

# **Synthesis of biomimetic elastin-like polypeptides as molecular springs for the activation of Cu(I) bis(NHC) mechanocatalysts**

## **Dissertation**

zur Erlangung des Doktorgrades der Naturwissenschaften  
(Dr. rer. nat.)

der

Naturwissenschaftlichen Fakultät II  
Chemie, Physik und Mathematik

der Martin-Luther-Universität  
Halle-Wittenberg

vorgelegt von

Herrn Sebastian Funtan  
geb. am 07.08.1989 in Kassel

Gutachter

1. Prof. Dr. Wolfgang H. Binder

2. Prof. Dr. Ulrich Schubert

Tag der Verteidigung: 01.12.2020

## **Danksagung**

An dieser Stelle möchte ich mich bei allen bedanken, die mich während meiner Promotion unterstützt und die zu deren Gelingen beigetragen haben.

Mein erster Dank gilt Herrn Prof. Dr. Wolfgang H. Binder für die Bereitstellung des interessanten Themas, der Betreuung und Unterstützung während der Promotion sowie der zahlreichen Möglichkeiten zur individuellen Umsetzung des Themas.

Bei der gesamten Arbeitsgruppe Binder sowie deren ehemaligen Mitgliedern möchte ich mich für die angenehme Arbeitsatmosphäre und die gute Zusammenarbeit bedanken. Insbesondere Susanne Tanner und Julia Großert danke ich für die durchgeführten ESI-, MALDI-TOF-MS und GPC-Messungen sowie für die Bereitstellung von Chemikalien und Glasgeräten. Anke Hassi danke ich für die Unterstützung in allen administrativen Angelegenheiten.

Mein besonderer Dank gilt meinen Kollegen aus dem Labor 3.23, dem Büro 3.10, Dr. Philipp Michael und Dr. Diana Döhler. Ich habe die fachlichen Diskussionen zur Lösung von aufgetretenen Problemen mit euch immer sehr zu schätzen gewusst. Außerdem hat der humorvolle Umgang miteinander im Labor 3.23 das Arbeiten nie monoton werden lassen und mir viel Freude bereitet. Vielen Dank dafür! Dr. Philipp Michael danke ich außerdem für die kritische Durchsicht meiner Arbeit.

Herrn Dr. Ströhl und seinem Team danke ich für die Anfertigung der NMR-Spektren während meiner Promotion, insbesondere der zahlreichen aufgenommenen NMR-Spektren während der Ultraschallexperimente.

Meiner Frau Anne Funtan und Herrn Prof. Dr. Reinhard Paschke vom Biozentrum danke ich für die Toxizitätstests der hergestellten Kupferkomplexe.

Mein weiterer Dank gilt Frau Zeynep Atris, Herrn Amirmasoud Gharavian und Frau Reinhild Dünnebacke vom Max-Planck-Institut für Kolloid- und Grenzflächenforschung in Potsdam für die Durchführung der AFM-Nanoindentierungsexperimente an den hergestellten Hydrogelen.

Zu guter letzt gilt ein großer Dank meiner Frau Anne Funtan, meiner Familie und meinen Freunden, die immer ein offenes Ohr für mich hatten und mir sowohl während des Studiums als auch während der Promotion stets Rückhalt gegeben haben.

## Abstract

Mechanochemistry is a comparably new field of research investigating the impact of mechanical forces that lead to defined chemical changes in macromolecules. The incorporation of selectively cleavable bonds, which are able to react in a predictable way under the influence of an external mechanical force, led to the construction of mechanophores with a wide range of applications. Their common aim is to redirect a usually destructive force into a productive event, which can take place after the rupture of the “weakest” link.

Aim of this thesis was the synthesis of latent elastin-like polypeptide (ELP) bearing Cu(I) bis *N*-heterocyclic carbene (NHC) catalysts which could be activated after application of an external force *via* ultrasound (in solution) or compression (in bulk). The ELPs were chosen due to their ability to form a  $\beta$ -spiral which could be exploited as “molecular spring” for an efficient force transmission. In order to enable a more flexible modification of the catalysts, two low molecular weight Cu(I) bis(NHC) complexes were synthesized from the respective imidazolium precursors by means of Cu<sub>2</sub>O. The generated complexes bore either two carboxyl or two amino groups, thus allowing a postmodification and extension of the attached NHC ligands by peptide coupling of ELP sequences with varying chain lengths.

One of the most frequently used ELP sequences is the pentapeptide Val-Pro-Gly-Val-Gly (VPGVG) which was synthesized *via* solution phase peptide synthesis and required an orthogonal protection group strategy (*N*-terminus: *tert*-butoxycarbonyl (Boc), *C*-terminus: methyl ester group (OMe)). Further elongation of the Boc-VPGVG-OMe sequence generated Boc-(VPGVG)<sub>4</sub>-OMe, thus increasing the length of the “molecular spring”. The  $\beta$ -spiral formation for the VPGVG sequence was proven *via* secondary structure analysis (IR- and CD-spectroscopy) and was retained even after coupling to the mechanophoric catalyst, thus allowing “molecular spring” behavior.

Coupling the catalysts with the *N*-terminus of ELP sequences of varying chain lengths, generated a multitude of peptide bearing mechanophores whose catalytic activities were tested in solution. After application of ultrasound, one of the NHC ligands was removed thus transforming the latent Cu(I) bis(NHC) complex into the active Cu(I) mono(NHC) complex which in turn could be exploited for the copper(I)-catalyzed alkyne-azide cycloaddition (CuAAC).

Furthermore, the VPGVG sequence was additionally linked between the carboxyl- and amino-functionalized mechanocatalyst, thus generating a chain-extended catalyst bearing the “molecular spring” as a repetitive unit between the latent Cu(I) bis(NHC) moieties. A model CuAAC reaction of phenylacetylene and benzyl azide revealed conversions between 3.4 % and 9.9 % depending on the investigated mechanocatalyst.

Moreover, a supramolecular mechanocatalyst was embedded into a bulk material by coupling the carboxyl functionalized mechanocatalyst to an amine modified barbiturate. This mechanocatalyst was incorporated into two different matrices (either PTHF or a barbiturate modified PEG) and the activation after compression was investigated by a fluorogenic “click” reaction between an azide functionalized coumarin and phenylacetylene revealing conversions up to 1.9 %.

Incorporating the amino functionalized catalyst, the azide functionalized coumarin and phenylacetylene into commercially available elastin using varying amounts of hexamethylenediisocyanate (HDI) generated hydrogels with different crosslinking densities. However, a proper characterization of the mechanical properties of the hydrogels failed due to their fragility in the completely swollen state, their changing mechanical properties in dependence from the degree of hydration and their stickiness. Therefore, detailed investigations were not possible with the available instruments.

## Kurzzusammenfassung

Mechanochemie ist ein vergleichsweise neues Forschungsgebiet, welches den Einfluss von externen Kräften auf definierte und gezielt hervorrufbare Veränderungen in Makromolekülen untersucht. Der Einbau von mechanolabilen Bindungen, die in der Lage sind unter externer Kraftbeanspruchung auf eine vorhersehbare Weise zu reagieren, hat zur Synthese zahlreicher Mechanophore mit unterschiedlichsten Anwendungsmöglichkeiten geführt. Ihr gemeinsames Ziel ist es, eine normalerweise destruktive Kraft in ein produktives Ereignis umzuleiten, das nach dem Bruch der schwächsten Bindung stattfinden kann.

Ziel dieser Arbeit war die Synthese von latenten Cu(I) bis(NHC) Katalysatoren, die mit Elastin-ähnlichen Polypeptiden (ELPs) modifiziert wurden und anschließend durch Einwirken einer externen Kraft (Ultraschall bzw. Kompression) aktiviert werden konnten. Die ELPs wurden auf Grund ihrer Fähigkeit zur Ausbildung von  $\beta$ -Spiralen verwendet, die während der Aktivierung als „molekulare Sprungfeder“ für eine verbesserte Kraftübertragung genutzt werden sollte. Um einen modularen Aufbau der Katalysatoren zu gewährleisten, wurden zwei niedermolekulare Cu(I) bis(NHC) Komplexe aus dem entsprechenden Imidazoliumsalz mittels der Cu<sub>2</sub>O Methode synthetisiert. Die hergestellten Komplexe trugen entweder zwei Carboxyl- oder Aminogruppen und erlaubten eine nachträgliche Modifizierung und Verlängerung der NHC Liganden durch Peptidkupplung von ELP Sequenzen mit unterschiedlicher Kettenlänge.

Eine der am häufigsten verwendeten ELP Sequenzen ist das Pentapeptid Val-Pro-Gly-Val-Gly (VPGVG), das im Rahmen dieser Arbeit mittels Peptidsynthese in Lösung hergestellt wurde und eine orthogonale Schutzgruppenstrategie erforderte (*N*-Terminus: *tert*-Butoxycarbonyl-Gruppe (Boc), *C*-Terminus: Methylster-Gruppe (OMe)). Das erhaltende Pentapeptid wurde noch weiter bis zum Boc-(VPGVG)<sub>4</sub>-OMe verlängert. Die Ausbildung der  $\beta$ -Spirale konnte mit Hilfe von Sekundärstrukturanalyse (IR- und CD-Spektroskopie) nachgewiesen werden und war auch noch nach der Kupplung an den mechanophoren Katalysator vorhanden.

Kupplung der Katalysatoren mit dem *N*-Terminus der ELPs mit verschiedenen Kettenlänge führte zu einer Vielzahl an Mechanophoren, deren katalytische Aktivität in Lösung getestet wurde. Ultraschall führte zur Abspaltung eines NHC Liganden und überführte den latenten Cu(I) bis(NHC) Komplex in den aktiven Cu(I) mono(NHC) Komplex, der im Folgenden für die Kupfer(I)-katalysierte Alkin-Azid Cycloaddition (CuAAC) zur Verfügung stand.

Zusätzlich wurde die VPGVG Sequenz auch zwischen dem Carboxyl- und dem Amino-funktionalisierten Katalysator eingebaut, was zu einem Mechanophor führte, der die „molekulare Sprungfeder“ als repetitive Einheit zwischen den einzelnen Cu(I) bis(NHC) Spezies trug. Die als Modellreaktionen verwendete CuAAC zwischen Phenylacetylen und Benzylazid führte zu Umsätzen zwischen 3.4 % und 9.9 % für die getesteten Mechanokatalysatoren.

Um die Aktivierbarkeit der Katalysatoren auch im festen Zustand zu testen, wurde der Carboxyl-funktionalisierte Katalysator außerdem an ein Amino-modifiziertes Barbiturat gekoppelt. Dieser Mechanokatalysator wurde in zwei verschiedene Matrices (PTHF oder Barbiturat-PEG) eingebaut und die Aktivierung nach Kompression mit Hilfe der fluorogenen „Click“-Reaktion zwischen einem Azid-funktionalisierten Cumarin und Phenylacetylen überprüft. Fluoreszenzmessungen zeigten dabei einen Umsatz von 1.9 % zum stark fluoreszierenden „Click“-Produkt.

Das Einbringen des Amin-funktionalisierten Katalysators, dem Azid-funktionalisierten Cumarin und dem Phenylacetylen in käufliches Elastin unter Verwendung verschiedener Mengen Hexamethylen-diisocyanat führte zu Hydrogelen mit unterschiedlicher Vernetzungsdichte. Eine genaue Charakterisierung der mechanischen Eigenschaften konnte allerdings auf Grund der Fragilität der Hydrogele im komplett gequollenen Zustand, der extremen Klebrigkeit sowie der Abhängigkeit der mechanischen Eigenschaften vom Hydratationsgrad mit Hilfe der zur Verfügung stehenden Instrumente nicht realisiert werden.

## Table of contents

<b>1</b>	<b>Introduction .....</b>	<b>1</b>
1.1	Mechanochemistry .....	1
1.1.1	Tribochemistry .....	1
1.1.2	Trituration.....	2
1.1.3	Sonochemistry .....	2
1.1.4	Macromolecular mechanochemistry.....	3
1.1.4.1	Soft mechanochemistry .....	3
1.1.4.2	Mechanochemistry of synthetic polymers.....	4
1.1.5	Activation of mechanophores.....	5
1.1.6	Metal-based polymeric mechanocatalysts.....	7
1.1.6.1	Silver/ruthenium <i>N</i> -heterocyclic carbene mechanocatalysts.....	8
1.1.6.2	Copper <i>N</i> -heterocyclic carbene mechanocatalysts .....	9
1.1.6.3	Ferrocene-based polymeric mechanophores .....	14
1.1.6.4	Ruthenocene-based polymeric mechanophores.....	17
1.2	Copper(I)-catalyzed alkyne-azide cycloaddition.....	17
1.3	Lever-arm effect .....	20
1.4	Elastin.....	20
1.4.1	Models for elastin elasticity.....	22
1.4.1.1	Random chain model.....	22
1.4.1.2	Liquid drop model .....	23
1.4.1.3	Oiled coil model .....	24
1.4.1.4	Fibrillar model.....	25
1.4.2	Elastin-like polypeptides .....	26
1.4.2.1	Thermoresponsivity.....	27
1.4.2.2	Elasticity.....	29
1.4.2.3	Applications.....	30
<b>2</b>	<b>Aim and concept .....</b>	<b>32</b>
2.1	Scope of the thesis .....	32
2.2	Concept.....	33
<b>3</b>	<b>Results and Discussion .....</b>	<b>36</b>
3.1	Synthesis and characterization of the COOH-functionalized mechanocatalysts ( <b>4</b> ).....	36
3.2	Synthesis and characterization of the elastin-like polypeptide sequence .....	38
3.2.1	Synthesis and characterization of the Boc-VPGVG-OMe sequence ( <b>16</b> ).....	38
3.2.2	Secondary structure analysis of Boc-VPGVG-OMe ( <b>16</b> ) .....	41
3.2.3	Chain elongation of Boc-VPGVG-OMe ( <b>16</b> ).....	43
3.3	Synthesis, characterization and mechanochemical activity of the linear mechanocatalysts .	46
3.3.1	Coupling reactions of the carboxyl-functionalized mechanocatalyst <b>4b</b> with <i>N</i> -terminus deprotected peptides .....	46
3.3.2	Secondary structure analysis of [Cu(C <sub>10</sub> COOH-VPGVG-NHC) <sub>2</sub> ] <b>X</b> ( <b>27e</b> ) .....	49
3.3.3	Mechanophoric activity of the linear catalysts .....	50

3.4	Synthesis, characterization and mechanochemical activity of the chain-extended mechanocatalysts ( <b>35</b> ) .....	55
3.4.1	Synthesis and characterization of the NH <sub>2</sub> -functionalized mechanocatalyst ( <b>34</b> ) .....	56
3.4.2	Synthesis of the chain-extended mechanocatalysts ( <b>35</b> ) .....	57
3.4.3	Mechanophoric activity of the chain-extended catalysts <b>35</b> .....	59
3.5	Synthesis, characterization and mechanochemical activity of the supramolecular mechanocatalyst .....	60
3.5.1	Synthesis and characterization of the supramolecular catalyst ( <b>42</b> ).....	60
3.5.2	Activation of the supramolecular catalyst <b>42</b> in solution .....	62
3.5.3	Activation of the supramolecular catalyst <b>42</b> in bulk .....	62
3.6	Synthesis of elastin-based hydrogels ( <b>49</b> ) .....	65
3.7	Cytotoxicity of the synthesized mechanocatalysts .....	67
<b>4</b>	<b>Experimental part</b> .....	<b>69</b>
4.1	Materials and methods.....	69
4.2	Synthesis of the carboxyl functionalized mechanophoric catalysts .....	71
4.2.1	Synthesis of <i>n</i> -bromoalkanoic acid methyl esters ( <b>1</b> ).....	71
4.2.2	Synthesis of the methyl ester protected NHC precursors ( <b>2</b> ) .....	72
4.2.3	Synthesis of the methyl ester protected Cu(I) bis(NHC) complexes [Cu(C <sub>n</sub> OOOMe-NHC) <sub>2</sub> ]X ( <b>3</b> ).....	73
4.2.4	Deprotection of the methyl ester protected Cu(I) bis(NHC) complexes [Cu(C <sub>n</sub> OOOMe-NHC) <sub>2</sub> ]X ( <b>4</b> ).....	74
4.2.5	Synthesis of the unprotected NHC precursors ( <b>5</b> ) .....	74
4.3	Synthesis and characterization of the elastin-like polypeptide sequence .....	75
4.3.1	Boc-protection reactions of single amino acids ( <b>6, 7</b> ) .....	75
4.3.2	Methyl ester protection reactions of single amino acids ( <b>8, 9</b> ).....	76
4.3.3	Synthesis of the pentapeptide sequence ( <b>10-17</b> ).....	77
4.3.4	Elongation of the elastin-like polypeptide sequence ( <b>18-26</b> ) .....	80
4.4	Synthesis of the linear mechanocatalysts ( <b>27a-g</b> ) .....	83
4.5	Synthesis of benzyl azide ( <b>29</b> ).....	86
4.6	Mechanochemical activation of the linear catalysts in solution by ultrasonication .....	86
4.7	Synthesis of the chain-extended mechanocatalysts .....	87
4.7.1	Synthesis of the imidazolium-based NH <sub>2</sub> -functionalized mechanocatalyst .....	87
4.7.1.1	Synthesis of <i>N</i> -( <i>tert</i> -butoxycarbonyl)-3-bromopropylamine ( <b>31</b> ) .....	87
4.7.1.2	Synthesis of 3-[3-[[[(1,1-dimethylethoxy)carbonyl]amino]propyl]-1-methyl-1 <i>H</i> -imidazolium bromide ( <b>32</b> ).....	88
4.7.1.3	Synthesis of bis(1-methylimidazol-3-[3-(((1,1-dimethylethoxy)carbonyl)amino)propyl]ylidene)copper(I) halogenide ( <b>33</b> ).....	88
4.7.1.4	Deprotection of the Boc-protected mechanocatalyst ( <b>34</b> ) .....	89
4.7.2	Synthesis of the chain-extended mechanocatalysts ( <b>35</b> ) .....	89
4.7.3	Mechanochemical activation of the chain-extended mechanocatalysts .....	90
4.8	Synthesis of the supramolecular catalyst.....	90
4.8.1	Synthesis of diethyl 2-ethyl-2-(1-hexyn-6-yl) malonate ( <b>36</b> ).....	90
4.8.2	Synthesis of 2-ethyl-2-(1-hexyn-6-yl) barbituric acid ( <b>37</b> ) .....	91

4.8.3	Synthesis of <i>N</i> -( <i>tert</i> -butoxycarbonyl)-3-chloropropylamine ( <b>38</b> ) .....	91
4.8.4	Synthesis of <i>N</i> -( <i>tert</i> -butoxycarbonyl)-3-azidopropylamine ( <b>39</b> ).....	92
4.8.5	“Click” reaction of <b>37</b> and <b>39</b> .....	92
4.8.6	Boc-deprotection of the clicked barbiturate <b>40</b> .....	93
4.8.7	Synthesis of the supramolecular mechanocatalyst ( <b>42</b> ).....	93
4.9	Activation of the supramolecular catalyst <b>42</b> in solution <i>via</i> ultrasonication.....	94
4.10	Synthesis of the fluorescence dye.....	94
4.10.1	Synthesis of 3-azido-7-hydroxycoumarin ( <b>43</b> ).....	94
4.10.2	Synthesis of 7-hydroxy-3-(4-phenyl-1 <i>H</i> -[1,2,3]triazole-1-yl)-coumarin ( <b>44</b> ) .....	95
4.11	Synthesis of high molecular weight PTHF ( <b>45</b> ).....	96
4.12	Synthesis of the barbiturate modified polymeric matrix .....	96
4.12.1	Synthesis of poly(ethylene glycol)-di-mesylate ( <b>46</b> ).....	96
4.12.2	Synthesis of poly(ethylene glycol)-di-azide ( <b>47</b> ) .....	96
4.12.3	Synthesis of poly(ethylene glycol)-di-barbiturate ( <b>48</b> ) .....	97
4.13	Activation of the supramolecular catalyst in bulk <i>via</i> compression.....	97
4.13.1	General calibration of the fluorescence spectrometer .....	97
4.14	Synthesis of elastin-based hydrogels ( <b>49</b> ) .....	98
4.15	Cytotoxicity of the mechanophoric catalysts .....	98
4.16	Synthesis of the histidinum based mechanocatalyst ( <b>55</b> ).....	99
4.16.1	Synthesis of <i>L</i> -histidine methyl ester dihydrochloride ( <b>51</b> ) .....	100
4.16.2	Synthesis of <i>N</i> - $\alpha$ -( <i>tert</i> -butoxycarbonyl)-1- <i>tert</i> -butoxycarbonyl- <i>L</i> -histidine methyl ester ( <b>52</b> ) .....	100
4.16.3	Synthesis of <i>N</i> - $\alpha$ -( <i>tert</i> -butoxycarbonyl)- <i>L</i> -histidine methyl ester ( <b>53</b> ).....	101
4.16.4	Synthesis of 4-[2-[[[(1,1-dimethylethoxy)carbonyl]amino]-3-methoxy-3-oxopropyl]-1,3-dimethyl-1 <i>H</i> -imidazolium iodide ( <b>54</b> ) .....	101
4.16.5	Synthesis of bis(4-[2-[[[(1,1-dimethylethoxy)carbonyl]amino]-3-methoxy-3-oxopropyl])-1,3-dimethyl-1 <i>H</i> -imidazol-2-ylidene copper(I) halogenide ( <b>55</b> ) .....	102
4.16.6	Mechanochemical activation of the histidinum based catalyst <b>55</b> .....	102
<b>5</b>	<b>Summary</b> .....	<b>103</b>
<b>6</b>	<b>References</b> .....	<b>108</b>
<b>7</b>	<b>Appendix</b> .....	<b>124</b>
7.1	Characterization of the COOH-functionalized mechanocatalyst synthesis ( <b>1-5</b> ).....	124
7.2	Characterization of the ELP sequence peptides ( <b>6-17</b> ) .....	130
7.3	Characterization of the ELP sequence elongation ( <b>18-26</b> ).....	136
7.4	Characterization of the linear mechanocatalysts ( <b>27a-g</b> ) .....	141
7.5	Characterization of benzyl azide ( <b>29</b> ).....	146
7.6	Characterization of the NH <sub>2</sub> -functionalized mechanocatalyst synthesis ( <b>31-34</b> ) .....	147
7.7	Characterization of the chain-extended mechanocatalyst ( <b>35a</b> ).....	149
7.8	Characterization of the supramolecular mechanocatalyst synthesis ( <b>36-42</b> ).....	149
7.9	Characterization of the fluorogenic dye ( <b>43-44</b> ) .....	154
7.10	Characterization of the PEG modification ( <b>46-48</b> ).....	155
7.11	Characterization of crosslinked elastin hydrogels ( <b>49</b> ) .....	158
7.12	Characterization of the histidinum based mechanocatalyst synthesis ( <b>51-55</b> ).....	161

<b>8</b>	<b>Curriculum Vitae .....</b>	<b>164</b>
<b>9</b>	<b>Eigenständigkeitserklärung.....</b>	<b>166</b>

## List of abbreviations

ACN	acetonitrile
Ac <sub>2</sub> O	acetic anhydride
Ad	adamantyl
AFM	atomic force microscopy
Ala / A	<i>L</i> -alanine
Arg / R	<i>L</i> -arginine
Asp / D	<i>L</i> -aspartic acid
atm	atmospheric pressure
ATRP	atom transfer radical polymerization
AzN	8-azidonaphtalene-2-ol
BDO	1,4-butanediol
BFP	blue fluorescent protein
Boc	<i>tert</i> -butoxycarbonyl (protection group)
CalM	calmodulin
CAT	chloramphenicol acetyltransferase
CCP	cell penetrating peptide
CD	circular dichroism
COGEF	constrained geometry simulates external force
Cp	cyclopentadiene (ligand)
CTA	chain transfer agent
CuAAC	copper(I)-catalyzed alkyne-azide cycloaddition
Cy	cyclohexyl
Cys / C	<i>L</i> -cysteine
DBTDL	dibutyltin dilaurate
DBU	1,8-diazabicyclo[5.4.0]undec-7-ene
DCC	<i>N,N'</i> -dicyclohexylcarbodiimide
DCM	dichloromethane
DCU	1,3-dicyclohexylurea
DHA	2,3-dihaloalkene
DFT	density functional theory
DIPEA	<i>N,N</i> -diisopropylethylamine
DMF	<i>N,N</i> -dimethylformamide
DMSO	dimethyl sulfoxide
DtBP	2,6-di- <i>tert</i> -butylpyridine
ECM	extracellular matrix
EDC	1-ethyl-3-(3-dimethylaminopropyl)carbodiimide
EDU	1-ethyl-3-(3-dimethylaminopropyl)urea
ELP	elastin-like polypeptide
EPR	enhanced permeability and retention
ESI	electrospray ionization
ESR	electron spin resonance
EtOAc	ethyl acetate
eq.	equivalent
<i>g</i> DBC	<i>gem</i> -dibromocyclopropane
<i>g</i> DCC	<i>gem</i> -dichlorocyclopropane
<i>g</i> DHC	<i>gem</i> -dihalocyclopropane
GFP	green fluorescent protein

Glu / E	<i>L</i> -glutamic acid
Gly / G	glycine
HDI	hexamethylenediisocyanate
His / H	<i>L</i> -histidine
HOBt	hydroxybenzotriazole
HPA	3-hydroxyphenylacetylene
<i>i</i> PrPh	diisopropylphenyl
IR	infrared
s	strong
m	middle
w	weak
ITC	inverse transition cycling
ITT	inverse transition temperature
KHMDS	potassium bis(trimethylsilyl)amide
LCCP	living carbocationic polymerization
LCST	lower critical solution temperature
LiTf <sub>2</sub> N	lithium(I) bis(trifluoromethanesulfonyl)imide
Lys / K	<i>L</i> -lysine
MCO	5-methoxycyclooctene
<i>m</i> CPBA	<i>meta</i> -chloroperoxybenzoic acid
MDI	methylene diphenyl diisocyanate
Mes	mesityl
MFS	molecular force sensors
$M_{lim}$	limiting molecular weight
$M_n$	number average molar mass
MS	mass spectrometry
$M_w$	weight average molecular weight
NEt <sub>3</sub>	triethylamine
NHC	<i>N</i> -heterocyclic carbene
NHS	<i>N</i> -hydroxysuccinimide
NMR	nuclear magnetic resonance spectroscopy
s	singlet
d	doublet
dd	doublet of doublets
t	triplet
td	triplet of doublets
q	quartet
m	multiplet
OMe	methyl ester (protection group)
PBD	poly(1,4-butadiene)
PDI	polydispersity index (PDI = $M_w/M_n$ )
PEG	poly(ethylene glycol)
PIB	poly(isobutylene)
PNB	poly(norbornene)
PMA	poly(methylacrylate)
PMDETA	<i>N,N,N',N',N''</i> -pentamethyldiethylenetriamine
PS	poly(styrene)
PTHF	poly(tetrahydrofuran)

PU	polyurethane
Pro / P	<i>L</i> -proline
RAFT	reversible addition-fragmentation chain-transfer
RCM	ring-closing metathesis
RI	refractive index
ROMP	ring-opening metathesis polymerization
SCFS	single-cell force spectroscopy
SMFS	single-molecule force spectroscopy
SPPS	solution phase peptide synthesis
SRB	sulforhodamine-B
TABS	thermally activated barrier to scission
<i>t</i> Bu	<i>tert</i> -butyl
TBTA	tris[(1-benzyl-1 <i>H</i> -1,2,4-triazol-4-yl)methyl]amine)
TEMPO	2,2,6,6-tetramethylpiperidinyloxy
TFM	traction force microscopy
$T_g$	glass transition temperature
THF	tetrahydrofuran
TLC	thin-layer chromatography
TMP	trimethanolpropane
TOF	time of flight
TON	turnover number
Tpy	2,2':6',2''-terpyridine
Trx	thioredoxin
UV	ultraviolet
Val / V	<i>L</i> -valine
vis	visible
VWF	von Willebrand factor
X <sub>aa</sub>	unspecified amino acid
YFP	yellow fluorescent protein

**Parts of this thesis have been published in:**

Funtan, S.; Michael, P.; Binder, W. H., Synthesis and Mechanochemical Activity of Peptide-Based Cu(I) Bis(*N*-Heterocyclic Carbene) Complexes, *Biomimetics* **2019**, 4 (1), 24.

Funtan, S.; Funtan, A.; Paschke, R.; Binder, W. H., Biomimetic Elastin-Like Polypeptides as Materials for the Activation of Mechanophoric Catalysts, *Organic Materials* **2020**, 2 (2), 116.

Parts of the Results and Discussion part as well as from the Experimental Part were adapted with permission from MDPI (Copyright 2019) and Thieme Gruppe (Copyright 2020).

# 1 Introduction

## 1.1 Mechanochemistry

Triggering of chemical reactions is commonly realized by conventional methods including heat, light or electrical stimuli<sup>1-3</sup>. While the provided energy is usually sufficient to overcome the activation barrier of a reaction, the introduced energy is commonly undirected in terms of time and spatial orientation in turn facilitating undesired side reactions. Mechanochemistry, the triggering of chemical reactions by an applied external mechanical force, is a promising alternative to the aforementioned activation methods. Besides the well known tribochemistry and trituration techniques also the comparatively new sonochemistry and macromolecular mechanochemistry can be counted to this topic (see Figure 1)<sup>4</sup>. In the following part, the four different subtopics of mechanochemistry should be briefly discussed with the main focus being the macromolecular mechanochemistry.

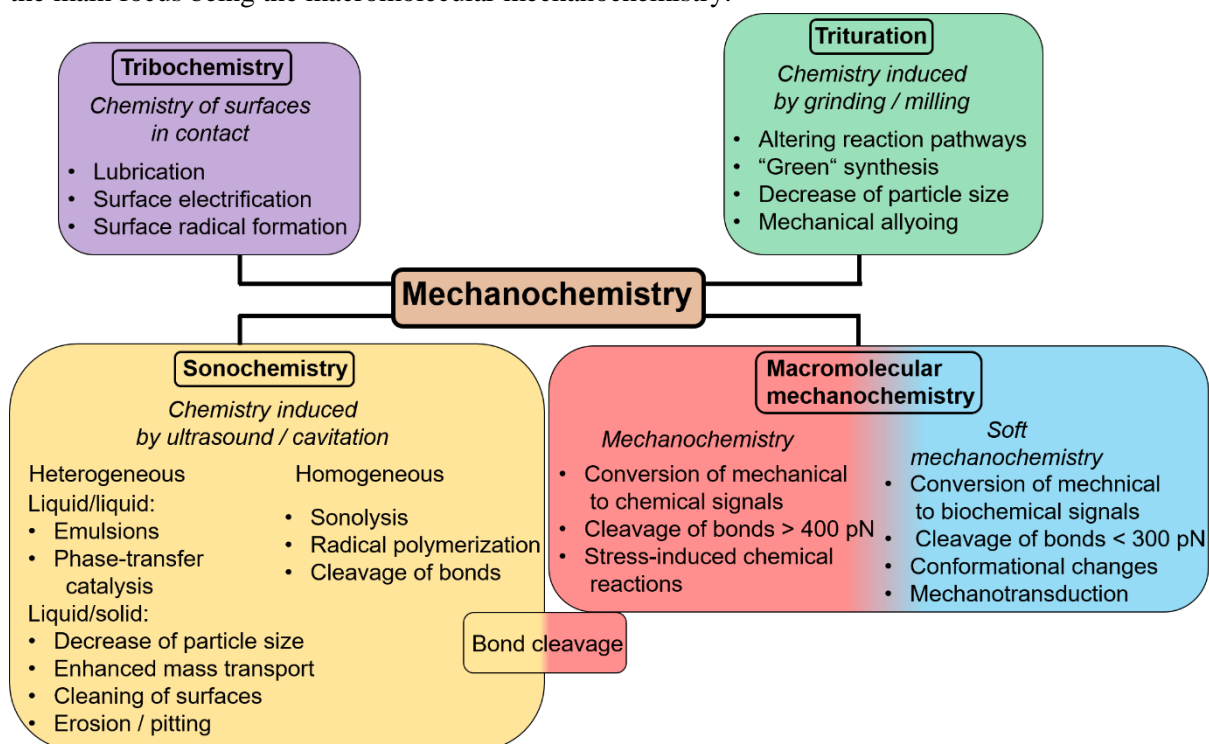


**Figure 1.** Mechanochemistry can be subdivided into tribochemistry (purple), trituration (green), sonochemistry (yellow) and macromolecular chemistry (red and blue)<sup>4</sup>.

### 1.1.1 Tribochemistry

Tribochemistry is the chemistry of contacting surfaces<sup>4</sup> and is strongly related to friction, wear and lubrication<sup>5</sup>. Production of fire by rubbing of dry wood might be the oldest application of this type of mechanochemistry<sup>6</sup>. However, tribochemistry still plays a crucial role nowadays. Every machine or engine suffers from wear due to friction of different components. In order to reduce the friction and the wear, lubricants are indispensable. The effect of lubricants is often based on tribochemical processes, e.g. hydrocarbons are polymerized due to the friction between two surfaces. Besides the reduction of the vapor pressure, the resulting polymers can also act as a film between the surfaces by reducing the occurring friction<sup>6</sup>. In some cases, even the metal surface participated in the polymerization process of the lubricant, thus generating organometallic polymers<sup>7</sup>. Friction of surfaces can also lead to charge separation and to the buildup of electrostatic potentials (also referred to as triboelectricity) which can be easily visualized by a balloon which is rubbed against hair. Modelling of tribochemical processes is difficult due to the many parameters (such as surface topology, mechanical contact stress and wear processes) that have to be considered when two surfaces are rubbed against each other<sup>6</sup>. Since friction

can also generate huge amounts of heat, it is often difficult to discriminate whether a reaction was induced thermally or by tribochemistry<sup>5-6</sup>.

### 1.1.2 Trituration

Trituration includes mechanochemical processes that are induced by grinding and milling<sup>4</sup>. Therefore, it practically exists for quite a long time since people were already using mortar and pestle for the processing of food, paints, medicines and minerals in early times<sup>8</sup>. However, at this time differentiation between chemical changes and a purely physical size reduction as a consequence of mechanical stress was hardly possible. In 1893, Lea was the first who described that mechanical force might alter commonly thermal driven reaction pathways<sup>9</sup>. It was found, that mercuric chloride and silver chloride decomposed when grinded in a mortar, while mercuric chloride sublimated when heated and silver chloride melted without decomposition. Mechanical alloying in ball mills for the synthesis of highly resistant and durable materials further increased the attention of scientists to mechanochemistry<sup>8</sup>.

Nowadays, trituration also found its way into laboratories as a common synthesis method since a physical reduction of the particle size usually results in an increased reactivity due to the increase of the surface. Trituration is also used for mechanochemical metal catalyzed reactions<sup>10</sup> including copper(I)-catalyzed alkyne-azide cycloadditions (CuAAC)<sup>11-13</sup>, olefin metathesis<sup>14</sup>, Suzuki coupling reactions<sup>15-16</sup>, Sonogashira coupling reactions<sup>17</sup>, Heck-Mizoroki reactions<sup>18-19</sup>, Michael additions<sup>20</sup> and can also be used for the synthesis of nanoparticles<sup>21-22</sup>. Furthermore, trituration allows the preparation of molecules which are not accessible *via* solution synthesis<sup>23-25</sup>. Ball mills or mortar and pestle also offer the apparent advantage of avoiding solvents, thus offering alternative, “green” synthetic pathways<sup>26</sup>.

### 1.1.3 Sonochemistry

Sonochemistry makes use of ultrasound to trigger, enhance or alter chemical reactions<sup>27</sup>. Application of ultrasound to liquids leads to the formation, growth and collapse of cavitation bubbles accompanied by significant changes of temperature and pressure. Experimental results revealed pressures of 1000 atm, temperatures of more than 5000 K with cooling rates of  $10^{10}$  K/s and lifetimes of the bubbles less than  $10 \mu\text{s}$ <sup>28-30</sup>. Sonochemistry can be divided into homogenous and heterogenous sonochemistry<sup>31</sup>. Homogenous sonochemistry is one of the main activation methods of mechanophores in solution<sup>32-38</sup> and will be discussed in detail in Chapter 1.1.5. Besides its use for the activation of mechanophores, the extreme conditions upon the collapse of the cavitation bubbles are exploited for the fragmentation of volatile solvent or reactant molecules into highly reactive radicals (also called sonolysis). The formed radicals then can be used for ultrasound induced radical polymerizations<sup>39</sup>.

Heterogenous sonochemistry covers liquid-liquid and liquid-solid systems. Ultrasonication of two immiscible liquids leads to the formation of very fine emulsions which is of particular interest for biphasic or phase-transfer-catalyzed reactions due to the increased surface area<sup>27</sup>. For liquid-solid systems, the size of the solid plays a crucial role for the formation of the cavitation bubbles<sup>31</sup>. Small particles ( $< 200 \mu\text{m}$ ) do not influence the formation and collapse of the cavitation bubbles, thus leading to homogenous cavitation. Upon collapse, the created shockwaves can strongly accelerate nearby solid particles. If the particles collide with each other they will fragmentate into smaller pieces due to their high kinetic energy<sup>27</sup>. Therefore, continuous ultrasonication can decrease the size of solid particles from  $240 \mu\text{m}$  to  $15 - 20 \mu\text{m}$  within 15 minutes<sup>40</sup>. Fragmentation drastically increases the surface of the solid particles and therefore can strongly increase reaction rates<sup>31</sup>.

Extended liquid-solid interfaces influence the nearby cavitation bubbles which will lead to their deformation. When the asymmetric cavitation bubbles collapse they produce microjets of the solvent with a speed of  $100 \text{ m/s}$ <sup>31</sup>. Due to their high velocity, these microjets can lead to erosion or pitting of surfaces, the same phenomenon that is used for the cleansing of equipment in the ultrasonication bath<sup>27</sup>.

### 1.1.4 Macromolecular mechanochemistry

Macromolecular mechanochemistry deals with the influence of stress onto polymers. It is reasonable, to further subdivide macromolecular mechanochemistry due to the large force range it encompasses. Soft mechanochemistry usually refers to mechanotransduction processes of cells and bacteria within the human body<sup>41</sup>. These processes only require a minimum of force within the range of 1 – 300 pN and mostly rely on conformational changes of proteins. Contrary, mechanochemistry of polymers (from now on only referred to as mechanochemistry) requires high energy input for the activation and cleavage of mechanophoric bonds in the range of 400 – 6000 pN<sup>42-46</sup>. However, the stronger the mechanophoric bond, the bigger is the probability for unintended C–C (6900 pN), C–N (7200 pN) or C–O (7600 pN) cleavages from the polymeric backbone<sup>47</sup>. Even if there is a striking difference between the necessary forces, the ultimate goal of both soft mechanochemistry and mechanochemistry is the transformation of the applied force into a (bio-)chemical signal (see Figure 2)<sup>41</sup>. On a molecular level, the occurring responses of biomacromolecules and synthetic polymers to the exerted force are fundamental different from each other due to the different force scales. The major differences will be discussed in the following section.

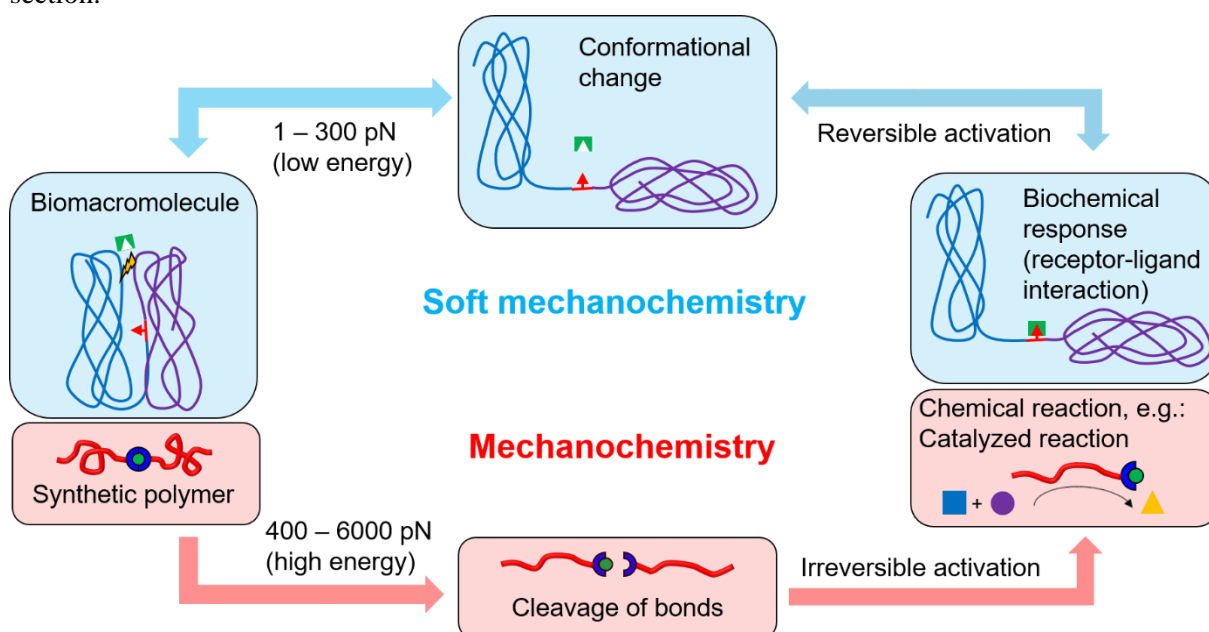


**Figure 2.** Soft mechanochemical processes involve significantly lower forces than mechanochemical processes. Therefore, soft mechanochemistry often relies on reversible conformational changes which allow receptor-ligand interactions while in mechanochemistry the cleavage of covalent bonds triggers a chemical reaction<sup>41</sup>.

#### 1.1.4.1 Soft mechanochemistry

Cells are located within the extracellular matrix (ECM) which provides them with a structural framework and biochemical support<sup>48</sup>. A constant exchange of mechanical signals between the ECM and the cells allows them to test the physical properties of their surrounding environment<sup>49</sup>. This exchange is of high importance to fulfill numerous vital processes such as cell growth<sup>50</sup>, differentiation<sup>51</sup>, adhesion<sup>52</sup>, activation of ion channels<sup>53-54</sup>, blood clotting<sup>55</sup>, the sense of touch<sup>56</sup> and spatial orientation<sup>57</sup>. The forces involved in soft mechanochemistry are several orders of magnitude lower than covalent bond dissociation energies. Hence, the transformation of a (weak) mechanical signal into a biochemical response is often based on conformational changes of proteins<sup>58</sup> or supramolecular protein structures<sup>59-60</sup>. These conformational changes lead to exposure of so-called cryptic sites that are buried within a protein in the absence of force but are exposed to a ligand after a conformational change. Once exposed, receptor-ligand interactions can take place to induce a biochemical signal (also see Figure 2)<sup>59-60</sup>. Conformational changes are much more energy saving and efficient than the breakage of covalent

bonds<sup>41</sup>. Furthermore, changes in the spatial arrangement of a protein are usually reversible, guaranteeing a return to the initial state after the force is no longer present

An example for soft mechanochemical processes within the human body is the von Willebrand factor (VWF) which is a large glycoprotein that is responsible for blood clotting after vascular damage<sup>55</sup>. VWF adopts a globular conformation and changes to an elongated form in the presence of shear force. The force, exerted from the occurring blood flow after an injury is enough, to trigger this conformational change and also exposes enzymatically cleavable sites. The exposed cryptic sites can interact with receptors which participate in the blood clotting, while the cleaved sites are responsible for clot resorption<sup>41, 55</sup>.

Some effort has been put into the synthesis of artificial cryptic site exhibition systems that only allow ligand-receptor interactions upon stretching since they are shielded by polymer or peptide chains in the unstretched conformation<sup>61-62</sup>.

Forces as low as 1 – 10 pN are omnipresent in the field of soft mechanochemistry<sup>63-64</sup> and require special measuring methods such as atomic force microscopy (AFM) or cellular traction force microscopy (TFM)<sup>48, 65</sup>. A major drawback of AFM based analyzing methods is, that often only isolated cells (single-cell force spectroscopy, SCFS)<sup>66</sup> or single receptor-ligand interactions (single-molecule force spectroscopy, SMFS)<sup>67</sup> are investigated. Thus, the obtained results do not have to reflect the *in vivo* behavior of the cells respectively proteins<sup>48</sup>. Furthermore, the cantilever tip can only exert local stress to the cells while in their natural environment they experience stress from all three dimensions<sup>41</sup>. Contrary, TFM can be used for the analysis of two dimensional and three dimensional substrates<sup>65</sup>. For TFM measurements, the deformation of a synthetic, elastic polymer matrix as a result of cellular forces is determined. Deformations can be visualized temporally and spatially by fluorescence beads with sizes much smaller than cells, however, the experimental and computational effort is enormous. Additionally, the maximal spatial resolution is limited to the micrometer range<sup>48</sup>. Accordingly, the forces obtained from TFM measurements are usually in the range of nanonewton and are the sum of numerous receptor-ligand interactions. Therefore, they are significantly higher than the forces obtained *via* SCFS or SMFS measurements and calculation of single receptor-ligand interactions is hardly possible<sup>48</sup>.

Molecular force sensors (MFSs) allow to reach single molecule force resolution (5 – 10 pN) and to observe many force induced interactions at once, thus combining the advantages of both SMFS and TFM<sup>48</sup>. The lowest possible resolutions can be obtained by replacing the AFM cantilever through single molecules. Common replacements are short double-stranded DNA molecules, DNA hairpins or PEGs, which are mechanically well characterized<sup>48</sup>. Visualization can be achieved *via* fluorescence measurements using the Förster resonance energy transfer (FRET). Force induced conformational changes will separate a previously neighbored FRET pair, thus leading to increased fluorescence at a distinct force<sup>48</sup>. The green fluorescent protein (GFP) and yellow fluorescent protein (YFP) are commonly used sensors for the measurement of force induced conformational changes<sup>68-69</sup>.

The mechanical properties of a material are also depending from the contact area between the material and the probe as well as the moved length of the probe for the measurement. Therefore, macroscopic measuring methods such as uniaxial tensile testing or rheology are problematic since they will not reflect the mechanical properties that are relevant to single cells which directly interact with the ECM at the microscopic scale<sup>65</sup>.

#### **1.1.4.2 Mechanochemistry of synthetic polymers**

Mechanochemistry of synthetic polymers involves macromolecules containing one or more initially latent mechanically labile bonds or functional groups which respond to an applied external force. Once activated by force, such mechanophores are able to undergo mechanochemical transformations such as color changes<sup>36, 46, 70-78</sup>, chemiluminescence<sup>77, 79-82</sup>, activation of latent metal catalysts<sup>37-38, 42, 83-98</sup>, biased reactivity<sup>3</sup>, release of small molecules<sup>99-100</sup>, generation of protons<sup>101</sup>, stabilization of radicals<sup>102</sup>, and also remodeling of polymers<sup>103-105</sup>.

The polymer chains fulfill the role of macromolecular handles by directing and accumulating the force along the polymer backbone to the labile bond. Exploitation of aforementioned mechanochemical transformations, especially in the fields of self-healing, stress-sensing and catalysis led to a rethinking of mechanochemistry from being “destructive to (being) productive”<sup>106</sup>. Previous treatment of mechanochemistry as a destructive process mostly arose from the times of its discovery in the 1930s when Staudinger first described the mechanical rupture of rubber under mastication using either a ball mill (bulk) or an extruder (solution)<sup>107-109</sup>. In 1940 Kauzmann and Eyring suggested that the molecular weight loss might be the result of a homolytic C–C-bond cleavage<sup>110</sup> which was later proven by several groups using electron spin resonance (ESR) spectroscopy<sup>111</sup>. First reports about chain scission experiments in solution showed that polymer mechanochemistry is not limited to the solid state<sup>112</sup>. In 1980 peroxide linkages were selectively incorporated into polymers as weak bonds, allowing specific bond scission of the chains and thus forming the basis for productive mechanochemistry<sup>113</sup>. Since a predictable and defined reaction of a molecule in response to an external mechanical force is essential for a mechanophore, major effort has been put in the identification of such weak links. A variety of mechanophoric moieties has been identified up to date including homolytic bond cleavage of peroxides<sup>113</sup>, azo-groups<sup>114</sup> and disulfides<sup>115</sup>, heterolytic bond cleavage of carbon-oxygen bonds<sup>116</sup> as well as carbon-sulfur bonds<sup>117</sup>, cleavage of coordination bonds<sup>38, 84, 88, 96, 98</sup>, pericyclic reactions<sup>46, 79, 103</sup> and bond isomerizations<sup>105, 118</sup>.

### 1.1.5 Activation of mechanophores

Prior to the cleavage of a mechanophoric bond, the covalently attached polymer chains first have to partially uncoil, in turn leading to the stretching of the labile bond which finally results in bond cleavage. Weakening of the labile bond can be described mathematically with the Morse potential under consideration of the thermally activated barrier to scission (TABS) theory and the constrained geometries simulate external force (COGEF) method<sup>47, 119-121</sup>. Application of an external pulling force leads to a constrained geometry optimization and thus to a deformation of the Morse potential which displays a lower dissociation energy ( $D_e$ ) than the force-free Morse potential and allows activation of mechanophores at lower temperatures.

Mechanophores can either be activated in solution using common methods such as ultrasonication<sup>32-38</sup> and shear stress exerted by turbulent, respectively elongation flow<sup>35, 122-123</sup> or in bulk using compression<sup>37, 46, 94-95, 124</sup>, tensile testing<sup>46, 125-126</sup> or torsional shear force<sup>79, 127-128</sup>. Even though solid-state methods can achieve higher maximum forces ( $\sim 10^5$  N), ultrasound ( $\sim 10^9$  N) is the most effective method to apply force to polymer chains due to the faster strain rates (solid state methods:  $10^0 - 10^2$  s<sup>-1</sup>, ultrasound:  $10^6 - 10^7$  s<sup>-1</sup>), giving an explanation for the higher activation efficiencies when using ultrasound compared to solid state<sup>35, 129</sup>.

Ultrasound-induced activation in solution by irradiation with high-frequency ultrasound relies on the formation, growth and collapse of cavitation bubbles as shown in Figure 3 (also see Chapter 1.1.3).

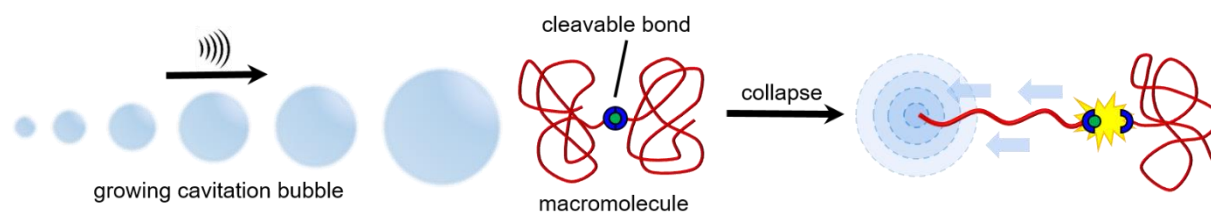


**Figure 3.** Ultrasound induced scission of a polymeric mechanophore. Under the influence of ultrasound cavitation bubbles start to form, grow and collapse, in turn generating a void volume. Due to the created void volume the nearer chain end of a randomly coiled polymer is pulled into the collapsing bubble, leading to stretching and cleavage of the polymer chain at the position of the weakest bond.

Upon collapse of a cavitation bubble, a void volume is generated, in turn pulling the closer end from a polymer chain into the void volume. As a consequence, the polymer chain starts to uncoil and force is generated upon stretching which accumulates in the midpoint of the polymer chain, subsequently activating the mechanophore<sup>129</sup>. However, full elongation of the chain is not necessary as also a partially coiled polymer chain can undergo chain scission<sup>120, 130-131</sup>.

A variety of parameters influences the activation efficiency of a mechanophore in solution. An increase in sonication power generally promotes the activation of a mechanophore since it increases the amount and size of cavitation bubbles<sup>129, 132</sup>. Surprisingly, temperature shows a contrary behavior. An increase of temperature leads to an increase of the vapor pressure and thus to a bigger amount of solvent entering the cavitation bubbles which can cushion the collapse of the cavitation bubbles<sup>30, 129, 132</sup>.

The proper choice of the solvent is crucial as it strongly affects the activation of mechanophores in solution due to several effects. First, the solvent should have a low vapor pressure to avoid the aforementioned cushioning effect of the cavitation bubbles, leading to a weaker shear field. Secondly, a good solvent-polymer interaction will lead to an extended conformation of the polymer chain which facilitates the coil-stretch transition and thus facilitates mechanophore cleavage<sup>129, 132-134</sup>. Accordingly, common solvents for ultrasound induced cleavage of mechanophores are e.g. THF, toluene and ethyl acetate, which possess comparably low vapor pressures<sup>30</sup>.

Moreover, the structure of the mechanophore is important. The force that is directed along the polymer backbone accumulates in the midpoint of the chain, thus the positioning of the mechanophoric labile bond in the center of the chain is advantageous (see Figure 4a). Calculations and experimental data proved an optimal activation when placing the labile bond within ~15 % of the center of the chain<sup>129, 135</sup>. Contrary, placing the mechanophoric bond apart the center rises the homolytic C–C bond cleavage probability and decreases thus the activation efficiency<sup>136</sup>.

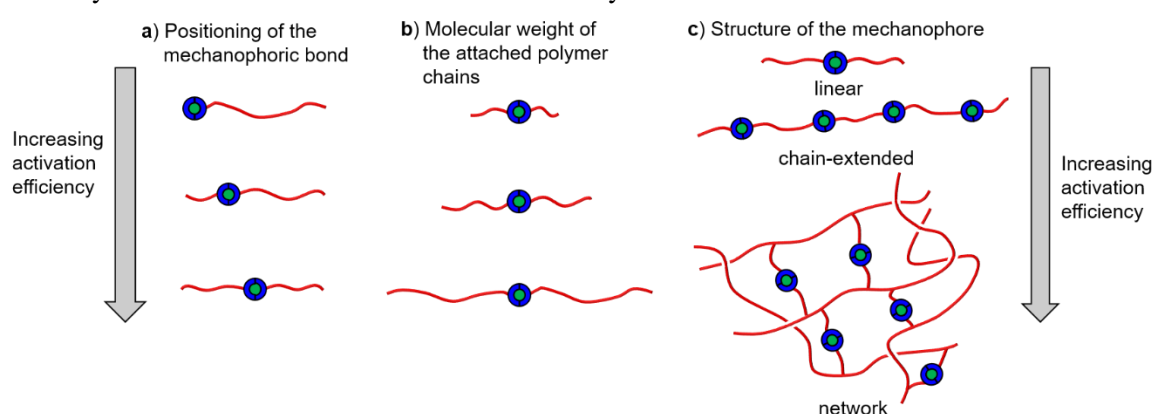


**Figure 4.** Activation efficiency of a mechanophore in dependence from a) the positioning of the mechanophoric bond, b) the molecular weight of the attached polymer chains and c) the structure of the mechanophore.

An increasing molecular weight and therefore an elongation of the polymer chains can also increase the activation efficiency, as the relaxation time of longer polymer chains back to the random coil state is higher than for shorter chains (see Figure 4b)<sup>137-138</sup>. In addition, it has been found that a limiting molecular weight ( $M_{lim}$ ) exists, below which the chain scission efficiency is drastically decreasing. However,  $M_{lim}$  usually varies strongly for different polymers<sup>134, 136</sup>. Decrease in activation efficiency relies on the inability of short chains to accumulate the required force for mechanophoric bond cleavage due to their faster relaxation to the random coil state.  $M_{lim}$  for a specific polymer has no fixed value and can differ, e.g. a higher ultrasound intensity results in a decrease of  $M_{lim}$ <sup>138</sup>.

Polymer concentration has also been taken into account for a variety of reasons. Higher polymer concentrations lead to an increase in the viscosity and thus to a hindered formation of cavitation bubbles which hampers mechanophore activation<sup>30, 122, 133</sup>. A higher polymer concentration also increases the probability for the backreaction to the initial latent state.

Activation of mechanophores in bulk is important in technical applications as the majority of polymeric materials is used in the solid state. Activation can be done using several methods such as compression<sup>37, 46, 94-95, 124</sup>, tensile testing<sup>46, 125-126</sup> or torsional shear force<sup>79, 127-128</sup>. The chain length of the polymeric handles is also of importance for activation in the solid state, as the chains must be sufficiently long to entangle with the used matrix thus acting as anchor. If the chains are too short, slipping from the chains out of the polymer matrix can occur, which prevents force transmission from the polymeric handles to the mechanophoric bond thus impeding their activation. If the polymeric handles are sufficiently entangled with the matrix, an external force will lead to a stretching of both the matrix and the anchored polymeric handles. Continuous application of force leads to further uncoiling of the chains. Once stretched, the exerted stress falls onto the polymeric handles leading to cleavage of the mechanophoric bond.

If the molecular weight of the mechanophore exceeds a critical value, physical entanglement is sufficient to ensure an efficient activation<sup>37, 95</sup>. Partial crystallinity of the polymeric matrix can also be advantageous due to a better force transmission to the mechanophoric bond along the crystalline lamellae of the matrix. Crystallinity of the matrix can further enhance the activation behavior of the mechanophore if both are able to cocrystallize with each other<sup>93</sup>.

Force transmission can be further improved by incorporation of multiple mechanophoric motifs within one polymer chain (chain-extended structures)<sup>95</sup>, by chemical crosslinking of the mechanophore into a network<sup>70, 128, 139</sup> (see Figure 4c) or by incorporation of supramolecular bonds<sup>70, 73, 140</sup>. Incorporating mechanophores into chemically crosslinked networks has the obvious advantage that chain disentanglements can no longer take place since mobility of the polymer chains is limited. The swelling of networks in solvents can also be used for the activation of mechanophores<sup>74</sup>. Furthermore, it was shown that only mechanophores oriented parallel to the direction of applied force are activated. Crosslinking points can redirect the force which allows usage of the perpendicular parts of the force to also activate differently aligned mechanophores in turn increasing activation efficiency<sup>126, 141</sup>. However, the amount of different inter- and intrachain interactions and their contributions to force transmission in such a bulk material as well as the appearance of localized regions of high stress concentrations, leading to inhomogeneous activation of the mechanophore, remain challenges in the field of bulk mechanochemistry<sup>120, 142</sup>.

Besides sufficient entanglement of the mechanophore in the matrix, the glass transition temperature ( $T_g$ ) plays an important role<sup>37, 46, 120, 125</sup>. Only above or slightly below  $T_g$ , chain mobility is sufficient for an efficient force transmission. Acting below  $T_g$ , the polymer chains are glassy and will not transmit force due to their brittleness and a predominant C-C bond scission will appear.

### 1.1.6 Metal-based polymeric mechanocatalysts

In the following section, different metal-based mechanocatalysts and their possible applications are discussed. The term “mechanocatalyst” refers to catalysts that are inactive or latent in their initial state due to steric shielding of the attached polymeric ligands (see Figure 5). When an external force is applied, the inactive catalyst switches to its active form by cleavage of one of the ligands, thus allowing the exposed metal center to catalyze the desired reaction.

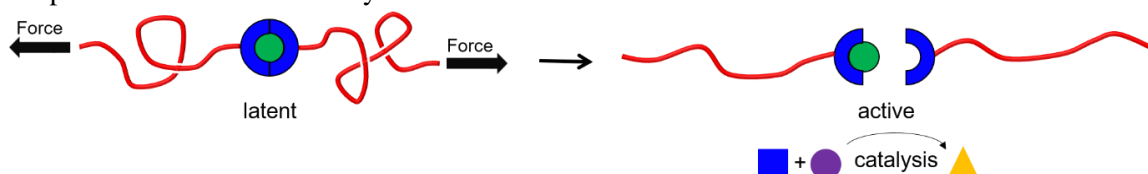


**Figure 5.** Switching of a latent catalyst to its catalytically active form by an external force.

The first metal-based polymeric mechanophores ( $[\text{PdCl}_2(\text{PPh}_2\text{-PTHF-PPh}_2)]_m$ ) were synthesized by Sijbesma *et al.* in 2004 and contained several Pd-P coordination bonds<sup>83</sup>. Ultrasonication of these

polymers led to a reversible reduction of the molecular weight, thus proving the selective cleavage of the coordination bonds instead of covalent bonds.

The observation of a specific, non-random cleavage of the coordination bond *via* ultrasonication can be seen as the beginning of modern mechanochemistry because it was the inspiration for the synthesis of a plenty of transition metal coordination complexes which afterwards were extensively tested in the field of mechanophoric catalysis. In the following years, the same working group performed a series of other experiments, further deepening the understanding of the synthesis of high molecular weight metal-based coordination polymers<sup>84-86</sup>.

In an attempt to investigate cleavage selectivity, a mechanophore  $([\text{PdCl}_2(\text{PCy}_2\text{-PTHF-PCy}_2)]_m[\text{PtCl}_2(\text{PCy}_2\text{-PTHF-PCy}_2)]_p)$  containing Pd-P bonds (141 kJ/mol) and Pt-P bonds (169 kJ/mol) with similar dissociation energies was synthesized<sup>86</sup>. Even though the Pd-P bonds were the preferential cleavage sites, breakage of the Pt-P bonds could not be completely avoided, showing that a sufficient difference in bond energies is a necessary requirement for selective bond scission.

Although these systems were often referred to as mechanophoric catalysts, their catalytic activity never has been tested.

### 1.1.6.1 Silver/ruthenium *N*-heterocyclic carbene mechanocatalysts

First mechanophoric catalysts with proven catalytic activity were also synthesized from the working group of Sijbesma and contained either silver or ruthenium as coordination metal<sup>42, 87-93</sup>. The first reported polymeric silver(I) bis(*N*-heterocyclic carbene) (NHC) complexes  $[\text{Ag}(\text{PTHF-NHC})_2]\text{PF}_6$  were synthesized in 2008 using *N*-ethyl imidazole terminated PTHF<sup>87</sup>, followed by the synthesis of ruthenium-based bis(NHC) complexes  $[\text{Ru}=\text{CHPh}(\text{PTHF-NHC})_2\text{Cl}_2]$  in 2009, bearing imidazolidine functionalized PTHF<sup>88</sup>, as shown in Figure 6a and 6b.

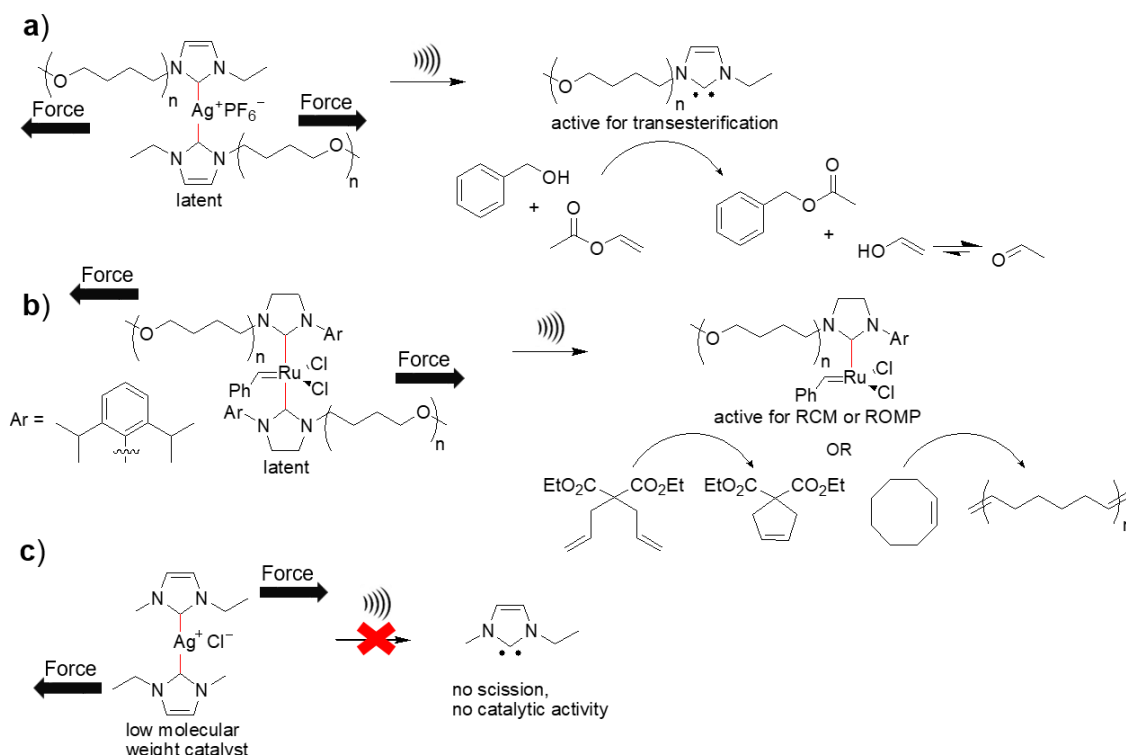


**Figure 6.** Testing of mechanophoric catalysts in solution *via* ultrasonication. a) Applying ultrasound to  $[\text{Ag}(\text{PTHF-NHC})_2]\text{PF}_6$  generates a free carbene ligand which can in turn catalyzes transesterification reactions. b) Subjecting  $[\text{Ru}=\text{CHPh}(\text{PTHF-NHC})_2\text{Cl}_2]$  to ultrasound generates a free coordination site at the Ru-center, thus allowing catalysis of ring-closing metathesis reactions or ring-opening metathesis polymerizations. c) Due to the missing polymeric handles, activation of the low molecular weight complex is hampered and thus does not show catalytic activity<sup>88, 90, 92-93</sup>.

The functionality of these complexes relied on blocking their catalytic activity in the latent state due to the coordinated ligands, which shielded the catalytic center from the reactants. Once activated by an external applied force, one of the shielding ligands was cleaved off, in turn exposing the catalytic active center to the reactants. The catalytic center could either be the metal as it was the case for the ruthenium complex which subsequently catalyzes ring-closing metathesis (RCM) reactions of diethyl diallylmalonate<sup>88,91-92</sup> or ring-opening metathesis polymerization (ROMP) of cyclooctene<sup>88</sup>, respectively disubstituted norbornenes<sup>92</sup>. Alternatively, the carbene could be the catalytic center as it was the case for the silver complex in turn catalyzing the transesterification reaction between benzyl alcohol and vinyl acetate<sup>88,90-91</sup>.

Detailed studies have been done to investigate the influence of several parameters on the activation behavior of those catalysts in solution, showing the previously described trends (see Chapter 1.1.5). Increasing the mechanophore concentration favored the activation efficiency of the catalyst and thus led to an increase of the turnover number (TON) for the transesterification reaction between benzyl alcohol and vinyl acetate using  $[\text{Ag}(\text{PTHF-NHC})_2]\text{PF}_6$  complexes<sup>90</sup>. Influence of the molecular weight of the polymeric handles followed the expected trend for both, the Ag- and the Ru-based mechanophores, with the activation being more efficient when the length of the polymeric handles was increased<sup>87-88, 90</sup>. While the molecular weight dependency was a first hint for the pure mechanical activation *via* an external applied force, testing of low molecular weight complexes bearing no polymeric handles did not show any conversion under the influence of ultrasound (see Figure 6c), clearly proving the catalysts to be mechanochemically active<sup>88,92</sup>. Cleavage efficiency could be improved by preventing recoordination of the ligands to the metal center and thus the return to the latent state. This was realized by the addition of small amounts of water (0.1 % v/v) which was able to react with the formed free carbene, forming the imidazolium salt and thus preventing the back reaction or alternatively by the addition of carbon disulfide (1 % v/v)<sup>87</sup>.

While previously mentioned examples were limited to homogenous catalysis in solution, mechanophoric activation of the Ru-based catalyst  $[\text{Ru}=\text{CHPh}(\text{PTHF-NHC})_2\text{Cl}_2]$  was also successfully transferred to the solid state by incorporation into a semicrystalline, high molecular weight PTHF matrix as shown in Figure 7. Five cycles of compression led to polymerization of a monofunctional norbornene with a conversion of up to 25 %. Using a bifunctional norbornene even allowed to trigger crosslinking reactions, underscoring the application possibilities for self-healing applications of mechanophoric catalysts<sup>93</sup>.

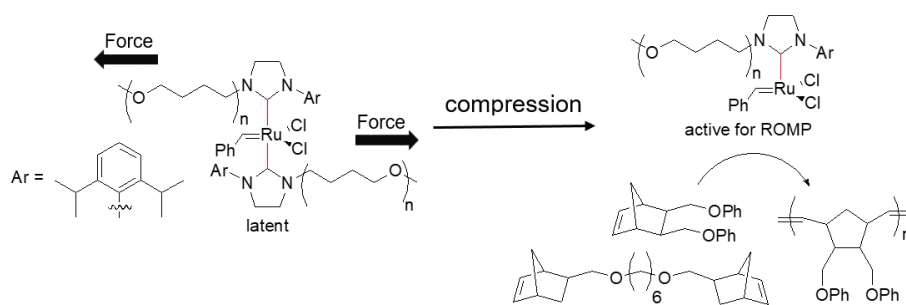


**Figure 7.** Activation of the mechanophoric catalyst  $[\text{Ru}=\text{CHPh}(\text{PTHF-NHC})_2\text{Cl}_2]$  in bulk *via* compressional forces. Once activated, the mechanophore triggers the ROMP of mono- and bifunctional norbornene monomers leading to linear polymers, respectively crosslinked networks. Selective activation of the catalyst, followed by spatially controlled polymerization holds great potential for autonomous self-healing materials<sup>93</sup>.

### 1.1.6.2 Copper N-heterocyclic carbene mechanocatalysts

With the applicability of Ag- and Ru-based carbene complexes being proven in the field of mechanocatalysis, utilization of latent Cu(I) bis(NHC) complexes for the mechanochemically triggered CuAAC was reported by Binder *et al.* in 2015<sup>37-38, 94-95</sup>. Exploiting the force triggered CuAAC offered a broad range of applications as site- and stress-specific “click” reactions were enabled, that potentially

can be used for self-healing and stress-sensing purposes as shown in Figure 8 (For the CuAAC also check Chapter 1.2).

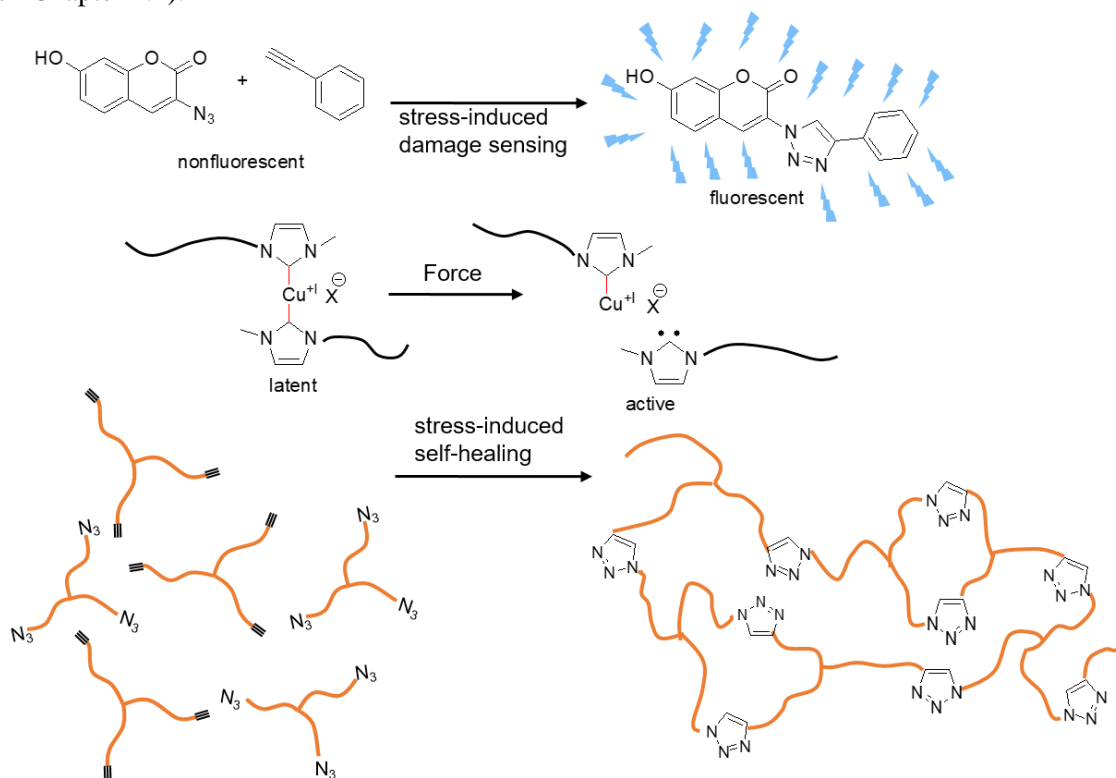


**Figure 8.** Activation of a latent Cu(I) catalyst by force can either be used for fluorogenic “click” reactions as stress-sensing tool or for self-healing crosslinking approaches.

Several polymeric Cu(I) bis(NHC) complexes have been synthesized using either living carbocationic polymerization (LCCP) or atom transfer radical polymerization (ATRP) and their efficiency for stress-induced “click” reactions have been tested in dependence from several parameters, including various types of polymers with a different  $T_g$ , the influence of the molecular weight as well as the mechanophore architecture and the method of activation<sup>37-38, 94-95</sup>. An overview about the synthesized catalysts is given in Figure 9 and Table 1.

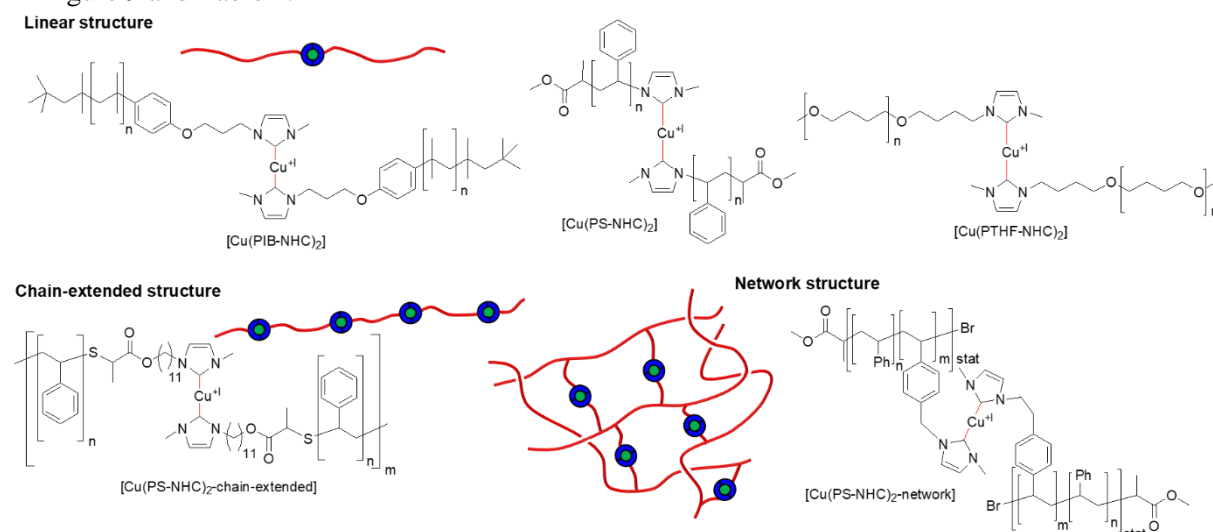


**Figure 9.** Overview about Cu(I) bis(NHC) complexes with linear, chain-extended and network structures<sup>37-38, 94-95</sup>.

**Table 1.** Overview about the synthesized Cu(I) bis(NHC) complexes and their catalytic activity<sup>37-38, 94-95</sup>.

Ent.	Catalyst	Structure	$M_n$ (GPC) [g/mol]	Polym. method	Method of activation <sup>a)</sup>	„Click“ conv. [%] <sup>b)</sup>
1		linear	4750	LCCP	Ultrasound	10
2		linear	4750	LCCP	Compression	0.5 ± 0.2
3		linear	8900	LCCP	Ultrasound	17
4	[Cu(PIB-NHC) <sub>2</sub> ]	linear	8900	LCCP	Compression	0.4 ± 0.2
5		linear	17200	LCCP	Ultrasound	27
6		linear	17200	LCCP	Compression	4.3 ± 1.0 7.2 ± 0.3
7		linear	6800	ATRP	Ultrasound	23
8		linear	6800	ATRP	Compression	0.5 ± 0.2
9		linear	11600	ATRP	Ultrasound	34
10		linear	11600	ATRP	Compression	2.0 ± 0.3
11		linear	12000	RAFT	Compression	11.1
12		linear	13100	ATRP	Ultrasound	44
13	[Cu(PS-NHC) <sub>2</sub> ]	linear	13600	ATRP	Ultrasound	52
14		linear	13600	ATRP	Compression	7.9 ± 0.5
15		linear	23000	RAFT	Compression	12.1
16		linear	50500	RAFT	Compression	16.2
17		chain- extended	15000	RAFT	Compression	16.1
18		chain- extended	21500	RAFT	Compression	44.2 (3-4) <sup>c)</sup>
19		network	network	ATRP	Compression	44.1
20	[Cu(PTHF-NHC) <sub>2</sub> ]	linear	15600	CROP	Ultrasound	97 (24) <sup>c)</sup>

<sup>a)</sup> Ultrasonication experiments were conducted in *d*<sub>8</sub>-THF/MeOH (30:1 v/v), following the “click” reaction between benzyl azide and phenylacetylene (*c* = 75.0 mM) after addition of 0.01 eq. Cu(I) catalyst. Ten cycles were performed with 90 min pulsing at 20 kHz with 30 % of maximal amplitude of 125 μm with a pulse sequence of 5 s pulse, 10 s break, 60 min without pulsing. Compression experiments were conducted in a high molecular weight PTHF-matrix with a catalyst concentration of 5.17 × 10<sup>-6</sup> mmol/mg<sub>sample</sub> and coumarin and phenylacetylene concentrations of 1.56 × 10<sup>-4</sup> mmol/mg<sub>sample</sub>. For every experiment 20 cycles of compression with a pressure of 10 tons for 30 min, followed by 30 min of waiting time were performed

<sup>b)</sup> “Click” conversions for ultrasound-induced experiments refer to the conversion of benzyl azide and phenylacetylene after ten cycles of ultrasound and were calculated *via* <sup>1</sup>H-NMR. “Click” conversions for compression experiments were calculated *via* fluorescence measurements after 20 cycles of compression to observe the fluorogenic CuAAC of 3-azido-7-hydroxy-coumarin and phenylacetylene. <sup>c)</sup> These complexes were not completely latent and showed a ground activity (given in brackets) in the absence of an applied force.

First experiments were conducted in solution by activating the catalysts *via* ultrasound and monitoring their activation by a model “click” reaction between benzyl azide and phenylacetylene. Cu(I) bis(NHC) complexes have been synthesized with poly(isobutylene) (PIB), poly(styrene) (PS) and PTHF as polymeric handles. The imidazolium moiety, which was necessary for the Cu(I) bis(NHC) complex formation was introduced as a post modification step after the polymerization. Cleavage efficiency of the complexes (*via* GPC) and their catalytic activity (*via*  $^1\text{H-NMR}$  spectroscopy) were compared in dependence from the molecular weight and among each other, taking their different polymer-solvent interactions into account<sup>37-38</sup>. In general, increasing the molecular weight of the polymeric handles led to an increase of the cleavage efficiency and in turn to an increased “click” conversion. The three tested PIB-based catalysts with molecular weights of 4700 g/mol [Cu(PIB-NHC)<sub>2</sub>-4.7], 8900 g/mol [Cu(PIB-NHC)<sub>2</sub>-8.9] and 17 200 g/mol [Cu(PIB-NHC)<sub>2</sub>-17.2] showed cleavage efficiencies of 45 %, 55 % and 84 % after 20 cycles of ultrasound. In concordance “click” conversions increased in the order 10 %, 17 % and 27 % after ten cycles of ultrasonication. The PS-based catalysts with molecular weights of 6800 g/mol [Cu(PS-NHC)<sub>2</sub>-6.8], 11 600 g/mol [Cu(PS-NHC)<sub>2</sub>-11.6] and 13 600 g/mol [Cu(PS-NHC)<sub>2</sub>-13.6] showed a similar behavior with increasing cleavage efficiencies in the order 46 %, 69 % and 80 % and “click” conversions of 23 %, 34 % and 52 %. Even though, the molecular weights for the PIB-based catalysts were higher, the PS-based catalysts showed better cleavage efficiencies and “click” conversions, which can be attributed to better polymer-solvent interactions between the PS-chains and the used solvent THF in comparison to the PIB-chains. This assumption was proven by testing the pTHF-based catalyst with a molecular weight of 15 600 g/mol for its catalytic activity. Due to the even better polymer-solvent interactions, “click” conversions of 97 % could be reached. However, this catalyst was no longer inactive in the absence of ultrasound and showed “click” conversions of up to 24 %, making it unsuitable as mechanophoric catalyst.

Activation of the catalysts was also performed in the solid state *via* compression experiments to test their applicability in stress-sensing materials. The applied stress was visualized by the fluorogenic “click” reaction between the two non-fluorescent starting materials 3-azido-7-hydroxy coumarin and phenylacetylene, which was catalyzed after stress-induced activation of the latent catalysts (see Figure 8). The influence of the molecular weight, the type of polymer and the polymeric architecture were investigated systematically as shown in Table 1<sup>37, 94-95</sup>. Increasing the molecular weight led to an increase for both, the PS-based and the PIB-based linear mechanocatalysts. Increasing the molecular weight of [Cu(PS-NHC)<sub>2</sub>-linear] from 6800 g/mol, to 11 600 g/mol and 13 600 g/mol led to an increase of the “click” conversion from 0.5 %, to 2.0 % and 7.9 %. Similarly, increasing the molecular weight of [Cu(PIB-NHC)<sub>2</sub>-linear] from 4800 g/mol, to 8900 g/mol and 17 200 g/mol led to an increase of the “click” conversion from 0.5 %, to 0.4 % and 7.2 %. Again, the PS-based catalysts showed higher conversions than the PIB-based catalysts, even though their molecular weight was lower. In contrast to solution measurements, polymer-solvent interactions do not play a role here. However, as a result of the much higher  $T_g$  of PS ( $T_g \sim 100$  °C) in contrast to PIB ( $T_g = -80$  °C) the PS chains are stiffer and allow a better force transmission, thus facilitating the mechanophore cleavage. Synthesis of mechanophoric catalysts with even longer polymer chains and thus higher activation efficiency was not possible due to the low yields of the quaternization reaction that was necessary as post modification step after the polymerization to introduce the imidazolium moiety for a subsequent complexation.

To circumvent this problem the imidazolium moieties were incorporated during the polymerization step using RAFT polymerization with an imidazolium containing chain transfer agent (CTA)<sup>95</sup>. The obtained polymers were transformed to the corresponding complexes [Cu(PS-NHC)<sub>2</sub>-linear] with molecular weights up to 50 500 g/mol, further improving the “click” conversion up to 16.2 %. In an attempt to further increase the catalytic activity a combination of RAFT and thio-bromo “click” reaction was used to incorporate the imidazolium moiety at both chain ends, subsequently allowing the synthesis of chain-

extended structures with multiple Cu(I) centers per chain<sup>94-95</sup>. The obtained catalysts [Cu(PS-NHC)<sub>2</sub>-chain-extended] with molecular weights of 15 000 g/mol and 21 500 g/mol contained in average three to four Cu(I) centers per chain and displayed a higher catalytic activity due to multiple potential scission points under applied stress. These modifications led to an increased “click” conversion up to 44.2 % during compression. However, it turned out that these catalysts were no longer inactive in the absence of an applied force and showed a ground activity of 3 – 4 %.

Therefore, a random copolymer of 1-methyl-3(4-vinylbenzyl)imidazolium hexafluorophosphate and styrene was synthesized, bearing several imidazolium groups in the polymer chain<sup>94</sup>. Transformation of these imidazolium groups to the Cu(I) bis(NHC) complex [Cu(PS-NHC)<sub>2</sub>-network] led to the formation of a network with the Cu(I) centers being the crosslinking points. The network structure offered two apparent advantages: 1) The effective chain length between the Cu(I) bis(NHC) moieties was shortened, which should hamper premature activation of the catalyst without applied stress and 2) the crosslinking points were able to redirect the applied force and allowed additional usage of the perpendicular parts of the force. This improved the activation efficiency as parallel orientated mechanophores activate better (see Chapter 1.1.5). Indeed, the “click” conversion of the synthesized network was 44.1 % which was comparable with the activity of the high molecular weight complex [Cu(PS-NHC)<sub>2</sub>-chain-extended]. However, the network based approach did not show any ground activity in the absence of force, making this catalyst a suitable candidate for stress-sensing applications.

In order to further extend the network concept, poly(urethane) (PU) networks containing Cu(I) bis(NHC) complexes were synthesized as shown in Figure 10a<sup>143</sup>. Besides the comparatively easy access to the networks *via* a multicomponent polyaddition (bis(OH)-functionalized Cu(I) bis(NHC) complex ([Cu(C<sub>11</sub>OH-NHC)<sub>2</sub>], pTHF, hexamethylenediisocyanate (HDI), trimethanolpropane (TMP), 8-azidonaphtalene-2-ol (AzN) and 3-hydroxyphenylacetylene (HPA)), the crosslinking density could be easily tuned by variation of the bi- ([Cu(C<sub>11</sub>OH-NHC)<sub>2</sub>] and pTHF) and trivalent alcohols (TMP) from 2/10 (tri/bivalent) (PU20) to 8/10 (PU80). Changing the chain length between crosslinking points also affected the activation efficiency of the Cu(I) bis(NHC) catalyst since longer chain segments (= lower crosslinking densities) were better capable of force accumulation and transmission. Covalent embedding of AzN and HPA generated a transparent network and allowed a homogenous distribution and stable incorporation into the networks. A variety of PU networks with different crosslinking densities and different *E*-moduli (PU20 (0.04 MPa), PU30 (0.10 MPa), PU40 (0.19 MPa), PU50 (0.32 MPa), PU60 (0.68 MPa), PU70 (1.00 MPa) and PU80 (1.20 MPa) have been synthesized and their mechanochemical activation behavior as well as their mechanical properties were investigated by oscillating tensile rheology (see Figure 10b) *via* the CuAAC, leading to the highly fluorescent 8-(4-(3-hydroxyphenyl)-1,2,3-triazole-1-yl)naphtalene-2-ol (see Figure 10).

The influence of the used frequency on the activation rate was tested for PU60 in the range of 0.25 to 1.0 Hz, keeping the deformation constant at  $\gamma = 60$  %. In all cases a maximal conversion of 12 % could be detected. However, the number of necessary cycles for 12 % conversion increased with decreasing frequency (12 % conversion at  $\sim 2.5 \times 10^4$  cycles (1.00 Hz),  $\sim 6.0 \times 10^4$  cycles (0.75 Hz),  $1.3 \times 10^5$  cycles (0.5 Hz) and  $\sim 2.6 \times 10^5$  cycles (0.25 Hz). As supposed, an increase of the applied deformation at the same frequency (0.5 Hz) led to an increase of the conversion for PU60 ( $\gamma = 40$  %: 5 % conversion),  $\gamma = 60$  %: 12 % conversion and  $\gamma = 80$  %: 17 % conversion).

The influence of the different crosslinking densities (and therefore different *E*-moduli) was tested for the different PUs at a frequency of 0.5 Hz and a deformation of  $\gamma = 80$  %. A decrease of the crosslinking density led to an increased chain length between the crosslinking points and therefore enhanced the mechanophoric activity. Accordingly, PU40 showed the highest conversion (25 %), which was gradually decreasing for PU50 (10.1 %), PU60 (8.5 %) and PU70 (5.2 %).

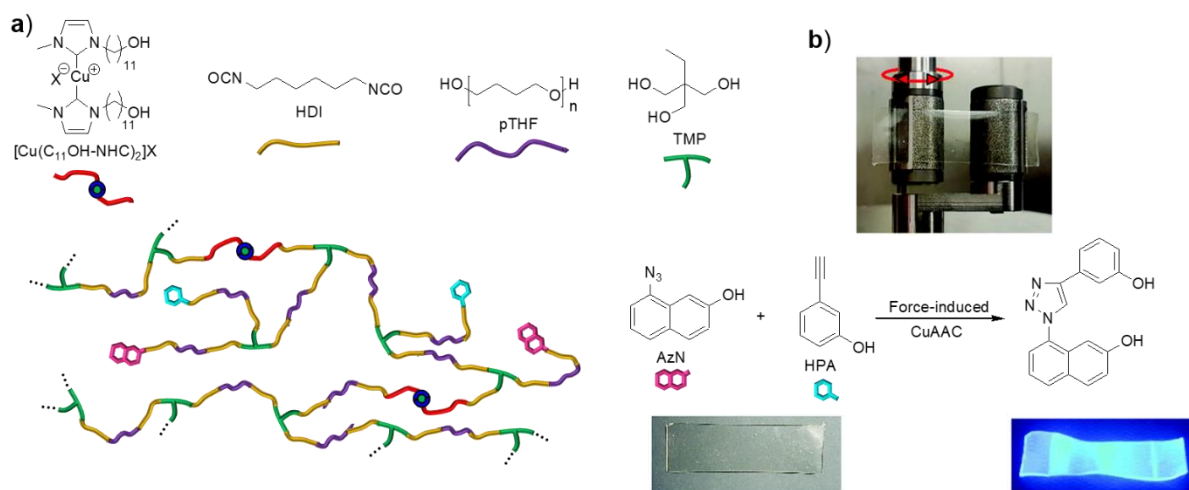


**Figure 10.** a) All-in-one approach for the synthesis of mechanoresponsive poly(urethane) networks. b) Activation of the PU foils could be done *via* oscillating tensile rheology, thus triggering the fluorogenic “click” reaction of the non-fluorescent 8-azidonaphtalene-2-ol (AzN) and 3-hydroxyphenylacetylene (HPA). Parts of Figure a) and b) were reproduced from reference<sup>143</sup> with permission from The Royal Society of Chemistry.

### 1.1.6.3 Ferrocene-based polymeric mechanophores

The force triggered release of Fe(II) and subsequent oxidation to Fe(III) has been independently described by the working groups of Fromm and Tang in 2018 using ferrocene based mechanophores<sup>96-97</sup>. Ferrocenes are used for a widespread range of applications, such as catalysis<sup>144</sup>, biomedical applications<sup>145</sup> or electrochemical applications<sup>146</sup> and therefore are another promising candidate for polymeric mechanophores, especially in respect to their high thermal stability. Fromm *et al.* incorporated ferrocene into poly(methylacrylate)s (PMA) [Fc-PMA] ( $M_n = 133\,000$  g/mol) and polyurethanes (PU) [Fc-PU] ( $M_n = 100\,000$  g/mol) (see Figure 11) to test their applicability as sensor materials as well as for potential medical applications<sup>96</sup>. Upon ultrasonication of [Fc-PMA], GPC measurements showed a much faster decrease of the molecular weight in comparison to a pure PMA [ref-PMA] without a ferrocene unit. Notably, the molecular weight was nearly halved for [Fc-PMA] after 90 minutes, indicating preferential cleavage near the center of the chain at the position of the ferrocene unit.

A heterolytic cleavage of the ferrocene unit *via* ultrasonication was proven in the presence of potassium thiocyanate. The released Fe(II) ions were oxidized to Fe(III) before they reacted with the added potassium thiocyanate thus forming the red complex  $[\text{Fe}(\text{SCN})_n(\text{H}_2\text{O})_{6-n}]^{(3-n)+}$ . As calculated by kinetic models using the GPC data, the specific cleavage of the ferrocene unit was ten times faster than the unspecific, homolytic C–C cleavage, which led to a cleavage of 52 % of the ferrocene groups after 90 minutes. To increase the number of ferrocene cleaving events per chains, ferrocene was incorporated *via* polycondensation with 1,4-butanediol (BDO), methylene diphenyl diisocyanate (MDI) and PTHF into a polyurethane, which resulted in the formation of [Fc-PU] ( $M_n = 100\,000$  g/mol) bearing in average six ferrocene groups per chain. Again, the molecular weight decreased much faster in comparison to a reference [ref-Pu] without ferrocene groups according to GPC. However, in comparison to [Fc-PMA] the GPC trace of [Fc-PU] was much broader which was explained due to several potential cleaving points leading to several scission events for one chain. Addition of  $\text{K}_4[\text{Fe}(\text{CN})_6]$  led to the formation of the blue complex  $\text{Fe}_4[\text{Fe}(\text{CN})_6]_3$ , proving the preferred cleavage at the ferrocene groups. Again, calculations using the obtained GPC data showed a three times faster specific cleavage of the ferrocene groups in comparison to nonspecific C–C cleavage leading to cleavage of 25 % of the ferrocene moieties. For both polymers, [Fc-PMA] and [Fc-PU],  $M_{\text{lim}}$  was found to be around 40 000 – 45 000 g/mol.

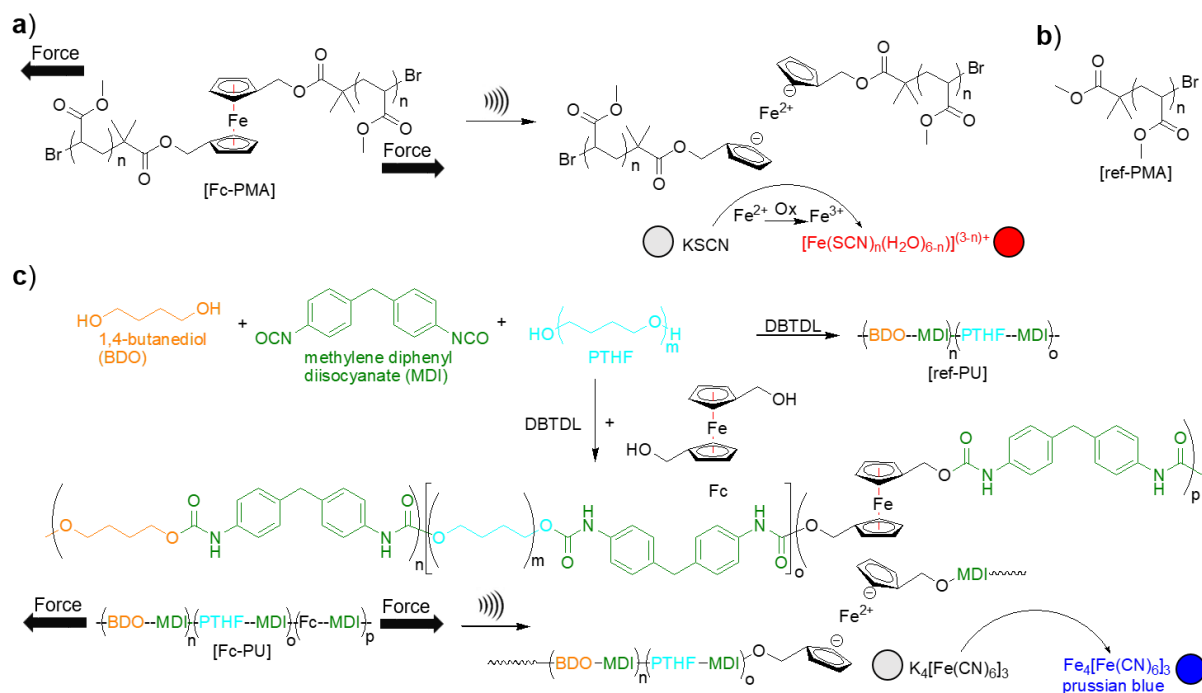


**Figure 11.** Testing of mechanophoric ferrocene catalysts. a) Activation of [Fc-PMA] led to formation of the red colored complex  $[\text{Fe}(\text{SCN})_n(\text{H}_2\text{O})_{6-n}]^{(3-n)+}$ . b) [ref-PMA] was synthesized as a control polymer without ferrocene moieties. c) Polyurethanes [Fc-PU], containing multiple ferrocene moieties and [ref-PU]. Again, cleavage of the ferrocene moieties for [Fc-PU] was followed by a color change originating from the formed blue complex  $\text{Fe}_4[\text{Fe}(\text{CN})_6]_3$ .

Tang *et al.* incorporated multiple ferrocene moieties into poly(butadiene)-derived polymers (see Figure 12a), thus creating multi-mechanophore copolymers and studied their cleavage behavior under the influence of pulsed ultrasound<sup>97</sup>. Applying ultrasound to a ferrocene-5-methoxycyclooctene (MCO) copolymer [Fe-MCO] ( $M_n = 111\,000$  g/mol) led to a decrease of the molecular weight in the course of 120 minutes until reaching  $M_{\text{lim}} = 17\,600$  g/mol. The cleavage caused the formation of cyclopentadienyl anions, which subsequently were reprotonated to form the cyclopentadiene (Cp) ligands as proven by  $^1\text{H-NMR}$  spectroscopic investigations during sonication. The addition of isopropyl alcohol (10 % v/v) strongly increased the cleavage rate, proving the cleavage and subsequent reprotonation of the ligands. Comparing the total amount of chain scission events (quantified by GPC) with the ferrocene scission events (quantified by  $^1\text{H-NMR}$ ) revealed a much more specific scission of the ferrocene moieties of  $97 \pm 3$  % in comparison to the results of Fromm *et al.*.

There were also some doubts whether the cleavage of the ferrocene is of heterolytic or homolytic origin. The group of Fromm assumed a heterolytic mechanism but did not give a proof for this assumption<sup>96</sup>. However, both mechanisms can be discriminated from each other because homolytic cleavage would result in temporary presence of radicals while heterolytic cleavage would lead to formation of  $[\text{CpFe}]^+$  and  $\text{Cp}^-$  (see Figure 12a). In an attempt to catch the formed radicals, 2,2:6,6-tetramethylpiperidinyloxyl (TEMPO) was added to a solution of [Fe-MCO] before sonication, showing no apparent influence on both the molecular weight degradation (*via* GPC) and the polymer structure (*via*  $^1\text{H-NMR}$ ). Additional density functional theory (DFT) calculations with a COGEF method were performed, also suggesting a heterolytic cleavage leading to formation of  $[\text{CpFe}]^+$  and  $\text{Cp}^-$ .

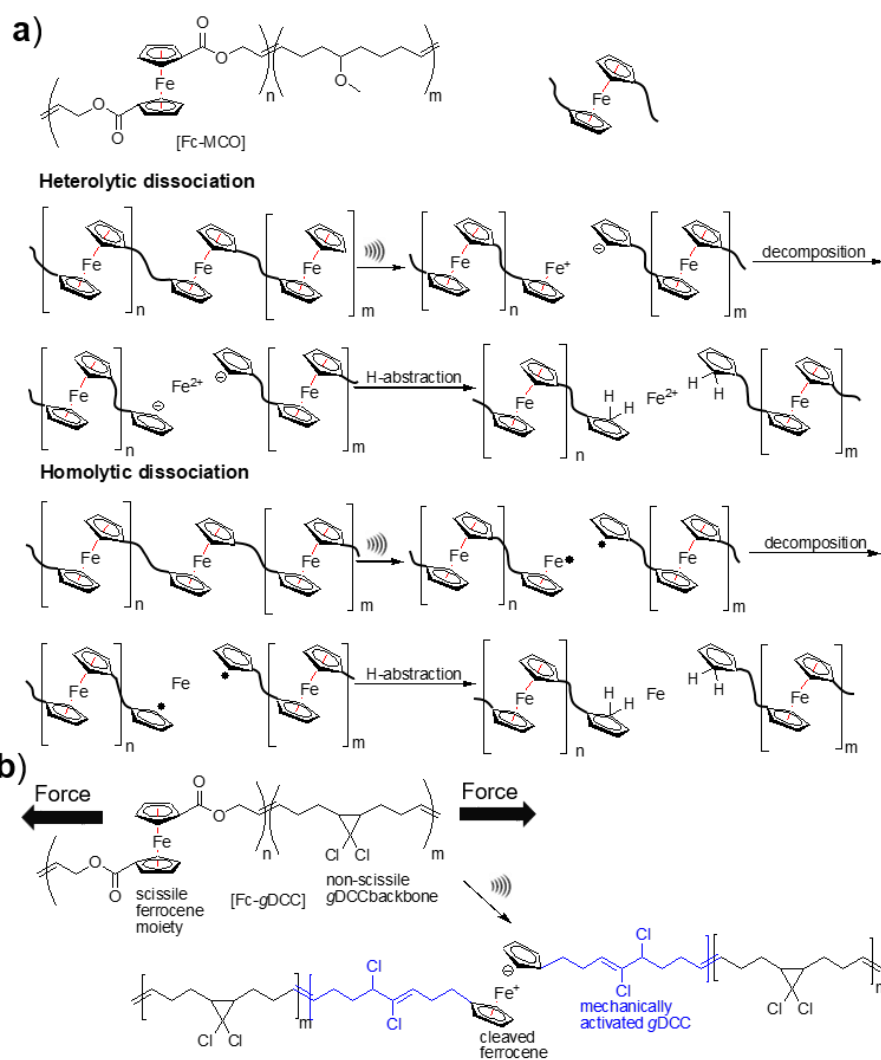


**Figure 12.** a) Structure of the polymer [Fc-MCO] with the heterolytic and homolytic dissociation mechanism of the ferrocene containing polymer. b) Multicentered [Fc-gDCC] possesses two potential mechanophoric groups, one being the ferrocene and the other being the gDCC moieties. Both possible reactions are shown (breakage of the ferrocene moieties and mechanical activation of gDCC)<sup>97</sup>.

Incorporation of *gem*-dichlorocyclopropane (gDCC) units led to a competing activation of the two mechanophoric bonds in the polymer [Fc-gDCC] (see Figure 12b) (also see Chapter 1.3 for a detailed description concerning gDCC mechanochemistry). gDCCs are three-membered rings with high ring strain that easily can undergo electrocyclic ring opening under the influence of an externally applied force. While activation of the ferrocene led to cleavage of the polymer chain, activation of gDCC is a non-scissile event and only led to ring opening, in turn generating 2,3-dihaloalkenes (DHA). Thus, comparing the scissile and non-scissile events allowed a rough estimation of the relative bond strength of the ferrocene moiety compared to the gDCC moiety. In comparison to a pure gDCC-based polymer [gDCC], the amount of non-scissile cleaved gDCC-units in the copolymer [Fc-gDCC] was considerably lower, indicating that the ferrocene units were more mechanically labile than the C–C bonds of the gDCC units.

### 1.1.6.4 Ruthenocene-based polymeric mechanophores

Based on their findings concerning ferrocene mechanophores, the group of Tang also synthesized single- and multicentered ruthenocene main-chain polymers (see Figure 13) and investigated their cleavage behavior under the influence of ultrasound<sup>98</sup>.

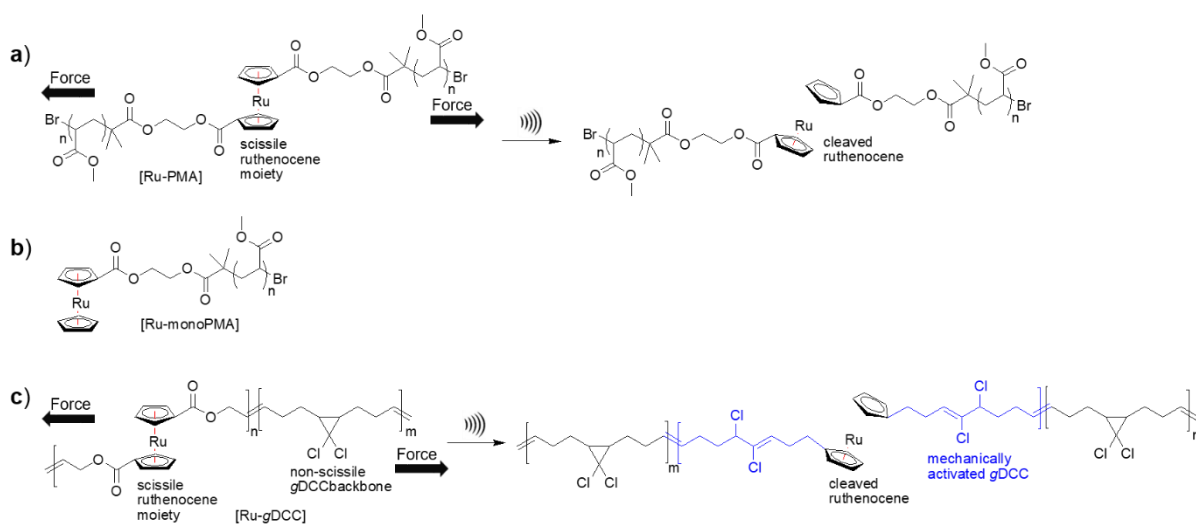


**Figure 13.** Activation of ruthenocene-based mechanophores *via* ultrasonication. a) The single-centered mechanophore [Ru-PMA] preferentially breaks at the ruthenocene moiety. b) [Ru-monoPMA] is not mechanophoric active due to the unfavorable positioning of the ruthenocene moiety at the chain end, preventing an effective force transmission. c) Multicentered [Ru-gDCC] possesses two potential mechanophoric groups, one being the ruthenocene and the other being the gDCC moieties. While breakage of the ruthenocene leads to a shortening of the polymer chains, mechanical activation of gDCC is a non-cleavage event. Even though both groups are mechanically active, breakage of the ruthenocene occurs more often due to the lower bond strength<sup>98</sup>.

The mechanophore with only one Ru-center was synthesized using a bifunctional ruthenocene-based atom transfer radical polymerization (ATRP) initiator and methyl acrylate as monomer, yielding [Ru-PMA] with a molecular weight of  $M_n = 76\,400$  g/mol. Sonication of this polymer for one hour led to a decrease of the molecular weight to 52 600 g/mol, corresponding to a scission of  $58 \pm 2\%$  of the ruthenocene moieties. Again, the ruthenocene was found to be the preferential cleaving site. Ultrasonication of a methyl acrylate polymer [Ru-monoPMA], bearing the ruthenocene at the end of the chain did not show any ruthenocene scissions in <sup>1</sup>H-NMR spectroscopy, clearly proving the mechanochemical origin of the cleavage. Copolymerization of ruthenocene with gDCC generated [Ru-gDCC] ( $M_n = 104\,000$  g/mol), as done previously for [Fe-gDCC]<sup>97</sup> (see Figure 13c). Comparison of the scissile and non-scissile events again allowed an estimation of the relative bond strength of both mechanophoric groups. Surprisingly, the amount of ruthenocene cleavage events was halved compared to the ferrocene indicating a higher bond strength for the ruthenocenes compared to the ferrocenes. However, the larger Ru-Cp centroid bond distance (1.823 Å) in comparison to the Fe-Cp centroid bond distance (1.661 Å) would have suggested a contrary behavior. COGEF simulations revealed a two-step heterolytic dissociation mechanism of the ruthenocene due to the richer coordination structure of ruthenium being a result of an additional orbital shell, compared to iron. As a result, the Ru-Cp bond has to be stretched  $\sim 7$  Å before heterolytic dissociation into [RuCp]<sup>+</sup> and Cp<sup>-</sup>, while Fe-Cp dissociation follows an one-step mechanism with a maximal stretching distance of 5.5 Å, thus explaining the higher mechanochemical strength of ruthenocene.

## 1.2 Copper(I)-catalyzed alkyne-azide cycloaddition

The copper(I)-catalyzed alkyne-azide cycloaddition (CuAAC) is one of the most impactful discoveries for polymer science as it allows easy modification of polymers by the “clicking” of alkynes and azides under the formation of 1,4-substituted triazoles<sup>147-148</sup>. Catalytic amounts of Cu(I) accelerate the reaction

by a factor of  $\sim 10^6$ , compared to the thermal, uncatalyzed Huisgen 1,3-dipolar cycloaddition<sup>149-150</sup>. The CuAAC fulfills almost all criteria that are necessary for a “click” reaction according to Sharpless including high yields, tolerance against other functional groups, stereospecificity, modularity, absence of byproducts, mild reaction conditions including usage of nontoxic solvents and simple product isolation *via* distillation or crystallization<sup>151</sup>. Most of the assumptions are a consequence of the high thermodynamic driving force that usually is greater than 84 kJ/mol. While plenty of the criteria are fulfilled, two remaining problems are the insensitivity against oxygen and water. Oxygen leads to oxidation of Cu(I) to Cu(II), which can in turn catalyze the Glaser coupling as side reaction<sup>152</sup>. Furthermore, it is well known that Cu(I) in aqueous solution undergoes disproportionation to Cu(0) and Cu(II). Circumventing oxidation of Cu(I) is possible by adding sodium ascorbate to the solution to steadily reduce the formed Cu(II)<sup>147</sup>. Alternatively, an addition of ligands can protect the Cu(I) from oxidation as well as disproportionation and can also increase the solubility and the reaction rates<sup>153-156</sup>. Aliphatic, tridentate *N*-donor ligands such as *N,N,N',N'',N'''*-pentamethyldiethylenetriamine (PMDETA) and tris[(1-benzyl-1*H*-1,2,4-triazol-4-yl)methyl]amin (TBTA) have been found to be perfect candidates for this task, however, also some aromatic chelating ligands such as 2,2':6',2''-terpyridine (Tpy) can strongly increase reaction rates<sup>157-158</sup>. Another class of usable ligands are *N*-heterocyclic carbene (NHC) ligands. The coordination of two NHC ligands to one Cu(I) center leads to the formation of [Cu(NHC)<sub>2</sub>]X complexes (see Figure 14) which have been proven to be efficient catalysts for the CuAAC with high tolerance against water and oxygen<sup>159</sup>.

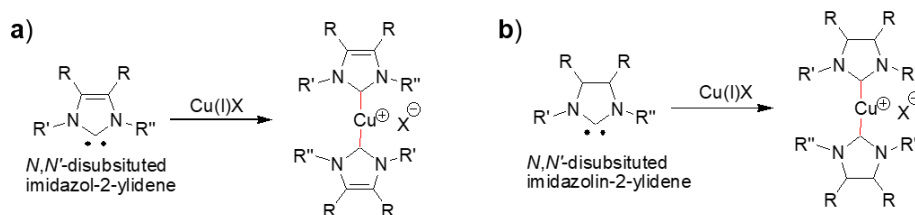


**Figure 14.** a) *N,N'*-disubstituted imidazol-2-ylidenes and b) *N,N'*-disubstituted imidazolin-2-ylidenes are two common NHC-ligands for the synthesis of Cu(I) bis(NHC) complexes.

NHCs as ligands are of special interest as the attachment of different substituents *R'* and *R''* can be used to tune the steric and electronic properties, which have a strong impact on the stability and reactivity of the resulting catalyst<sup>159-163</sup>. Ligand tuning is particularly effective for imidazole-2-ylidene- (see Figure 14a) and imidazolin-2-ylidene-based (see Figure 14b) complexes as in this case a substitution of *R'* and *R''* can have pronounced effects. Accordingly, the incorporation of less bulkier or electron-withdrawing groups such as cyclohexyl (Cy), *tert*-butyl (*t*Bu) or alkyl leads to less stable complexes with higher reactivity. Contrary, incorporation of bulky and electron-donating groups such as diisopropylphenyl (*i*PrPh), mesityl (Mes) or adamantyl (Ad) generates more stable complexes with less reactivity<sup>159</sup>.

While the Cu(I) bis(NHC) catalyzed CuAAC in general follows the commonly accepted catalytic cycle which involves multiple Cu(I) centers<sup>155, 164-165</sup>, there are some differences in the activation step due to the basic nature of the NHC ligand<sup>159, 163</sup> (see Figure 15). Once cleaved off, the NHC ligand is able to interact as internal base in turn deprotonating the alkyne and making an additional base redundant. Subsequently, the formation of the Cu(I)-acetylide (**II**) can take place. The coordination of the azide (**III**) involves multiple Cu(I) centers in which one of the Cu(I) centers is part of the formed six-membered intermediate (**IV**). The exclusion of the Cu(I) forms the 1,2,3-triazole intermediate (**V**) that still bears the Cu(I) at the 5-position. Reprotonating the triazole by the protonated NHC ligand releases the final 1,4-disubstituted-1,2,3-triazole under reformation of the initial Cu(I) bis(NHC) complex (**I**).

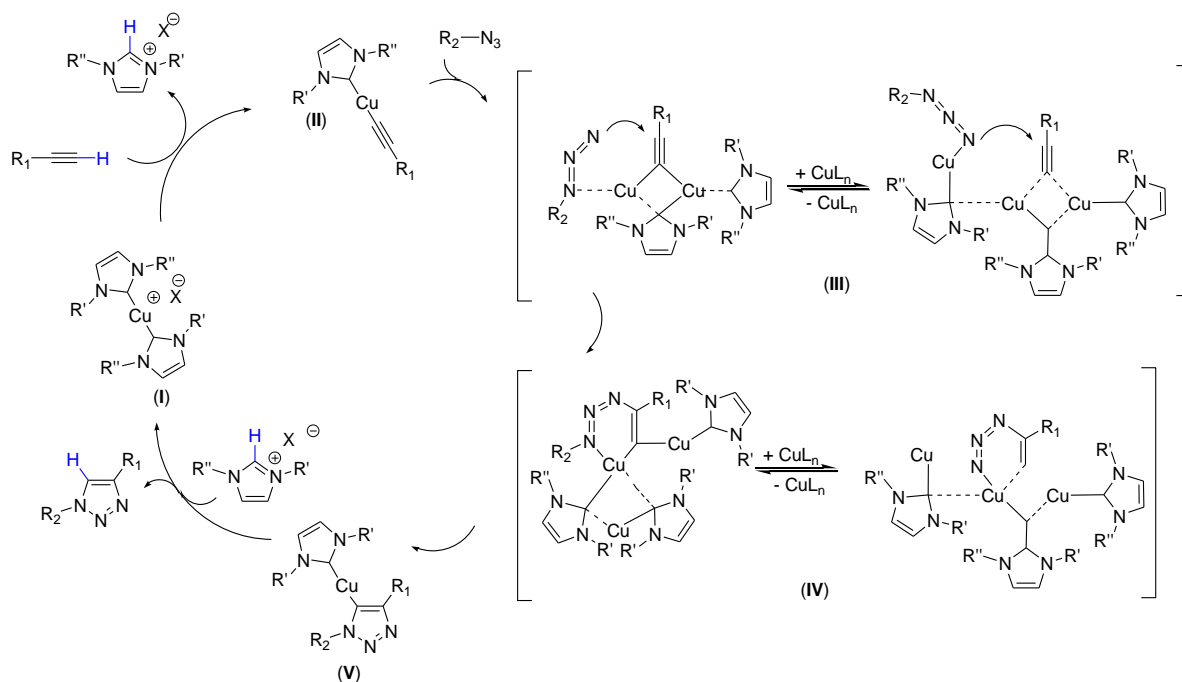


**Figure 15.** Catalytic cycle of the CuAAC using Cu(I) bis(NHC) complexes. Activation of the catalyst (I) takes place by removal of one NHC ligand, subsequently deprotonating the alkyne and allowing formation of the Cu(I)-acetylide (II). After coordination of the azide (III), ring-closure takes place forming a six-membered ring which contains a Cu(I) center (IV). Exclusion of the Cu(I) center leads to the Cu(I) bearing 1,2,3-triazole intermediate (V) which is then re-protonated by the free imidazolium ligand, thus regenerating the Cu(I) bis(NHC) complex (I).

Nowadays, the CuAAC is indispensable from (bio-)chemistry as a versatile tool for the synthesis of simple organic molecules or modification of synthetic polymers including conjugation of peptides or drugs<sup>166-167</sup>. Moreover, a time and spatial controlled CuAAC allows an on demand “click” chemistry for stress-sensing and self-healing applications. In case of stress-sensing, a non-fluorescent alkyne and a non-fluorescent azide react to a fluorogenic product through elongation of the conjugated  $\pi$ -system *via* triazole ring formation<sup>168</sup>. CuAAC based self-healing reactions are triggered through crosslinking reactions of multivalent, fluid alkynes and azides leading to network formation and thus restoration of the materials properties (also see Chapter 1.1.6.2 and Figure 8)<sup>169</sup>. However, in both cases a proper separation of the individual click components is necessary to avoid a premature, undesired reaction. Therefore, usually encapsulation methods are used, allowing a local release and “click” reaction upon rupture of the capsules<sup>170</sup>.

Another approach is the usage of Cu(I) bis(NHC) mechanophoric catalysts. The major advantage of this method is, that the individual compounds do not have to be separated from each other (e.g. by encapsulation) since the catalyst only switches to its active form after application of an external force. Again, an inevitable requirement for a stress-induced “click” reaction is to prevent the unintended catalyst activation, meaning a premature cleavage of one of the NHC ligand in the absence of force. This cleavage would start the catalytic cycle in turn leading to stress-sensing and/or self-healing reactions that usually should have taken place after an external force led to a damage event. A possible method to prevent the unintended cleavage is the attachment of polymer chains to the NHC ligands. Considering their bulkiness and their random coil configuration in the absence of an external force, they are able to strongly increase the stability of the Cu(I) complex because they can prevent the alkyne from coordination to the Cu(I) center. Consequently, the latent catalyst does not show any activity until an external force leads to copper-carbene scission, in turn activating the catalyst by exposure of the Cu(I) center to the alkyne<sup>37-38, 94-95</sup>.

### 1.3 Lever-arm effect

The polymeric chains that are attached to a mechanophore are frequently treated as passive handles with the sole purpose to transmit an applied force to the mechanophoric bond without actively influencing the mechanophoric behavior (also see Chapter 1.1.5). However, it was pointed out that the structure of the polymer backbone might have a bigger influence on the activation behavior than assumed so far<sup>171</sup>. While this assumption was made as a result of theoretical calculations, shortly after, the working group of Craig was able to give an experimental proof for the participation of the polymer backbone on the activation efficiency of mechanophoric bonds using *gem*-dihalocyclopropanes (gDHCs)<sup>45, 172-173</sup>. gDHCs belong to the class of cyclic mechanophores and are able to undergo ring opening under mechanical stress due to their increased ring strain<sup>45, 102-104, 172-175</sup>. They can be easily incorporated into polymers by treating commercially available *cis*-poly(1,4-butadiene) (PBD) with *in situ* generated dihalocarbenes<sup>103, 124</sup>. Both, the *gem*-dibromocyclopropan- (gDBC) and the *gem*-dichlorocyclopropan (gDCC)-PBD copolymers are accessible<sup>45, 103-104, 174-175</sup>. Upon mechanical activation they are able to undergo electrocyclic ring opening, thus forming 2,3-dihaloalkenes (DHA) as shown in Figure 16a.

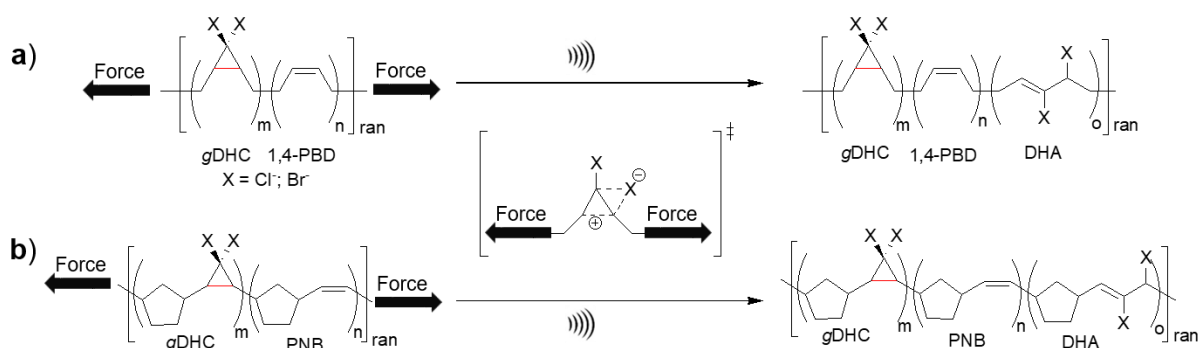


**Figure 16.** Ultrasonication of a) gDHC-modified PBD and b) gDHC-modified PNB. The applied force leads to force induced ring opening, thus generating 2,3-dihaloalkenes (DHA). Redrawn with permission from reference<sup>103</sup>.

Using AFM, the ring opening of *cis*-gDBC was found to require slightly lower forces (1210 pN) than the ring opening of *cis*-gDCC (1330 pN) (see Figure 16a)<sup>45</sup>. However, a pronounced drop in the required forces for ring opening was found when exchanging the polymer backbone from PBD to *cis*-poly(norbornene) (PNB) (> 85 % *cis* content) (see Figure 16b). Both ring opening for the *cis*-gDBC (740 pN) and the *cis*-gDCC (900 pN) occurred at forces, approximately one-third lower than their *cis*-gDBC PBD and *cis*-gDCC PBD counterparts. The lever-arm effect, exerted from the PNB scaffold positively promoted force transmission in comparison to the PBD backbone. The limited chain internal conformational changes due to the stiffer cyclopentane ring of the PNB backbone is thought to be responsible for the lever-arm effect which thus can decrease the required energy for the ring opening reaction.

This effect was not limited to the ring opening of gDHCs and was even more pronounced when ultrasound was applied to PBD ( $M_n = 384\,000$  g/mol) and PNB ( $M_n = 965\,000$  g/mol) that previously were epoxidized with *meta*-chloroperoxybenzoic acid (*m*CPBA) (50 – 80 % functionalization of the double bonds)<sup>172</sup>. The lever-arm effect exerted from the PNB backbone allowed ring opening of both the gDHCs (bond dissociation energy: 125 – 188 kJ/mol)<sup>172</sup> and the epoxide (bond dissociation energy: 271 kJ/mol)<sup>176</sup> while the transmitted force of the PBD was high enough for the ring opening of the easier cleavable gDHCs but too low to open the more stable epoxides.

### 1.4 Elastin

The lever-arm effect clearly indicates that the chosen polymeric backbone is more than a simple and passive force transmission tool. It does not simply transmit an applied force from the chain end to the mechanophoric center but can also actively influence the activation behavior. Therefore, it can be

advantageous to search for new polymers that are usable as effective force transmitters. One of the promising polymer classes for this task are shock-absorbing proteins including the proteins elastin, titin, talin and resilin<sup>177-180</sup>. Usually they are responsible for energy dissipation after appearance of mechanical stress in the human body to protect cells from damage. Elastin in particular is of note as a potential force transmitter due to its “molecular spring” behavior which is further described in detail in the following chapter<sup>181-182</sup>.

Elastin is a highly crosslinked, extracellular matrix (ECM) protein, being responsible for the elasticity and resilience of tissues that repeatedly undergo extension and retraction such as ligaments and arteries. It is also present as a minor component in other connective tissues, e.g. skin, lung or tendons that are exposed to repeated cycles of stretching and relaxation<sup>183-184</sup>. Its *in vivo* half-life time of about 70 years underscores the persistence of elastin which undergoes billions of cycles of extension and recoiling during this time without significant loss of mechanical properties<sup>185</sup>. The longevity of elastin is of great importance for mammals since its production is mostly limited to the late fetal, neonatal and early growth phase<sup>186</sup>. Upon injury and wound healing the elastin production can be reinitiated even in later years. However, the aberrant deposition of the newly expressed elastin and collagen leads to scarring due to a disrupted fiber network revealing only reduced elasticity and resilience<sup>187</sup>.

Mature elastin is synthesized from a soluble precursor, called tropoelastin, which is expressed by different cells such as smooth muscle cells, fibroblasts, endothelial cells and chondrocytes<sup>188-192</sup>. Tropoelastin is a ~70 000 g/mol polypeptide of modular structure consisting of two alternating domains, one being hydrophobic while the other is hydrophilic<sup>193-194</sup>. The latter domains are rich in *L*-lysine (Lys) and *L*-alanine (Ala) and are referred to as crosslinking domains. Crosslinking is triggered by the copper-dependent enzyme lysyl oxidase which catalyzes the oxidative deamination of  $\epsilon$ -amino groups on lysine residues leading to formation of allysine<sup>195-196</sup> (see Figure 17a).

Subsequent condensation reactions between lysine side chains and allysine occur spontaneously without further catalysis and lead to a variety of crosslinks with desmosine and isodesmosine being the most common ones (see Figure 17b). However, there are also reports about other types of Lys-based crosslinks<sup>197-199</sup>. Usually two tropoelastin molecules are involved in the formation of one crosslinking point. From one molecule two allysine residues, separated by two or three Ala moieties, undergo condensation with one allysine unit and one Lys side chain, again separated by two or three Ala residues, from the other molecule as shown in Figure 17c<sup>200</sup>.

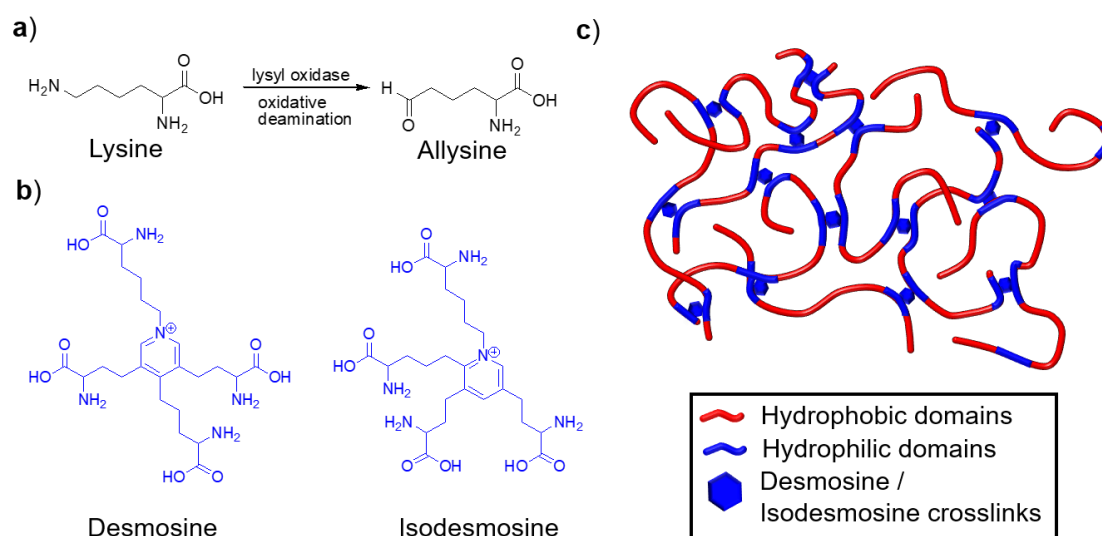


**Figure 17.** a) Oxidative deamination of lysine to allysine by the enzyme lysyl oxidase. b) The majority of crosslinking points are either desmosine or isodesmosine, originating from the condensation of one Lys side chain and three allysines which are located in the hydrophilic domains of tropoelastin. c) Usually two elastin chains are connected by one crosslinking point resulting in a highly elastic network.

Almost all Lys residues of tropoelastin are involved in the formation of crosslinks, which suggests a molecular ordering to facilitate the crosslinking process and contradicting thus the proposed random network model for elastin<sup>201</sup>. Urry *et al.* calculated in a simplified model a gelation time of  $10^{40}$  years for a random tropoelastin system to establish 20 potential crosslinks, clearly disproving the random nature of crosslinked elastin<sup>202</sup>. Hence, a previous alignment of the tropoelastin chains is necessary which juxtaposes the limited amount of potential crosslinking lysine residues<sup>203</sup>. This preorganization is achieved by the hydrophobic domains, mainly consisting of glycine (Gly), *L*-valine (Val), *L*-proline (Pro) and Ala, contributing up to 75 % of the complete protein composition<sup>194, 204</sup>. The thermoresponsive behavior of this domains, also called inverse temperature transition (ITT), leads to coacervation at body temperature<sup>205-206</sup> (also see Chapter 1.4.2.1). Below the ITT tropoelastin is randomly dispersed in aqueous solution, showing an expanded conformation with approximately 40 % local  $\beta$ -spiral structure and a large solvent-accessible surface area<sup>203, 207</sup>. When the ITT is exceeded, expulsion of hydration water leads to an increase in the molecular ordering of the tropoelastin molecules due to interaction of the exposed hydrophobic domains which in turn start to form filamentous arrays<sup>200, 203</sup>. Hydrophobic interaction mostly involves the oligopeptide repetitive sequences GVGVP, GGVP and GVGVP<sup>208</sup>. Even though the ordering of the tropoelastin chains is increasing, coacervation is an entropically driven process as the entropy gained due to the release of the hydration water overcompensates the entropy loss of the ordering process<sup>200, 203</sup>. The hydrophobic collapse also aligns the hydrophilic domains to each other in turn triggering the crosslinking reaction to form mature elastin. Above the ITT, elastin possesses a highly dynamic, compact amorphous structure with distorted  $\beta$ -strands, fluctuating turns, buried hydrophobic residues and main-chain polar groups that still can form hydrogen bonds with the surrounding water molecules<sup>207, 209-210</sup>. Coacervation is strongly influenced by protein concentration, salt concentration and to a lesser extent from the pH and is optimally tuned for physiological conditions in the ECM to take place at 37 °C, 150 mM NaCl and a pH of 7-8<sup>200, 211</sup>. The process of coacervation is fully reversible if the solution is cooled down after heating above the ITT. However, if this temperature is kept for longer times, the formed aggregates are no longer soluble due to maturation<sup>212-213</sup>.

### 1.4.1 Models for elastin elasticity

Several models were developed to explain the elasticity of elastin, which originates from the ability of the chains to recoil after they have been stretched.<sup>214-219</sup> Commonly, the elasticity of elastin is explained by entropic reasons. However, there are two different assumptions underlying the individual models. The first approach treats elastin as amorphous network which is isotropic and lacks any ordered structure, while the second approach treats elastin as anisotropic with ordered regions<sup>200, 208</sup>.

#### 1.4.1.1 Random chain model

In the random chain model<sup>216-217</sup> from Hovee and Flory elastin is seen as a typical rubber with flexible chains that are kinetically free and move randomly due to Brownian motion. Random cross links act as connection points between the single chains, resulting in an amorphous material as shown in Figure 18.

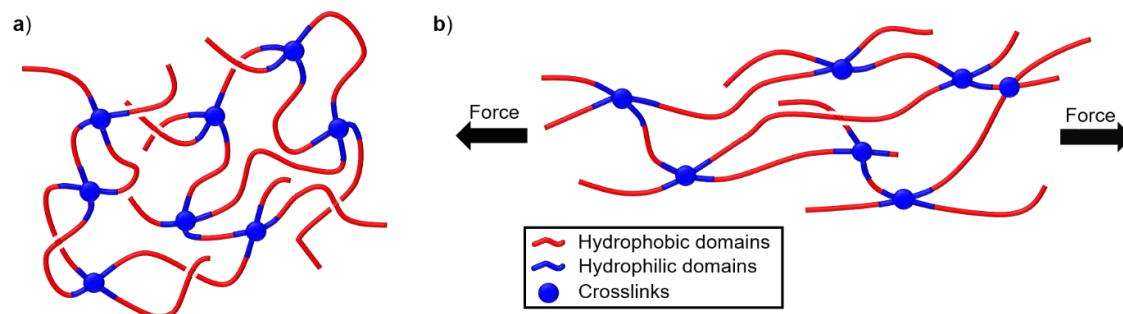


**Figure 18.** Random chain model: a) Chain segments between the randomly placed crosslinks are kinetically free and can move undirected. b) Stretching of the network forces the chains in more ordered conformations which leads to a decrease of the entropy, thus providing the restoring force and elasticity of the network.

When the network is stretched, the chains are forced in a more ordered state causing thus a partial loss of their conformational freedom. Accordingly, the entropy of the system is decreasing and the recovery to the original random coil state is the driving force for the elasticity. Several observations support the assumption that elastin can be seen as an amorphous network. First of all the amino acid sequence of elastin itself implies a randomly dispersed nature due to the high amount of Gly, being advantageous for a high degree of kinetic freedom of the chains which also has been proven by NMR-spectroscopy<sup>220</sup>. Additionally the remarkably content of Pro, which is known to be a helix breaker, also favors the free motion of the chains<sup>221</sup>. Secondly, several experimental results also indicate an amorphous structure of elastin, e.g. the presence of a glass transition typical for rubbers<sup>201, 222</sup>, the lack of birefringence during polarized light microscopy which is an indication for isotropic conformation<sup>223</sup> and the mechanical state being typical for a disordered polymer in a viscoelastic transition phase<sup>208, 224</sup>. Furthermore, experimental results obtained by Raman spectroscopy are indicative of a disordered structure<sup>225</sup>. In contrast to classical rubbers, elastin reveals elasticity solely in the presence of water while it is a brittle material in the absence of water<sup>226</sup>. The hydrophobic hydration of elastin is essential for the elasticity which differs from the classical model for rubberlike materials. Those materials usually have a one-phase network structure and any diluent present is randomly distributed within the whole material<sup>227</sup>. Nevertheless, slight modifications of the random chain model still allowed its validity. Gosline *et al.* modified the model proving the hydrophobic hydration of elastin, which leads to an additional decrease in entropy due to the ordering of water molecules around the non-polar residues of the peptide via calorimetric studies. The return to the relaxed state of the chains, accompanied by the release of the hydration water leads to an increase in entropy, providing an additional restoring force<sup>208, 228</sup>.

However, some observations are incompatible with the random chain model: Electron microscopy clearly proved the fibrous nature of elastin which indicates the necessity of order and contradicts the assumption of kinetically free and randomly moving chains<sup>203</sup>. Effective crosslinking of tropoelastin only takes place above the transition temperature in the coacervate state, again indicating an increase in molecular order which is thought to be necessary for the juxtaposition of the hydrophilic domains that consecutively form the crosslinks<sup>208</sup>. Concerns were also expressed regarding the choice of solvents that were used for most experiments. Hovee and Flory observed a decrease in the degree of swelling for elastin in pure water with increasing temperature and thus used a mixture of water and 30 % ethylene glycol to circumvent this problem.<sup>216, 229-230</sup> Using this mixture, the volume of the swollen network was no longer dependent from the temperature, however, there is some evidence that ethylene glycol might have affected the physical properties of elastin.

#### **1.4.1.2 Liquid drop model**

The liquid drop model<sup>214</sup> by Weis-Fogh and Andersen considers elastin swollen in water to be a two-phase system. Each tropoelastin molecule can be treated as a globular molecule that is crosslinked with other tropoelastin molecules as shown in Figure 19. To avoid contact with water, the hydrophobic side chains are buried in the interior of the globules with the hydrophilic parts of the tropoelastin covering them and forming the interface between the hydrophobic side chains and water. However, it was also noted that the amount of hydrophilic groups in tropoelastin is not sufficient to provide a full coverage of the globule, meaning the interface contains both hydrophilic and hydrophobic side chains. The idea of exposing the hydrophobic side chains upon stretching also was the basis for Goselines model. Even though, a random network arrangement was assumed for this model<sup>221, 228</sup>. When elastin is stretched, the globules start to deform. Consequently, they not only lose entropy due to restriction of the chains but also because of a generated restoring force originating from an increased interface between the hydrophobic groups and the solvent water.

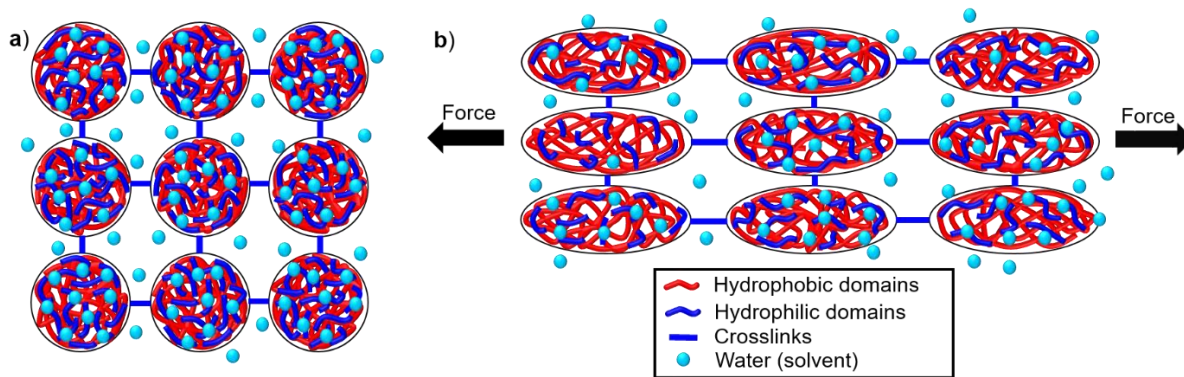


**Figure 19.** Liquid drop model: a) The hydrophobic domains are buried within the tropoelastin spheres, while the hydrophilic domains cover as much of the surface as possible. b) Stretching of the network results in deformation of the tropoelastin spheres, accompanied by an increase in their surface. Thus interaction of the hydrophobic domains with water occurs which provides an additional restoring force for elasticity<sup>208, 214</sup>.

Since the entropy loss of typical rubber materials is solely based on changes in configurational entropy, the entropy loss during stretching should be higher for elastin, according to the liquid drop model, considering these two complementary effects. Indeed, it was found that deformation of elastin in water produces heat several times larger in terms of energy than the corresponding applied mechanical work when measuring the heat exchange of elastin samples during stretching and relaxation experiments which is the consequence of the increased interfacial area between the hydrophobic domains and water. This contradicts the assumption of the random chain model that entropy loss is solely a consequence of forcing the chains in more ordered conformations<sup>231</sup>. Even though there has been some experimental evidence for the globular shape of the crosslinked domains, the elasticity mechanism based on hydrophobic interactions was rejected, mostly because the non-inclusion of hydration water of elastin. The consideration to treat elastin swollen in water as a biphasic system consisting of elastin and water is not sufficient. A more precise description would have been achieved when using a triphasic system (elastin, hydration water and solvent water). Moreover, the hydrophobic mechanism was criticized for neglecting the high mobility of the hydrophobic regions<sup>208, 231-233</sup>.

### 1.4.1.3 Oiled coil model

Gray *et al.* came up with another model termed the oiled coil model<sup>215</sup>, which basically is a modified version of the liquid drop model also focusing on the hydrocarbon-water interactions (see Figure 20).

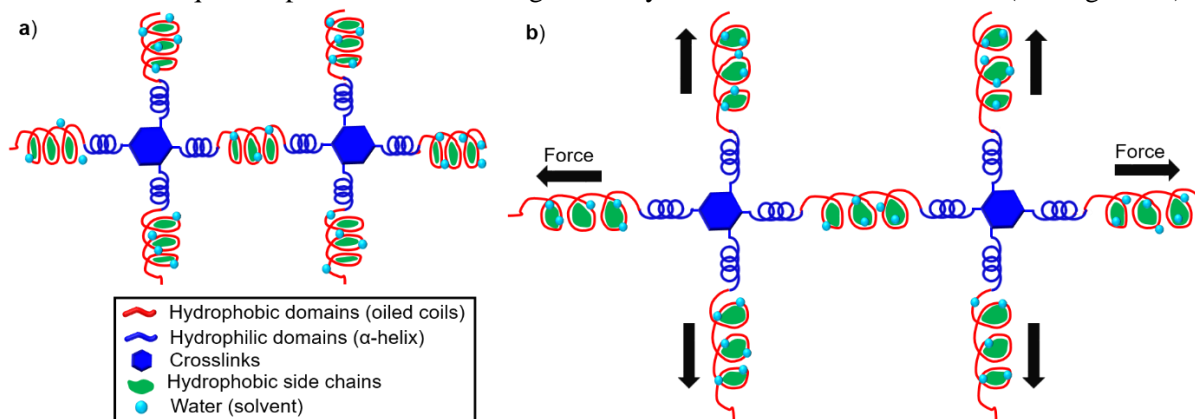


**Figure 20.** Oiled coil model: a) The surface of the oiled coils is mostly covered by Gly to minimize hydrocarbon-water interactions between the hydrophobic side chains (Val and Pro) and the solvent. b) When the network is stretched, the hydrophobic side chains are exposed to water, leading to unfavorable hydrocarbon-water interactions which provides an additional restoring force for elasticity. Only water molecules near the oiled coils are shown for better clarity<sup>208, 215</sup>.

In contrast to the liquid drop model, the oiled coil model treats the tropoelastin molecules as fibrillar instead of globular. Each fibrillar unit is build up from alternating  $\alpha$ -helical crosslinking domains being rich in Ala and Lys and broad coils being rich in Gly, Val and Pro. While former domains are hydrophilic and are responsible for the network structure and rigidity of elastin, latter domains are hydrophobic and are responsible for flexibility. The exterior of the oiled coils is occupied by Gly which forms the interface between solvent water and Pro, Val and other hydrophobic residues which are buried within the coils. When elastin is stretched, the buried hydrophobic domains are exposed to water resulting in a larger hydrocarbon-water interface and providing the restoration force which is in accordance with the liquid drop model<sup>214</sup>. Assuming the peptide backbone as the site of hydration instead of the amino side chains, the brittleness and loss of extensibility in the absence of water can be explained by this model. Nevertheless, the stationarity that is the basis of this model, meaning the return to the same conformation after each stretching and relaxation process, is incompatible with the high mobility of the hydrophobic domains. Therefore it has been rejected as well as the liquid drop model<sup>220, 232-233</sup>.

#### 1.4.1.4 Fibrillar model

The fibrillar model<sup>218, 234-238</sup>, developed by Urry *et al.* mostly relies on the experimental data that were obtained from experiments using polypeptides of short, repetitive amino acid sequences, found in the hydrophobic domains of elastin, called elastin-like polypeptides (ELPs) (for details see Chapter 1.4.2). The regular repeating amino acid sequences have been previously described by Sandberg *et al.* most commonly with Val-Pro-Gly-Val-Gly, Val-Pro-Gly-Gly and Ala-Pro-Gly-Val-Gly-Val<sup>239</sup>. Secondary structure investigation *via* NMR-spectroscopy<sup>234, 240-241</sup>, circular dichroism (CD) spectroscopy<sup>242</sup> and X-ray diffraction<sup>243</sup> revealed the formation of type-II  $\beta$ -turns between the carbonyl group of the first amino acid (Val<sub>1</sub>) and the amino group of the fourth amino acid (Val<sub>4</sub>), thus allowing Pro and Gly at the second (Pro<sub>2</sub>), respectively third position (Gly<sub>3</sub>) to form the turning point as shown in Figure 21a. The fifth amino acid (Gly<sub>5</sub>) does not contribute to the  $\beta$ -turn formation but is of high importance for the flexibility of the peptide chain.

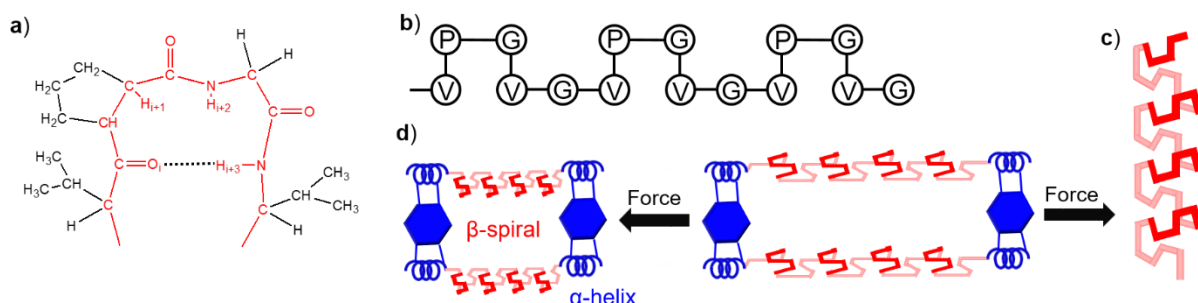


**Figure 21.** Fibrillar model: a) Type-II  $\beta$ -turn formation from the tetrapeptide sequence Val<sub>1</sub>-Pro<sub>2</sub>-Gly<sub>3</sub>-Val<sub>4</sub>. b) Schematic drawing of three consecutive  $\beta$ -turns from a (VPGVG)<sub>3</sub> sequence. c) Formation of the  $\beta$ -spiral by stacking  $\beta$ -turns. d)  $\beta$ -Spirals are crosslinked with each other by the hydrophilic domains which adopt  $\alpha$ -helical structures<sup>244</sup>.

Even though, the aforementioned results were obtained by the investigation of the cyclic polypeptides, Urry *et al.* successfully developed a linear, ring-opened helical conformation model by adjusting the torsion angles of the cyclic polypeptides<sup>218</sup>. Upon increase of the temperature, the  $\beta$ -turns start to aggregate due to hydrophobic interactions, thus forming a loose helix, also called  $\beta$ -spiral. The term spiral implies that the helix is formed from repeating units that contain intrarepeat secondary structures. Contrary, in a classical helix hydrogen bonding only occurs between repeating units. The prefix  $\beta$  clarifies that a  $\beta$ -turn is the recurring hydrogen-bonding moiety<sup>235</sup>. The stability of the  $\beta$ -spiral originates from the  $\beta$ -turns which act as spacers between each turn of the helix. Within the  $\beta$ -spiral, the  $\beta$ -turn is responsible for a downward movement of the helix and the Val<sub>4</sub>-Gly<sub>5</sub>-Val<sub>1</sub> sequence produces an upwards shift as shown in Figure 21b, 21c and 21d. The upward movement of one turn stacks with the

downward movement of the turn below, thus creating a void volume in the interior of the helix that is accessible to solvent molecules. Those solvent molecules can freely exchange with bulk water<sup>218</sup>. The Val<sub>4</sub>-Gly<sub>5</sub>-Val<sub>1</sub> sequence is kinetically free to undergo librational or rocking motions, which, together with the flexible  $\beta$ -turn, allows many states of equivalent energy and also gives an explanation for the absence of a birefringence in polarized optical microscopy<sup>235-236</sup>. The  $\beta$ -spirals are crosslinked with each other by the hydrophilic domains which adopt  $\alpha$ -helical structures. Upon stretching of the peptide chains these motions are damped, leading to a decrease in the amount of states of equivalent energy and thus providing the restoring force for elasticity. The necessity of high mobility for the peptide was proven by exchanging Gly<sub>5</sub> with Ala<sub>5</sub>. Gly<sub>5</sub> is implemented to fulfill a key role in the elastic behavior because it allows many librated states due to the absence of a side chain. Indeed, the exchange of Gly<sub>5</sub> with Ala<sub>5</sub> strongly decreased the peptides mobility due to the additional methyl group, in turn strongly decreasing elasticity<sup>235, 245</sup>. In order to further optimize hydrophobic interactions, several  $\beta$ -spirals can aggregate which explains the observation of twisted filaments that start to form above the inverse transition temperature<sup>246</sup>. While the formation of fibrils is advantageous for the  $\beta$ -spiral model since the effect on accessible configurations is minimal, the effect on a single random chain in the concentrated state is significant due to the resulting entanglements.<sup>235</sup> The assumption that elasticity originates from the  $\beta$ -spiral formation of the peptide and thus from an increase in order clearly contradicts the approach of elasticity being the result of random moving chains. Therefore, it is incompatible with the theory of rubber elasticity which is the basis for the random chain model<sup>216</sup>.

Even though the fibrillar model mostly relies on conclusions that were obtained from experiments involving ELPs and not the native elastin, it is commonly accepted due to the huge amount of experimental data that are consistent with this model. There are a lot of similarities between native elastin, its precursor tropoelastin and ELPs (for detailed description check Chapter 1.4.2). When reaching the inverse transition temperature there is an apparent increase in molecular order due to coacervation which is attributed to the formation of type-II  $\beta$ -turns<sup>247-248</sup> and which subsequently leads to fiber formation<sup>247-248</sup>. Furthermore, chemical crosslinking of ELPs results in networks whose elasticity is similar to that of native elastin<sup>249-250</sup>.

Another model developed by Tamburro *et al.* is based on  $\beta$ -turn formation involving the amino acid sequence (X-Gly-Gly)<sub>n</sub><sup>251</sup>. In compliance to Urrys model, the bend of the  $\beta$ -turn is formed by the second (X<sub>2</sub>) and third (Gly<sub>3</sub>) amino acid while hydrogen bonding occurs between the first (Gly<sub>1</sub>) and the fourth (Gly<sub>4</sub>) glycine. Due to the comparably high content of glycine the turns are intended to be much more flexible and labile compared to the (VPGVG)<sub>n</sub> sequence, thus assuming a random chain model as origin of elasticity.

#### 1.4.2 Elastin-like polypeptides

Structural investigation and characterization of native elastin remain challenging due to the complete insolubility being a result of the crosslinking process. To enable analysis of native elastin, solubilization is necessary which requires harsh methods involving either strong alkaline ( $\kappa$ -elastin) or acidic ( $\alpha$ -elastin) conditions, denaturants or enzymatic degradation. Moreover, harsh solubilization conditions may cause an enhanced fragmentation of the sequence, which is important for a proper function<sup>208, 244, 252</sup>. Another possibility is to isolate the precursor molecule tropoelastin from pigs or chicken, which were put on a copper-deficient diet directly after birth. Due to the lack of the copper-dependent enzyme lysyl oxidase, that is necessary for the crosslinking, the tropoelastin can be isolated for analysis<sup>193, 253-254</sup>. Although elastin respectively tropoelastin were produced in the past according to this method, currently recombinant peptide synthesis is the preferred synthetic pathway since it eliminates the necessity of using kilograms of animal tissue for the production of a small amount of purified protein accompanied by a much easier purification<sup>255-256</sup>. Besides recombinant peptide synthesis of elastin, the isolation of the recurring sequences Gly-Gly-Val-Pro, Val-Pro-Gly-Val-Gly and Pro-Gly-Val-Gly-Val-Ala (see Figure 22) being present in solubilized elastin was one of the key achievements since it also

opened the possibility for solid phase synthesis and solution phase synthesis of short sequences<sup>215, 239, 257-258</sup>.

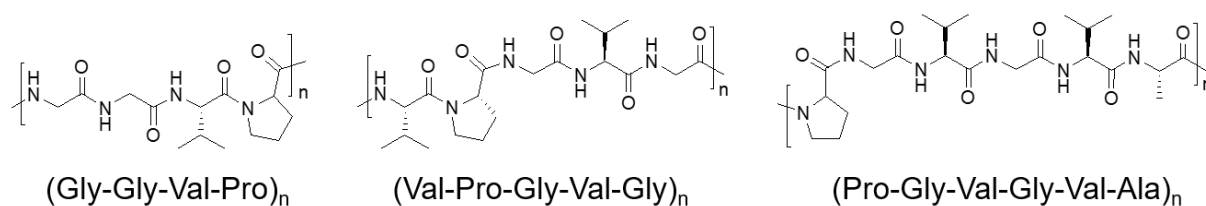


**Figure 22.** Common elastin-like polypeptide (ELP) sequences that are used to study the thermal and mechanical properties of native elastin.

The pentapeptide VPGVG is of special interest because it is recurring up to 50 times in one tropoelastin molecule, being the most repeating sequence of native elastin within the hydrophobic domains<sup>258-259</sup>. Polymerization of afore mentioned short amino acid sequences yields polypeptides that show similar thermoresponsivity and even elastic behavior (when crosslinked) compared to native elastin and are therefore called elastin-like polypeptides (ELPs)<sup>210, 248, 260</sup>. The often used ELP  $(\text{VPGVG})_n$  is soluble in water below 25 °C up to a chain length of  $n = 50$  but undergoes phase transition above 25 °C<sup>210</sup>.

#### 1.4.2.1 Thermoresponsivity

Just as native elastin, ELPs also show thermoresponsive behavior. With increasing temperature, the strength of the hydrogen bonds between the peptide chains and the hydration water gradually become weaker. When the inverse transition temperature (ITT) is reached, the majority of hydration water is released, thus exposing the hydrophobic side chains of the ELPs. Consequential, hydrophobic domains of the ELP chains can interact with each other, leading to an increase of the order and a minimized solvent accessible surface area of the ELP. Even though this leads to an increase in order, the ITT is an entropic driven process due to the gained entropy from the released hydration water<sup>200, 261</sup>.

While the thermoresponsive behavior of tropoelastin respectively crosslinked elastin in large part is predetermined by its natural amino acid sequence, the ITT of ELPs is tunable over a broad temperature range making them perfect candidates for the usage as stimuli responsive polymers. Numerous factors can be adjusted to tune the ITT of ELPs including chain length, composition and concentration<sup>262-266</sup>. For the tuning of the transition temperature, often the fourth amino acid (Gly) in the ELP sequence  $(\text{VPGVG})_n$  is replaced which is depicted as  $(\text{VPGX}_{aa}\text{G})_n$ .  $\text{X}_{aa}$  is also called guest residue and can be any amino acid except Pro which would prevent the ELP from coacervation<sup>267</sup>. If more than one amino acid is used as guest residue, usually  $\text{ELP}[\text{X}_i\text{Y}_j\text{Z}_k-n]$  is chosen as notation method. X, Y and Z are again referring to the amino acids used as guest residues while the subscripts  $i, j$  and  $k$  are indicating the ratio of the amino acids at the fourth position. The letter  $n$  refers to the number of repeating pentapeptide units. The guest residue strongly affects the transition temperature of the ELP due to changes in the hydrophobicity. In general, when decreasing the overall hydrophobicity of the ELP, the transition temperature is increasing as shown in Figure 23a. When partially exchanging the guest residue Val from  $\text{ELP}[\text{V}_5]$  with the less hydrophobic amino acids Ala and Gly ( $\text{ELP}[\text{V}_5\text{A}_2\text{G}_3]$ ) the transition temperature is increasing by ~10 °C. Further substitution of Val with Ala and Gly ( $\text{ELP}[\text{V}_1\text{A}_8\text{G}_7]$ ) leads to a further increase of the transition temperature. As mentioned previously, every amino acid except Pro can be used as guest residue and therefore a variety of ELPs with different compositions have been synthesized up do date<sup>249, 266, 268-271</sup>. Moreover, a significant dependence of the transition temperature from the molecular weight is known. When increasing the number of repetitive units the transition temperature decreases independently of the chosen guest residues as can be seen in both Figure 23a and Figure 23b. This effect is usually more pronounced for smaller molecular weights. Additionally, the concentration of the ELP in the aqueous solution plays a crucial role for the transition temperature. Figure 23b shows an increase of the transition temperature with decreasing ELP concentration. The main reason for this

behavior is thought to be the concentration dependent change of the extent of hydrophobic interactions which also influences the balance between the hydration water and bulk water<sup>263</sup>.

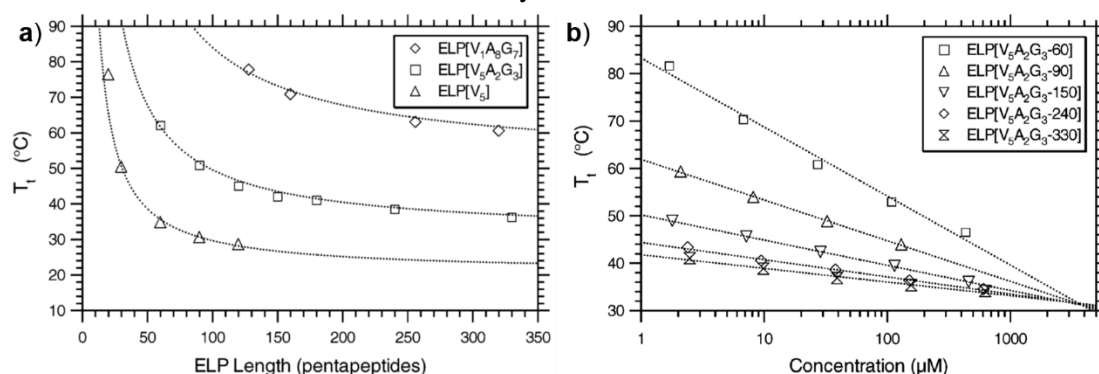


**Figure 23.** a) Chain length and composition dependency of the transition temperature of ELPs. b) Chain length, composition and concentration dependency of the transition temperature of ELPs. Increasing the chain length and increasing the concentration of the ELP in aqueous solution both lower the transition temperature while the reduction of the hydrophobicity of the guest residue increases the transition temperature. Reprinted with permission from<sup>263</sup>. Copyright (2004) American Chemical Society.

Salt addition is another parameter that can be used for the tuning of the thermoresponsive properties of ELPs. According to the Hofmeister series, salts can influence the solubility of macromolecules in solution in different ways and hence are divided into two classes known as kosmotropes and chaotropes<sup>272</sup>. Anions to the left of Cl<sup>-</sup> in the Hofmeister series (see Figure 24a) are called kosmotropes and are able to interact with the water molecules that are hydrogen bonded to the amide bonds of peptides. These interactions weaken the hydrogen bonds which results in a salting-out effect. Contrary, anions to the right of Cl<sup>-</sup> are able to directly bind to the amide bonds and are therefore called chaotropes, because they increase the protein solubility.

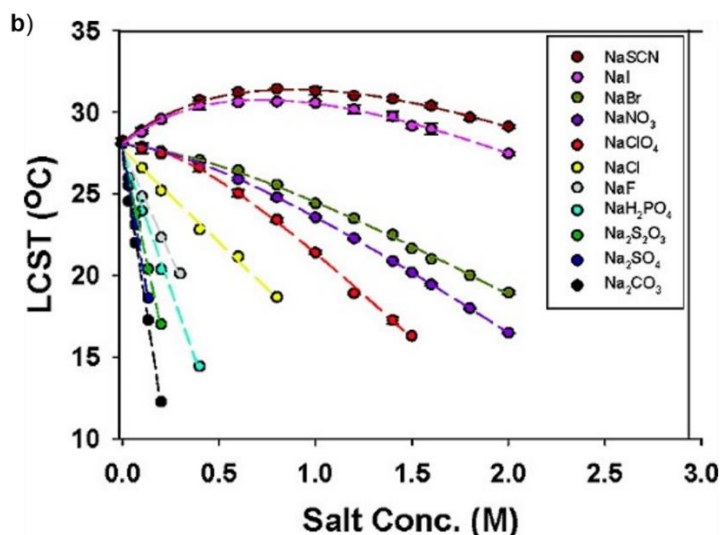
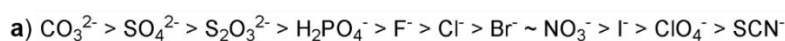


**Figure 24.** a) The Hofmeister series of the anions. b) Influence of different anions on the thermoresponsive behavior of ELP[V<sub>5</sub>-120]. Reprinted with permission from reference<sup>273</sup>. Copyright (2008) American Chemical Society.

Figure 24b shows the influence of eleven different anions on the thermoresponsive behavior of ELP[V<sub>5</sub>-120] with an transition temperature of 28 °C in pure water. The kosmotropic anions (F<sup>-</sup>, Cl<sup>-</sup>, H<sub>2</sub>PO<sub>4</sub><sup>-</sup>, S<sub>2</sub>O<sub>3</sub><sup>2-</sup>, SO<sub>4</sub><sup>2-</sup> and CO<sub>3</sub><sup>2-</sup> follow the Hofmeister series by decreasing the solubility of the peptide due to weakening of the hydrogen bonds thus leading to a nearly linear decrease of the transition temperature

in the tested concentration range. Contrary, chaotropes ( $\text{SCN}^-$ ,  $\text{I}^-$ ,  $\text{ClO}_4^-$ ,  $\text{Br}^-$ ,  $\text{NO}_3^-$ ) show nonlinear behavior since they increase the solubility of the ELP at low concentrations but also show salting-out at higher concentrations. At lower salt concentrations the chaotropic anions are unable to polarize the hydration water molecules and thus directly bind to the amide moieties which act as dipoles in turn preventing the hydrophobic collapse. Further increasing the concentration of the chaotropes caused a destabilization of the hydrophobic hydration shell which leads to a depression of the transition temperature<sup>273</sup>.

The incorporation of the pH sensitive amino acids glutamic acid (Glu) (ELP[V<sub>1</sub>I<sub>3</sub>E<sub>1</sub>-160]) and histidine (His) (ELP[V<sub>1</sub>H<sub>2</sub>G<sub>1</sub>A<sub>1</sub>-120]) as guest residues also offers the possibility to trigger phase transition of an ELP by changing the pH<sup>271, 274</sup>.

### 1.4.2.2 Elasticity

Crosslinking of ELPs results in networks whose elastic behavior is comparable to that of native elastin<sup>275</sup>. Similar to the thermoresponsivity, there is little scope when tuning the mechanical properties of native elastin since they are mostly predetermined by the natural amino acid sequence as well as the desmosine and isodesmosine crosslinks. However, two external parameters that can be used for the tuning of mechanical properties of native elastin are the temperature and the hydration level. Both parameters are in close dependence from each other<sup>276</sup>. In contrast, variations in the molecular weight of ELPs, the incorporation of different guest residues ( $X_{\text{aa}}$ ) or the variation of the crosslinking density as well as the structure of the crosslinker can be used to synthesize networks with different mechanical properties specifically tailored for their applications<sup>249</sup>. Because the ITT is preserved in the crosslinked ELPs, temperature and the level of hydration can also be used for further adjustment of the mechanical properties<sup>249-250</sup>. Crosslinking of ELPs commonly is realized by the incorporation of amino acids bearing functional groups in their side chain at the guest residue position  $X_{\text{aa}}$ . Lys<sup>249-250, 277-278</sup> or Glu<sup>277</sup> are frequently used for this purpose, allowing subsequent amidation reactions. Besides amidation, several other crosslinking strategies involve reaction with isocyanates<sup>219, 279</sup>, photoinitiation<sup>280</sup>,  $\gamma$ -irradiation<sup>277, 281-282</sup>, enzymes<sup>283</sup> or peroxides<sup>277</sup>. The usage of elastin-based block copolymers also allows the formation of physically crosslinked networks above their ITT<sup>284-285</sup>.

Beyond the crosslinking of ELPs *via* the guest residue  $X_{\text{aa}}$  other approaches were developed. Desai *et al.* used the amino group from the *N*-terminus as well as an amino modified *C*-terminus from three different ELPs (VPGVG)<sub>n</sub> with varying chain lengths (21 100 g/mol (V50CK1), 31 400 g/mol (V75CK1) and 41 700 g/mol (V100CK1)) for crosslinking reactions with a tetravalent polyethylene glycol (PEG) bearing terminal *N*-hydroxysuccinimide (NHS) ester groups<sup>278</sup>. The obtained isotropic, homogeneously crosslinked networks showed excellent elasticity with maximum strains up to ~1500 % and linear elasticity up to 1100 % (see Figure 25a).

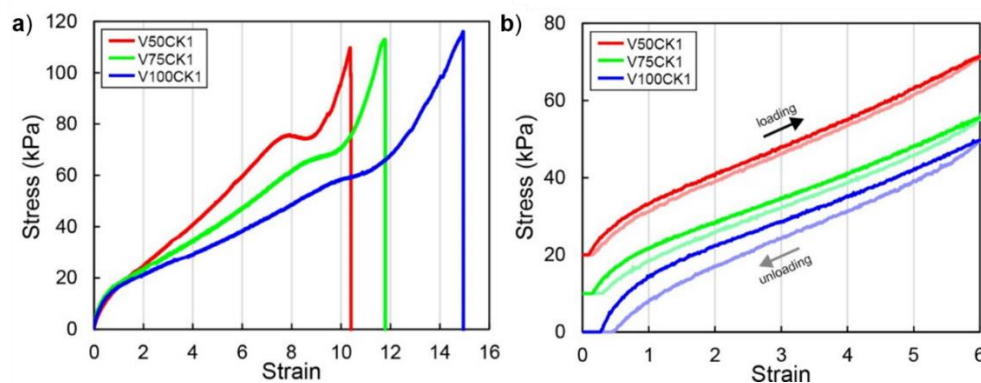


**Figure 25.** a) Stress-strain curves for the three hydrogels show an increase in the maximum strain with increasing ELP size. b) The energy recovery in cyclic tensile tests increases with decreasing ELP length. The curve for V50CK1 is shifted by 20 kPa and the curve for V75CK1 is shifted by 10 kPa for better clarity. Reprinted with permission from literature<sup>278</sup>. Copyright (2016) American Chemical Society.

The ultimate tensile stress for all three networks was similar with a maximum value of around 100 kPa, while the rupture event happened at different strains. V50CK1 disrupted first at 1030 %, V75CK1 as second at 1210 % and V100CK1 as the last one at 1440 %. The elastic moduli were also quite similar with values around 19 kPa. Because at low strains the applied stress is borne by unraveling of entangled chains and inter/intra-chain interactions the elastic moduli are nearly indistinguishable at the beginning of the tensile test. However, due to shorter chain lengths, unraveling was faster accomplished for V50CK1 and C75CK1 compared to V100CK1. Thus the region of nonlinear deformation, where the applied stress directly falls on the chains and crosslinks is reached earlier for the network with the shortest chains (V50CK1), followed by the network with the medium chain length (V75CK1) and ultimately for the network with the longest chain length (V100CK1). Cyclic tensile tests within the linear elastic region of the networks also revealed high resilience and low stress softening for all three networks (see Figure 25b). The hysteresis increased with increasing chain length (94 % recovery for V50CK1, 88 % recovery for V75CK1 and 83 % V100CK1) which was attributed to the increased hydrophobic chain interactions for longer chain lengths.

Using atomic force microscopy (AFM) Urry *et al.* were also able to prove single chain elasticity for a Cys-(VPGVG)<sub>251</sub>-Cys ELP by fixing a single chain between a gold coated surface and a gold coated AFM tip further proving the “molecular spring” behavior of ELPs<sup>244</sup>.

### 1.4.2.3 Applications

Besides their thermoresponsive and elastic behavior, several other properties like biocompatibility and low immunogenicity are exploited, making ELPs to suitable candidates for biomedical applications and an alternative to synthetic polymers such as polyethylene glycol<sup>286-287</sup>. The synthesis of monodisperse ELPs with specified chain lengths *via* gene expression allows exact tuning of the plasma half-life of the ELP as well as its route and rate of clearance<sup>288-289</sup>. The incorporation of amino acids bearing functional groups in their side chains allow subsequent conjugation of drugs<sup>290</sup>, imaging agents<sup>291-292</sup> or bioactive ligands<sup>293-294</sup>. As ELPs are composed of natural occurring amino acids, a high biocompatibility<sup>295</sup>, low immunogenicity<sup>296</sup> and an enzymatically degradation is given<sup>297</sup> leading to nontoxic degradation products<sup>298</sup>. Application of ELPs involves both linear and crosslinked ELPs, depending on the type of application.

Conjugation of drugs to linear ELPs is usually performed to increase the circulation rate of a drug in the body by either increasing the hydrodynamic radius of the drug and thus reduce the renal clearance rate or to avoid enzymatic degradation of the drug by a shielding effect, exerted from the conjugated polymer<sup>299-300</sup>.

Furthermore, conjugation is a common method to increase the solubility of hydrophobic drugs<sup>301</sup> or to increase the cellular uptake by the linkage of cell penetrating peptides (CPP)<sup>302</sup>.

For tumor therapy conjugation of ELPs to drugs is used due to the enhanced permeability and retention (EPR) effect leading to increased accumulation of the ELP-drug conjugate in the tumor, an effect that is further amplified through the thermoresponsive behavior of the conjugate during externally focused hyperthermia of the tumor<sup>292, 303</sup>.

Exploitation of the ELPs thermoresponsivity is also possible by incorporation of drugs into ELP-nanoparticles<sup>274, 304</sup> or coacervates<sup>299</sup>. When injected into the body, ideally, the ITT is exceeded and the drug is incorporated and steadily released from the formed nanoparticles, respectively the coacervate thus acting as a drug depot.

The thermoresponsive behavior of linear ELPs can also be exploited for protein purification, termed inverse transition cycling (ITC)<sup>288, 305</sup>. Fusion of an ELP tag to the target protein at the gene level allows separation from the cell lysate by centrifugation when exceeding the ITT as shown for several peptides including chloramphenicol acetyltransferase (CAT), blue fluorescent protein (BFP), thioredoxin (Trx), calmodulin (CaM) and green fluorescent protein (GFP)<sup>306-307</sup>. Incorporation of a thrombin cleavage

site<sup>306</sup> or an intein sequence<sup>308-309</sup> between the target protein and ELP subsequently allows cleavage of the ELP which in turn can be removed by another ITC to obtain the target peptide with high purity. Application of crosslinked ELPs mostly involves the usage as scaffolds for tissue engineering which is reasonable because elastin is a substantial part of the ECM and is thus an appropriate matrix-replacement for cells and tissues to grow<sup>288, 310</sup>. Even though ELP coacervates<sup>311</sup> and physically crosslinked ELPs<sup>312</sup> are used for tissue engineering, their applicability is often limited due to the lack of the required mechanical strength. Contrary, chemical crosslinking of ELPs allows precise tuning of the mechanical properties of the scaffold in the range of 1 – 1000 kPa<sup>313</sup>. However, non-toxicity and solubility of the chosen crosslinker in aqueous solution has to be considered<sup>288, 314</sup>. Besides biocompatibility of the ELP-matrix, proper cell adhesion is necessary to guarantee cell growth which commonly is realized by incorporation of the cell recognition motif RGD (arginine-glycine-aspartic acid)<sup>315</sup>. Up to now, ELPs with different mechanical properties have been synthesized for tissue engineering of small diameter vascular grafts<sup>316-317</sup>, cartilaginous repair<sup>283</sup>, hepatic tissue repair<sup>318</sup>, epithelial cell growth for ocular surface transplantations<sup>319</sup> and for stem cell differentiation<sup>320</sup>. ELPs were also successfully used for the production of cell sheets meaning the culturing of cells on a surface in the absence of a scaffold. The formed cell sheet with ECM subsequently can be transplanted to a host tissue<sup>321</sup>.

## 2 Aim and concept

### 2.1 Scope of the thesis

Aim of this thesis was the development of peptide functionalized latent Cu(I) bis(*N*-heterocyclic carbene) (NHC) catalysts that could be activated by a mechanical force (see Figure 26a), thus offering the possibility for a time and spatial controlled copper(I)-catalyzed alkyne-azide “click” reaction (CuAAC). Incorporation into biological systems might enable the detection of stress by exploitation of the force induced CuAAC. The force transmission should be realized by the attached elastin-like polypeptide (ELP) sequences which are known for their ability to adopt a  $\beta$ -spiral structure in turn acting as “molecular springs”<sup>244</sup>.

The incorporation of several Cu(I) centers into one peptide chain should be done to achieve chain-extended catalysts which bear the ELP “molecular spring” motif as repetitive unit between the mechanophoric linkages (see Figure 26b). The mechanophoric activity of these complexes should be probed *via* ultrasonication which is a common tool for application of force in solution, thus triggering a stress-induced CuAAC of terminal alkynes and azides. The application of biomimetic ELP sequences, capable of adopting the  $\beta$ -spiral thus might be a promising way to further study force transmission since the resulting structures could be exploited as “molecular springs”.

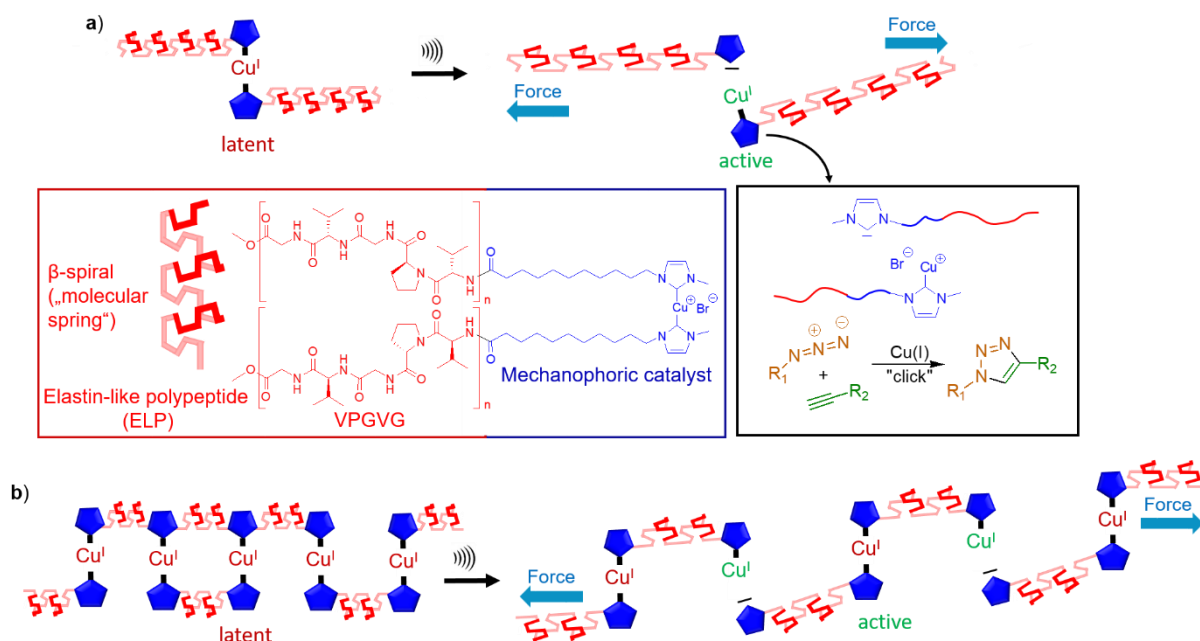


**Figure 26.** a) “Molecular spring” bearing latent Cu(I) bis(NHC) mechanocatalysts are able to adopt  $\beta$ -spirals *via* their ELP sequences for an optimized force transmission to the labile copper-carbene bond: Cleaving one shielding NHC-ligand activates the catalyst and thus triggers the CuAAC in a time and spatial controlled manner. b) Chain-extended mechanocatalysts incorporate the “molecular spring” motif between several Cu(I) bis(NHC) centers.

In order to test the activation behavior in the solid state, a barbiturate modified mechanocatalyst (devoid of a peptide sequence) should be prepared and incorporated into a barbiturate modified matrix to combine the mechanochemical stress-sensing and supramolecular self-healing behavior. Barbiturates are well known motifs to establish a reversible cluster formation *via* their hydrogen bonds<sup>322-324</sup> enabling a multiple restoration of the origin material stiffness by reforming the clusters after occurred damage by e.g. compressional forces as shown in Figure 27. Moreover, the destruction of eventually formed supramolecular clusters may dissipate parts of the rupture energy and can prevent thus the materials from further damage.

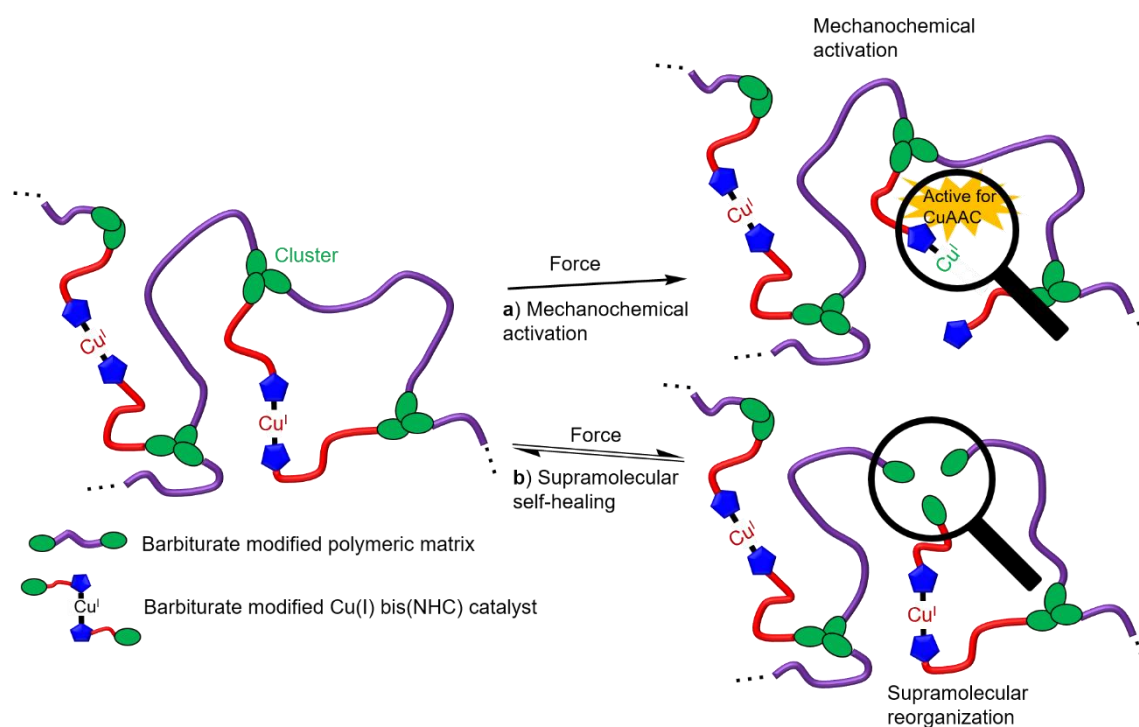


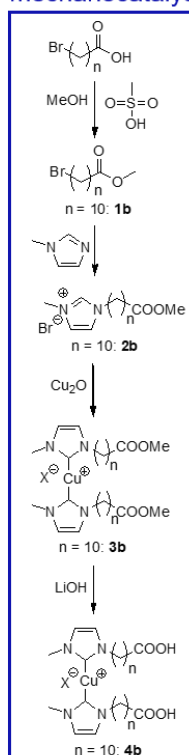
**Figure 27.** Incorporation of a barbiturate modified latent Cu(I) bis(NHC) catalyst into a barbiturate bearing polymeric matrix to investigate the activation behavior of the mechanocatalyst in the solid state. Compression can either lead to the a) activation of the catalyst, thus triggering the time and spatial controlled CuAAC or to b) breakage of supramolecular bonds.

Finally, a mechanophoric catalyst should be chemically crosslinked into an elastin network to investigate the mechanoactivity within the formed hydrogels. Crosslinking points can further increase the activation efficiency of the mechanocatalysts because they are able to redirect the applied force. Therefore, the perpendicular parts of the force can be used to also activate differently aligned mechanophores in turn increasing the catalytic activity<sup>126, 141</sup>.

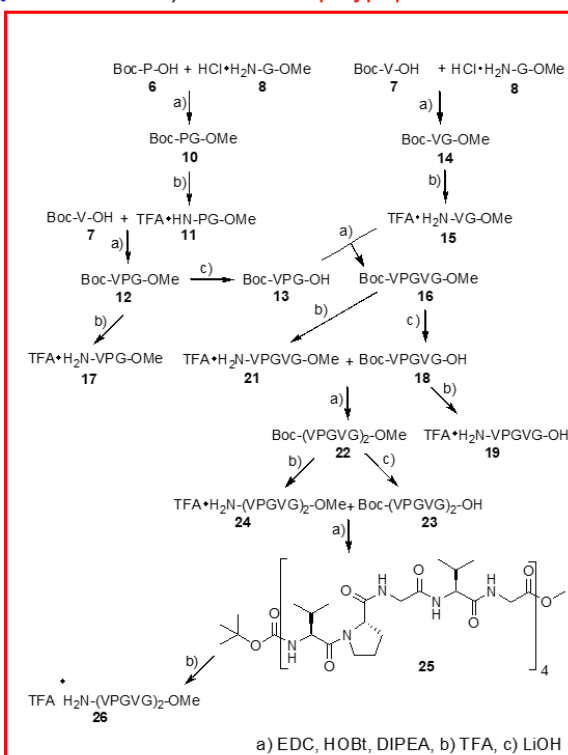
## 2.2 Concept

The synthetic approach for the peptide-based mechanocatalysts is shown in Scheme 1. The combination of a Cu(I) bis(NHC) complex and the ELPs requires the synthesis of a carboxyl functionalized latent mechanocatalyst  $[\text{Cu}(\text{C}_{10}\text{COOH-NHC})_2]\text{X}$  (**4b**) (see Scheme 1-I) which allows a subsequent peptide coupling with the *N*-terminus of peptides. Ideally, the complex should be built up symmetrically with two carboxyl groups to guarantee a positioning of the mechanophoric bond in the midpoint of the chain which is crucial for an efficient activation (see Chapter 1.1.5). Previously, the polymeric handles were attached to the NHC precursors and subsequently transformed to the Cu(I) bis(NHC) catalysts by means of a strong base and coordination to a copper(I) salt<sup>37-38, 95</sup>. However, this turns out as an unsuitable method for macroligands bearing a large amount of reactive functional groups, like amines or peptides, due to their inherent reactivity towards bases. The direct incorporation of functional groups into the NHC precursors will allow the initial synthesis of a low molecular weight catalyst which will lower the impact of side reactions. A subsequent attachment of the different peptide chains *via* peptide coupling will yield the polymeric mechanophore, thus offering much more variability in the design of the catalysts. Furthermore, the synthesis of an amine functionalized catalyst  $[\text{Cu}(\text{C}_3\text{NH}_2\cdot\text{TFA-NHC})_2]\text{X}$  (**34**) (see Scheme 1-III) will allow the synthesis of chain-extended mechanocatalysts **35b** by incorporation of the ELP sequence  $\text{H}_2\text{N-VPGVG-OH}$  (**19**) between **4b** and **34**.

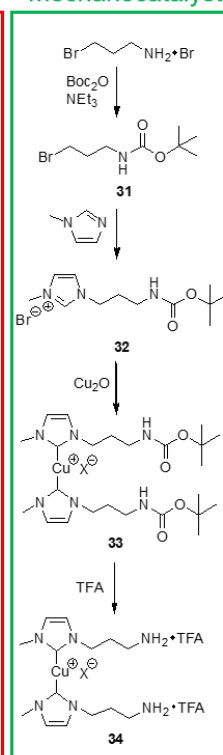
I) COOH-  
mechanocatalyst



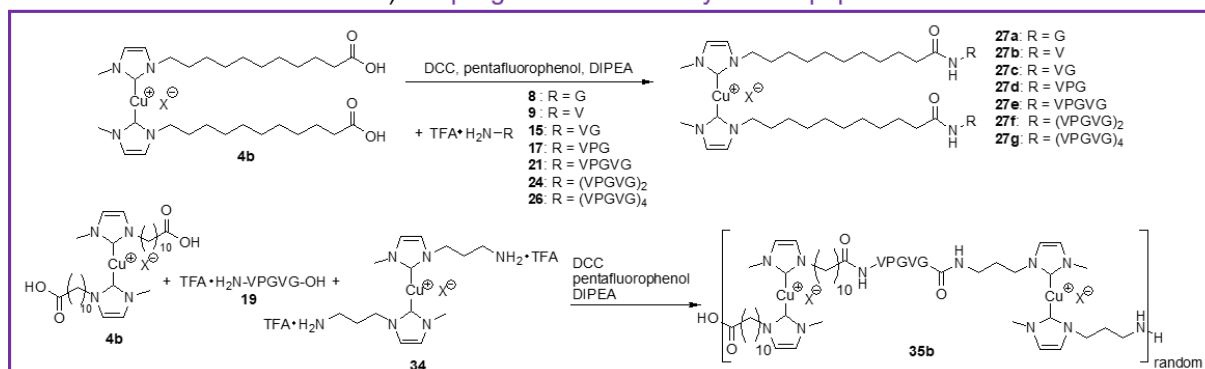
II) Elastin-like polypeptide



III) NH2-  
mechanocatalyst



IV) Coupling of mechanocatalysts with peptides



**Scheme 1.** Synthetic approach to the peptide modified latent Cu(I) bis(NHC) complexes. Both low molecular weight complexes (**4b** and **34**) are synthesized from the respective methyl ester- (**3b**) or Boc-protected (**33**) imidazolium precursor (**2b** and **32**) using the Cu<sub>2</sub>O method and are afterwards deprotected. The ELP sequence is build up using common peptide coupling agents (EDC•HCl, HOBT) and the Boc- and methyl ester groups as orthogonal protection groups. Linkage of the peptides to the mechanocatalyst is realized *via* coupling of the *N*-terminus to the carboxyl groups from **4b**, thus generating mechanocatalysts **27a-g**. Polycondensation of **4b**, **34** and the double deprotected pentapeptide **19** generates a chain-extended catalyst **35b** with multiple Cu(I) centers.

Mechanocatalysts **4b** and **34** will be synthesized from the corresponding imidazolium precursors with Cu<sub>2</sub>O as both internal base and copper(I) source as once. Since protection of the respective functional groups is necessary for a successful synthesis, the obtained catalysts need to be Boc- (**33**) or methyl ester deprotected (**3b**) before the coupling with peptides. The ELP sequence is build up in solution using common peptide coupling protocols<sup>257</sup> and the aforementioned protection group strategy (Boc- and methyl ester), thus allowing sequence specific synthesis of different peptides up to Boc-(VPGVG)<sub>4</sub>-OMe (**25**) (see Scheme 1-II). A variety of peptides (H<sub>2</sub>N-G-OMe (**8**), H<sub>2</sub>N-V-OMe (**9**), H<sub>2</sub>N-VG-OMe (**15**), H<sub>2</sub>N-VPG-OMe (**17**), H<sub>2</sub>N-VPGVG-OMe (**21**), H<sub>2</sub>N-(VPGVG)<sub>2</sub>-OMe (**24**), H<sub>2</sub>N-(VPGVG)<sub>4</sub>-OMe (**26**)) with different chain lengths will be coupled to mechanocatalyst **4b**, thus generating mechanophores **27a-g** (see Scheme 1-IV). Hence, the influence of the increasing molecular

weight of the attached peptide on the mechanophoric activity can be probed. Furthermore, only mechanocatalysts **27e-g** bear peptide sequences that are capable of  $\beta$ -spiral formation while mechanocatalysts **27a-d** cannot show “molecular spring” behavior. The mechanocatalytic activity of the obtained complexes will be tested in solution by using a model CuAAC “click” reaction of phenylacetylene (**28**) and benzyl azide (**29**).

For the solid state experiments mechanocatalyst **42** is synthesized by coupling of an amino modified barbiturate **41** to mechanocatalyst **4b** (see Figure 28a). The mechanochemical activation in bulk will be probed *via* a fluorogenic “click” reaction of the non-fluorescent 3-azido-7-hydroxycoumarin (**43**) with phenylacetylene (**28**) which generates the highly fluorescent 7-hydroxy-3-(4-phenyl-1*H*-[1,2,3]triazole-1-yl)-coumarin dye (**44**) (see Figure 28b).

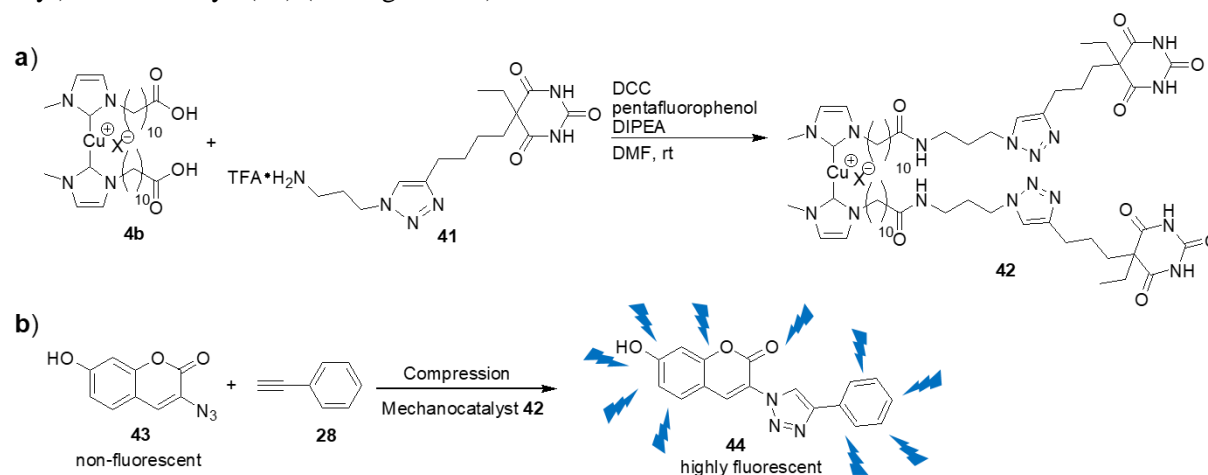


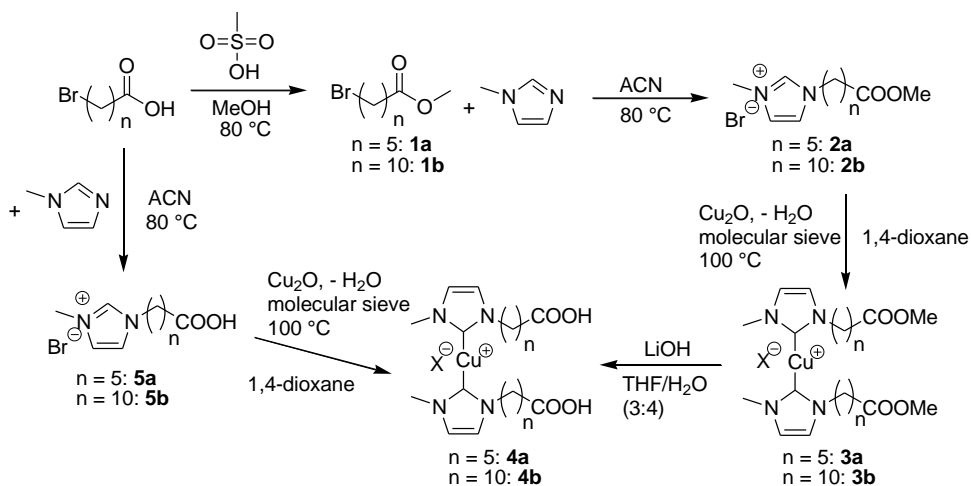
**Figure 28.** a) Synthesis of the barbiturate modified mechanocatalyst **42**. b) Activation of the latent catalyst **42** in bulk leads to the fluorogenic “click” reaction of the non-fluorescent 3-azido-7-hydroxycoumarin (**43**) with phenylacetylene (**28**) which generates the highly fluorescent 7-hydroxy-3-(4-phenyl-1*H*-[1,2,3]triazole-1-yl)-coumarin dye (**44**).

Finally, mechanocatalyst **34** and the non-fluorogenic dye **43** are chemically crosslinked into a commercially available solubilized elastin. The thus generated hydrogels will be tested for their mechanical properties as well as for their mechanochemical activation behavior.

### 3 Results and Discussion

#### 3.1 Synthesis and characterization of the COOH-functionalized mechanocatalysts (4)

In a first step, two Cu(I) bis(NHC) complexes were synthesized in a four step synthesis, bearing two carboxylic acid moieties which only differed in their alkyl chain length ( $n = 5$ , **4a** and  $n = 10$ , **4b**). The carboxyl functionalization was of high importance since it allowed subsequent coupling reactions with the *N*-terminus of peptides. Due to the bifunctionality of the catalyst a positioning of the mechanophoric bond in the midpoint of the chain was also possible, which was crucial for an efficient activation (also see Chapter 1.1.5)<sup>129, 135</sup>. The synthetic approach was similar for both complexes as apparent from Scheme 2, therefore only the details for the synthesis of **4b** are described (for **4a** see Experimental Part 4.2).



**Scheme 2.** Synthetic pathway for the synthesis of the two mechanophoric catalysts **4a** and **4b** bearing two carboxyl groups.

First, 11-bromoundecanoic acid was refluxed in methanol in the presence of catalytic amounts of methanesulfonic acid in turn yielding the 11-bromoundecanoic acid methyl ester (**1b**). The subsequent quaternization reaction was performed with *N*-methylimidazole and generated the NHC precursor **2b** in quantitative yields which in turn was able to act as ligand for the desired Cu(I) bis(NHC) complexes. For deprotonation and complexation, Cu<sub>2</sub>O was chosen as internal base and Cu(I) source at once<sup>325</sup>, thus yielding the mechanophoric complex [Cu(C<sub>10</sub>COOMe-NHC)<sub>2</sub>]X (**3b**) with a yield of 41 %. The commonly used method for complex formation involving strong bases such as potassium bis(trimethylsilyl)amide (KHMDs) (pK<sub>a</sub>(water) = 26<sup>326</sup>) or sodium *tert*-butoxide (pK<sub>a</sub>(water) = 19<sup>327</sup>) could not be applied due to the lability of the methyl ester protection group under basic conditions<sup>37</sup>. While a synthesis of the Cu(I) bis(NHC) complexes using the aforementioned bases usually can be performed at room temperature, reaction with Cu<sub>2</sub>O only proceeds at higher temperatures. Therefore, synthesis of the complexes was accomplished at 100 °C. Finally, lithium hydroxide was used for deprotection of **3b**, thus quantitatively yielding the carboxyl-functionalized catalyst [Cu(C<sub>10</sub>COOH-NHC)<sub>2</sub>]X (**4b**). In contrast to catalyst **3b**, the yield for complex **3a**, bearing the shorter alkyl chain, was reduced to 9 % (41 % for **3b**). Therefore, following reactions were performed with mechanocatalyst **4b**. To facilitate the reaction, it was also attempted to directly quaternize the unprotected 6-bromohexanoic acid, respectively the unprotected 11-bromoundecanoic acid. While these reactions proceeded quantitatively to the NHC precursors **5a** and **5b** (for details see Experimental Part 4.2.5 and Appendix 7.1), the subsequent Cu(I) bis(NHC) formation had very poor yields (< 5 %) and therefore was neglected. A possible reason for the low conversions might be the complexation of the Cu(I) to the free carboxyl groups which prevented the formation of the Cu(I) bis(NHC) complexes<sup>328-329</sup>.

The successful synthesis of complex **4b** was proven by comparing the <sup>1</sup>H-NMR spectrum of the imidazolium precursor **2b** (Figure 29a) with the <sup>1</sup>H-NMR spectrum of the protected catalyst **3b**

(Figure 29b) and deprotected catalyst **4b** (Figure 29c). A full characterization of all compounds is given in the Experimental Part 4.2, while the according spectra are presented in the Appendix 7.1.

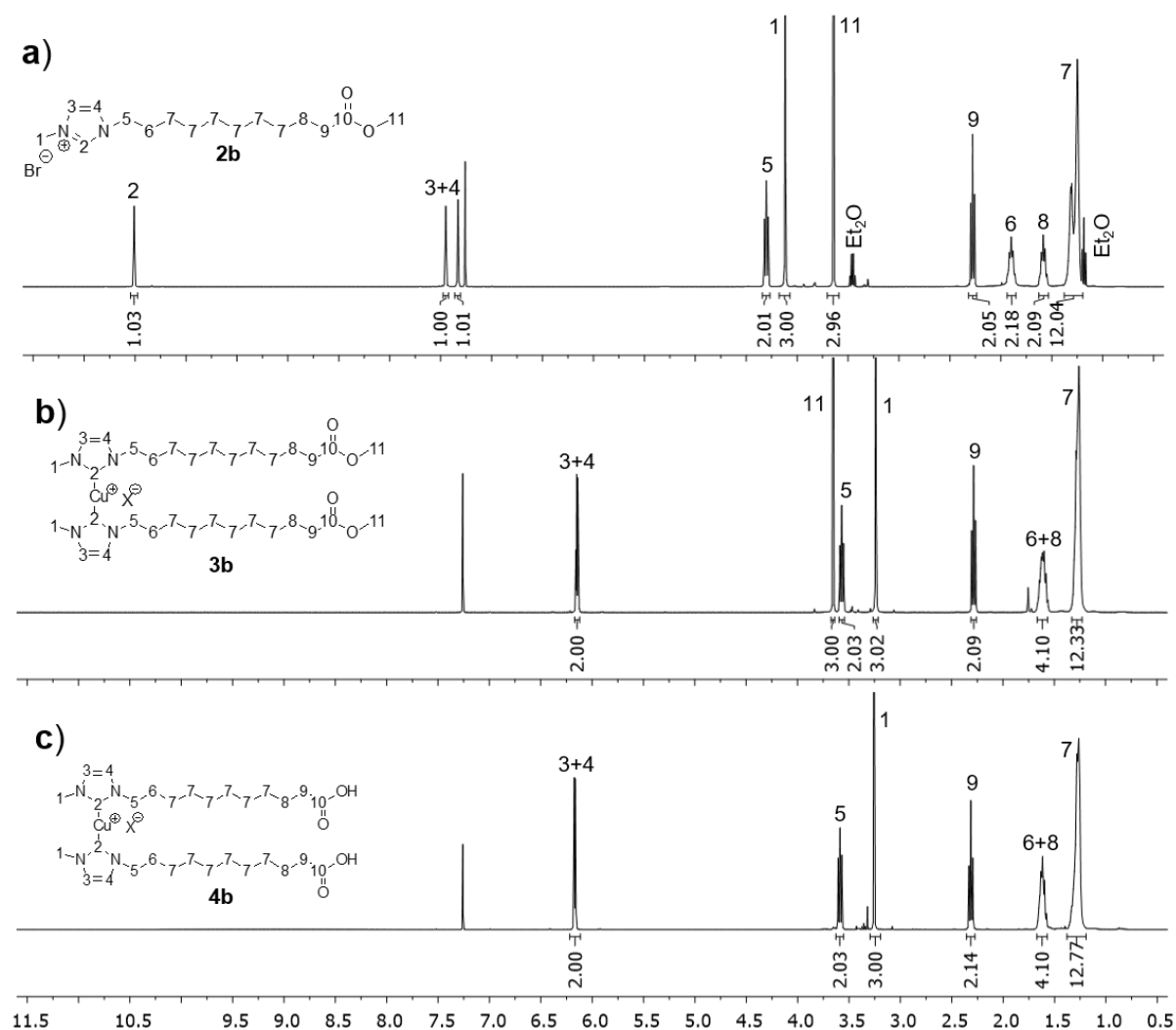


**Figure 29.**  $^1\text{H-NMR}$  spectra of a) the NHC precursor **2b**, b) the methyl ester protected complex **3b** and c) the deprotected complex **4b** bearing two carboxyl groups.

The absence of proton resonances  $H_2$  ( $-\text{NCHN}-$ ) at 10.51 ppm from precursor **2b** to complex **3b** together with the significant shift of protons  $H_3$  and  $H_4$  ( $-\text{NCH}=\text{CHN}-$ ) from 7.45 and 7.33 ppm to 6.15 ppm proved the successful deprotonation and formation of the Cu(I) bis(NHC) complex **3b** and was thus in good compliance with literature<sup>94</sup>. Comparison of these  $^1\text{H-NMR}$  spectra with the  $^1\text{H-NMR}$  spectrum from the deprotected catalyst **4b** revealed the successful removal of the protection group due to the absence of protons  $H_{11}$  ( $-\text{C}(\text{O})\text{OCH}_3$ ), while the signals  $H_3$  and  $H_4$  ( $-\text{NCH}=\text{CHN}-$ ) stayed unaffected. Together with the absence of  $H_2$  ( $-\text{NCHN}-$ ) at 10.51 ppm it could be shown that no decomposition, followed by reprotonation of the complex took place. Successful deprotonation and formation of the copper-carbene bond could also be proven *via*  $^{13}\text{C-NMR}$  spectroscopy due to a pronounced shift of  $C_2$  ( $-\text{NCHN}-$ ) from  $\delta = 137.8$  to  $\delta = 153.2$  ppm which was in accordance with literature<sup>37</sup> (see Appendix 7.1).

Additionally, a histidinium based mechanocatalyst (**55**) was synthesized for two reasons. First, since *L*-histidine possesses a carboxyl and an amino group, this catalyst allowed even more flexibility since coupling of the *N*- as well as the *C*-terminus of peptides would be possible. Second, the influence of the substitution pattern (1,3-substitution for imidazolium and 1,3,4-substitution for histidinium) on the mechanophoric activity should be tested. However, this catalyst did not show mechanoresponsivity and

therefore was not investigated in detail. The synthetic approach of this catalyst as well as the conducted ultrasonication experiments are shown in the Experimental Part 4.16.

### 3.2 Synthesis and characterization of the elastin-like polypeptide sequence

#### 3.2.1 Synthesis and characterization of the Boc-VPGVG-OMe sequence (16)

In a next step, the elastin-like polypeptide (ELP) sequence had to be synthesized, which in turn could be coupled to the mechanophoric catalyst  $[\text{Cu}(\text{C}_{10}\text{COOH-NHC})_2]\text{X}$  (**4b**) for chain extension. Therefore, the pentapeptide sequence Val-Pro-Gly-Val-Gly (VPGVG) was chosen since it is the most prominent amino acid sequence within the hydrophobic domains of native elastin<sup>239, 330</sup>. Accordingly, it is one of the best investigated ELP sequences which was also used for the development of Urrys fibrillar model<sup>218, 234-238</sup>. The excellent elastic properties of the VPGVG sequence originate from its ability to adopt a  $\beta$ -spiral as a result of consecutive stacking type-II  $\beta$ -turns, formed from every pentapeptide unit (see Chapter 1.4.1.4). Formation of the  $\beta$ -spiral allows elastin to behave like a “molecular spring”<sup>244</sup> under influence of an external force and thus is thought to be an ideal force transmitter for the activation of mechanophoric catalysts.

Starting from the single, unprotected amino acids the peptide sequence was built up *via* solution phase peptide synthesis (SPPS) following common coupling protocols<sup>257</sup>. The *tert*-butoxycarbonyl (Boc)<sup>331</sup> protection group was used for the *N*-terminus, while the *C*-terminus was methyl ester (OMe)<sup>332</sup> protected to assure an orthogonal protecting group strategy. One of the major advantages of the Boc-group is its residue-free, selective cleavage under acidic conditions with trifluoroacetic acid (TFA), leading to the release of carbon dioxide and isobutylene. Contrary, the *C*-terminus could be selectively deprotected under basic conditions using lithium hydroxide. Since the next coupling step with a methyl ester protected amino acid, respectively Boc-protected amino acid generated a Boc- and methyl ester protected peptide, unintended side reactions could be avoided as shown in Figure 30, thus allowing synthesis of sequence specific peptides.

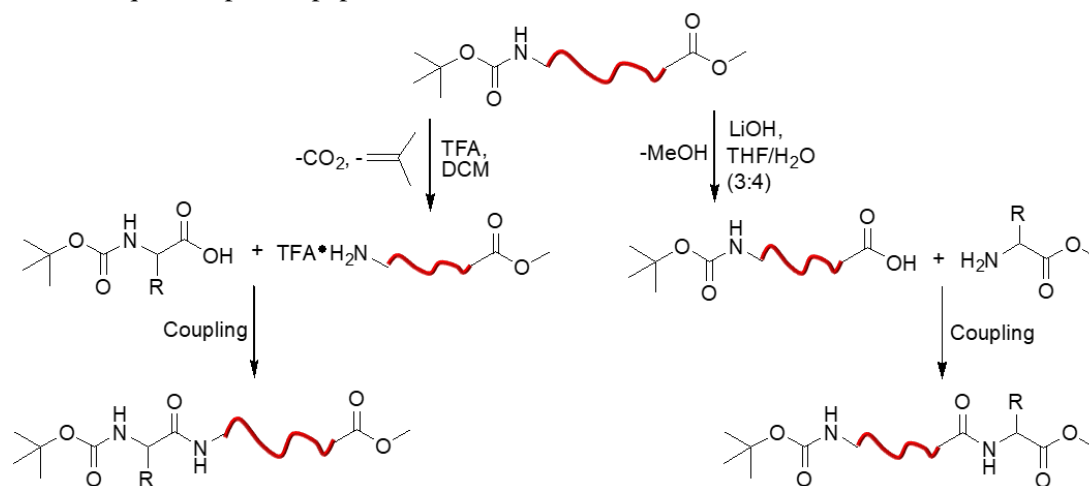
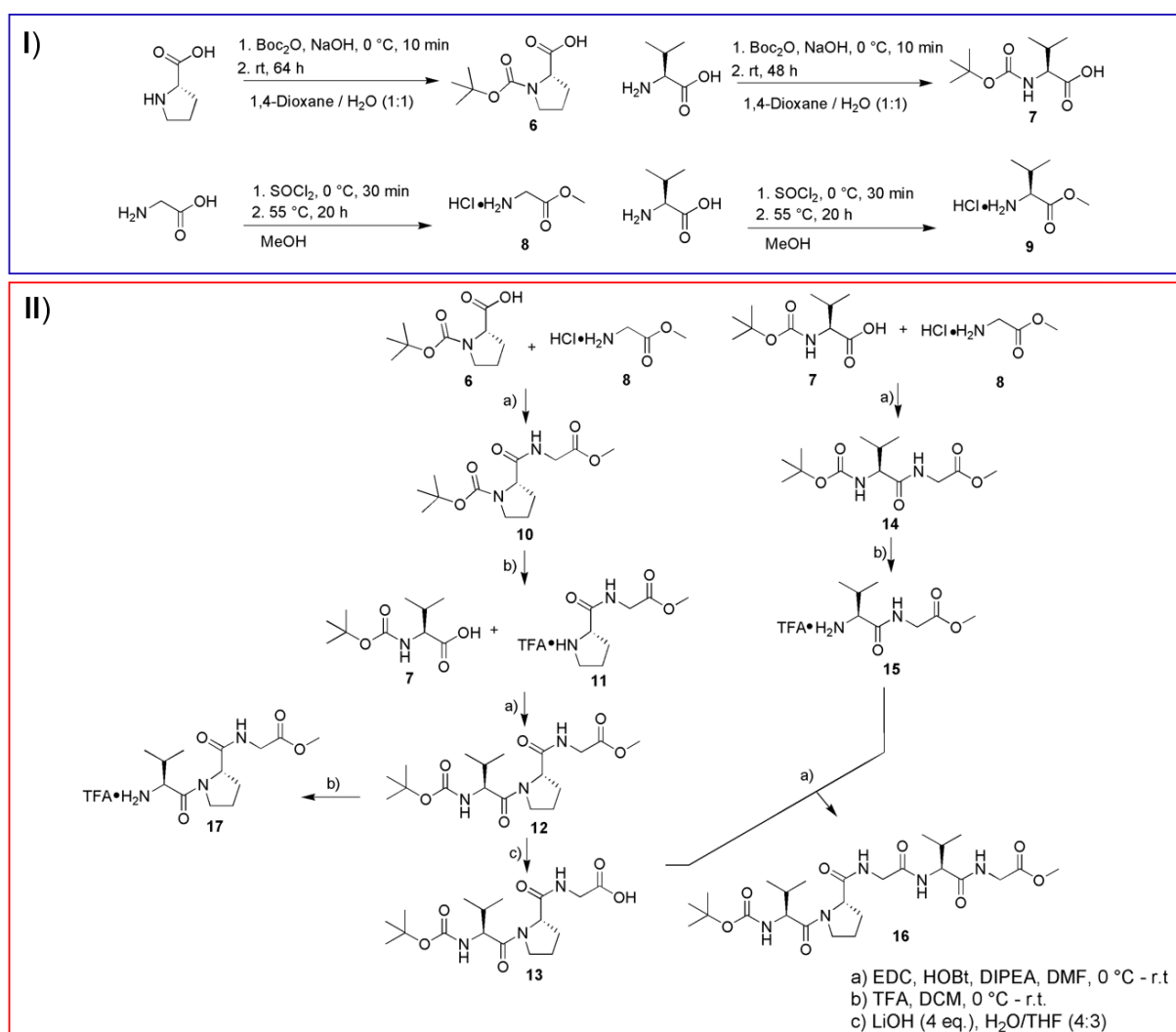


**Figure 30.** Orthogonal protection group strategy allows the synthesis of sequence specific peptides. Hence, reaction of one Boc-protected with one methyl ester protected amino acids generates a *N*- and *C*-terminus protected peptide which is unable to undergo further coupling reactions.

Subsequent peptide couplings were performed with 1-ethyl-3-(3-dimethylaminopropyl)carbodiimide hydrochloride (EDC·HCl) and hydroxybenzotriazole (HOBt) as coupling agents. Carbodiimides are often used because they are able to minimize the occurrence of the [1,3]-acyl shift which would lead to formation of the *N*-acylurea as byproduct<sup>333</sup>. The commonly used *N,N'*-dicyclohexylcarbodiimide (DCC) was avoided for the building up of the pentapeptide sequence since it is known that complete separation of the formed 1,3-dicyclohexylurea (DCU) is hardly possible<sup>333</sup>. Therefore, EDC·HCl offered a reasonable alternative because the formed 1-ethyl-3-(3-dimethylaminopropyl)urea (EDU) was water soluble and thus could be easily separated from the synthesized peptide. The *O*-acylurea intermediate,

formed from the unprotected *C*-terminus of a peptide and the carbodiimide is prone to epimerization<sup>334</sup>. However, the epimerization level can be significantly reduced by additives such as HOBT<sup>335</sup>. HOBT immediately reacts with the formed *O*-acylurea in turn generating an active ester which stabilizes the approach of the amine *via* hydrogen bonding, thus preventing epimerization.<sup>336</sup>

An overview about the synthetic approach for the pentapeptide sequence is given in Scheme 3, also including the necessary Boc- and methyl ester protection reactions. A full characterization of all compounds is given in the Experimental Part 4.3, while the according spectra are presented in the Appendix 7.2. In a first step, Boc-protection reactions of *L*-proline (Pro) and *L*-valine (Val) were accomplished according to known procedures using di-*tert*-butyl dicarbonate<sup>331, 337</sup> and generated the corresponding Boc-protected amino acids Boc-Pro (**6**) and Boc-Val (**7**) in quantitative yields. For the methyl ester protection, the corresponding amino acid was refluxed in methanol in the presence of thionyl chloride and thus generated Gly-OMe (**8**) and Val-OMe (**9**)<sup>332, 338</sup>.



**Scheme 3.** I) Boc- and methyl ester protection reactions of the single amino acids. II) Solution phase peptide synthesis (SPPS) of the Boc-VPGVG-OMe (**16**) sequence.

The peptide sequence was assembled from a tripeptide and a dipeptide which were synthesized individually. For the tripeptide, Boc-Pro (**6**) and Gly-OMe (**8**) were coupled to the dipeptide Boc-PG-OMe (**10**) which subsequently was deprotected with TFA, generating the *N*-terminus deprotected H<sub>2</sub>N-PG-OMe (**11**). Subsequently, the tripeptide Boc-VPG-OMe (**12**) was generated by coupling of Boc-Val (**7**) with H<sub>2</sub>N-PG-OMe (**11**) and was methyl ester deprotected to Boc-VPG-OH (**13**) with lithium

hydroxide. Boc-deprotection of Boc-VPG-OMe (**12**) to H<sub>2</sub>N-VPG-OMe (**17**) was also performed for a later coupling reaction to the mechanophoric catalyst [Cu(C<sub>10</sub>COOH-NHC)<sub>2</sub>]X (**4b**) (see Chapter 3.3), even though it was not necessary for the buildup of the pentapeptide sequence. The purified <sup>1</sup>H-NMR spectrum of the tripeptide Boc-VPG-OMe (**12**) is shown in Figure 31a. Both protection groups were still present at 3.60 ppm (*H*<sub>15</sub>, –C(O)OCH<sub>3</sub>) and 1.35 ppm (*H*<sub>1</sub>, –C(CH<sub>3</sub>)<sub>3</sub>), meaning that unintended coupling reactions could be avoided. The integral of the resonance at 3.60 ppm was five instead of three due to overlapping with protons *H*<sub>8</sub> (N–CH<sub>2</sub>–CH<sub>2</sub>–). Comparison with the methyl ester deprotected peptide **13** proved successful deprotection of the C-terminus (see Figure 31b). The resonance of the methyl group was no longer present at 3.60 ppm. Due to the missing methyl group, protons *H*<sub>13</sub> (–HN–CH<sub>2</sub>–C(O)OH) were slightly shifted to the highfield and were now overlapping with protons *H*<sub>8</sub> (N–CH<sub>2</sub>–CH<sub>2</sub>–) resulting in an integral of four. Contrary, stirring the peptide in the presence of TFA successfully removed the Boc-group (missing resonance at 1.35 ppm), while the methyl ester protection group was still visible at 3.60 ppm (*H*<sub>12</sub>, –C(O)OCH<sub>3</sub>) as shown in Figure 31c. Because the product was used without further neutralization, it was obtained as TFA-salt as visible from the broad signal at 8.06 ppm (–CH–NH<sub>3</sub><sup>+</sup>).

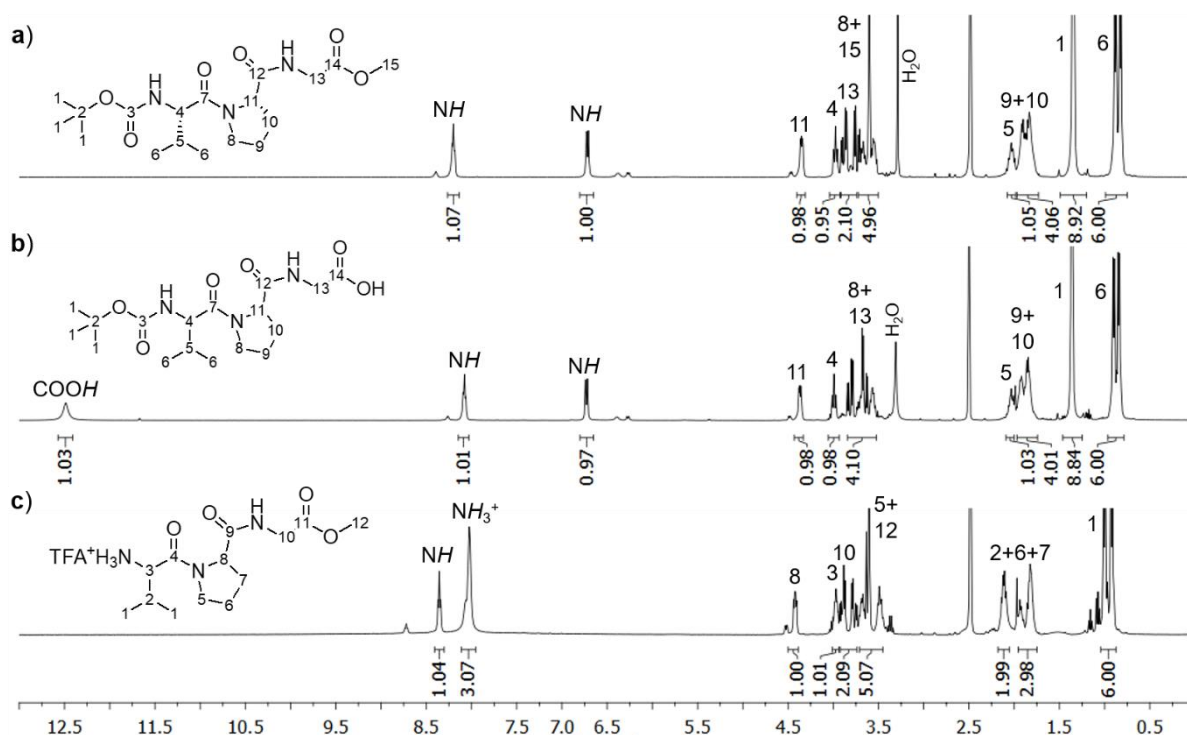


**Figure 31.** <sup>1</sup>H-NMR spectra of a) Boc-VPG-OMe (**12**), b) methyl ester deprotected tripeptide Boc-VPG-OH (**13**) and c) Boc-deprotected tripeptide TFA•H<sub>2</sub>N-VPG-OMe (**17**).

With the tripeptide finished, the missing dipeptide Boc-VG-OMe (**14**) was synthesized by coupling of Boc-Val (**7**) and Gly-OMe (**8**). Deprotection with TFA led to formation of H<sub>2</sub>N-VG-OMe (**15**), which then could be coupled with (**13**) to the pentapeptide Boc-VPGVG-OMe (**16**).

Purity of Boc-VPGVG-OMe (**16**) was proven *via* <sup>1</sup>H-NMR spectroscopy and ESI-TOF-MS (see Figure 32). In the <sup>1</sup>H-NMR spectrum both protection groups were visible at 1.35 ppm (*H*<sub>1</sub>, –C(CH<sub>3</sub>)<sub>3</sub>) and 3.60 ppm (*H*<sub>21</sub>, –C(O)OCH<sub>3</sub>). There were only four resonances that could be assigned to NH protons due to the presence of Pro, which is not bearing an NH since it is a secondary amine. Purity was also proven *via* ESI-TOF-MS, clearly showing only one peak that could be identified as the pentapeptide with both protection groups and an additional sodium cation. The measured peak also fitted well with the simulation ([C<sub>25</sub>H<sub>43</sub>N<sub>5</sub>O<sub>8</sub>Na]<sup>+</sup>), proving the successful synthesis and purification of Boc-VPGVG-OMe (**16**).

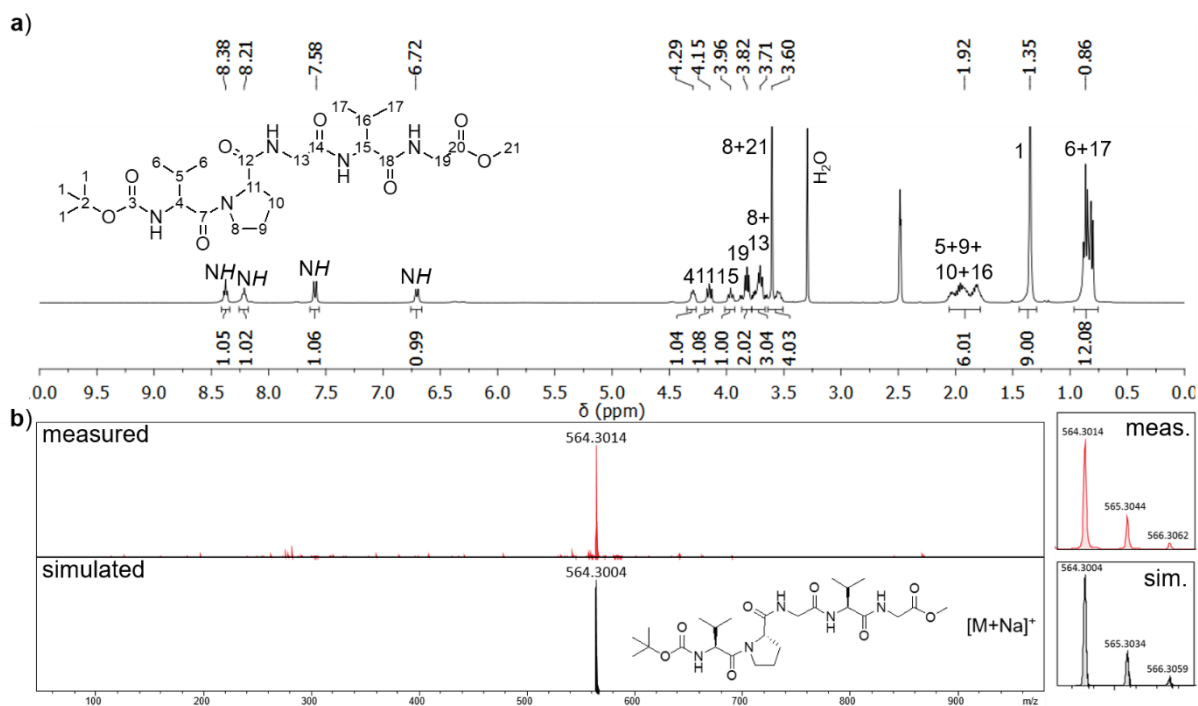


**Figure 32.** a) <sup>1</sup>H-NMR spectrum of Boc-VPGVG-OMe (**16**) and b) ESI-TOF-MS of Boc-VPGVG-OMe (**16**).

### 3.2.2 Secondary structure analysis of Boc-VPGVG-OMe (**16**)

With the successful synthesis of the pentapeptide Boc-VPGVG-OMe (**16**) it was necessary, to ensure that the pentapeptide sequence is adopting the  $\beta$ -spiral structure as reported in literature<sup>218, 234-238</sup>. Formation of the  $\beta$ -spiral was crucial since it was the scope of this work to exploit the “molecular spring” behavior of the ELP-sequence for an enhanced force transmission and thus a facilitated activation of the previously synthesized catalyst [Cu(C<sub>10</sub>COOH-NHC)<sub>2</sub>]X (**4b**) (see Chapter 3.1).

IR-spectroscopy is a common method to obtain information about the secondary structure of peptides<sup>339</sup> and can be divided into several bands (A, B and I – VII)<sup>340</sup> from which the amide I (1600 – 1690 cm<sup>-1</sup>) and amide II (1480 – 1575 cm<sup>-1</sup>) bands contain the most information. The amide I band is the most sensitive region of the IR-spectrum and mostly is the result of C=O stretch vibrations of the peptide bonds (~80 %) while in-plane NH bending only plays a minor role (< 20 %)<sup>339, 341</sup>. C=O stretching is strongly influenced by the hydrogen bonds that are formed between the C=O and the NH groups of the peptide backbone. Since the ability to form hydrogen bonds is strongly dependent from the conformation of the peptide backbone, secondary structure formation also affects the vibrational bands of the IR-spectrum and thus allows a breakdown of the different present secondary structures. The different secondary structures within the amide I band can be divided into  $\alpha$ -helix (1650 – 1658 cm<sup>-1</sup>), <sub>310</sub> helix (1663 cm<sup>-1</sup>),  $\beta$ -sheet (1620 – 1640 cm<sup>-1</sup> and 1690 – 1695 cm<sup>-1</sup>) and random coil (1640 – 1648 cm<sup>-1</sup>)<sup>339, 341-342</sup>. Major contributions of in-plane NH (40 – 60 %) and CN stretching vibrations (18 – 40 %) can be found in the amide II band of the IR-spectrum<sup>341</sup>. Contrary to the amide I band, the amide II band is less sensitive to conformational changes and therefore commonly is only used as double check to verify the results obtained from the amide I band.

The used solvent for the IR-analysis should also be selected carefully. Commonly H<sub>2</sub>O is the preferred solvent for the secondary structure analysis of peptides to mimic the native environmental conditions of the peptide and minimize disturbing influences. However, the H–O–H bond shows vibrational bands at 1645 cm<sup>-1</sup> which are overlapping with the amide I band (1600 – 1690 cm<sup>-1</sup>)<sup>339</sup>. The intensity of the water absorbance is approximately an order of magnitude higher than the absorbance of peptides in the amide I band and thus complicates the analysis. To circumvent this overlapping, often D<sub>2</sub>O is used due to the absence of any absorption in the amide I and amide II region. However, using a deuterated and protic

solvent provides the possibility for an H-D exchange of the peptide moieties which can affect the length and strength of hydrogen bonds and thus can alter the secondary structure<sup>343</sup>. Nevertheless, IR-measurements of **16** were performed in D<sub>2</sub>O to avoid the aforementioned overlapping with the amide I band.

Results from the IR-measurements in D<sub>2</sub>O of **16** are shown in Figure 33. As discussed previously, the amide I band contains the most information about the secondary structure of peptides and therefore only the region between 1550 cm<sup>-1</sup> and 1800 cm<sup>-1</sup> is shown. The measurement was performed at three different concentrations (5.0, 7.5 and 10.0 mg/mL in D<sub>2</sub>O) and revealed two maxima at 1654 cm<sup>-1</sup> and 1618 cm<sup>-1</sup> (see Figure 33a). The maximum at 1618 cm<sup>-1</sup> is unusually shifted to low wavenumbers and in literature is interpreted as aggregated  $\beta$ -sheet<sup>344</sup>. The second maximum at 1654 cm<sup>-1</sup> commonly would be associated with the presence of  $\alpha$ -helical structures (1653  $\pm$  4 cm<sup>-1</sup>)<sup>339</sup>. However, considering the assumed  $\beta$ -spiral structure of the ELP and the tendency of the pentapeptide sequence VPGVG to form  $\beta$ -turns it seemed improper to conclude an  $\alpha$ -helical structure for **16**. As proven by Franzen *et al.* with both experimental and theoretical experiments, the occurrence of the double-peaked amide I band with two maxima around 1615 cm<sup>-1</sup> (being indicative of  $\beta$ -sheet formation) and 1650 cm<sup>-1</sup> is characteristic for a  $\beta$ -spiral<sup>345</sup>. Hence, a comparison of the obtained results for secondary structure analysis with generalized data from other peptides is not reasonable due to the unique feature of  $\beta$ -spiral formation which is exclusive to elastin, respectively ELPs. It is also noteworthy that  $\beta$ -spiral formation was concentration independent in the range of 5 – 10 mg/mL (see Figure 33b). Thus, the obtained IR-spectra looked almost identically after normalization to the maximum at 1740 cm<sup>-1</sup> of the methyl ester protection group.

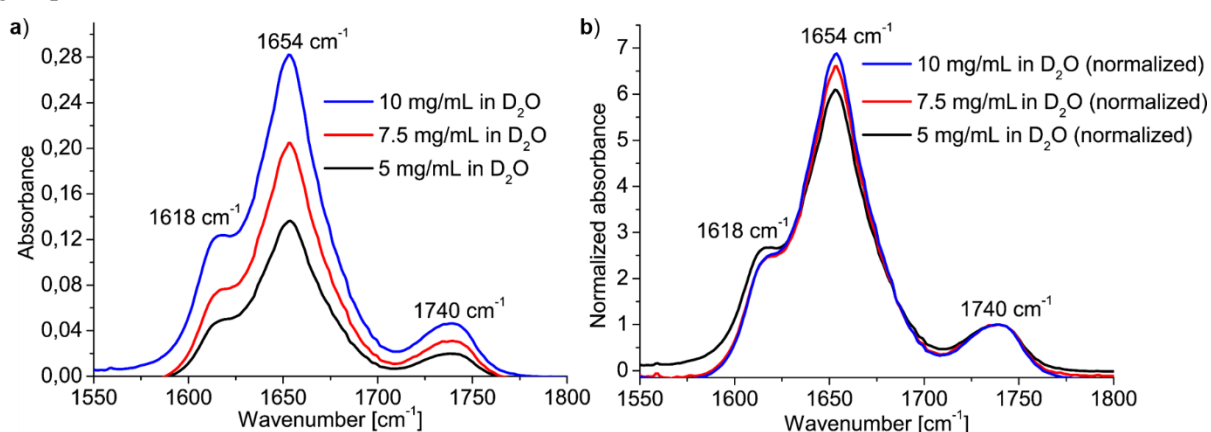


**Figure 33.** a) Obtained IR-spectra for the measurement of Boc-VPGVG-OMe (**16**) in D<sub>2</sub>O at three different concentrations (5.0, 7.5 and 10.0 mg/mL). b) Normalization of the measured spectra to the band originating from the methyl ester protection group at 1740 cm<sup>-1</sup>.

In order to double check the presence of the  $\beta$ -spiral and the absence of  $\alpha$ -helical structures, circular dichroism (CD) spectroscopy was performed. CD-spectroscopy is another tool to quickly get information about the secondary structure of peptides<sup>346</sup>. Measurements rely on the unequal absorption of right-handed and left-handed circular polarized light in the far ultraviolet (UV) region and involve  $n \rightarrow \pi^*$  and  $\pi \rightarrow \pi^*$  transitions of the amide bonds<sup>347</sup>. These transitions are influenced by the spatial arrangement of the peptide backbone, namely the  $\phi$ ,  $\Psi$  angles. Thus, the recorded CD-spectra are reflective of the secondary structures that are present in a peptide or protein<sup>347</sup>.  $\alpha$ -Helical proteins reveal two negative bands (around 222 nm and 208 nm) and one positive band (around 193 nm)<sup>348</sup> while  $\beta$ -sheet structures have one negative (around 218 nm) and one positive band (around 195 nm)<sup>349</sup> in their CD-spectra. Best results are achieved for helical secondary structures because they usually are of high regularity and order (similar  $\phi$ ,  $\Psi$  angles), thus leading to similar CD-spectra<sup>347</sup>. Furthermore, very high intensities are characteristic in the CD-spectrum which easily allows the identification of small fractions of helical secondary structures. Contrary, CD-spectra from  $\beta$ -sheet proteins can differ from each other

due to different orientations (parallel or antiparallel) of adjacent strands and different  $\phi$ ,  $\Psi$  angles, leading to a shift of the minimum of the negative band as well as a shift of the maximum of the positive band<sup>347</sup>. The intensities of  $\beta$ -sheet secondary structures in the CD-spectra also tend to be two-third lower in comparison to  $\alpha$ -helical secondary structures, further impeding evaluation of CD-spectra with high  $\alpha$ -helical and low  $\beta$ -sheet content<sup>347</sup>.

The results from CD-measurements in D<sub>2</sub>O at a concentration of 0.4 mg/mL are shown in Figure 34. The presence of one maximum at 208 nm and one minimum at 226 nm clearly indicated  $\beta$ -sheets as the major secondary structure element. There was no evidence for  $\alpha$ -helical structures which usually show much higher intensities as signals that originate from  $\beta$ -sheet structures (see above). Thus, the “molecular spring” behavior was assumed for the synthesized ELP as previously described in literature<sup>218, 234-238, 345</sup>.

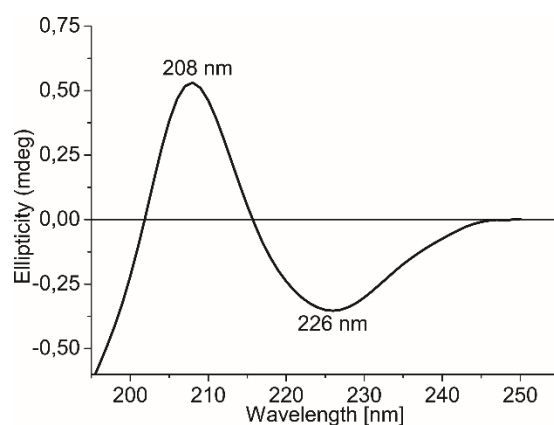
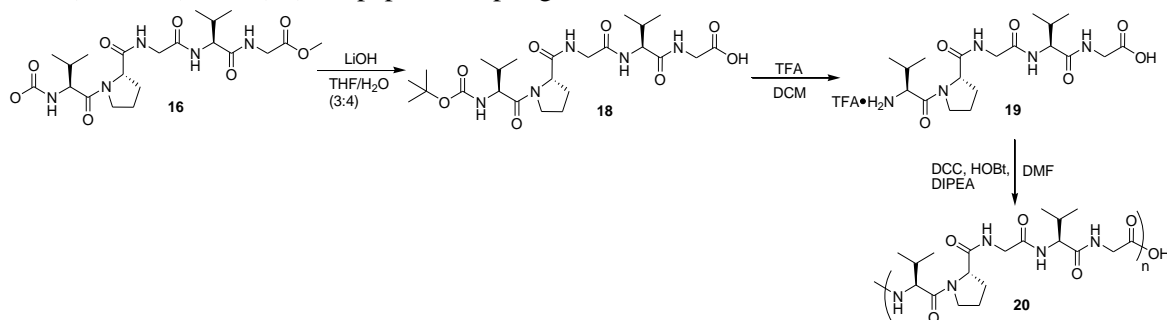


**Figure 34.** Obtained CD-spectrum for the measurement of Boc-VPGVG-OMe (**16**) in D<sub>2</sub>O at a concentration of 0.4 mg/mL.

### 3.2.3 Chain elongation of Boc-VPGVG-OMe (**16**)

In order to elongate the force transmitting peptide backbone, the previously synthesized pentapeptide Boc-VPGVG-OMe (**16**) was extended. Initially, pentapeptide **16** was methyl ester deprotected which generated Boc-VPGVG-OH (**18**) as shown in Scheme 4. In a next step **18** was also deprotected at the *N*-terminus to the double-deprotected TFA•H<sub>2</sub>N-VPGVG-OH (**19**) which then could be polymerized to H<sub>2</sub>N-(VPGVG)<sub>n</sub>-OH (**20**) *via* peptide coupling.



**Scheme 4.** Synthetic approach for the polymerization of Boc-VPGVG-OMe (**16**).

The polymerization of **19** was performed in DMF with DCC and HOBt as coupling agents and could be followed with GPC. Figure 35 shows the GPC measurement of the resulting ELP after 72 h stirring at room temperature. Due to the step-growth character of the coupling polycondensation, the obtained polypeptide showed a multimodal distribution with broad polydispersity corresponding to ELPs of different chain length. The GPC trace revealed the presence of monomeric and several oligomeric species ((VPGVG)<sub>2</sub>, (VPGVG)<sub>3</sub>, (VPGVG)<sub>4</sub>) as well as polypeptides with an average molecular weight of 5900 g/mol. Using this mixture for subsequent coupling reactions to the mechanophoric catalyst

would be disadvantageous as it significantly lowers the validity of the subsequently performed mechanochemical “click” reactions. Due to the multimodality of the ELP chains, the resulting catalysts would possess force transmitting handles of different chain lengths, in turn leading to unequal activation behavior. Moreover, the reproducibility of the mechanophoric activation behavior would be further impeded since a positioning of the mechanophoric bond in the center of the catalyst would be impossible as a consequence of the polydispersity.

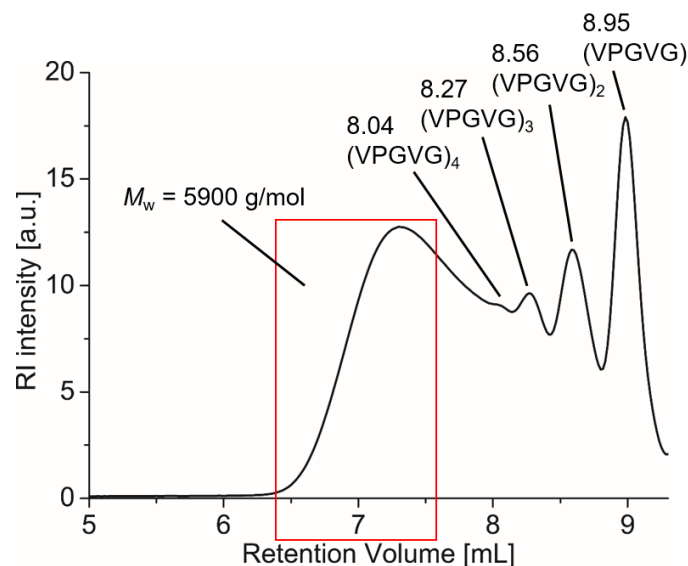
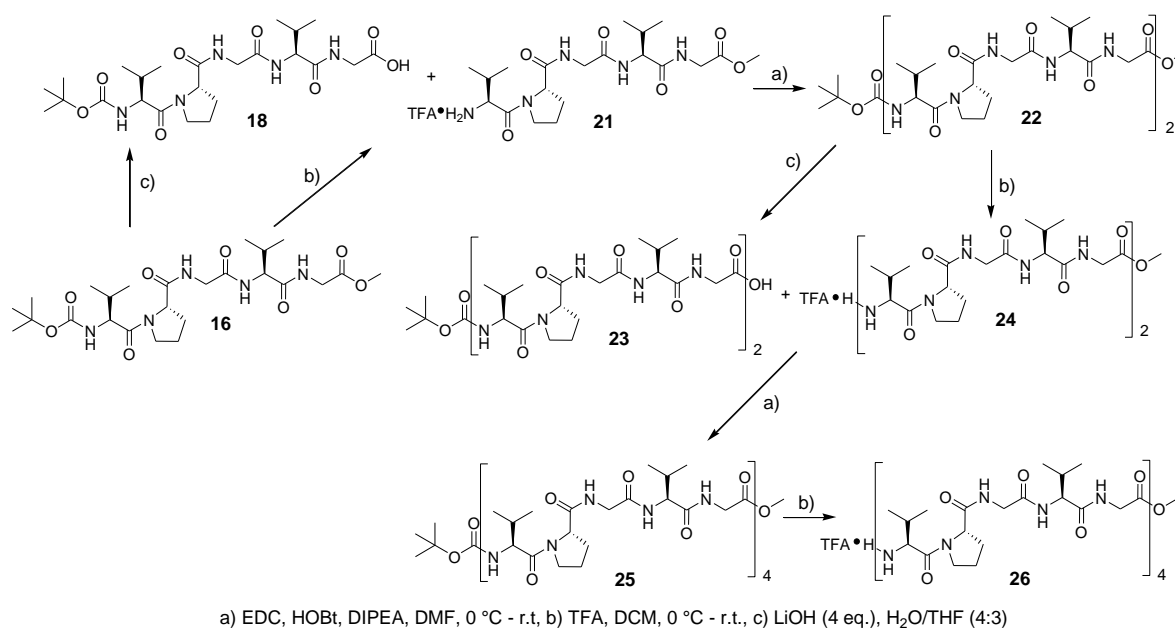


**Figure 35.** GPC of the polymerized pentapeptide sequence  $\text{H}_2\text{N}-(\text{VPGVG})_n-\text{OH}$  (**20**) after a reaction time of 72 h.

In order to avoid a high polydispersity of the elongated peptide chain, the peptide was built up in a step-by-step process by repeatedly performing deprotection and coupling reactions as shown in Scheme 5. This method allowed the buildup of a monodisperse eicosapeptide ( $\text{Boc}-(\text{VPGVG})_4-\text{OMe}$ ) since every coupling step generated a peptide with C- and N-protected termini, thus preventing undesired side reactions.



**Scheme 5.** Solution phase peptide synthesis (SPPS) of the  $\text{TFA}\cdot\text{H}_2\text{N}-(\text{VPGVG})_4-\text{OMe}$  (**26**) sequence.

All deprotection and coupling steps were conducted analogous to the previously described synthesis of the pentapeptide sequence (see Chapter 3.2.1). In a first step, the previously synthesized Boc-VPGVG-OMe (**16**) was split. One half was deprotected at the C-terminus with lithium hydroxide and generated Boc-VPGVG-OH (**18**) while the other half was N-terminus deprotected with TFA and thus generated TFA•H<sub>2</sub>N-VPGVG-OMe (**21**). Coupling of these two pentapeptides generated the decapeptide Boc-(VPGVG)<sub>2</sub>-OMe (**22**) which was split once more. Deprotection generated the C-terminus deprotected Boc-(VPGVG)<sub>2</sub>-OH (**23**) and the N-terminus deprotected TFA•H<sub>2</sub>N-(VPGVG)<sub>2</sub>-OMe (**24**) which subsequently were coupled to the eicosapeptide Boc-(VPGVG)<sub>4</sub>-OMe (**25**). The following deprotection generated TFA•H<sub>2</sub>N-(VPGVG)<sub>4</sub>-OMe (**26**) which was necessary for the coupling reaction with the mechanophoric catalyst **4b** (see Chapter 3.3.1). The stepwise elongation of the peptide chain could be followed *via* <sup>1</sup>H-NMR spectroscopy as shown in Figure 36. The resonance from the Boc-protection group at 1.35 ppm (*H*<sub>1</sub>, -C(CH<sub>3</sub>)<sub>3</sub>) was used as reference since it stayed constant for all three synthesized peptides Boc-VPGVG-OMe (**16**), Boc-(VPGVG)<sub>2</sub>-OMe (**22**) and Boc-(VPGVG)<sub>4</sub>-OMe (**25**). Using the resonance from the methyl ester protection group at 3.60 ppm (*H*<sub>21</sub>, -C(O)OCH<sub>3</sub>) was more difficult due to the overlap with protons *H*<sub>8</sub> (N-CH<sub>2</sub>-CH<sub>2</sub>-). Since all other protons became part of the repetitive unit after successful coupling reactions, the integral of their resonances was always doubling. Doubling of the integrals could be followed easily, especially for protons *H*<sub>6</sub> and *H*<sub>17</sub> (-CH(CH<sub>3</sub>)<sub>2</sub>) (12 → 24 → 48) and protons *H*<sub>5</sub> (-CH(CH<sub>3</sub>)<sub>2</sub>), *H*<sub>9</sub> (-CH<sub>2</sub>-CH<sub>2</sub>-CH<sub>2</sub>-), *H*<sub>10</sub> (-CH<sub>2</sub>-CH<sub>2</sub>-CH<sub>2</sub>-) and *H*<sub>16</sub> (-CH(CH<sub>3</sub>)<sub>2</sub>) (6 → 12 → 24), clearly proving the successful elongation of the peptide.

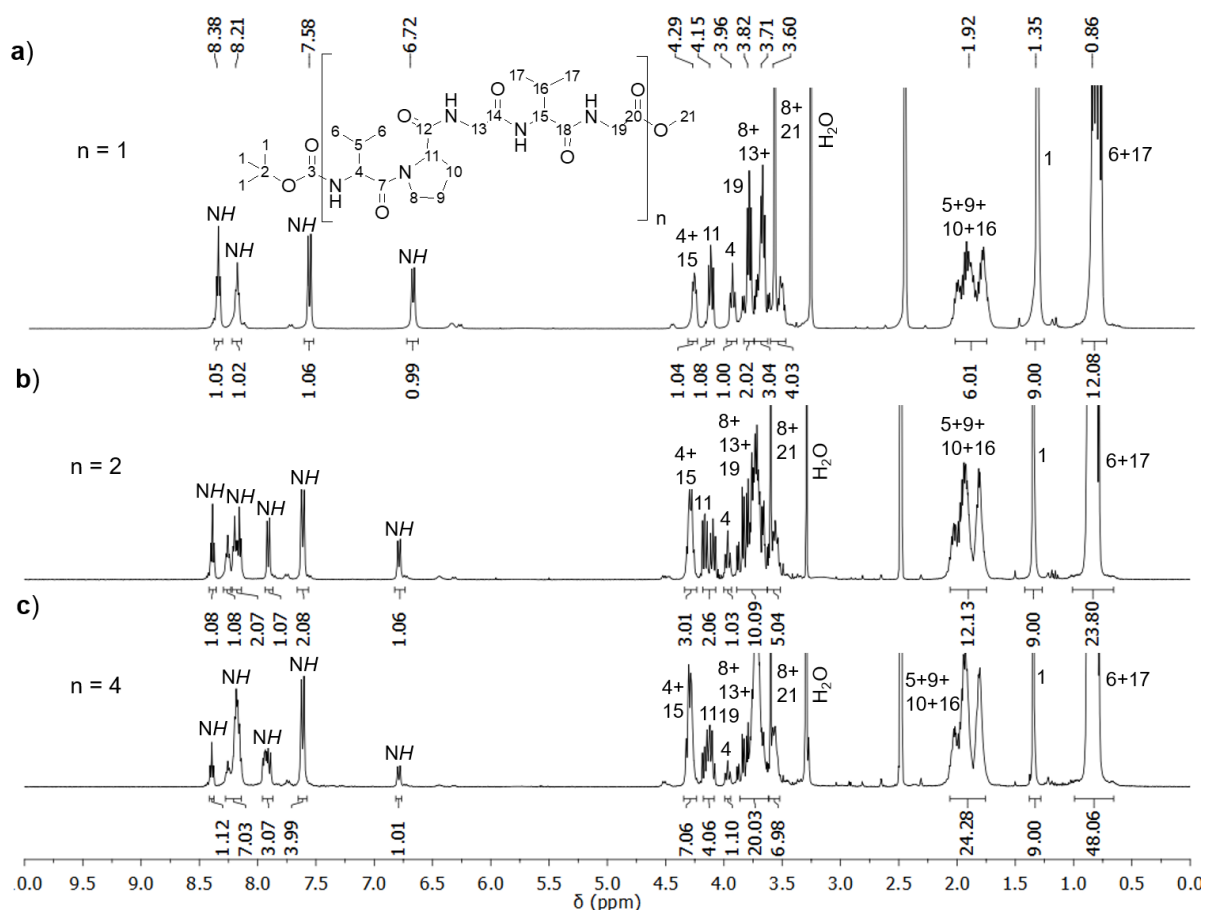


**Figure 36.** <sup>1</sup>H-NMR spectra of a) Boc-VPGVG-OMe (**16**), b) Boc-(VPGVG)<sub>2</sub>-OMe (**22**) and c) Boc-(VPGVG)<sub>4</sub>-OMe (**25**).

The increasing chain length could also be proven with decreasing retention times in the GPC as apparent from Figure 37. The GPC measurements also illustrated the advantage of the step-by-step coupling

approach in contrast to the polymerization approach of TFA•H<sub>2</sub>N-VPGVG-OH. The obtained ELPs were monodisperse and thus allowed generation of precise mechanophoric catalysts, bearing equally long force transmitting handles with the mechanophoric bond in the center of the chain.

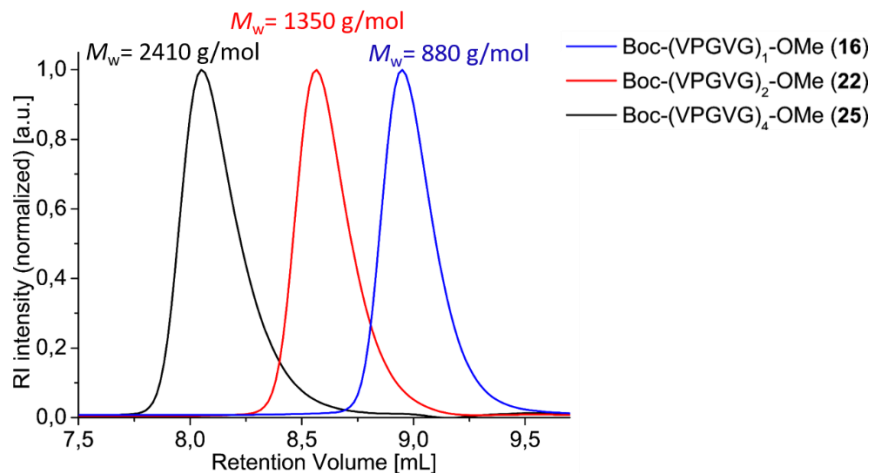


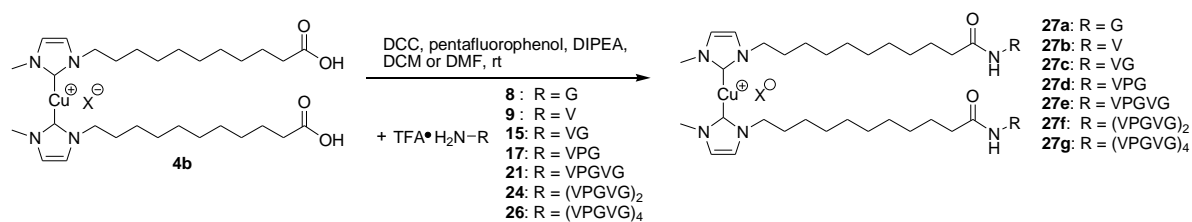
**Figure 37.** GPC traces of the three ELPs Boc-VPGVG-OMe (**16**), Boc-(VPGVG)<sub>2</sub>-OMe (**22**) and Boc-(VPGVG)<sub>4</sub>-OMe (**25**).

A full characterization of all compounds (<sup>1</sup>H-NMR, <sup>13</sup>C-NMR, IR-spectroscopy and ESI-TOF-MS) is given in the Experimental Part 4.3.4, while the according spectra are presented in the Appendix 7.3.

### 3.3 Synthesis, characterization and mechanochemical activity of the linear mechanocatalysts

#### 3.3.1 Coupling reactions of the carboxyl-functionalized mechanocatalyst **4b** with *N*-terminus deprotected peptides

With the successful synthesis of the mechanocatalyst [Cu(C<sub>10</sub>COOH-NHC)<sub>2</sub>]<sup>+</sup>X<sup>-</sup> (**4b**) and a variety of ELPs with different chain length the next step was their coupling reaction, thus generating mechanophoric catalysts with peptide based force transmitting handles. Force transmission of hitherto existing Cu(I) bis(NHC) complexes solely relied on addition of synthetic polymers (see Chapter 1.1.6.2)<sup>37-38, 94-95, 143</sup>. Exchanging the synthetic polymeric handles with ELPs might be a promising way to further study force transmission, since the resulting β-spiral could be exploited as “molecular spring”. Several mechanophoric catalysts with peptide chains of different chain lengths have been synthesized as shown in Scheme 6 and Table 2.



**Scheme 6.** Performed coupling reactions between the carboxyl functionalized Cu(I) bis(NHC) complex **4b** and peptides of different chain length.

**Table 2.** Overview about the synthesized mechanocatalysts **27a-g**, including the attached peptide sequence, the molecular weight and the obtained yield after purification.

Entry	Catalyst	Peptide sequence	Calculated molecular weight (g/mol)	Yield (%)
1	<b>4b</b>	/	675.96	/
2	<b>27a</b>	G-OMe	818.06	54
3	<b>27b</b>	V-OMe	870.19	45
4	<b>27c</b>	VG-OMe	1064.24	42
5	<b>27d</b>	VPG-OMe	1258.37	31
6	<b>27e</b>	VPGVG-OMe	1522.16	38
7	<b>27f</b>	(VPGVG) <sub>2</sub> -OMe	2341.22	11
8	<b>27g</b>	(VPGVG) <sub>4</sub> -OMe	3978.43	14

Since the Cu(I) bis(NHC) complex was carboxyl functionalized, methyl ester protected peptides were used for coupling reactions *via* the *N*-terminus. First experiments were conducted with the single amino acids Gly-OMe (**8**) and Val-OMe (**9**) to check whether a proper attachment to the catalyst was possible without unintended destruction of the mechanophore. Adoption of the previously used coupling conditions (EDC•HCl, HOBt) led to no conversion in case of Gly-OMe and to low yields in case of Val-OMe (< 10 %). However, exchanging the coupling reagents to DCC and pentafluorophenol led to acceptable yields in the range of 50 % for both [Cu(C<sub>10</sub>COOH-G-NHC)<sub>2</sub>]X (**27a**) and [Cu(C<sub>10</sub>COOH-V-NHC)<sub>2</sub>]X (**27b**). Pentafluorophenol is a frequently used coupling agent which forms the pentafluorophenyl active ester as an intermediate, followed by the formation of the peptide bond<sup>350-351</sup>. Successful synthesis and purification of the catalysts could be proven *via* <sup>1</sup>H-NMR spectroscopy and is exemplary shown in Figure 38 for complex **27a**. For a full characterization of all synthesized mechanocatalyst-peptide conjugates check the Experimental Part 4.4 as well as the Appendix 7.4.

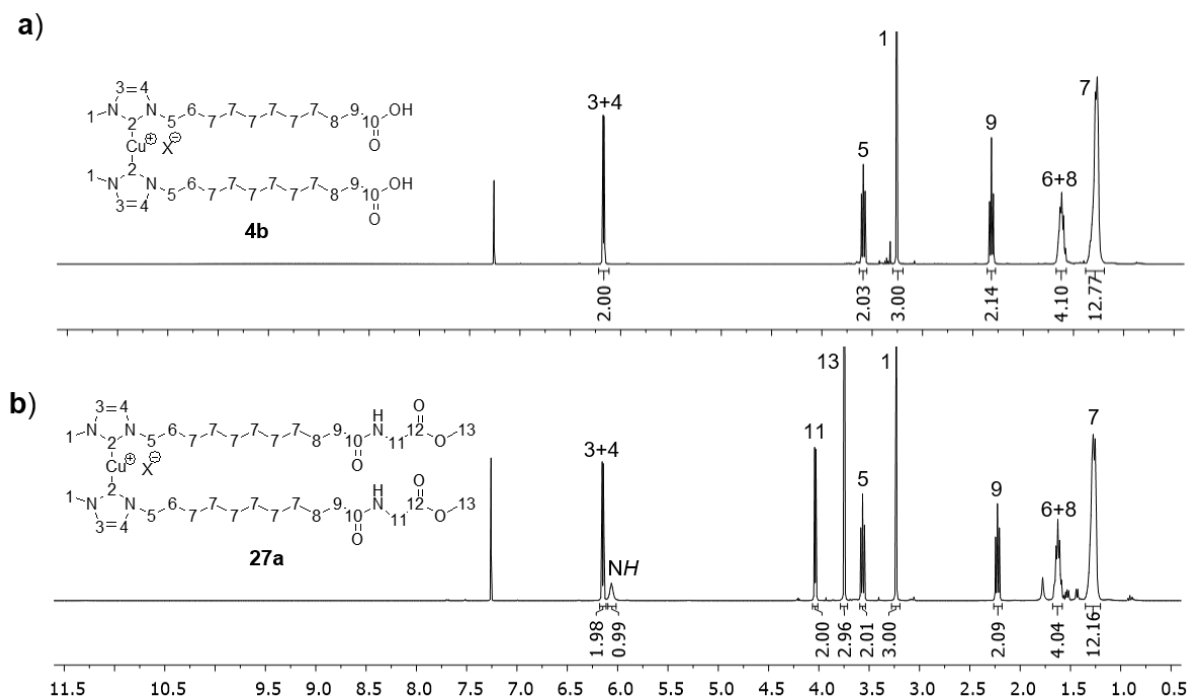


**Figure 38.** <sup>1</sup>H-NMR spectra of a) [Cu(C<sub>10</sub>COOH-NHC)<sub>2</sub>]X (**4b**) and b) [Cu(C<sub>10</sub>COOH-G-NHC)<sub>2</sub>]X (**27a**).

Figure 38a shows the <sup>1</sup>H-NMR spectrum from the pure catalyst [Cu(C<sub>10</sub>COOH-NHC)<sub>2</sub>]X as reference. Comparing it with the <sup>1</sup>H-NMR spectrum of [Cu(C<sub>10</sub>COOH-G-NHC)<sub>2</sub>]X (Figure 38b) the NH of the formed peptide bond could be detected at 6.06 ppm, while protons H<sub>11</sub> (–NHCH<sub>2</sub>–) and H<sub>13</sub> (–C(O)OCH<sub>3</sub>) from the coupled glycine methyl ester were present at 4.03 and 3.75 ppm. The resonances

of protons  $H_3$  and  $H_4$  ( $-NCH=CHN-$ ) of the Cu(I) bis(NHC) ring at 6.15 and 6.06 ppm verified that the complex was not destroyed during the coupling. Additionally, no signal at 10.50 ppm was detected which would be indicative of a catalyst cleavage and reprotonation of the NHC ( $C_2$ ).

In a next step, the attachment of a di- and tripeptide was probed. The peptides TFA•H<sub>2</sub>N-VG-OMe (**15**) and TFA•H<sub>2</sub>N-VPG-OMe (**17**) were the building blocks for the ELP sequence VPGVG and generated catalysts [Cu(C<sub>10</sub>COOH-VG-NHC)<sub>2</sub>]X (**27c**) and [Cu(C<sub>10</sub>COOH-VPG-NHC)<sub>2</sub>]X (**27d**). These catalysts were of interest for two reasons. First, both amino acid sequences are too short to adopt the  $\beta$ -spiral structure since they are missing the necessary VPGV sequence for the type-II  $\beta$ -turn formation<sup>243</sup>. This might influence the mechanophoric behavior of this catalyst since the “molecular spring” behavior is not present in these catalysts. Second, the reactivity and yield of the previously tested coupling protocol also should be tested for longer chains and not solely for single amino acids. Both syntheses were successful, even though the yield decreased to 42 % for [Cu(C<sub>10</sub>COOH-VG-NHC)<sub>2</sub>]X (**27c**) and to 31 % for [Cu(C<sub>10</sub>COOH-VPG-NHC)<sub>2</sub>]X (**27d**). Purification of the products was also no longer possible *via* column chromatography in pure CHCl<sub>3</sub> due to the increasing polarity from the longer peptide chains. Therefore small amounts of MeOH (CHCl<sub>3</sub>/MeOH, 40:1) had to be used. MeOH is a protic solvent which potentially can reprotonate the NHC carbene but <sup>1</sup>H-NMR spectroscopy (see Appendix 7.4) proved that both catalysts were not destroyed during the reaction as well as during the workup.

Hence, the incorporation of the ELP sequence with varying chain length (VPGVG, (VPGVG)<sub>2</sub> and (VPGVG)<sub>4</sub>) was performed. Contrary to the previously performed coupling reactions the solvent was changed from DCM to DMF due to the polarity of the ELPs. While the yield for [Cu(C<sub>10</sub>COOH-VPGVG-NHC)<sub>2</sub>]X (**27e**) was reasonable (38 %), it further dropped with increasing chain length for [Cu(C<sub>10</sub>COOH-(VPGVG)<sub>2</sub>-NHC)<sub>2</sub>]X (**27f**) (11 %) and [Cu(C<sub>10</sub>COOH-(VPGVG)<sub>4</sub>-NHC)<sub>2</sub>]X (**27g**) (14 %). Separation of the uncoupled peptide from the product also got difficult with increasing ELP length. While purification of [Cu(C<sub>10</sub>COOH-(VPGVG)<sub>2</sub>-NHC)<sub>2</sub>]X (**27f**) was still possible with gradient column chromatography (CHCl<sub>3</sub>/MeOH (60:1) → DCM/MeOH (40:1) → DCM/MeOH (20:1) → DCM/MeOH (10:1), complete separation of the uncoupled peptide from [Cu(C<sub>10</sub>COOH-(VPGVG)<sub>4</sub>-NHC)<sub>2</sub>]X (**27g**) was no longer possible.

The <sup>1</sup>H-NMR spectrum from [Cu(C<sub>10</sub>COOH-VPGVG-NHC)<sub>2</sub>]X (**27e**) is exemplarily shown in Figure 39 (for all other characterization data see Experimental Part 4.4 and Appendix 7.4). The presence of a *NH* resonance at 7.93 ppm proved the successful formation of the mechanophore-ELP peptide bond. Furthermore, resonances of protons  $H_3$  and  $H_4$  ( $-NCH=CHN-$ ) of the Cu(I) bis(NHC) at 6.46 ppm and the absence of a signal at 10.50 ppm (reprotonated carbene) verified that the complex was not destroyed during the coupling. An additional proof could be provided by the shift of the retention volume during the GPC measurement. Due to the attachment of two peptide chains to the mechanophoric catalyst the signal for the conjugate was shifted to a lower retention volume as shown in Figure 40.

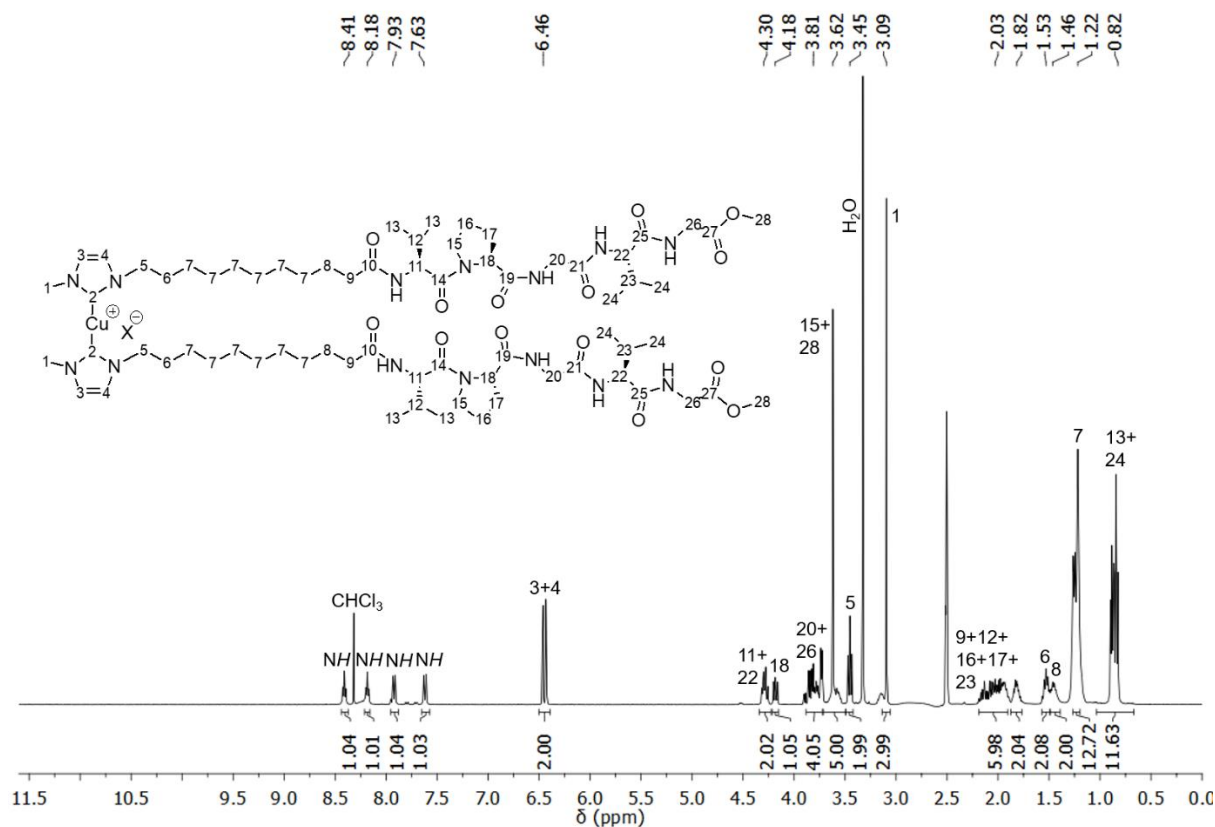


**Figure 39.**  $^1\text{H-NMR}$  spectrum of  $[\text{Cu}(\text{C}_{10}\text{COOH-VPGVG-NHC})_2]\text{X}$  (**27e**).

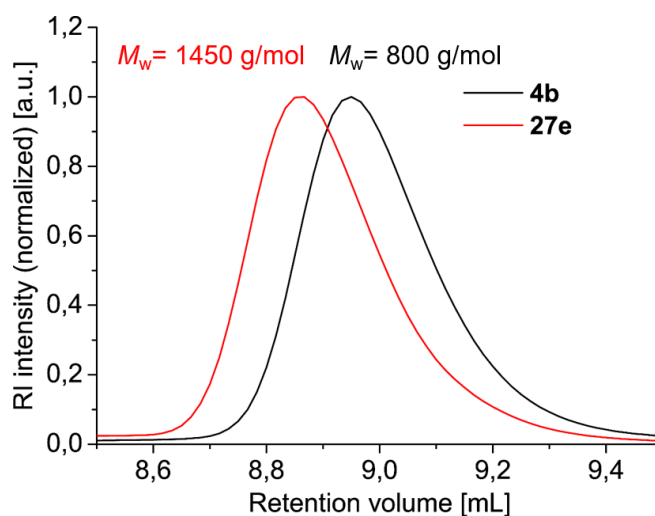


**Figure 40.** GPC traces of  $[\text{Cu}(\text{C}_{10}\text{COOH-NHC})_2]\text{X}$  (black) and  $[\text{Cu}(\text{C}_{10}\text{COOH-VPGVG-NHC})_2]\text{X}$  (red).

### 3.3.2 Secondary structure analysis of $[\text{Cu}(\text{C}_{10}\text{COOH-VPGVG-NHC})_2]\text{X}$ (**27e**)

Since the ELPs were attached to the mechanophoric catalyst with the aim to exploit their “molecular spring” behavior, it was crucial to check the persistence of the  $\beta$ -spiral conformation after the coupling. Therefore, secondary structure analysis was performed for the mechanocatalyst  $[\text{Cu}(\text{C}_{10}\text{COOH-VPGVG-NHC})_2]\text{X}$  (**27e**) bearing the VPGVG pentapeptide sequence. First, IR-experiments were conducted under the same conditions (5.0, 7.5 and 10.0 mg/mL in  $\text{D}_2\text{O}$ ) as for Boc-VPGVG-OMe (**16**) (see Chapter 3.2.2, Figure 33 and Figure 34). The results are shown in Figures 41a-c, proving that the  $\beta$ -spiral formation was not affected by the coupling reaction.

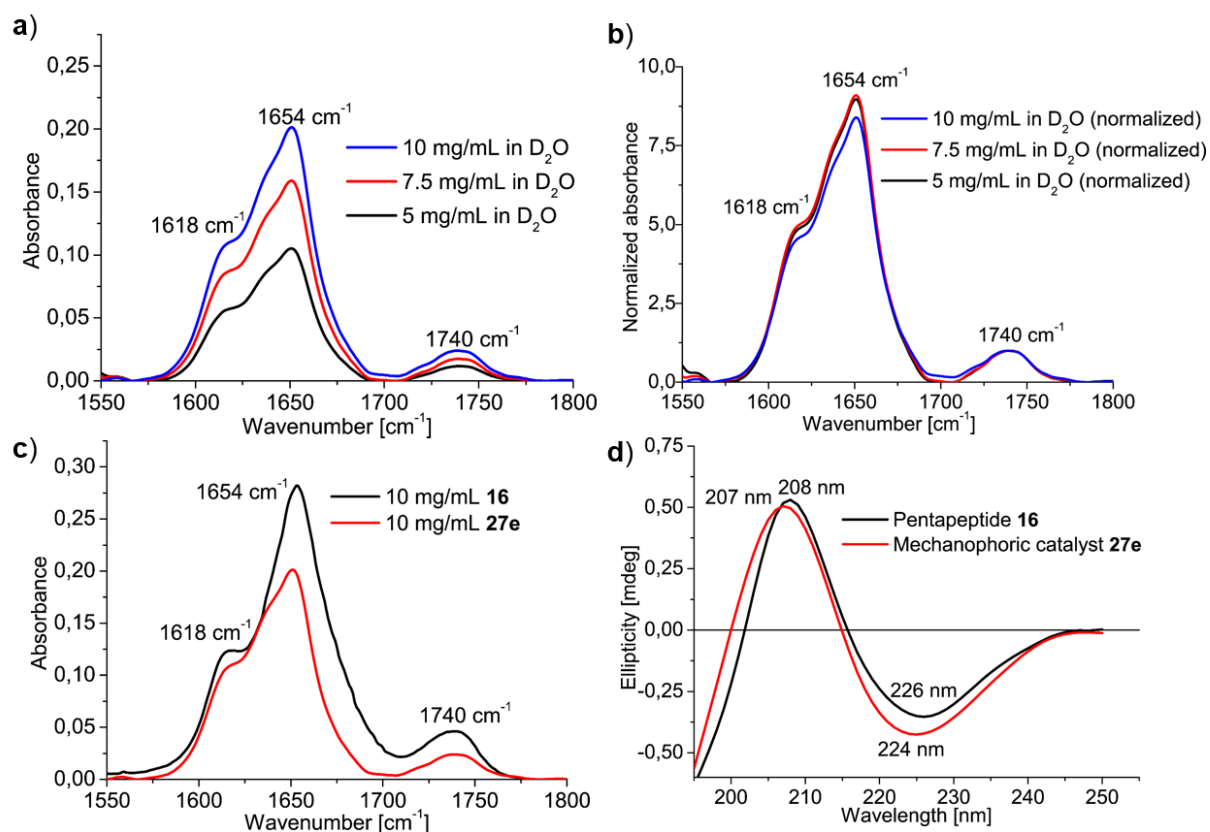


**Figure 41.** a) IR-spectra of  $[\text{Cu}(\text{C}_{10}\text{COOH-VPGVG-NHC})_2]\text{X}$  (**27e**) in  $\text{D}_2\text{O}$  at three different concentrations (5.0, 7.5 and 10.0 mg/mL). b) Normalization of the measured spectra to the band originating from the methyl ester protection group at  $1740\text{ cm}^{-1}$ . c) Overlay of the two measurements of Boc-VPGVG-OMe (**16**) and  $[\text{Cu}(\text{C}_{10}\text{COOH-VPGVG-NHC})_2]\text{X}$  (**27e**) at a concentration of 10.0 mg/mL. d) Overlay of the CD-spectra of Boc-VPGVG-OMe (**16**) and  $[\text{Cu}(\text{C}_{10}\text{COOH-VPGVG-NHC})_2]\text{X}$  (**27e**) in  $\text{D}_2\text{O}$  at a concentration of 0.4 mg/mL.

The two  $\beta$ -spiral indicating maxima at  $1618\text{ cm}^{-1}$  and  $1654\text{ cm}^{-1}$  were still present<sup>345</sup> proving again an independent  $\beta$ -Spiral formation within the tested concentration range (5.0 – 10.0 mg/ml). A perfect match of all three IR-spectra was obtained after normalization to the band at  $1740\text{ cm}^{-1}$ , which originated from the methyl ester protection group (see Figure 41b). For clarification, the measurements of Boc-VPGVG-OMe (**16**) and  $[\text{Cu}(\text{C}_{10}\text{COOH-VPGVG-NHC})_2]\text{X}$  (**27e**) at 10 mg/mL are also shown as overlay (see Figure 41c). Since in both cases 10 mg of sample were used, the variations in the absorbance intensities were the result of different molecular weights. As discussed in Chapter 3.2.2, the evaluation of IR-spectra of ELPs with generalized data from other peptides is difficult due to the unique property of  $\beta$ -spiral formation. To exclude the presence of  $\alpha$ -helical structures, which also would show an IR-band in the same range ( $1650 - 1658\text{ cm}^{-1}$ )<sup>339</sup>, additional CD-measurements were performed in  $\text{D}_2\text{O}$  with a concentration of 0.4 mg/mL. The comparison with spectra of Boc-VPGVG-OMe (**16**) revealed a significant similarity to the pure pentapeptide except small shifts of both maxima (see Figure 41d), still showing only  $\beta$ -sheet conformation and no  $\alpha$ -helical structures.

Accordingly, the  $\beta$ -spiral formation was not prevented by the linkage of two pentapeptide units *via* the mechanophoric catalyst, thus allowing the ELP sequence to act as “molecular spring”. It was demonstrated earlier that each pentapeptide unit forms the  $\beta$ -spiral structure independently from other pentapeptide units<sup>257</sup>.

### 3.3.3 Mechanophoric activity of the linear catalysts

After the successful synthesis of a variety of peptide-modified mechanophoric catalysts **27a-g**, their mechanoresponsive behavior and their catalytic properties towards the CuAAC were tested. Therefore, ultrasonication experiments were performed to apply external force. Ultrasonication is a common

method for the application of stress in solution<sup>33, 37, 88, 120, 129-130, 136</sup> (also see Chapter 1.1.5). The applied force is transmitted along the peptide backbone to the labile copper-carbene bond, thus generating a free coordination site at the Cu(I) center as shown in Figure 42. Hence, the coordination of an alkyne is no longer sterically hindered, in turn allowing the “click” reaction to take place (also see Chapters 1.1.6.2 and 1.2). In order to prove the initial latency and the mechanophoric origin of the catalytic activity, control experiments had to be performed in the absence of ultrasound to exclude thermal influences. Accordingly, a model “click” reaction between phenylacetylene (**28**) and benzyl azide (**29**) (for synthesis and characterization see Experimental Part 4.5 and Appendix 7.5) was used monitoring the catalytic behavior of the initial as well as the activated mechanocatalysts in the absence and presence of ultrasound *via* <sup>1</sup>H-NMR spectroscopy (see Figure 42).

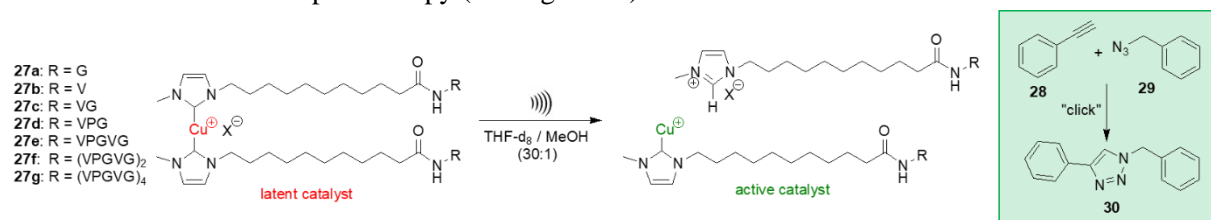


**Figure 42.** Ultrasound induced activation of the mechanophoric complexes **27a-g** leading to scission of the labile copper-carbene bond. Removal of one of the sterically shielding NHC ligands allows coordination of an alkyne to the Cu(I) center and thus the CuAAC reaction between phenylacetylene (**28**) and benzyl azide (**29**) can take place.

For the ultrasonication experiments, the respective mechanocatalyst (**3a**, **3b**, **4b** or **27a-g**) was dissolved in a mixture of THF-d<sub>8</sub> and MeOH (30:1) with a concentration of 0.75 mmol/L. The addition of MeOH was crucial since it protonated the cleaved carbene, thus preventing the backreaction to the Cu(I) bis(NHC) and increasing the conversion of the CuAAC<sup>37</sup>. After addition of 100 eq. of **28** and **29** the mixture was subjected to repeated cycles of pulsed ultrasound while it was cooled in a water bath to avoid the temperature from rising above room temperature. Samples were taken before each experiment as well as after the 3<sup>rd</sup>, 5<sup>th</sup>, 10<sup>th</sup>, 14<sup>th</sup> and 17<sup>th</sup> cycle and the “click” conversion was calculated *via* <sup>1</sup>H-NMR spectroscopy. Therefore, the shift of the methylene group from **29** at 4.35 ppm to 5.59 ppm for **30** could be observed as well as an increasing resonance for the triazole ring at 8.10 ppm. The results for all conducted ultrasonication experiments are summarized in Table 3 as well as in Figure 43. An overview about the sonication dependent conversions is also given in the Experimental Part 4.6 (Table 8).

Blind experiments at room temperature in the absence of any mechanophoric catalyst proved that the “click” reaction between **28** and **29** did not take place in the presence of ultrasonication (Table 3, entry 1). Therefore, any participation of ultrasound to the uncatalyzed “click” reaction could be excluded. Furthermore, the latent nature of the synthesized mechanophores was proven by stirring **28** and **29** at room temperature in the presence of mechanophoric catalysts but in the absence of ultrasound (ent. 9, 12, 15, 18, 21, 27). After 42.5 hours (corresponding to the time needed for 17 cycles of ultrasonication), no formation of the “click” product could be observed in all cases. To also exclude thermal influences, all control experiments were repeated at 60 °C (ent. 10, 13, 16, 19, 22, 28) and revealed only small conversions (< 2 %) in the range of the thermal 1,3-dipolar Huisgen cycloaddition (ent. 2) after 42.5 hours.

**Table 3.** Ultrasonication induced "click" reactions between phenylacetylene (**28**) and benzyl azide (**29**)<sup>a</sup>. Sonication cycle dependent conversions are shown in Figure 43 as well as in the Experimental Part 4.6.

Entry	Catalyst	Ultrasound	Amplitude (%)	t (h)	US cycles <sup>b</sup>	T (°C)	Final conversion (%) <sup>c</sup>
1	without	off	-	42.5	-	rt	0
2	without	off	-	42.5	-	60	2.0
3	without	on	20	42.5	17	rt	0
4	<b>3a</b>	on	30	25	10	rt	0
5	<b>3a</b>	on	20	35	14	rt	1.0
6	<b>3b</b>	on	30	25	10	rt	0
7	<b>3b</b>	on	30	25	10	0	0
8	<b>3b</b>	on	20	42.5	17	rt	3.8
9	<b>3b</b>	off	-	42.5	-	rt	0
10	<b>3b</b>	off	-	42.5	-	60	1.9
11	<b>4b</b>	on	20	42.5	17	rt	3.4
12	<b>4b</b>	off	-	42.5	-	rt	0
13	<b>4b</b>	off	-	42.5	-	60	1.9
14	<b>27a</b>	on	20	42.5	17	rt	3.8
15	<b>27a</b>	off	-	42.5	-	rt	0
16	<b>27a</b>	off	-	42.5	-	60	1.9
17	<b>27b</b>	on	20	42.5	17	rt	3.8
18	<b>27b</b>	off	-	42.5	-	rt	0
19	<b>27b</b>	off	-	42.5	-	60	2.0
20	<b>27c</b>	on	20	42.5	17	rt	4.3
21	<b>27c</b>	off	-	42.5	-	rt	0
22	<b>27c</b>	off	-	42.5	-	60	1.9
23	<b>27d</b>	on	20	42.5	17	rt	4.3
24	<b>27e</b>	on	20	42.5	17	rt	4.7
25	<b>27f</b>	on	20	42.5	17	rt	5.2
26	<b>27g</b>	on	20	42.5	17	rt	5.6
27	<b>27g</b>	off	-	42.5	-	rt	0
28	<b>27g</b>	off	-	42.5	-	60	2.9

<sup>a</sup>For all reactions 1.0 eq. of azide **28**, 1.0 eq. of alkyne **29** and 0.01 eq. of the Cu(I) catalyst (0.75 mM) were used in THF-d<sub>8</sub>/MeOH (30:1) (v/v). <sup>b</sup>One cycle consisted of 90 min pulsing at 20 kHz with 20 % or 30 % amplitude of 125 μm with a pulse sequence of 5 s/pulse, 10 s/break followed by 60 min without pulsing. <sup>c</sup>The "click" reaction was followed by the increasing triazole resonance originating from product **30** in the <sup>1</sup>H-NMR spectrum at δ = 8.11 ppm as well as the shift from the methylene group of **29** from δ = 4.35 ppm to δ = 5.59 ppm with a standard deviation of ± 1 %.

First ultrasonication experiments were conducted with the pure mechanophoric catalysts [Cu(C<sub>6</sub>COOMe-NHC)<sub>2</sub>]<sub>2</sub>X (**3a**), [Cu(C<sub>10</sub>COOMe-NHC)<sub>2</sub>]<sub>2</sub>X (**3b**) and [Cu(C<sub>10</sub>COOH-NHC)<sub>2</sub>]<sub>2</sub>X (**4b**) which did not bear any amino acid or peptide. These experiments were also conducted with a higher energy input by using an amplitude of 30 % (ent. 4, 6, 7) which is commonly used in literature<sup>37-38, 88</sup>. However, a rapid formation of a grey precipitate during the first two cycles was observed and no "click" conversion could be detected *via* <sup>1</sup>H-NMR spectroscopy. Therefore, a rapid decomposition of the catalyst was concluded which prevented catalysis of the CuAAC. A variation of the temperature (0 °C and room temperature) did not show any effect. Thus, the amplitude was decreased to 20 % to reduce the energy input and to avoid a premature destruction of the catalyst. Since the energy input was lower

due to the decreased amplitude (20 % amplitude: sonication intensity of  $4.66 \text{ W cm}^{-1}$  and an energy input of 11 kJ per cycle, 30 % amplitude: sonication intensity of  $8.75 \text{ W cm}^{-1}$  and an energy input of 21 kJ per cycle), ultrasonication experiments were conducted for 17 cycles instead of ten cycles. Repeating the ultrasonication experiments of  $[\text{Cu}(\text{C}_6\text{COOMe-NHC})_2]\text{X}$  (**3a**),  $[\text{Cu}(\text{C}_{10}\text{COOMe-NHC})_2]\text{X}$  (**3b**) and  $[\text{Cu}(\text{C}_{10}\text{COOH-NHC})_2]\text{X}$  (**4b**) with the lower amplitude at room temperature led to small conversions of the “click” reaction for **3b** and **4b** in the range of 3.5 % after the 17<sup>th</sup> cycle. Contrary to **4b** which showed a conversion of 2.0 % after the tenth cycle, catalyst **3b** already showed a small conversion (0.5 %) after the fifth cycle. Solely catalyst **3a** showed a comparably smaller conversion of 1.0 % after the 14<sup>th</sup> cycle. Due to the smaller activity and the low yield during synthesis (see Chapter 3.1) all following experiments were therefore performed with catalyst **4b** as building block for the peptide coupling reactions.

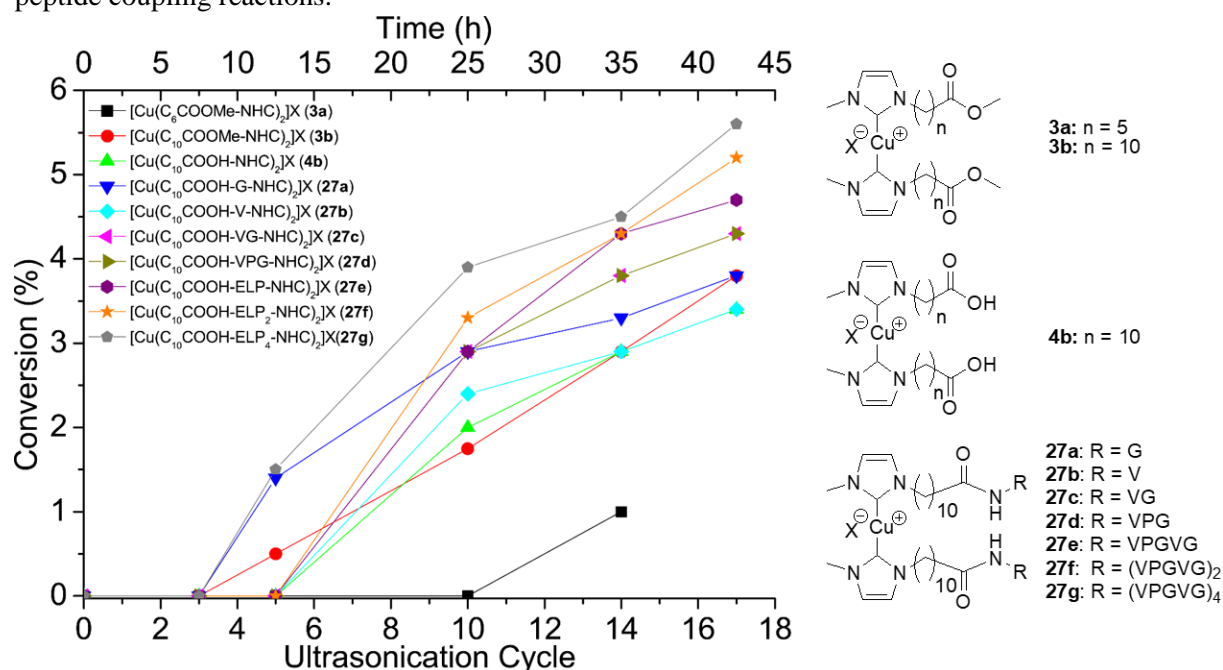


**Figure 43.** Time and ultrasonication cycle dependent conversion of an equimolar mixture of phenylacetylene (**28**) and benzyl azide (**29**) in a mixture of THF- $d_8$  and MeOH (30:1) using different mechanophoric catalysts.

In a next step, catalysts  $[\text{Cu}(\text{C}_{10}\text{COOH-G-NHC})_2]\text{X}$  (**27a**) and  $[\text{Cu}(\text{C}_{10}\text{COOH-V-NHC})_2]\text{X}$  (**27b**) were tested since it was crucial to prove that the catalysts retained their mechanophoric behavior after the peptide coupling reactions. Calculation of the “click” conversion revealed an unchanged mechanophoric activity with conversions around 3.5 % after the last cycle. Therefore, catalysts  $[\text{Cu}(\text{C}_{10}\text{COOH-VG-NHC})_2]\text{X}$  (**27c**) and  $[\text{Cu}(\text{C}_{10}\text{COOH-VPG-NHC})_2]\text{X}$  (**27d**) were tested for their mechanoresponsivity. Both catalysts showed identical activity with first conversions after the tenth cycle (2.9 %) that were increasing to 4.3 % after the last cycle. Up to now, the tested catalysts were only modified with short amino acid sequences that were not able to adopt the  $\beta$ -spiral structure. Thus, mechanocatalysts  $[\text{Cu}(\text{C}_{10}\text{COOH-VPGVG-NHC})_2]\text{X}$  (**27e**),  $[\text{Cu}(\text{C}_{10}\text{COOH-(VPGVG)}_2\text{-NHC})_2]\text{X}$  (**27f**) and  $[\text{Cu}(\text{C}_{10}\text{COOH-(VPGVG)}_4\text{-NHC})_2]\text{X}$  (**27g**) were tested which could show the “molecular spring” behavior as previously proven (see Chapter 3.3.2). Extension of the  $\beta$ -spiral led to stepwise increase of the conversion from 4.7 % (**27e**) to 5.2 % (**27f**) and 5.6 % (**27g**) after the last ultrasonication cycle. Furthermore, catalyst **27g** also showed the highest conversion after the fifth cycle (1.5 %). Even though the observed catalytic activity scaled with an increasing chain length of the attached peptide, the conversions were comparably low. One explanation might be the shorter chain length of the attached polymeric handles in comparison to other mechanocatalysts that are known in literature (commonly  $M_w > 10\,000 \text{ g/mol}$ )<sup>37-38</sup>. It is well known that an increasing chain length favors the activation

of the catalyst<sup>137-138</sup>. Therefore, the amount of activated catalyst in dependence from the ultrasonication cycle was also calculated *via* <sup>1</sup>H-NMR spectroscopy as exemplary shown for **27e** in Figure 44.

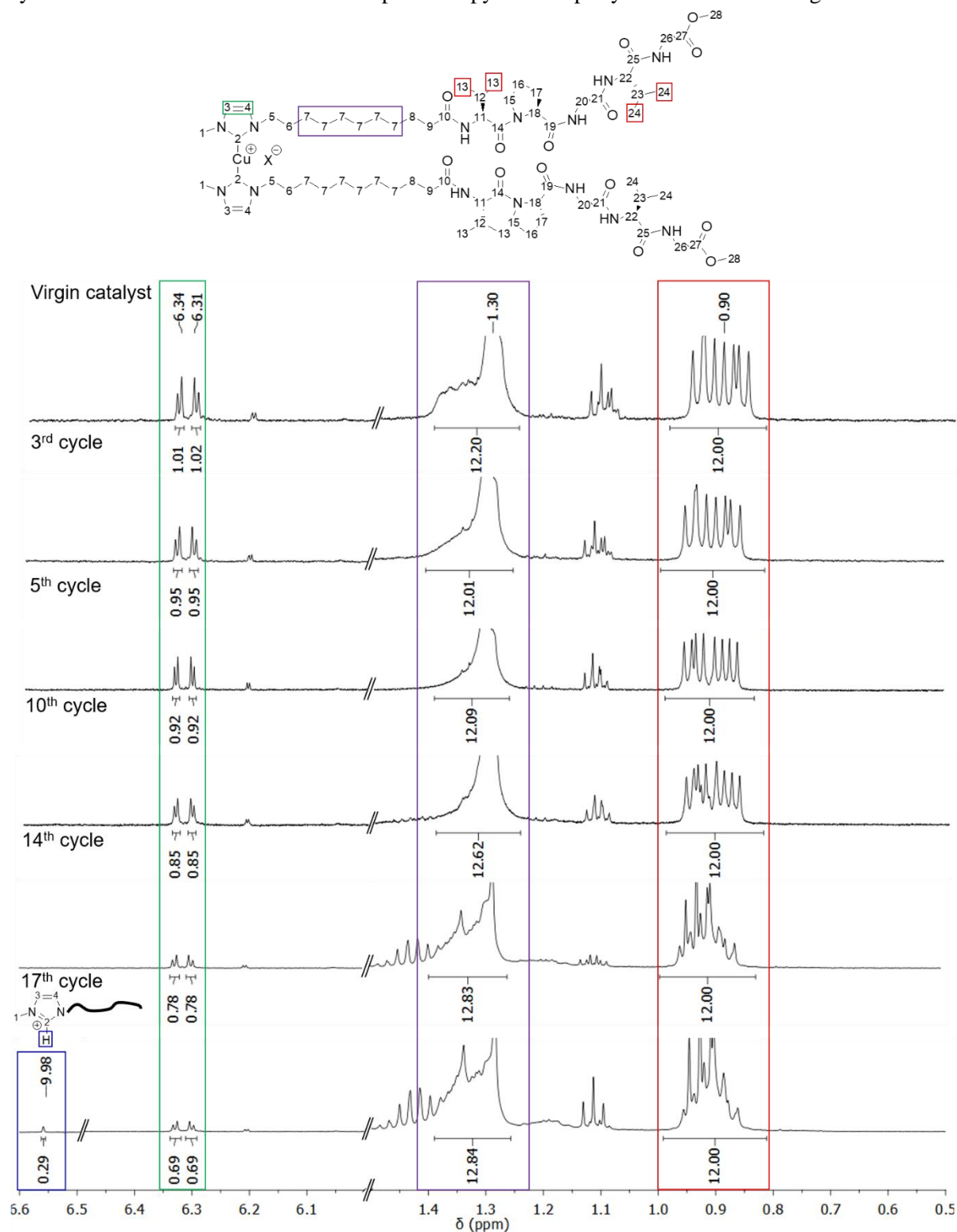


**Figure 44.** Cutouts from the stacked <sup>1</sup>H-NMR spectra of **27e**, showing the stepwise activation of the catalyst by following the reduction of the bis(NHC) resonances from protons  $H_3$  and  $H_4$  (green) at 6.34 and 6.31 ppm in dependence from the applied ultrasonication cycles. Additionally, reprotonation of the cleaved NHC ligand by MeOH is visible due to the increasing resonance at 9.98 ppm, originating from proton  $H_2$  (blue).

Only the necessary resonances for the calculation are shown. Protons  $H_{13}$  and  $H_{24}$  ( $-\text{CH}(\text{CH}_3)_2$ ) (red) at 0.90 ppm were used as reference since they stayed constant over the complete ultrasonication

experiment. As double check, also the resonances from protons  $H_7$  (purple) originating from the alkyl chain were integrated since they also should stay constant. The resonances at 6.34 and 6.31 ppm from protons  $H_3$  and  $H_4$  ( $-NCH=CHN-$ ) (green) belonged to the uncleaved Cu(I)-imidazol-2-ylidene moieties. Hence, following their reduction of the integral allowed to calculate the amount of activated mechanocatalyst. Additionally, the increasing resonance at 9.98 ppm (blue, only shown for the last cycle) proved the cleavage of the mechanocatalyst and the subsequent reprotonation of the generated NHC ligand by MeOH. It is worth mentioning that no occurrence of the Cu(I) mono(NHC) signal could be detected (around 6.40 and 6.55 ppm). Presumably, the presence of a large amount of heteroatoms within the polymer backbone favored a rapid degradation of the monocarbene complex once it was formed. As calculated from the  $^1\text{H-NMR}$  spectrum, only eight percent of the Cu(I) bis(NHC) catalyst were activated after the 5<sup>th</sup> cycle of ultrasonication, also giving an explanation why most catalysts did not show any catalytic activity until the 10<sup>th</sup> cycle of ultrasonication when 15 % of the catalyst were activated. After the last cycle of ultrasonication, approximately 30 % of the catalyst were activated while 70 % were still in the latent form. Thus, activation behavior of the mechanocatalysts differed from the Cu(I) bis(NHC) complexes with synthetic polymeric handles which usually showed an efficient activation within the first five cycles of ultrasonication (20 – 30 % conversion of the “click” product **30**)<sup>37-38</sup>. The most conclusive explanation for the comparably slow activation behavior of the peptide bearing mechanocatalyst is the shorter chain length. Hence, force accumulation is less effective as for mechanocatalysts with longer polymeric handles, leading to inferior activation and to smaller conversions for the CuAAC. However, further elongation of the peptide chains was not viable due to the diminishing yields for both the peptide coupling reactions as well as the coupling reactions to the mechanophoric catalyst. Especially the yields for the coupling reactions to the mechanophore were pretty low ( $[\text{Cu}(\text{C}_{10}\text{COOH}-(\text{VPGVG})_2\text{-NHC})_2]\text{X}$  (**27f**) (11 %) and  $[\text{Cu}(\text{C}_{10}\text{COOH}-(\text{VPGVG})_4\text{-NHC})_2]\text{X}$  (**27g**) (14 %)), making further elongation of the chains rather uneconomic. Additionally, the previously mentioned rapid degradation of the Cu(I) mono(NHC) complex might also play a role, which most probably is the result of the high amounts of heteroatoms within the backbone.

### 3.4 Synthesis, characterization and mechanochemical activity of the chain-extended mechanocatalysts (**35**)

Since a further elongation and coupling of the (VPGVG)<sub>4</sub> sequence to the mechanophoric catalyst was not viable due to the diminishing yields of the coupling reactions, in a second approach chain-extended catalysts were synthesized to further increase the mechanocatalytic activity (see Figure 45).

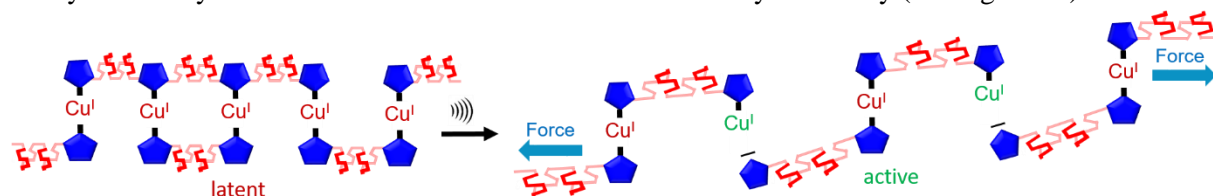
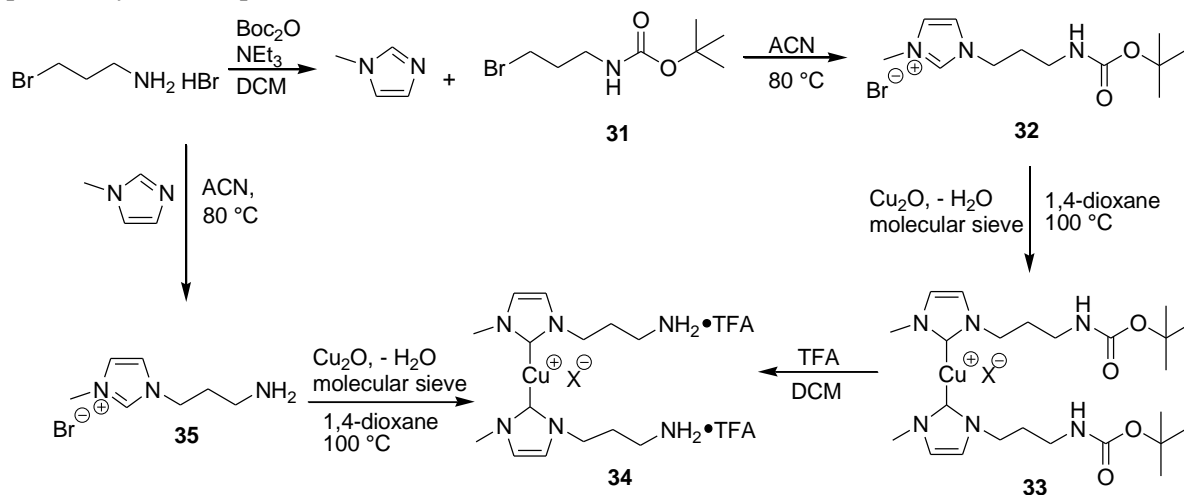


**Figure 45.** Chain-extended catalysts bear more than one Cu(I) bis(NHC) center and therefore offer several possible cleaving points when ultrasound is applied. Furthermore, incorporation of the VPGVG sequence (red) allowed exploitation of the “molecular spring” behavior due to formation of the  $\beta$ -spiral.

The chain-extended catalysts bore more than one Cu(I) center and combined two advantages: First, incorporating several Cu(I) bis(NHC) moieties into one polymer chain offered more than one possible cleaving point which led to generation of more than one catalytic active center after ultrasound was applied. Second, chain-extended catalysts were easily accessible through the reaction of a bifunctional mechanocatalyst and the double deprotected pentapeptide  $\text{TFA}\cdot\text{H}_2\text{N-VPGVG-OH}$  (**19**), thus also incorporating the  $\beta$ -spiral into the chain-extended mechanocatalysts. However, using mechanocatalyst **4b** for chain-extension was not sufficient since for the polycondensation reaction with **19** and **4b** a second mechanocatalyst with two amino groups was needed.

### 3.4.1 Synthesis and characterization of the NH<sub>2</sub>-functionalized mechanocatalyst (**34**)

Hence, mechanocatalyst **34** was synthesized in a four step synthesis as shown in Scheme 7. The catalyst was chosen since it had a similar structure compared to catalyst **4b**, which was also build up from imidazolium based NHC precursors and which was investigated for its mechanophoric behavior in detail previously (see Chapter 3.3.3).



**Scheme 7.** Synthetic approach for the NH<sub>2</sub>-functionalized mechanocatalyst **34**.

In a first step, the 3-bromopropan-1-amine hydrobromide was Boc-protected, thus generating **31** in quantitative yields. The quaternization reaction was performed with *N*-methylimidazole in ACN and generated the NHC precursor **32**. Synthesis of [Cu(C<sub>3</sub>NHBoc-NHC)<sub>2</sub>]X (**33**) was accomplished analogous to the synthesis of the carboxyl functionalized catalyst by refluxing at 100 °C in the presence of Cu<sub>2</sub>O in 1,4-dioxane<sup>325</sup>. Compared to the synthesis of **3b** (40 % yield), the yield was slightly lower with 25 %. However, the subsequent Boc-deprotection with TFA was again quantitative, thus generating [Cu(C<sub>3</sub>NH<sub>2</sub>•TFA-NHC)<sub>2</sub>]X (**34**) with two unprotected amino groups. Direct quaternization of 3-bromopropan-1-amine hydrobromide to **35** was also tested since it would allow to avoid the accomplished Boc-protection and deprotection step, further simplifying the reaction. However, separation of the unprotected NHC precursor from unreacted 3-bromopropan-1-amine hydrobromide and *N*-methylimidazole was not possible which prevented a successful purification of **35**.

The successful synthesis of **34** could be proven by comparing the <sup>1</sup>H-NMR spectrum of the imidazolium precursor **32** (Figure 46a) with the <sup>1</sup>H-NMR spectrum of the protected catalyst **33** (Figure 46b) and the deprotected catalyst **34** (Figure 46c). A full characterization of all compounds is given in the Experimental Part 4.7, while the according spectra are presented in the Appendix 7.6. Deprotonation and formation of the Cu(I) bis(NHC) complex could be proven by the missing resonance at 10.30 ppm originating from proton H<sub>2</sub> (–NCHN–) for compound **33** (see Figure 46b). Furthermore, protons H<sub>3</sub> and H<sub>4</sub> (–NCH=CHN–) significantly shifted from 7.38 and 7.63 ppm to 6.18 ppm. The <sup>1</sup>H-NMR spectrum of complex **34** (see Figure 46c) revealed the successful removal of the Boc-protection group which was no longer visible at 1.42 ppm. Moreover, the <sup>1</sup>H-NMR spectrum indicated that both amino groups of **34** were protonated after deprotection due to the TFA (resonance at 7.80 ppm corresponding to –NH<sub>3</sub><sup>+</sup>TFA<sup>–</sup>). Successful deprotonation and formation of the copper-carbene bond could also be proven *via* <sup>13</sup>C-NMR spectroscopy due to a pronounced shift of C<sub>2</sub> (–NCHN–) from δ = 138.0 to δ = 153.6 ppm which was in accordance with literature<sup>37</sup> (see Appendix 7.6).

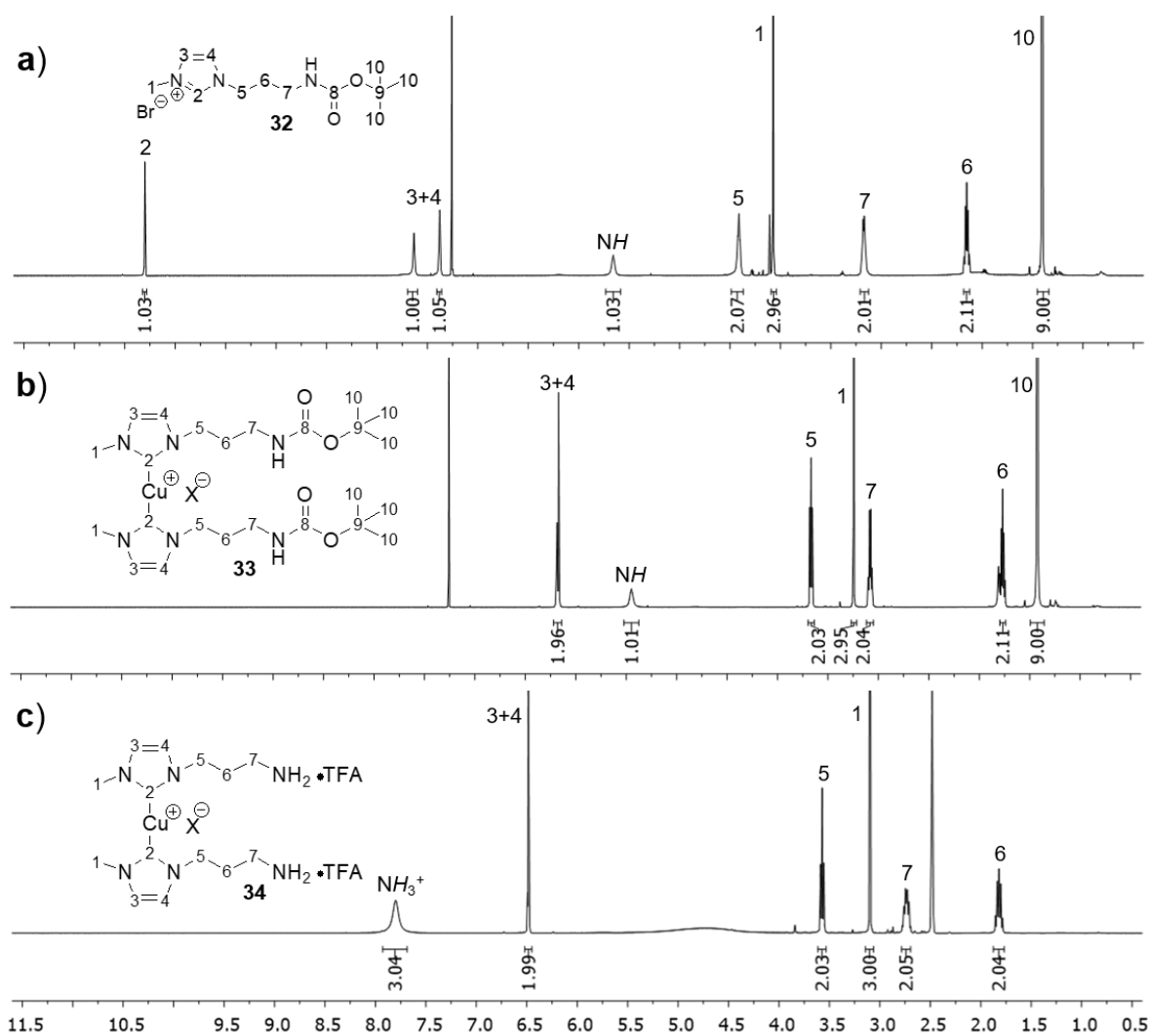
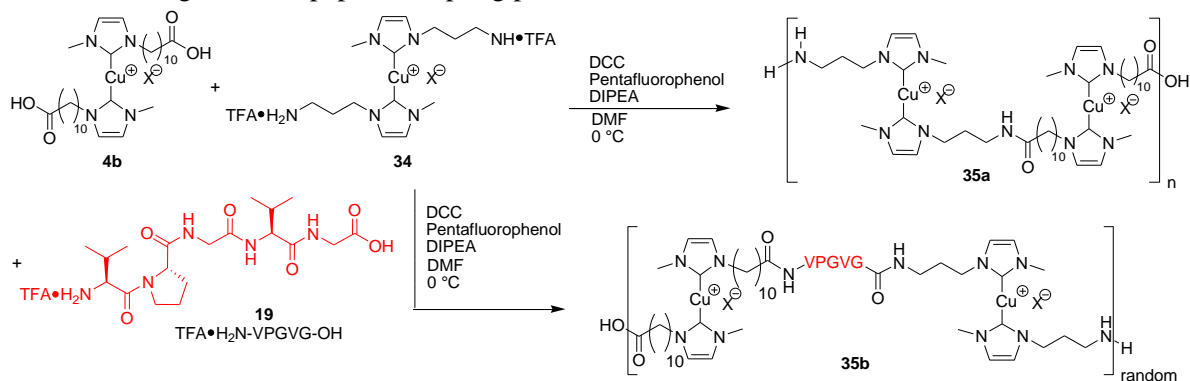


**Figure 46.**  $^1\text{H}$ -NMR spectra of a) the NHC precursor **32**, b) the Boc-protected complex **33** and c) the deprotected complex **34** bearing two amino groups.

### 3.4.2 Synthesis of the chain-extended mechanocatalysts (**35**)

Consecutively, the two chain-extended mechanocatalysts **35a** and **35b** were synthesized according to Scheme 8 using common peptide coupling protocols<sup>257</sup>.



**Scheme 8.** Synthesis of the chain-extended mechanophores **35a** and **35b**.

First, mechanophore **35a** was generated *via* polycondensation of the two low molecular weight complexes **4b** and **34**. Due to the bifunctional character of both catalysts, an equimolar polycondensation

under the formation of amide bonds took place, embedding the Cu(I) bis(NHC) complex within a polyamide chain. For the coupling reaction DCC and pentafluorophenol were used as previously done for the buildup of the linear mechanocatalysts **27a-g**. The reaction could be followed with GPC measurements and the results are shown in Figure 47a. Formation of dimeric structures (1100 g/mol) could be observed at the early stage of the reaction (one hour), while bigger condensates (5400 g/mol up to 13200 g/mol) could be observed after ongoing reaction time (up to 75 h). Due to the step-growth character of the polycondensation the obtained mechanocatalysts showed comparably broad molecular weight distributions. Further elongation of the reaction time (> 90 h) caused a decomposition of the once formed catalyst as indicated by a decrease of the molecular weight. Most probably, a premature cleavage of the mechanolabile copper-carbene bonds appeared presumably due to the rapidly increasing chain length. Nevertheless, quenching the reaction after 75 h and purifying *via* column chromatography yielded the pure **35a**. The successful synthesis was proven *via*  $^1\text{H-NMR}$  spectroscopy due to the absence of any resonance at 10.50 ppm which would originate from reprotonation of the NHC ligand ( $\text{H}_2$ ,  $-\text{NCHN}-$ ) (see Figure 47b). Additionally, the remaining resonances from protons  $\text{H}_3$ ,  $\text{H}_4$ ,  $\text{H}_{14}$  and  $\text{H}_{15}$  ( $-\text{NCH}=\text{CHN}-$ ) indicated the persistence of the Cu(I) bis(NHC) species.

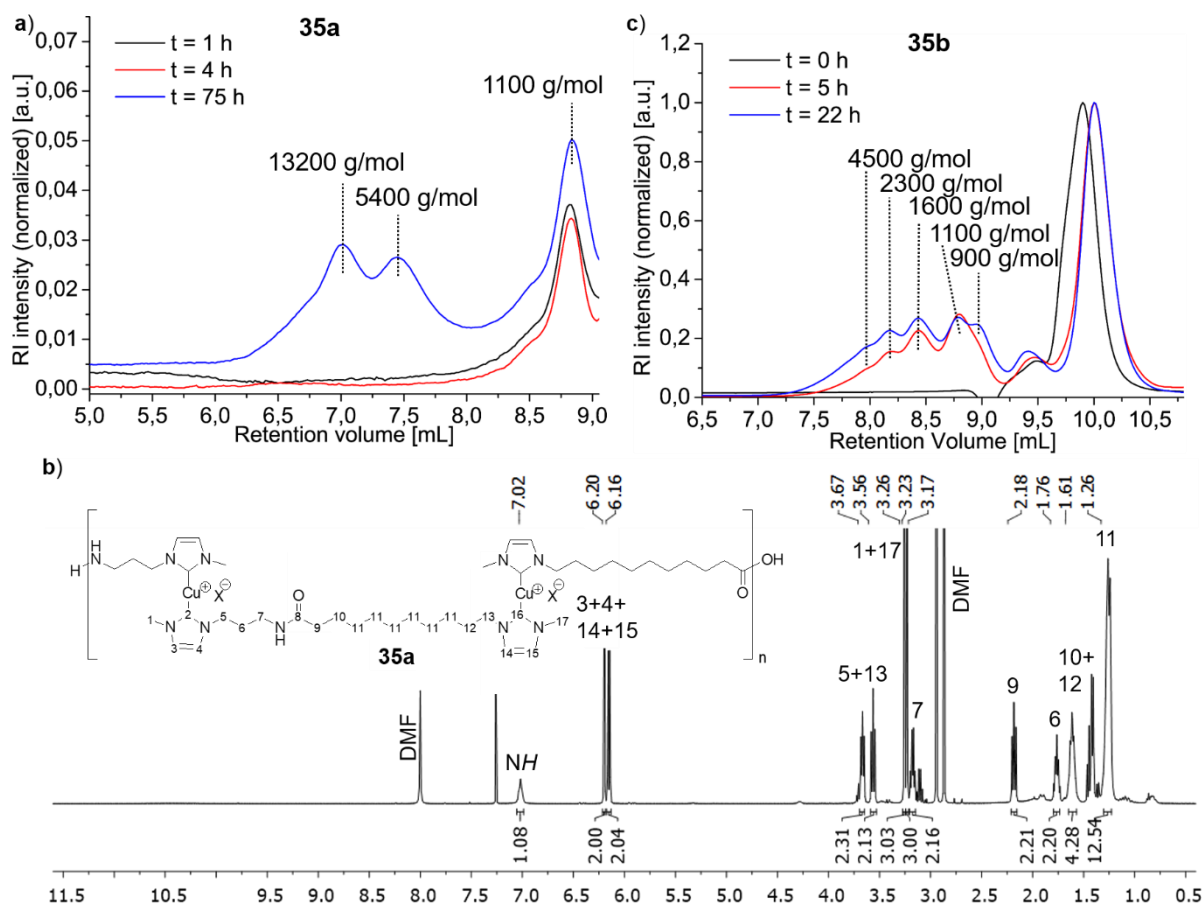


**Figure 47.** a) Time dependent GPC traces for the synthesis of **35a**. b)  $^1\text{H-NMR}$  spectrum from **35a**. c) Time dependent GPC traces for the synthesis of **35b**.

In order to incorporate the  $\beta$ -spiral into the chain-extended catalysts, equimolar amounts of the low molecular weight catalysts **4b** and **34** were mixed with five equivalents of the double deprotected pentapeptide  $\text{TFA}\cdot\text{H}_2\text{N-VPGVG-OH}$  (**19**). Thus, the “molecular spring” behavior could be introduced into catalyst **35b** by polycondensation after addition of DCC and pentafluorophenol. Likewise for the first mechanophore, the reaction could be followed by GPC measurements as shown in Figure 47c. Again, at the beginning of the reaction ( $t = 0$  h) only monomeric and dimeric species could be observed while higher molecular weight species (up to 4500 g/mol) could be observed with ongoing reaction. To

avoid an unintended premature cleavage of the chain-extended catalyst, the reaction was stopped after 22 hours.

The mechanophoric activity of catalyst **35b** is thought to be better in comparison to **35a** since the incorporated pentapeptide sequence can act as “molecular spring”. Furthermore, incorporation of the peptide sequence increases the distance between two Cu(I) centers and therefore increases the ability to accumulate and transmit the force. Contrary, the distance between two Cu(I) centers for **35a** is shorter which will lead to inferior force accumulation and transmission. However, catalyst **35a** should show an alternating structure as a consequence of the bifunctionality of both catalysts. Hence, every carboxyl group from **4b** should react with the amino group from **34** and *vice versa*. Contrary, the addition of **19** will lead to a more random structure of the resulting catalyst **35b**.

### 3.4.3 Mechanophoric activity of the chain-extended catalysts **35**

Similarly to mechanocatalysts **27a-g**, the mechanocatalytic activity of complexes **33**, **34** and **35a,b** towards the CuAAC was tested *via* ultrasonication experiments by following the “click” reaction between phenylacetylene (**28**) and benzyl azide (**29**) (see Chapter 3.3.3). Again, the conversion was calculated by <sup>1</sup>H-NMR spectroscopy *via* the shift of the methylene group from **29** at 4.35 ppm to 5.59 ppm for **30** as well as an increasing resonance for the triazole ring at 8.10 ppm. Samples were taken before each experiment as well as after the 3<sup>rd</sup>, 5<sup>th</sup>, 10<sup>th</sup>, 14<sup>th</sup> and 17<sup>th</sup> cycle. The results for all conducted ultrasonication experiments are summarized in Table 4 as well as in Figure 48. An overview about the sonication dependent conversions is also given in the Experimental Part 4.7.3 (Table 9). For comparison also the results for [Cu(C<sub>10</sub>COOH-NHC)<sub>2</sub>]X (**4b**) are shown.

**Table 4.** Ultrasonication induced “click” reactions between phenylacetylene (**28**) and benzyl azide (**29**)<sup>a</sup>. Sonication cycle dependent conversions are shown in Figure 48 as well as in the Experimental Part 4.7.3.

Entry	Catalyst	Ultrasound	Amplitude (%)	t (h)	US cycles <sup>b</sup>	T (°C)	Final conversion (%) <sup>c</sup>
1	<b>4b</b>	on	20	42.5	17	rt	3.4
2	<b>33</b>	on	20	42.5	17	rt	9.9
3	<b>33</b>	off	-	42.5	-	rt	0
4	<b>33</b>	off	-	42.5	-	60	2.5
5	<b>34</b>	on	20	42.5	17	rt	4.8
6	<b>34</b>	off	-	42.5	-	rt	0
7	<b>34</b>	off	-	42.5	-	60	2.4
8	<b>35a</b>	on	20	42.5	17	rt	3.9
9	<b>35a</b>	off	-	42.5	-	rt	0
10	<b>35a</b>	off	-	42.5	-	60	1.5
11	<b>35b</b>	on	20	42.5	17	rt	4.7

<sup>a</sup>For all reactions 1.0 eq. of azide **28**, 1.0 eq. of alkyne **29** and 0.01 eq. of the Cu(I) catalyst (0.75 mM) were used in THF-d<sub>8</sub>/MeOH (30:1) (v/v). <sup>b</sup>One cycle consisted of 90 min pulsing at 20 kHz with 20 % or 30 % amplitude of 125 μm with a pulse sequence of 5 s/pulse, 10 s/break followed by 60 min without pulsing. <sup>c</sup>The “click” reaction was followed by the increasing triazole resonance originating from product **30** in the <sup>1</sup>H-NMR spectrum at δ = 8.11 ppm as well as the shift from the methylene group of **29** from δ = 4.35 ppm to δ = 5.59 ppm with a standard deviation of ± 1 %.

The Boc-protected amine-based catalyst [Cu(C<sub>3</sub>NHBoc-NHC)<sub>2</sub>]Br (**33**) showed a significantly higher activity than its deprotected pendant [Cu(C<sub>3</sub>NH<sub>2</sub>•TFA-NHC)<sub>2</sub>]Br (**34**). A conversion of 4.8 % could already be detected after the 3<sup>rd</sup> cycle and increased linearly during the next cycles up to 9.9 % after the 17<sup>th</sup> cycle. Therefore, **33** is the only tested mechanocatalyst that already showed activity after the 3<sup>rd</sup> cycle. The deprotection of catalyst to **34** had a bigger influence on the mechanoresponsivity in comparison to [Cu(C<sub>10</sub>COOH-NHC)<sub>2</sub>]Br (**4b**): An activation could only be detected after the 10<sup>th</sup> cycle (2.9 % conversion), subsequently increasing linearly to a conversion of 4.8 % after the 17<sup>th</sup> cycle which

is only the half of the Boc-protected catalyst **33**. It can be hypothesized that the sterically demanding Boc-groups caused a pre-stretching of the copper-carbene bond and facilitated its cleavage<sup>37, 159</sup>. The higher conversion using **34** instead of the carboxyl-based catalyst **4b** could be explained by the ionic endgroup structure ( $-\text{NH}_3^+\text{TFA}^-$ ; see  $^1\text{H-NMR}$  spectrum, Figure 46c) of catalyst **34** which was able to facilitate the protonation of the cleaved free NHC and thus accelerated the copper(I)-acetylide formation.

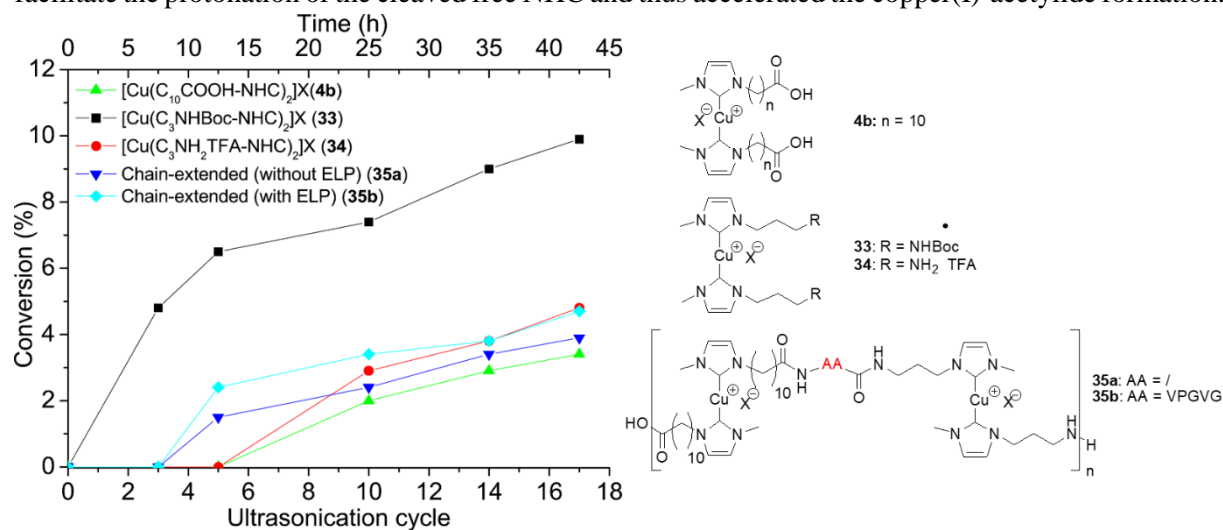


**Figure 48.** Time and ultrasonication cycle dependent conversion of an equimolar mixture of phenylacetylene (**28**) and benzyl azide (**29**) in a mixture of THF- $d_8$  and MeOH (30:1) using different mechanophoric catalysts.

The chain-extended catalyst **35b** with incorporated ELP sequences showed higher mechanophoric activity (4.7 % conversion after the last cycle) than the chain-extended catalyst **35a** without ELP sequences (3.9 % conversion after the last cycle). Even though the overall catalytic activity could not be increased in comparison to the linear mechanocatalysts **27a-g**, both catalysts already showed catalytic activity after the 5<sup>th</sup> cycle with conversions of 2.4 % (**35b**), respectively 1.5 % (**35a**). The majority of the linear mechanocatalysts **27a-g** (except **27a** and **27g**) only showed activation after the 10<sup>th</sup> cycle. Therefore, a facilitated activation due to the chain-extended structure and the increased concentration of Cu(I) bis(NHC) centers could be concluded.

The mechanochemical origin of the CuAAC was again proven by control experiments at room temperature as well as at 60 °C in the absence of ultrasonication. At room temperature no conversion could be detected *via*  $^1\text{H-NMR}$  spectroscopy after 42.5 hours (corresponding to the time needed for 17 cycles of ultrasonication) for all performed experiments (Table 4, entry 3, 6 and 9). The calculated conversions for the conducted experiments at 60 °C (Table 4, entry 4, 7 and 10) revealed only small conversions (< 2.5 %) in the range of the thermal 1,3-dipolar Huisgen cycloaddition.

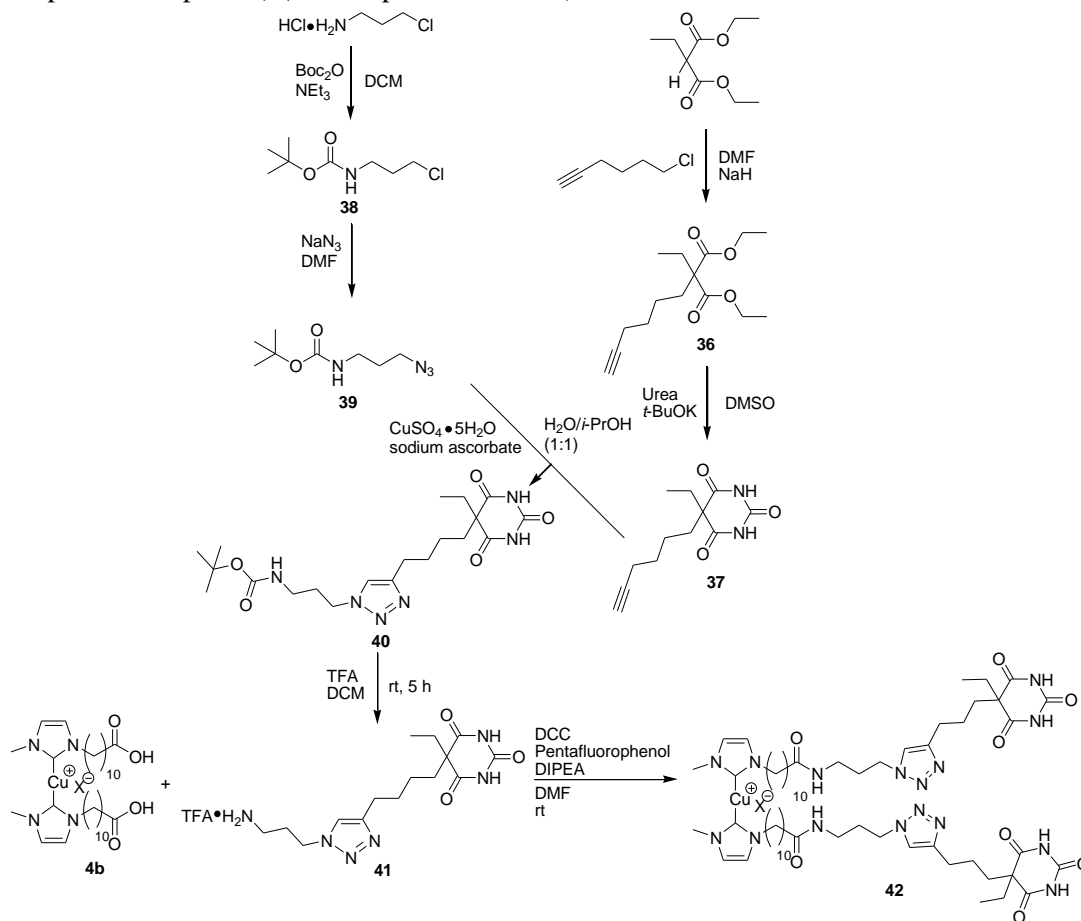
### 3.5 Synthesis, characterization and mechanochemical activity of the supramolecular mechanocatalyst

#### 3.5.1 Synthesis and characterization of the supramolecular catalyst (**42**)

Besides the synthesis of linear and chain-extended mechanocatalysts, in a third approach, mechanocatalysts containing supramolecular groups were synthesized. Incorporation and combination of mechanochemistry and supramolecular interactions might give rise to a series of interesting materials that combine strength, toughness and self-healing properties by sacrificial bonds<sup>70, 72-73, 127, 140</sup>. Barbiturates are well-known for their ability to form supramolecular cluster which can be used for self-healing approaches due to the reversible dissociation and association under stress<sup>322-324</sup>.

Therefore, the alkyne modified barbiturate **37** was synthesized as shown in Scheme 9. In order to allow a coupling of the barbiturate to the mechanocatalyst catalyst  $[\text{Cu}(\text{C}_{10}\text{COOH-NHC})_2]\text{X}$  (**4b**) the linker molecule *N*-(*tert*-butoxycarbonyl)-3-azidopropylamine **39** was also synthesized. This molecule initially allowed the CuAAC with the alkyne modified barbiturate thus generating **40**. Boc-deprotection then

generated a free amino group that could be coupled to the mechanocatalyst **4b**, using the same conditions that previously were described for the synthesis of the linear and chain-extended mechanocatalysts (DCC, pentafluorophenol) (see Chapter 3.3 and 3.4).



**Scheme 9.** Synthetic approach for the barbiturate-modified mechanocatalyst **42**.

A full characterization of all compounds is given in the Experimental Part 4.8 as well as in the Appendix 7.8. The  $^1\text{H-NMR}$  spectrum of **42** is shown in Figure 49, proving the successful synthesis and purification.

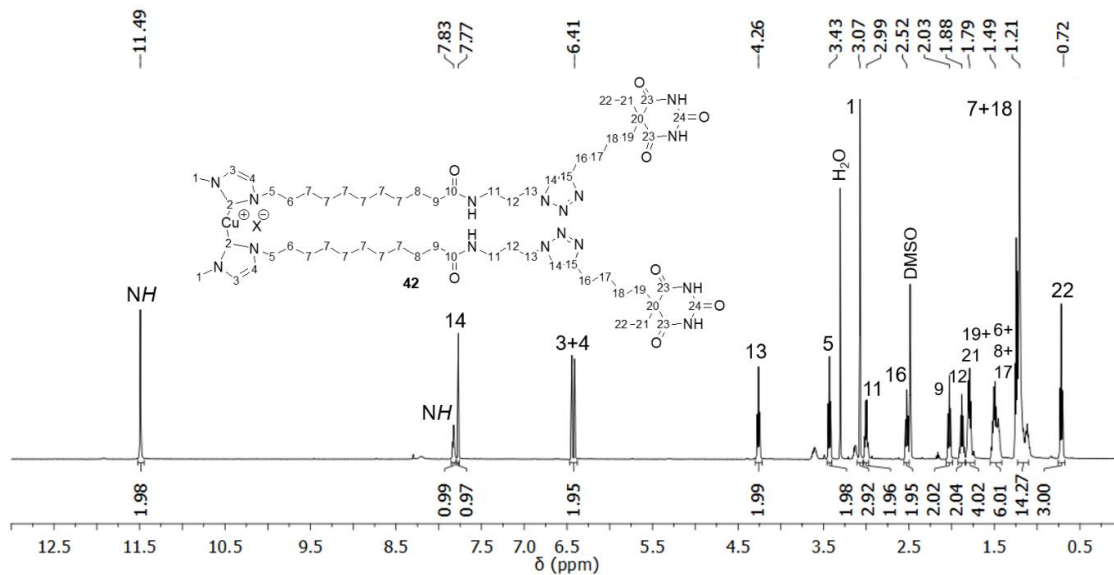


**Figure 49.**  $^1\text{H-NMR}$  spectrum of the supramolecular catalyst **42**.

The resonance at 7.83 ppm, originating from NH ( $-\text{C}(\text{O})\text{NHCH}_2-$ ) proved the formation of the peptide bond while the absence of proton resonances  $H_2$  ( $-\text{NCHN}-$ ) at 10.51 ppm showed that the catalyst was not destroyed during the reaction and the workup.

### 3.5.2 Activation of the supramolecular catalyst **42** in solution

Similarly to mechanocatalysts **27a-g**, the mechanocatalytic activity of complex **42** towards the CuAAC was tested *via* ultrasonication experiments by following the “click” reaction between phenylacetylene (**28**) and benzyl azide (**29**) (see Chapter 3.3.3). The conversion was calculated with  $^1\text{H-NMR}$  spectroscopy *via* the shift of the methylene group from **29** at 4.35 ppm to 5.59 ppm for **30** as well as an increasing resonance for the triazole ring at 8.10 ppm following the procedure that was described previously (see Chapter 3.3.3 and Experimental Part 4.9) The catalyst showed low activity with a conversion of 3.4 % after the last cycle which was comparable with the activity of  $[\text{Cu}(\text{C}_{10}\text{COOH-NHC})_2]\text{X}$  (**4b**) (3.4 %). However, the mechanophoric origin of the CuAAC could be proven *via* control experiments in the absence of ultrasonication at room temperature and at 60 °C. At room temperature no conversion could be detected after 42.5 hours (corresponding to the time needed for 17 cycles of ultrasonication). At 60 °C a conversion of 1.9 % could be detected which is in the range of the thermal 1,3-dipolar Huisgen cycloaddition. An overview about the sonication dependent conversions is also given in the Experimental Part 4.9 (Table 10).

### 3.5.3 Activation of the supramolecular catalyst **42** in bulk

Testing of the mechanocatalyst **42** in bulk was particularly interesting due to the occurring supramolecular interactions. However, activation in bulk required another detection method for the activation since  $^1\text{H-NMR}$  spectroscopy was not applicable. Hence, the highly fluorescent dye 7-hydroxy-3-(4-phenyl-1*H*-[1,2,3]triazole-1-yl)-coumarin (**44**) ( $\lambda_{\text{Em}} = 427$  nm and  $\lambda_{\text{Ex}} = 360$  nm, for synthesis, UV-vis and fluorescence spectra see Experimental Part 4.10 and Appendix 7.9) was used as detection tool which was successfully used for stress-sensing applications previously<sup>37</sup>. **44** was formed after the fluorogenic “click” reaction of 3-azido-7-hydroxycoumarin (**43**) and phenylacetylene (**28**) that could only take place after activation of the mechanocatalyst as shown in Figure 50.

Entanglement and cocrystallization of the catalyst **42** with the matrix might only play a minor role for the activation by compression due to the low molecular weight of **42**. Nevertheless, crystallinity of the matrix allows a better force transmission to the mechanophoric bond along the crystalline lamellae of the matrix (for details see Chapter 1.1.5). The catalyst was embedded into two different matrices which are shown in Figure 50a. The synthesis of both matrices is described in the Experimental Part 4.11 and 4.12. **45** was obtained *via* cationic ring opening polymerization of THF (112 000 g/mol according to GPC) while **48** was obtained *via* postmodification of a commercial  $\alpha,\omega$ -bis-hydroxy-PEG (8000 g/mol according to GPC) (for GPCs see Appendix 7.10). **45** was chosen since previous experiments proved the applicability of this matrix<sup>37, 94-95</sup>. However, to enable supramolecular interactions between the mechanocatalyst **42** and the matrix, the barbiturate modified PEG **48** was also tested. The primary difference between both matrices (**45** and **48**) is that the supramolecular mechanocatalyst **42** is able to participate in the cluster formation of **48** (compare Figure 50b and 50c). The huge amount of formed supramolecular clusters could also lead to a competitive reaction when compressional forces are applied which is the breakage of supramolecular clusters. Force dissipation by breakage of the supramolecular bonds might prevent an efficient activation of the Cu(I) bis(NHC) catalyst.

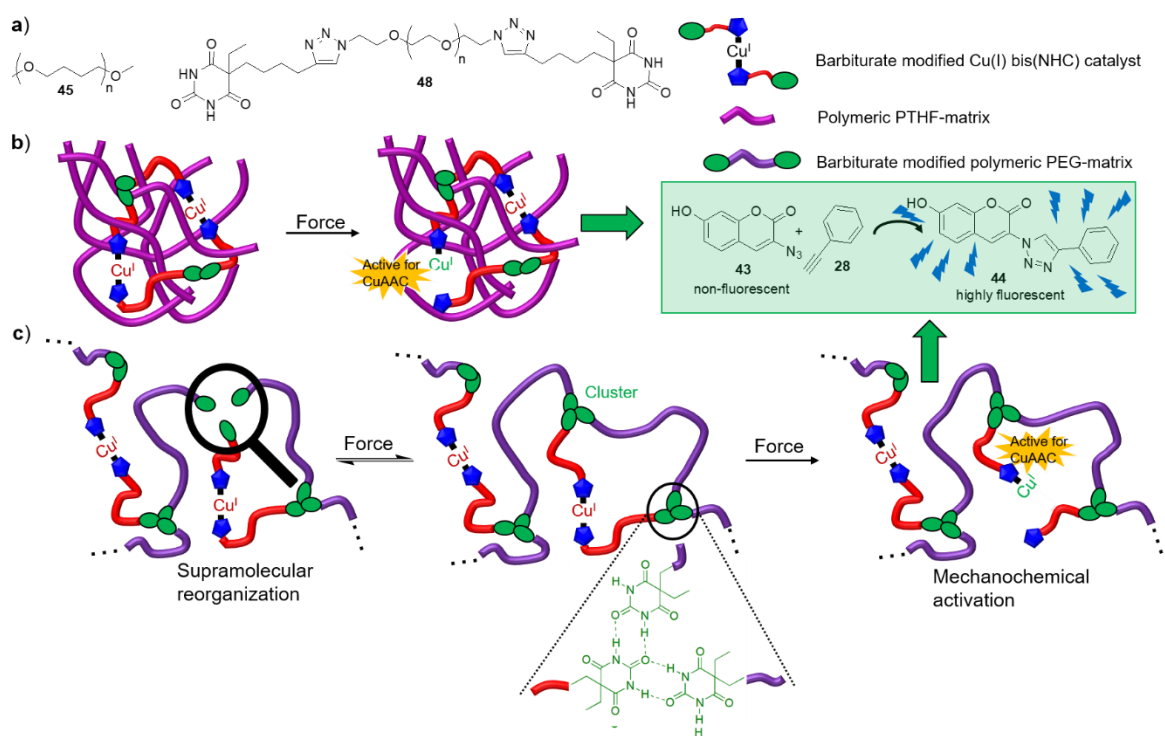


**Figure 50.** a) High molecular weight PTHF (**45**) and barbiturate modified PEG (**48**) were used as matrices for the compression experiments. b) Compression of the randomly distributed catalyst **42** in the matrix **45**. c) Catalyst **42** can participate in the supramolecular cluster formation of matrix **48**. Application of compressional forces can either lead to activation of the mechanocatalyst or to destruction of the supramolecular clusters.

Compression experiments were conducted by embedding the non-fluorescent 3-azido-7-hydroxycoumarin (**43**) and phenylacetylene (**28**) into 200 mg of the corresponding matrix (**45** or **48**) with a concentration of  $1.56 \cdot 10^{-4} \text{ mmol}_{\text{Cu}}/\text{mg}_{\text{sample}}$ . For the mechanocatalyst **42** a concentration of  $5.17 \cdot 10^{-6} \text{ mmol}_{\text{Cu}}/\text{mg}_{\text{sample}}$  was chosen. For the embedding all compounds were dissolved in THF to achieve a homogenous distribution within the matrix. After the solvent was removed, the samples were stored in the fridge for one week for crystallization. Subsequently, activation of the catalyst was achieved by compression cycles *via* an automatic hydraulic press. In total, 20 compression cycles were conducted for every experiment at which one cycle consisted out of 30 min of compression with a pressure of 10 tons, followed by 30 minutes without pressure. Due to the activation of **42**, a compression cycle dependent increase in the fluorescence activity at  $\lambda_{\text{Em}} = 427 \text{ nm}$  could be observed after excitation at  $\lambda_{\text{Ex}} = 360 \text{ nm}$ . Previously performed concentration dependent calibration measurements by incorporation of varying amounts of the fluorescence dye **44** and the non-fluorescent dye **43** into the PTHF matrix **45** were done according to a general protocol and allowed a conversion of the measured fluorescence intensity into the “click” conversion (for calibration and equation see Experimental Part 4.13.1).

The results for compression of **42** in the PTHF matrix **45** is shown in Figure 51. A conversion of 1.9 % could be calculated after the last compression cycle. The low conversion most probably was the consequence of the low molecular weight of **42**, preventing an efficient entanglement of the catalyst within the matrix. Furthermore, incorporation of the supramolecular catalyst strongly influenced the crystallinity of the resulting sample. Before incorporation, the crystallinity of the pure PTHF was 68 % which dropped down to 32 % ( $\Delta H_{\text{m}} = 55.6 \text{ J/g}$ , proven *via* DSC measurements) after the embedding. While the drop in crystallinity might also have affected the activation behavior, it also impeded handling of the sample which was extremely brittle. Therefore, removal of the complete tablet after compression was difficult.

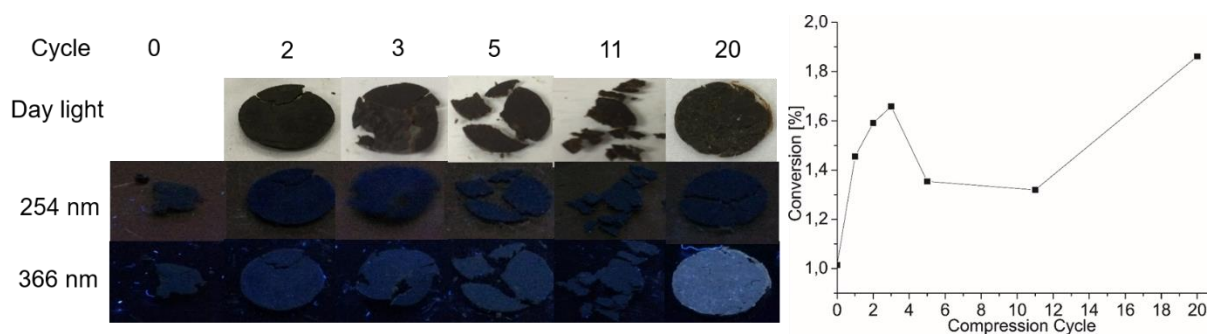


**Figure 51.** Compression led to mechanophoric activation of **42**, thus triggering the fluorogenic “click” reaction of **28** and **43**. Fluorescence intensity was increasing with ongoing compression cycles. However, due to the brittleness of the sample, accurate measurement of the tablet after the 5<sup>th</sup> and 11<sup>th</sup> cycle was not possible. Therefore, the fluorescence beam did not hit the complete sample during excitation, thus leading to smaller fluorescence.

Since the sample became very brittle and fragmented after the 5<sup>th</sup> and the 11<sup>th</sup> compression cycle, the fluorescence measurements were defective. A complete focusing of the fluorescence beam to the sample was not possible, thus leading to decreasing fluorescence intensities. However, control experiments without addition of the catalyst did not show an increase of the fluorescence intensity, proving the mechanochemical origin of the fluorogenic “click” reaction.

In order to circumvent the brittleness of the sample, a second polymeric matrix was probed. Therefore, **42** was also embedded into **48**, which also bore barbiturate groups. It was assumed that the crystallinity would be less affected which could also be proven *via* DSC measurements. The crystallinity of pure **48** was found to be 73 % and dropped to 61 % after incorporation of **28**, **42** and **43**. The results from the compression experiments are shown in Figure 52.

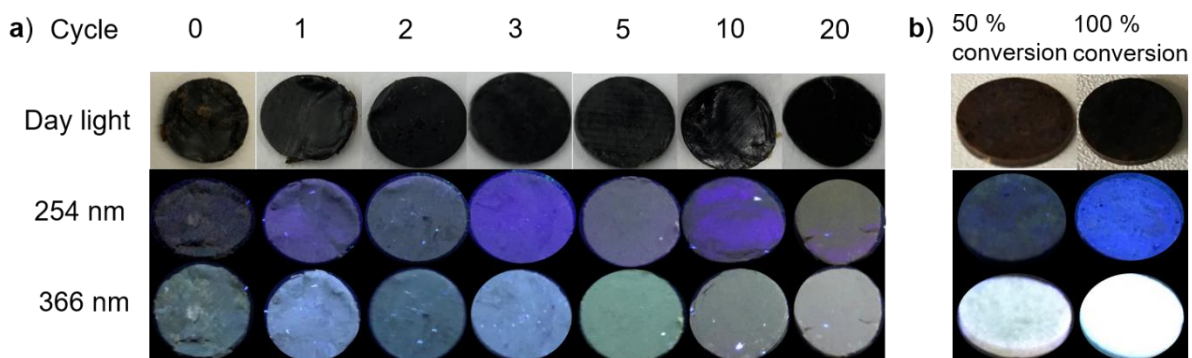


**Figure 52.** a) Compression of mechanocatalyst **42** in the presence of **28** and **43** did not lead to an increase of the fluorescence intensity. However, due to the changing properties of the sample from a soft tablet with a rough surface to a hard tablet with a smooth surface, the color appeared to change due to different reflection of the fluorescence light. b) Incorporation of dye **44** into the barbiturate modified PEG matrix **48** instead of the PTHF matrix did not influence the excitation and emission wavelength of the dye.

Measuring of the fluorescence did not reveal an increase of the intensity with proceeding compression cycles. Additionally to the non-activation of the mechanocatalyst, compression strongly affected the properties of the sample. During the first cycles, the tablet was soft and had a rough surface texture. During the compression experiment, the sample gradually got hard and brittle with a very smooth surface texture, which might be attributed to stress induced crystallization<sup>70</sup> of the PEG-matrix. Thus, the crystallinity increased from 61 % before the first compression cycle to 69 % after the 20<sup>th</sup> compression cycle (proven *via* DSC). Due to the changing surface texture the color of the sample in Figure 52 also appeared to change because of differences in the reflection of the fluorescence light. In order to test, if the emission and excitation wavelength of the fluorescence dye **44** were influenced by the exchange of the matrix, the “clicked” dye was directly incorporated into the matrix, thus mimicking a conversion of 50 % and 100 % (see Figure 52b). In case of the 50 % conversion, the missing 50 % were filled up with

the “unclicked” dye **43**. As apparent from Figure 52b, the excitation wavelength did not change (corresponding spectra are presented in the Appendix 7.10). Thus, non-activation of the catalyst could be concluded. Presumably, the supramolecular hydrogen bonds of the barbiturate were weaker than the copper-carbene bonds, leading to their preferential cleavage under stress and preventing an activation of the mechanophore (see Figure 50c).

### 3.6 Synthesis of elastin-based hydrogels (**49**)

In order to also incorporate a mechanophoric catalyst into a chemically crosslinked network, commercially available solubilized elastin was crosslinked *via* isocyanate chemistry. Usage of hexamethyldiisocyanate (HDI) allowed an easy incorporation of the  $[\text{Cu}(\text{C}_3\text{NH}_2\cdot\text{TFA-NHC})_2]\text{X}$  (**34**) since isocyanates can react with both the amino groups from the mechanocatalyst as well as from elastin thus generating ureas. Amino groups from solubilized elastin mostly originated from the *L*-lysine (Lys) side chains as well as from the *N*-terminus. Free amino groups from Lys side chains were obtained during the solubilization process of crosslinked elastin through destruction of the desmosine and isodesmosine crosslinks (see Chapter 1.4.2). Due to the destruction of crosslinking points, the solubilized elastin contained a variety of species with different molecular weights (see Appendix 7.11). The incorporation of the mechanocatalyst **34** into a network was also favorable since the crosslinking points allow a redirection of the applied directional force, thus also the perpendicular parts of the force can be used for the activation (see Chapter 1.1.5)<sup>126, 141</sup>.

In first experiments, the solubilized elastin was crosslinked with HDI in varying ratios to test the ideal composition of the resulting hydrogels **49** as shown in Table 5.

**Table 5.** Synthesis of elastin-based hydrogels **49** with varying ratios of elastin and HDI. Hydrogels **49j** and **49k** were also synthesized by using the trivalent crosslinker TMP (ratio HDI:TMP, 3:1). Hydrogels **49c**, **49g**, **49i** and **49k** contained mechanocatalyst **34** with a concentration of  $5.17 \cdot 10^{-6} \text{ mmol}_{\text{Cu}}/\text{mg}_{\text{sample}}$  and 3-azido-7-hydroxycoumarin (**43**) and phenylacetylene (**28**) with a concentration of  $1.56 \cdot 10^{-4} \text{ mmol}_{\text{Cu}}/\text{mg}_{\text{sample}}$ .

Entry	Compound	Elastin:HDI	DBU	TMP <sup>a</sup>	$[\text{Cu}(\text{C}_3\text{NH}_2\cdot\text{TFA-NHC})_2]\text{X}$ ( <b>34</b> )	Appearance
1	<b>49a</b>	1:1.4	yes	no	no	solid
2	<b>49b</b>	1.4:1	yes	no	no	hydrogel
3	<b>49c</b>	2.9:1	yes	no	yes	hydrogel
4	<b>49d</b>	4.8:1	no	no	no	hydrogel
5	<b>49e</b>	4.8:1	yes	no	no	hydrogel
6	<b>49f</b>	23.8:1	yes	no	no	hydrogel
7	<b>49g</b>	23.8:1	yes	no	yes	hydrogel
8	<b>49h</b>	30:1	yes	no	no	hydrogel
9	<b>49i</b>	30:1	yes	no	yes	hydrogel
10	<b>49j</b>	47.6:1	yes	yes	no	hydrogel
11	<b>49k</b>	47.6:1	yes	yes	yes	hydrogel
12	<b>49l</b>	50:1	yes	no	no	hydrogel
13	<b>49m</b>	60:1	yes	no	no	soluble

Additionally, hydrogels **49j,k** were synthesized in the presence of trimethanolpropane (TMP) to also incorporate a trivalent crosslinker. For the hydrogel synthesis elastin was dissolved in DMF by stirring for at least one hour. A concentration of  $100 \text{ mg}_{\text{elastin}}/\text{mL}_{\text{DMF}}$  was found to be ideal since the solution was not too viscous and still could be transferred to teflon molds with a glass pipette after addition of HDI (see Figure 53a).

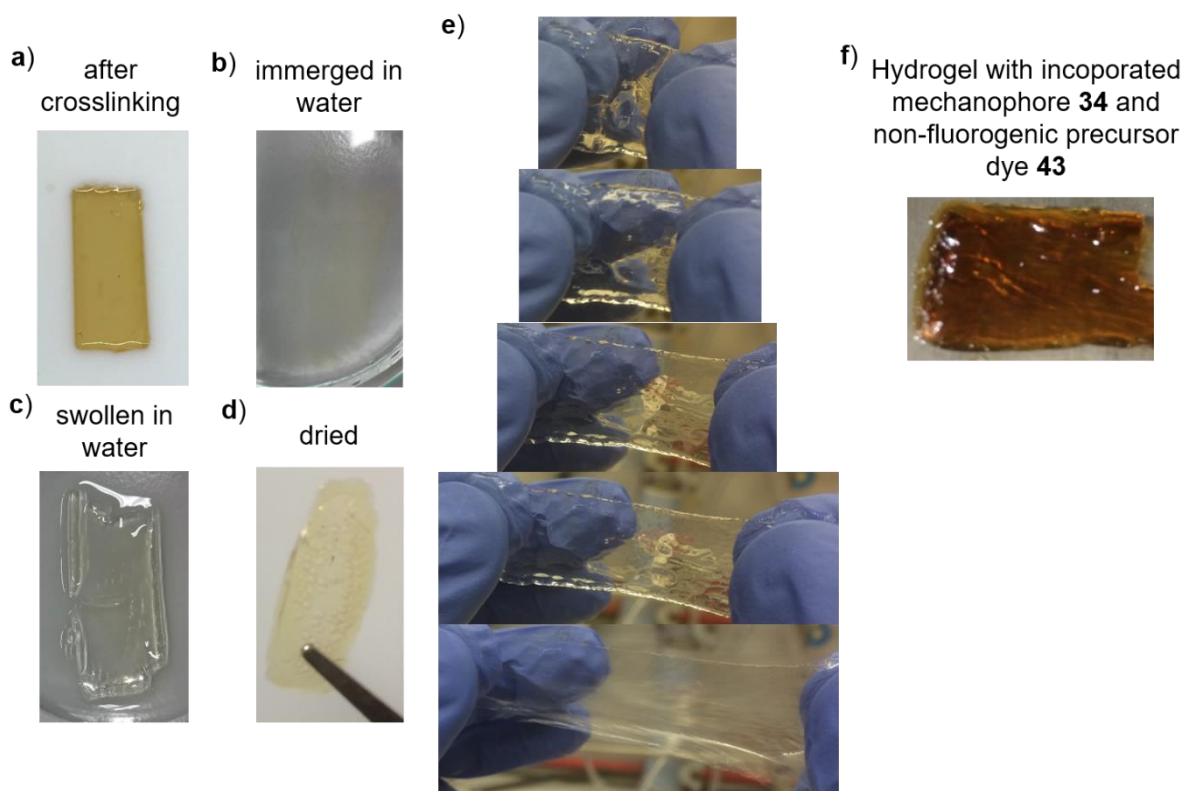


**Figure 53.** Synthesis of elastin-based hydrogels **49**. a) After crosslinking in the teflon mold. b) Immersed in water to exchange the DMF. c) When completely swollen the hydrogels were fragile and were not extendable. d) When completely dried the hydrogels were rigid and brittle solids. e) When not completely swollen the hydrogels could be extended. f) Incorporation of mechanocatalyst **34**, phenylacetylene (**28**) and the non-fluorogenic precursor dye **43** into the hydrogel.

The teflon mold was then placed in a desiccator with nitrogen atmosphere overnight for crosslinking. Applying vacuum was not practicable since in this case the formation of bubbles could be observed within the networks. Afterwards, the formed hydrogel was stored in water to exchange the DMF (see Figure 53b). The presence of water is known to be crucial for the elasticity of elastin since it is a prerequisite for the flexibility of the adopted  $\beta$ -spiral<sup>226, 352</sup> (see Chapter 1.4.1).

In case of the hydrogel **49a** the elastin was immediately crosslinked after addition of the HDI, thus leading to an inhomogenous and turbid solid. By using a ratio of 60:1 (elastin:HDI), the resulting hydrogel **49m** dissolved after transferring it into water, thus indicating insufficient crosslinking. The hydrogels were fragile and were not extendable when fully swollen (see Figure 53c) and rigid and brittle when completely dried (see Figure 53d). However, they could be extended, when not fully swollen (see Figure 53e) which was in accordance with literature<sup>278</sup>. Since the degree of hydration has a pronounced effect on the mechanical properties of the hydrogels, tensile testing<sup>278, 281</sup> and rheologic measurements<sup>249</sup> are usually performed while the hydrogels are immersed in PBS or water. Maintaining a distinct temperature then allows to guarantee a defined degree of hydration. However, characterization of the mechanical properties of the synthesized hydrogels was difficult due to their sticky and gelatinous properties. Their hydration degree dependent elasticity also impeded detailed investigations of the mechanical properties with rheology, tensile testing as well as with nanoindentation experiments *via* AFM since the necessary setup for a measurement when immersed in PBS or water was not available. Due to quick dehydration of the samples (also see Appendix 7.11) during the measurements no reliable results could be obtained. Therefore, the influence of the added trivalent crosslinker TMP (**49j,k**) could also not be tested. Nevertheless, mechanocatalyst **34** was incorporated into hydrogels together with 3-azido-7-hydroxycoumarin (**43**) and phenylacetylene (**28**), generating the hydrogels **49c** (Elastin:HDI, 2.9:1), **49g** (Elastin:HDI, 23.8:1), **49i** (Elastin:HDI, 30:1) and **49k** (Elastin:HDI, 47.6:1) with different

crosslinking densities (see Figure 53f). Though, trying to activate the mechanophoric networks **49c**, **49g**, **49i** and **49k** with stretching in the rheometer as well as compression failed due to the same reasons as mentioned above, namely their sticky and gelatinous properties and the dependency of elasticity from the degree of hydration. Additionally, the hydrogels showed a ground fluorescence even in the absence of the fluorogenic dye **44** (see Appendix 7.11). While the excitation maximum was found to be  $\lambda_{Ex,max} = 370$  nm, the hydrogel could also be excited at a wavelength of  $\lambda_{Ex} = 360$  nm (which is the wavelength that is used for the excitation of **44**). The resulting emission maximum also overlapped with  $\lambda_{Em,max} = 427$  nm from the fluorogenic dye **44**. Presumably, the fluorescence originated from fluorescence active amino acids such as tryptophan, phenyl alanine or tyrosine which are part of the native elastine sequence<sup>239</sup>. Hence, activation experiments of the hydrogels **49c**, **49g**, **49i** and **49k** with incorporated catalyst  $[Cu(C_3NH_2 \cdot TFA-NHC)_2]X$  (**34**) and the non-fluorogenic dye **43** could not be exerted.

### 3.7 Cytotoxicity of the synthesized mechanocatalysts

While the attachment of the ELP sequences was primarily performed to introduce the “molecular spring” behavior, it was also tested whether the incorporation of peptide chains as well as the bis(NHC) structure affected the cell toxicity of the Cu(I) bis(NHC) complexes. As known from literature, Cu(I) usually tends to be highly cell toxic<sup>353-356</sup>. The toxicity originates from the ability of copper to denature proteins through chelate formation<sup>355</sup> as well as the ability to catalyze the generation of reactive oxygen species (ROS) which also can cause damage to most biological molecules<sup>356</sup>. There are several reports that indicated the cell toxicity of neutral and cationic Cu(I) mono(NHC) complexes<sup>357-358</sup>. Though, it was tested whether the incorporation of a second NHC ligand also could influence cell toxicity due to the shielding of the Cu(I) center exerted from the bis(NHC) structure. Therefore, the cytotoxicity of  $[Cu(C_{10}COOH-NHC)_2]X$  (**4b**),  $[Cu(C_{10}COOH-VPGVG-NHC)_2]X$  (**27e**),  $[Cu(C_3NH_2 \cdot TFA-NHC)_2]X$  (**34**) and fluorotris(triphenylphosphine)copper(I) (**50**) were tested against the MCF7 and the NIH/3T3 cell lines. Comparing the cytotoxicity against a breast cancer cell line (MCF7) and a cell line that was derived from mouse embryonic fibroblasts (NIH/3T3) also allowed to check the selectivity of the Cu(I) bis(NHC) complexes. The concentration dependent decrease of the cell growth is shown in Figure 54 (for tabular overview check Experimental Part 4.15). At first, **50** was tested for its cytotoxicity. As expected this complex showed a high cytotoxicity with 50 % of the cells being alive at concentrations as low as 4  $\mu\text{mol/L}$  for both cell lines (MCF7 and NIH/3T3). At a concentration of 10  $\mu\text{mol/L}$  the amount of living cells dropped to 5.6 % (MCF7) respectively below 1 % (NIH/3T3) (for close-up of the low concentration range see Experimental Part 4.15). In a next step the cytotoxicity of mechanocatalysts **4b** and **34** was tested and already showed decreased cytotoxicity. 50 % of the cells were still alive at a concentration of 50  $\mu\text{mol/L}$  (**4b**, NIH/3T3 and **34**, MCF7) and 92  $\mu\text{mol/L}$  (**4b**, MCF7) while even for the highest concentration of 100  $\mu\text{mol/L}$  for complex **34**, 52 % of the NIH/3T3 cells were still alive. It was assumed that the two NHC ligands were able to shield the Cu(I) which did hinder its interaction with the cells and thus decreased the cytotoxicity. Comparatively, a variety of cationic and neutral 2,2'-bis-pyridil coordinated Cu(I) mono(NHC) complexes showed significantly higher toxicity with 50 % of the MCF7 cells being alive at concentrations in the range of 0.015 to 1.6  $\mu\text{mol/L}$ <sup>358</sup>. The toxicity was further decreased for catalyst **27e** which bore the VPGVG pentapeptide sequence. While for the MCF7 cell line 50 % of the cells were still alive at a concentration of 132  $\mu\text{mol/L}$ , 67 % of the NIH/3T3 cells were alive at the highest measured concentration of 150  $\mu\text{mol/L}$  proving an increased biocompatibility. Presumably, an attachment of the peptide chains further extended the length of the shielding ligands which further prevented an interaction between the cells and the Cu(I). However, for all tested complexes the results were similar for both cell lines (MCF7 and NIH/3T3), showing low selectivity for tumor cells.

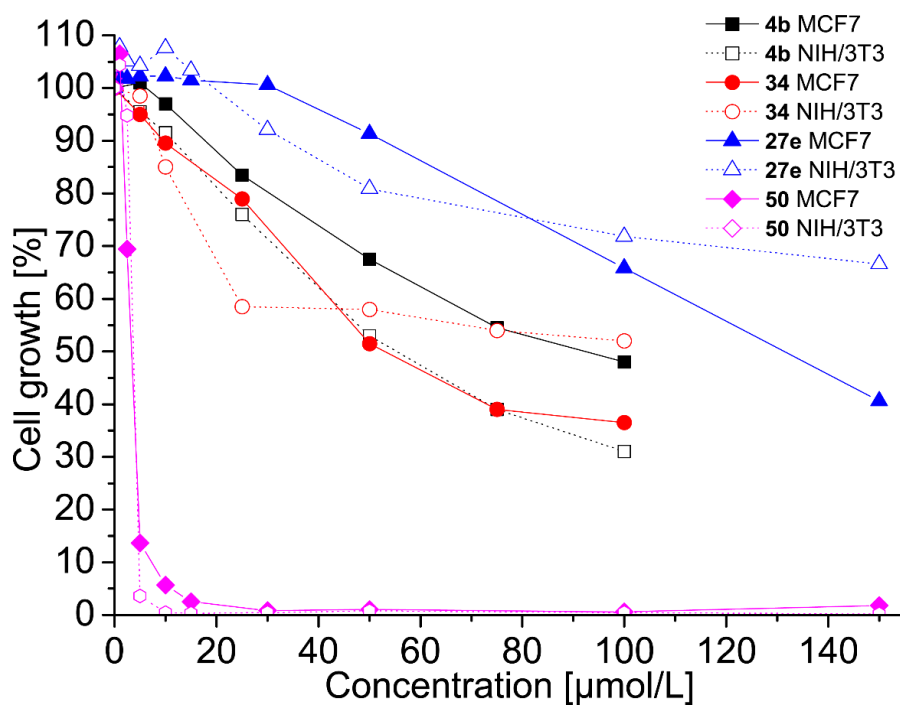


**Figure 54.** Cytotoxicity tests of mechanocatalysts **4b** (black), **34** (red) and **27e** (blue) as well as for complex **50** (magenta). Filled symbols refer to the toxicity tests against the MCF7 cell line (breast cancer) and open symbols refer to toxicity tests against the NIH/3T3 cell line (mouse embryonic fibroblasts).

## 4 Experimental part

### 4.1 Materials and methods

All reactions were conducted under dry, inert argon atmosphere using common Schlenk techniques unless otherwise noted. All solvents were purchased in technical grade and were distilled before usage. Dichloromethane was predried over calcium chloride. 1,4-Dioxane, acetonitrile (ACN), dichloromethane (DCM), *N,N*-dimethylformamide (DMF), dimethylsulfoxide (DMSO) and methanol (MeOH) were dried by refluxing over calcium hydride for several hours. Tetrahydrofuran (THF) was predried over potassium hydroxide. Final drying was achieved by refluxing THF in the presence of sodium/benzophenone until the blue color persisted.

The following chemicals were purchased from Sigma Aldrich: 1-Methylimidazole (99 %), copper(I) oxide (97 %), lithium hydroxide monohydrate, 3-bromopropan-1-amine hydrobromide (98 %), 3-chloropropan-1-amine hydrochloride (98 %), triethylamine (Et<sub>3</sub>N) (99%), trifluoroacetic acid (99 %), thionyl chloride (99 %), *N,N'*-dicyclohexylcarbodiimide (DCC) (99 %), pentafluorophenol (99 %), *N,N*-diisopropylethylamine (DIPEA) (99 %), sodium azide (99.5 %), iodomethane (99 %), sodium *tert*-butoxide (97 %), potassium *tert*-butoxide (95 %), tetrakis(acetonitrile)copper(I) hexafluorophosphate (97 %), sodium hydride (60 % dispersion in mineral oil), benzophenone (99 %), sodium ascorbate, hydroxybenzotriazole monohydrate (HOBt) (97 %), methane sulfonylchloride (98 %), sodium iodide (99.9 %), sodium nitrite, potassium permanganate,  $\alpha,\omega$ -bis-hydroxy-PEG (8000 g/mol), trimethylolpropane (TMP) (97 %), elastin (soluble from bovine neck ligament) and deuterium oxide. Phenylacetylene (98 %), hexamethylenediisocyanate (HDI) (> 98 %), urea and sodium (in mineral oil) were obtained from Merck. 6-Bromohexanoic acid (98 %), 11-bromoundecanoic acid (99 %) and diethyl malonate (99 %) were bought from TCI and di-*tert*-butyl dicarbonate (99 %) and *N'*-(3-dimethylaminopropyl)-*N'*-ethylcarbodiimide hydrochloride (EDC·HCl) (98 %) were obtained from Carbolution Chemicals. Sodium chloride, sodium sulfate, glycine (>99 %), *L*-proline (>98.5 %), *L*-histidine (99 %) and *L*-valine (>99 %) were purchased from Roth. The following chemicals were purchased from Fluka: Methanesulfonic acid (98 %), trichloroacetic acid, 1,8-diazabicyclo[5.4.0]undec-7-ene (DBU) (98 %) and benzyl bromide (98 %). Hydrochloric acid (37 %), sodium hydroxide (99 %), acetic acid (99.9 %) and sodium bicarbonate were obtained from Guessing. Magnesium sulfate (99 %), 2,4-dihydroxy benzaldehyde (98 %), 6-chloro-1-hexyne (98 %) and calcium hydride (92 %) were purchased from Alfa Aesar. HPLC-grade methanol and *N*-acetyl glycine were obtained from VWR and HPLC-grade dimethylformamide (DMF) was obtained from VWR BDH Prolabo. Ce(SO<sub>4</sub>) · 4 H<sub>2</sub>O, (NH<sub>4</sub>)<sub>6</sub>Mo<sub>7</sub>O<sub>24</sub> · 4 H<sub>2</sub>O and copper(II) sulfate pentahydrate were obtained from VEB. Lithium(I) bis(trifluoromethanesulfonyl)imide (LiTf<sub>2</sub>N) was purchased from J&K Chemicals. Anhydrous sodium acetate and potassium carbonate were bought from Bernd Kraft and pyridine (99 %) was purchased from Acros Organics. Potassium bisulfate was obtained from Lachema and sulforhodamine-B was bought from abcr GmbH. Deuterated chloroform (CDCl<sub>3</sub>), deuterated dimethyl sulfoxide (DMSO-d<sub>6</sub>) and deuterated tetrahydrofuran (THF-d<sub>8</sub>) were purchased from Chemotrade.

<sup>1</sup>H-NMR and <sup>13</sup>C-NMR spectra were recorded either on a Varian Gemini 2000 (400 MHz) or on a Varian Unity Inova 500 (500 MHz) using MestReNova software (version 6.0.2-5475) for the evaluation of the results. The spectra were measured at 27 °C using deuterated chloroform (CDCl<sub>3</sub>), deuterated dimethyl sulfoxide (DMSO-d<sub>6</sub>) or deuterated tetrahydrofuran (THF-d<sub>8</sub>). All chemical shifts ( $\delta$ ) were given in parts per million (ppm) and were referred to the solvent residual signal (CDCl<sub>3</sub>: 7.26 ppm (<sup>1</sup>H), 77.0 ppm (<sup>13</sup>C), DMSO-d<sub>6</sub>: 2.50 ppm (<sup>1</sup>H), 39.5 ppm (<sup>13</sup>C), THF-d<sub>8</sub>: 1.72 ppm (<sup>1</sup>H), 67.2 ppm (<sup>13</sup>C)). Subscript letters of protons (*H<sub>y</sub>*) and carbons (*C<sub>y</sub>*) indicate the corresponding atoms within the structures shown on the <sup>1</sup>H-NMR and <sup>13</sup>C-NMR spectrum.

Gel permeation chromatography (GPC) measurements were performed on a Viscotek GPCmax VE 2001 using a H<sub>HR</sub>-H Guard-17369 and a GMH<sub>HR</sub>-N-18055 column with DMF containing 10 mM

LiTf<sub>2</sub>N as eluent at 60 °C and via detection of the refractive index with a VE 3580 RI detector from Viscotek at 35 °C. The injection volume was 100 µL and a sample concentration of 5 mg/mL was used while the flow rate was set to 1 mL/min. The external calibration was done using polystyrene standards (MP = 1000 – 115000 g/mol).

ESI-TOF-MS measurements were performed on a Bruker Daltonics microTOF *via* direct injection with a flow rate of 180 µL/h using either the positive or negative mode. The obtained spectra were processed with the software Bruker Data Analysis 4.0. Samples were prepared by dissolving the sample in HPLC grade solvent at a concentration of 0.01 mg/mL - 1 mg/mL either without salt addition or with sodium iodide, depending from the measured substance.

FTIR-spectroscopy was performed on a VERTEX 70 IR-spectrometer by using a single reflex-diamond attenuated total reflectance unit for solid-state investigations. Solution experiments were performed in D<sub>2</sub>O using a Specac Omni Cell demountable cell with CaF<sub>2</sub> windows and PTFE spacer of 0.1 mm. The pure solvent was measured as background and the absorption bands are reported in cm<sup>-1</sup>.

CD-spectroscopy measurements were performed on a Jasco J-810 at 20 °C using a cuvette with a space length of 0.1 mm and a sample concentration of 0.4 mg/mL in D<sub>2</sub>O. Spectra were measured with a wavelength range of 250 to 195 nm with a scan rate of 1 nm/s performing 50 accumulations.

UV-vis measurements were performed on a Perkin Elmer UV/vis Lambda 365 using quartz glass cuvettes (d = 10 mm) from Helma analytics. The used concentration was 0.20 mmol/L in HPLC grade THF.

Fluorescence measurements in bulk were carried out on a Cary Eclipse fluorescence spectrometer from Agilent. The samples were fixed in a solid sample holder between two quartz glass object slides. Emission spectra were recorded in a wavelength range from 380 nm to 700 nm with a maximum emission wavelength of 427 nm, when excited at 360 nm. The excitation spectra were recorded in a wavelength range from 220 nm to 500 nm with the maximum of emission at 427 nm, when excited at 360 nm. Every measurement was performed three times at different positions of the sample.

DSC measurements were performed on a Netzsch Phoenix DSC 204 F1 with sample amounts of 3 – 10 mg which were weighed into standard alumina pans. Usually the measurements were performed with a heating rate of either 5 K/min or 10 K/min in a temperature range of -50 °C to 100 °C.

Ultrasonication experiments were conducted with a VCX 500 ultrasonic processor equipped with a long full wave solid probe out of titanium alloy (Ti-Al-4V) and an internally threaded stainless steel adapter. The used frequency was 20 kHz with a maximal amplitude of 20 % and a sequence of 5 s pulse and 10 s break for 90 min. One ultrasonication cycle corresponded to an ultrasound power intensity of 4.66 W cm<sup>-1</sup> and an energy input of 11 kJ. During this time the mixture was cooled in a water bath to prevent the temperature from rising above 25 °C. Each cycle was followed by a waiting time of 60 min. All experiments were conducted under inert and dry conditions in a 10 mL reaction vessel with two additional side necks. Control experiments without ultrasound were carried out in two-necked flasks at room temperature as well as at 60 °C to prove the activation of the catalyst by ultrasound.

Compression experiments were conducted on an automatic hydraulic Atlas Press T15 from Specac together with an Atlas 13 mm evacuable pellet die applying ten tons of pressure.

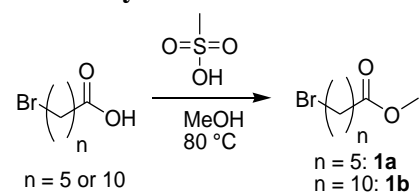
Cytotoxicity tests were evaluated by the sulforhodamine-B (SRB) micro culture colorimetric assay. Exponentially growing cells were seeded into 96-well plates at the appropriate cell densities to prevent confluence of the cells during the period of the experiment. After 24 hours the cells were treated with serial dilutions of the compounds (0-150 µM) for 72 h. After 72 h, the supernatant medium was discarded from the 96-well plates and the cells were fixed with 10 % trichloroacetic acid. For a thorough fixation the cells were allowed to stand at 4 °C for at least two hours. After fixation, the cells were

washed in a plate washer. The washing step was done five times with water using alternate dispensing and aspiration procedures. The plates were then stained with 100  $\mu$ L of 0.4 % SRB in a 1 % acetic acid solution for 45 min. After staining, the plates were washed with 1 % acetic acid to remove the dye and allowed to air-dry overnight. 100  $\mu$ L of 10 mM tris base solution were added to each well and the absorbance was measured at a wavelength of 570 nm using a Tecan Infinite F200 Pro plate reader.

Thin-layer chromatography (TLC) was performed using Merck silica gel 60 plates. Spots on the TLC were visualized using an oxidizing agent blue stain or potassium permanganate solution or UV light (256 or 366 nm). The blue staining solution was prepared as follows:  $(\text{NH}_4)_6\text{Mo}_7\text{O}_{24}\cdot 4\text{H}_2\text{O}$  (1.0 g) and  $\text{Ce}(\text{SO}_4)_2\cdot 4\text{H}_2\text{O}$  (1.0 g) were dissolved in a mixture of distilled water (90.0 mL) and concentrated sulfuric acid (6.0 mL). The potassium permanganate solution was prepared as follows:  $\text{KMnO}_4$  (3.0 g) and  $\text{K}_2\text{CO}_3$  (20.0 g) were dissolved in  $\text{H}_2\text{O}$  (300.0 mL) and 10 %  $\text{NaOH}$  (5.0 mL). Column chromatography was carried out using silica gel high-purity grade, 60  $\text{\AA}$  pore size, 230-400 mesh particle size.

## 4.2 Synthesis of the carboxyl functionalized mechanophoric catalysts

### 4.2.1 Synthesis of *n*-bromoalkanoic acid methyl esters (1)



**Scheme 10.** Synthesis of the *n*-bromoalkanoic acid methyl esters (1).

**General procedure:** The respective *n*-bromoalkanoic acid (42.01 mmol, 1.0 eq.) was dissolved in MeOH (120 mL) and subsequently catalytic amounts of methanesulfonic acid were added. The mixture was refluxed for 48 hours at 80 °C. Afterwards the solvent was removed, the crude product was redissolved in  $\text{Et}_2\text{O}$  (80 mL) and washed with saturated  $\text{NaHCO}_3$  (40 mL), water (40 mL) and brine (40 mL). The organic phase was dried with  $\text{MgSO}_4$ , filtered and the solvent was removed to yield the product as a yellow liquid.

#### Characterization of 1a:

Yield: 3.42 g, 17.3 mmol, 57 %

$^1\text{H-NMR}$  (400 MHz,  $\text{CDCl}_3$ , 27 °C):  $\delta$  (ppm) = 3.67 (s, 3H,  $H_7$ ), 3.40 (t, 2H,  $H_1$ ,  $^3J = 6.8$  Hz), 2.33 (t, 2H,  $H_5$ ,  $^3J = 7.4$  Hz), 1.87 (m, 2H,  $H_2$ ), 1.66 (m, 2H,  $H_4$ ), 1.48 (m, 2H,  $H_3$ ).

$^{13}\text{C-NMR}$  (100 MHz,  $\text{CDCl}_3$ , 27 °C):  $\delta$  (ppm) = 173.8 ( $C_6$ ), 51.5 ( $C_7$ ), 33.7 ( $C_1$ ), 33.4 ( $C_5$ ), 32.4 ( $C_2$ ), 27.6 ( $C_3$ ), 24.1 ( $C_4$ ).

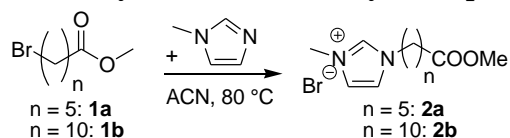
#### Characterization of 1b:

Yield: 11.1 g, 39.8 mmol, 95 %

$^1\text{H-NMR}$  (400 MHz,  $\text{CDCl}_3$ , 27 °C):  $\delta$  (ppm) = 3.66 (s, 3H,  $H_8$ ), 3.40 (t, 2H,  $H_1$ ,  $^3J = 6.9$  Hz), 2.30 (t, 2H,  $H_6$ ,  $^3J = 7.5$  Hz), 1.84 (m, 2H,  $H_2$ ), 1.61 (m, 2H,  $H_5$ ), 1.41 (m, 2H,  $H_3$ ), 1.28 (m, 10H,  $H_4$ ).

$^{13}\text{C-NMR}$  (100 MHz,  $\text{CDCl}_3$ , 27 °C):  $\delta$  (ppm) = 174.3 ( $C_7$ ), 51.4 ( $C_8$ ), 34.1 ( $C_1$ ), 34.0 ( $C_6$ ), 32.8 ( $C_2$ ), 29.3 ( $C_4$ ), 29.3 ( $C_4$ ), 29.2 ( $C_4$ ), 29.1 ( $C_4$ ), 28.7 ( $C_4$ ), 28.1 ( $C_3$ ), 24.9 ( $C_5$ ).

#### 4.2.2 Synthesis of the methyl ester protected NHC precursors (2)



**Scheme 11.** Synthesis of the imidazolium based NHC precursors (2).

**Procedure for 2a:** **1a** (3.40 g, 16.27 mmol) and 1-methylimidazole (1.11 g, 1.08 mL, 13.55 mmol) were dissolved in ACN (10 mL). The reaction mixture was stirred for 65 hours at 80 °C. Afterwards the solvent was removed and the obtained yellow, sticky liquid was dissolved in H<sub>2</sub>O (30 mL). The aqueous phase was washed with Et<sub>2</sub>O (4 x 20 mL). Subsequently, the water was removed and the crude product was redissolved in DCM (40 mL), dried over Na<sub>2</sub>SO<sub>4</sub> and subsequently was filtered. Removing the solvent yielded the product as a viscous, yellow liquid.

**Procedure for 2b:** **1b** (7.9 g, 28.27 mmol) and 1-methylimidazole (1.93 g, 1.88 mL, 23.56 mmol) were dissolved in ACN (16 mL). The reaction mixture was stirred for 48 hours at 80 °C. Afterwards the solvent was removed and the crude product was stored in the fridge until it was completely crystallized. The solid product was washed with Et<sub>2</sub>O (5 x 20 mL) until the washing solution was no longer yellow. The pure product was dried at the rotary evaporator afterwards.

##### Characterization of 2a:

Yield: 3.70 g, 12.7 mmol, 93 %

<sup>1</sup>H-NMR (400 MHz, CDCl<sub>3</sub>, 27 °C):  $\delta$  (ppm) = 10.36 (s, 1H,  $H_2$ ), 7.52 (s, 1H,  $H_4$ ), 7.47 (s, 1H,  $H_3$ ), 4.34 (t, 2H,  $H_5$ ,  $^3J = 7.4$  Hz), 4.09 (s, 3H,  $H_1$ ), 3.62 (s, 3H,  $H_{11}$ ), 2.30 (t, 2H,  $H_9$ ,  $^3J = 7.2$  Hz), 1.93 (m, 2H,  $H_6$ ), 1.64 (m, 2H,  $H_8$ ), 1.37 (m, 2H,  $H_7$ ).

<sup>13</sup>C-NMR (100 MHz, CDCl<sub>3</sub>, 27 °C):  $\delta$  (ppm) = 173.7 ( $C_{10}$ ), 137.6 ( $C_2$ ), 123.6 ( $C_4$ ), 122.1 ( $C_3$ ), 51.6 ( $C_{11}$ ), 49.7 ( $C_5$ ), 36.7 ( $C_1$ ), 33.4 ( $C_9$ ), 29.9 ( $C_6$ ), 25.5 ( $C_7$ ), 24.0 ( $C_8$ ).

MS (ESI),  $m/z$  calculated for [C<sub>11</sub>H<sub>19</sub>N<sub>2</sub>O<sub>2</sub>]<sup>+</sup> = 211.1464; found 211.1441.

##### Characterization of 2b:

Yield: 8.22 g, 22.8 mmol, 97 %

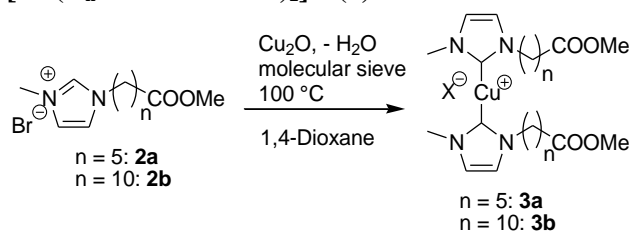
<sup>1</sup>H-NMR (400 MHz, CDCl<sub>3</sub>, 27 °C):  $\delta$  (ppm) = 10.51 (s, 1H,  $H_2$ ), 7.45 (s, 1H,  $H_4$ ), 7.33 (s, 1H,  $H_3$ ), 4.30 (t, 2H,  $H_5$ ,  $^3J = 7.4$  Hz), 4.12 (s, 3H,  $H_1$ ), 3.64 (s, 3H,  $H_{11}$ ), 2.28 (t, 2H,  $H_9$ ,  $^3J = 7.5$  Hz), 1.88 (m, 2H,  $H_6$ ), 1.58 (m, 2H,  $H_8$ ), 1.25 (m, 12H,  $H_7$ ).

<sup>13</sup>C-NMR (100 MHz, CDCl<sub>3</sub>, 27 °C):  $\delta$  (ppm) = 174.2 ( $C_{10}$ ), 137.8 ( $C_2$ ), 123.2 ( $C_4$ ), 121.6 ( $C_3$ ), 51.4 ( $C_{11}$ ), 50.1 ( $C_5$ ), 36.7 ( $C_1$ ), 34.0 ( $C_9$ ), 30.2 ( $C_6$ ), 29.1 ( $C_7$ ), 29.1 ( $C_7$ ), 29.0 ( $C_7$ ), 29.0 ( $C_7$ ), 28.8 ( $C_7$ ), 26.1 ( $C_7$ ), 24.8 ( $C_8$ ).

MS (ESI),  $m/z$  calculated for [C<sub>16</sub>H<sub>29</sub>N<sub>2</sub>O<sub>2</sub>]<sup>+</sup> = 281.2238; found 281.2224.

IR (bulk):  $\nu_{\max}$  (cm<sup>-1</sup>) = 3418 (w), 3063 (w), 2923 (m), 2853 (m), 1730 (s), 1562 (m), 1469 (m), 1418 (m), 1361 (m), 1335 (m), 1305 (w), 1272 (w), 1240 (m), 1207 (m), 1162 (s), 1110 (w), 1035 (w), 1014(w), 986 (w), 969 (w), 881 (m), 832 (s), 786 (w), 744 (m), 722 (m), 654 (w), 617 (s).

### 4.2.3 Synthesis of the methyl ester protected Cu(I) bis(NHC) complexes [Cu(C<sub>n</sub>OOMe-NHC)<sub>2</sub>]<sup>+</sup>X<sup>-</sup> (**3**)



**Scheme 12.** Synthesis of the methyl ester protected Cu(I) bis(NHC) complexes (**3**).

**General procedure:** **2** (2.76 mmol, 1.0 eq.), Cu<sub>2</sub>O (13.61 mmol, 5.0 eq.) and activated molecular sieve (3 Å) were suspended in 1,4-dioxane (10 mL) and were refluxed for 68 hours. Afterwards the solution was centrifuged and filtered and the solvent was removed. Further purification was done *via* column chromatography (see below) to yield the pure product as colorless solid.

Purification of **3a** *via* column chromatography: (CHCl<sub>3</sub> (R<sub>f</sub> = 0.1) → CHCl<sub>3</sub>/MeOH (40:1) (R<sub>f</sub> = 0.33) → CHCl<sub>3</sub>/MeOH (20:1) (R<sub>f</sub> = 0.55).

Purification of **3b** *via* column chromatography: (CHCl<sub>3</sub> (R<sub>f</sub> = 0.04) → CHCl<sub>3</sub>/MeOH (40:1) (R<sub>f</sub> = 0.22) → CHCl<sub>3</sub>/MeOH (20:1) (R<sub>f</sub> = 0.31).

#### Characterization of **3a**:

Yield: 62.2 mg, 0.12 mmol, 7 %

<sup>1</sup>H-NMR (400 MHz, CDCl<sub>3</sub>, 27 °C): δ (ppm) = 6.15 (dd, 2H, H<sub>3</sub> + H<sub>4</sub>), 3.65 (s, 3H, H<sub>11</sub>), 3.59 (t, 2H, H<sub>5</sub>, <sup>3</sup>J = 7.2 Hz), 3.24 (s, 3H, H<sub>1</sub>), 2.30 (t, 2H, H<sub>9</sub>, <sup>3</sup>J = 7.5 Hz), 1.68 (m, 4H, H<sub>6</sub> + H<sub>8</sub>), 1.35 (m, 2H, H<sub>7</sub>).

<sup>13</sup>C-NMR (100 MHz, CDCl<sub>3</sub>, 27 °C): δ (ppm) = 173.9 (C<sub>10</sub>), 153.2 (C<sub>2</sub>), 111.2 (C<sub>4</sub>), 109.9 (C<sub>3</sub>), 51.4 (C<sub>11</sub>), 43.3 (C<sub>5</sub>), 33.9 (C<sub>1</sub>), 30.3 (C<sub>9</sub>), 29.2 (C<sub>6</sub>), 26.1 (C<sub>7</sub>), 24.5 (C<sub>8</sub>).

#### Characterization of **3b**:

Yield: 397.0 mg, 0.56 mmol, 41 %

<sup>1</sup>H-NMR (400 MHz, CDCl<sub>3</sub>, 27 °C): δ (ppm) = 6.15 (dd, 2H, H<sub>3</sub> + H<sub>4</sub>), 3.65 (s, 3H, H<sub>11</sub>), 3.58 (t, 2H, H<sub>5</sub>, <sup>3</sup>J = 7.2 Hz), 3.25 (s, 3H, H<sub>1</sub>), 2.29 (t, 2H, H<sub>9</sub>, <sup>3</sup>J = 7.5 Hz), 1.62 (m, 4H, H<sub>6</sub> + H<sub>8</sub>), 1.26 (m, 12H, H<sub>7</sub>).

<sup>13</sup>C-NMR (100 MHz, CDCl<sub>3</sub>, 27 °C): δ (ppm) = 174.3 (C<sub>10</sub>), 153.2 (C<sub>2</sub>), 111.0 (C<sub>4</sub>), 109.9 (C<sub>3</sub>), 51.4 (C<sub>11</sub>), 43.6 (C<sub>5</sub>), 34.1 (C<sub>1</sub>), 30.3 (C<sub>9</sub>), 29.5 (C<sub>6</sub>), 29.4 (C<sub>7</sub>), 29.3 (C<sub>7</sub>), 29.2 (C<sub>7</sub>), 29.1 (C<sub>7</sub>), 26.6 (C<sub>7</sub>), 24.9 (C<sub>8</sub>).

IR (bulk): ν<sub>max</sub> (cm<sup>-1</sup>) = 2919 (m), 2850 (m), 1729 (s), 1664 (s), 1489 (m), 1463 (m), 1448 (m), 1424 (m), 1390 (w), 1379 (w), 1365 (w), 1271 (m), 1244 (w), 1205 (m), 1171 (w), 1113 (m), 982 (w), 767 (w), 673 (s), 652 (m), 556 (w).



**Procedure for 5b:** 11-Bromoundecanoic acid (1.5 g, 5.66 mmol) and 1-methylimidazole (0.47 mL, 5.94 mmol) were dissolved in ACN (4 mL). The reaction mixture was stirred for 20 hours at 80 °C. Afterwards the solution was cooled down and the formed precipitate was filtered and washed with Et<sub>2</sub>O (5 x 10 mL). The pure product was dried at the rotary evaporator afterwards.

#### Characterization of 5a:

Yield: 1.44 g, 5.18 mmol, 73 %

<sup>1</sup>H-NMR (400 MHz, DMSO-d<sub>6</sub>, 27 °C): δ (ppm) = 11.99 (s, 1H, COOH), 9.15 (s, 1H, H<sub>2</sub>), 7.76 (s, 1H, H<sub>3</sub>), 7.69 (s, 1H, H<sub>4</sub>), 4.14 (t, 2H, H<sub>5</sub>, <sup>3</sup>J = 7.2 Hz), 3.83 (s, 3H, H<sub>1</sub>), 2.19 (t, 2H, H<sub>9</sub>, <sup>3</sup>J = 7.3 Hz), 1.77 (m, 2H, H<sub>6</sub>), 1.52 (m, 2H, H<sub>7</sub>), 1.25 (m, 2H, H<sub>8</sub>).

<sup>13</sup>C-NMR (100 MHz, DMSO-d<sub>6</sub>, 27 °C): δ (ppm) = 174.7 (C<sub>10</sub>), 137.0 (C<sub>2</sub>), 124.0 (C<sub>4</sub>), 122.7 (C<sub>3</sub>), 49.0 (C<sub>5</sub>), 36.2 (C<sub>1</sub>), 33.8 (C<sub>9</sub>), 29.5 (C<sub>6</sub>), 29.4 (C<sub>7</sub>), 24.2 (C<sub>8</sub>).

#### Characterization of 5b:

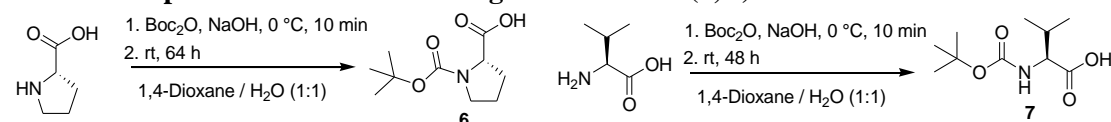
Yield: 1.76 g, 4.98 mmol, 88 %

<sup>1</sup>H-NMR (400 MHz, DMSO-d<sub>6</sub>, 27 °C): δ (ppm) = 11.94 (s, 1H, COOH), 9.13 (s, 1H, H<sub>2</sub>), 7.76 (s, 1H, H<sub>4</sub>), 7.69 (s, 1H, H<sub>3</sub>), 4.14 (t, 2H, H<sub>5</sub>, <sup>3</sup>J = 7.2 Hz), 3.83 (s, 3H, H<sub>1</sub>), 2.16 (t, 2H, H<sub>9</sub>, <sup>3</sup>J = 7.3 Hz), 1.75 (m, 2H, H<sub>6</sub>), 1.46 (m, 2H, H<sub>8</sub>), 1.22 (m, 12H, H<sub>7</sub>).

<sup>13</sup>C-NMR (100 MHz, DMSO-d<sub>6</sub>, 27 °C): δ (ppm) = 174.9 (C<sub>10</sub>), 137.0 (C<sub>2</sub>), 124.0 (C<sub>4</sub>), 122.7 (C<sub>3</sub>), 49.2 (C<sub>5</sub>), 36.2 (C<sub>1</sub>), 34.1 (C<sub>9</sub>), 29.8 (C<sub>6</sub>), 29.2 (C<sub>7</sub>), 29.2 (C<sub>7</sub>), 29.1 (C<sub>7</sub>), 29.0 (C<sub>7</sub>), 28.8 (C<sub>7</sub>), 25.9 (C<sub>7</sub>), 24.9 (C<sub>8</sub>).

### 4.3 Synthesis and characterization of the elastin-like polypeptide sequence

#### 4.3.1 Boc-protection reactions of single amino acids (6, 7)



**Scheme 15.** Synthesis of the Boc-protected amino acids **6** and **7**.

**General procedure:** Protection of the *N*-terminus was done according to literature<sup>331, 337</sup>. The corresponding amino acid (43.0 mmol, 1.0 eq.) and NaOH (45.15 mmol, 1.05 eq.) were dissolved in water (80 mL). Di-*tert*-butyl dicarbonate (51.6 mmol, 1.10 eq.) was dissolved in 1,4-dioxane (80 mL) and was slowly added to the reaction mixture which was cooled *via* ice bath. The mixture was left to stir for 48 hours at room temperature and afterwards was concentrated to ~ 50 mL. EtOAc (150 mL) was added and the pH was adjusted to 2 with aqueous KHSO<sub>4</sub> (10 wt%). The aqueous phase was extracted with EtOAc (1 x 150 mL, 6 x 50 mL) and the combined organic phases were washed with water (20 mL) afterwards. After drying over Na<sub>2</sub>SO<sub>4</sub> and filtration, the solvent was removed. In case of **6**, the crude product was recrystallized from boiling EtOAc to obtain the pure product as colorless solid. **7** was obtained as a highly viscous and sticky oil which slowly started to crystallize in the fridge.

#### Characterization of 6:

Yield: 8.45 g, 39.1 mmol, 91 %

<sup>1</sup>H-NMR (400 MHz, CDCl<sub>3</sub>, 27 °C): δ (ppm) = 9.57 (s, 1H, COOH), 4.33 (m, 1H, H<sub>7</sub>), 3.45 (m, 2H, H<sub>4</sub>), 2.27 (m, 2H, H<sub>6</sub>), 1.93 (m, 2H, H<sub>5</sub>), 1.47 (d, 9H, H<sub>1</sub>).

<sup>13</sup>C-NMR (100 MHz, CDCl<sub>3</sub>, 27 °C): δ (ppm) = 178.8/175.0 (C<sub>8</sub>), 156.4/154.1 (C<sub>3</sub>), 81.5/80.3 (C<sub>2</sub>), 59.2/58.9 (C<sub>7</sub>), 47.0/46.3 (C<sub>4</sub>), 30.8/28.5 (C<sub>6</sub>), 28.4 (C<sub>1</sub>), 24.3/23.6 (C<sub>5</sub>).

MS (ESI),  $m/z$  calculated for  $[C_{10}H_{16}NO_4]^- = 214.1074$ ; found 214.1161.

IR (bulk):  $\nu_{\max}$  ( $\text{cm}^{-1}$ ) = 2968 (w), 2895 (w), 1735 (s), 1632 (s), 1478 (w), 1425 (s), 1367 (w), 1332 (w), 1253 (w), 1208 (m), 1187 (w), 1161 (m), 1129 (m), 1089 (w), 978 (w), 898 (w), 852 (w), 791 (w), 774 (w), 761 (w), 640 (w), 587 (w).

#### Characterization of 7:

Yield: 8.12 g, 37.4 mmol, 88 %

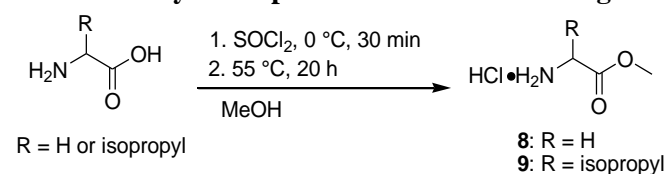
$^1\text{H-NMR}$  (400 MHz, DMSO- $d_6$ , 27 °C):  $\delta$  (ppm) = 12.43 (s, 1H, COOH), 6.88 (d, 1H, NH,  $^3J = 8.5$  Hz), 3.76 (dd, 1H,  $H_3$ ,  $J = 8.5, 6.1$  Hz), 1.97 (td, 1H,  $H_2$ ,  $J = 13.4, 6.8$  Hz), 1.36 (s, 9H,  $H_7$ ), 0.85 (t, 6H,  $H_1$ ,  $^3J = 6.5$  Hz).

$^{13}\text{C-NMR}$  (100 MHz, DMSO- $d_6$ , 27 °C):  $\delta$  (ppm) = 173.4 ( $C_4$ ), 155.8 ( $C_5$ ), 77.9 ( $C_6$ ), 59.0 ( $C_3$ ), 29.4 ( $C_2$ ), 28.1 ( $C_7$ ), 19.1 ( $C_1$ ), 18.1 ( $C_1$ ).

MS (ESI),  $m/z$  calculated for  $[C_{10}H_{18}NO_4]^- = 216.1241$ ; found 216.1310.

IR (bulk):  $\nu_{\max}$  ( $\text{cm}^{-1}$ ) = 3302 (w), 2973 (w), 2937 (w), 2512 (w), 1702 (s), 1644 (s), 1476 (w), 1456 (w), 1405 (s), 1369 (m), 1346 (w), 1310 (w), 1274 (m), 1254 (w), 1188 (w), 1158 (s), 1125 (w), 1094 (w), 1010 (w), 982 (w), 959 (w), 897 (w), 857 (w), 842 (w), 781 (w), 744 (w), 685 (w), 658 (w), 595 (w).

#### 4.3.2 Methyl ester protection reactions of single amino acids (8, 9)



**Scheme 16.** Synthesis of the methyl ester protected amino acids **8** and **9**.

General procedure: Synthesis of the methyl ester protected amino acids was done according to literature<sup>332, 338</sup>. The corresponding amino acid (42.68 mmol, 1.0 eq.) was dissolved in dry methanol (60 mL) and was cooled down to 0 °C. Freshly distilled thionyl chloride (64.02 mmol, 1.5 eq.) was slowly added and after stirring for 30 minutes the temperature was increased to 80 °C and the mixture was refluxed for another 20 hours until completion of the reaction. After removal of the solvent and the excess of thionyl chloride the product was recrystallized from methanol followed by filtration to obtain the pure product as colorless powder.

#### Characterization of 8:

Yield: 6.58 g, 52.37 mmol, 79 %

$^1\text{H-NMR}$  (400 MHz, DMSO- $d_6$ , 27 °C):  $\delta$  (ppm) = 8.54 (s, 3H, NH), 3.77 (s, 2H,  $H_3$ ), 3.73 (s, 3H,  $H_1$ ).

$^{13}\text{C-NMR}$  (100 MHz, DMSO- $d_6$ , 27 °C):  $\delta$  (ppm) = 167.9 ( $C_2$ ), 52.4 ( $C_1$ ), 39.4 ( $C_3$ ).

MS (ESI),  $m/z$  calculated for  $[C_3H_8NO_2]^+ = 90.1429$ ; found 90.0550.

IR (bulk):  $\nu_{\max}$  ( $\text{cm}^{-1}$ ) = 2880 (s), 2686 (w), 2634 (w), 1742 (s), 1583 (m), 1556 (w), 1494 (m), 1458 (w), 1437 (w), 1423 (w), 1400 (w), 1245 (s), 1140 (w), 1096 (w), 1058 (s), 955 (m), 899 (s), 878 (s), 677 (w), 588 (w).

#### Characterization of 9:

Yield: 6.21 g, 37.1 mmol, 87 %

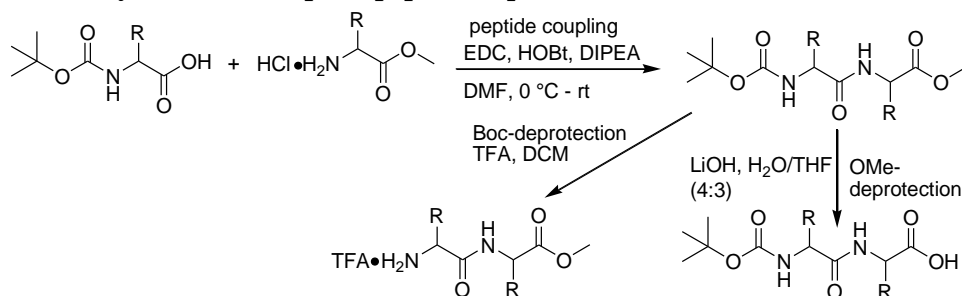
$^1\text{H-NMR}$  (400 MHz, DMSO- $d_6$ , 27 °C):  $\delta$  (ppm) = 8.68 (s, 3H, NH), 3.80 (d, 1H,  $H_4$ ,  $^3J = 4.8$  Hz), 3.72 (s, 3H,  $H_6$ ), 2.19 (m, 1H,  $H_3$ ), 0.93 (dd, 6H,  $H_1 + H_2$ ,  $J = 19.7, 6.9$  Hz).

$^{13}\text{C}$ -NMR (100 MHz, DMSO- $d_6$ , 27 °C):  $\delta$  (ppm) = 169.1 ( $C_5$ ), 57.2 ( $C_4$ ), 52.4 ( $C_6$ ), 29.2 ( $C_3$ ), 18.4 ( $C_1$ ), 17.5 ( $C_2$ ).

MS (ESI),  $m/z$  calculated for  $[\text{C}_6\text{H}_{14}\text{NO}_2]^+$  = 132.1026; found 132.1019.

IR (bulk):  $\nu_{\text{max}}$  ( $\text{cm}^{-1}$ ) = 2967 (w), 2828 (m), 2604 (w), 1735 (s), 1592 (m), 1568 (m), 1504 (s), 1434 (m), 1378 (w), 1333 (w), 1286 (m), 1237 (s), 1174 (w), 1157 (w), 1107 (w), 1071 (w), 1038 (m), 1020 (w), 971 (w), 927 (w), 879 (w), 814 (w), 771 (w), 650 (w), 583 (w).

### 4.3.3 Synthesis of the pentapeptide sequence (10-17)



**Scheme 17.** Generalized peptide coupling, Boc-deprotection and methyl ester deprotection steps for the buildup of the ELP sequence.

The coupling as well as the deprotection steps were performed as previously described in literature<sup>257</sup>.

General procedure for the coupling reaction: The Boc-protected peptide (7.96 mmol; 1.0 eq.), EDC•HCl (9.56 mmol; 1.2 eq.) and HOBT (9.56 mmol; 1.2 eq.) were dissolved in dry DMF (80 mL). The mixture was cooled down to 0 °C in an ice bath and was stirred for 30 minutes after the addition of DIPEA (28.67 mmol; 3.6 eq.). Subsequently the methyl ester protected peptide (7.96 mmol; 1.0 eq.) was dissolved in DMF (40 mL) and was slowly added to the solution. The reaction was stirred for further 48 hours before the solvent was removed under reduced pressure. The residue was dissolved in EtOAc (150 mL) and water (100 mL). Afterwards the organic layer was washed with HCl (1M, 20 mL), saturated  $\text{NaHCO}_3$  solution (20 mL) and brine (50 mL). The organic layer was dried over  $\text{Na}_2\text{SO}_4$  before it was filtrated and the solvent was removed. For purification of the respective peptide check the information below.

Purification of **10**: Recrystallization from DCM/petrol ether.

Purification of **12**: Column chromatography: DCM ( $R_f = 0.1$ )  $\rightarrow$  DCM/MeOH (20:1) ( $R_f = 0.3$ ).

Purification of **14**: Recrystallization from EtOAc/petrol ether.

Purification of **16**: Column chromatography: DCM ( $R_f = 0.0$ )  $\rightarrow$  DCM/MeOH (80:1)  $\rightarrow$  DCM/MeOH (60:1)  $\rightarrow$  DCM/MeOH (30:1)  $\rightarrow$  DCM/MeOH (20:1) ( $R_f = 0.16$ ).

General procedure for the Boc-deprotection: The Boc-protected peptide (4.58 mmol; 1.0 eq.) was dissolved in DCM (10 mL). The mixture was cooled down to 0 °C with an ice bath before TFA (51.75 mmol; 11.3 eq.) was added. The mixture was stirred for 17 hours at room temperature. Afterwards the solvent and the TFA were removed under vacuum.

General procedure for the OMe-deprotection: The peptide (5.50 mmol; 1.0 eq.) was dissolved in THF (55 mL) and the mixture was cooled down to 0 °C.  $\text{LiOH}\cdot\text{H}_2\text{O}$  (22.16 mmol; 4 eq.) was dissolved in water (72 mL) and was added to the reaction mixture. After 14 hours of stirring at room temperature the pH was adjusted to 4 by adding 1M HCl. After extraction with EtOAc (6 x 50 mL), the combined organic phases were dried over  $\text{Na}_2\text{SO}_4$ , filtered and the solvent was removed.

An overview about all synthesized intermediate products for the synthesis of the Boc-VPGVG-OMe (**16**) sequence is given in Table 6.

**Table 6.** Synthesized intermediate products for the buildup of the pentapeptide sequence **16**. The column *N*-terminus refers to whether it is Boc-protected or deprotected (TFA•H<sub>2</sub>N) while the column *C*-terminus refers to whether it is methyl ester protected (OMe) or deprotected (OH).

Entry	Compound	<i>N</i> -Terminus	Amino acid sequence	<i>C</i> -Terminus
1	10	Boc	PG	OMe
2	11	TFA•H <sub>2</sub> N	PG	OMe
3	12	Boc	VPG	OMe
4	13	Boc	VPG	OH
5	14	Boc	VG	OMe
6	15	TFA•H <sub>2</sub> N	VG	OMe
7	16	Boc	VPGVG	OMe
8	17	TFA•H <sub>2</sub> N	VPG	OMe

#### Characterization of 10:

Yield: 11.72 g, 40.94 mmol, 52 %

<sup>1</sup>H-NMR (400 MHz, DMSO-d<sub>6</sub>, 27 °C): δ (ppm) = 8.22 (s, 1H, NH), 4.08 (m, 1H, H<sub>7</sub>), 3.81 (qd, 2H, H<sub>9</sub>, *J* = 17.3, 5.9 Hz), 3.60 (s, 3H, H<sub>11</sub>), 3.36 (m, 1H, H<sub>4</sub>), 3.26 (m, 1H, H<sub>4</sub>), 2.09 + 1.79 (m, 4H, H<sub>5</sub> + H<sub>6</sub>), 1.32 (d, 9H, H<sub>1</sub>).

<sup>13</sup>C-NMR (100 MHz, DMSO-d<sub>6</sub>, 27 °C): δ (ppm) = 173.5 (C<sub>8</sub>), 170.6 (C<sub>10</sub>), 153.6 (C<sub>3</sub>), 78.9 (C<sub>2</sub>), 60.0 (C<sub>7</sub>), 52.1 (C<sub>11</sub>), 46.8 (C<sub>4</sub>), 40.9 (C<sub>9</sub>), 31.4 (C<sub>6</sub>), 28.6 (C<sub>1</sub>), 28.4 (C<sub>1</sub>), 23.5 (C<sub>5</sub>).

MS (ESI), *m/z* calculated for [C<sub>13</sub>H<sub>22</sub>N<sub>2</sub>O<sub>5</sub>Na]<sup>+</sup> = 309.1418; found 309.1421.

IR (bulk): ν<sub>max</sub> (cm<sup>-1</sup>) = 3300 (w), 2973 (w), 1753 (m), 1704 (w), 1685 (m), 1660 (m), 1529 (w), 1479 (w), 1409 (s), 1364 (m), 1258 (w), 1213 (w), 1159 (s), 1124 (w), 1089 (w), 1039 (w), 1020 (w), 978 (w), 921 (w), 854 (w), 782 (w), 755 (w).

#### Characterization of 11:

Yield: 12.01 g, 40.01 mmol, 98 %

<sup>1</sup>H-NMR (400 MHz, DMSO-d<sub>6</sub>, 27 °C): δ (ppm) = 9.50 (s, 1H, NH<sub>2</sub><sup>+</sup>), 8.99 (t, 1H, NH, <sup>3</sup>*J* = 5.8 Hz), 8.59 (s, 1H, NH<sub>2</sub><sup>+</sup>), 4.25 (s, 1H, H<sub>4</sub>), 3.96 (m, 2H, H<sub>6</sub>), 3.65 (s, 3H, H<sub>8</sub>), 3.23 (s, 2H, H<sub>1</sub>), 2.33 (m, 1H, H<sub>2</sub>), 1.89 (m, 3H, H<sub>2</sub> + H<sub>3</sub>).

<sup>13</sup>C-NMR (100 MHz, DMSO-d<sub>6</sub>, 27 °C): δ (ppm) = 170.2 (C<sub>5</sub>), 169.2 (C<sub>7</sub>), 59.3 (C<sub>4</sub>), 52.4 (C<sub>8</sub>), 46.1 (C<sub>1</sub>), 41.2 (C<sub>6</sub>), 29.9 (C<sub>3</sub>), 23.8 (C<sub>2</sub>).

MS (ESI), *m/z* calculated for [C<sub>8</sub>H<sub>15</sub>N<sub>2</sub>O<sub>3</sub>]<sup>+</sup> = 187.1077; found 187.1083.

IR (bulk): ν<sub>max</sub> (cm<sup>-1</sup>) = 2959 (w), 1745 (w), 1665 (s), 1563 (m), 1413 (w), 1370 (w), 1175 (s), 1126 (s), 1027 (w), 983 (w), 832 (m), 798 (m), 720 (s).

#### Characterization of 12:

Yield: 12.70 g, 32.96 mmol, 81 %

<sup>1</sup>H-NMR (400 MHz, DMSO-d<sub>6</sub>, 27 °C): δ (ppm) = 8.20 (t, 1H, NH, <sup>3</sup>*J* = 5.6 Hz), 6.73 (d, 1H, NH, <sup>3</sup>*J* = 8.4 Hz), 4.35 (dd, 1H, H<sub>11</sub>, *J* = 8.2, 3.7 Hz), 3.98 (t, 1H, H<sub>4</sub>, <sup>3</sup>*J* = 8.2 Hz), 3.85 (m, 2H, H<sub>13</sub>), 3.60 (m, 5H, H<sub>8</sub> + H<sub>15</sub>), 2.03 (m, 1H, H<sub>5</sub>), 1.83 (m, 4H, H<sub>9</sub> + H<sub>10</sub>), 0.89 (dd, 6H, H<sub>6</sub>, *J* = 21.9, 6.6 Hz).

<sup>13</sup>C-NMR (100 MHz, DMSO-d<sub>6</sub>, 27 °C): δ (ppm) = 172.6 (C<sub>7</sub>), 170.8 (C<sub>12</sub>), 170.7 (C<sub>14</sub>), 156.0 (C<sub>3</sub>), 78.4 (C<sub>2</sub>), 59.5 (C<sub>11</sub>), 57.7 (C<sub>4</sub>), 52.1 (C<sub>15</sub>), 47.4 (C<sub>8</sub>), 41.0 (C<sub>13</sub>), 30.2 (C<sub>5</sub>), 29.6 (C<sub>10</sub>), 28.6 (C<sub>1</sub>), 24.9 (C<sub>9</sub>), 19.6 (C<sub>6</sub>), 18.8 (C<sub>6</sub>).

MS (ESI),  $m/z$  calculated for  $[\text{C}_{18}\text{H}_{31}\text{N}_3\text{O}_6\text{Na}]^+ = 408.2096$ ; found 408.2105.

IR (bulk):  $\nu_{\text{max}}$  ( $\text{cm}^{-1}$ ) = 3314 (w), 2971 (w), 1751 (w), 1689 (m), 1629 (w), 1509 (w), 1435 (w), 1390 (w), 1365 (w), 1204 (w), 1163 (s), 1090 (w), 1043 (w), 1013 (w), 881 (w).

#### Characterization of 13:

Yield: 11.81 g, 31.80 mmol, 97 %

$^1\text{H-NMR}$  (400 MHz,  $\text{DMSO-d}_6$ , 27 °C):  $\delta$  (ppm) = 12.49 (s, 1H, COOH), 8.08 (t, 1H, NH,  $^3J = 5.6$  Hz), 6.72 (d, 1H, NH,  $^3J = 8.5$  Hz), 4.37 (dd, 1H,  $H_{11}$ ,  $J = 8.2, 3.5$  Hz), 3.99 (t, 1H,  $H_4$ ,  $^3J = 8.2$  Hz), 3.78 (m, 4H,  $H_8 + H_{13}$ ), 2.03 (m, 1H,  $H_5$ ), 1.85 (m, 4H,  $H_9 + H_{10}$ ), 0.89 (dd, 6H,  $H_6$ ,  $J = 22.6, 6.7$  Hz).

$^{13}\text{C-NMR}$  (100 MHz,  $\text{DMSO-d}_6$ , 27 °C):  $\delta$  (ppm) = 172.3 ( $C_7$ ), 171.6 ( $C_{14}$ ), 170.8 ( $C_{12}$ ), 155.9 ( $C_3$ ), 78.4 ( $C_2$ ), 59.5 ( $C_{11}$ ), 57.7 ( $C_4$ ), 47.4 ( $C_8$ ), 41.0 ( $C_{13}$ ), 30.2 ( $C_5$ ), 29.6 ( $C_{10}$ ), 28.6 ( $C_1$ ), 24.9 ( $C_9$ ), 19.6 ( $C_6$ ), 18.8 ( $C_6$ ).

MS (ESI),  $m/z$  calculated for  $[\text{C}_{17}\text{H}_{28}\text{N}_3\text{O}_6]^- = 370.2098$ ; found 370.1973.

IR (bulk):  $\nu_{\text{max}}$  ( $\text{cm}^{-1}$ ) = 3312 (w), 2972 (w), 1628 (m), 1519 (w), 1443 (w), 1391 (w), 1366 (w), 1242 (w), 1161 (s), 1043 (w), 1015 (w), 878 (w), 602 (w).

#### Characterization of 14:

Yield: 16.60 g, 57.60 mmol, 72 %

$^1\text{H-NMR}$  (400 MHz,  $\text{CDCl}_3$ , 27 °C):  $\delta$  (ppm) = 6.59 (s, 1H, NH), 5.08 (d, 1H, NH,  $^3J = 7.7$  Hz), 4.04 (m, 3H,  $H_4 + H_8$ ), 3.74 (s, 3H,  $H_{10}$ ), 2.18 (td, 1H,  $H_5$ ,  $J = 13.4, 6.8$  Hz), 1.43 (s, 9H,  $H_1$ ), 0.97 (dd, 6H,  $H_6$ ,  $J = 20.0, 6.8$  Hz).

$^{13}\text{C-NMR}$  (100 MHz,  $\text{CDCl}_3$ , 27 °C):  $\delta$  (ppm) = 171.8 ( $C_7$ ), 170.0 ( $C_9$ ), 155.8 ( $C_3$ ), 79.9 ( $C_2$ ), 59.8 ( $C_4$ ), 52.3 ( $C_{10}$ ), 41.0 ( $C_8$ ), 30.7 ( $C_5$ ), 28.2 ( $C_1$ ), 19.1 ( $C_6$ ), 17.5 ( $C_6$ ). MS (ESI),  $m/z$  calculated for  $[\text{C}_{13}\text{H}_{24}\text{N}_2\text{O}_5\text{Na}]^+ = 311.2485$ ; found 311.1577.

IR (bulk):  $\nu_{\text{max}}$  ( $\text{cm}^{-1}$ ) = 3314 (w), 2959 (w), 1749 (m), 1687 (w), 1655 (s), 1551 (w), 1524 (s), 1438 (w), 1416 (w), 1386 (w), 1367 (w), 1298 (w), 1246 (w), 1210 (m), 1168 (w), 1087 (w), 1045 (w), 1020 (w), 985 (w), 914 (w), 705 (w), 660 (w), 573 (w).

#### Characterization of 15:

Yield: 9.32 g, 32.12 mmol, 98 %

$^1\text{H-NMR}$  (400 MHz,  $\text{DMSO-d}_6$ , 27 °C):  $\delta$  (ppm) = 8.87 (t, 1H, NH,  $^3J = 5.7$  Hz), 8.13 (s, 3H,  $\text{NH}_3^+$ ), 3.89 (m, 2H,  $H_5$ ), 3.63 (m, 4H,  $H_3 + H_7$ ), 2.07 (m, 1H,  $H_2$ ), 0.93 (dd, 6H,  $H_1$ ,  $^3J = 6.9, 3.5$  Hz).

$^{13}\text{C-NMR}$  (100 MHz,  $\text{DMSO-d}_6$ , 27 °C):  $\delta$  (ppm) = 170.2 ( $C_4$ ), 168.9 ( $C_6$ ), 57.6 ( $C_3$ ), 52.2 ( $C_7$ ), 41.0 ( $C_5$ ), 30.2 ( $C_2$ ), 18.5 ( $C_1$ ), 18.0 ( $C_1$ ).

MS (ESI),  $m/z$  calculated for  $[\text{C}_8\text{H}_{17}\text{N}_2\text{O}_3]^+ = 189.1234$ ; found 189.1242.

IR (bulk):  $\nu_{\text{max}}$  ( $\text{cm}^{-1}$ ) = 2970 (w), 1744 (m), 1665 (s), 1530 (w), 1438 (w), 1369 (w), 1178 (s), 1132 (s), 1034 (w), 981 (w), 837 (m), 799 (m), 721 (s), 596 (w).

#### Characterization of 16:

Yield: 12.65 g, 23.99 mmol, 73 %

$^1\text{H-NMR}$  (400 MHz,  $\text{DMSO-d}_6$ , 27 °C):  $\delta$  (ppm) = 8.38 (t, 1H, NH,  $^3J = 5.8$  Hz), 8.21 (t, 1H, NH,  $^3J = 5.5$  Hz), 7.58 (d, 1H, NH,  $^3J = 8.9$  Hz), 6.72 (d, 1H, NH,  $^3J = 8.3$  Hz), 4.29 (dd, 1H,  $H_4$ ,  $J = 7.5, 5.0$  Hz), 4.15 (dd, 1H,  $H_{11}$ ,  $J = 8.7, 7.3$  Hz), 3.96 (t, 1H,  $H_{15}$ ,  $^3J = 8.3$  Hz), 3.82 (m, 2H,  $H_{19}$ ), 3.71 (m, 3H,  $H_8 + H_{13}$ ), 3.60 (m, 4H,  $H_8 + H_{21}$ ), 1.92 (m, 6H,  $H_5 + H_9 + H_{10} + H_{16}$ ), 1.35 (s, 9H,  $H_1$ ), 0.86 (m, 12H,  $H_6 + H_{17}$ ).

$^{13}\text{C}$ -NMR (100 MHz, DMSO- $d_6$ , 27 °C):  $\delta$  (ppm) = 172.5 ( $C_7$ ), 171.8 ( $C_{18}$ ), 171.0 ( $C_{12}$ ), 170.6 ( $C_{20}$ ), 169.1 ( $C_{14}$ ), 156.0 ( $C_3$ ), 78.4 ( $C_2$ ), 60.1 ( $C_{15}$ ), 58.1 ( $C_{11}$ ), 57.8 ( $C_4$ ), 52.1 ( $C_{21}$ ), 47.6 ( $C_8$ ), 42.6 ( $C_{13}$ ), 41.0 ( $C_{19}$ ), 30.9 ( $C_{16}$ ), 30.2 ( $C_5$ ), 29.6 ( $C_{10}$ ), 28.6 ( $C_1$ ), 25.0 ( $C_9$ ), 19.5 ( $C_{17}$ ), 19.5 ( $C_6$ ), 18.9 ( $C_6$ ), 18.6 ( $C_{17}$ ). MS (ESI),  $m/z$  calculated for  $[\text{C}_{25}\text{H}_{43}\text{N}_5\text{O}_8\text{Na}]^+$  = 564.3014; found 564.3004. IR (bulk):  $\nu_{\text{max}}$  ( $\text{cm}^{-1}$ ) = 3311 (w), 2966 (w), 1746 (w), 1626 (s), 1522 (m), 1439 (w), 1390 (w), 1366 (w), 1311 (w), 1207 (w), 1162 (s), 1039 (w), 1013 (w), 675 (w), 563 (w).

#### Characterization of 17:

Yield: 66.5 mg, 0.16 mmol, 98 %

$^1\text{H}$ -NMR (400 MHz, DMSO- $d_6$ , 27 °C):  $\delta$  (ppm) = 8.37 (t, 1H, NH,  $^3J = 5.8$  Hz), 8.06 (s, 3H,  $\text{NH}_3^+$ ), 4.42 (dd, 1H,  $H_8$ ,  $J = 8.4, 5.1$  Hz), 3.97 (m, 1H,  $H_3$ ), 3.87 (m, 2H,  $H_{10}$ ), 3.60 (m, 5H,  $H_5 + H_{12}$ ), 2.11 (m, 2H,  $H_2 + H_7$ ), 1.81 (m, 3H,  $H_6 + H_7$ ), 0.99 (dd, 6H,  $H_I$ ,  $J = 31.8, 6.9$  Hz).

$^{13}\text{C}$ -NMR (100 MHz, DMSO- $d_6$ , 27 °C):  $\delta$  (ppm) = 172.0 ( $C_4$ ), 170.6 ( $C_9$ ), 167.2 ( $C_{11}$ ), 59.8 ( $C_8$ ), 56.2 ( $C_3$ ), 52.1 ( $C_{12}$ ), 47.8 ( $C_5$ ), 40.9 ( $C_{10}$ ), 27.9 ( $C_2$ ), 29.7 ( $C_7$ ), 25.0 ( $C_6$ ), 18.9 ( $C_1$ ), 17.5 ( $C_1$ ).

#### 4.3.4 Elongation of the elastin-like polypeptide sequence (18-26)

The peptide coupling reactions as well as the deprotection reactions were conducted analogous to the reactions which were already described for the buildup of the pentapeptide **16** in the Experimental Part 4.3.3. The products from the peptide coupling reactions had to be purified *via* column chromatography (see below) while workup of the Boc- and methyl ester deprotection followed the procedures as described in the Experimental Part 4.3.3.

Column chromatography of **22**: DCM/MeOH (60:1) ( $R_f = 0.0$ )  $\rightarrow$  DCM/MeOH (40:1) ( $R_f = 0.02$ )  $\rightarrow$  DCM/MeOH (30:1) ( $R_f = 0.04$ )  $\rightarrow$  DCM/MeOH (20:1) ( $R_f = 0.06$ )  $\rightarrow$  DCM/MeOH (10:1) ( $R_f = 0.12$ ). Column chromatography of **25**: DCM/MeOH (60:1) ( $R_f = 0.0$ )  $\rightarrow$  DCM/MeOH (40:1) ( $R_f = 0.0$ )  $\rightarrow$  DCM/MeOH (20:1) ( $R_f = 0.05$ )  $\rightarrow$  DCM/MeOH (10:1) ( $R_f = 0.09$ )  $\rightarrow$  DCM/MeOH (5:1) ( $R_f = 0.20$ ).

An overview about all synthesized intermediate products for the synthesis of the TFA• $\text{H}_2\text{N}$ -(VPGVG) $_4$ -OMe (**26**) sequence is given in Table 7.

**Table 7.** Synthesized intermediate products for the buildup of the eicosapeptide sequence **26**. The column *N*-terminus refers to whether it is Boc-protected or deprotected (TFA• $\text{H}_2\text{N}$ ) while the column *C*-terminus refers to whether it is methyl ester protected (OMe) or deprotected (OH).

Entry	Compound	<i>N</i> -Terminus	Amino acid sequence	<i>C</i> -Terminus
1	18	Boc	VPGVG	OH
2	19	TFA• $\text{H}_2\text{N}$	VPGVG	OH
3	20	TFA• $\text{H}_2\text{N}$	(VPGVG) $_n$	OH
4	21	TFA• $\text{H}_2\text{N}$	VPGVG	OMe
5	22	Boc	(VPGVG) $_2$	OMe
6	23	Boc	(VPGVG) $_2$	OH
7	24	TFA• $\text{H}_2\text{N}$	(VPGVG) $_2$	OMe
8	25	Boc	(VPGVG) $_4$	OMe
9	26	TFA• $\text{H}_2\text{N}$	(VPGVG) $_4$	OMe

#### Characterization of 18:

Yield: 2.83 g, 5.47 mmol, 98 %

$^1\text{H}$ -NMR (400 MHz, DMSO- $d_6$ , 27 °C):  $\delta$  (ppm) = 12.48 (s, 1H, COOH), 8.27 (t, 1H, NH,  $^3J = 5.9$  Hz), 8.21 (t, 1H, NH,  $^3J = 5.6$  Hz), 7.59 (d, 1H, NH,  $^3J = 9.0$  Hz), 6.71 (d, 1H, NH,  $^3J = 8.4$  Hz), 4.30 (dd, 1H,  $H_4$ ,  $J = 7.5, 5.3$  Hz), 4.16 (dd, 1H,  $H_{11}$ ,  $J = 8.8, 7.2$  Hz), 3.96 (t, 1H,  $H_{15}$ ,  $^3J = 8.3$  Hz), 3.73 (m, 5H,

$H_8 + H_{13} + H_{19}$ ), 3.56 (m, 1H,  $H_8$ ), 1.94 (m, 6H,  $H_5 + H_9 + H_{10} + H_{16}$ ), 1.35 (s, 9H,  $H_1$ ), 0.85 (m, 12H,  $H_6 + H_{17}$ ).

$^{13}\text{C-NMR}$  (100 MHz, DMSO- $d_6$ , 27 °C):  $\delta$  (ppm) = 172.4 ( $C_7$ ), 171.6 ( $C_{18} + C_{20}$ ), 171.0 ( $C_{12}$ ), 169.1 ( $C_{14}$ ), 156.0 ( $C_3$ ), 78.4 ( $C_2$ ), 60.1 ( $C_{15}$ ), 58.1 ( $C_{11}$ ), 57.8 ( $C_4$ ), 47.6 ( $C_8$ ), 42.6 ( $C_{13}$ ), 41.0 ( $C_{19}$ ), 31.0 ( $C_{16}$ ), 30.2 ( $C_5$ ), 29.6 ( $C_{10}$ ), 28.6 ( $C_1$ ), 25.0 ( $C_9$ ), 19.6 ( $C_{17}$ ), 19.5 ( $C_6$ ), 18.9 ( $C_6$ ), 18.6 ( $C_{17}$ ).

MS (ESI),  $m/z$  calculated for  $[\text{C}_{24}\text{H}_{40}\text{N}_5\text{O}_8]^- = 526.2871$ ; found 526.2959.

IR (bulk):  $\nu_{\text{max}}$  ( $\text{cm}^{-1}$ ) = 3298 (w), 2968 (w), 1627 (s), 1521 (m), 1447 (w), 1391 (w), 1367 (w), 1162 (m), 1015 (w), 878 (w), 677 (w), 620 (w).

#### Characterization of 19:

Yield: 154.3 mg, 0.28 mmol, 98 %

$^1\text{H-NMR}$  (400 MHz, DMSO- $d_6$ , 27 °C):  $\delta$  (ppm) = 12.43 (s, 1H, COOH), 8.31 (t, 1H, NH,  $^3J = 6.0$  Hz), 8.20 (t, 1H, NH,  $^3J = 5.7$  Hz), 8.03 (s, 3H,  $\text{NH}_3^+$ ), 7.67 (d, 1H, NH,  $^3J = 8.9$  Hz), 4.41 (dd, 1H,  $H_3$ ,  $J = 8.2, 5.2$  Hz), 4.18 (dd, 1H,  $H_8$ ,  $J = 10.4, 5.0$  Hz), 3.95 (m, 1H,  $H_{12}$ ), 3.70 (m, 5H,  $H_5 + H_{10} + H_{16}$ ), 3.50 (m, 1H,  $H_5$ ), 2.09 (m, 2H,  $H_2 + H_{13}$ ), 1.95 (m, 2H,  $H_6 + H_7$ ), 1.82 (m, 2H,  $H_6 + H_7$ ), 0.92 (m, 12H,  $H_1 + H_{14}$ ).

$^{13}\text{C-NMR}$  (100 MHz, DMSO- $d_6$ , 27 °C):  $\delta$  (ppm) = 171.8 ( $C_4$ ), 171.6 ( $C_{17}$ ), 171.5 ( $C_{15}$ ), 171.0 ( $C_{12}$ ), 168.9 ( $C_{11}$ ), 167.3 ( $C_9$ ), 60.0 ( $C_{12}$ ), 57.8 ( $C_8$ ), 56.2 ( $C_3$ ), 47.8 ( $C_5$ ), 42.4 ( $C_{10}$ ), 41.0 ( $C_{16}$ ), 31.1 ( $C_{13}$ ), 29.8 ( $C_7$ ), 29.7 ( $C_2$ ), 25.0 ( $C_6$ ), 19.6 ( $C_{14}$ ), 18.9 ( $C_{14}$ ), 18.4 ( $C_1$ ), 17.6 ( $C_1$ ).

MS (ESI),  $m/z$  calculated for  $[\text{C}_{19}\text{H}_{32}\text{N}_5\text{O}_6]^- = 426.2347$ ; found 426.2336.

IR (bulk):  $\nu_{\text{max}}$  ( $\text{cm}^{-1}$ ) = 2969 (w), 1642 (s), 1523 (m), 1372 (w), 1179 (s), 1133 (s), 1034 (w), 835 (w), 799 (w), 720 (w), 599 (w).

#### Characterization of 21:

Yield: 2.50 g, 4.50 mmol, 98 %

$^1\text{H-NMR}$  (400 MHz, DMSO- $d_6$ , 27 °C):  $\delta$  (ppm) = 8.42 (t, 1H, NH,  $^3J = 5.9$  Hz), 8.20 (t, 1H, NH,  $^3J = 5.7$  Hz), 8.01 (s, 3H,  $\text{NH}_3^+$ ), 7.67 (dd, 1H, NH,  $^3J = 8.8$  Hz), 4.42 (dd, 1H,  $H_3$ ,  $J = 8.3, 5.3$  Hz), 4.18 (dd, 1H,  $H_8$ ,  $J = 8.8, 6.7$  Hz), 3.95 (m, 1H,  $H_{12}$ ), 3.83 (m, 2H,  $H_{16}$ ), 3.70 (m, 3H,  $H_5 + H_{10}$ ), 3.60 (s, 3H,  $H_{18}$ ), 3.50 (m, 1H,  $H_5$ ), 2.09 – 1.82 (m, 6H,  $H_2 + H_6 + H_7 + H_{13}$ ), 0.87 (m, 12H,  $H_1 + H_{14}$ ).

$^{13}\text{C-NMR}$  (100 MHz, DMSO- $d_6$ , 27 °C):  $\delta$  (ppm) = 171.8 ( $C_4 + C_{15}$ ), 170.6 ( $C_9$ ), 169.0 ( $C_{11}$ ), 167.3 ( $C_{17}$ ), 60.0 ( $C_{12}$ ), 57.8 ( $C_8$ ), 56.2 ( $C_3$ ), 52.1 ( $C_{18}$ ), 47.9 ( $C_5$ ), 42.4 ( $C_{10}$ ), 40.9 ( $C_{16}$ ), 31.1 ( $C_{13}$ ), 29.7 ( $C_2 + C_7$ ), 25.0 ( $C_6$ ), 19.5 ( $C_{14}$ ), 18.9 ( $C_{14}$ ), 18.4 ( $C_1$ ), 17.6 ( $C_1$ ).

MS (ESI),  $m/z$  calculated for  $[\text{C}_{20}\text{H}_{36}\text{N}_5\text{O}_6]^+ = 442.2660$ ; found 442.2680.

IR (bulk):  $\nu_{\text{max}}$  ( $\text{cm}^{-1}$ ) = 3290 (w), 2967 (w), 1748 (w), 1644 (s), 1524 (m), 1454 (w), 1731 (w), 1199 (s), 1176 (s), 1132 (s), 1036 (w), 835 (w), 800 (w), 720 (w), 599 (w).

#### Characterization of 22:

Yield: 1.809 g, 1.90 mmol, 47 %

$^1\text{H-NMR}$  (400 MHz, DMSO- $d_6$ , 27 °C):  $\delta$  (ppm) = 8.39 (t, 1H, NH,  $^3J = 5.9$  Hz), 8.26 (t, 1H, NH,  $^3J = 5.8$  Hz), 8.20 (t, 1H, NH,  $^3J = 5.7$  Hz), 8.16 (t, 1H, NH,  $^3J = 5.8$  Hz), 7.90 (d, 1H, NH,  $^3J = 8.5$  Hz), 7.62 (d, 2H, NH,  $^3J = 8.9$  Hz), 6.78 (d, 1H, NH,  $^3J = 8.4$  Hz), 4.27 (m, 3H,  $H_4 + H_{15}$ ), 4.16 (m, 2H,  $H_{11}$ ), 3.97 (t, 1H,  $H_4$ ,  $^3J = 8.4$  Hz), 3.73 (m, 10H,  $H_8 + H_{13} + H_{19}$ ), 3.60 (m, 5H,  $H_8 + H_{21}$ ), 1.92 (m, 12H,  $H_5 + H_9 + H_{10} + H_{16}$ ), 1.35 (s, 9H,  $H_1$ ), 0.87 (m, 24H,  $H_6 + H_{17}$ ).

$^{13}\text{C-NMR}$  (100 MHz, DMSO- $d_6$ , 27 °C):  $\delta$  (ppm) = 171.9 ( $C_7$ ), 171.9 ( $C_7$ ), 171.3 ( $C_{18}$ ), 170.9 ( $C_{18}$ ), 170.8 ( $C_{12}$ ), 170.1 ( $C_{20}$ ), 169.8 ( $C_{12}$ ), 168.6 ( $C_{20}$ ), 168.6 ( $C_{14}$ ), 168.6 ( $C_{14}$ ), 155.5 ( $C_3$ ), 78.0 ( $C_2$ ), 59.7 ( $C_{15}$ ), 59.5 ( $C_{15}$ ), 58.3 ( $C_{11}$ ), 57.5 ( $C_{11}$ ), 57.4 ( $C_4$ ), 55.6 ( $C_4$ ), 51.6 ( $C_{21}$ ), 47.3 ( $C_8$ ), 47.2 ( $C_8$ ), 42.1 ( $C_{13}$ ), 42.0 ( $C_{13}$ ), 41.6 ( $C_{19}$ ), 40.5 ( $C_{19}$ ), 30.5 ( $C_{16}$ ), 30.4 ( $C_{16}$ ), 30.1 ( $C_5$ ), 29.7 ( $C_5$ ), 29.2 ( $C_{10}$ ), 29.1 ( $C_{10}$ ), 28.2

(C<sub>1</sub>), 24.6 (C<sub>9</sub>), 24.4 (C<sub>9</sub>), 19.1 (C<sub>17</sub>), 19.0 (C<sub>6</sub> + C<sub>17</sub>), 19.0 (C<sub>6</sub>), 18.5 (C<sub>17</sub>), 18.4 (C<sub>6</sub>), 18.3 (C<sub>17</sub>), 18.0 (C<sub>6</sub>).

MS (ESI),  $m/z$  calculated for [C<sub>44</sub>H<sub>74</sub>N<sub>10</sub>O<sub>13</sub>Na]<sup>+</sup> = 973.5329; found 973.5324.

IR (bulk):  $\nu_{\max}$  (cm<sup>-1</sup>) = 3300 (w), 2965 (w), 1626 (s), 1518 (m), 1440 (w), 1390 (w), 1367 (w), 1206 (w), 1164 (m), 1012 (w), 879 (w), 665 (w), 614 (w).

#### Characterization of 23:

Yield: 849.2 mg, 0.91 mmol, 91 %

<sup>1</sup>H-NMR (400 MHz, DMSO-d<sub>6</sub>, 27 °C):  $\delta$  (ppm) = 12.47 (s, 1H, COOH), 8.27 (dd, 2H, NH,  $J$  = 11.2, 5.6 Hz), 8.20 (t, 1H, NH,  $^3J$  = 5.7 Hz), 8.16 (t, 1H, NH,  $^3J$  = 5.8 Hz), 7.92 (d, 1H, NH,  $^3J$  = 8.5 Hz), 7.61 (t, 2H, NH,  $^3J$  = 9.4 Hz), 6.80 (d, 1H, NH,  $^3J$  = 8.5 Hz), 4.29 (m, 3H, H<sub>4</sub> + H<sub>11</sub>), 4.17 (dd, 1H, H<sub>11</sub>,  $J$  = 8.9, 6.9 Hz), 4.10 (dd, 1H, H<sub>15</sub>,  $J$  = 8.6, 7.8 Hz), 3.97 (t, 1H, H<sub>15</sub>,  $^3J$  = 8.3 Hz), 3.73 (m, 10H, H<sub>8</sub> + H<sub>13</sub> + H<sub>19</sub>), 3.56 (m, 2H, H<sub>8</sub>), 1.94 (m, 12H, H<sub>5</sub> + H<sub>9</sub> + H<sub>10</sub> + H<sub>16</sub>), 1.35 (s, 9H, H<sub>1</sub>), 0.83 (m, 24H, H<sub>6</sub> + H<sub>17</sub>).

<sup>13</sup>C-NMR (100 MHz, DMSO-d<sub>6</sub>, 27 °C):  $\delta$  (ppm) = 172.0 (C<sub>7</sub>), 171.9 (C<sub>7</sub>), 171.1 (C<sub>18</sub>), 171.1 (C<sub>12</sub>), 171.0 (C<sub>18</sub>), 170.8 (C<sub>12</sub>), 169.8 (C<sub>20</sub>), 168.6 (C<sub>14</sub>), 168.6 (C<sub>20</sub>), 155.5 (C<sub>3</sub>), 78.0 (C<sub>2</sub>), 59.7 (C<sub>15</sub>), 59.5 (C<sub>15</sub>), 58.3 (C<sub>11</sub>), 57.5 (C<sub>11</sub>), 57.4 (C<sub>4</sub>), 55.6 (C<sub>4</sub>), 47.2 (C<sub>8</sub>), 47.2 (C<sub>8</sub>), 42.1 (C<sub>13</sub>), 42.0 (C<sub>13</sub>), 41.6 (C<sub>19</sub>), 40.6 (C<sub>19</sub>), 30.6 (C<sub>16</sub>), 30.5 (C<sub>16</sub>), 30.1 (C<sub>5</sub>), 29.8 (C<sub>5</sub>), 29.2 (C<sub>10</sub>), 29.1 (C<sub>10</sub>), 28.2 (C<sub>1</sub>), 24.6 (C<sub>9</sub>), 24.4 (C<sub>9</sub>), 19.1 (C<sub>17</sub>), 19.1 (C<sub>17</sub>), 19.0 (C<sub>6</sub>), 18.4 (C<sub>17</sub>), 18.3 (C<sub>6</sub>), 18.0 (C<sub>6</sub>).

MS (ESI),  $m/z$  calculated for [C<sub>43</sub>H<sub>71</sub>N<sub>10</sub>O<sub>13</sub>]<sup>-</sup> = 935.5189; found 935.5197.

IR (bulk):  $\nu_{\max}$  (cm<sup>-1</sup>) = 3287 (w), 2965 (w), 1622 (s), 1523 (m), 1444 (w), 1390 (w), 1367 (w), 1236 (w), 1165 (m), 1042 (w), 880 (w), 660 (w), 618 (w).

#### Characterization of 24:

Yield: 850.0 mg, 0.88 mmol, 98 %

<sup>1</sup>H-NMR (400 MHz, DMSO-d<sub>6</sub>, 27 °C):  $\delta$  (ppm) = 8.42 (t, 1H, NH,  $^3J$  = 5.9 Hz), 8.20 (dd, 2H, NH,  $J$  = 12.3 Hz, 5.9 Hz), 8.16 (t, 1H, NH,  $^3J$  = 5.8 Hz), 8.02 (s, 3H, NH<sub>3</sub><sup>+</sup>), 7.89 (d, 1H, NH,  $^3J$  = 8.6 Hz), 7.69 (d, 1H, NH,  $^3J$  = 8.7 Hz), 7.62 (d, 1H, NH,  $^3J$  = 8.9 Hz), 4.43 (dd, 1H, H<sub>3</sub>,  $J$  = 8.3, 5.3 Hz), 4.32 (m, 2H, H<sub>8</sub>), 4.18 (m, 2H, H<sub>12</sub>), 3.97 (m, 1H, H<sub>3</sub>), 3.73 (m, 10H, H<sub>5</sub> + H<sub>10</sub> + H<sub>16</sub>), 3.62 (s, 3H, H<sub>18</sub>), 3.49 (m, 2H, H<sub>5</sub>), 2.13 – 1.79 (m, 12H, H<sub>2</sub> + H<sub>6</sub> + H<sub>7</sub> + H<sub>13</sub>), 0.87 (m, 24H, H<sub>1</sub> + H<sub>14</sub>).

<sup>13</sup>C-NMR (100 MHz, DMSO-d<sub>6</sub>, 27 °C):  $\delta$  (ppm) = 172.3 (C<sub>4</sub>), 171.8 (C<sub>4</sub> + C<sub>15</sub>), 171.5 (C<sub>15</sub>), 170.6 (C<sub>9</sub>), 170.3 (C<sub>9</sub>), 169.1 (C<sub>11</sub>), 169.0 (C<sub>11</sub>), 168.9 (C<sub>17</sub>), 167.3 (C<sub>17</sub>), 60.0 (C<sub>12</sub>), 59.9 (C<sub>12</sub>), 58.1 (C<sub>8</sub>), 57.9 (C<sub>8</sub>), 56.2 (C<sub>3</sub>), 56.1 (C<sub>3</sub>), 52.1 (C<sub>18</sub>), 47.9 (C<sub>5</sub>), 47.6 (C<sub>5</sub>), 42.5 (C<sub>10</sub>), 42.4 (C<sub>10</sub>), 42.0 (C<sub>16</sub>), 41.0 (C<sub>16</sub>), 31.0 (C<sub>13</sub>), 31.0 (C<sub>13</sub>), 30.6 (C<sub>2</sub>), 29.8 (C<sub>2</sub>), 29.7 (C<sub>7</sub>), 29.7 (C<sub>7</sub>), 25.1 (C<sub>6</sub>), 24.9 (C<sub>6</sub>), 19.6 (C<sub>14</sub>), 19.5 (C<sub>1</sub>), 18.9 (C<sub>14</sub>), 18.5 (C<sub>1</sub>), 18.5 (C<sub>14</sub>), 17.6 (C<sub>1</sub>).

MS (ESI),  $m/z$  calculated for [C<sub>39</sub>H<sub>67</sub>N<sub>10</sub>O<sub>11</sub>]<sup>+</sup> = 851.4975; found 851.4985.

IR (bulk):  $\nu_{\max}$  (cm<sup>-1</sup>) = 3299 (w), 2965 (w), 1749 (w), 1641 (s), 1522 (m), 1448 (w), 1200 (m), 1173 (m), 1034 (w), 835 (w), 719 (w), 701 (w), 602 (w).

#### Characterization of 25:

Yield: 383.0 mg, 0.22 mmol, 24 %

<sup>1</sup>H-NMR (400 MHz, DMSO-d<sub>6</sub>, 27 °C):  $\delta$  (ppm) = 8.39 (t, 1H, NH,  $^3J$  = 5.9 Hz), 8.20 (m, 7H, NH), 7.92 (m, 3H, NH), 7.62 (d, 4H, NH,  $^3J$  = 8.8 Hz), 6.79 (d, 1H, NH,  $^3J$  = 8.4 Hz), 4.28 (m, 7H, H<sub>4</sub> + H<sub>15</sub>), 4.15 (m, 4H, H<sub>11</sub>), 3.97 (t, 1H, H<sub>4</sub>,  $^3J$  = 8.4 Hz), 3.72 (m, 20H, H<sub>8</sub> + H<sub>13</sub> + H<sub>19</sub>), 3.60 (m, 7H, H<sub>8</sub> + H<sub>21</sub>), 1.92 (m, 24H, H<sub>5</sub> + H<sub>9</sub> + H<sub>10</sub> + H<sub>16</sub>), 1.35 (s, 9H, H<sub>1</sub>), 0.87 (m, 48H, H<sub>6</sub> + H<sub>17</sub>).

MS (ESI),  $m/z$  calculated for [C<sub>82</sub>H<sub>136</sub>N<sub>20</sub>O<sub>23</sub>Na]<sup>+</sup> = 1791.9979; found: 1791.9966.

IR (bulk):  $\nu_{\max}$  (cm<sup>-1</sup>) = 3298 (w), 2967 (w), 1627 (s), 1523 (m), 1443 (w), 1391 (w), 1369 (w), 1202 (w), 1172 (m), 1132 (w), 10126(w), 719 (w).

#### Characterization of **26**:

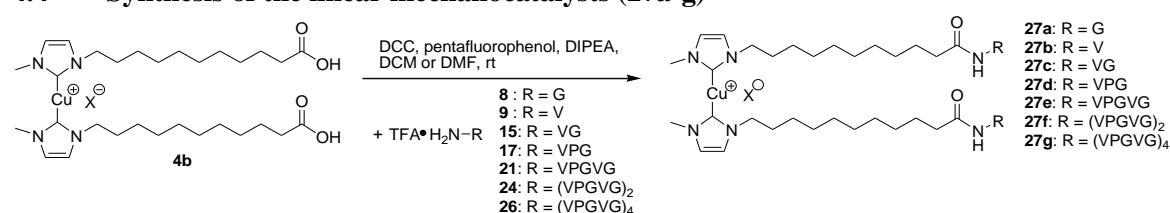
Yield: 701.3 mg, 0.39 mmol, 99 %

<sup>1</sup>H-NMR (400 MHz, DMSO-d<sub>6</sub>, 27 °C):  $\delta$  (ppm) = 8.40 (t, 1H, NH, <sup>3</sup>J = 5.8 Hz), 8.19 (m, 7H, NH), 8.03 (m, 3H, NH<sub>3</sub><sup>+</sup>), 7.91 (m, 3H, NH), 7.61 (d, 4H, NH, <sup>3</sup>J = 8.8 Hz), 4.42 (dd, 1H, H<sub>3</sub>, J = 8.2, 5.3 Hz), 4.31 (m, 6H, H<sub>3</sub> + H<sub>8</sub>), 4.15 (m, 4H, H<sub>12</sub>), 3.96 (m, 1H, H<sub>3</sub>), 3.72 (m, 20H, H<sub>5</sub> + H<sub>10</sub> + H<sub>16</sub>), 3.60 (m, 7H, H<sub>5</sub> + H<sub>18</sub>), 1.94 (m, 24H, H<sub>2</sub> + H<sub>6</sub> + H<sub>7</sub> + H<sub>13</sub>), 0.83 (m, 48H, H<sub>1</sub> + H<sub>14</sub>).

MS (ESI), *m/z* calculated for [C<sub>77</sub>H<sub>129</sub>N<sub>20</sub>O<sub>21</sub>]<sup>+</sup> = 1669.9636; found 1669.9434.

IR (bulk):  $\nu_{\max}$  (cm<sup>-1</sup>) = 3287 (w), 2965 (w), 1627 (s), 1525 (m), 1448 (w), 1200 (w), 1177 (w), 1131 (w), 719 (w).

#### 4.4 Synthesis of the linear mechanocatalysts (**27a-g**)



**Scheme 18.** Synthesis of the linear mechanocatalysts **27a-g** via peptide coupling reactions.

**General procedure for the coupling reaction:** **4b** (0.065 mmol, 1.0 eq.) was dissolved in DCM (**27a-d**) or DMF (**27e-g**) (500.0  $\mu$ L). The mixture was cooled down to 0 °C in an ice bath and molecular sieve (3 Å) and DCC (0.143 mmol, 2.2 eq.) were added. The mixture was stirred for ten minutes before pentafluorophenol (0.143 mmol, 2.2 eq.), dissolved in DCM (**27a-d**) or DMF (**27e-g**) (200.0  $\mu$ L) was added. After stirring for another 15 minutes the *N*-terminus deprotected peptide (0.13 mmol, 2.0 eq.) was dissolved in DCM (**27a-d**) or DMF (**27e-g**) (500.0  $\mu$ L) and DIPEA (0.286 mmol, 4.4 eq.) and was also added to the reaction. The reaction was further stirred for 48 hours until completion of the reaction (checked *via* TLC, for R<sub>f</sub> values see below). The formed precipitate was removed by filtration and the product was concentrated in vacuo. Purification was accomplished by gradient column chromatography (see below).

Column chromatography of **27a**: CHCl<sub>3</sub> (R<sub>f</sub> = 0.1).

Column chromatography of **27b**: CHCl<sub>3</sub> (R<sub>f</sub> = 0.1).

Column chromatography of **27c**: CHCl<sub>3</sub> (R<sub>f</sub> = 0.10)  $\rightarrow$  CHCl<sub>3</sub>/MeOH (20:1) (R<sub>f</sub> = 0.18).

Column chromatography of **27d**: CHCl<sub>3</sub> (R<sub>f</sub> = 0.05)  $\rightarrow$  CHCl<sub>3</sub>/MeOH (40:1) (R<sub>f</sub> = 0.11).

Column chromatography of **27e**: CHCl<sub>3</sub> (R<sub>f</sub> = 0.00)  $\rightarrow$  CHCl<sub>3</sub>/MeOH (40:1) (R<sub>f</sub> = 0.04)  $\rightarrow$  CHCl<sub>3</sub>/MeOH (20:1) (R<sub>f</sub> = 0.08).

Column chromatography of **27f**: DCM/MeOH (60:1) (R<sub>f</sub> = 0.00)  $\rightarrow$  DCM/MeOH (40:1) (R<sub>f</sub> = 0.05)  $\rightarrow$  DCM/MeOH (20:1) (R<sub>f</sub> = 0.10)  $\rightarrow$  DCM/MeOH (10:1) (R<sub>f</sub> = 0.26).

Column chromatography of **27g**: DCM/MeOH (60:1) (R<sub>f</sub> = 0.00)  $\rightarrow$  DCM/MeOH (40:1) (R<sub>f</sub> = 0.00)  $\rightarrow$  DCM/MeOH (20:1) (R<sub>f</sub> = 0.00)  $\rightarrow$  DCM/MeOH (10:1) (R<sub>f</sub> = 0.09)  $\rightarrow$  DCM/MeOH (5:1) (R<sub>f</sub> = 0.18).

#### Characterization of **27a**:

Yield: 11.9 mg, 0.015 mmol, 54 %

<sup>1</sup>H-NMR (400 MHz, CDCl<sub>3</sub>, 27 °C):  $\delta$  (ppm) = 6.15 (dd, 2H, H<sub>3</sub> + H<sub>4</sub>), 6.06 (s, 1H, NH), 4.03 (d, 2H, H<sub>11</sub>, <sup>3</sup>J = 5.2 Hz), 3.75 (s, 3H, H<sub>13</sub>), 3.57 (m, 2H, H<sub>5</sub>), 3.23 (s, 3H, H<sub>1</sub>), 2.23 (m, 2H, H<sub>9</sub>), 1.63 (m, 4H, H<sub>6</sub> + H<sub>8</sub>), 1.27 (m, 12H, H<sub>7</sub>).

<sup>13</sup>C-NMR (100 MHz, CDCl<sub>3</sub>, 27 °C): δ (ppm) = 173.3 (C<sub>10</sub>), 170.6 (C<sub>12</sub>), 153.2 (C<sub>2</sub>), 111.1 (C<sub>4</sub>), 109.9 (C<sub>3</sub>), 52.3 (C<sub>13</sub>), 43.6 (C<sub>5</sub>), 41.1 (C<sub>11</sub>), 36.3 (C<sub>1</sub>), 30.3 (C<sub>9</sub>), 29.5 (C<sub>6</sub>), 29.3 (C<sub>7</sub>), 29.2 (C<sub>7</sub>), 29.1 (C<sub>7</sub>), 29.1 (C<sub>7</sub>), 26.5 (C<sub>7</sub>), 25.5 (C<sub>8</sub>).

IR (bulk): ν<sub>max</sub> (cm<sup>-1</sup>) = 3324 (m), 3131 (w), 2919 (s), 2849 (m), 1744 (s), 1684 (s), 1637 (s), 1541 (s), 1471 (s), 1458 (w), 1437 (m), 1412 (m), 1370 (m), 1353 (m), 1305 (w), 1253 (m), 1240 (m), 1208 (s), 1184 (s), 1115 (w), 1095 (w), 1052 (w), 1042 (w), 1010 (w), 974 (w), 898 (w), 806 (w), 772 (w), 753 (w), 718 (w), 665 (s), 634 (w), 590 (w), 574 (w).

#### Characterization of 27b:

Yield: 28.8 mg, 0.033 mmol, 45 %

<sup>1</sup>H-NMR (400 MHz, CDCl<sub>3</sub>, 27 °C): δ (ppm) = 6.13 (dd, 2H, H<sub>3</sub> + H<sub>4</sub>), 5.96 (d, 1H, NH, <sup>3</sup>J = 8.6 Hz), 4.55 (dd, 2H, H<sub>11</sub>, J = 8.8, 5.0 Hz), 3.71 (s, 3H, H<sub>15</sub>), 3.54 (m, 2H, H<sub>5</sub>), 3.22 (s, 3H, H<sub>1</sub>), 2.21 (m, 2H, H<sub>9</sub>), 2.13 (dtd, 1H, H<sub>12</sub>, J = 13.7, 6.9, 5.2 Hz), 1.61 (m, 4H, H<sub>6</sub> + H<sub>8</sub>), 1.27 (m, 12H, H<sub>7</sub>), 0.89 (dd, 6H, H<sub>13</sub>, J = 12.8, 6.9 Hz).

<sup>13</sup>C-NMR (100 MHz, CDCl<sub>3</sub>, 27 °C): δ (ppm) = 173.0 (C<sub>10</sub>), 172.7 (C<sub>14</sub>), 153.3 (C<sub>2</sub>), 111.1 (C<sub>4</sub>), 110.0 (C<sub>3</sub>), 56.8 (C<sub>11</sub>), 52.1 (C<sub>15</sub>), 43.7 (C<sub>5</sub>), 36.7 (C<sub>1</sub>), 31.3 (C<sub>12</sub>), 30.3 (C<sub>9</sub>), 29.5 (C<sub>6</sub>), 29.3 (C<sub>7</sub>), 29.3 (C<sub>7</sub>), 29.2 (C<sub>7</sub>), 29.1 (C<sub>7</sub>), 29.1 (C<sub>7</sub>), 26.5 (C<sub>7</sub>), 25.6 (C<sub>8</sub>), 18.9 (C<sub>13</sub>), 17.8 (C<sub>13</sub>).

IR (bulk): ν<sub>max</sub> (cm<sup>-1</sup>) = 3284 (w), 2926 (m), 2854 (m), 1743 (m), 1655 (s), 1533 (m), 1468 (m), 1411 (w), 1372 (w), 1328 (m), 1202 (m), 1153 (m), 1002 (w), 658 (m), 553 (w).

#### Characterization of 27c:

Yield: 26.2 mg, 0.015 mmol, 42 %

<sup>1</sup>H-NMR (400 MHz, CDCl<sub>3</sub>, 27 °C): δ (ppm) = 6.97 (t, 1H, NH, <sup>3</sup>J = 5.3 Hz), 6.27 (d, 1H, NH, <sup>3</sup>J = 8.7 Hz), 6.14 (dd, 2H, H<sub>3</sub> + H<sub>4</sub>), 4.35 (dd, 1H, H<sub>11</sub>, <sup>3</sup>J = 7.0 Hz), 4.07 + 3.95 (dd, 1H, H<sub>15</sub>), 3.72 (s, 3H, H<sub>17</sub>), 3.56 (m, 2H, H<sub>5</sub>), 3.22 (s, 3H, H<sub>1</sub>), 2.20 (t, 2H, H<sub>9</sub>, <sup>3</sup>J = 7.6 Hz), 2.09 (m, 1H, H<sub>12</sub>), 1.59 (m, 4H, H<sub>6</sub> + H<sub>8</sub>), 1.24 (m, 12H, H<sub>7</sub>), 0.94 (dd, 6H, H<sub>13</sub>, J = 8.8, 6.8 Hz).

<sup>13</sup>C-NMR (100 MHz, CDCl<sub>3</sub>, 27 °C): δ (ppm) = 173.3 (C<sub>10</sub>), 171.8 (C<sub>14</sub>), 169.9 (C<sub>16</sub>), 153.2 (C<sub>2</sub>), 111.1 (C<sub>4</sub>), 109.9 (C<sub>3</sub>), 58.1 (C<sub>11</sub>), 52.2 (C<sub>17</sub>), 43.6 (C<sub>5</sub>), 41.1 (C<sub>15</sub>), 36.6 (C<sub>1</sub>), 31.0 (C<sub>12</sub>), 30.3 (C<sub>9</sub>), 29.5 (C<sub>6</sub>), 29.3 (C<sub>7</sub>), 29.2 (C<sub>7</sub>), 29.2 (C<sub>7</sub>), 29.1 (C<sub>7</sub>), 29.1 (C<sub>7</sub>), 26.5 (C<sub>7</sub>), 25.6 (C<sub>8</sub>), 19.1 (C<sub>13</sub>), 18.2 (C<sub>13</sub>).

IR (bulk): ν<sub>max</sub> (cm<sup>-1</sup>) = 3284 (s), 2923 (s), 2852 (m), 1735 (m), 1668 (s), 1631 (s), 1631 (s), 1544 (m), 1469 (w), 1409 (w), 1387 (w), 1341 (w), 1296 (w), 1240 (m), 1152 (w), 1112 (w), 1041 (w), 1013 (w), 846 (w), 674 (m).

#### Characterization of 27d:

Yield: 31.7 mg, 0.025 mmol, 31 %

<sup>1</sup>H-NMR (400 MHz, CDCl<sub>3</sub>, 27 °C): δ (ppm) = 7.30 (t, 1H, NH, <sup>3</sup>J = 4.9 Hz), 6.16 (d, 1H, NH, <sup>3</sup>J = 9.0 Hz), 6.14 (dd, 2H, H<sub>3</sub> + H<sub>4</sub>), 4.60 (m, 2H, H<sub>11</sub> + H<sub>18</sub>), 3.99 (m, 2H, H<sub>20</sub>), 3.71 (m, 5H, H<sub>15</sub> + H<sub>22</sub>), 3.55 (t, 2H, H<sub>5</sub>, <sup>3</sup>J = 7.3 Hz), 3.22 (s, 3H, H<sub>1</sub>), 2.33 (m, 1H, H<sub>12</sub>), 2.18 (t, 2H, H<sub>9</sub>, <sup>3</sup>J = 7.6 Hz), 2.00 (m, 4H, H<sub>16</sub> + H<sub>17</sub>), 1.61 (m, 4H, H<sub>6</sub> + H<sub>8</sub>), 1.25 (m, 12H, H<sub>7</sub>), 0.92 (dd, 6H, H<sub>13</sub>, J = 23.9, 6.7 Hz).

<sup>13</sup>C-NMR (100 MHz, CDCl<sub>3</sub>, 27 °C): δ (ppm) = 173.1 (C<sub>10</sub>), 172.3 (C<sub>14</sub>), 171.2 (C<sub>19</sub>), 170.0 (C<sub>21</sub>), 153.2 (C<sub>2</sub>), 111.0 (C<sub>4</sub>), 109.9 (C<sub>3</sub>), 59.7 (C<sub>18</sub>), 55.3 (C<sub>11</sub>), 52.2 (C<sub>22</sub>), 47.7 (C<sub>15</sub>), 43.6 (C<sub>5</sub>), 41.2 (C<sub>20</sub>), 36.6 (C<sub>1</sub>), 31.4 (C<sub>12</sub>), 30.3 (C<sub>9</sub>), 29.5 (C<sub>6</sub>), 29.3 (C<sub>7</sub>), 29.3 (C<sub>7</sub>), 29.2 (C<sub>7</sub>), 29.1 (C<sub>7</sub>), 27.2 (C<sub>17</sub>), 26.5 (C<sub>7</sub>), 25.6 (C<sub>8</sub>), 25.0 (C<sub>16</sub>), 19.4 (C<sub>13</sub>), 17.7 (C<sub>13</sub>).

IR (bulk): ν<sub>max</sub> (cm<sup>-1</sup>) = 3289 (m), 1926 (s), 2854 (m), 1753 (m), 1629 (s), 1531 (m), 1436 (s), 1369 (m), 1237 (m), 1201 (s), 1108 (w), 1013 (w), 662 (m).

### Characterization of 27e:

Yield: 37.4 mg, 0.024 mmol, 38 %

<sup>1</sup>H-NMR (400 MHz, DMSO-d<sub>6</sub>, 27 °C): δ (ppm) = 8.41 (t, 1H, NH, <sup>3</sup>J = 5.9 Hz), 8.18 (t, 1H, NH, <sup>3</sup>J = 5.8 Hz), 7.93 (d, 1H, NH, <sup>3</sup>J = 8.4 Hz), 7.63 (d, 1H, NH, <sup>3</sup>J = 8.9 Hz), 6.46 (dd, 2H, H<sub>3</sub> + H<sub>4</sub>), 4.30 (m, 2H, H<sub>11</sub> + H<sub>22</sub>), 4.18 (dd, 1H, H<sub>18</sub>, J = 8.8, 7.0 Hz), 3.81 (m, 4H, H<sub>20</sub> + H<sub>26</sub>), 3.62 (m, 5H, H<sub>15</sub> + H<sub>28</sub>), 3.45 (t, 2H, H<sub>5</sub>, <sup>3</sup>J = 7.1 Hz), 3.09 (s, 3H, H<sub>1</sub>), 2.17 – 1.78 (m, 8H, H<sub>9</sub> + H<sub>12</sub> + H<sub>16</sub> + H<sub>17</sub> + H<sub>23</sub>), 1.53 (m, 2H, H<sub>6</sub>), 1.46 (m, 2H, H<sub>8</sub>), 1.22 (s, 12H, H<sub>7</sub>), 0.82 (m, 12H, H<sub>13</sub> + H<sub>24</sub>).

<sup>13</sup>C-NMR (100 MHz, DMSO-d<sub>6</sub>, 27 °C): δ (ppm) = 172.5 (C<sub>14</sub>), 172.4 (C<sub>10</sub>), 171.8 (C<sub>25</sub>), 170.7 (C<sub>21</sub>), 170.6 (C<sub>27</sub>), 169.1 (C<sub>19</sub>), 153.0 (C<sub>2</sub>), 111.7 (C<sub>4</sub>), 110.6 (C<sub>3</sub>), 59.9 (C<sub>22</sub>), 58.0 (C<sub>18</sub>), 56.2 (C<sub>11</sub>), 52.1 (C<sub>28</sub>), 47.6 (C<sub>15</sub>), 43.0 (C<sub>5</sub> + C<sub>20</sub>), 41.0 (C<sub>26</sub>), 35.3 (C<sub>1</sub>), 31.0 (C<sub>23</sub>), 30.3 (C<sub>12</sub>), 30.2 (C<sub>9</sub>), 29.7 (C<sub>17</sub>), 29.4 (C<sub>6</sub>), 29.3 (C<sub>7</sub>), 29.1 (C<sub>7</sub>), 29.0 (C<sub>7</sub>), 29.0 (C<sub>7</sub>), 26.4 (C<sub>7</sub>), 25.7 (C<sub>8</sub>), 24.9 (C<sub>16</sub>), 19.6 (C<sub>24</sub>), 19.5 (C<sub>13</sub>), 19.0 (C<sub>24</sub>), 18.5 (C<sub>13</sub>).

IR (bulk): ν<sub>max</sub> (cm<sup>-1</sup>) = 3305 (w), 2929 (w), 2855 (w), 1754 (w), 1652 (s), 1544 (w), 1412 (m), 1387 (m), 1312 (s), 1206 (w), 1104 (w), 1037 (w), 824 (w), 672 (m).

### Characterization of 27f:

Yield: 32.7 mg, 0.014 mmol, 11 %

<sup>1</sup>H-NMR (400 MHz, DMSO-d<sub>6</sub>, 27 °C): δ (ppm) = 8.41 (t, 1H, NH, <sup>3</sup>J = 5.9 Hz), 8.21 (m, 3H, NH), 7.95 (t, 2H, NH, <sup>3</sup>J = 8.1 Hz), 7.64 (d, 1H, NH, <sup>3</sup>J = 8.9 Hz), 6.45 (dd, 2H, H<sub>3</sub> + H<sub>4</sub>), 4.30 (m, 4H, H<sub>11</sub> + H<sub>22</sub>), 4.15 (m, 2H, H<sub>18</sub>), 3.73 (m, 10H, H<sub>15</sub> + H<sub>20</sub> + H<sub>26</sub>), 3.62 (m, 5H, H<sub>15</sub> + H<sub>28</sub>), 3.45 (t, 2H, H<sub>5</sub>, <sup>3</sup>J = 7.1 Hz), 3.09 (s, 3H, H<sub>1</sub>), 2.18 – 1.79 (m, 14H, H<sub>9</sub> + H<sub>12</sub> + H<sub>16</sub> + H<sub>17</sub> + H<sub>23</sub>), 1.53 (m, 2H, H<sub>6</sub>), 1.46 (m, 2H, H<sub>8</sub>), 1.21 (s, 12H, H<sub>7</sub>), 0.84 (m, 24H, H<sub>13</sub> + H<sub>24</sub>).

<sup>13</sup>C-NMR (100 MHz, DMSO-d<sub>6</sub>, 27 °C): δ (ppm) = 172.1 (C<sub>14</sub>), 171.9 (C<sub>14</sub>), 171.9 (C<sub>10</sub>), 171.3 (C<sub>25</sub>), 171.0 (C<sub>25</sub>), 170.5 (C<sub>19</sub>), 170.1 (C<sub>19</sub>), 169.8 (C<sub>27</sub>), 168.6 (C<sub>27</sub>), 168.6 (C<sub>21</sub>), 168.6 (C<sub>21</sub>), 152.5 (C<sub>2</sub>), 111.3 (C<sub>4</sub>), 110.1 (C<sub>3</sub>), 59.6 (C<sub>22</sub>), 59.5 (C<sub>22</sub>), 58.1 (C<sub>18</sub>), 57.5 (C<sub>18</sub>), 55.8 (C<sub>11</sub>), 55.7 (C<sub>11</sub>), 51.6 (C<sub>28</sub>), 47.3 (C<sub>15</sub>), 47.2 (C<sub>15</sub>), 42.5 (C<sub>5</sub> + C<sub>20</sub>), 40.5 (C<sub>26</sub>), 40.2 (C<sub>26</sub>), 34.9 (C<sub>1</sub>), 30.5 (C<sub>23</sub>), 30.1 (C<sub>12</sub>), 29.9 (C<sub>12</sub>), 29.8 (C<sub>9</sub>), 29.2 (C<sub>17</sub>), 29.2 (C<sub>17</sub>), 28.9 (C<sub>6</sub>), 28.8 (C<sub>7</sub>), 28.7 (C<sub>7</sub>), 28.6 (C<sub>7</sub>), 28.5 (C<sub>7</sub>), 25.9 (C<sub>7</sub>), 25.3 (C<sub>8</sub>), 24.4 (C<sub>16</sub>), 24.4 (C<sub>16</sub>), 19.1 (C<sub>24</sub>), 19.0 (C<sub>13</sub>), 18.6 (C<sub>24</sub>), 18.4 (C<sub>13</sub>), 18.3 (C<sub>24</sub>), 18.0 (C<sub>13</sub>).

IR (bulk): ν<sub>max</sub> (cm<sup>-1</sup>) = 3285 (w), 2931 (w), 1752 (w), 1620 (s), 1523 (m), 1443 (w), 1202 (w), 1131 (w), 1034 (w), 660 (w).

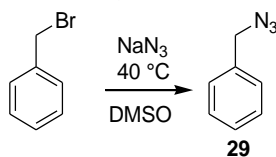
### Characterization of 27g:

Yield: 107 mg, 0.027 mmol, 14 %

<sup>1</sup>H-NMR (400 MHz, DMSO-d<sub>6</sub>, 27 °C): δ (ppm) = 8.40 (t, 2H, NH, <sup>3</sup>J = 5.9 Hz), 8.18 (m, 6H, NH), 7.92 (m, 4H, NH), 7.62 (d, 4H, NH, <sup>3</sup>J = 8.8 Hz), 6.44 (dd, 2H, H<sub>3</sub> + H<sub>4</sub>), 4.30 (m, 8H, H<sub>11</sub> + H<sub>22</sub>), 4.12 (m, 4H, H<sub>18</sub>), 3.72 (m, 20H, H<sub>15</sub> + H<sub>20</sub> + H<sub>26</sub>), 3.60 (m, 7H, H<sub>15</sub> + H<sub>28</sub>), 3.43 (m, 2H, H<sub>5</sub>), 3.07 (s, 3H, H<sub>1</sub>), 2.18 – 1.72 (m, 26H, H<sub>9</sub> + H<sub>12</sub> + H<sub>16</sub> + H<sub>17</sub> + H<sub>23</sub>), 1.49 (m, 2H, H<sub>6</sub>), 1.43 (m, 2H, H<sub>8</sub>), 1.20 (s, 12H, H<sub>7</sub>), 0.82 (m, 48H, H<sub>13</sub> + H<sub>24</sub>).

IR (bulk): ν<sub>max</sub> (cm<sup>-1</sup>) = 3285 (w), 2964 (w), 1752 (w), 1620 (s), 1523 (m), 1443 (w), 1202 (w), 1131 (w), 1034 (w), 660 (w).

#### 4.5 Synthesis of benzyl azide (29)



**Scheme 19.** Synthesis of benzyl azide (29).

Synthesis of benzyl azide (29) was accomplished according to literature<sup>359</sup>. Sodium azide (5.5 g, 84.7 mmol) and benzyl bromide (13.2 g, 9.17 mL, 77.0 mmol) were dissolved in DMSO (170 mL). The reaction mixture was stirred at 40 °C for 90 hours. Afterwards, water (50 mL) was added and the reaction was further stirred until it was cooled down to room temperature. The mixture was extracted with Et<sub>2</sub>O (3 x 30 mL) and the combined organic phases were washed with water (2 x 50 mL) and brine (50 mL). Subsequently the organic phase was dried over Na<sub>2</sub>SO<sub>4</sub>, filtered and the solvent was removed under reduced pressure.

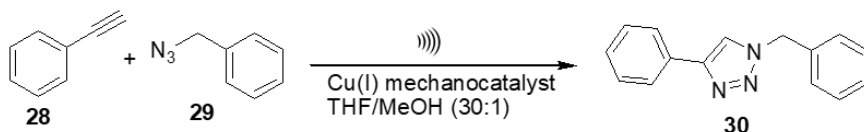
Yield: 9.45 g, 71.0 mmol, 92 %

<sup>1</sup>H-NMR (400 MHz, CDCl<sub>3</sub>, 27 °C): δ (ppm) = 7.38 (m, 5H, H<sub>3</sub> + H<sub>4</sub> + H<sub>5</sub>), 4.35 (s, 2H, H<sub>1</sub>).

<sup>13</sup>C-NMR (100 MHz, CDCl<sub>3</sub>, 27 °C): δ (ppm) = 135.4 (C<sub>2</sub>), 129.0 (C<sub>4</sub>), 128.3 (C<sub>5</sub>), 128.2 (C<sub>3</sub>), 54.8 (C<sub>1</sub>).

IR (bulk): ν<sub>max</sub> (cm<sup>-1</sup>) = 3032 (w), 2090 (s), 1496 (w), 1454 (w), 1349 (w), 1253 (m), 1201 (w), 1077 (w), 1028 (w), 875 (w), 736 (m), 697 (s), 651 (w), 566 (w).

#### 4.6 Mechanochemical activation of the linear catalysts in solution by ultrasonication



**Scheme 20.** Model „click“ reaction between phenylacetylene (28) and benzyl azide (29) for the investigation of the catalytic activity of mechanocatalysts **3a**, **3b**, **3b** and **27a-g**.

The catalytic activity of mechanocatalysts **3a**, **3b**, **3b** and **27a-g** was investigated *via* a model „click“ reaction between phenylacetylene (28) and benzyl azide (29). Ultrasonication experiments were conducted by placing the latent mechanocatalyst (**3a**, **3b**, **3b** or **27a-g**) (7.50 μmol, 0.01 eq.) into a 10 mL reaction vessel with two additional side necks attached to a Sonics VCX 500 ultrasonic processor equipped with a long full wave solid probe and an internally threaded stainless steel adapter. The vessel was evacuated and flushed with nitrogen at least three times to remove oxygen. Subsequently, **28** (82.0 μL, 750.0 μmol, 100.0 eq.) and **29** (97.0 μL, 750.0 μmol, 100.0 eq.) were added as well as 10.0 mL of a THF-d<sub>8</sub>/MeOH mixture (30:1) which resulted in a catalyst concentration of 0.75 mM. To the mixture, successive cycles of pulsed ultrasound with a frequency of 20 kHz using 20 % of the maximal amplitude with a sequence of 5 s pulse and 10 s break for 90 minutes were applied corresponding to an ultrasound power intensity of 4.66 W/cm<sup>2</sup> and an energy input of 11 kJ. During this time the mixture was cooled in a water bath to prevent the temperature from rising above 25 °C. Each cycle was followed by a waiting time of 60 minutes. Samples were taken before each experiment and after the 3<sup>rd</sup>, 5<sup>th</sup>, 10<sup>th</sup>, 14<sup>th</sup> and 17<sup>th</sup> cycle and the conversion of the „click“ reaction was calculated *via* <sup>1</sup>H-NMR spectroscopy by observing the increasing triazole resonance at 8.11 ppm as well as the shift of the methylene group from 4.35 ppm to 5.59 ppm. Control experiments without ultrasound were carried out in two-necked flasks at room temperature as well as at 60 °C under reflux to prove the mechanochemical origin of the catalyst activation. Samples for the acquired <sup>1</sup>H-NMR spectra were directly taken out of the mixture without further purification after the corresponding ultrasonication

cycles. The ultrasonication cycle dependent conversions for all mechanocatalysts are presented in Table 8.

**Table 8.** Sonication cycle dependent conversions for the ultrasonication induced "click" reactions between phenylacetylene (**28**) and benzyl azide (**29**)<sup>a</sup>.

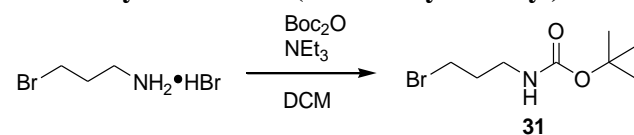
Entry	Catalyst	Conversion after US cycle (%) <sup>b</sup>					
		0	3	5	10	14	17
1	<b>3a</b>	0	0	0	0	1.0	- <sup>c</sup>
2	<b>3b</b>	0	0	0.5	1.8	2.9	3.8
3	<b>4b</b>	0	0	0	2	2.9	3.4
4	<b>27a</b>	0	0	1.4	2.9	3.3	3.8
5	<b>27b</b>	0	0	0	2.4	2.9	3.4
6	<b>27c</b>	0	0	0	2.9	3.8	4.3
7	<b>27d</b>	0	0	0	2.9	3.8	4.3
8	<b>27e</b>	0	0	0	2.9	4.3	4.7
9	<b>27f</b>	0	0	0	3.3	4.3	5.2
10	<b>27g</b>	0	0	1.5	3.9	4.5	5.6

<sup>a</sup>For all reactions 1.0 eq. of azide **28**, 1.0 eq. of alkyne **29** and 0.01 eq. of the Cu(I) catalyst (0.75 mM) were used in THF-d<sub>6</sub>/MeOH (30:1) (v/v). <sup>b</sup>One cycle consisted of 90 min pulsing at 20 kHz with 20 % or 30 % amplitude of 125 μm with a pulse sequence of 5 s/pulse, 10 s/break followed by 60 min without pulsing. The "click" reaction was followed by the increasing triazole resonance originating from product **30** in the <sup>1</sup>H-NMR spectrum at δ = 8.11 ppm as well as the shift from the methylene group of **29** from δ = 4.35 ppm to δ = 5.59 ppm with a standard deviation of ± 1 %. <sup>c</sup>Samples were only taken until the 14<sup>th</sup> cycle.

## 4.7 Synthesis of the chain-extended mechanocatalysts

### 4.7.1 Synthesis of the imidazolium-based NH<sub>2</sub>-functionalized mechanocatalyst

#### 4.7.1.1 Synthesis of *N*-(*tert*-butoxycarbonyl)-3-bromopropylamine (**31**)



**Scheme 21.** Synthesis of *N*-(*tert*-butoxycarbonyl)-3-bromopropylamine (**31**).

The synthesis of **31** was accomplished according to literature<sup>360</sup>. 3-Bromopropan-1-amine hydrobromide (6.55 g, 30.0 mmol) was suspended in DCM (12 mL). The mixture was cooled down to 0 °C by means of an ice bath and triethylamine (3.49 g, 4.78 mL, 34.5 mmol) was added. Di-*tert*-butyl dicarbonate (5.04 g, 23.0 mmol) was dissolved in DCM (12.5 mL) and was also added to the reaction mixture. After stirring for 24 hours the solution was washed with HCl (1M, 4 x 20 mL). Subsequently, the organic phase was washed with brine (20 mL) and was dried over Na<sub>2</sub>SO<sub>4</sub>. After filtration and removal of the solvent the pure product was obtained as a slightly yellow oil that crystallized in the freezer.

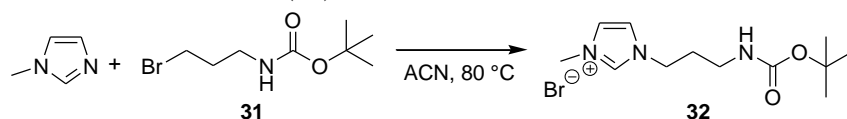
Yield: 5.30 g, 22.2 mmol, 97 %

<sup>1</sup>H-NMR (400 MHz, CDCl<sub>3</sub>, 27 °C): δ (ppm) = 4.65 (s, 1H, NH), 3.43 (t, 2H, H<sub>1</sub>, <sup>3</sup>J = 6.5 Hz), 3.27 (dd, 2H, H<sub>3</sub>, <sup>3</sup>J = 12.6, 6.3 Hz), 2.04 (p, 2H, H<sub>2</sub>, <sup>3</sup>J = 6.5 Hz), 1.44 (s, 9H, H<sub>6</sub>).

<sup>13</sup>C-NMR (100 MHz, CDCl<sub>3</sub>, 27 °C): δ (ppm) = 155.9 (C<sub>4</sub>), 79.4 (C<sub>5</sub>), 39.0 (C<sub>3</sub>), 32.7 (C<sub>2</sub>), 30.8 (C<sub>1</sub>), 28.4 (C<sub>6</sub>).

IR (bulk): ν<sub>max</sub> (cm<sup>-1</sup>) = 2965 (s), 1669 (s), 1487 (s), 1448 (m), 1374 (w), 1295 (s), 1240 (w), 1114 (s), 1074 (s), 994 (w), 947 (w), 908 (w), 817 (w), 764 (s), 682 (m), 555 (m).

#### 4.7.1.2 Synthesis of 3-[3-[[[(1,1-dimethylethoxy)carbonyl]amino]propyl]-1-methyl-1H-imidazolium bromide (32)



**Scheme 22.** Synthesis of imidazolium salt **32**.

**31** (5.30 g, 22.2 mmol) and 1-methylimidazole (2.13 mL, 26.7 mmol) were dissolved in ACN (12.2 mL). The reaction mixture was stirred for 40 hours at 80 °C. Afterwards the solvent was removed and the crude product was redissolved in water (20 mL). The aqueous phase was washed with CHCl<sub>3</sub> (10 x 15 mL) and EtOAc (10 x 15 mL). Subsequently, the water was removed, the product was redissolved in CHCl<sub>3</sub> and dried over Na<sub>2</sub>SO<sub>4</sub>. Filtration and removal of the solvent yielded the pure product as yellow, highly viscous liquid.

Yield: 5.67 g, 17.7 mmol, 80 %

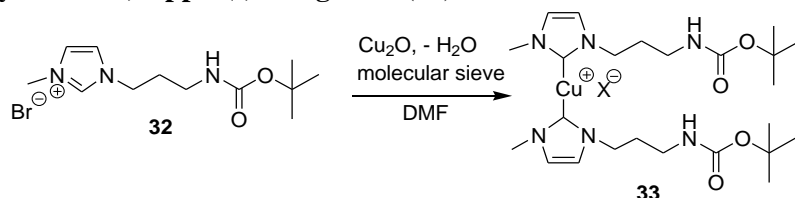
<sup>1</sup>H-NMR (400 MHz, CDCl<sub>3</sub>, 27 °C): δ (ppm) = 10.30 (s, 1H, H<sub>2</sub>), 7.63 (s, 1H, H<sub>4</sub>), 7.38 (s, 1H, H<sub>3</sub>), 5.66 (s, 1H, NH), 4.41 (t, 2H, H<sub>5</sub>, <sup>3</sup>J = 5.9 Hz), 4.07 (s, 3H, H<sub>1</sub>), 3.18 (dd, 2H, H<sub>7</sub>, J = 11.2, 5.4 Hz), 2.15 (m, 2H, H<sub>6</sub>), 1.41 (s, 9H, H<sub>10</sub>).

<sup>13</sup>C-NMR (100 MHz, CDCl<sub>3</sub>, 27 °C): δ (ppm) = 156.6 (C<sub>8</sub>), 138.0 (C<sub>2</sub>), 123.1 (C<sub>4</sub>), 122.7 (C<sub>3</sub>), 79.4 (C<sub>9</sub>), 47.5 (C<sub>5</sub>), 36.7 (C<sub>1</sub> + C<sub>7</sub>), 30.6 (C<sub>6</sub>), 28.4 (C<sub>10</sub>).

MS (ESI), *m/z* calculated for [C<sub>12</sub>H<sub>22</sub>N<sub>3</sub>O<sub>2</sub>]<sup>+</sup> = 240.1727; found 240.1707.

IR (bulk): ν<sub>max</sub> (cm<sup>-1</sup>) = 3265 (m), 2976 (m), 1690 (s), 1572 (w), 1514 (m), 1454 (w), 1391 (w), 1364 (m), 1270 (m), 1250 (m), 1163 (s), 1005 (w), 853 (w), 752 (w), 651 (m), 620 (m).

#### 4.7.1.3 Synthesis of bis(1-methylimidazol-3-[3-(((1,1-dimethylethoxy)carbonyl)amino)propyl]ylidene-2-ene)copper(I) halogenide (33)



**Scheme 23.** Synthesis of the Boc-protected mechanocatalyst **33**.

**32** (0.83 g, 2.58 mmol), Cu<sub>2</sub>O (1.85 g, 12.90 mmol) and activated molecular sieve (3 Å) were suspended in DMF (5 mL) and were refluxed for 70 hours. The solution was filtered afterwards and the solvent was removed. Further purification was done *via* column chromatography (CHCl<sub>3</sub> (R<sub>f</sub> = 0.09) → CHCl<sub>3</sub>/MeOH (60:1) (R<sub>f</sub> = 0.17). After removal of the solvent the product was obtained as a yellow, sticky liquid that slowly crystallized.

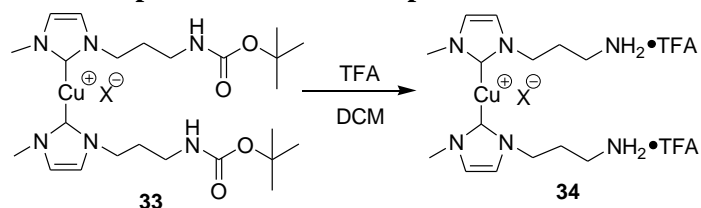
Yield: 159 mg, 0.32 mmol, 25 %

<sup>1</sup>H-NMR (400 MHz, CDCl<sub>3</sub>, 27 °C): δ (ppm) = 6.18 (dd, 2H, H<sub>3</sub> + H<sub>4</sub>), 5.45 (s, 1H, NH), 3.67 (t, 2H, H<sub>5</sub>, <sup>3</sup>J = 6.2 Hz), 3.25 (s, 3H, H<sub>1</sub>), 3.08 (dd, 2H, H<sub>7</sub>, J = 12.2, 6.1 Hz), 1.75 (m, 2H, H<sub>6</sub>), 1.42 (s, 9H, H<sub>10</sub>).

<sup>13</sup>C-NMR (100 MHz, CDCl<sub>3</sub>, 27 °C): δ (ppm) = 156.1 (C<sub>8</sub>), 153.6 (C<sub>2</sub>), 111.6 (C<sub>3</sub>), 110.1 (C<sub>4</sub>), 78.9 (C<sub>9</sub>), 40.5 (C<sub>5</sub>), 36.8 (C<sub>7</sub>), 30.4 (C<sub>1</sub>), 29.9 (C<sub>6</sub>), 28.4 (C<sub>10</sub>).

IR (bulk): ν<sub>max</sub> (cm<sup>-1</sup>) = 3289 (w), 2971 (w), 1694 (w), 1661 (s), 1517 (m), 1475 (w), 1443 (w), 1412 (w), 1390 (w), 1364 (w), 1348 (w), 1279 (m), 1249 (m), 1222 (w), 1163 (m), 1137 (m), 1049 (w), 974 (m), 945 (m), 853 (w), 819 (w), 783 (w), 748 (w), 679 (s), 608 (s), 586 (w).

#### 4.7.1.4 Deprotection of the Boc-protected mechanocatalyst (**34**)



**Scheme 24.** Synthesis of the NH<sub>2</sub>-functionalized mechanocatalyst **34**.

**33** (50.0 mg, 0.10 mmol) was dissolved in DCM (500.0  $\mu$ L). The mixture was cooled down to 0 °C with an ice bath before TFA (289.3 mg, 195.5  $\mu$ L, 2.54 mmol) was added. Completion of the reaction was followed *via* TLC (CHCl<sub>3</sub>/MeOH (20:1), R<sub>f</sub> = 0.04). After complete consumption of the starting material, the solvent and the TFA were removed under reduced pressure to yield the product as a yellow, sticky liquid that slowly crystallized.

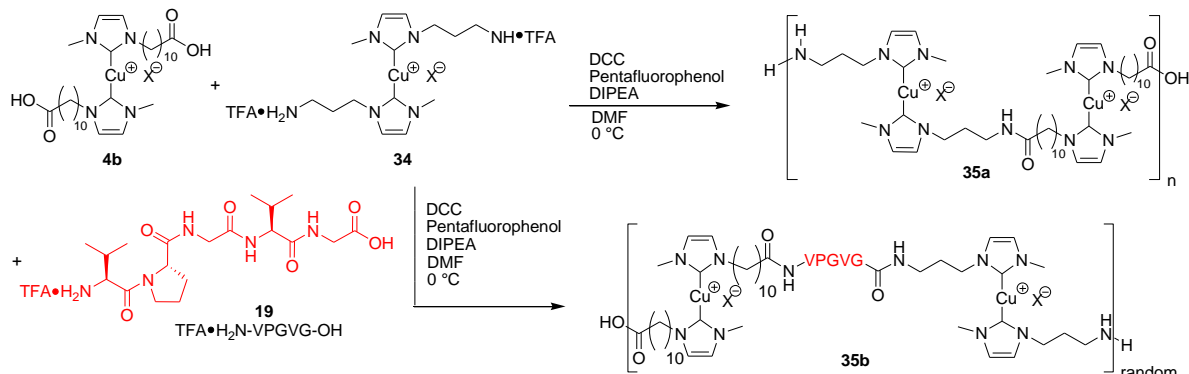
Yield: 51.1 mg, 0.08 mmol, 98 %

<sup>1</sup>H-NMR (400 MHz, DMSO-d<sub>6</sub>, 27 °C):  $\delta$  (ppm) = 7.80 (s, 3H, NH<sub>3</sub><sup>+</sup>), 6.49 (dd, 2H, H<sub>3</sub> + H<sub>4</sub>), 3.57 (t, 2H, H<sub>5</sub>, <sup>3</sup>J = 6.7 Hz), 3.10 (s, 3H, H<sub>1</sub>), 2.75 (m, 2H, H<sub>7</sub>), 1.82 (m, 2H, H<sub>6</sub>).

<sup>13</sup>C-NMR (100 MHz, DMSO-d<sub>6</sub>, 27 °C):  $\delta$  (ppm) = 153.2 (C<sub>2</sub>), 112.3 (C<sub>3</sub>), 110.7 (C<sub>4</sub>), 40.3 (C<sub>5</sub>), 36.7 (C<sub>7</sub>), 30.3 (C<sub>1</sub>), 27.7 (C<sub>6</sub>).

IR (bulk):  $\nu_{\text{max}}$  (cm<sup>-1</sup>) = 2958 (m), 1719 (s), 1672 (s), 1597 (m), 1481 (s), 1443 (w), 1411 (m), 1377 (w), 1304 (w), 1251 (w), 1169 (s), 1111 (s), 1019 (m), 995 (m), 850 (m), 830 (m), 810 (m), 795 (m), 784 (m), 762 (w), 750 (w), 719 (s), 649 (s), 632 (m), 595 (w), 552 (w).

#### 4.7.2 Synthesis of the chain-extended mechanocatalysts (**35**)



**Scheme 25.** Synthetic approach for the generation of chain-extended mechanocatalysts **35**.

**General procedure:** **4b** (31.09 mg, 46.0  $\mu$ mol) and DIPEA (4.8 eq.) were dissolved in DMF (200.0  $\mu$ L) followed by the addition of molecular sieve (3 Å) and DCC (6 eq.) in the countercurrent of nitrogen. The mixture was stirred for five minutes before pentafluorophenol (6 eq.) was added. Subsequently, **34** (1.0 eq) and DIPEA (4.8 eq.) were dissolved in DMF (150.0  $\mu$ L) and added to the mixture (for **35b**: also 5.0 eq. of **19** were added), which was stirred afterwards for 75 hours at 30 °C. After the reaction was finished, CHCl<sub>3</sub> (2.0 mL) was added and the solution was filtered. The crude product was purified *via* column chromatography on silica changing the solvent polarity gradually from pure CHCl<sub>3</sub> (R<sub>f</sub> = 0.0)  $\rightarrow$  CHCl<sub>3</sub>/MeOH (40:1) (R<sub>f</sub> = 0.20)  $\rightarrow$  CHCl<sub>3</sub>/MeOH (20:1) (R<sub>f</sub> = 0.42).

## Characterization of **35a**:

$^1\text{H-NMR}$  (400 MHz,  $\text{CDCl}_3$ , 27 °C):  $\delta$  (ppm) = 7.02 (t, NH,  $^3J = 7.4$  Hz), 6.20 (s, 2H,  $H_3 + H_4$ ), 6.16 (dd, 2H,  $H_{14} + H_{15}$ ), 3.67 (m, 2H,  $H_5$ ), 3.56 (t, 2H,  $H_{13}$ ,  $^3J = 7.3$  Hz), 3.26 (s, 3H,  $H_1$ ), 3.23 (s, 3H,  $H_{17}$ ), 3.17 (dd, 2H,  $H_7$ ,  $J = 12.1, 6.2$  Hz), 2.18 (m 2H,  $H_9$ ), 1.76 (dt, 2H,  $H_6$ ,  $J = 12.1, 6.1$  Hz), 1.61 (m, 4H,  $H_{10} + H_{12}$ ), 1.26 (m, 12H,  $H_{11}$ ).

$^{13}\text{C-NMR}$  (100 MHz,  $\text{CDCl}_3$ , 27 °C):  $\delta$  (ppm) = 173.6 ( $C_8$ ), 153.6 ( $C_2$ ), 153.1 ( $C_{16}$ ), 111.9 ( $C_3$ ), 111.1 ( $C_4$ ), 110.2 ( $C_{14}$ ), 110.0 ( $C_{15}$ ), 43.6 ( $C_{13}$ ), 40.5 ( $C_5$ ), 36.9 ( $C_{17}$ ), 35.2 ( $C_7$ ), 30.5 ( $C_1$ ), 30.3 ( $C_9$ ), 29.5 ( $C_{12}$ ), 29.3 ( $C_6$ ), 29.3 ( $C_{11}$ ), 29.2 ( $C_{11}$ ), 29.2 ( $C_{11}$ ), 29.2 ( $C_{11}$ ), 29.1 ( $C_{11}$ ), 26.5 ( $C_{11}$ ), 25.7 ( $C_{10}$ ).

IR (bulk):  $\nu_{\text{max}}$  ( $\text{cm}^{-1}$ ) = 3268 (w), 2925 (m), 2853 (w), 1655 (s), 1545 (m), 1472 (m), 1410 (w), 1377 (w), 1239 (m), 1200 (w), 1129 (w) 826 (w), 660 (s).

### 4.7.3 Mechanochemical activation of the chain-extended mechanocatalysts

Ultrasonication experiments of mechanocatalysts **33**, **34** and **35a,b** were accomplished analogous to the procedure already given in the Experimental Part 4.6 for the linear mechanocatalysts. Control experiments without ultrasound were carried out in two-necked flasks at room temperature as well as at 60 °C under reflux to prove the mechanochemical origin of the catalyst activation. Samples for the acquired  $^1\text{H-NMR}$  spectra were directly taken out of the mixture without further purification after the corresponding ultrasonication cycles. The ultrasonication cycle dependent conversions for all mechanocatalysts are presented in Table 9.

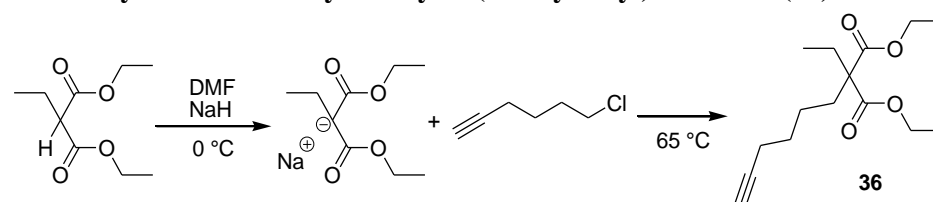
**Table 9.** Sonication cycle dependent conversions for the ultrasonication induced "click" reactions between phenylacetylene (**28**) and benzyl azide (**29**)<sup>a</sup>.

Entry	Catalyst	Conversion after US cycle (%) <sup>b</sup>					
		0	3	5	10	14	17
1	<b>4b</b>	0	0	0	2	2.9	3.4
2	<b>33</b>	0	4.8	6.5	7.4	9.0	9.9
3	<b>34</b>	0	0	0	2.9	3.8	4.8
4	<b>35a</b>	0	0	1.5	2.4	3.4	3.9
5	<b>35b</b>	0	0	2.4	3.4	3.8	4.7

<sup>a</sup>For all reactions 1.0 eq. of azide **28**, 1.0 eq. of alkyne **29** and 0.01 eq. of the Cu(I) catalyst (0.75 mM) were used in THF- $d_6$ /MeOH (30:1) (v/v). <sup>b</sup>One cycle consisted of 90 min pulsing at 20 kHz with 20 % or 30 % amplitude of 125  $\mu\text{m}$  with a pulse sequence of 5 s/pulse, 10 s/break followed by 60 min without pulsing. The "click" reaction was followed by the increasing triazole resonance originating from product **30** in the  $^1\text{H-NMR}$  spectrum at  $\delta = 8.11$  ppm as well as the shift from the methylene group of **29** from  $\delta = 4.35$  ppm to  $\delta = 5.59$  ppm with a standard deviation of  $\pm 1$  %.

## 4.8 Synthesis of the supramolecular catalyst

### 4.8.1 Synthesis of diethyl 2-ethyl-2-(1-hexyn-6-yl) malonate (**36**)



**Scheme 26.** Synthesis of diethyl 2-ethyl-2-(1-hexyn-6-yl) malonate (**36**).

The synthesis of the malonate (**36**) was conducted according to literature<sup>361</sup>. Sodium hydride (1.53 g, 38.25 mmol) was suspended in dry DMF (12 mL). The mixture was cooled down to 0 °C by means of an ice bath. Diethyl malonate (5.98 mL, 31.88 mmol) was slowly added *via* a dropping funnel in the course of one hour. The mixture was further stirred until no more hydrogen formation was observed. Subsequently, 6-chloro-1-hexyne (3.86 mL, 31.88 mmol) was added *via* syringe. The mixture was stirred at 65 °C for 60 hours. After removal of the solvent the sticky residue was extracted with Et<sub>2</sub>O

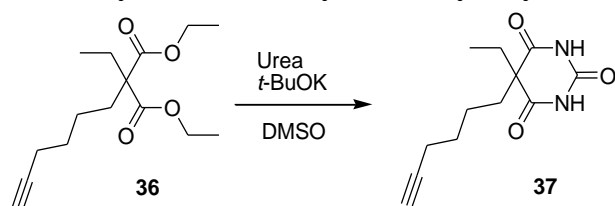
(3 x 25 mL) and the combined organic phases were dried over Na<sub>2</sub>SO<sub>4</sub>, filtrated and the solvent was removed. The residual impurities were removed *via* flash chromatography with *n*-hexane (R<sub>f</sub> = 0). The purified product was obtained by changing the solvent to pure CHCl<sub>3</sub> (R<sub>f</sub> = 0.75).

Yield: 3.53 g, 13.14 mmol, 41 %

<sup>1</sup>H-NMR (400 MHz, CDCl<sub>3</sub>, 27 °C): δ (ppm) = 4.18 (q, 4H, H<sub>11</sub>, <sup>3</sup>J = 7.1 Hz), 2.19 (td, 2H, H<sub>3</sub>, J = 7.1, 2.6 Hz), 1.92 (m, 3H, H<sub>1</sub> + H<sub>8</sub>), 1.87 (m, 2H, H<sub>6</sub>), 1.53 (m, 2H, H<sub>5</sub>), 1.28 (m, 2H, H<sub>4</sub>), 1.24 (t, 6H, H<sub>12</sub>, <sup>3</sup>J = 7.1 Hz), 0.81 (t, 3H, H<sub>9</sub>, <sup>3</sup>J = 7.6 Hz).

<sup>13</sup>C-NMR (100 MHz, CDCl<sub>3</sub>, 27 °C): δ (ppm) = 171.7 (C<sub>10</sub>), 84.1 (C<sub>2</sub>), 68.4 (C<sub>1</sub>), 61.0 (C<sub>11</sub>), 57.8 (C<sub>7</sub>), 31.0 (C<sub>6</sub>), 28.6 (C<sub>8</sub>), 25.2 (C<sub>4</sub>), 22.9 (C<sub>5</sub>), 18.1 (C<sub>3</sub>), 14.1 (C<sub>12</sub>), 8.4 (C<sub>9</sub>).

#### 4.8.2 Synthesis of 2-ethyl-2-(1-hexyn-6-yl) barbituric acid (**37**)



**Scheme 27.** Synthesis of 2-ethyl-2-(1-hexyn-6-yl) barbituric acid (**37**).

The synthesis of **37** was accomplished according to literature<sup>361</sup>. Urea (23.68 g, 394.24 mmol) and potassium *tert*-butoxide (3.10 g, 26.28 mmol) were dissolved in dry DMSO (100 mL). When everything was dissolved, **36** (3.53 g, 13.14 mmol) was added *via* syringe and the mixture was stirred for 30 hours at room temperature. Water (400 mL) was added and the pH was checked to be 10. The aqueous phase was washed with Et<sub>2</sub>O (2 x 250 mL) afterwards. The organic phase was discarded and the pH of the aqueous phase was adjusted to 2 with HCl (1M). Subsequently the aqueous phase was extracted with Et<sub>2</sub>O (3 x 150 mL) and the combined organic phases were washed with water (200 mL). After drying over Na<sub>2</sub>SO<sub>4</sub> and filtration the solvent was removed and the crude product was recrystallized from toluene.

Yield: 2.88 g, 12.2 mmol, 93 %

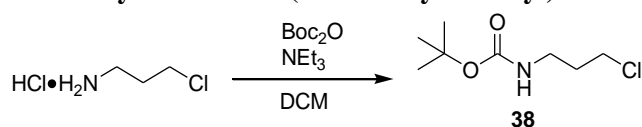
<sup>1</sup>H-NMR (400 MHz, DMSO-d<sub>6</sub>, 27 °C): δ (ppm) = 11.51 (s, 2H, NH), 2.69 (t, 1H, H<sub>1</sub>, <sup>3</sup>J = 2.6 Hz), 2.09 (td, 2H, H<sub>3</sub>, J = 6.9, 2.6 Hz), 1.77 (m, 4H, H<sub>6</sub> + H<sub>8</sub>), 1.34 (m, 2H, H<sub>4</sub>), 1.17 (m, 2H, H<sub>5</sub>), 0.72 (t, 3H, H<sub>9</sub>, <sup>3</sup>J = 7.4 Hz).

<sup>13</sup>C-NMR (100 MHz, DMSO-d<sub>6</sub>, 27 °C): δ (ppm) = 173.5 (C<sub>10</sub>), 150.3 (C<sub>1</sub>), 84.6 (C<sub>2</sub>), 71.8 (C<sub>1</sub>), 56.1 (C<sub>7</sub>), 37.9 (C<sub>8</sub>), 32.0 (C<sub>6</sub>), 28.3 (C<sub>4</sub>), 24.1 (C<sub>5</sub>), 17.9 (C<sub>3</sub>), 9.5 (C<sub>9</sub>).

MS (ESI), *m/z* calculated for [C<sub>12</sub>H<sub>15</sub>N<sub>2</sub>O<sub>3</sub>]<sup>-</sup> = 235.1177; found 235.1077.

IR (bulk): ν<sub>max</sub> (cm<sup>-1</sup>) = 3290 (m), 2945 (w), 1755 (s), 1716 (s), 1676 (s), 1462 (m), 1418 (m), 1372 (m), 1336 (m), 1316 (m), 1235 (m), 1035 (w), 955 (w), 823 (w), 787 (w), 761 (w), 731 (w), 670 (w), 623 (w).

#### 4.8.3 Synthesis of *N*-(*tert*-butoxycarbonyl)-3-chloropropylamine (**38**)



**Scheme 28.** Synthesis of *N*-(*tert*-butoxycarbonyl)-3-chloropropylamine (**38**).

The synthesis of **38** was done according to literature<sup>362</sup>. 3-Chloropropan-1-amine hydrochloride (4.0 g, 30.76 mmol) was suspended in DCM (17.0 mL). The mixture was cooled down to 0 °C by means of an

ice bath and triethylamine (3.77 g, 5.16 mL, 37.24 mmol) was added. Di-*tert*-butyl dicarbonate (6.80 g, 31.16 mmol) was dissolved in DCM (17.0 mL) and was also added to the reaction mixture. After stirring for 24 hours the solution was washed with HCl (1M, 3 x 20 mL). Subsequently the organic phase was washed with brine (20 mL) and dried over MgSO<sub>4</sub>. After filtration and removal of the solvent, the pure product was obtained as a slightly yellow oil.

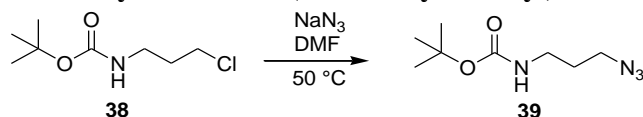
Yield: 5.44 g, 28.08 mmol, 91 %

<sup>1</sup>H-NMR (400 MHz, CDCl<sub>3</sub>, 27 °C): δ (ppm) = 4.66 (s, 1H, NH), 3.59 (t, 2H, H<sub>1</sub>, <sup>3</sup>J = 6.4 Hz), 3.25 (q, 2H, H<sub>3</sub>, <sup>3</sup>J = 6.4 Hz), 1.94 (p, 2H, H<sub>2</sub>, <sup>3</sup>J = 6.5 Hz), 1.44 (s, 9H, H<sub>6</sub>).

<sup>13</sup>C-NMR (100 MHz, CDCl<sub>3</sub>, 27 °C): δ (ppm) = 156.1 (C<sub>4</sub>), 79.6 (C<sub>5</sub>), 42.5 (C<sub>1</sub>), 38.1 (C<sub>3</sub>), 32.7 (C<sub>2</sub>), 28.5 (C<sub>6</sub>).

IR (bulk): ν<sub>max</sub> (cm<sup>-1</sup>) = 3341 (m), 2976 (m), 1685 (s), 1513 (m), 1391 (w), 1365 (m), 1250 (s), 1163 (s), 1079 (s), 993 (w), 853 (w), 779 (w), 653 (w).

#### 4.8.4 Synthesis of *N*-(*tert*-butoxycarbonyl)-3-azidopropylamine (**39**)



**Scheme 29.** Synthesis of *N*-(*tert*-butoxycarbonyl)-3-azidopropylamine (**39**).

Azidation was performed according to literature<sup>363</sup>. Therefore, **38** (5.44 g, 28.08 mmol) and sodium azide (3.65 g, 56.15 mmol) were dissolved in DMF (40 mL). The mixture was stirred for 100 hours at 50 °C. Afterwards, the solvent was removed and the residue was redissolved in CHCl<sub>3</sub> (100 mL). The organic phase was washed with water (1 x 70 mL, 2 x 30 mL) and brine (30 mL). After drying over Na<sub>2</sub>SO<sub>4</sub> and filtration the solvent was removed to yield the product as yellow liquid.

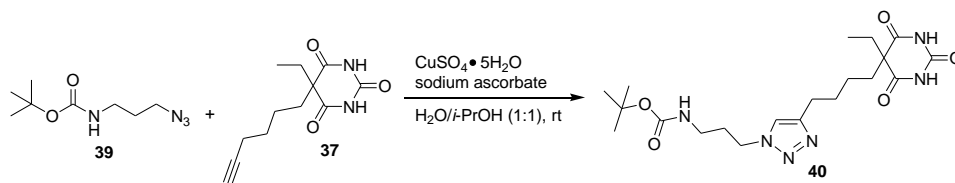
Yield: 5.29 g, 26.44 mmol, 94 %

<sup>1</sup>H-NMR (400 MHz, CDCl<sub>3</sub>, 27 °C): δ (ppm) = 4.64 (s, 1H, NH), 3.34 (t, 2H, H<sub>1</sub>, <sup>3</sup>J = 6.7 Hz), 3.23 (q, 2H, H<sub>3</sub>, <sup>3</sup>J = 6.4 Hz), 1.77 (p, 2H, H<sub>2</sub>, <sup>3</sup>J = 6.7 Hz), 1.44 (s, 9H, H<sub>6</sub>).

<sup>13</sup>C-NMR (100 MHz, CDCl<sub>3</sub>, 27 °C): δ (ppm) = 156.0 (C<sub>4</sub>), 79.4 (C<sub>5</sub>), 49.3 (C<sub>1</sub>), 38.2 (C<sub>3</sub>), 29.5 (C<sub>2</sub>), 28.5 (C<sub>6</sub>).

IR (bulk): ν<sub>max</sub> (cm<sup>-1</sup>) = 3347 (w), 2977 (w), 2093 (s), 1687 (s), 1513 (s), 1453 (w), 1391 (w), 1365 (s), 1249 (s), 1165 (s), 1007 (w), 863 (w), 780 (w), 660 (m).

#### 4.8.5 “Click” reaction of **37** and **39**



**Scheme 30.** “Click” reaction for the synthesis of **40**.

**37** (1.0 g, 5.0 mmol), CuSO<sub>4</sub>·5 H<sub>2</sub>O (662.4 mg, 0.25 mmol), **39** (1.18 g, 5.0 mmol), sodium ascorbate (98.8 mg, 0.5 mmol), water (20 mL) and *iso*-propanol (20 mL) were added to a round bottom flask. In order to remove oxygen out of the reaction system, three freeze-thaw cycles were performed. The reaction mixture was stirred at 60 °C for 160 hours before the solvent was removed. The residue was dissolved in CHCl<sub>3</sub> (20 mL) and all insoluble compounds were removed by centrifugation. Subsequently, the organic phase was dried over Na<sub>2</sub>SO<sub>4</sub>, filtered and the solvent was removed. The

sticky residue was washed with Et<sub>2</sub>O (3 x 10 mL). The product started to crystallize upon drying to yield a white, slightly yellow solid.

Yield: 1.39 g, 3.18 mmol, 64 %

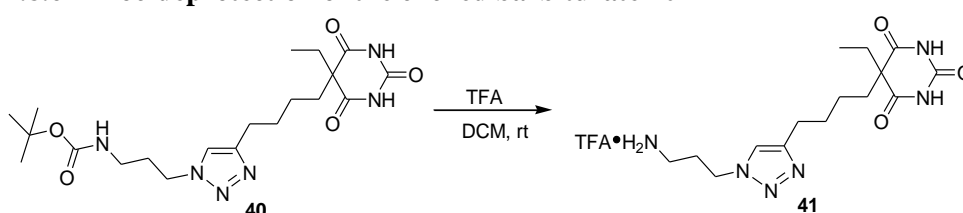
<sup>1</sup>H-NMR (400 MHz, DMSO-d<sub>6</sub>, 27 °C): δ (ppm) = 11.49 (s, 2H, NH), 7.75 (s, 1H, H<sub>7</sub>), 6.89 (s, 1H, NH), 4.26 (t, 2H, H<sub>6</sub>, <sup>3</sup>J = 7.1 Hz), 2.89 (m, 2H, H<sub>4</sub>), 2.49 (t, 2H, H<sub>9</sub>, <sup>3</sup>J = 7.1 Hz), 1.84 (m, 6H, H<sub>5</sub> + H<sub>12</sub> + H<sub>14</sub>), 1.49 (m, 2H, H<sub>10</sub>), 1.36 (s, 9H, H<sub>1</sub>), 1.12 (m, 2H, H<sub>11</sub>), 0.72 (t, 3H, H<sub>15</sub>).

<sup>13</sup>C-NMR (100 MHz, DMSO-d<sub>6</sub>, 27 °C): δ (ppm) = 173.1 (C<sub>16</sub>), 155.9 (C<sub>3</sub>), 149.8 (C<sub>17</sub>), 146.8 (C<sub>8</sub>), 122.4 (C<sub>7</sub>), 78.0 (C<sub>2</sub>), 56.1 (C<sub>13</sub>), 47.2 (C<sub>6</sub>), 37.9 (C<sub>4</sub>), 37.6 (C<sub>9</sub>), 32.1 (C<sub>10</sub>), 30.7 (C<sub>12</sub>), 29.3 (C<sub>14</sub>), 28.7 (C<sub>1</sub>), 25.1 (C<sub>5</sub>), 24.5 (C<sub>11</sub>) 9.5 (C<sub>15</sub>).

MS (ESI), *m/z* calculated for [C<sub>20</sub>H<sub>31</sub>N<sub>6</sub>O<sub>5</sub>]<sup>-</sup> = 435.2515; found 435.2350.

IR (bulk): ν<sub>max</sub> (cm<sup>-1</sup>) = 2935 (w), 2858 (w), 1690 (s), 1522 (w), 1410 (w), 1364 (w), 1333 (w), 1307 (w), 1249 (w), 1164 (w), 1049 (w), 852 (w), 759 (w), 667 (w).

#### 4.8.6 Boc-deprotection of the clicked barbiturate **40**



**Scheme 31.** Boc-deprotection of **40**.

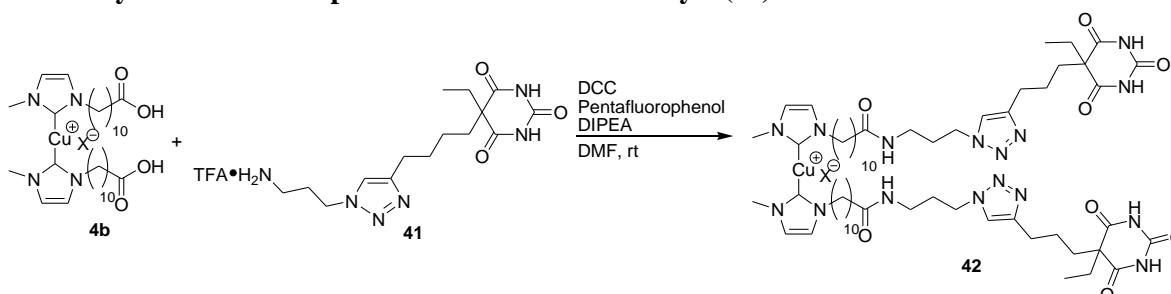
Boc-deprotection of **40** was performed according to literature<sup>257</sup>. Therefore, **40** (60.0 mg, 0.138 mmol) was dissolved in DCM (240.0 μL) and the mixture was cooled down to 0 °C before TFA (172.5 mg, 116.5 μL, 1.50 mmol) was added. The mixture was stirred for five hours at room temperature. After evaporation the product was obtained as TFA-salt.

Yield: 61.7 mg, 0.136 mmol, 99 %

<sup>1</sup>H-NMR (400 MHz, DMSO-d<sub>6</sub>, 27 °C): δ (ppm) = 11.51 (s, 2H, NH), 7.81 (m, 4H, H<sub>4</sub> + NH<sub>3</sub><sup>+</sup>), 4.38 (t, 2H, H<sub>3</sub>, <sup>3</sup>J = 6.8 Hz), 2.77 (m, 2H, H<sub>1</sub>), 2.55 (t, 2H, H<sub>6</sub>, <sup>3</sup>J = 7.5 Hz), 2.07 (m, 2H, H<sub>2</sub>, <sup>3</sup>J = 7.1 Hz), 1.81 (m, 4H, H<sub>9</sub> + H<sub>11</sub>), 1.52 (m, 2H, H<sub>7</sub>), 1.14 (m, 2H, H<sub>8</sub>), 0.75 (t, 3H, H<sub>12</sub>, <sup>3</sup>J = 7.4 Hz).

<sup>13</sup>C-NMR (100 MHz, DMSO-d<sub>6</sub>, 27 °C): δ (ppm) = 173.5 (C<sub>13</sub>), 150.3 (C<sub>14</sub>), 147.2 (C<sub>5</sub>), 122.5 (C<sub>4</sub>), 56.1 (C<sub>10</sub>), 46.8 (C<sub>3</sub>), 38.0 (C<sub>1</sub>), 36.9 (C<sub>6</sub>), 32.1 (C<sub>7</sub>), 29.4 (C<sub>9</sub>), 28.3 (C<sub>11</sub>), 25.0 (C<sub>2</sub>), 24.6 (C<sub>8</sub>), 9.6 (C<sub>12</sub>).

#### 4.8.7 Synthesis of the supramolecular mechanocatalyst (**42**)



**Scheme 32.** Coupling reaction for the generation of the supramolecular mechanocatalyst **42**.

**4b** (50.0 mg, 0.0743 mmol) was dissolved in DMF (500.0 μL). The solution was stirred at room temperature and molecular sieve (3 Å) and DCC (33.7 mg, 0.1635 mmol) were added. After stirring for ten minutes pentafluorophenol (30.1 mg, 0.1635 mmol), dissolved in DMF (200.0 μL) was added. After stirring for another ten minutes **41** (66.91 mg, 0.1486 mmol) and DIPEA (42.5 mg, 55.6 μL,

0.327 mmol) were dissolved in DMF (400.0  $\mu$ L) and were also added to the reaction. The mixture was stirred for 63 hours at room temperature before the formed precipitate was removed by filtration and the product was concentrated in vacuo. Purification by column chromatography  $\text{CHCl}_3 \rightarrow \text{CHCl}_3/\text{MeOH}$  (40:1) ( $R_f = 0.00$ )  $\rightarrow \text{CHCl}_3/\text{MeOH}$  (20:1) ( $R_f = 0.08$ )  $\rightarrow \text{CHCl}_3/\text{MeOH}$  (10:1) ( $R_f = 0.13$ ) yielded the pure product as white solid.

Yield: 70.6 mg, 0.015 mmol, 75 %

$^1\text{H-NMR}$  (400 MHz,  $\text{DMSO-d}_6$ , 27  $^\circ\text{C}$ ):  $\delta$  (ppm) = 11.49 (s, 2H, NH), 7.83 (t, 1H, NH,  $^3J = 5.5$  Hz), 7.77 (s, 1H,  $H_{14}$ ), 6.41 (dd, 2H,  $H_3 + H_4$ ), 4.26 (t, 2H,  $H_{13}$ ,  $^3J = 7.0$  Hz), 3.43 (t, 2H,  $H_5$ ,  $^3J = 7.1$  Hz), 3.07 (s, 3H,  $H_1$ ), 2.99 (dd, 2H,  $H_{11}$ ,  $^3J = 12.5, 7.7$  Hz), 2.52 (t, 2H,  $H_{16}$ ,  $^3J = 7.6$  Hz), 2.03 (t, 2H,  $H_9$ ,  $^3J = 7.4$  Hz), 1.88 (p, 2H,  $H_{12}$ ,  $^3J = 6.9$  Hz), 1.79 (m, 4H,  $H_{19} + H_{21}$ ), 1.49 (m, 6H,  $H_6 + H_8 + H_{17}$ ), 1.21 (m, 14H,  $H_7 + H_{18}$ ), 0.72 (t, 3H,  $H_{22}$ ,  $^3J = 7.4$  Hz).

$^{13}\text{C-NMR}$  (100 MHz,  $\text{DMSO-d}_6$ , 27  $^\circ\text{C}$ ):  $\delta$  (ppm) = 173.5 ( $C_{23}$ ), 172.7 ( $C_{10}$ ), 153.0 ( $C_2$ ), 150.3 ( $C_{24}$ ), 146.9 ( $C_{15}$ ), 122.2 ( $C_{14}$ ), 111.7 ( $C_4$ ), 110.6 ( $C_3$ ), 56.1 ( $C_{20}$ ), 47.5 ( $C_{13}$ ), 43.0 ( $C_5$ ), 38.0 ( $C_{16}$ ), 36.2 ( $C_1$ ), 35.8 ( $C_{11}$ ), 32.1 ( $C_{17}$ ), 30.4 ( $C_{19}$ ), 30.2 ( $C_9$ ), 29.4 ( $C_6 + C_{21}$ ), 29.3 ( $C_7$ ), 29.3 ( $C_7$ ), 29.2 ( $C_7$ ), 29.1 ( $C_7$ ), 29.0 ( $C_7$ ), 26.4 ( $C_7$ ), 25.7 ( $C_8$ ), 25.1 ( $C_{12}$ ), 24.6 ( $C_{18}$ ), 9.5 ( $C_{22}$ ).

IR (bulk):  $\nu_{\text{max}}$  ( $\text{cm}^{-1}$ ) = 2928 (w), 2854 (w), 1712 (w), 1642 (s), 1555 (w), 1411 (w), 1308 (s), 1236 (w), 1035 (w), 823 (w), 733 (w), 669 (w).

#### 4.9 Activation of the supramolecular catalyst **42** in solution *via* ultrasonication

Ultrasonication experiments of mechanocatalyst **42** were accomplished analogous to the procedure already given in the Experimental Part 4.6 for the linear mechanocatalysts. Control experiments without ultrasound were carried out in two-necked flasks at room temperature as well as at 60  $^\circ\text{C}$  under reflux to prove the mechanochemical origin of the catalyst activation. Samples for the acquired  $^1\text{H-NMR}$  spectra were directly taken out of the mixture without further purification after the corresponding ultrasonication cycles. The ultrasonication cycle dependent conversions for all mechanocatalysts are presented in Table 10.

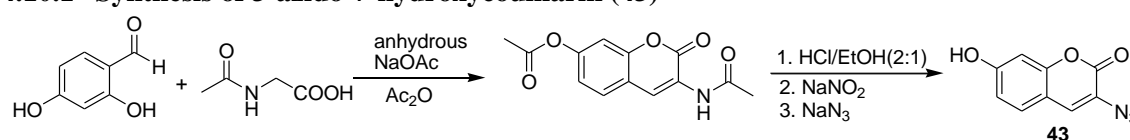
**Table 10.** Sonication cycle dependent conversions for the ultrasonication induced "click" reactions between phenylacetylene (**28**) and benzyl azide (**29**)<sup>a</sup>.

Entry	Catalyst	Conversion after US cycle (%) <sup>b</sup>					
		0	3	5	10	14	17
1	<b>4b</b>	0	0	0	2	2.9	3.4
2	<b>42</b>	0	0	0	1.5	2.4	3.4

<sup>a</sup>For all reactions 1.0 eq. of azide **28**, 1.0 eq. of alkyne **29** and 0.01 eq. of the Cu(I) catalyst (0.75 mM) were used in  $\text{THF-d}_8/\text{MeOH}$  (30:1) (v/v). <sup>b</sup>One cycle consisted of 90 min pulsing at 20 kHz with 20 % or 30 % amplitude of 125  $\mu\text{m}$  with a pulse sequence of 5 s/pulse, 10 s/break followed by 60 min without pulsing. The "click" reaction was followed by the increasing triazole resonance originating from product **30** in the  $^1\text{H-NMR}$  spectrum at  $\delta = 8.11$  ppm as well as the shift from the methylene group of **29** from  $\delta = 4.35$  ppm to  $\delta = 5.59$  ppm with a standard deviation of  $\pm 1$  %.

#### 4.10 Synthesis of the fluorescence dye

##### 4.10.1 Synthesis of 3-azido-7-hydroxycoumarin (**43**)



**Scheme 33.** Synthesis of 3-azido-7-hydroxycoumarin (**43**).

The synthesis of **43** was accomplished according to literature<sup>364</sup>. 2,4-Dihydroxy benzaldehyde (5.52 g, 40.0 mmol), *N*-acetylglycine (4.68 g, 40.0 mmol) and anhydrous sodium acetate (11.98 g, 146.0 mmol) were refluxed in acetic anhydride (200 mL) for four hours. The hot solution was poured onto ice, in turn

forming a yellow-brownish precipitate. The precipitate was washed with ice water (400 mL) and afterwards was refluxed in a 2:1 mixture of concentrated hydrochloric acid and ethanol (60 mL) for one hour. Subsequently, the mixture was cooled down to -5 °C by addition of ice water (80 mL) and cooling with an ice / sodium chloride bath. Sodium nitrite (5.52 g, 80.0 mmol) was slowly added and the mixture was further stirred for 15 minutes. Sodium azide (7.80 g, 120.0 mmol) was added in small portions to avoid an increase of the temperature above -5 °C. After stirring for another 20 minutes the brown precipitate was filtered, washed with water (300 mL) and was dried under vacuum.

Yield: 0.96 g, 4.27 mmol, 12 %

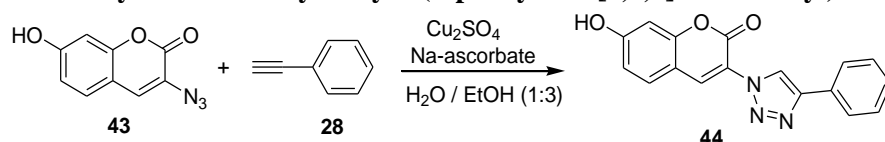
<sup>1</sup>H-NMR (400 MHz, DMSO-d<sub>6</sub>, 27 °C): δ (ppm) = 10.50 (s, 1H, OH), 7.57 (s, 1H, H<sub>5</sub>), 7.45 (d, 1H, H<sub>7</sub>, <sup>3</sup>J = 8.5 Hz), 6.80 (dd, 1H, H<sub>8</sub>, J = 8.5, 1.8 Hz), 6.74 (s, 1H, H<sub>1</sub>).

<sup>13</sup>C-NMR (100 MHz, DMSO-d<sub>6</sub>, 27 °C): δ (ppm) = 160.7 (C<sub>9</sub>), 157.7 (C<sub>3</sub>), 153.2 (C<sub>2</sub>), 129.5 (C<sub>7</sub>), 128.3 (C<sub>1</sub>), 121.6 (C<sub>4</sub>), 114.2 (C<sub>8</sub>), 111.8 (C<sub>6</sub>), 102.5 (C<sub>5</sub>).

MS (ESI), *m/z* calculated for [C<sub>9</sub>H<sub>6</sub>N<sub>3</sub>O<sub>3</sub>]<sup>+</sup> = 204.0400; found 204.0530.

IR (bulk): ν<sub>max</sub> (cm<sup>-1</sup>) = 3298 (m), 2113 (s), 1677 (s), 1619 (s), 1598 (s), 1566 (w), 1452 (w), 1372 (w), 1343 (s), 1319 (s), 1299 (s), 1257 (s), 1208 (s), 1180 (s), 1155 (w), 1123 (m), 1068 (m), 923 (m), 858 (m), 836 (m), 814 (m), 756 (m), 744 (w), 722 (w), 625 (w), 582 (w).

#### 4.10.2 Synthesis of 7-hydroxy-3-(4-phenyl-1*H*-[1,2,3]triazole-1-yl)-coumarin (**44**)



**Scheme 34.** Synthesis of 7-hydroxy-3-(4-phenyl-1*H*-[1,2,3]triazole-1-yl)-coumarin (**44**).

**44** was synthesized following synthetic protocols from literature<sup>364</sup>. Therefore, **43** (150.0 mg, 0.74 mmol), **28** (78.3 mg, 84.6 μL, 0.77 mmol), Cu<sub>2</sub>SO<sub>4</sub>•5 H<sub>2</sub>O (11.2 mg, 0.045 mmol) and sodium ascorbate (35.9 mg, 0.18 mmol) were dissolved in a mixture of water (1.87 mL) and ethanol (5.62 mL). Three freeze-thaw cycles were performed, to remove the oxygen before the mixture was stirred for 48 hours at room temperature in the dark. Subsequently, the ethanol was removed under reduced pressure and the remaining solution was stored in the fridge overnight. The brown precipitate was filtered, washed with ice water (15 mL) and was dried under vacuum.

Yield: 134 mg, 0.44 mmol, 60 %

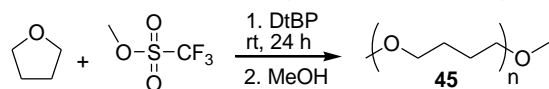
<sup>1</sup>H-NMR (400 MHz, DMSO-d<sub>6</sub>, 27 °C): δ (ppm) = 10.92 (s, 1H, OH), 9.01 (s, 1H, H<sub>10</sub>), 8.66 (s, 1H, H<sub>5</sub>), 7.96 (d, 2H H<sub>13</sub>, <sup>3</sup>J = 7.5 Hz), 7.78 (d, 1H H<sub>7</sub>, <sup>3</sup>J = 8.3 Hz), 7.49 (t, 2H, H<sub>14</sub>, <sup>3</sup>J = 7.6 Hz), 7.38 (t, 1H, H<sub>15</sub>, <sup>3</sup>J = 7.3 Hz), 6.92 (d, 1H, H<sub>8</sub>, J = 8.2 Hz), 6.88 (s, 1H, H<sub>1</sub>).

<sup>13</sup>C-NMR (100 MHz, DMSO-d<sub>6</sub>, 27 °C): δ (ppm) = 163.1 (C<sub>4</sub>), 156.7 (C<sub>7</sub>), 155.2 (C<sub>5</sub>), 146.9 (C<sub>2</sub>), 137.2 (C<sub>12</sub>), 131.5 (C<sub>1</sub>), 130.5 (C<sub>3</sub>), 129.5 (C<sub>13</sub>), 128.7 (C<sub>9</sub>), 125.7 (C<sub>14</sub>), 122.8 (C<sub>15</sub>), 119.8 (C<sub>11</sub>), 114.9 (C<sub>10</sub>), 110.7 (C<sub>8</sub>), 102.5 (C<sub>6</sub>).

MS (ESI), *m/z* calculated for [C<sub>17</sub>H<sub>11</sub>N<sub>3</sub>O<sub>3</sub>Na]<sup>+</sup> = 328.069; found 328.050.

IR (bulk): ν<sub>max</sub> (cm<sup>-1</sup>) = 1732 (w), 1707 (m), 1604 (s), 1411 (w), 1232 (s), 1176 (w), 1129 (w), 1077 (w), 766 (m), 694 (m), 634 (m).

#### 4.11 Synthesis of high molecular weight PTHF (45)

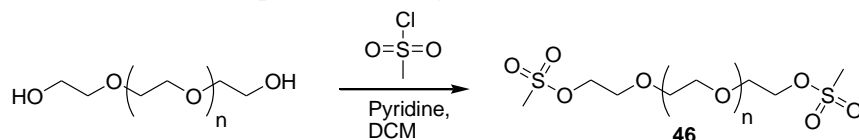


**Scheme 35.** Synthesis of the high molecular weight PTHF (45).

High molecular weight PTHF was synthesized as described in literature<sup>93</sup> *via* cationic ring opening polymerization. Therefore, freshly distilled THF (600 mL, 7.4 mol), methyl trifluoromethanesulfonate (60  $\mu$ L, 547  $\mu$ mol) and 2,6-di-*tert*-butylpyridine (DtBP) (3  $\mu$ L, 139  $\mu$ mol) were placed in a 1 L two-neck flask. The reaction was stirred at room temperature for 24 hours before MeOH (50 mL) was added. Subsequently, the mixture was stirred overnight before it was precipitated two times in MeOH. After drying, the high molecular weight PTHF was obtained in a yield of 10 %. GPC measurements revealed a molecular weight of 112 000 g/mol. The melting point was determined *via* DSC and was found to be 46 °C and the melting enthalpy was 117.8 J/g which corresponds to a crystallinity of 68 % (literature:  $\Delta H_{m,100\%} = 172$  J/g)<sup>365</sup>.

#### 4.12 Synthesis of the barbiturate modified polymeric matrix

##### 4.12.1 Synthesis of poly(ethylene glycol)-di-mesylate (46)



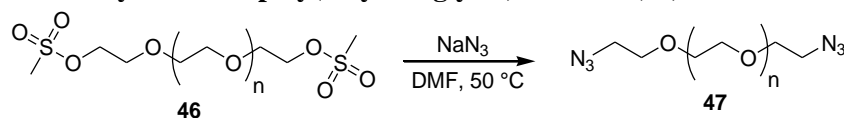
**Scheme 36.** Synthesis of poly(ethylene glycol)-di-mesylate (46).

The mesylation of the poly(ethylene glycol) was done according to literature<sup>366</sup>. HO-PEG-OH (10.0 g, 1.25 mmol) and pyridine (1.5 mL, 19.35 mmol) were cooled down to 0 °C in an ice bath. Methanesulfonyl chloride (0.484 mL, 6.25 mmol) was dissolved in DCM (20 mL) and was added dropwise to the reaction. Afterwards the mixture was stirred for 24 hours and saturated NaHCO<sub>3</sub> solution (70 mL) was added. The aqueous solution was extracted with DCM (6 x 30 mL) and the combined organic phases were dried with Na<sub>2</sub>SO<sub>4</sub>. After filtration, the solvent was removed and the yellow oil was precipitated in cold Et<sub>2</sub>O to obtain the product as white solid which was filtered and dried in vacuum.

Yield: 9.04 g, 1.13 mmol, 90 %

<sup>1</sup>H-NMR (400 MHz, CDCl<sub>3</sub>, 27 °C):  $\delta$  (ppm) = 4.36 (m, 4H, H<sub>2</sub>), 3.75 (m, 4H, H<sub>3</sub>), 3.62 (m, 637H, H<sub>4</sub>), 3.06 (s, 6H, H<sub>1</sub>).

##### 4.12.2 Synthesis of poly(ethylene glycol)-di-azide (47)



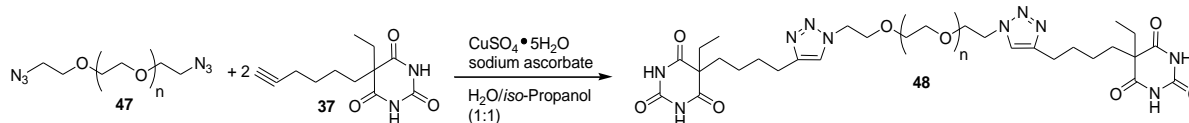
**Scheme 37.** Synthesis of poly(ethylene glycol)-di-azide (47).

46 (8.6 g, 1.1 mmol) and sodium azide (0.35 g, 5.4 mmol) were dissolved in DMF (50.0 mL) and the mixture was stirred for 42 hours at 50 °C. The solvent was removed and the crude product was redissolved in DCM (100 mL). After centrifugation and filtration the DCM was removed and the yellow oil was precipitated in cold Et<sub>2</sub>O to obtain the product as a white solid, which was filtered and dried in vacuum.

Yield: 7.73 g, 0.96 mmol, 90 %

$^1\text{H-NMR}$  (400 MHz,  $\text{CDCl}_3$ , 27 °C):  $\delta$  (ppm) = 3.62 (m, 648H,  $H_2 + H_3$ ), 3.36 (m, 4H,  $H_1$ ).

### 4.12.3 Synthesis of poly(ethylene glycol)-di-barbiturate (**48**)



**Scheme 38.** Synthesis of poly(ethylene glycol)-di-barbiturate (**48**).

**47** (5.0 g, 0.625 mmol), **37** (0.44 g, 1.88 mmol),  $\text{Cu}_2\text{SO}_4 \cdot 5 \text{H}_2\text{O}$  (30.0 mg, 0.19 mmol) and sodium ascorbate (29.7 mg, 0.15 mmol) were dissolved in water (39 mL) and *iso*-propanol (39 mL). Oxygen was removed *via* freeze-thaw cycles before the mixture was stirred for six days at 60 °C. Subsequently, the solvent was removed and the crude product was redissolved in DCM, dried with  $\text{Na}_2\text{SO}_4$  and filtered. After removal of the solvent, the polymer was precipitated three times in cold  $\text{Et}_2\text{O}$ , filtered and dried in vacuum. The melting point was determined *via* DSC and was found to be 58 °C and the melting enthalpy was 122.0 J/g which corresponds to a crystallinity of 61 % (literature:  $\Delta H_{\text{m},100\%} = 196.8 \text{ J/g}$ )<sup>367</sup>.

Yield: 4.1 g, 0.51 mmol, 82 %

$^1\text{H-NMR}$  (400 MHz,  $\text{DMSO-d}_6$ , 27 °C):  $\delta$  (ppm) = 11.49 (s, 4H,  $\text{NH}$ ), 7.74 (s, 2H,  $H_{11}$ ), 4.43 (t, 4H,  $H_{12}$ ,  $^3J = 5.3 \text{ Hz}$ ), 3.76 (t, 4H,  $H_{13}$ ,  $^3J = 5.3 \text{ Hz}$ ), 3.49 (m, 596H,  $H_{14}$ ), 2.53 (m, 4H,  $H_9$ ), 1.79 (m, 8H,  $H_4 + H_6$ ), 1.50 (dt, 4H,  $H_8$ ,  $J = 15.2, 7.6 \text{ Hz}$ ), 1.13 (m, 4H,  $H_7$ ), 0.72 (t, 6H,  $H_5$ ,  $^3J = 7.4 \text{ Hz}$ ).

## 4.13 Activation of the supramolecular catalyst in bulk *via* compression

### 4.13.1 General calibration of the fluorescence spectrometer

For the calibration varying amounts of **28**, **43** and **44** were dissolved in THF and were mixed with high molecular weight PTHF (200 mg, 112 000 g/mol) to reach bulk concentrations for **44** of 0,  $1.58 \cdot 10^{-6}$ ,  $3.17 \cdot 10^{-6}$ ,  $7.93 \cdot 10^{-6}$ ,  $1.59 \cdot 10^{-5}$ ,  $3.19 \cdot 10^{-5}$ ,  $6.42 \cdot 10^{-5}$  and  $1.64 \cdot 10^{-5} \text{ mmol}_{\text{dye}}/\text{mg}_{\text{sample}}$ , corresponding to “click” conversions of 0, 1.0, 1.9, 4.8, 9.6, 19.2, 38.9 and 100.0 %. Missing amounts to 100 % conversion were filled up with the “unclicked” dye **43**. The solvent was removed afterwards and all samples were kept in the fridge for one week. Subsequently, three compression cycles with a pressure of ten tons were performed. The obtained tablets were fixed in between two quartz glass holders for the fluorescence measurements. All measurements were conducted three times, using different positions of the tablets at an excitation wavelength of  $\lambda_{\text{Ex}} = 360 \text{ nm}$  and an emission wavelength of  $\lambda_{\text{Em}} = 427 \text{ nm}$ . Results for the calibration are shown in Figure 55. Fitting of the graph in Figure 55b led to equation 1, which was used for the calculation of the conversion.

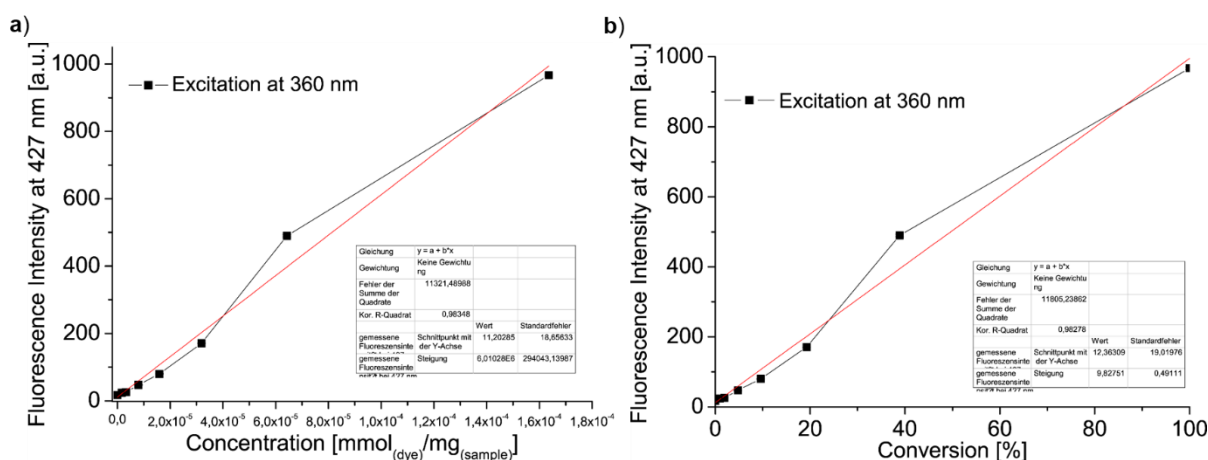


**Figure 55.** Calibration measurements for different degrees of conversion of the fluorogenic “click” reaction of **28** and **43** to **44** in a high molecular weight PTHF (112 000 g/mol) matrix.

Excitation at 360 nm:

$$y = 9.8275x + 12.3631$$

(eq1)

#### 4.14 Synthesis of elastin-based hydrogels (49)

Solubilized elastin (100 mg) was dissolved in DMF by stirring for one hour at room temperature. To the slightly yellow solution, the corresponding amount of HDI as well as a drop of DBU were added under vigorous stirring to achieve a homogenous mixture. The mixture was quickly transferred into a teflon mold before it became too viscous and then was placed in a desiccator. The desiccator was flushed with nitrogen for 15 minutes to remove most of the oxygen. Vacuum could not be applied since a reduction of the pressure led to formation of bubbles which were trapped within the formed hydrogel. After twelve hours, the formed network was removed from the teflon mold, was placed in a petri dish and was washed with *n*-pentane three times. Afterwards, the hydrogels were immersed in water for at least three days and the water was regularly exchanged to remove the DMF and the *n*-pentane.

For dehydration of the samples, the hydrogels were placed in a petri dish and were put in the vacuum oven at 40 °C. Afterwards, the pressure was gradually decreased over ten hours to avoid an expansion and destruction of the networks due to the evaporating water.

#### 4.15 Cytotoxicity of the mechanophoric catalysts

**Table 11.** Cell viability of complexes **4b**, **34**, **27e** and **50** against the breast cancer cell line MCF7 and the cell line from mouse embryonic fibroblasts (NIH/3T3). Italic numbers were extrapolated from the graphs.

Concentration [ $\mu\text{mol/L}$ ]	<b>4b</b>		<b>34</b>		<b>27e</b>		<b>50</b>	
	Cell viability		Cell viability		Cell viability		Cell viability	
	MCF7 [%]	NIH/3T3 [%]	MCF7 [%]	NIH/3T3 [%]	MCF7 [%]	NIH/3T3 [%]	MCF7 [%]	NIH/3T3 [%]
0	100.0	100.0	100.0	100.0	100.0	100	100.0	100.0
1	98.0	98.6	91.0	99.6	102.3	107.8	106.5	104.3
2.5	100.5	97.5	97.3	98.9	101.8	105.1	69.4	94.7
5	101.0	95.0	95.0	98.5	102.2	104.3	13.6	3.6
10	97.0	91.5	89.5	85.0	102.2	107.6	5.6	0.5
15	92.6	86.9	85.9	76.0	101.5	103.4	2.5	0.3
25	83.5	76.0	79.0	58.5	100.6	95.8	0.8	0.4
30	80.0	71.3	73.8	58.5	100.6	92.1	0.8	0.4
50	67.5	53.0	51.5	58.0	91.3	80.9	1.0	0.7
75	54.5	39.0	39.0	54.0	78.6	75.1	0.7	0.6
100	48	31.0	36.5	52.0	65.8	71.8	0.6	0.4
150	-	-	-	-	40.5	66.6	1.8	0.2

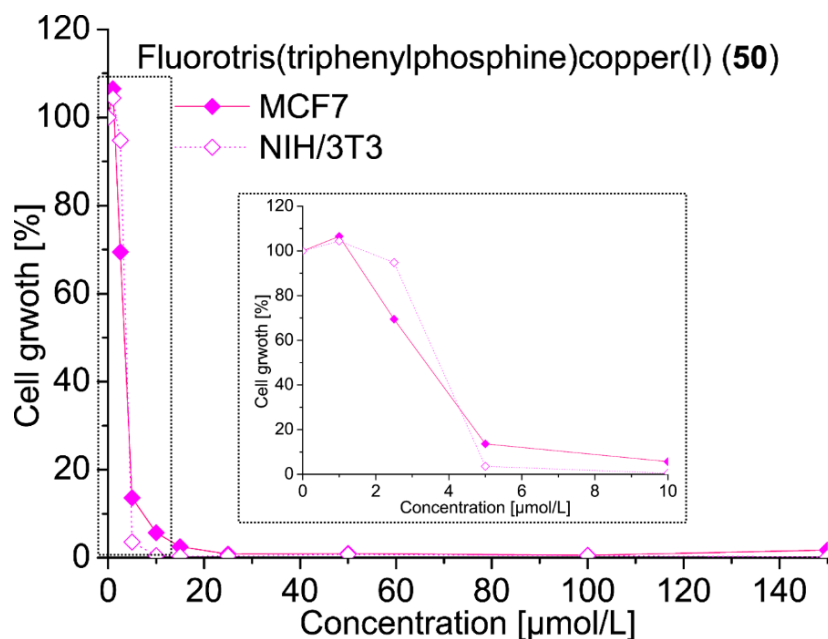
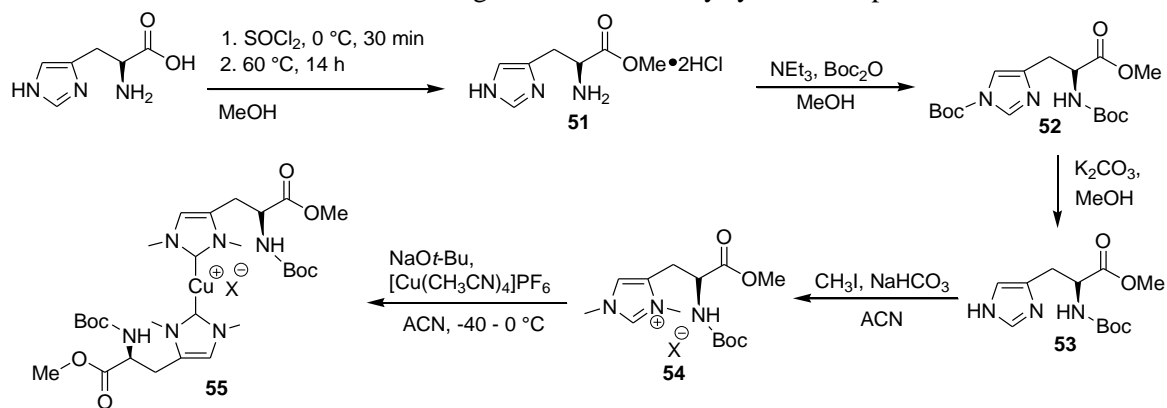


**Figure 56.** Cytotoxicity tests of complex **50**. Filled symbols refer to the toxicity tests against the MCF7 cell line (breast cancer) and open symbols refer to toxicity tests against the NIH/3T3 cell line (mouse embryonic fibroblasts).

#### 4.16 Synthesis of the histidinium based mechanocatalyst (**55**)

The histidine-based mechanocatalyst **55** was synthesized since it allowed more variety for the peptide coupling reactions. Depending from whether the carboxyl- or the amine group of the catalyst was cleaved off, coupling of the *N*-terminus as well as the *C*-terminus of peptides was possible. Contrary, mechanocatalyst **4b** necessarily required a *N*-terminus deprotected peptide. Furthermore, a possible impact of the substitution from 1,3-unsymmetrically substituted imidazolium to 1,3,4-unsymmetrically substituted histidinium should be investigated. The necessary synthetic steps are shown in Scheme 39.

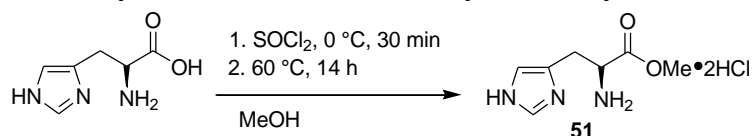


**Scheme 39.** Synthetic approach for mechanocatalyst **55**.

First, *L*-histidine methyl ester dihydrochloride (**51**) was synthesized following common protocols<sup>368</sup>. The following Boc-protection generated the double Boc-protected intermediate **52** which then had to be selectively Boc-deprotected with potassium carbonate at the the NH imidazole, thus yielding **53**<sup>369</sup>. Stirring **53** in the presence of iodomethane led to formation of the histidinium salt **54** through methylation of the NH imidazole. The obtained compound was highly hygroscopic and light sensitive, therefore storage in a desiccator in the dark was mandatory. Subsequent transformation to the mechanocatalyst **55** was not successful by choosing the previously used Cu<sub>2</sub>O method (see Chapter 3.1)<sup>325</sup>. Therefore, deprotonation was accomplished with sodium *tert*-butoxide in ACN, while [Cu(CH<sub>3</sub>CN)<sub>4</sub>]PF<sub>6</sub> was used for the Cu(I) bis(NHC) formation as previously described (see Chapter 3.1)<sup>37</sup>. However, conducting the

reaction at room temperature led to decomposition of the product. Contrary, conducting the reaction at  $-40\text{ }^{\circ}\text{C}$  in ACN generated the desired complex **55** with a yield of 25 %. The successful synthesis and purity was proven *via*  $^1\text{H-NMR}$  spectroscopy by the missing resonance of  $H_{10}$  ( $-\text{NCHN}-$ ) at 8.99 ppm from precursor **54** to complex **55** as well as the significant shift of proton  $H_9$  ( $-\text{NCH}=\text{C}-$ ) from 7.42 to 6.15 ppm (see Appendix 7.12). A full characterization of all intermediates as well as the final product is given in the Experimental Part 4.16 while the corresponding spectra are presented in the Appendix 7.12.

#### 4.16.1 Synthesis of *L*-histidine methyl ester dihydrochloride (**51**)



**Scheme 40.** Synthesis of *L*-histidine methyl ester dihydrochloride (**51**).

The synthesis of *L*-histidine methyl ester dihydrochloride (**51**) was done according to literature<sup>368</sup>. *L*-Histidine (10.0 g, 64.0 mmol) was dissolved in dry methanol (120 mL) and was cooled down to  $0\text{ }^{\circ}\text{C}$  prior to the dropwise addition of freshly distilled thionyl chloride (19.68 g, 12 mL, 166.0 mmol). After stirring for 30 minutes the temperature was increased to  $80\text{ }^{\circ}\text{C}$  and the mixture was refluxed for another 14 hours. After removal of the solvent and the excess of thionyl chloride the product was recrystallized twice from methanol, followed by filtration and additional washing with methanol to obtain the pure product as colorless powder.

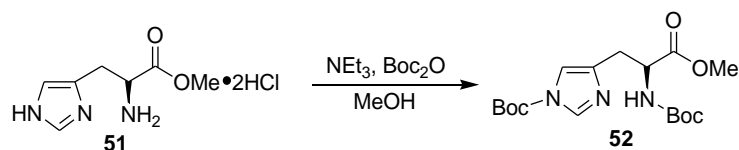
Yield: 14.41 g, 59.50 mmol, 93 %

$^1\text{H-NMR}$  (400 MHz,  $\text{DMSO-d}_6$ ,  $27\text{ }^{\circ}\text{C}$ ):  $\delta$  (ppm) = 9.05 (s, 1H,  $H_7$ ), 7.51 (s, 1H,  $H_6$ ), 4.46 (t, 1H,  $H_3$ ,  $^3J = 7.0\text{ Hz}$ ), 3.70 (s, 3H,  $H_1$ ), 3.31 (d, 2H,  $H_4$ ,  $^3J = 7.1\text{ Hz}$ ).

$^{13}\text{C-NMR}$  (100 MHz,  $\text{DMSO-d}_6$ ,  $27\text{ }^{\circ}\text{C}$ ):  $\delta$  (ppm) = 168.5 ( $C_2$ ), 134.0 ( $C_7$ ), 126.4 ( $C_5$ ), 118.1 ( $C_6$ ), 53.0 ( $C_1$ ), 51.0 ( $C_3$ ), 25.0 ( $C_4$ ).

MS (ESI),  $m/z$  calculated for  $[\text{C}_7\text{H}_{12}\text{N}_3\text{O}_2]^+ = 170.1686$ ; found 170.0924.

#### 4.16.2 Synthesis of *N*- $\alpha$ -(*tert*-butoxycarbonyl)-1-*tert*-butoxycarbonyl-*L*-histidine methyl ester (**52**)



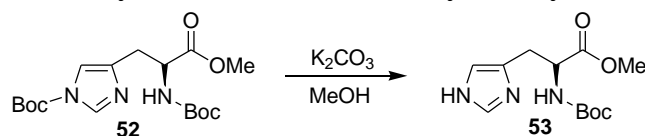
**Scheme 41.** Synthesis of *N*- $\alpha$ -(*tert*-butoxycarbonyl)-1-*tert*-butoxycarbonyl-*L*-histidine methyl ester (**52**).

The synthesis of **52** was accomplished according to literature<sup>369</sup>. To a cooled suspension of **51** (6.0 g, 24.80 mmol) in methanol (90 mL) was added dropwise the triethylamine (5.0 g, 6.84 mL, 49.60 mmol). Afterwards di-*tert*-butyl dicarbonate (12.44 g, 57.04 mmol) was melted in a water bath and was slowly added, followed by stirring at  $0\text{ }^{\circ}\text{C}$  for one hour. The reaction was finished after further stirring at room temperature for 20 hours. After removal of the solvent the crude product was purified by column chromatography (DCM/MeOH (20:1) ( $R_f = 0.66$ ) to obtain a white, glassy solid.

Yield: 7.46 g, 20.20 mmol, 81 %

$^1\text{H-NMR}$  (400 MHz,  $\text{DMSO-d}_6$ ,  $27\text{ }^{\circ}\text{C}$ ):  $\delta$  (ppm) = 7.97 (d, 1H,  $H_{10}$ ,  $^4J = 1.1\text{ Hz}$ ), 7.13 (d, 1H,  $H_9$ ,  $^4J = 0.8\text{ Hz}$ ), 5.70 (d, 1H,  $\text{NH}$ ,  $^3J = 7.9\text{ Hz}$ ), 4.57 (m, 1H,  $H_6$ ), 3.72 (s, 3H,  $H_4$ ), 3.04 (m, 2H,  $H_7$ ), 1.60 (s, 9H,  $H_{12}$ ), 1.43 (s, 9H,  $H_1$ ).

#### 4.16.3 Synthesis of *N*- $\alpha$ -(*tert*-butoxycarbonyl)-*L*-histidine methyl ester (**53**)



**Scheme 42.** Synthesis of *N*- $\alpha$ -(*tert*-butoxycarbonyl)-*L*-histidine methyl ester (**53**).

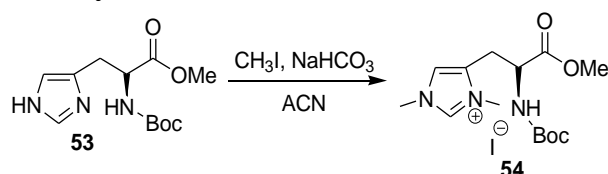
Synthesis of **53** was done according to literature<sup>369</sup>. Therefore, **52** (5.59 g, 15.14 mmol) was dissolved in dry methanol (40 mL) and  $K_2CO_3$  (0.21 g, 1.51 mmol) was added in a counterflow of nitrogen. The mixture was refluxed for six hours at 70 °C to give a yellow, clear solution. The solvent was removed and the crude product was redissolved in EtOAc (100 mL) and washed with water (3 x 50 mL). The combined aqueous phases were backextracted with EtOAc (3 x 50 mL) and the organic phases were combined, washed with brine (20 mL), dried over  $MgSO_4$  and filtrated. Afterwards the product was further purified by column chromatography (DCM/MeOH (10 : 1) ( $R_f$  = 0.16) to give a white solid.

Yield: 3.0 g, 11.14 mmol, 74 %

$^1H$ -NMR (400 MHz, DMSO - $d_6$ , 27 °C):  $\delta$  (ppm) = 7.56 (d, 1H,  $H_7$ ,  $^3J$  = 1.1 Hz), 7.14 (d, 1H, NH,  $^3J$  = 7.8 Hz), 6.79 (s, 1H,  $H_6$ ), 4.21 (td, 1H,  $H_3$ ,  $J$  = 7.8, 6.0 Hz), 3.57 (s, 3H,  $H_1$ ), 2.84 (m, 2H,  $H_4$ ), 1.34 (s, 9H,  $H_{10}$ ).

$^{13}C$ -NMR (100 MHz, DMSO - $d_6$ , 27 °C):  $\delta$  (ppm) = 172.7 ( $C_2$ ), 155.8 ( $C_8$ ), 135.3 ( $C_7$ ), 134.0 ( $C_5$ ), 116.5 ( $C_6$ ), 80.1 ( $C_9$ ), 53.7 ( $C_3$ ), 52.5 ( $C_1$ ), 29.8 ( $C_4$ ), 28.4 ( $C_{10}$ ).

#### 4.16.4 Synthesis of 4-[2-[[1,1-dimethylethoxy)carbonyl]amino]-3-methoxy-3-oxopropyl]-1,3-dimethyl-1*H*-imidazolium iodide (**54**)



**Scheme 43.** Synthesis of histidinium salt **54**.

To a mixture of **53** (1.5 g, 5.58 mmol) and  $NaHCO_3$  (1.88 g, 22.32 mmol) ACN was added (10.5 mL). The mixture was heated to 40 °C followed by the addition of iodomethane (19.0 g, 8.49 mL, 136.2 mmol) and was stirred for 150 h. The yellow suspension was filtered and subsequently the ACN was removed under reduced pressure. The residue was redissolved in  $CHCl_3$  (15.0 mL) and was extracted with water (7 x 10 mL). The aqueous phases were combined, the solvent was removed under reduced pressure and the product was redissolved in ACN (10 mL). After drying with  $Na_2SO_4$ , filtration and removal of the solvent the product was obtained as a white, slightly yellowish solid which was highly hygroscopic and was stored in a desiccator in the dark.

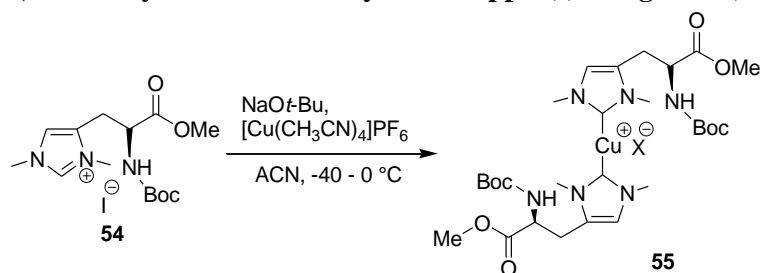
Yield: 2.25 g, 5.32 mmol, 95 %

$^1H$ -NMR (400 MHz, DMSO  $d_6$ , 27 °C):  $\delta$  (ppm) = 8.99 (s, 1H,  $H_{10}$ ), 7.42 (s, 1H,  $H_9$ ), 7.38 (d, 1H, NH,  $^3J$  = 8.4 Hz), 4.34 (td, 1H,  $H_6$ ,  $J$  = 9.4 Hz, 4.8 Hz), 3.79 (s, 3H,  $H_{11}$ ), 3.76 (s, 3H,  $H_{11}$ ), 3.65 (s, 3H,  $H_4$ ), 3.11 (dd, 1H,  $H_7$ ,  $J$  = 15.7 Hz, 4.7 Hz), 2.96 (dd, 1H,  $H_7$ ,  $J$  = 15.8 Hz, 9.8 Hz), 1.33 (s, 9H,  $H_1$ ).

$^{13}C$ -NMR (100 MHz, DMSO - $d_6$ , 27 °C):  $\delta$  (ppm) = 171.2 ( $C_5$ ), 155.3 ( $C_3$ ), 136.7 ( $C_{10}$ ), 131.2 ( $C_8$ ), 121.4 ( $C_9$ ), 78.7 ( $C_2$ ), 52.2 ( $C_4$ ), 51.7 ( $C_6$ ), 35.7 ( $C_{11}$ ), 33.3 ( $C_{11}$ ), 28.0 ( $C_1$ ), 24.9 ( $C_7$ ).

MS (ESI),  $m/z$  calculated for  $[C_{14}H_{16}N_3O_4]^+$  = 298.1761; found 298.1759.

#### 4.16.5 Synthesis of bis(4-[2-[[[(1,1-dimethylethoxy)carbonyl]amino]-3-methoxy-3-oxopropyl])-1,3-dimethyl-1*H*-imidazol-2-ylidene copper(I) halogenide (**55**)



**Scheme 44.** Synthesis of **55**.

**54** (0.50 g, 1.18 mmol) was weighed into a Schlenk flask and cooled down to  $-40\text{ }^{\circ}\text{C}$  by means of a MeOH / liquid nitrogen bath. Sodium *tert*-butoxide (175.6 mg, 1.83 mmol) was suspended in ACN (5.0 mL) and was added *via* syringe. The mixture was stirred for ten minutes prior to the addition of tetrakis(acetonitrile)copper(I) hexafluorophosphate (228.7 mg, 0.61 mmol), dissolved in ACN (3.5 mL). The mixture was stirred for another three hours at  $-40\text{ }^{\circ}\text{C}$  and afterwards for 16 hours at room temperature. The resulting, slightly greenish, suspension was filtered and the solvent was removed under reduced pressure. Column chromatography (EtOAc/MeOH (5:1) ( $R_f = 0.44$ )) yielded the pure product.

Yield: 228.6 mg, 0.28 mmol, 25 %

$^1\text{H-NMR}$  (400 MHz, DMSO- $d_6$ ,  $27\text{ }^{\circ}\text{C}$ ):  $\delta$  (ppm) = 7.25 (d, 1H, NH,  $^3J = 8.0$  Hz), 6.15 (s, 1H,  $H_9$ ), 4.13 (td, 1H,  $H_6$ ,  $J = 8.5$  Hz, 4.9 Hz), 3.61 (s, 3H,  $H_4$ ), 3.03 (s, 6H,  $H_{11}$ ). 2.80 (dd, 1H,  $H_7$ ,  $J = 15.2$  Hz, 5.1 Hz), 2.66 (dd, 1H,  $H_7$ ,  $J = 15.5$  Hz, 9.5 Hz), 1.34 (s, 9H,  $H_1$ ).

$^{13}\text{C-NMR}$  (100 MHz, DMSO- $d_6$ ,  $27\text{ }^{\circ}\text{C}$ ):  $\delta$  (ppm) = 171.9 ( $C_5$ ), 155.3 ( $C_{10}$ ), 152.9 ( $C_3$ ), 117.9 ( $C_8$ ), 108.9 ( $C_9$ ), 78.4 ( $C_2$ ), 52.2 ( $C_6$ ), 51.9 ( $C_4$ ), 29.6 ( $C_{11}$ ), 28.1 ( $C_1$ ), 27.04 ( $C_{11}$ ), 26.2 ( $C_7$ ).

#### 4.16.6 Mechanochemical activation of the histidinum based catalyst **55**

Ultrasonication experiments of mechanocatalyst **55** were accomplished analogous to the procedure already given in the Experimental Part 4.6 for the linear mechanocatalysts. Samples for the acquired  $^1\text{H-NMR}$  spectra were directly taken out of the mixture without further purification after the corresponding ultrasonication cycles. Several parameters were varied for the ultrasonication experiments but no “click” conversion could be detected in all cases. An overview about the accomplished experiments is shown in Table 12.

**Table 12.** Ultrasonication induced “click” reactions between phenylacetylene (**28**) and benzyl azide (**29**)<sup>a</sup>.

Entry	Temperature ( $^{\circ}\text{C}$ )	Amplitude (%)	Time (h)	US cycles <sup>b</sup>	Remarks
1	0	30	15	6	
2	0	20	15	6	
3	0	30	25	10	
4	0	20	25	10	
5	40	30	25	10	
6	0	30	15	10	no waiting time between US cycles
7	25	30	25	10	addition of 2.0 eq. sodium ascorbate

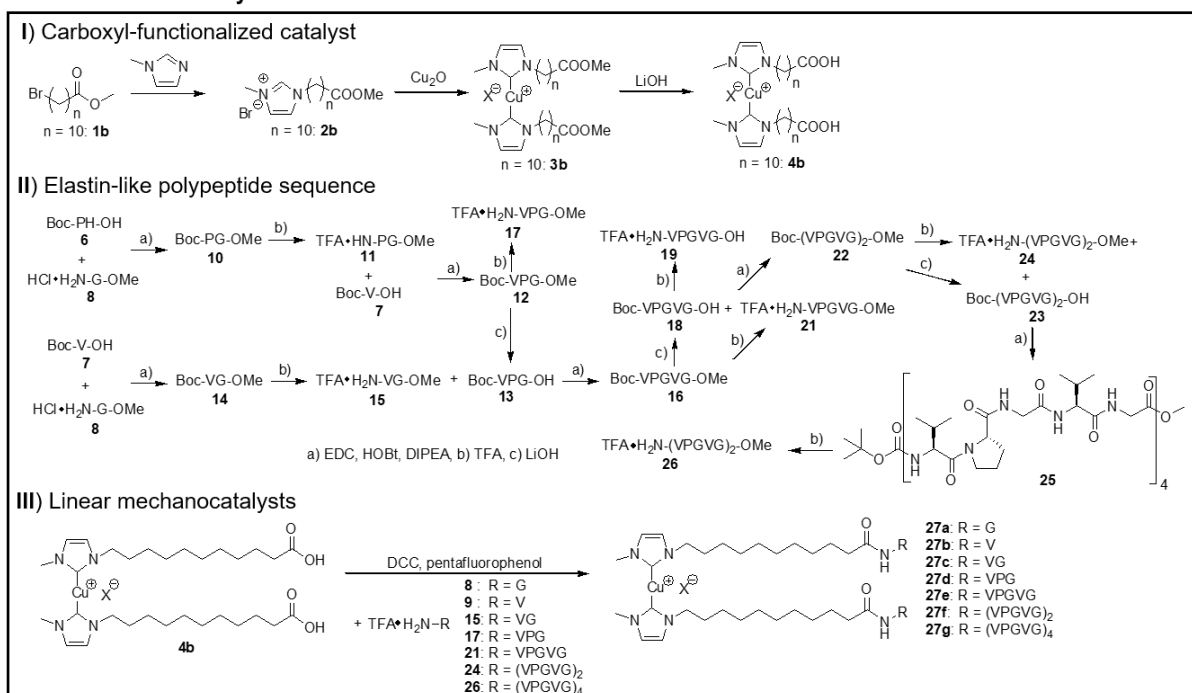
<sup>a</sup>For all reactions 1.0 eq. of azide **28**, 1.0 eq. of alkyne **29** and 0.01 eq. of the Cu(I) catalyst **55** (0.75 mM) were used in THF- $d_8$ /MeOH (30:1) (v/v). <sup>b</sup>One cycle consisted of 90 min pulsing at 20 kHz with 20 % or 30 % amplitude of 125  $\mu\text{m}$  with a pulse sequence of 5 s/pulse, 10 s/break followed by 60 min without pulsing.

## 5 Summary

The aim of this work was the synthesis and characterization of peptide bearing latent Cu(I) bis(NHC) mechanocatalysts for a force-induced copper(I)-catalyzed alkyne-azide cycloaddition (CuAAC). These catalysts should be activated with an external force like ultrasonication (solution) or compression (bulk). Elastin-like polypeptides (ELPs) were chosen as peptidic force transmission handles as they enabled the establishing of  $\beta$ -spiral structures, which could be exploited as “molecular spring” for an enhanced force transmission to the mechanolabile copper-carbene bond.

Therefore, a variety of low molecular weight mechanophoric complexes have been synthesized. Especially  $[\text{Cu}(\text{C}_{10}\text{COOH-NHC})_2]\text{X}$  (**4b**) (Figure 57-I) and  $[\text{Cu}(\text{C}_3\text{NH}_2\cdot\text{TFA-NHC})_2]\text{X}$  (**34**) (Figure 57-IV) were found to be suitable complexes since they were accessible in good yields, already showed mechanophoric activity and allowed peptide coupling reactions with either the *N*- or the *C*-terminus of peptides. Previous methyl ester- and Boc-protection of the respective NHC precursors **2b** and **32** was necessary for a successful formation of the protected catalysts  $[\text{Cu}(\text{C}_{10}\text{COOMe-NHC})_2]\text{X}$  (**3b**) and  $[\text{Cu}(\text{C}_3\text{NHBoc-NHC})_2]\text{X}$  (**33**) using the  $\text{Cu}_2\text{O}$  method. Strong bases such as potassium bis(trimethylsilyl)amide (KHMDs) or sodium *tert*-butoxide were not applicable for the synthesis of **3b** due to the reactivity of the methyl ester protection group towards bases.

### Linear mechanocatalysts



### Chain-extended mechanocatalyst

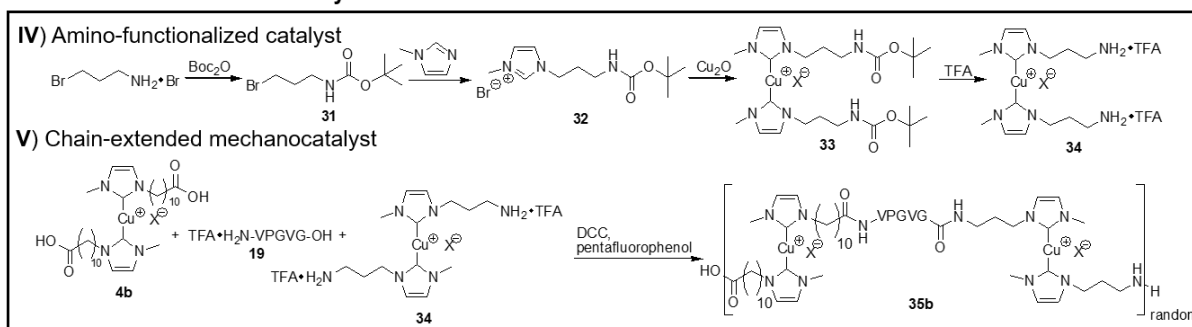


**Figure 57.** Synthetic pathway for I) the carboxyl functionalized low molecular weight complex **4b**, II) the ELP sequence which was built up using common peptide coupling agents (EDC·HCl, HOBT), III) the linear mechanocatalysts **27a-g**, IV) the amine functionalized low molecular weight complex **34** and V) the chain-extended catalyst **35b** with multiple Cu(I) centers.

The synthesis of the ELP sequence was done in solution with EDC•HCl and HOBt which are common coupling agents in the field of peptide chemistry (Figure 57-II). The *tert*-butoxycarbonyl (Boc) protection group for the *N*-terminus and the methyl ester (OMe) protection group for the *C*-terminus guaranteed a sequence specific buildup of the peptide. A variety of ELP sequences with different chain lengths up to Boc-(VPGVG)<sub>4</sub>-OMe (**25**) have been synthesized. Several peptides (H<sub>2</sub>N-G-OMe (**8**), H<sub>2</sub>N-V-OMe (**9**), H<sub>2</sub>N-VG-OMe (**15**), H<sub>2</sub>N-VPG-OMe (**17**), H<sub>2</sub>N-VPGVG-OMe (**21**), H<sub>2</sub>N-(VPGVG)<sub>2</sub>-OMe (**24**), H<sub>2</sub>N-(VPGVG)<sub>4</sub>-OMe (**26**)) could be successfully coupled to the carboxyl groups of mechanocatalyst **4b** *via* the *N*-terminus of the peptides, thus generating the linear mechanophores **27a-g** (Figure 57-III).

Both the peptide coupling reactions and the coupling to the mechanocatalyst **4b** suffered from low yields, making a further elongation of the linear catalysts rather uneconomic. Therefore, polycondensation of **4b** and **34** with the double deprotected pentapeptide TFA•H<sub>2</sub>N-VPGVG-OH (**19**) was conducted to generate the chain-extended mechanocatalyst **35b** which contained the “molecular spring” as a repetitive unit in between several Cu(I) centers (Figure 57-V).

Secondary structure analysis *via* IR- and CD-spectroscopy in D<sub>2</sub>O revealed the ability of the Boc-VPGVG-OMe (**16**) to truly adopt the  $\beta$ -spiral which was a prerequisite for the “molecular spring” behavior (see Figure 58). The  $\beta$ -spiral formation is an ability that is exclusive to elastin, respectively ELPs. Repeating the measurements with mechanocatalyst [Cu(C<sub>10</sub>COOH-VPGVG-NHC)<sub>2</sub>]X (**27e**) which also bore the VPGVG sequence, revealed nearly identical results for both IR- and CD-measurements and proved that the secondary structure formation was not affected by the peptide coupling. Therefore, the “molecular spring” behavior of the attached peptides could be concluded.

The activation behavior of the synthesized complexes was tested *via* ultrasonication experiments in solution (THF-d<sub>8</sub>/MeOH (30:1)). The application of ultrasound cleaved one of the shielding ligands, in turn allowing the coordination of the alkyne to the Cu(I) center which started the “click” reaction of phenylacetylene (**28**) and benzyl azide (**29**) (see Figure 58). This reaction could be monitored by taking aliquots before ultrasound application and after the 3<sup>rd</sup>, 5<sup>th</sup>, 10<sup>th</sup>, 14<sup>th</sup> and 17<sup>th</sup> cycle to calculate the “click” conversion *via* <sup>1</sup>H-NMR spectroscopy.

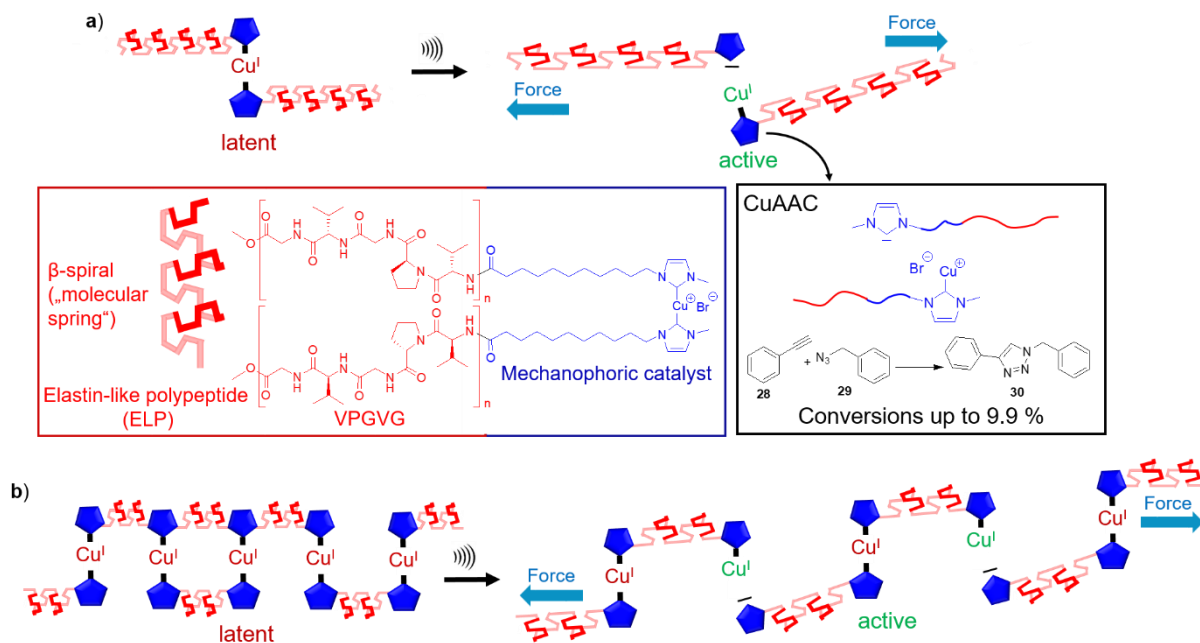


**Figure 58.** Catalytic activity was tested in solution with ultrasound by following the sonication cycle dependent model “click” reaction of phenylacetylene (**28**) and benzyl azide (**29**) for a) the linear catalysts **27a-g** and b) the chain-extended catalyst **35b**.

For the linear catalysts a steady increase of the conversion could be observed from the shortest catalyst without attached peptide chains  $[\text{Cu}(\text{C}_{10}\text{COOH-NHC})_2]\text{X}$  (**4b**) (3.4 %) to  $\text{Cu}(\text{C}_{10}\text{COOH-(VPGVG)}_4\text{-NHC})_2]\text{X}$  (**27g**) (5.6 %) after the 17<sup>th</sup> ultrasonication cycle. Commonly, the mechanocatalysts did not show catalytic activity before the 10<sup>th</sup> cycle. Solely **27g**, bearing the longest peptide chains showed catalytic activity after the 5<sup>th</sup> cycle (1.5 %). The chain-extended mechanocatalyst **35b** also showed catalytic activity after the 5<sup>th</sup> cycle (2.4 %) which increased to 4.7 % after the last cycle.

Presumably, the low conversions could be attributed to the comparably low molecular weight peptides that were attached to mechanophore **4b**. Thus, the limiting molecular weight which was necessary for an efficient activation of the catalyst has not been reached. This assumption could be proven by calculating the sonication cycle dependent amount of activated catalyst **27e** via <sup>1</sup>H-NMR spectroscopy. Only 8 % of the Cu(I) bis(NHC) complex was cleaved after the 10<sup>th</sup> ultrasonication while after the 17<sup>th</sup> cycle 31 % of the catalyst was activated. Commercially obtained solubilized elastin with a higher molecular weight could not be used for the synthesis of linear catalysts with longer chains for two reasons: First, solubilized elastin is obtained by refluxing the crosslinked elastin under basic conditions thus leading to destruction of the crosslinks. Therefore, the obtained solubilized elastin is a heterogeneous mixture of a variety of different elastin fragments. Secondly, the molecular weight distribution of the solubilized elastin is very broad (see Appendix 7.11), preventing a reliable positioning of the Cu(I) bis(NHC) near the midst point of the peptidic catalyst. Hence, a reproducible activation behavior could not be achieved.

Nevertheless, the commercial elastin could be used for the synthesis of hydrogels using the free amine groups and hexamethylenediisocyanate (HDI) for crosslinking (see Figure 59).

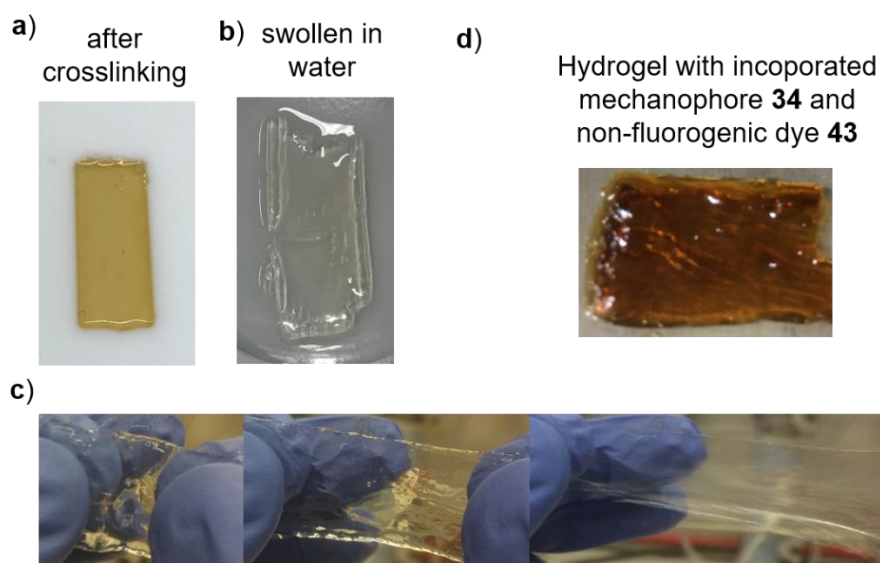


**Figure 59.** Synthesis of elastin-based hydrogels **49**. a) After crosslinking in the teflon mold. b) When completely swollen the hydrogels were fragile and were not extendable. c) When not completely swollen the hydrogels could be extended. d) Incorporation of mechanocatalyst **34**, phenylacetylene (**28**) and the non-fluorogenic dye **43** into the hydrogel.

Addition of **34** also offered the possibility to incorporate the mechanophoric catalyst together with 3-azido-7-hydroxycoumarin (**43**) and phenylacetylene (**28**) into the hydrogels (see Figure 59d). Stable hydrogels could be formed with elastin/HDI ratios between 1.4:1 and 50:1. Further decrease of the ratio (1:1.4) led to immediate solidification of the resulting network after addition of the HDI. Contrary, increasing the elastin/HDI ratio to (60:1) led to insufficiently crosslinked networks that were dissolving upon placement in water for swelling. Characterization of the samples was difficult due to the fragility of the hydrogels in the fully swollen state and due to their stickiness (see Figure 59b). Furthermore, the

strong dependency of elasticity from the degree of hydration prevented a meaningful mechanical characterization with available instruments.

In order to test the activation behavior of the synthesized catalysts in the solid state, an amine modified barbiturate **41** was synthesized which could be coupled to **4b** *via* peptide coupling (see Figure 60a). The resulting complex **42**, 3-azido-7-hydroxycoumarin (**43**) and phenylacetylene (**28**) were incorporated into two different matrices (high molecular weight PTHF (112 000 g/mol) (**45**) and barbiturate modified PEG (8000 g/mol) (**48**)) (see Figure 60b) to follow the activation of the catalyst with the fluorogenic “click” reaction due to formation of 7-hydroxy-3-(4-phenyl-1*H*-[1,2,3]triazole-1-yl)-coumarin (**44**) (see Figure 60c). The increasing conversion could be calculated with fluorescence spectroscopy. Activation of the catalyst was achieved by repeating cycles of compression with a pressure of ten tons, followed by release of the stress. A conversion of 1.9 % could be calculated for the compression experiment in the PTHF matrix. Testing of the barbiturate modified matrix did not reveal any conversion. Presumably the barbiturate clusters were preferentially destroyed thus acting as sacrificial bonds and preventing cleavage of the Cu(I) bis(NHC) catalyst.

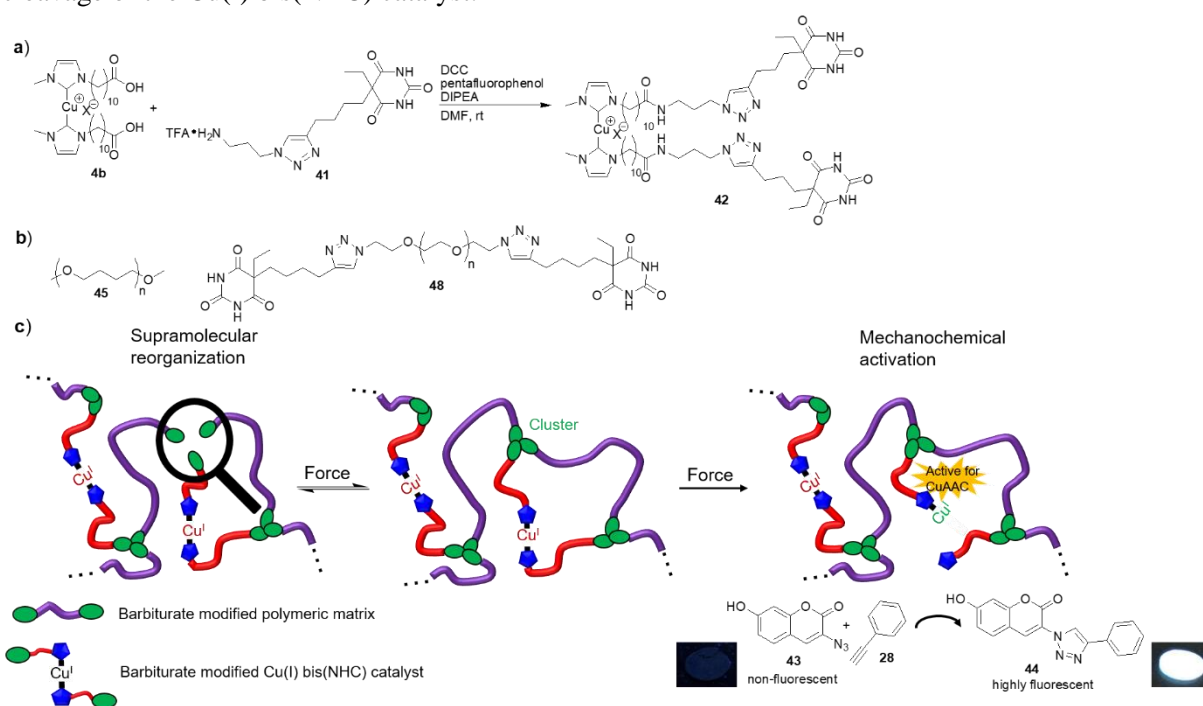


**Figure 60.** a) Synthesis of the barbiturate modified Cu(I) bis(NHC) complex **42**. b) Compression experiments of **42** were conducted within two different matrices (PTHF (**45**) or barbiturate modified PEG (**48**)). c) Compression of the catalyst within the matrix **48** could either lead to destruction of the supramolecular barbiturate clusters or to the activation of **42** by cleavage of one of the NHC ligands. After activation of **42**, the fluorogenic “click” reaction of 3-azido-7-hydroxycoumarin (**43**) and phenylacetylene (**28**) generated the highly fluorescent 7-hydroxy-3-(4-phenyl-1*H*-[1,2,3]triazole-1-yl)-coumarin (**44**).

The successful incorporation of Cu(I) bis(NHC) catalysts into ELPs and elastine based hydrogels might also allow a prospective usage as an autonomous stress detection system in biological systems. However, copper tends to be highly toxic (see Chapter 3.7). Therefore, the cytotoxicity of the synthesized Cu(I) bis(NHC) complexes  $[\text{Cu}(\text{C}_{10}\text{COOH-NHC})_2]\text{X}$  (**4b**),  $[\text{Cu}(\text{C}_{10}\text{COOH-VPGVG-NHC})_2]\text{X}$  (**27e**),  $[\text{Cu}(\text{C}_3\text{NH}_2\cdot\text{TFA-NHC})_2]\text{X}$  (**34**) as well as fluorotris(triphenylphosphine)copper(I) (**50**) were tested against the MCF7 (breast cancer) and the NIH/3T3 (mouse embryonic fibroblasts) cell lines. Testing of complex **50** revealed a high cytotoxicity against both cell lines with 50 % of the cells being alive at concentrations as low as 4  $\mu\text{mol/L}$ . The cytotoxicity for complexes **4b** and **34** could be significantly reduced with 50 % of the cells being alive at a concentration of 50  $\mu\text{mol/L}$  (**4b**, NIH/3T3 and **34**, MCF7) and 92  $\mu\text{mol/L}$  (**4b**, MCF7), while even for the highest concentration of 100  $\mu\text{mol/L}$  for complex **34**,

52 % of the NIH/3T3 cells were still alive. Presumably the two attached NHC ligands exerted a shielding effect, thus preventing an interaction of the cells with the Cu(I) center. This shielding effect could be even enhanced by addition of peptides to the catalyst, thus increasing the length of the NHC ligands. Hence, the cytotoxicity of **27e** which bore the VPGVG sequence could be further decreased. 50 % of the MCF7 cells were still alive at a concentration of 132  $\mu\text{mol/L}$ , while 67 % of the NIH/3T3 cells were alive at the highest measured concentration of 150  $\mu\text{mol/L}$ . The comparatively low cytotoxicity of the synthesized Cu(I) bis(NHC) complexes might allow their use for future biologic applications.

## 6 References

1. Beyer, M. K.; Clausen-Schaumann, H., Mechanochemistry: The Mechanical Activation of Covalent Bonds. *Chem. Rev* **2005**, *105* (8), 2921-2948.
2. Brantley, J. N.; Wiggins, K. M.; Bielawski, C. W., Polymer mechanochemistry: the design and study of mechanophores. *Polym. Int.* **2013**, *62* (1), 2-12.
3. Hickenboth, C. R.; Moore, J. S.; White, S. R.; Sottos, N. R.; Baudry, J.; Wilson, S. R., Biasing reaction pathways with mechanical force. *Nature* **2007**, *446* (7134), 423-427.
4. Suslick, K. S., Mechanochemistry and sonochemistry: concluding remarks. *Faraday Discuss.* **2014**, *170* (0), 411-422.
5. Hsu, S. M.; Zhang, J.; Yin, Z., The Nature and Origin of Tribochemistry. *Tribol. Lett.* **2002**, *13* (2), 131-139.
6. Fischer, T. E., Tribochemistry. *Annu. Rev. Mater. Sci.* **1988**, *18* (1), 303-323.
7. Gates, R. S.; Jewett, K. L.; Hsu, S. M., A Study on the Nature of Boundary Lubricating Film: Analytical Method Development. *Tribol. Trans.* **1989**, *32* (4), 423-430.
8. Takacs, L., The historical development of mechanochemistry. *Chem. Soc. Rev.* **2013**, *42* (18), 7649-7659.
9. Lea, M. C., On endothermic decompositions obtained by pressure; Part II, Transformations of energy by shearing stress. *Am. J. Sci.* **1893**, *46*, 413-420.
10. Hernández, J. G.; Frišćić, T., Metal-catalyzed organic reactions using mechanochemistry. *Tetrahedron Lett.* **2015**, *56* (29), 4253-4265.
11. Thorwirth, R.; Stolle, A.; Ondruschka, B.; Wild, A.; Schubert, U. S., Fast, ligand- and solvent-free copper-catalyzed click reactions in a ball mill. *Chem. Commun.* **2011**, *47* (15), 4370-4372.
12. Cook, T. L.; Walker, J. A.; Mack, J., Scratching the catalytic surface of mechanochemistry: a multi-component CuAAC reaction using a copper reaction vial. *Green Chem.* **2013**, *15* (3), 617-619.
13. Mukherjee, N.; Ahammed, S.; Bhadra, S.; Ranu, B. C., Solvent-free one-pot synthesis of 1,2,3-triazole derivatives by the 'Click' reaction of alkyl halides or aryl boronic acids, sodium azide and terminal alkynes over a Cu/Al<sub>2</sub>O<sub>3</sub> surface under ball-milling. *Green Chem.* **2013**, *15* (2), 389-397.
14. Do, J.-L.; Mottillo, C.; Tan, D.; Štrukil, V.; Frišćić, T., Mechanochemical Ruthenium-Catalyzed Olefin Metathesis. *J. Am. Chem. Soc.* **2015**, *137* (7), 2476-2479.
15. Braga, D.; D'Addari, D.; Polito, M.; Grepioni, F., Mechanically Induced Expeditious and Selective Preparation of Disubstituted Pyridine/Pyrimidine Ferrocenyl Complexes. *Organometallics* **2004**, *23* (11), 2810-2812.
16. Cravotto, G.; Garella, D.; Tagliapietra, S.; Stolle, A.; Schüßler, S.; Leonhardt, S. E. S.; Ondruschka, B., Suzuki cross-couplings of (hetero)aryl chlorides in the solid-state. *New J. Chem.* **2012**, *36* (6), 1304-1307.
17. Fulmer, D. A.; Shearouse, W. C.; Medonza, S. T.; Mack, J., Solvent-free Sonogashira coupling reaction via high speed ball milling. *Green Chem.* **2009**, *11* (11), 1821-1825.
18. Tullberg, E.; Peters, D.; Frejd, T., The Heck reaction under ball-milling conditions. *J. Organomet. Chem.* **2004**, *689* (23), 3778-3781.
19. Zhu, X.; Liu, J.; Chen, T.; Su, W., Mechanically activated synthesis of (E)-stilbene derivatives by high-speed ball milling. *Appl. Organomet. Chem.* **2012**, *26* (3), 145-147.
20. Jörres, M.; Mersmann, S.; Raabe, G.; Bolm, C., Organocatalytic solvent-free hydrogen bonding-mediated asymmetric Michael additions under ball milling conditions. *Green Chem.* **2013**, *15* (3), 612-616.
21. Rak, M. J.; Saadé, N. K.; Frišćić, T.; Moores, A., Mechanochemical synthesis of ultra-small monodisperse amine-stabilized gold nanoparticles with controllable size. *Green Chem.* **2014**, *16* (1), 86-89.
22. Tsuzuki, T.; McCormick, P. G., Mechanochemical synthesis of nanoparticles. *J. Mater. Sci.* **2004**, *39* (16), 5143-5146.
23. Rightmire, N. R.; Hanusa, T. P.; Rheingold, A. L., Mechanochemical Synthesis of [1,3-(SiMe<sub>3</sub>)<sub>2</sub>C<sub>3</sub>H<sub>3</sub>]<sub>3</sub>(Al,Sc), a Base-Free Tris(allyl)aluminum Complex and Its Scandium Analogue. *Organometallics* **2014**, *33* (21), 5952-5955.
24. Shi, Y. X.; Xu, K.; Clegg, J. K.; Ganguly, R.; Hirao, H.; Frišćić, T.; García, F., The First Synthesis of the Sterically Encumbered Adamantoid Phosphazane P<sub>4</sub>(NtBu)<sub>6</sub>: Enabled by Mechanochemistry. *Angew. Chem. Int. Ed.* **2016**, *55* (41), 12736-12740.

25. Štrukil, V.; Gracin, D.; Magdysyuk, O. V.; Dinnebier, R. E.; Friščić, T., Trapping Reactive Intermediates by Mechanochemistry: Elusive Aryl N-Thiocarbamoylbenzotriazoles as Bench-Stable Reagents. *Angew. Chem. Int. Ed.* **2015**, *54* (29), 8440-8443.
26. Do, J.-L.; Friščić, T., Mechanochemistry: A Force of Synthesis. *ACS Cent. Sci.* **2017**, *3* (1), 13-19.
27. Thompson, L. H.; Doraiswamy, L. K., Sonochemistry: Science and Engineering. *Ind. Eng. Chem. Res.* **1999**, *38* (4), 1215-1249.
28. Flint, E. B.; Suslick, K. S., The Temperature of Cavitation. *Science* **1991**, *253* (5026), 1397-1399.
29. Blake-Perutz, J. R.; Suslick, K. S.; Didenko, Y.; Fang, M. M.; Hyeon, T.; Kolbeck, K. J.; McNamara, W. B.; Mdeleleni, M. M.; Wong, M., Acoustic cavitation and its chemical consequences. *Philos. Trans. R. Soc. A* **1999**, *357* (1751), 335-353.
30. Akbulatov, S.; Boulatov, R., Experimental Polymer Mechanochemistry and its Interpretational Frameworks. *ChemPhysChem* **2017**, *18* (11), 1422-1450.
31. Suslick, K. S., Sonochemistry. *Science* **1990**, *247* (4949), 1439-1445.
32. Cravotto, G.; Gaudino, E. C.; Cintas, P., On the mechanochemical activation by ultrasound. *Chem. Soc. Rev.* **2013**, *42* (18), 7521-7534.
33. Paulusse, J. M. J.; Sijbesma, R. P., Ultrasound in polymer chemistry: Revival of an established technique. *J. Polym. Sci., Part A: Polym. Chem.* **2006**, *44* (19), 5445-5453.
34. Kuijpers, M. W. A.; Iedema, P. D.; Kemmere, M. F.; Keurentjes, J. T. F., The mechanism of cavitation-induced polymer scission; experimental and computational verification. *Polymer* **2004**, *45* (19), 6461-6467.
35. Wiggins, K. M.; Brantley, J. N.; Bielawski, C. W., Methods for activating and characterizing mechanically responsive polymers. *Chem. Soc. Rev.* **2013**, *42* (17), 7130-7147.
36. Potisek, S. L.; Davis, D. A.; Sottos, N. R.; White, S. R.; Moore, J. S., Mechanophore-Linked Addition Polymers. *J. Am. Chem. Soc.* **2007**, *129* (45), 13808-13809.
37. Michael, P.; Binder, W. H., A Mechanochemically Triggered "Click" Catalyst. *Angew. Chem. Int. Ed.* **2015**, *54* (47), 13918-13922.
38. Michael, P.; Sheidaee Mehr, S. K.; Binder, W. H., Synthesis and characterization of polymer linked copper(I) bis(N-heterocyclic carbene) mechanocatalysts. *J. Polym. Sci., Part A: Polym. Chem.* **2017**, *55* (23), 3893-3907.
39. McKenzie, T. G.; Karimi, F.; Ashokkumar, M.; Qiao, G. G., Ultrasound and Sonochemistry for Radical Polymerization: Sound Synthesis. *Chem. Eur. J* **2019**, *25* (21), 5372-5388.
40. Ratoarinoro, N.; Wilhelm, A. M.; Berlan, J.; Delmas, H., Effects of ultrasound emitter type and power on a heterogeneous reaction. *Chem. Eng. J.* **1992**, *50* (1), 27-31.
41. Lavalle, P.; Boulmedais, F.; Schaaf, P.; Jierry, L., Soft-Mechanochemistry: Mechanochemistry Inspired by Nature. *Langmuir* **2016**, *32* (29), 7265-7276.
42. Groote, R.; Szyja, B. M.; Pidko, E. A.; Hensen, E. J. M.; Sijbesma, R. P., Unfolding and Mechanochemical Scission of Supramolecular Polymers Containing a Metal-Ligand Coordination Bond. *Macromolecules* **2011**, *44* (23), 9187-9195.
43. Kryger, M. J.; Munaretto, A. M.; Moore, J. S., Structure-Mechanochemical Activity Relationships for Cyclobutane Mechanophores. *J. Am. Chem. Soc.* **2011**, *133* (46), 18992-18998.
44. Kean, Z. S.; Black Ramirez, A. L.; Yan, Y.; Craig, S. L., Bicyclo[3.2.0]heptane Mechanophores for the Non-scissile and Photochemically Reversible Generation of Reactive Bis-enones. *J. Am. Chem. Soc.* **2012**, *134* (31), 12939-12942.
45. Klukovich, H. M.; Kouznetsova, T. B.; Kean, Z. S.; Lenhardt, J. M.; Craig, S. L., A backbone lever-arm effect enhances polymer mechanochemistry. *Nat. Chem.* **2013**, *5* (2), 110-114.
46. Davis, D. A.; Hamilton, A.; Yang, J.; Cremer, L. D.; Van Gough, D.; Potisek, S. L.; Ong, M. T.; Braun, P. V.; Martínez, T. J.; White, S. R.; Moore, J. S.; Sottos, N. R., Force-induced activation of covalent bonds in mechanoresponsive polymeric materials. *Nature* **2009**, *459*, 68.
47. Beyer, M. K., The mechanical strength of a covalent bond calculated by density functional theory. *J. Chem. Phys.* **2000**, *112* (17), 7307-7312.
48. Goktas, M.; Blank, K. G., Molecular Force Sensors: From Fundamental Concepts toward Applications in Cell Biology. *Adv. Mater. Interfaces* **2017**, *4* (1), 1600441.

49. Schoen, I.; Pruitt, B. L.; Vogel, V., The Yin-Yang of Rigidity Sensing: How Forces and Mechanical Properties Regulate the Cellular Response to Materials. *Annu. Rev. Mater. Res.* **2013**, *43* (1), 589-618.
50. Huang, H.; Kamm, R. D.; Lee, R. T., Cell mechanics and mechanotransduction: pathways, probes, and physiology. *Am. J. Physiol.-Cell Physiol.* **2004**, *287* (1), C1-C11.
51. García, A. J.; Vega, M. a. D.; Boettiger, D., Modulation of Cell Proliferation and Differentiation through Substrate-dependent Changes in Fibronectin Conformation. *Mol. Biol. Cell* **1999**, *10* (3), 785-798.
52. Evans, E. A.; Calderwood, D. A., Forces and Bond Dynamics in Cell Adhesion. *Science* **2007**, *316* (5828), 1148-1153.
53. Goodman, M. B.; Lumpkin, E. A.; Ricci, A.; Tracey, W. D.; Kernan, M.; Nicolson, T., Molecules and Mechanisms of Mechanotransduction. *J. Neurosci.* **2004**, *24* (42), 9220-9222.
54. Comrie, J. E.; Huck, W. T. S., Exploring Actuation and Mechanotransduction Properties of Polymer Brushes. *Macromol. Rapid Commun.* **2008**, *29* (7), 539-546.
55. Crawley, J. T. B.; de Groot, R.; Xiang, Y.; Luken, B. M.; Lane, D. A., Unraveling the scissile bond: how ADAMTS13 recognizes and cleaves von Willebrand factor. *Blood* **2011**, *118* (12), 3212-3221.
56. Gillespie, P. G.; Walker, R. G., Molecular basis of mechanosensory transduction. *Nature* **2001**, *413*, 194.
57. Woo, S.-H.; Lukacs, V.; de Nooij, J. C.; Zaytseva, D.; Criddle, C. R.; Francisco, A.; Jessell, T. M.; Wilkinson, K. A.; Patapoutian, A., Piezo2 is the principal mechanotransduction channel for proprioception. *Nat. Neurosci.* **2015**, *18*, 1756.
58. Vogel, V., Mechanotransduction involving multimodular Proteins: Converting Force into Biochemical Signals. *Annu. Rev. Biophys.* **2006**, *35* (1), 459-488.
59. Jasti, J.; Furukawa, H.; Gonzales, E. B.; Gouaux, E., Structure of acid-sensing ion channel 1 at 1.9 Å resolution and low pH. *Nature* **2007**, *449*, 316.
60. Chalfie, M., Neurosensory mechanotransduction. *Nat. Rev. Mol. Cell Biol.* **2009**, *10*, 44.
61. Mertz, D.; Vogt, C.; Hemmerlé, J.; Mutterer, J.; Ball, V.; Voegel, J.-C.; Schaaf, P.; Lavallo, P., Mechanotransductive surfaces for reversible biocatalysis activation. *Nat. Mater.* **2009**, *8*, 731.
62. Longo, J.; Yao, C.; Rios, C.; Chau, N. T. T.; Boulmedais, F.; Hemmerlé, J.; Lavallo, P.; Schiller, S. M.; Schaaf, P.; Jierry, L., Reversible biomechano-responsive surface based on green fluorescent protein genetically modified with unnatural amino acids. *Chem. Commun.* **2015**, *51* (1), 232-235.
63. Finer, J. T.; Simmons, R. M.; Spudich, J. A., Single myosin molecule mechanics: piconewton forces and nanometre steps. *Nature* **1994**, *368*, 113.
64. Jiang, G.; Giannone, G.; Critchley, D. R.; Fukumoto, E.; Sheetz, M. P., Two-piconewton slip bond between fibronectin and the cytoskeleton depends on talin. *Nature* **2003**, *424*, 334.
65. Polacheck, W. J.; Chen, C. S., Measuring cell-generated forces: a guide to the available tools. *Nat. Methods* **2016**, *13*, 415.
66. Helenius, J.; Heisenberg, C.-P.; Gaub, H. E.; Muller, D. J., Single-cell force spectroscopy. *J. Cell Sci.* **2008**, *121* (11), 1785-1791.
67. Kokkoli, E.; Ochsenhirt, S. E.; Tirrell, M., Collective and Single-Molecule Interactions of  $\alpha 5\beta 1$  Integrins. *Langmuir* **2004**, *20* (6), 2397-2404.
68. Wang, Y.; Wang, N., FRET and mechanobiology. *Integr. Biol.* **2009**, *1* (10), 565-573.
69. Perez-Jimenez, R.; Garcia-Manyes, S.; Ainarapu, S. R. K.; Fernandez, J. M., Mechanical Unfolding Pathways of the Enhanced Yellow Fluorescent Protein Revealed by Single Molecule Force Spectroscopy. *J. Biol. Chem.* **2006**, *281* (52), 40010-40014.
70. Zhang, H.; Chen, Y.; Lin, Y.; Fang, X.; Xu, Y.; Ruan, Y.; Weng, W., Spiropyran as a Mechanochromic Probe in Dual Cross-Linked Elastomers. *Macromolecules* **2014**, *47* (19), 6783-6790.
71. Gossweiler, G. R.; Kouznetsova, T. B.; Craig, S. L., Force-Rate Characterization of Two Spiropyran-Based Molecular Force Probes. *J. Am. Chem. Soc.* **2015**, *137* (19), 6148-6151.
72. Fang, X.; Zhang, H.; Chen, Y.; Lin, Y.; Xu, Y.; Weng, W., Biomimetic Modular Polymer with Tough and Stress Sensing Properties. *Macromolecules* **2013**, *46* (16), 6566-6574.
73. Hong, G.; Zhang, H.; Lin, Y.; Chen, Y.; Xu, Y.; Weng, W.; Xia, H., Mechanoresponsive Healable Metallosupramolecular Polymers. *Macromolecules* **2013**, *46* (21), 8649-8656.

74. Lee, C. K.; Diesendruck, C. E.; Lu, E.; Pickett, A. N.; May, P. A.; Moore, J. S.; Braun, P. V., Solvent Swelling Activation of a Mechanophore in a Polymer Network. *Macromolecules* **2014**, *47* (8), 2690-2694.
75. Zhang, H.; Gao, F.; Cao, X.; Li, Y.; Xu, Y.; Weng, W.; Boulatov, R., Mechanochromism and Mechanical-Force-Triggered Cross-Linking from a Single Reactive Moiety Incorporated into Polymer Chains. *Angew. Chem. Int. Ed.* **2016**, *55* (9), 3040-3044.
76. Göstl, R.; Sijbesma, R. P.,  $\pi$ -extended anthracenes as sensitive probes for mechanical stress. *Chem. Sci.* **2016**, *7* (1), 370-375.
77. Kim, G.; Lau, V. M.; Halmes, A. J.; Oelze, M. L.; Moore, J. S.; Li, K. C., High-intensity focused ultrasound-induced mechanochemical transduction in synthetic elastomers. *Proc. Natl. Acad. Sci.* **2019**, *116* (21), 10214-10222.
78. Wang, L.; Zhou, W.; Tang, Q.; Yang, H.; Zhou, Q.; Zhang, X., Rhodamine-Functionalized Mechanochromic and Mechanofluorescent Hydrogels with Enhanced Mechanoresponsive Sensitivity. *Polymers* **2018**, *10* (9), 994.
79. Chen, Y.; Spiering, A. J. H.; Karthikeyan, S.; Peters, G. W. M.; Meijer, E. W.; Sijbesma, R. P., Mechanically induced chemiluminescence from polymers incorporating a 1,2-dioxetane unit in the main chain. *Nat. Chem.* **2012**, *4*, 559.
80. Clough, J. M.; Balan, A.; van Daal, T. L. J.; Sijbesma, R. P., Probing Force with Mechanobase-Induced Chemiluminescence. *Angew. Chem. Int. Ed.* **2016**, *55* (4), 1445-1449.
81. Clough, J. M.; van der Gucht, J.; Sijbesma, R. P., Mechanoluminescent Imaging of Osmotic Stress-Induced Damage in a Glassy Polymer Network. *Macromolecules* **2017**, *50* (5), 2043-2053.
82. Yuan, Y.; Chen, W.; Ma, Z.; Deng, Y.; Chen, Y.; Chen, Y.; Hu, W., Enhanced optomechanical properties of mechanochemiluminescent poly(methyl acrylate) composites with granulated fluorescent conjugated microporous polymer fillers. *Chem. Sci.* **2019**, *10* (7), 2206-2211.
83. Paulusse, J. M. J.; Sijbesma, R. P., Reversible Mechanochemistry of a PdII Coordination Polymer. *Angew. Chem. Int. Ed.* **2004**, *43* (34), 4460-4462.
84. Paulusse, J. M. J.; Huijbers, J. P. J.; Sijbesma, R. P., Reversible, High Molecular Weight Palladium and Platinum Coordination Polymers Based on Phosphorus Ligands. *Macromolecules* **2005**, *38* (15), 6290-6298.
85. Paulusse, J. M. J.; Huijbers, J. P. J.; Sijbesma, R. P., Quantification of Ultrasound-Induced Chain Scission in PdII-Phosphine Coordination Polymers. *Chem. Eur. J* **2006**, *12* (18), 4928-4934.
86. Paulusse, J. M. J.; Sijbesma, R. P., Selectivity of mechanochemical chain scission in mixed palladium(ii) and platinum(ii) coordination polymers. *Chem. Commun.* **2008**, (37), 4416-4418.
87. Karthikeyan, S.; Potisek, S. L.; Piermattei, A.; Sijbesma, R. P., Highly Efficient Mechanochemical Scission of Silver-Carbene Coordination Polymers. *J. Am. Chem. Soc.* **2008**, *130* (45), 14968-14969.
88. Piermattei, A.; Karthikeyan, S.; Sijbesma, R. P., Activating catalysts with mechanical force. *Nat. Chem.* **2009**, *1* (2), 133-137.
89. Rooze, J.; Groote, R.; Jakobs, R. T. M.; Sijbesma, R. P.; van Iersel, M. M.; Rebrov, E. V.; Schouten, J. C.; Keurentjes, J. T. F., Mechanism of Ultrasound Scission of a Silver-Carbene Coordination Polymer. *J. Phys. Chem. B* **2011**, *115* (38), 11038-11043.
90. Groote, R.; van Haandel, L.; Sijbesma, R. P., The effect of molecular weight and catalyst concentration on catalytic activity in mechanochemically activated transesterification using silver(I)-N-heterocyclic carbene latent catalysts. *J. Polym. Sci., Part A: Polym. Chem.* **2012**, *50* (23), 4929-4935.
91. Groote, R.; Jakobs, R. T. M.; Sijbesma, R. P., Performance of Mechanochemically Activated Catalysts Is Enhanced by Suppression of the Thermal Effects of Ultrasound. *ACS Macro Let.* **2012**, *1* (8), 1012-1015.
92. Jakobs, R. T. M.; Sijbesma, R. P., Mechanical Activation of a Latent Olefin Metathesis Catalyst and Persistence of its Active Species in ROMP. *Organometallics* **2012**, *31* (6), 2476-2481.
93. Jakobs, R. T. M.; Ma, S.; Sijbesma, R. P., Mechanocatalytic Polymerization and Cross-Linking in a Polymeric Matrix. *ACS Macro Let.* **2013**, *2* (7), 613-616.
94. Michael, P.; Biewend, M.; Binder, W. H., Mechanochemical Activation of Fluorogenic CuAAC "Click" Reactions for Stress-Sensing Applications. *Macromol. Rapid Commun.* **2018**, *39* (22), 1800376.
95. Biewend, M.; Neumann, S.; Michael, P.; Binder, W. H., Synthesis of polymer-linked copper(i) bis(N-heterocyclic carbene) complexes of linear and chain extended architecture. *Polym. Chem.* **2019**, *10* (9), 1078-1088.

96. Di Giannantonio, M.; Ayer, M. A.; Verde-Sesto, E.; Lattuada, M.; Weder, C.; Fromm, K. M., Triggered Metal Ion Release and Oxidation: Ferrocene as a Mechanophore in Polymers. *Angew. Chem. Int. Ed.* **2018**, *57* (35), 11445-11450.
97. Sha, Y.; Zhang, Y.; Xu, E.; Wang, Z.; Zhu, T.; Craig, S. L.; Tang, C., Quantitative and Mechanistic Mechanochemistry in Ferrocene Dissociation. *ACS Macro Lett.* **2018**, *7* (10), 1174-1179.
98. Sha, Y.; Zhang, Y.; Xu, E.; McAlister, C. W.; Zhu, T.; Craig, Stephen L.; Tang, C., Generalizing metallocene mechanochemistry to ruthenocene mechanophores. *Chem. Sci.* **2019**, *10* (19), 4959-4965.
99. Larsen, M. B.; Boydston, A. J., "Flex-Activated" Mechanophores: Using Polymer Mechanochemistry To Direct Bond Bending Activation. *J. Am. Chem. Soc.* **2013**, *135* (22), 8189-8192.
100. Larsen, M. B.; Boydston, A. J., Successive Mechanochemical Activation and Small Molecule Release in an Elastomeric Material. *J. Am. Chem. Soc.* **2014**, *136* (4), 1276-1279.
101. Diesendruck, C. E.; Steinberg, B. D.; Sugai, N.; Silberstein, M. N.; Sottos, N. R.; White, S. R.; Braun, P. V.; Moore, J. S., Proton-Coupled Mechanochemical Transduction: A Mechanogenerated Acid. *J. Am. Chem. Soc.* **2012**, *134* (30), 12446-12449.
102. Lenhardt, J. M.; Ong, M. T.; Choe, R.; Evenhuis, C. R.; Martinez, T. J.; Craig, S. L., Trapping a Diradical Transition State by Mechanochemical Polymer Extension. *Science* **2010**, *329* (5995), 1057-1060.
103. Lenhardt, J. M.; Black, A. L.; Craig, S. L., gem-Dichlorocyclopropanes as Abundant and Efficient Mechanophores in Polybutadiene Copolymers under Mechanical Stress. *J. Am. Chem. Soc.* **2009**, *131* (31), 10818-10819.
104. Kean, Z. S.; Craig, S. L., Mechanochemical remodeling of synthetic polymers. *Polymer* **2012**, *53* (5), 1035-1048.
105. Radiom, M.; Kong, P.; Maroni, P.; Schäfer, M.; Kilbinger, A.; Borkovec, M., Mechanically Induced Cis-to-Trans Isomerization of Carbon-Carbon Double Bond Using Atomic Force Microscopy. *Phys. Chem. Chem. Phys.* **2016**, *18* (18).
106. Li, J.; Nagamani, C.; Moore, J. S., Polymer Mechanochemistry: From Destructive to Productive. *Acc. Chem. Res.* **2015**, *48* (8), 2181-2190.
107. Staudinger H.; Bondy H. F., Über Isopren und Kautschuk, 19. Mitteil.: Über die Molekülgröße des Kautschuks und der Balata. *Chem. Ber.* **1930**, *63* (3), 734-736.
108. Staudinger, H.; Leupold, E. O., Über Isopren und Kautschuk, 18. Mitteil.: Viscositäts-Untersuchungen an Balata. *Chem. Ber.* **1930**, *63* (3), 730-733.
109. Staudinger, H.; Heuer, W., Über hochpolymere Verbindungen, 93. Mitteil.: Über das Zerreißen der Faden-Moleküle des Poly-styrols. *Chem. Ber.* **1934**, *67* (7), 1159-1164.
110. Kauzmann, W.; Eyring, H., The Viscous Flow of Large Molecules. *J. Am. Chem. Soc.* **1940**, *62* (11), 3113-3125.
111. Sohma, J., Mechanochemistry of polymers. *Prog. Polym. Sci.* **1989**, *14* (4), 451-596.
112. Kuhn, W.; Kuhn, H., Wanderungsdoppelbrechung von Fadenmolekelionen im elektrischen Feld. *Helv. Chim. Acta* **1944**, *27* (1), 493-499.
113. Encina, M. V.; Lissi, E.; Sarasúa, M.; Gargallo, L.; Radic, D., Ultrasonic degradation of polyvinylpyrrolidone: Effect of peroxide linkages. *J. Polym. Sci., Polym. Lett. Ed.* **1980**, *18* (12), 757-760.
114. Berkowski, K. L.; Potisek, S. L.; Hickenboth, C. R.; Moore, J. S., Ultrasound-Induced Site-Specific Cleavage of Azo-Functionalized Poly(ethylene glycol). *Macromolecules* **2005**, *38* (22), 8975-8978.
115. Li, Y.; Nese, A.; Matyjaszewski, K.; Sheiko, S. S., Molecular Tensile Machines: Anti-Arrhenius Cleavage of Disulfide Bonds. *Macromolecules* **2013**, *46* (18), 7196-7201.
116. Diesendruck, C. E.; Peterson, G. I.; Kulik, H. J.; Kaitz, J. A.; Mar, B. D.; May, P. A.; White, S. R.; Martínez, T. J.; Boydston, A. J.; Moore, J. S., Mechanically triggered heterolytic unzipping of a low-ceiling-temperature polymer. *Nat. Chem.* **2014**, *6*, 623.
117. Shiraki, T.; Diesendruck, C. E.; Moore, J. S., The mechanochemical production of phenyl cations through heterolytic bond scission. *Faraday Discuss.* **2014**, *170* (0), 385-394.
118. Surampudi, S. K.; Patel, H. R.; Nagarjuna, G.; Venkataraman, D., Mechano-isomerization of azobenzene. *Chem. Commun.* **2013**, *49* (68), 7519-7521.
119. De Bo, G., Mechanochemistry of the mechanical bond. *Chem. Sci.* **2018**, *9* (1), 15-21.

120. Caruso, M. M.; Davis, D. A.; Shen, Q.; Odom, S. A.; Sottos, N. R.; White, S. R.; Moore, J. S., Mechanically-Induced Chemical Changes in Polymeric Materials. *Chem. Rev* **2009**, *109* (11), 5755-5798.
121. Ong, M. T.; Leiding, J.; Tao, H.; Virshup, A. M.; Martínez, T. J., First Principles Dynamics and Minimum Energy Pathways for Mechanochemical Ring Opening of Cyclobutene. *J. Am. Chem. Soc.* **2009**, *131* (18), 6377-6379.
122. May, P. A.; Moore, J. S., Polymer mechanochemistry: techniques to generate molecular force via elongational flows. *Chem. Soc. Rev.* **2013**, *42* (18), 7497-7506.
123. Buchholz, B. A.; Zahn, J. M.; Kenward, M.; Slater, G. W.; Barron, A. E., Flow-induced chain scission as a physical route to narrowly distributed, high molar mass polymers. *Polymer* **2004**, *45* (4), 1223-1234.
124. Lenhardt, J. M.; Black, A. L.; Beiermann, B. A.; Steinberg, B. D.; Rahman, F.; Samborski, T.; Elsagr, J.; Moore, J. S.; Sottos, N. R.; Craig, S. L., Characterizing the mechanochemically active domains in gem-dihalocyclopropanated polybutadiene under compression and tension. *J. Mater. Chem.* **2011**, *21* (23), 8454-8459.
125. Beiermann, B. A.; Davis, D. A.; Kramer, S. L. B.; Moore, J. S.; Sottos, N. R.; White, S. R., Environmental effects on mechanochemical activation of spiropyran in linear PMMA. *J. Mater. Chem.* **2011**, *21* (23), 8443-8447.
126. Beiermann, B. A.; Kramer, S. L. B.; May, P. A.; Moore, J. S.; White, S. R.; Sottos, N. R., The Effect of Polymer Chain Alignment and Relaxation on Force-Induced Chemical Reactions in an Elastomer. *Adv. Funct. Mater.* **2014**, *24* (11), 1529-1537.
127. Chen, Y.; Sijbesma, R. P., Dioxetanes as Mechanoluminescent Probes in Thermoplastic Elastomers. *Macromolecules* **2014**, *47* (12), 3797-3805.
128. Kingsbury, C. M.; May, P. A.; Davis, D. A.; White, S. R.; Moore, J. S.; Sottos, N. R., Shear activation of mechanophore-crosslinked polymers. *J. Mater. Chem.* **2011**, *21* (23), 8381-8388.
129. Suslick, K. S.; Price, G. J., Applications of Ultrasound to Materials Chemistry. *Annu. Rev. Mater. Sci.* **1999**, *29* (1), 295-326.
130. Gooberman, G., Ultrasonic degradation of polystyrene. Part 1. A proposed mechanism for degradation. *J. Polym. Sci.* **1960**, *42* (139), 25-33.
131. Okkuama, M.; Hirose, T., Mechanics of ultrasonic degradation of linear high polymer and ultrasonic cavitation. *J. Appl. Polym. Sci.* **1963**, *7* (2), 591-602.
132. Lenhardt, J. M.; Black Ramirez, A. L.; Lee, B.; Kouznetsova, T. B.; Craig, S. L., Mechanistic Insights into the Sonochemical Activation of Multimechanophore Cyclopropanated Polybutadiene Polymers. *Macromolecules* **2015**, *48* (18), 6396-6403.
133. Price, G. J.; Smith, P. F., Ultrasonic degradation of polymer solutions—III. The effect of changing solvent and solution concentration. *Eur. Polym. J.* **1993**, *29* (2), 419-424.
134. Vijayalakshmi, S. P.; Madras, G., Effect of initial molecular weight and solvents on the ultrasonic degradation of poly(ethylene oxide). *Polym. Degrad. Stab.* **2005**, *90* (1), 116-122.
135. Van der hoff, B. M. E.; Gall, C. E., A Method for Following Changes in Molecular Weight Distributions of Polymers on Degradation: Development and Comparison with Ultrasonic Degradation Experiments. *J. Macromol. Sci. A* **1977**, *11* (9), 1739-1758.
136. Boulatov, R., *Polymer Mechanochemistry*. Springer International Publishing: Heidelberg, 2015; Vol. 369.
137. Taghizadeh, M. T.; Asadpour, T., Effect of molecular weight on the ultrasonic degradation of poly(vinyl-pyrrolidone). *Ultrason. Sonochem.* **2009**, *16* (2), 280-286.
138. Price, G. J.; Smith, P. F., Ultrasonic degradation of polymer solutions. 1. Polystyrene revisited. *Polym. Int.* **1991**, *24* (3), 159-164.
139. Kean, Z. S.; Hawk, J. L.; Lin, S.; Zhao, X.; Sijbesma, R. P.; Craig, S. L., Increasing the Maximum Achievable Strain of a Covalent Polymer Gel Through the Addition of Mechanically Invisible Cross-Links. *Adv. Mater.* **2014**, *26* (34), 6013-6018.
140. Chen, Y.; Zhang, H.; Fang, X.; Lin, Y.; Xu, Y.; Weng, W., Mechanical Activation of Mechanophore Enhanced by Strong Hydrogen Bonding Interactions. *ACS Macro Lett.* **2014**, *3* (2), 141-145.
141. Beiermann, B. A.; Kramer, S. L. B.; Moore, J. S.; White, S. R.; Sottos, N. R., Role of Mechanophore Orientation in Mechanochemical Reactions. *ACS Macro Lett.* **2012**, *1* (1), 163-166.

142. Hossain, D.; Tschopp, M. A.; Ward, D. K.; Bouvard, J. L.; Wang, P.; Horstemeyer, M. F., Molecular dynamics simulations of deformation mechanisms of amorphous polyethylene. *Polymer* **2010**, *51* (25), 6071-6083.
143. Biewend, M.; Michael, P.; Binder, W. H., Detection of stress in polymers: mechanochemical activation of CuAAC click reactions in poly(urethane) networks. *Soft Matter* **2020**, *16* (5), 1137-1141.
144. Fu, G. C., Enantioselective Nucleophilic Catalysis with “Planar-Chiral” Heterocycles. *Acc. Chem. Res.* **2000**, *33* (6), 412-420.
145. Yan, Y.; Zhang, J.; Ren, L.; Tang, C., Metal-containing and related polymers for biomedical applications. *Chem. Soc. Rev.* **2016**, *45* (19), 5232-5263.
146. Astruc, D., Why is Ferrocene so Exceptional? *Eur. J. Inorg. Chem.* **2017**, *2017* (1), 6-29.
147. Rostovtsev, V. V.; Green, L. G.; Fokin, V. V.; Sharpless, K. B., A Stepwise Huisgen Cycloaddition Process: Copper(I)-Catalyzed Regioselective “Ligation” of Azides and Terminal Alkynes. *Angew. Chem. Int. Ed.* **2002**, *41* (14), 2596-2599.
148. Tornøe, C. W.; Christensen, C.; Meldal, M., Peptidotriazoles on Solid Phase: [1,2,3]-Triazoles by Regiospecific Copper(I)-Catalyzed 1,3-Dipolar Cycloadditions of Terminal Alkynes to Azides. *J. Org. Chem.* **2002**, *67* (9), 3057-3064.
149. Lewis, W. G.; Green, L. G.; Grynszpan, F.; Radić, Z.; Carlier, P. R.; Taylor, P.; Finn, M. G.; Sharpless, K. B., Click Chemistry In Situ: Acetylcholinesterase as a Reaction Vessel for the Selective Assembly of a Femtomolar Inhibitor from an Array of Building Blocks. *Angew. Chem. Int. Ed.* **2002**, *41* (6), 1053-1057.
150. Huisgen, R., 1.3-Dipolare Cycloadditionen Rückschau und Ausblick. *Angew. Chem.* **1963**, *75* (13), 604-637.
151. Kolb, H. C.; Finn, M. G.; Sharpless, K. B., Click Chemistry: Diverse Chemical Function from a Few Good Reactions. *Angew. Chem. Int. Ed.* **2001**, *40* (11), 2004-2021.
152. Glaser, C., Beiträge zur Kenntniss des Acetylnylbenzols. *Ber. Dtsch. Chem. Ges.* **1869**, *2* (1), 422-424.
153. Binder, W. H.; Sachsenhofer, R., ‘Click’ Chemistry in Polymer and Materials Science. *Macromol. Rapid Commun.* **2007**, *28* (1), 15-54.
154. Hein, J. E.; Fokin, V. V., Copper-catalyzed azide-alkyne cycloaddition (CuAAC) and beyond: new reactivity of copper(I) acetylides. *Chem. Soc. Rev.* **2010**, *39* (4), 1302-1315.
155. Binder, W. H.; Sachsenhofer, R., ‘Click’ Chemistry in Polymer and Material Science: An Update. *Macromol. Rapid Commun.* **2008**, *29* (12-13), 952-981.
156. Meldal, M.; Tornøe, C. W., Cu-Catalyzed Azide-Alkyne Cycloaddition. *Chem. Rev.* **2008**, *108* (8), 2952-3015.
157. Golas, P. L.; Tsarevsky, N. V.; Sumerlin, B. S.; Matyjaszewski, K., Catalyst Performance in “Click” Coupling Reactions of Polymers Prepared by ATRP: Ligand and Metal Effects. *Macromolecules* **2006**, *39* (19), 6451-6457.
158. Lewis, W. G.; Magallon, F. G.; Fokin, V. V.; Finn, M. G., Discovery and Characterization of Catalysts for Azide-Alkyne Cycloaddition by Fluorescence Quenching. *J. Am. Chem. Soc.* **2004**, *126* (30), 9152-9153.
159. Díez-González, S.; Nolan, S. P., [(NHC)<sub>2</sub>Cu]X Complexes as Efficient Catalysts for Azide-Alkyne Click Chemistry at Low Catalyst Loadings. *Angew. Chem.* **2008**, *120* (46), 9013-9016.
160. Lazreg, F.; Nahra, F.; Cazin, C. S. J., Copper-NHC complexes in catalysis. *Coord. Chem. Rev.* **2015**, *293-294*, 48-79.
161. Lazreg, F.; Slawin, A. M. Z.; Cazin, C. S. J., Heteroleptic Bis(N-heterocyclic carbene)Copper(I) Complexes: Highly Efficient Systems for the [3+2] Cycloaddition of Azides and Alkynes. *Organometallics* **2012**, *31* (22), 7969-7975.
162. Díez-González, S.; Correa, A.; Cavallo, L.; Nolan, S. P., (NHC)Copper(I)-Catalyzed [3+2] Cycloaddition of Azides and Mono- or Disubstituted Alkynes. *Chem. Eur. J.* **2006**, *12* (29), 7558-7564.
163. Egbert, J. D.; Cazin, C. S. J.; Nolan, S. P., Copper N-heterocyclic carbene complexes in catalysis. *Catal. Sci. Technol.* **2013**, *3* (4), 912-926.
164. Meldal, M., Polymer “Clicking” by CuAAC Reactions. *Macromol. Rapid Commun.* **2008**, *29* (12-13), 1016-1051.
165. Rodionov, V. O.; Fokin, V. V.; Finn, M. G., Mechanism of the Ligand-Free CuI-Catalyzed Azide-Alkyne Cycloaddition Reaction. *Angew. Chem. Int. Ed.* **2005**, *44* (15), 2210-2215.

166. Canalle, L. A.; Lowik, D. W. P. M.; van Hest, J. C. M., Polypeptide-polymer bioconjugates. *Chem. Soc. Rev.* **2010**, *39* (1), 329-353.
167. Ahmad Fuaad, A. A. H.; Azmi, F.; Skwarczynski, M.; Toth, I., Peptide conjugation via CuAAC 'click' chemistry. *Molecules (Basel, Switzerland)* **2013**, *18* (11), 13148-13174.
168. Le Droumaguet, C.; Wang, C.; Wang, Q., Fluorogenic click reaction. *Chem. Soc. Rev.* **2010**, *39* (4), 1233-1239.
169. Gragert, M.; Schunack, M.; Binder, W. H., Azide/Alkyne-“Click”-Reactions of Encapsulated Reagents: Toward Self-Healing Materials. *Macromol. Rapid Commun.* **2011**, *32* (5), 419-425.
170. Döhler, D.; Michael, P.; Binder, W. H., CuAAC-Based Click Chemistry in Self-Healing Polymers. *Acc. Chem. Res.* **2017**, *50* (10), 2610-2620.
171. Ribas-Arino, J.; Shiga, M.; Marx, D., Mechanochemical Transduction of Externally Applied Forces to Mechanophores. *J. Am. Chem. Soc.* **2010**, *132* (30), 10609-10614.
172. Klukovich, H. M.; Kean, Z. S.; Ramirez, A. L. B.; Lenhardt, J. M.; Lin, J.; Hu, X.; Craig, S. L., Tension Trapping of Carbonyl Ylides Facilitated by a Change in Polymer Backbone. *J. Am. Chem. Soc.* **2012**, *134* (23), 9577-9580.
173. Wang, J.; Kouznetsova, T. B.; Kean, Z. S.; Fan, L.; Mar, B. D.; Martínez, T. J.; Craig, S. L., A Remote Stereochemical Lever Arm Effect in Polymer Mechanochemistry. *J. Am. Chem. Soc.* **2014**, *136* (43), 15162-15165.
174. Ramirez, A. L. B.; Kean, Z. S.; Orlicki, J. A.; Champhekar, M.; Elsagr, S. M.; Krause, W. E.; Craig, S. L., Mechanochemical strengthening of a synthetic polymer in response to typically destructive shear forces. *Nat. Chem.* **2013**, *5* (9), 757-761.
175. Lee, B.; Niu, Z.; Wang, J.; Slobodnick, C.; Craig, S. L., Relative Mechanical Strengths of Weak Bonds in Sonochemical Polymer Mechanochemistry. *J. Am. Chem. Soc.* **2015**, *137* (33), 10826-10832.
176. Houk, K. N.; Rondan, N. G.; Santiago, C.; Gallo, C. J.; Gandour, R. W.; Griffin, G. W., Theoretical studies of the structures and reactions of substituted carbonyl ylides. *J. Am. Chem. Soc.* **1980**, *102* (5), 1504-1512.
177. Qin, G.; Hu, X.; Cebe, P.; Kaplan, D. L., Mechanism of resilin elasticity. *Nat. Commun.* **2012**, *3*, 1003.
178. Yeo, G. C.; Baldock, C.; Tuukkanen, A.; Roessle, M.; Dyksterhuis, L. B.; Wise, S. G.; Matthews, J.; Mithieux, S. M.; Weiss, A. S., Tropoelastin bridge region positions the cell-interactive C terminus and contributes to elastic fiber assembly. *Proc. Natl. Acad. Sci.* **2012**, *109* (8), 2878-2883.
179. Yao, M.; Goult, B. T.; Klapholz, B.; Hu, X.; Toseland, C. P.; Guo, Y.; Cong, P.; Sheetz, M. P.; Yan, J., The mechanical response of talin. *Nat. Commun.* **2016**, *7*, 11966.
180. Eckels, E. C.; Tapia-Rojo, R.; Rivas-Pardo, J. A.; Fernández, J. M., The Work of Titin Protein Folding as a Major Driver in Muscle Contraction. *Annu. Rev. Physiol.* **2018**, *80* (1), 327-351.
181. Baldock, C.; Oberhauser, A. F.; Ma, L.; Lammie, D.; Siegler, V.; Mithieux, S. M.; Tu, Y.; Chow, J. Y. H.; Suleman, F.; Malfois, M.; Rogers, S.; Guo, L.; Irving, T. C.; Wess, T. J.; Weiss, A. S., Shape of tropoelastin, the highly extensible protein that controls human tissue elasticity. *Proc. Natl. Acad. Sci.* **2011**, *108* (11), 4322-4327.
182. Green, E. M.; Mansfield, J. C.; Bell, J. S.; Winlove, C. P., The structure and micromechanics of elastic tissue. *Interface Focus* **2014**, *4* (2), 20130058-20130058.
183. Anwar, R. A., Elastin: A brief Review. *Biochem. Educ.* **1990**, *18* (4), 162-166.
184. Li, B.; Daggett, V., Molecular basis for the extensibility of elastin. *J. Muscle Res. Cell Motil.* **2002**, *23* (5-6), 561-573.
185. Keeley, F. W.; Bellingham, C. M.; Woodhouse, K. A., Elastin as a self-organizing biomaterial: use of recombinantly expressed human elastin polypeptides as a model for investigations of structure and self-assembly of elastin. *Philos. Trans. R. Soc. B* **2002**, *357* (1418), 185-189.
186. Mariani, T. J.; Sandefur, S.; Pierce, R. A., Elastin in Lung Development. *Exp. Lung Res.* **1997**, *23* (2), 131-145.
187. Almine, J.; Wise, S.; Weiss, A., Elastin signaling in wound repair. *Birth Defects Res.* **2012**, *96* (3), 248-57.
188. Jones, P. A.; Scott-Burden, T.; Gevers, W., Glycoprotein, elastin, and collagen secretion by rat smooth muscle cells. *Proc. Natl. Acad. Sci. U. S. A.* **1979**, *76* (1), 353-357.
189. Mecham, R. P.; Madaras, J.; McDonald, J. A.; Ryan, U., Elastin production by cultured calf pulmonary artery endothelial cells. *J. Cell. Physiol.* **1983**, *116* (3), 282-288.

190. Sephel, G. C.; Davidson, J. M., Elastin Production in Human Skin Fibroblast Cultures and Its Decline with Age. *J. Invest. Dermatol.* **1986**, *86* (3), 279-285.
191. Davis, E. C.; Mecham, R. P., Intracellular trafficking of tropoelastin. *Matrix Biol.* **1998**, *17* (4), 245-254.
192. Long, J. L.; Tranquillo, R. T., Elastic fiber production in cardiovascular tissue-equivalents. *Matrix Biol.* **2003**, *22* (4), 339-350.
193. Sandberg, L. B.; Weissman, N.; Smith, D. W., Purification and partial characterization of a soluble elastin-like protein from copper-deficient porcine aorta. *Biochemistry* **1969**, *8* (7), 2940-2945.
194. Daamen, W. F.; Veerkamp, J. H.; van Hest, J. C. M.; van Kuppevelt, T. H., Elastin as a biomaterial for tissue engineering. *Biomaterials* **2007**, *28* (30), 4378-4398.
195. Kagan, H. M.; Sullivan, K. A., Lysyl oxidase: Preparation and role in elastin biosynthesis. In *Methods Enzymol.*, Academic Press: 1982; Vol. 82, pp 637-650.
196. Kagan, H. M.; Cai, P., Isolation of active site peptides of lysyl oxidase. In *Methods Enzymol.*, Academic Press: 1995; Vol. 258, pp 122-132.
197. Thomas, J.; Elsdon, D. F.; Partridge, S. M., Degradation Products from Elastin: Partial Structure of Two Major Degradation Products from the Cross-linkages in Elastin. *Nature* **1963**, *200* (4907), 651-652.
198. Davis, N. R.; Anwar, R. A., Mechanism of formation of desmosine and isodesmosine cross-links of elastin. *J. Am. Chem. Soc.* **1970**, *92* (12), 3778-3782.
199. Umeda, H.; Takeuchi, M.; Suyama, K., Two New Elastin Cross-links Having Pyridine Skeleton: Implication of Ammonia in Elastin Cross-Linking in Vivo. *J. Biol. Chem.* **2001**, *276* (16), 12579-12587.
200. Mithieux, S. M.; Weiss, A. S., Elastin. In *Adv. Protein Chem.*, Academic Press: 2005; Vol. Volume 70, pp 437-461.
201. Kakivaya, S. R.; Hoeve, C. A., The glass point of elastin. *Proc. Natl. Acad. Sci. U. S. A.* **1975**, *72* (9), 3505-3507.
202. Urry, D. W., On the molecular mechanisms of elastin coacervation and coacervate calcification. *Faraday Discuss.* **1976**, *61* (0), 205-212.
203. Urry, D. W., Molecular perspectives of vascular wall structure and disease: The elastic component. *Perspect. Biol. Med.* **1978**, *21* (2), 265-295.
204. Indik, Z.; Yeh, H.; Ornstein-Goldstein, N.; Sheppard, P.; Anderson, N.; Rosenbloom, J. C.; Peltonen, L.; Rosenbloom, J., Alternative splicing of human elastin mRNA indicated by sequence analysis of cloned genomic and complementary DNA. *Proc. Natl. Acad. Sci. U. S. A.* **1987**, *84* (16), 5680-5684.
205. Perticaroli, S.; Ehlers, G.; Jalarvo, N.; Katsaras, J.; Nickels, J. D., Elasticity and Inverse Temperature Transition in Elastin. *J. Phys. Chem. Lett.* **2015**, *6* (20), 4018-4025.
206. Urry, D. W.; Starcher, B.; Partridge, S. M., Coacervation of solubilized elastin effects a notable conformational change. *Nature* **1969**, *222* (5195), 795-796.
207. Li, B.; Alonso, D. O. V.; Daggett, V., The molecular basis for the inverse temperature transition of elastin. *J. Mol. Biol.* **2001**, *305* (3), 581-592.
208. Vrhovski, B.; Weiss, A. S., Biochemistry of tropoelastin. *Eur. J. Biochem.* **1998**, *258* (1), 1-18.
209. Li, B.; Alonso, D. O. V.; Bennion, B. J.; Daggett, V., Hydrophobic Hydration Is an Important Source of Elasticity in Elastin-Based Biopolymers. *J. Am. Chem. Soc.* **2001**, *123* (48), 11991-11998.
210. Reiersen, H.; Clarke, A. R.; Rees, A. R., Short elastin-like peptides exhibit the same temperature-induced structural transitions as elastin polymers: implications for protein engineering. *J. Mol. Biol.* **1998**, *283* (1), 255-264.
211. Vrhovski, B.; Jensen, S.; Weiss, A. S., Coacervation Characteristics of Recombinant Human Tropoelastin. *Eur. J. Biochem.* **1997**, *250* (1), 92-98.
212. Yeo, G. C.; Keeley, F. W.; Weiss, A. S., Coacervation of tropoelastin. *Adv. Colloid Interface Sci.* **2011**, *167* (1), 94-103.
213. Bellingham, C. M.; Lillie, M. A.; Gosline, J. M.; Wright, G. M.; Starcher, B. C.; Bailey, A. J.; Woodhouse, K. A.; Keeley, F. W., Recombinant human elastin polypeptides self-assemble into biomaterials with elastin-like properties. *Biopolymers* **2003**, *70* (4), 445-455.
214. Weis-Fogh, T.; Andersen, S. O., New Molecular Model for the Long-range Elasticity of Elastin. *Nature* **1970**, *227* (5259), 718-721.
215. Gray, W. R.; Sandberg, L. B.; Foster, J. A., Molecular Model for Elastin Structure and Function. *Nature* **1973**, *246* (5434), 461-466.

216. Hoeve, C. A. J.; Flory, P. J., The elastic properties of elastin. *Biopolymers* **1974**, *13* (4), 677-686.
217. Dorrington, K. L.; McCrum, N. G., Elastin as a rubber. *Biopolymers* **1977**, *16* (6), 1201-1222.
218. Venkatachalam, C. M.; Urry, D. W., Development of a linear helical conformation from its cyclic correlate.  $\beta$ -Spiral model of the elastin poly(pentapeptide) (VPGVG)<sub>n</sub>. *Macromolecules* **1981**, *14* (5), 1225-1229.
219. Annabi, N.; Mithieux, S. M.; Boughton, E. A.; Ruys, A. J.; Weiss, A. S.; Dehghani, F., Synthesis of highly porous crosslinked elastin hydrogels and their interaction with fibroblasts in vitro. *Biomaterials* **2009**, *30* (27), 4550-4557.
220. Torchia, D. A.; Piez, K. A., Mobility of elastin chains as determined by <sup>13</sup>C nuclear magnetic resonance. *J. Mol. Biol.* **1973**, *76* (3), 419-424.
221. Gosline, J. M., The elastic properties of rubber-like proteins and highly extensible tissues. *Symp. Soc. Exp. Biol.* **1980**, *34*, 332-357.
222. Gosline, J. M.; French, C. J., Dynamic mechanical properties of elastin. *Biopolymers* **1979**, *18* (8), 2091-2103.
223. Aaron, B. B.; Gosline, J. M., Optical properties of single elastin fibres indicate random protein conformation. *Nature* **1980**, *287* (5785), 865-867.
224. Dorrington, K.; Grut, W.; McCrum, N. G., Mechanical state of elastin. *Nature* **1975**, *255* (5508), 476-478.
225. Prescott, B.; Renugopalakrishnan, V.; Thomas Jr., G. J., Appendix: Raman spectrum and structure of elastin in relation to type-II  $\beta$ -turns. *Biopolymers* **1987**, *26* (6), 934-936.
226. Debelle, L.; Alix, A. J. P., The structures of elastins and their function. *Biochimie* **1999**, *81* (10), 981-994.
227. Andrady, A. L.; Mark, J. E., Thermoelasticity of swollen elastin networks at constant composition. *Biopolymers* **1980**, *19* (4), 849-855.
228. Gosline, J. M., Hydrophobic interaction and a model for the elasticity of elastin. *Biopolymers* **1978**, *17* (3), 677-695.
229. Oplatka, A.; Michaeli, I.; Katchalsky, A., Thermoelasticity of open systems. *J. Polym. Sci.* **1960**, *46* (148), 365-374.
230. Volpin, D.; Ciferri, A., Thermoelasticity of Elastin. *Nature* **1970**, *225* (5230), 382-382.
231. Debelle, L.; Alix, A. J. P.; Jacob, M.-P.; Huvenne, J.-P.; Berjot, M.; Sombret, B.; Legrand, P., Bovine Elastin and  $\kappa$ -Elastin Secondary Structure Determination by Optical Spectroscopies. *J. Biol. Chem.* **1995**, *270* (44), 26099-26103.
232. Tamburro, A. M.; Guantieri, V.; Gordini, D. D., Synthesis and Structural Studies of a Pentapeptide Sequence of Elastin. Poly (Val-Gly-Gly-Leu-Gly). *J. Biomol. Struct. Dyn.* **1992**, *10* (3), 441-454.
233. Villani, V.; Tamburro, A. M., Molecular mechanics calculations of the conformers of the dipetide Boc-Gly-Leu-NMe and tripeptide Boc-Gly-Leu-Gly-NMe. Searching the conformational space by the build-up method. *Perkin Trans.* **1992**, (12), 2263-2270.
234. Urry, D. W.; Long, M. M.; Gross, E., Conformations of the Repeat Peptides of Elastin in Solution: An Application of Proton and Carbon-13 Magnetic Resonance to the Determination of Polypeptide Secondary Structure. *CRC Crit. Rev. Biochem.* **1976**, *4* (1), 1-45.
235. Urry, D. W.; Trapane, T. L.; Long, M. M.; Prasad, K. U., Test of the librational entropy mechanism of elasticity of the polypentapeptide of elastin. Effect of introducing a methyl group at residue 5. *J. Chem. Soc. Faraday Trans* **1983**, *79* (4), 853-868.
236. Urry, D. W.; Venkatachalam, C. M., A librational entropy mechanism for elastomers with repeating peptide sequences in helical array. *Int. J. Quantum Chem.* **1983**, *24* (S10), 81-93.
237. Urry, D. W., Entropic elastic processes in protein mechanisms. I. Elastic structure due to an inverse temperature transition and elasticity due to internal chain dynamics. *J. Protein. Chem.* **1988**, *7* (1), 1-34.
238. Urry, D. W., Entropic elastic processes in protein mechanisms. II. Simple (passive) and coupled (active) development of elastic forces. *J. Protein. Chem.* **1988**, *7* (2), 81-114.
239. Foster, J. A.; Bruenger, E.; Gray, W. R.; Sandberg, L. B., Isolation and Amino Acid Sequences of Tropoelastin Peptides. *J. Biol. Chem.* **1973**, *248* (8), 2876-2879.
240. Urry, D. W.; Ohnishi, T., Studies on the conformations and interactions of elastin. Proton magnetic resonance of the repeating tetramer. *Biopolymers* **1974**, *13* (6), 1223-1242.

241. Venkatachalam, C. M.; Khaled, M. A.; Sugano, H.; Urry, D. W., Nuclear magnetic resonance and conformational energy calculations of repeat peptides of elastin. Conformational characterization of cyclopentadecapeptide cyclo-(L-Val-L-Pro-Gly-L-Val-Gly)<sub>3</sub>. *J. Am. Chem. Soc.* **1981**, *103* (9), 2372-2379.
242. Urry, D. W.; Long, M. M.; Ohnishi, T.; Jacobs, M., Circular dichroism and absorption of the polytetrapeptide of elastin: A polymer model for the  $\beta$ -turn. *Biochem. Biophys. Res. Commun.* **1974**, *61* (4), 1427-1433.
243. Cook, W. J.; Einspahr, H.; Trapane, T. L.; Urry, D. W.; Bugg, C. E., Crystal structure and conformation of the cyclic trimer of a repeat pentapeptide of elastin, cyclo-(L-valyl-L-prolylglycyl-L-valylglycyl)<sub>3</sub>. *J. Am. Chem. Soc.* **1980**, *102* (17), 5502-5505.
244. Urry, D. W.; Hugel, T.; Seitz, M.; Gaub, H. E.; Sheiba, L.; Dea, J.; Xu, J.; Parker, T., Elastin: a representative ideal protein elastomer. *Philos. Trans. R. Soc. B* **2002**, *357* (1418), 169-184.
245. Urry, D. W.; Trapane, T. L.; Wood, S. A.; Walker, J. T.; Harris, R. D.; Prasad, K. U., D-Ala<sup>5</sup> analog of the elastin polypentapeptide. Physical characterization. *Int. J. Pept. Protein Res.* **1983**, *22* (2), 164-175.
246. Volpin, D.; Urry, D. W.; Pasquali-Ronchetti, I.; Gotte, L., Studies by electron microscopy on the structure of coacervates of synthetic polypeptides of tropoelastin. *Micron (1969)* **1976**, *7* (3), 193-198.
247. Cox, B. A.; Starcher, B. C.; Urry, D. W., Coacervation of Tropoelastin Results in Fiber Formation. *J. Biol. Chem.* **1974**, *249* (3), 997-998.
248. Urry, D. W.; Long, M. M.; Cox, B. A.; Ohnishi, T.; Mitchell, L. W.; Jacobs, M., The synthetic polypentapeptide of elastin coacervates and forms filamentous aggregates. *Biochim. Biophys. Acta* **1974**, *371* (2), 597-602.
249. Trabbic-Carlson, K.; Setton, L. A.; Chilkoti, A., Swelling and Mechanical Behaviors of Chemically Cross-Linked Hydrogels of Elastin-like Polypeptides. *Biomacromolecules* **2003**, *4* (3), 572-580.
250. Lim, D. W.; Nettles, D. L.; Setton, L. A.; Chilkoti, A., Rapid Cross-Linking of Elastin-like Polypeptides with (Hydroxymethyl)phosphines in Aqueous Solution. *Biomacromolecules* **2007**, *8* (5), 1463-1470.
251. Tamburro, A. M.; Guantieri, V.; Scopa, A.; Drabble, J. M., Polypeptide models of elastin: CD and NMR studies on synthetic poly(X-Gly-Gly). *Chirality* **1991**, *3* (4), 318-323.
252. Mecham, R. P., Methods in elastic tissue biology: Elastin isolation and purification. *Methods* **2008**, *45* (1), 32-41.
253. Weissman, N.; Shields, G. S.; Carnes, W. H., Cardiovascular Studies on Copper-deficient Swine: IV. Content and Solubility of the Aortic Elastin, Collagen, and Hexosamine. *J. Biol. Chem.* **1963**, *238* (9), 3115-3118.
254. Chou, W. S.; Savage, J. E.; O'Dell, B. L., Relation of Monoamine Oxidase Activity and Collagen Crosslinking in Copper-Deficient and Control Tissues. *Proc. Soc. Exp. Biol. Med.* **1968**, *128* (4), 948-952.
255. Martin, S. L.; Vrhovski, B.; Weiss, A. S., Total synthesis and expression in Escherichia coli of a gene encoding human tropoelastin. *Gene* **1995**, *154* (2), 159-166.
256. Rosano, G. L.; Ceccarelli, E. A., Recombinant protein expression in Escherichia coli: advances and challenges. *Front. Microbiol.* **2014**, *5*, 172-172.
257. Chen, Y.; Guan, Z., Bioinspired Modular Synthesis of Elastin-Mimic Polymers To Probe the Mechanism of Elastin Elasticity. *J. Am. Chem. Soc.* **2010**, *132* (13), 4577-4579.
258. Sandberg, L. B.; Leslie, J. G.; Leach, C. T.; Alvarez, V. L.; Torres, A. R.; Smith, D. W., Elastin covalent structure as determined by solid phase amino acid sequencing. *Pathol Biol (Paris)* **1985**, *33* (4), 266-274.
259. Yeh, H.; Ornstein-Goldstein, N.; Indik, Z.; Sheppard, P.; Anderson, N.; Rosenbloom, J. C.; Cicila, G.; Yoon, K.; Rosenbloom, J., Sequence Variation of Bovine Elastin mRNA Due to Alternative Splicing. *Matrix Biol.* **1987**, *7* (4), 235-247.
260. Urry, D. W.; Shaw, R. G.; Prasad, K. U., Polypentapeptide of elastin: Temperature dependence of ellipticity and correlation with elastomeric force. *Biochem. Biophys. Res. Commun.* **1985**, *130* (1), 50-57.
261. Li, N. K.; Quiroz, F. G.; Hall, C. K.; Chilkoti, A.; Yingling, Y. G., Molecular Description of the LCST Behavior of an Elastin-Like Polypeptide. *Biomacromolecules* **2014**, *15* (10), 3522-3530.

262. Chilkoti, A.; Dreher, M. R.; Meyer, D. E., Design of thermally responsive, recombinant polypeptide carriers for targeted drug delivery. *Adv. Drug Delivery. Rev.* **2002**, *54* (8), 1093-1111.
263. Meyer, D. E.; Chilkoti, A., Quantification of the Effects of Chain Length and Concentration on the Thermal Behavior of Elastin-like Polypeptides. *Biomacromolecules* **2004**, *5* (3), 846-851.
264. Zhao, B.; Li, N. K.; Yingling, Y. G.; Hall, C. K., LCST Behavior is Manifested in a Single Molecule: Elastin-Like polypeptide (VPGVG)<sub>n</sub>. *Biomacromolecules* **2016**, *17* (1), 111-118.
265. MacEwan, S. R.; Weitzhandler, I.; Hoffmann, I.; Genzer, J.; Gradzielski, M.; Chilkoti, A., Phase Behavior and Self-Assembly of Perfectly Sequence-Defined and Monodisperse Multiblock Copolypeptides. *Biomacromolecules* **2017**, *18* (2), 599-609.
266. Prhashanna, A.; Taylor, P. A.; Qin, J.; Kiick, K. L.; Jayaraman, A., Effect of Peptide Sequence on the LCST-Like Transition of Elastin-Like Peptides and Elastin-Like Peptide–Collagen-Like Peptide Conjugates: Simulations and Experiments. *Biomacromolecules* **2019**, *20* (3), 1178-1189.
267. Despanie, J.; Dhandhukia, J. P.; Hamm-Alvarez, S. F.; MacKay, J. A., Elastin-like polypeptides: Therapeutic applications for an emerging class of nanomedicines. *J. Control. Release* **2016**, *240*, 93-108.
268. Aladini, F.; Araman, C.; Becker, C. F. W., Chemical synthesis and characterization of elastin-like polypeptides (ELPs) with variable guest residues. *J. Pept. Sci.* **2016**, *22* (5), 334-342.
269. Petitdemange, R.; Garanger, E.; Bataille, L.; Dieryck, W.; Bathany, K.; Garbay, B.; Deming, T. J.; Lecommandoux, S., Selective Tuning of Elastin-like Polypeptide Properties via Methionine Oxidation. *Biomacromolecules* **2017**, *18* (2), 544-550.
270. Chen, Z.; Ding, Z.; Zhang, G.; Tian, L.; Zhang, X., Construction of Thermo-Responsive Elastin-Like Polypeptides (ELPs)-Aggregation-Induced-Emission (AIE) Conjugates for Temperature Sensing. *Molecules* **2018**, *23* (7), 1725.
271. Mackay, J. A.; Callahan, D. J.; Fitzgerald, K. N.; Chilkoti, A., Quantitative model of the phase behavior of recombinant pH-responsive elastin-like polypeptides. *Biomacromolecules* **2010**, *11* (11), 2873-2879.
272. Hofmeister, F., Zur Lehre von der Wirkung der Salze. *Arch. Exp. Pathol. Pharmacol.* **1888**, *24* (4), 247-260.
273. Cho, Y.; Zhang, Y.; Christensen, T.; Sagle, L. B.; Chilkoti, A.; Cremer, P. S., Effects of Hofmeister Anions on the Phase Transition Temperature of Elastin-like Polypeptides. *J. Phys. Chem. B* **2008**, *112* (44), 13765-13771.
274. Wu, Y.; MacKay, J. A.; R. McDaniel, J.; Chilkoti, A.; Clark, R. L., Fabrication of Elastin-Like Polypeptide Nanoparticles for Drug Delivery by Electrospraying. *Biomacromolecules* **2009**, *10* (1), 19-24.
275. Urry, D. W.; Henze, R.; Harris, R. D.; Prasad, K. U., Polypentapeptide of elastin: Temperature dependence correlation of elastomeric force and dielectric permittivity. *Biochem. Biophys. Res. Commun.* **1984**, *125* (3), 1082-1088.
276. Gosline, J.; Lillie, M.; Carrington, E.; Guerette, P.; Ortlepp, C.; Savage, K., Elastic proteins: biological roles and mechanical properties. *Philos. Trans. R. Soc. B* **2002**, *357* (1418), 121-132.
277. Lee, J.; Macosko, C. W.; Urry, D. W., Elastomeric Polypentapeptides Cross-Linked into Matrixes and Fibers. *Biomacromolecules* **2001**, *2* (1), 170-179.
278. Desai, M. S.; Wang, E.; Joyner, K.; Chung, T. W.; Jin, H.-E.; Lee, S.-W., Elastin-Based Rubber-Like Hydrogels. *Biomacromolecules* **2016**, *17* (7), 2409-2416.
279. Nowatzki, P. J.; Tirrell, D. A., Physical properties of artificial extracellular matrix protein films prepared by isocyanate crosslinking. *Biomaterials* **2004**, *25* (7), 1261-1267.
280. Nagapudi, K.; Brinkman, W. T.; Leisen, J. E.; Huang, L.; McMillan, R. A.; Apkarian, R. P.; Conticello, V. P.; Chaikof, E. L., Photomediated Solid-State Cross-Linking of an Elastin–Mimetic Recombinant Protein Polymer. *Macromolecules* **2002**, *35* (5), 1730-1737.
281. Lee, J.; Macosko, C. W.; Urry, D. W., Mechanical Properties of Cross-Linked Synthetic Elastomeric Polypentapeptides. *Macromolecules* **2001**, *34* (17), 5968-5974.
282. Lee, J.; Macosko, C. W.; Urry, D. W., Swelling Behavior of  $\gamma$ -Irradiation Cross-Linked Elastomeric Polypentapeptide-Based Hydrogels. *Macromolecules* **2001**, *34* (12), 4114-4123.
283. McHale, M. K.; Setton, L. A.; Chilkoti, A., Synthesis and in Vitro Evaluation of Enzymatically Cross-Linked Elastin-Like Polypeptide Gels for Cartilaginous Tissue Repair. *Tissue Eng.* **2005**, *11* (11-12), 1768-1779.

284. Wright, E. R.; Conticello, V. P., Self-assembly of block copolymers derived from elastin-mimetic polypeptide sequences. *Adv. Drug Delivery. Rev.* **2002**, *54* (8), 1057-1073.
285. Wright, E. R.; McMillan, R. A.; Cooper, A.; Apkarian, R. P.; Conticello, V. P., Thermoplastic Elastomer Hydrogels via Self-Assembly of an Elastin-Mimetic Triblock Polypeptide. *Adv. Funct. Mater.* **2002**, *12* (2), 149-154.
286. Abuchowski, A.; McCoy, J. R.; Palczuk, N. C.; van Es, T.; Davis, F. F., Effect of covalent attachment of polyethylene glycol on immunogenicity and circulating life of bovine liver catalase. *J. Biol. Chem.* **1977**, *252* (11), 3582-6.
287. Kim, W.; Chaikof, E. L., Recombinant elastin-mimetic biomaterials: Emerging applications in medicine. *Adv. Drug Delivery. Rev.* **2010**, *62* (15), 1468-1478.
288. MacEwan, S. R.; Chilkoti, A., Elastin-like polypeptides: Biomedical applications of tunable biopolymers. *Peptide Sci.* **2010**, *94* (1), 60-77.
289. Frandsen, J. L.; Ghandehari, H., Recombinant protein-based polymers for advanced drug delivery. *Chem. Soc. Rev.* **2012**, *41* (7), 2696-2706.
290. Dreher, M. R.; Raucher, D.; Balu, N.; Michael Colvin, O.; Ludeman, S. M.; Chilkoti, A., Evaluation of an elastin-like polypeptide–doxorubicin conjugate for cancer therapy. *J. Control. Release* **2003**, *91* (1), 31-43.
291. Janib, S. M.; Liu, S.; Park, R.; Pastuszka, M. K.; Shi, P.; Moses, A. S.; Orosco, M. M.; Lin, Y.-A.; Cui, H.; Conti, P. S.; Li, Z.; MacKay, J. A., Kinetic quantification of protein polymer nanoparticles using non-invasive imaging. *Integr. Biol.* **2012**, *5* (1), 183-194.
292. Meyer, D. E.; Shin, B. C.; Kong, G. A.; Dewhirst, M. W.; Chilkoti, A., Drug targeting using thermally responsive polymers and local hyperthermia. *J. Control. Release* **2001**, *74* (1), 213-224.
293. Cai, L.; Dinh, C. B.; Heilshorn, S. C., One-pot Synthesis of Elastin-like Polypeptide Hydrogels with Grafted VEGF-Mimetic Peptides. *Biomater. Sci.* **2014**, *2* (5), 757-765.
294. Kim, B.; Chilkoti, A., Allosteric Actuation of Inverse Phase Transition of a Stimulus-Responsive Fusion Polypeptide by Ligand Binding. *J. Am. Chem. Soc.* **2008**, *130* (52), 17867-17873.
295. Urry, D. W.; Parker, T. M.; Reid, M. C.; Gowda, D. C., Biocompatibility of the Bioelastic Materials, Poly(GVGVP) and Its  $\gamma$ -Irradiation Cross-Linked Matrix: Summary of Generic Biological Test Results. *J. Bioact. Compat. Polym.* **1991**, *6* (3), 263-282.
296. Nouri, F. S.; Wang, X.; Chen, X.; Hatefi, A., Reducing the Visibility of the Vector/DNA Nanocomplexes to the Immune System by Elastin-Like Peptides. *Pharm. Res.* **2015**, *32* (9), 3018-3028.
297. Liu, W.; Dreher, M. R.; Furgeson, D. Y.; Peixoto, K. V.; Yuan, H.; Zalutsky, M. R.; Chilkoti, A., Tumor accumulation, degradation and pharmacokinetics of elastin-like polypeptides in nude mice. *J. Control. Release* **2006**, *116* (2), 170-178.
298. Urry, D. W., Elastic molecular machines in metabolism and soft-tissue restoration. *Trends Biotechnol.* **1999**, *17* (6), 249-257.
299. Betre, H.; Liu, W.; Zalutsky, M. R.; Chilkoti, A.; Kraus, V. B.; Setton, L. A., A thermally responsive biopolymer for intra-articular drug delivery. *J. Control. Release* **2006**, *115* (2), 175-182.
300. Kuna, M.; Mahdi, F.; Chade, A. R.; Bidwell, G. L., 3rd, Molecular Size Modulates Pharmacokinetics, Biodistribution, and Renal Deposition of the Drug Delivery Biopolymer Elastin-like Polypeptide. *Sci. Rep.* **2018**, *8* (1), 7923-7923.
301. Jung, B.; Theato, P., Chemical Strategies for the Synthesis of Protein–Polymer Conjugates. In *Bio-synthetic Polymer Conjugates*, Schlaad, H., Ed. Springer Berlin Heidelberg: Berlin, Heidelberg, 2013; pp 37-70.
302. Massodi, I.; Bidwell, G. L.; Raucher, D., Evaluation of cell penetrating peptides fused to elastin-like polypeptide for drug delivery. *J. Control. Release* **2005**, *108* (2), 396-408.
303. Ryu, J. S.; Raucher, D., Elastin-like polypeptides: The influence of its molecular weight on local hyperthermia-induced tumor accumulation. *Eur. J. Pharm. Biopharm.* **2014**, *88* (2), 382-389.
304. Andrew MacKay, J.; Chen, M.; McDaniel, J. R.; Liu, W.; Simnick, A. J.; Chilkoti, A., Self-assembling chimeric polypeptide–doxorubicin conjugate nanoparticles that abolish tumours after a single injection. *Nat. Mater.* **2009**, *8*, 993.
305. Meyer, D. E.; Chilkoti, A., Purification of recombinant proteins by fusion with thermally-responsive polypeptides. *Nat. Biotechnol.* **1999**, *17* (11), 1112-1115.
306. Trabbic-Carlson, K.; Liu, L.; Kim, B.; Chilkoti, A., Expression and purification of recombinant proteins from *Escherichia coli*: Comparison of an elastin-like polypeptide fusion with an oligohistidine fusion. *Protein Sci.* **2004**, *13* (12), 3274-3284.

307. Trabbic-Carlson, K.; Meyer, D. E.; Liu, L.; Piervincenzi, R.; Nath, N.; LaBean, T.; Chilkoti, A., Effect of protein fusion on the transition temperature of an environmentally responsive elastin-like polypeptide: a role for surface hydrophobicity? *Protein Eng., Des. Sel.* **2004**, *17* (1), 57-66.
308. Ge, X.; Yang, D. S. C.; Trabbic-Carlson, K.; Kim, B.; Chilkoti, A.; Filipe, C. D. M., Self-Cleavable Stimulus Responsive Tags for Protein Purification without Chromatography. *J. Am. Chem. Soc.* **2005**, *127* (32), 11228-11229.
309. Banki, M. R.; Feng, L.; Wood, D. W., Simple bioseparations using self-cleaving elastin-like polypeptide tags. *Nat. Methods* **2005**, *2* (9), 659-662.
310. Nettles, D. L.; Chilkoti, A.; Setton, L. A., Applications of elastin-like polypeptides in tissue engineering. *Adv. Drug Delivery. Rev.* **2010**, *62* (15), 1479-1485.
311. Betre, H.; Setton, L. A.; Meyer, D. E.; Chilkoti, A., Characterization of a Genetically Engineered Elastin-like Polypeptide for Cartilaginous Tissue Repair. *Biomacromolecules* **2002**, *3* (5), 910-916.
312. Wu, X.; Sallach, R.; Haller, C. A.; Caves, J. A.; Nagapudi, K.; Conticello, V. P.; Levenston, M. E.; Chaikof, E. L., Alterations in Physical Cross-Linking Modulate Mechanical Properties of Two-Phase Protein Polymer Networks. *Biomacromolecules* **2005**, *6* (6), 3037-3044.
313. Rodríguez-Cabello, J. C.; González de Torre, I.; Ibañez-Fonseca, A.; Alonso, M., Bioactive scaffolds based on elastin-like materials for wound healing. *Adv. Drug Delivery. Rev.* **2018**, *129*, 118-133.
314. Lim, D. W.; Nettles, D. L.; Setton, L. A.; Chilkoti, A., In Situ Cross-Linking of Elastin-like Polypeptide Block Copolymers for Tissue Repair. *Biomacromolecules* **2008**, *9* (1), 222-230.
315. Liu, J. C.; Tirrell, D. A., Cell Response to RGD Density in Cross-Linked Artificial Extracellular Matrix Protein Films. *Biomacromolecules* **2008**, *9* (11), 2984-2988.
316. Di Zio, K.; Tirrell, D. A., Mechanical Properties of Artificial Protein Matrices Engineered for Control of Cell and Tissue Behavior. *Macromolecules* **2003**, *36* (5), 1553-1558.
317. Huang, L.; McMillan, R. A.; Apkarian, R. P.; Pourdeyhimi, B.; Conticello, V. P.; Chaikof, E. L., Generation of Synthetic Elastin-Mimetic Small Diameter Fibers and Fiber Networks. *Macromolecules* **2000**, *33* (8), 2989-2997.
318. Janorkar, A. V.; Rajagopalan, P.; Yarmush, M. L.; Megeed, Z., The use of elastin-like polypeptide-polyelectrolyte complexes to control hepatocyte morphology and function in vitro. *Biomaterials* **2008**, *29* (6), 625-632.
319. Martínez-Osorio, H.; Juárez-Campo, M.; Diebold, Y.; Girotti, A.; Alonso, M.; Arias, F. J.; Rodríguez-Cabello, J. C.; García-Vázquez, C.; Calonge, M., Genetically Engineered Elastin-Like Polymer as a Substratum to Culture Cells from the Ocular Surface. *Curr. Eye Res.* **2009**, *34* (1), 48-56.
320. Betre, H.; Ong, S. R.; Guilak, F.; Chilkoti, A.; Fermor, B.; Setton, L. A., Chondrocytic differentiation of human adipose-derived adult stem cells in elastin-like polypeptide. *Biomaterials* **2006**, *27* (1), 91-99.
321. Mie, M.; Mizushima, Y.; Kobatake, E., Novel extracellular matrix for cell sheet recovery using genetically engineered elastin-like protein. *J. Biomed. Mater. Res. B* **2008**, *86B* (1), 283-290.
322. Herbst, F.; Seiffert, S.; Binder, W. H., Dynamic supramolecular poly(isobutylene)s for self-healing materials. *Polym. Chem.* **2012**, *3* (11), 3084-3092.
323. Herbst, F.; Döhler, D.; Michael, P.; Binder, W. H., Self-Healing Polymers via Supramolecular Forces. *Macromol. Rapid Commun.* **2013**, *34* (3), 203-220.
324. Rupp, H.; Döhler, D.; Hilgeroth, P.; Mahmood, N.; Beiner, M.; Binder, W. H., 3D Printing of Supramolecular Polymers: Impact of Nanoparticles and Phase Separation on Printability. *Macromol. Rapid Commun.* **2019**, *40* (24), 1900467.
325. Chun, J.; Lee, H. S.; Jung, I. G.; Lee, S. W.; Kim, H. J.; Son, S. U., Cu<sub>2</sub>O: A Versatile Reagent for Base-Free Direct Synthesis of NHC-Copper Complexes and Decoration of 3D-MOF with Coordinatively Unsaturated NHC-Copper Species. *Organometallics* **2010**, *29* (7), 1518-1521.
326. Fraser, R. R.; Mansour, T. S.; Savard, S., Acidity measurements on pyridines in tetrahydrofuran using lithiated silylamines. *J. Org. Chem.* **1985**, *50* (17), 3232-3234.
327. Dewick, P. M., *Essentials of Organic Chemistry: For Students of Pharmacy, Medicinal Chemistry and Biological Chemistry*. Wiley: 2006.
328. Moore, L. R.; Cooks, S. M.; Anderson, M. S.; Schanz, H.-J.; Griffin, S. T.; Rogers, R. D.; Kirk, M. C.; Shaughnessy, K. H., Synthesis and Characterization of Water-Soluble Silver and Palladium Imidazol-2-ylidene Complexes with Noncoordinating Anionic Substituents. *Organometallics* **2006**, *25* (21), 5151-5158.

329. Papini, G.; Pellei, M.; Gioia Lobbia, G.; Burini, A.; Santini, C., Sulfonate- or carboxylate-functionalized N-heterocyclic bis-carbene ligands and related water soluble silver complexes. *Dalton Trans.* **2009**, (35), 6985-6990.
330. Urry, D. W.; Cunningham, W. D.; Ohnishi, T., Conformation and interactions of elastin. Proton magnetic resonance of the repeating pentapeptide. *Biochemistry* **1974**, *13* (3), 609-616.
331. Maity, S.; Kumar, P.; Haldar, D., Sonication-induced instant amyloid-like fibril formation and organogelation by a tripeptide. *Soft Matter* **2011**, *7* (11), 5239-5245.
332. Li, F.; Bravo-Rodriguez, K.; Phillips, C.; Seidel, R. W.; Wieberneit, F.; Stoll, R.; Doltsinis, N. L.; Sanchez-Garcia, E.; Sander, W., Conformation and Dynamics of a Cyclic Disulfide-Bridged Peptide: Effects of Temperature and Solvent. *J. Phys. Chem. B* **2013**, *117* (13), 3560-3570.
333. Han, S.-Y.; Kim, Y.-A., Recent Development of Peptide Coupling Reagents in Organic Synthesis. *Tetrahedron* **2004**, *60*.
334. Anderson, G. W.; Callahan, F. M., Racemization by the dicyclohexylcarbodiimide method of peptide synthesis. *J. Am. Chem. Soc.* **1958**, *80* (11), 2902-2903.
335. König, W.; Geiger, R., Eine neue Methode zur Synthese von Peptiden: Aktivierung der Carboxylgruppe mit Dicyclohexylcarbodiimid unter Zusatz von 1-Hydroxy-benzotriazolinen. *Chem. Ber.* **1970**, *103* (3), 788-798.
336. Valeur, E.; Bradley, M., Amide bond formation: beyond the myth of coupling reagents. *Chem. Soc. Rev.* **2009**, *38* (2), 606-631.
337. Al-Azemi, T. F.; Mohamad, A. A.; Vinodh, M., Ring-closing metathesis approach for the synthesis of optically active l-proline-based macrocycles. *Tetrahedron* **2015**, *71* (10), 1523-1528.
338. Tauchman, J.; Císařová, I.; Štěpnička, P., Chiral Phosphanylferrocenecarboxamides with Amino Acid Pendant Groups as Ligands for Cu-Mediated Asymmetric Conjugate Additions of Diethylzinc to Chalcones – Structural Characterisation of Precursors to the Cu Catalyst. *Eur. J. Org. Chem.* **2010**, *2010* (22), 4276-4287.
339. Kong, J.; Yu, S., Fourier Transform Infrared Spectroscopic Analysis of Protein Secondary Structures. *Acta Biochim. Biophys. Sin.* **2007**, *39* (8), 549-559.
340. Bandekar, J., Amide modes and protein conformation. *Biochim. Biophys. Acta Protein Struct. Molec. Enzym.* **1992**, *1120* (2), 123-143.
341. Krimm, S., Vibrational analysis of conformation in peptides, polypeptides, and proteins. *Biopolymers* **1983**, *22* (1), 217-25.
342. Susi, H.; Byler, D. M., Resolution-enhanced fourier transform infrared spectroscopy of enzymes. In *Methods Enzymol.*, Academic Press: 1986; Vol. 130, pp 290-311.
343. Byler, D. M.; Susi, H., Examination of the secondary structure of proteins by deconvolved FTIR spectra. *Biopolymers* **1986**, *25* (3), 469-487.
344. Lin, S.-Y.; Hsieh, T.-F.; Wei, Y.-S., pH- and thermal-dependent conformational transition of PGAIPG, a repeated hexapeptide sequence from tropoelastin. *Peptides* **2005**, *26* (4), 543-549.
345. Serrano, V.; Liu, W.; Franzen, S., An Infrared Spectroscopic Study of the Conformational Transition of Elastin-Like Polypeptides. *Biophys. J.* **2007**, *93* (7), 2429-2435.
346. Greenfield, N. J., Using circular dichroism spectra to estimate protein secondary structure. *Nat. Protoc.* **2006**, *1* (6), 2876-2890.
347. Whitmore, L.; Wallace, B. A., Protein secondary structure analyses from circular dichroism spectroscopy: Methods and reference databases. *Biopolymers* **2008**, *89* (5), 392-400.
348. Holzwarth, G.; Doty, P., The Ultraviolet Circular Dichroism of Polypeptides. *J. Am. Chem. Soc.* **1965**, *87* (2), 218-228.
349. Greenfield, N. J.; Fasman, G. D., Computed circular dichroism spectra for the evaluation of protein conformation. *Biochemistry* **1969**, *8* (10), 4108-4116.
350. Meneses, C.; Nicoll, S. L.; Trembleau, L., Multigram-Scale Synthesis of Short Peptides via a Simplified Repetitive Solution-Phase Procedure. *J. Org. Chem.* **2010**, *75* (3), 564-569.
351. Cinzia, C.; Anna, B., Synthesis of  $\alpha$ -N-Linked Glycopeptides. *Eur. J. Org. Chem.* **2011**, *2011* (20-21), 3911-3919.
352. Urry, D. W., Protein elasticity based on conformations of sequential polypeptides: The biological elastic fiber. *J. Protein. Chem.* **1984**, *3* (5), 403-436.
353. Tisato, F.; Marzano, C.; Porchia, M.; Pellei, M.; Santini, C., Copper in diseases and treatments, and copper-based anticancer strategies. *Med. Res. Rev.* **2010**, *30* (4), 708-749.

354. Gandin, V.; Porchia, M.; Tisato, F.; Zanella, A.; Severin, E.; Dolmella, A.; Marzano, C., Novel Mixed-Ligand Copper(I) Complexes: Role of Diimine Ligands on Cytotoxicity and Genotoxicity. *J. Med. Chem.* **2013**, *56* (18), 7416-7430.
355. Le Droumaguet, B.; Velonia, K., Click Chemistry: A Powerful Tool to Create Polymer-Based Macromolecular Chimeras. *Macromol. Rapid Commun.* **2008**, *29* (12-13), 1073-1089.
356. Brewer, G. J., Risks of Copper and Iron Toxicity during Aging in Humans. *Chem. Res. Toxicol.* **2010**, *23* (2), 319-326.
357. Streciwilk, W.; Hackenberg, F.; Müller-Bunz, H.; Tacke, M., Synthesis and cytotoxicity studies of p-benzyl substituted NHC–copper(I) bromide derivatives. *Polyhedron* **2014**, *80*, 3-9.
358. Elie, M.; Mahoro, G. U.; Duverger, E.; Renaud, J.-L.; Daniellou, R.; Gaillard, S., Cytotoxicity of cationic NHC copper(I) complexes coordinated to 2,2'-bis-pyridyl ligands. *J. Organomet. Chem.* **2019**, *893*, 21-31.
359. Alvarez, S. G.; Alvarez, M. T., A Practical Procedure for the Synthesis of Alkyl Azides at Ambient Temperature in Dimethyl Sulfoxide in High Purity and Yield. *Synthesis* **1997**, *1997* (04), 413-414.
360. Roy, S.; Eastman, A.; Gribble, G. W., Synthesis of bisindolylmaleimides related to GF109203x and their efficient conversion to the bioactive indolocarbazoles. *Org. Biomol. Chem.* **2006**, *4* (17), 3228-3234.
361. Srivastava, P. C.; Callahan, A. P.; Cunningham, E. B.; Knapp, F. F., Potential cerebral perfusion agents: synthesis and evaluation of a radioiodinated vinylalkylbarbituric acid analog. *J. Med. Chem.* **1983**, *26* (5), 742-746.
362. Wen, L.; Liu, Q.; Ma, J.; Tian, Y.; Li, C.; Bo, Z.; Jiang, L., Malachite Green Derivative–Functionalized Single Nanochannel: Light-and-pH Dual-Driven Ionic Gating. *Adv. Mater.* **2012**, *24* (46), 6193-6198.
363. Jain, A.; Kameswaran, M.; Pandey, U.; Prabhaskar, K.; Sarma, H. D.; Dash, A., <sup>68</sup>Ga labeled Erlotinib: A novel PET probe for imaging EGFR over-expressing tumors. *Bioorg. Med. Chem. Lett.* **2017**, *27* (19), 4552-4557.
364. Sivakumar, K.; Xie, F.; Cash, B. M.; Long, S.; Barnhill, H. N.; Wang, Q., A Fluorogenic 1,3-Dipolar Cycloaddition Reaction of 3-Azidocoumarins and Acetylenes. *Org. Lett.* **2004**, *6* (24), 4603-4606.
365. Yoshida, S.; Suga, H.; Seki, S., Thermodynamic Studies of Solid Polyethers. III. Poly(tetrahydrofuran),  $[-(\text{CH}_2)_4\text{O}]_n$ . *Polym. J. (Tokyo, Jpn.)* **1973**, *5* (1), 25-32.
366. Edward Semple, J.; Sullivan, B.; Vojtkovsky, T.; Sill, K. N., Synthesis and facile end-group quantification of functionalized PEG azides. *J. Polym. Sci., Part A: Polym. Chem.* **2016**, *54* (18), 2888-2895.
367. Pielichowski, K.; Flejtuch, K., Differential scanning calorimetry studies on poly(ethylene glycol) with different molecular weights for thermal energy storage materials. *Polym. Adv. Technol.* **2002**, *13* (10-12), 690-696.
368. Rasheed, A.; Theja, I.; Ashok Kumar, C. K.; Lavanya, Y.; Ravindra Royal, P.; Vamsee Krishna, S., Synthesis, hydrolysis studies and pharmacodynamic profile of novel colon-specific mutual prodrug of Aceclofenac with amino acids. *Der Pharma Chem.* **2009**, *1* (2), 59-71.
369. Abdo, M.-R.; Joseph, P.; Boigegrain, R.-A.; Liautard, J.-P.; Montero, J.-L.; Köhler, S.; Winum, J.-Y., Brucella suis histidinol dehydrogenase: Synthesis and inhibition studies of a series of substituted benzylic ketones derived from histidine. *Bioorg. Med. Chem.* **2007**, *15* (13), 4427-4433.

## 7 Appendix

### 7.1 Characterization of the COOH-functionalized mechanocatalyst synthesis (1-5)

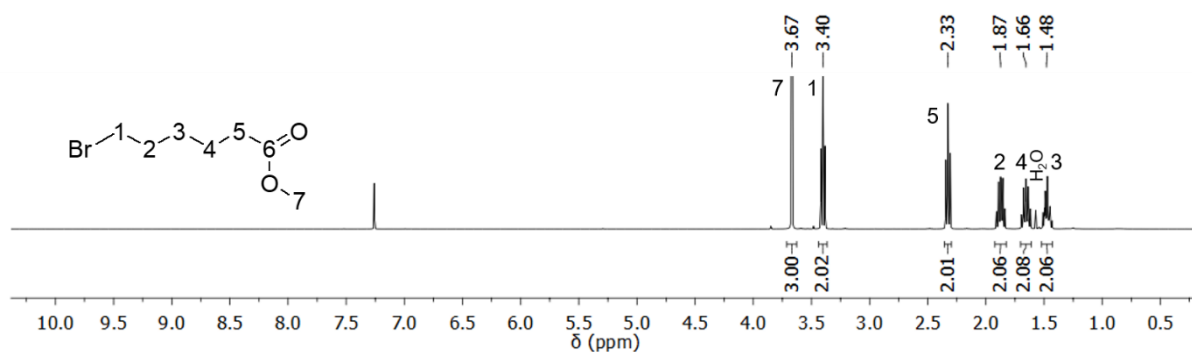


Figure A1. <sup>1</sup>H-NMR spectrum of 1a.

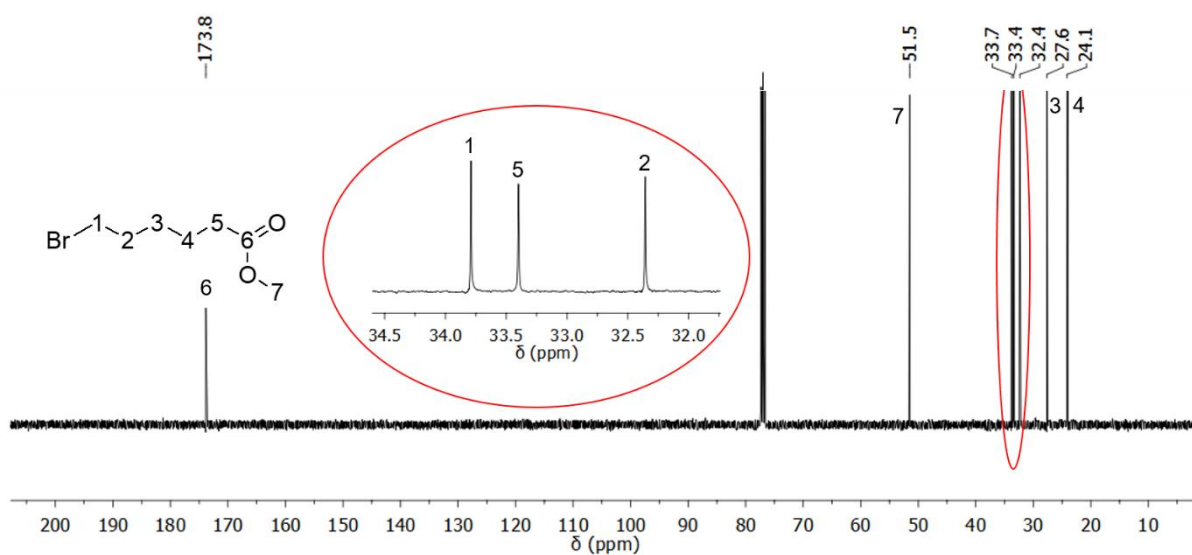


Figure A2. <sup>13</sup>C-NMR spectrum of 1a.

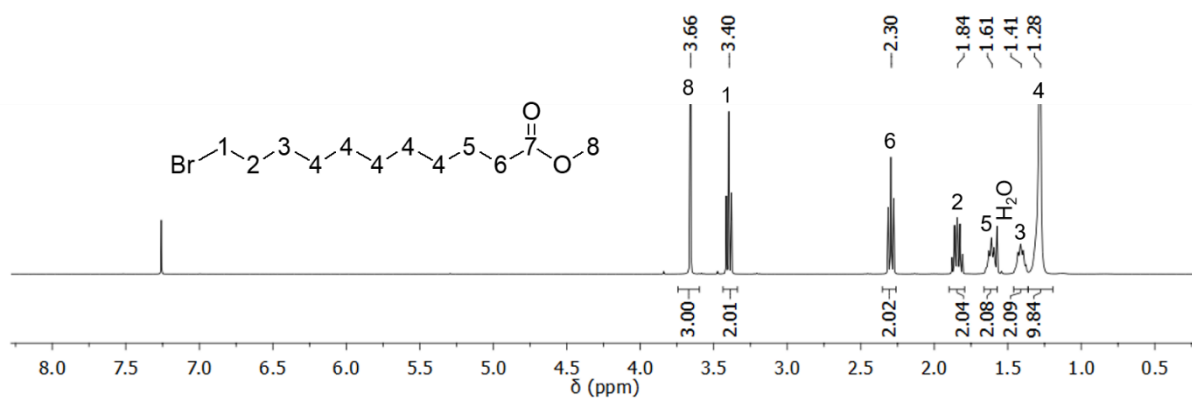


Figure A3. <sup>1</sup>H-NMR spectrum of 1b.

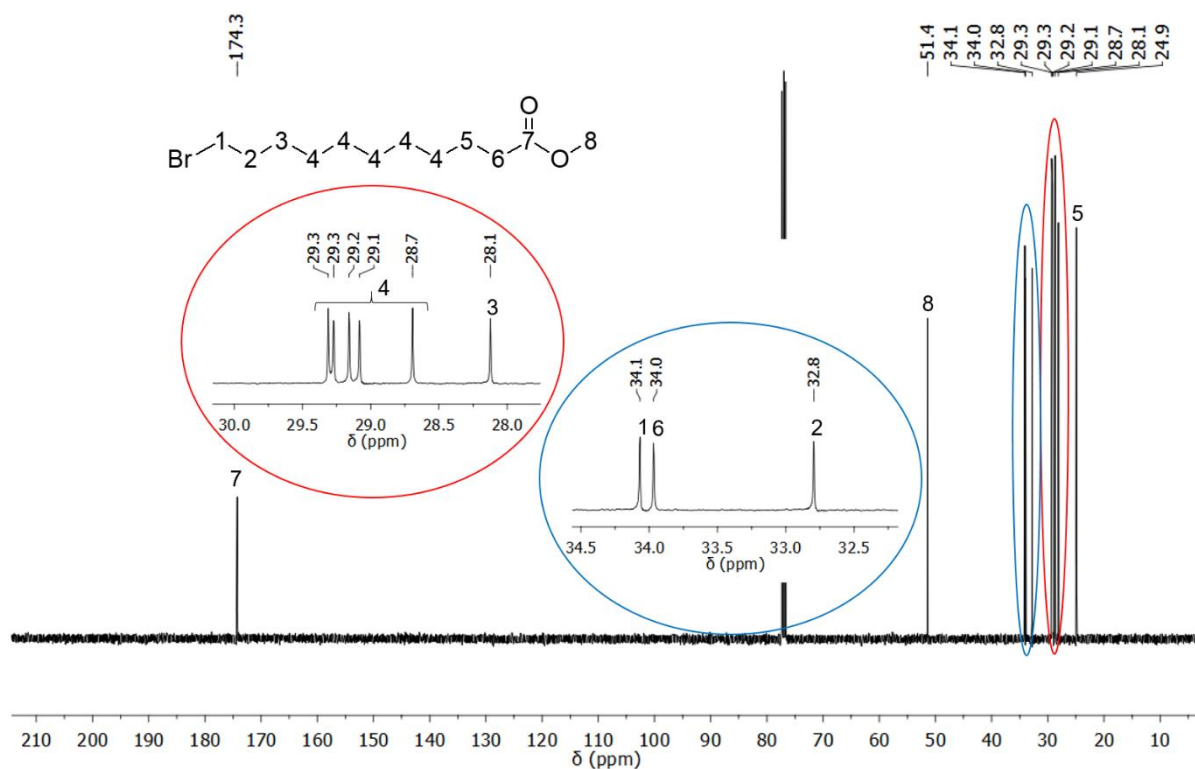


Figure A4.  $^{13}\text{C}$ -NMR spectrum of **1b**.

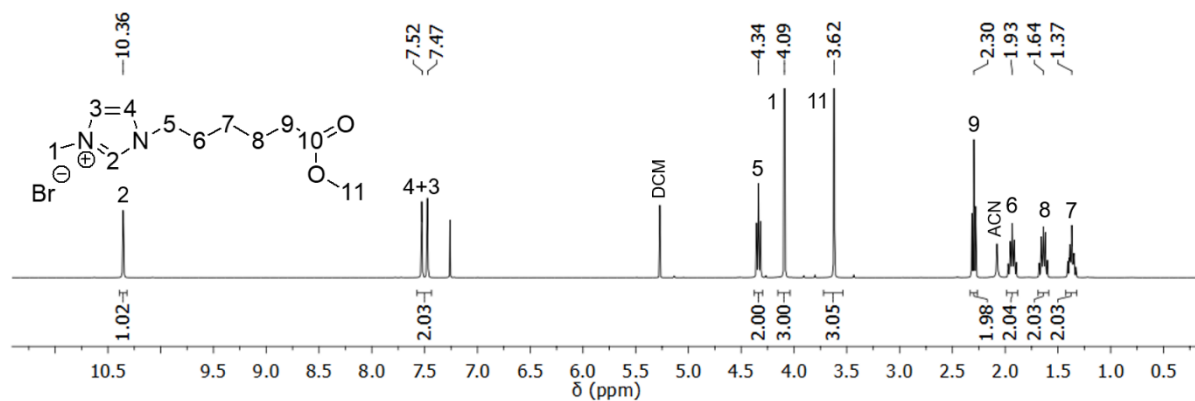


Figure A5.  $^1\text{H}$ -NMR spectrum of **2a**.

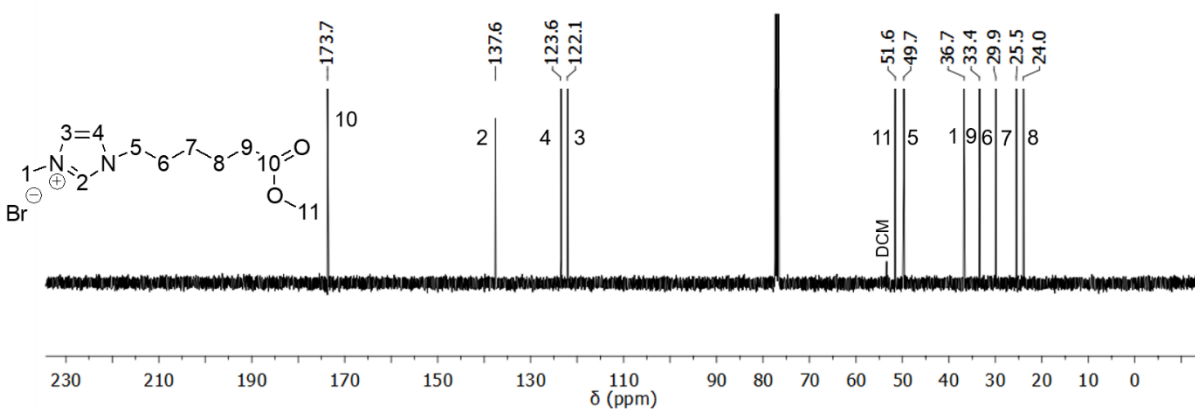


Figure A6.  $^{13}\text{C}$ -NMR spectrum of **2a**.

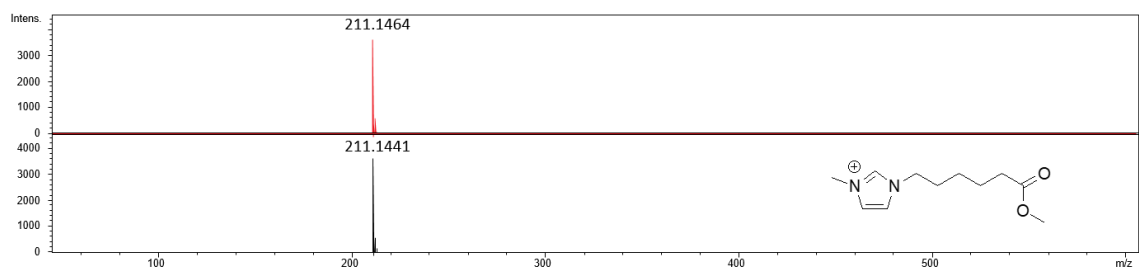


Figure A7. ESI-TOF-MS of 2a.

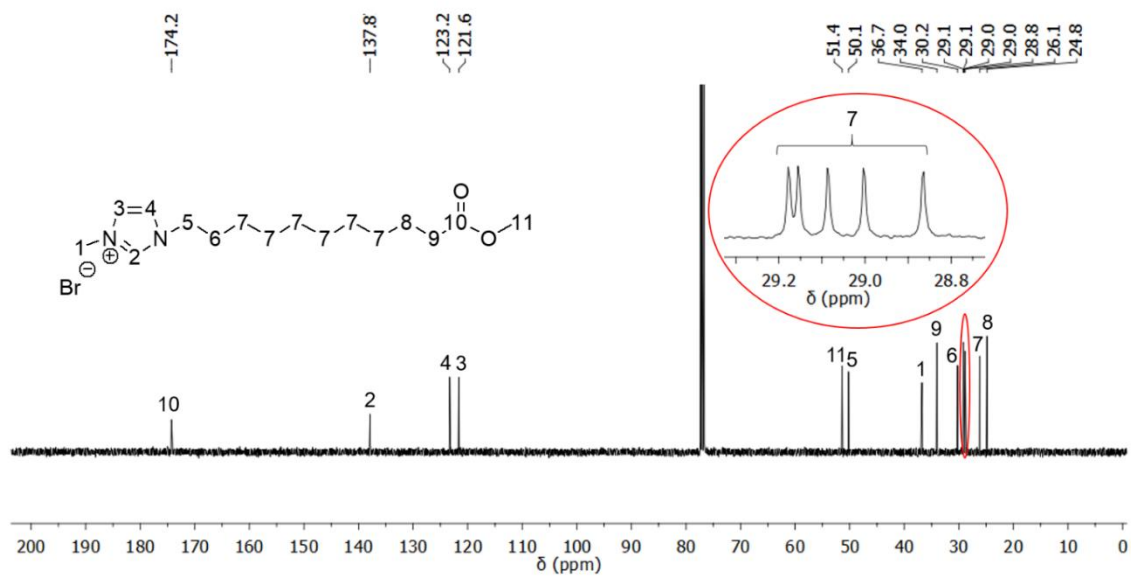


Figure A8.  $^{13}\text{C}$ -NMR spectrum of 2b.

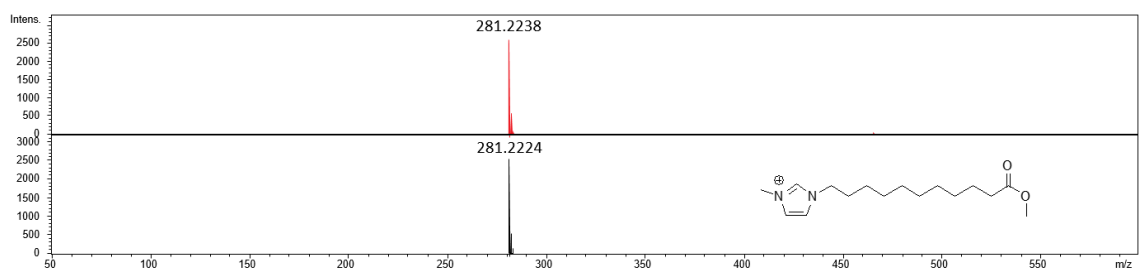


Figure A9. ESI-TOF-MS of 2b.

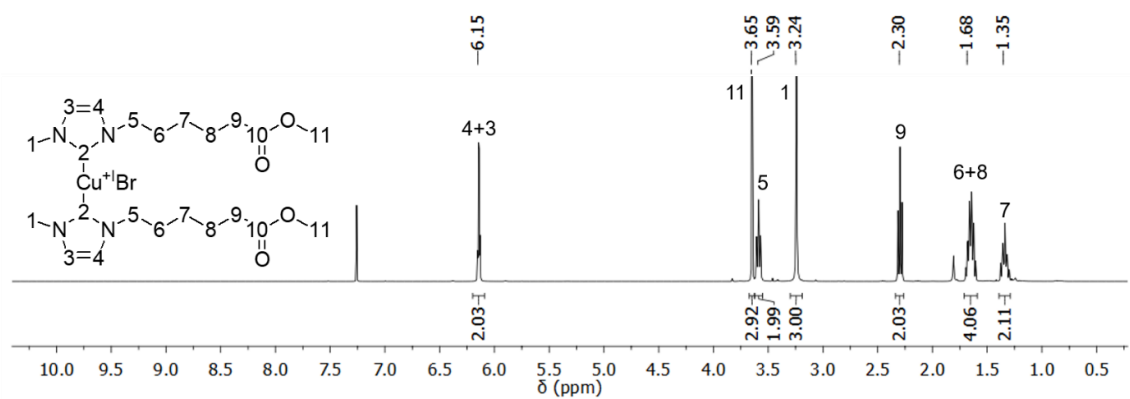
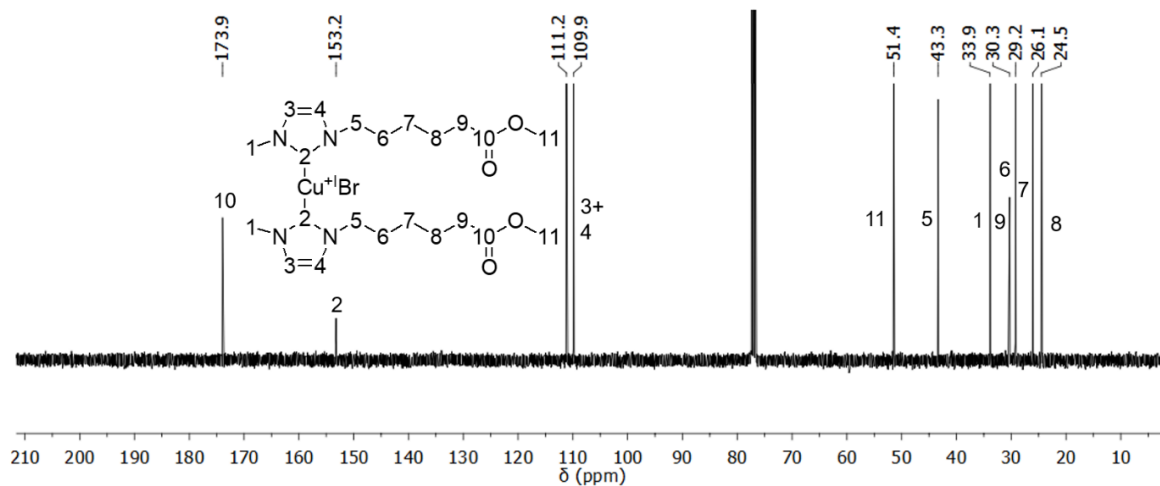
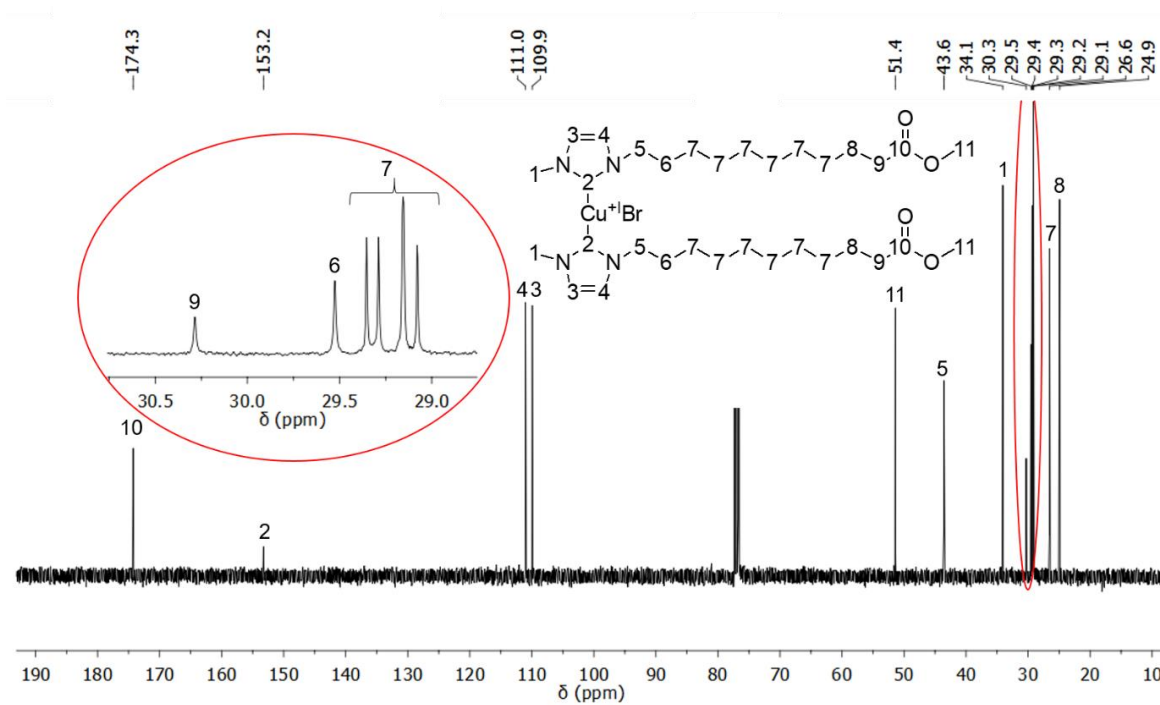


Figure A10.  $^1\text{H}$ -NMR spectrum of 3a.



**Figure A11.**  $^{13}\text{C}$ -NMR spectrum of **3a**.



**Figure A12.**  $^{13}\text{C}$ -NMR spectrum of **3b**.

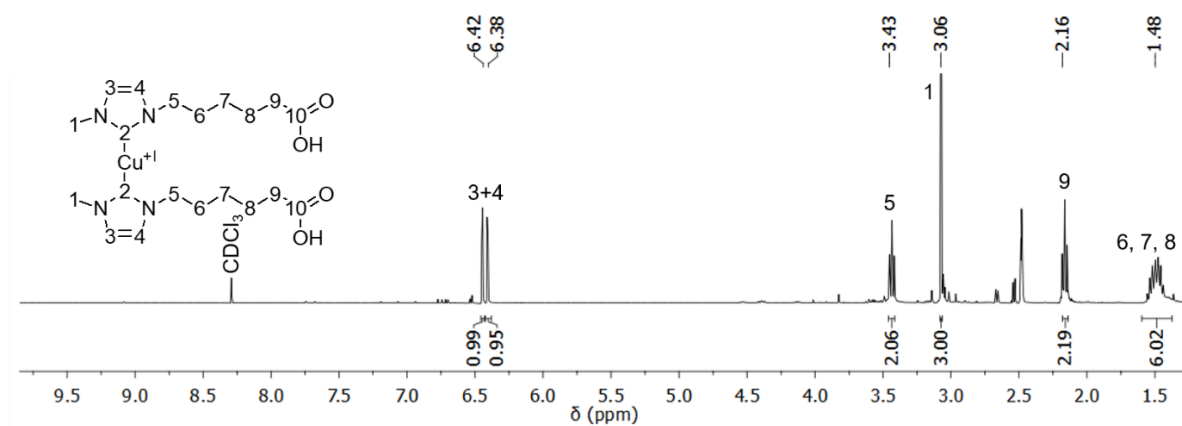


**Figure A13.**  $^1\text{H}$ -NMR spectrum of **4a**.

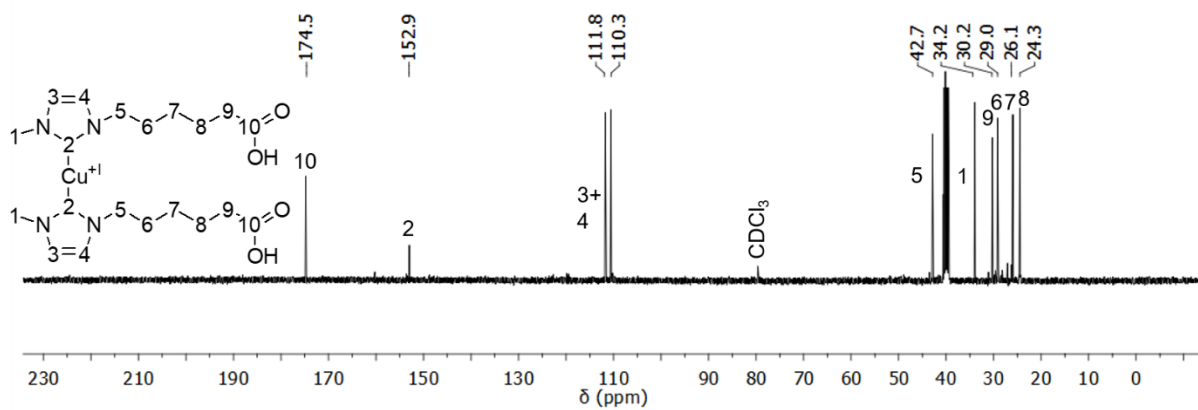


**Figure A14.**  $^{13}\text{C}$ -NMR spectrum of **4a**.

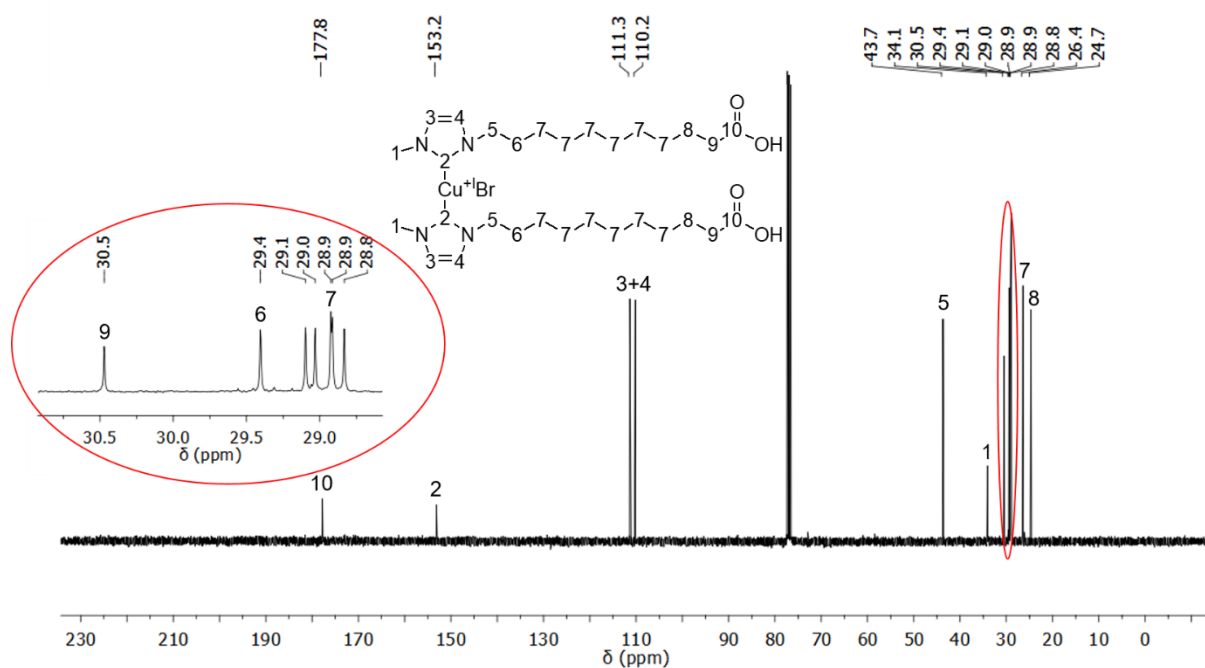


**Figure A15.**  $^{13}\text{C}$ -NMR spectrum of **4b**.

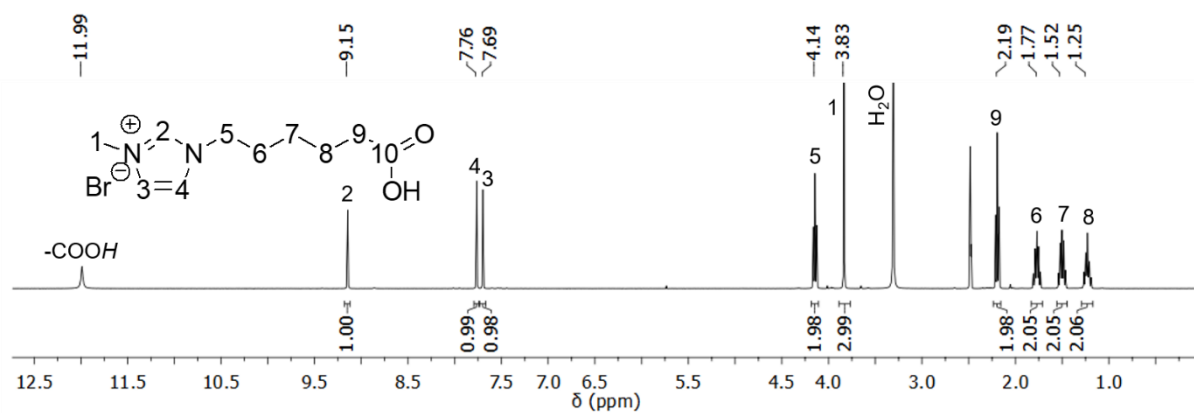


**Figure A16.**  $^1\text{H}$ -NMR spectrum of **5a**.

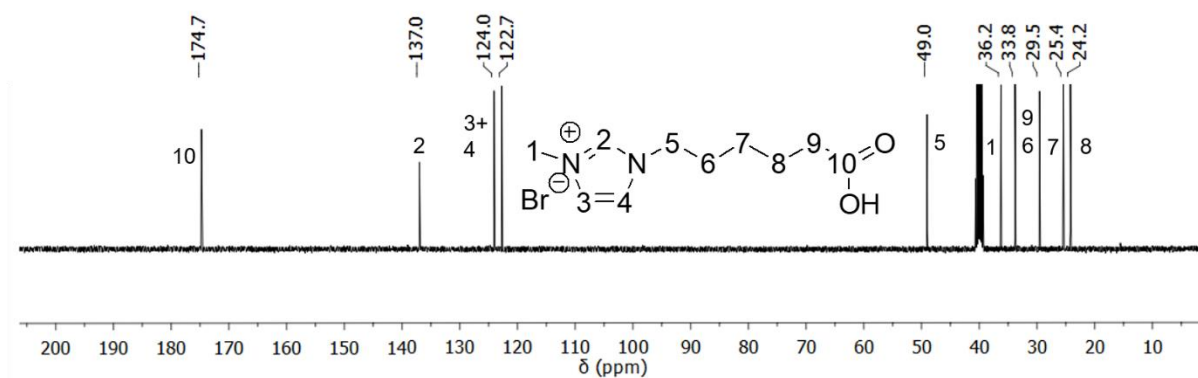


**Figure A17.**  $^{13}\text{C}$ -NMR spectrum of **5a**.

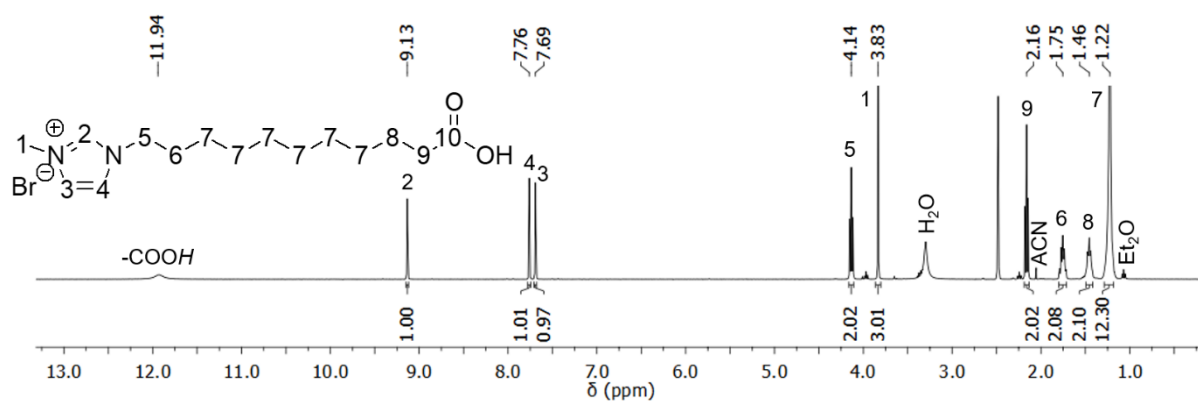


**Figure A18.**  $^1\text{H}$ -NMR spectrum of **5b**.

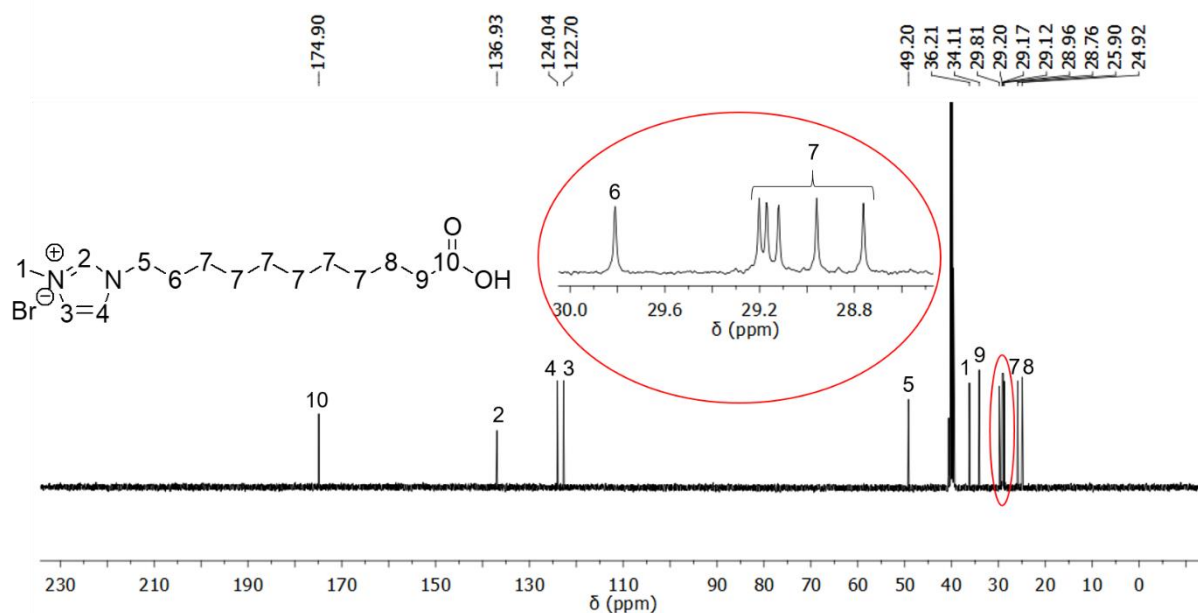


**Figure A19.**  $^{13}\text{C}$ -NMR spectrum of **5b**.

## 7.2 Characterization of the ELP sequence peptides (6-17)

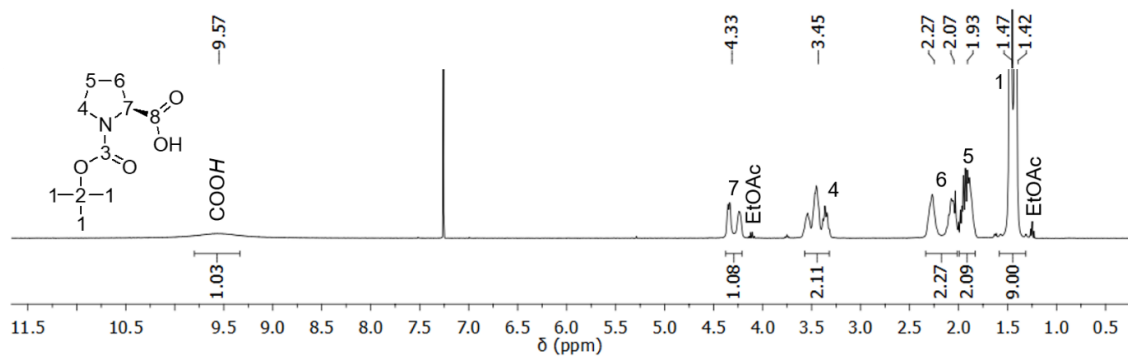


**Figure A20.**  $^1\text{H-NMR}$  spectrum of **6**.

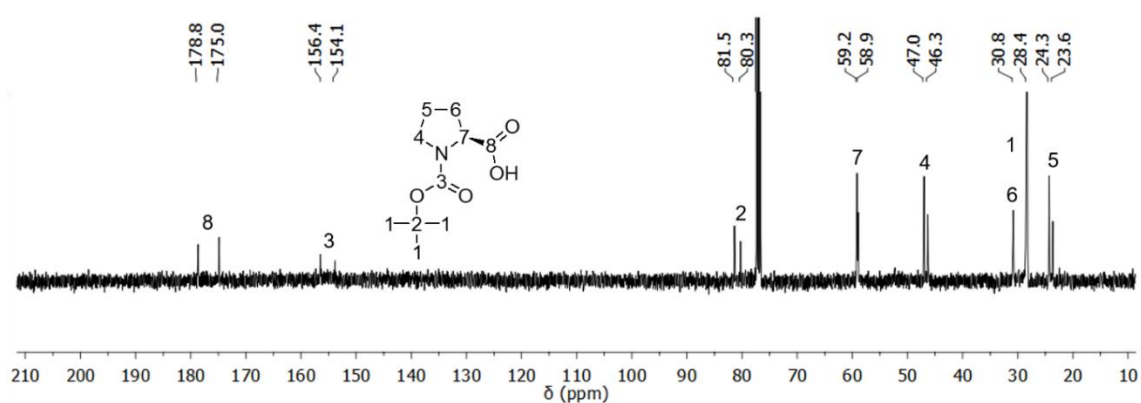


**Figure A21.**  $^{13}\text{C-NMR}$  spectrum of **6**.

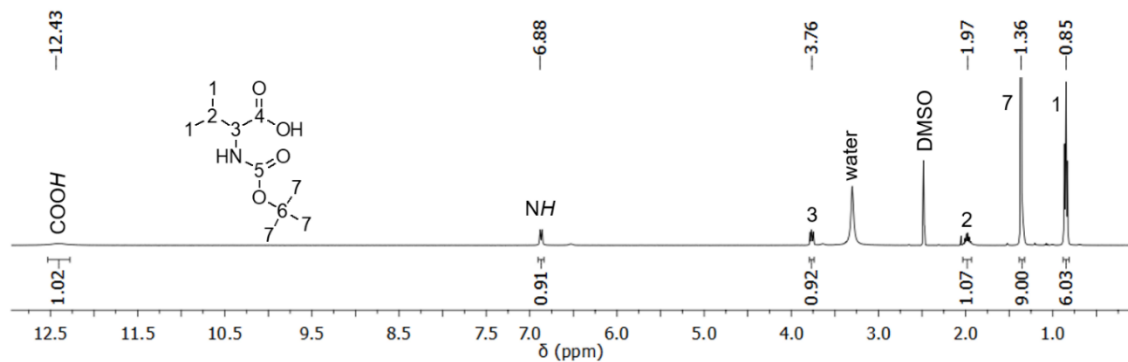


**Figure A22.**  $^1\text{H-NMR}$  spectrum of **7**.

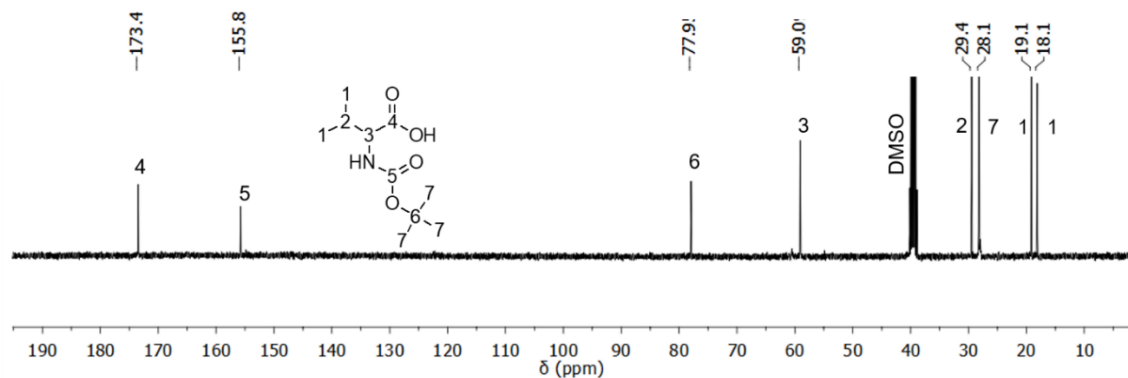


**Figure A23.**  $^{13}\text{C-NMR}$  spectrum of **7**.

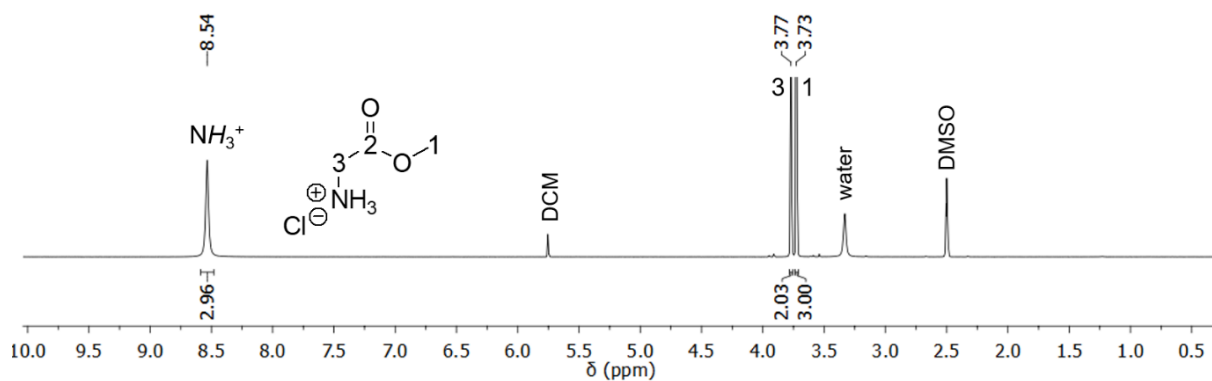


Figure A24. <sup>1</sup>H-NMR spectrum of 8.

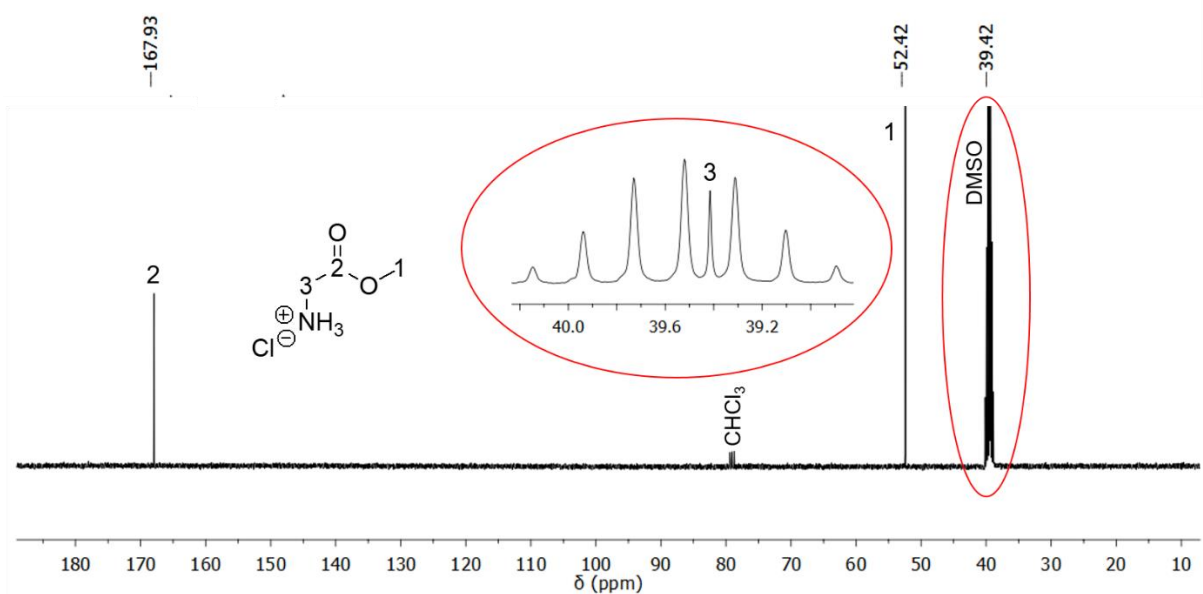


Figure A25. <sup>13</sup>C-NMR spectrum of 8.

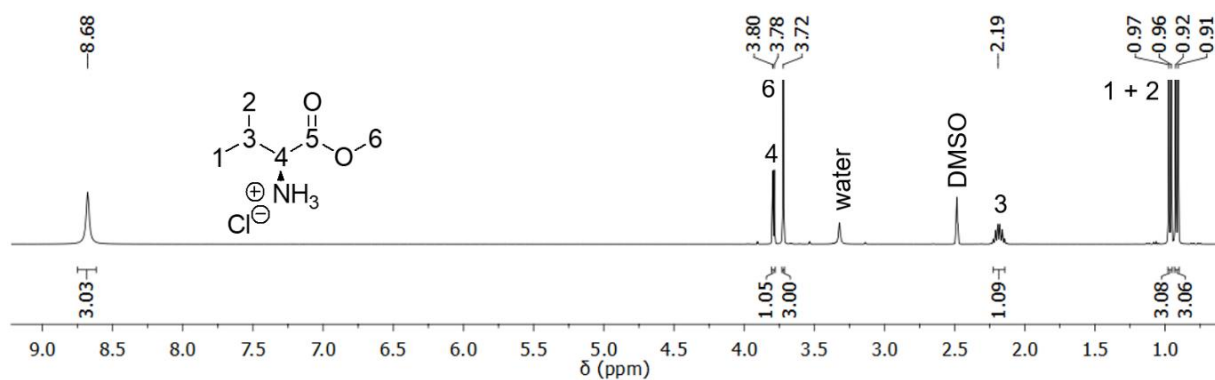


Figure A26. <sup>1</sup>H-NMR spectrum of 9.

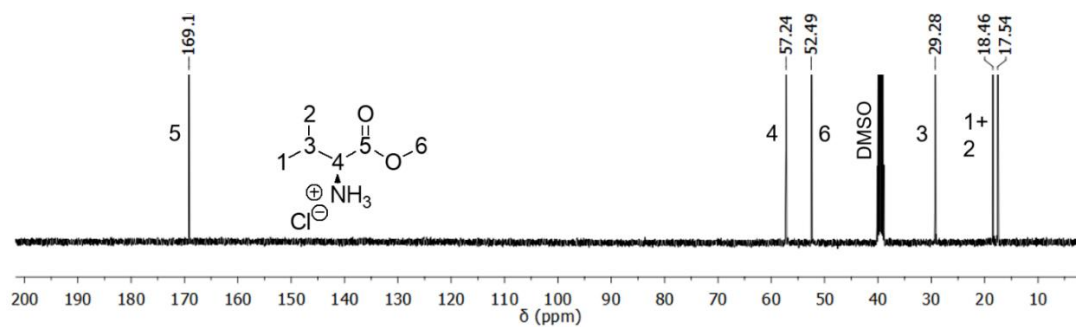


Figure A27.  $^1\text{H-NMR}$  spectrum of **9**.

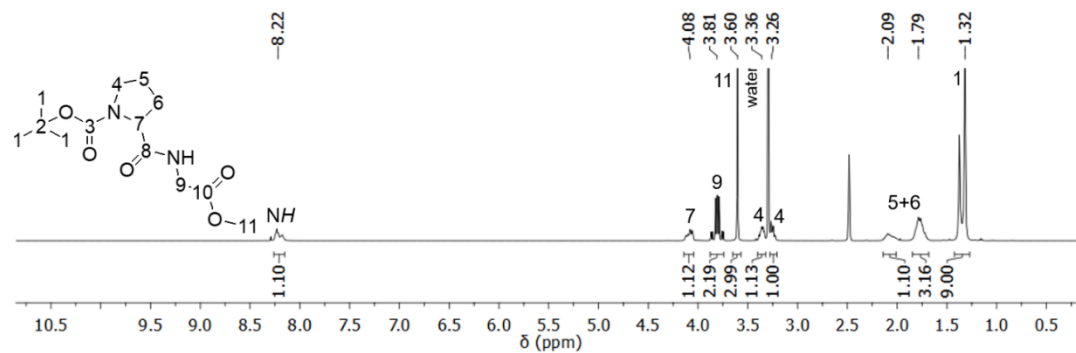


Figure A28.  $^1\text{H-NMR}$  spectrum of **10**.

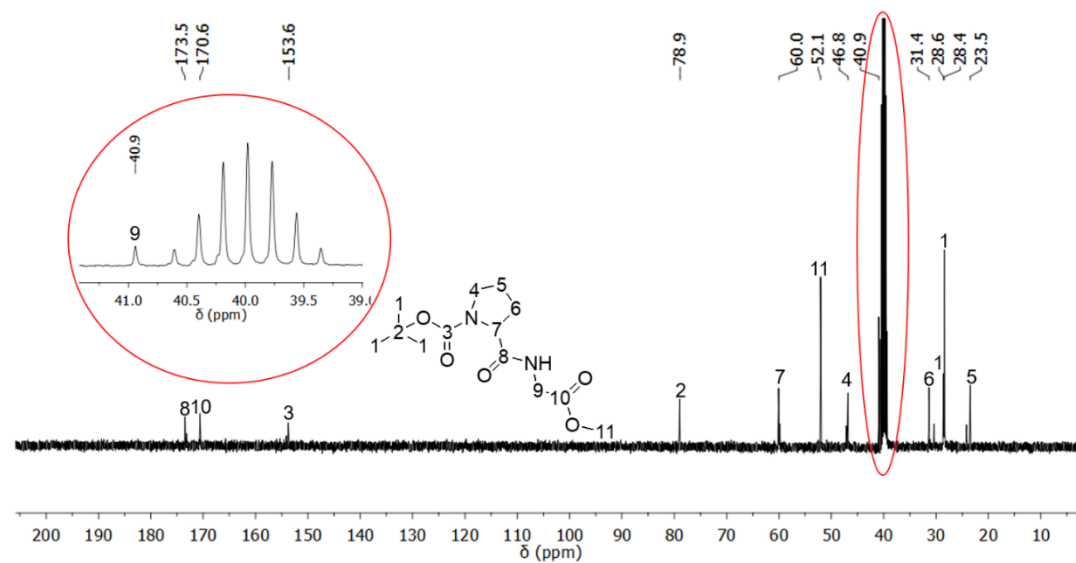


Figure A29.  $^{13}\text{C-NMR}$  spectrum of **10**.

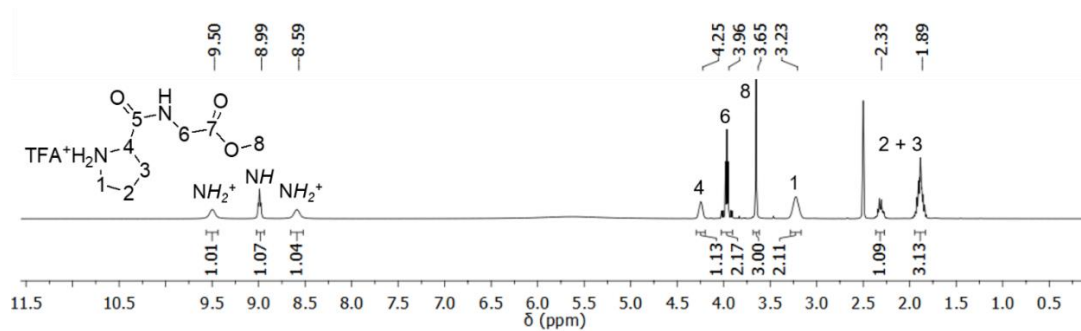
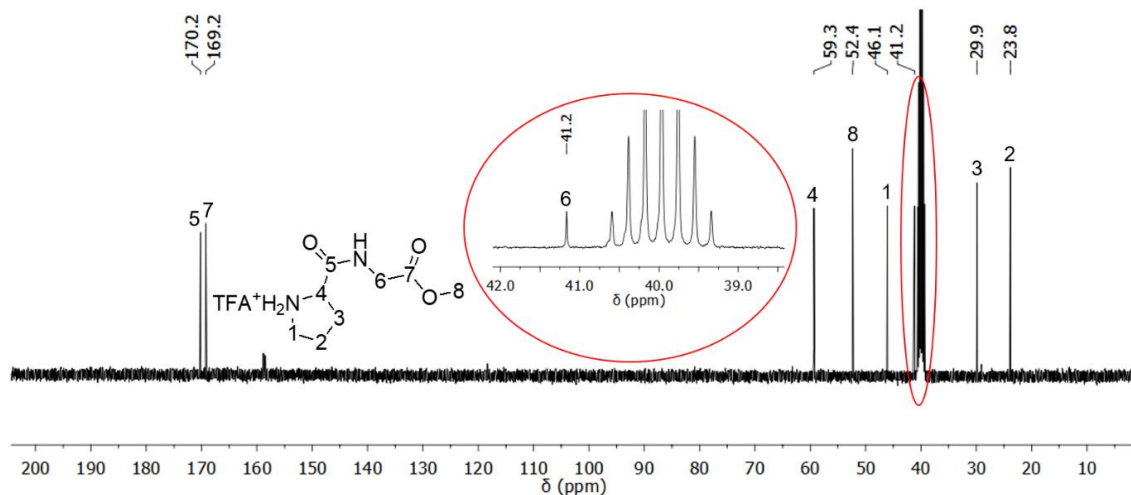
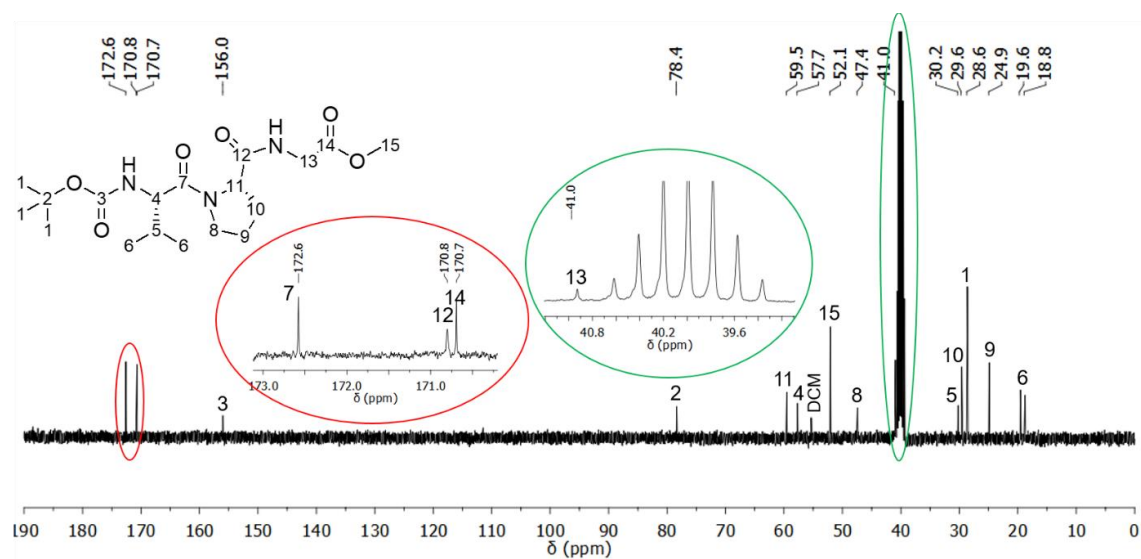


Figure A30.  $^1\text{H-NMR}$  spectrum of **11**.



**Figure A31.**  $^{13}\text{C}$ -NMR spectrum of **11**.



**Figure A32.**  $^{13}\text{C}$ -NMR spectrum of **12**.

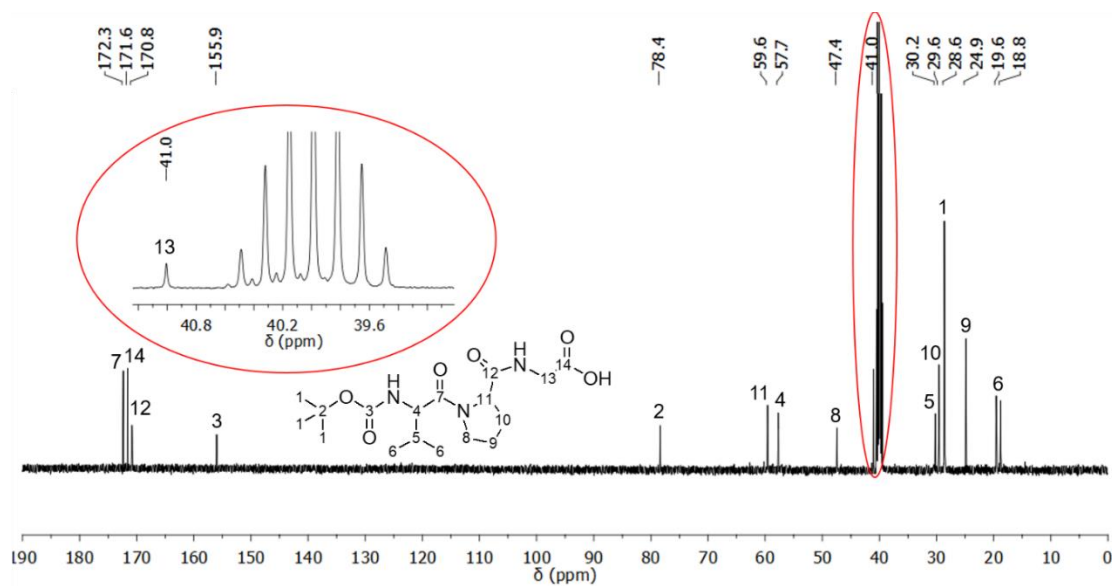


**Figure A33.**  $^{13}\text{C}$ -NMR spectrum of **13**.

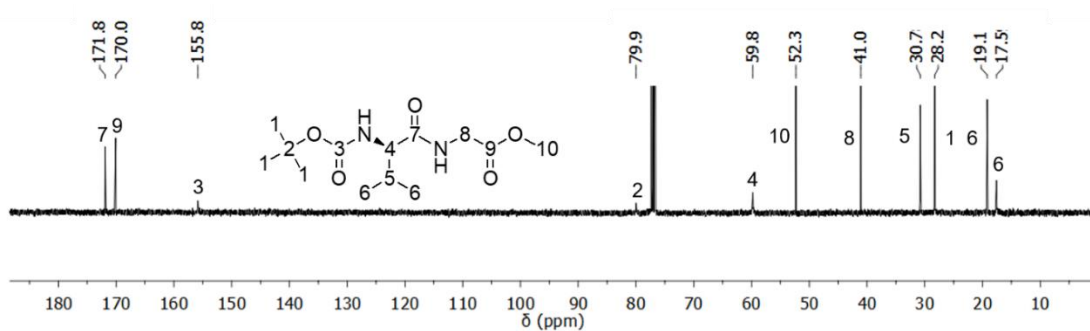
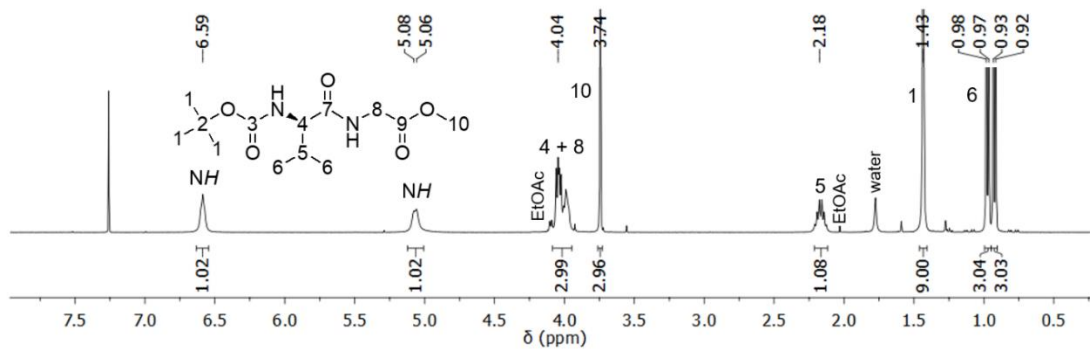


**Figure A35.**  $^{13}\text{C-NMR}$  spectrum of **14**.

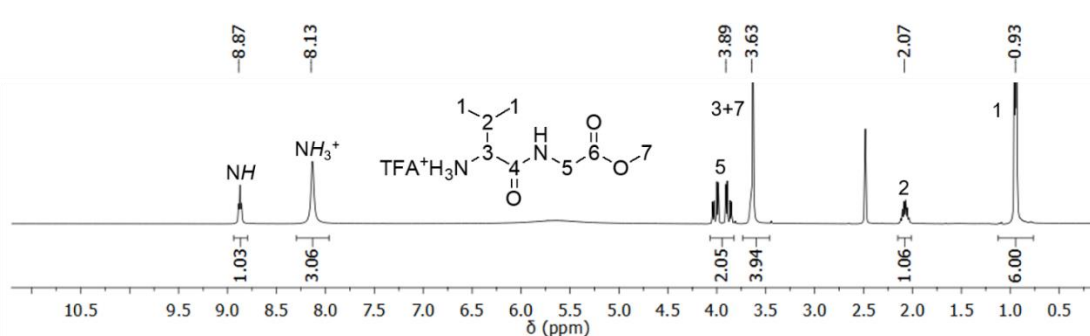


**Figure A36.**  $^1\text{H-NMR}$  spectrum of **15**.

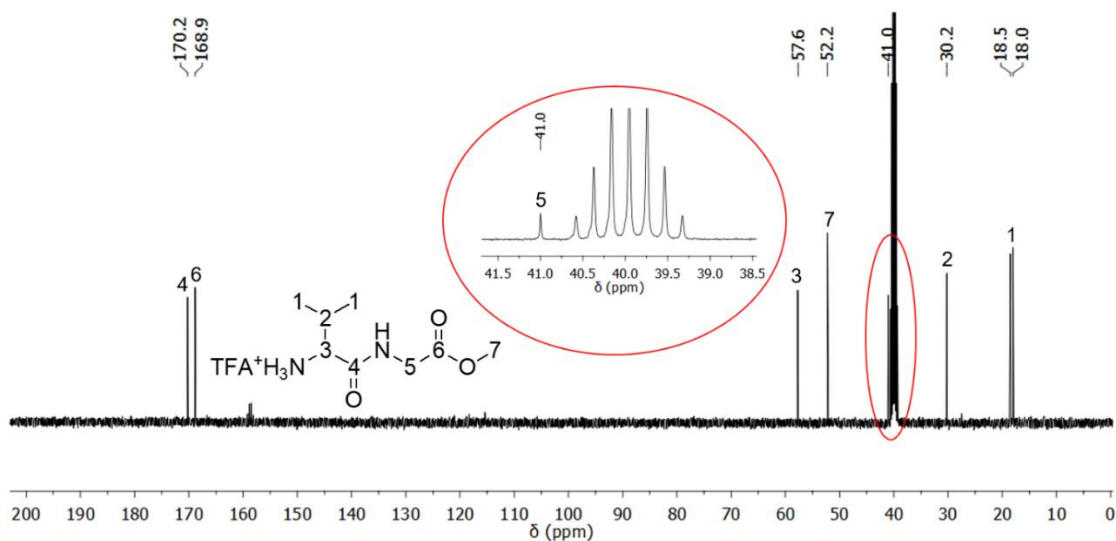


**Figure A37.**  $^{13}\text{C-NMR}$  spectrum of **15**.

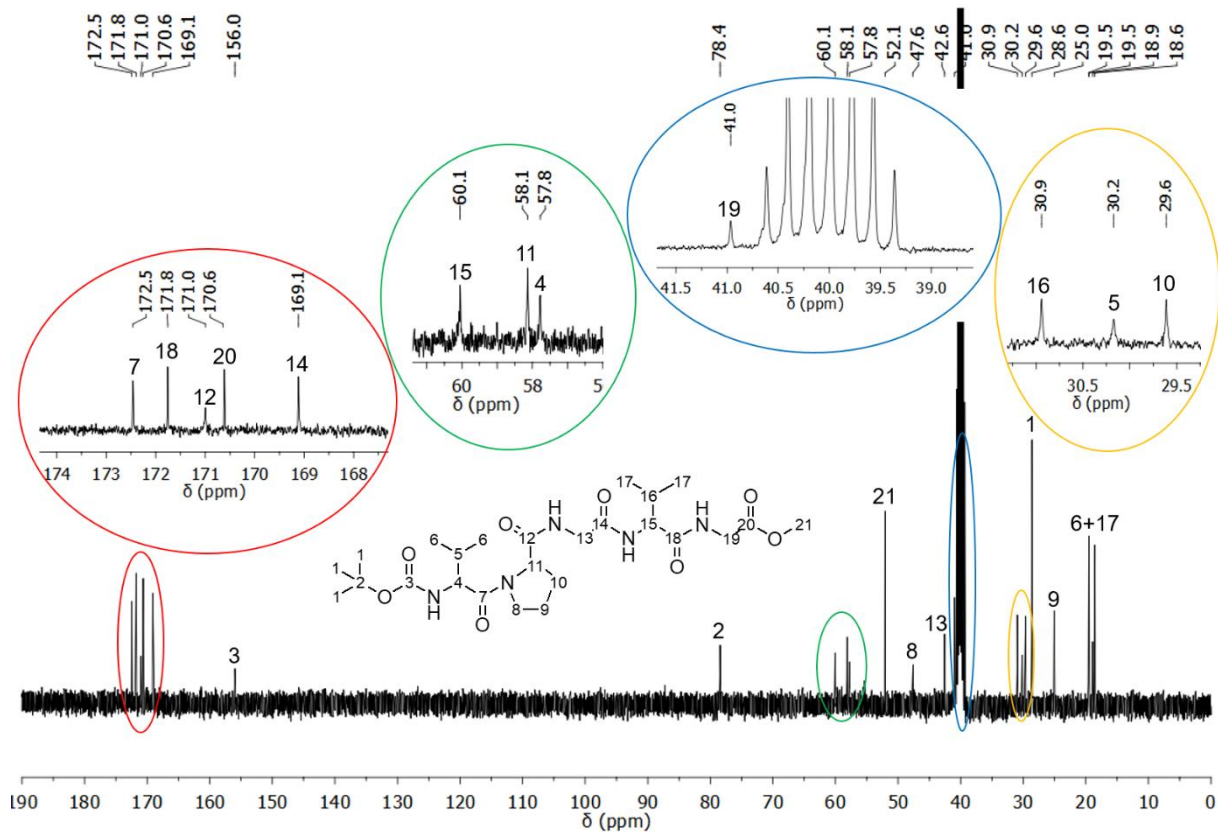


Figure A38.  $^{13}\text{C}$ -NMR spectrum of 16.

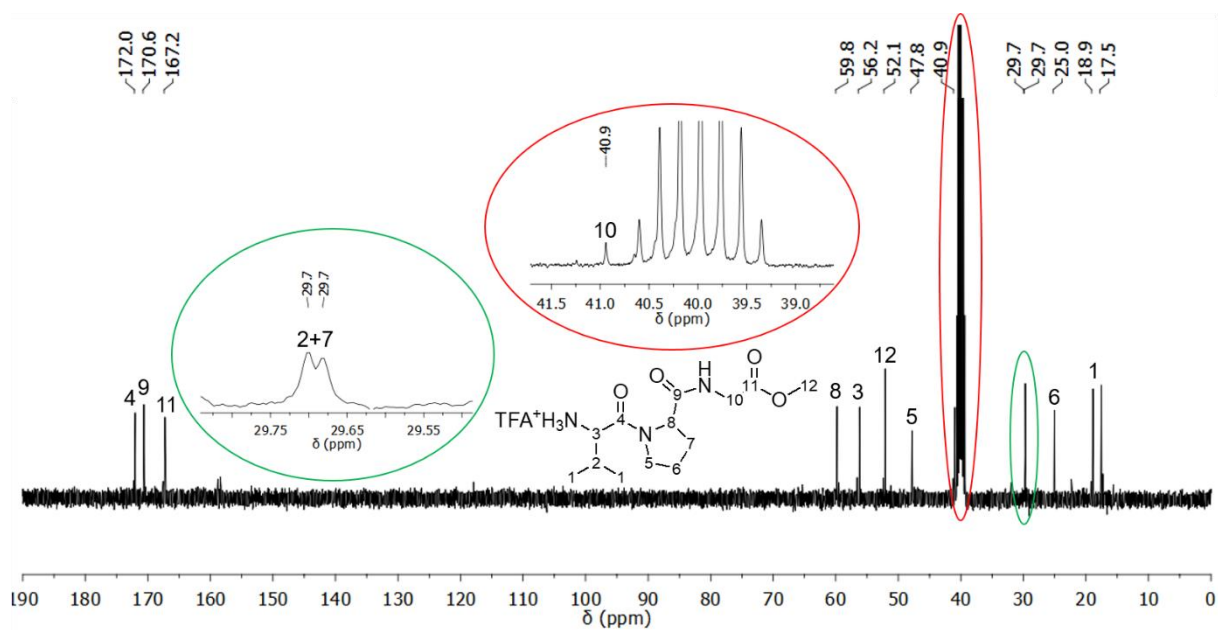


Figure A39.  $^{13}\text{C}$ -NMR spectrum of 17.

### 7.3 Characterization of the ELP sequence elongation (18-26)

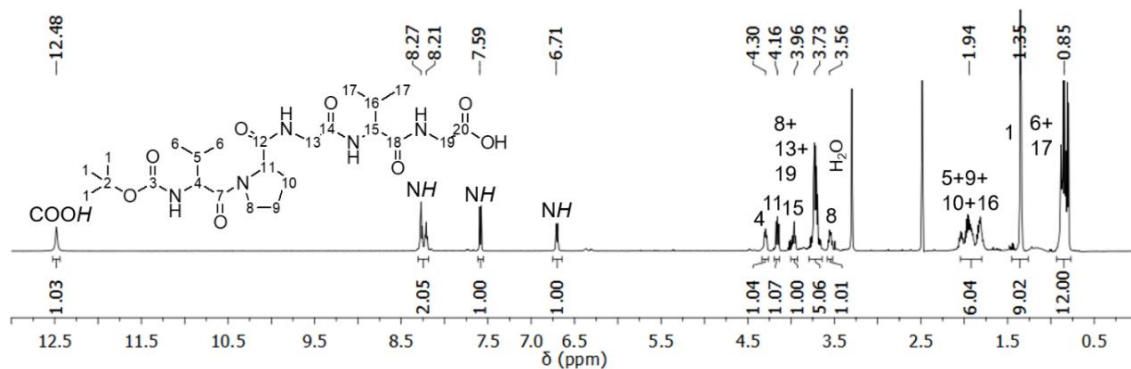


Figure A40. <sup>1</sup>H-NMR spectrum of 18.

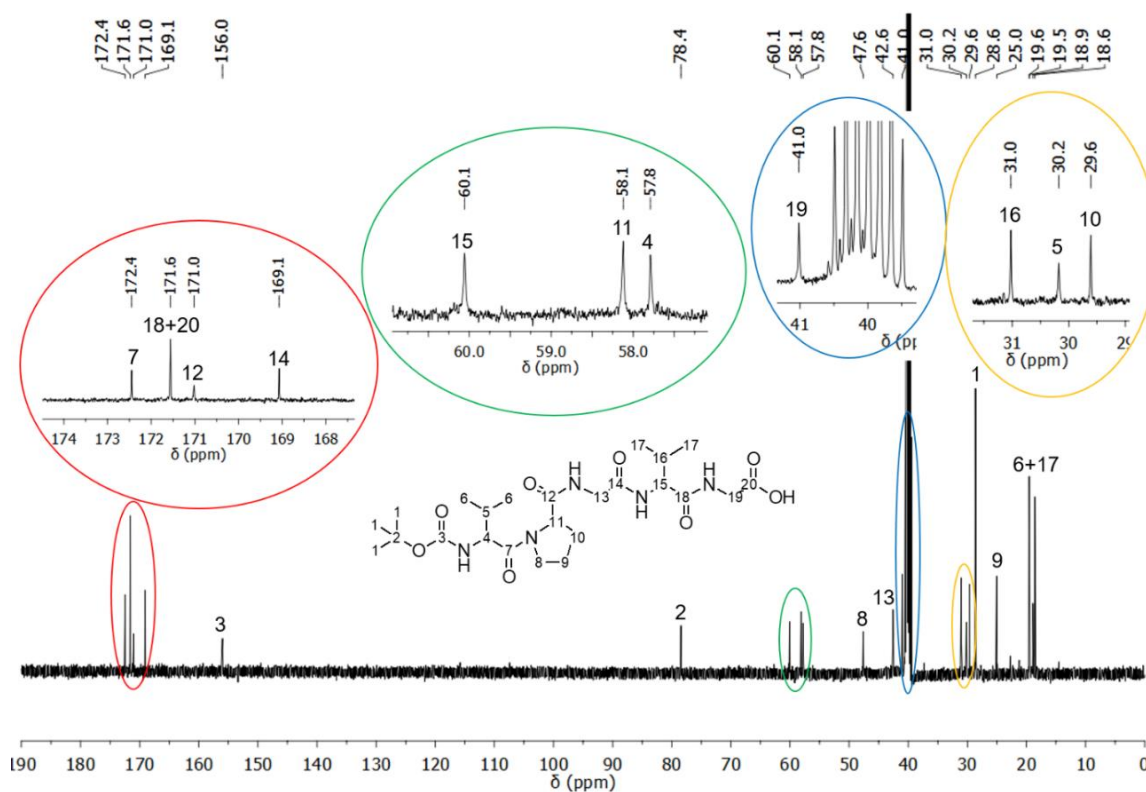


Figure A41. <sup>13</sup>C-NMR spectrum of 18.

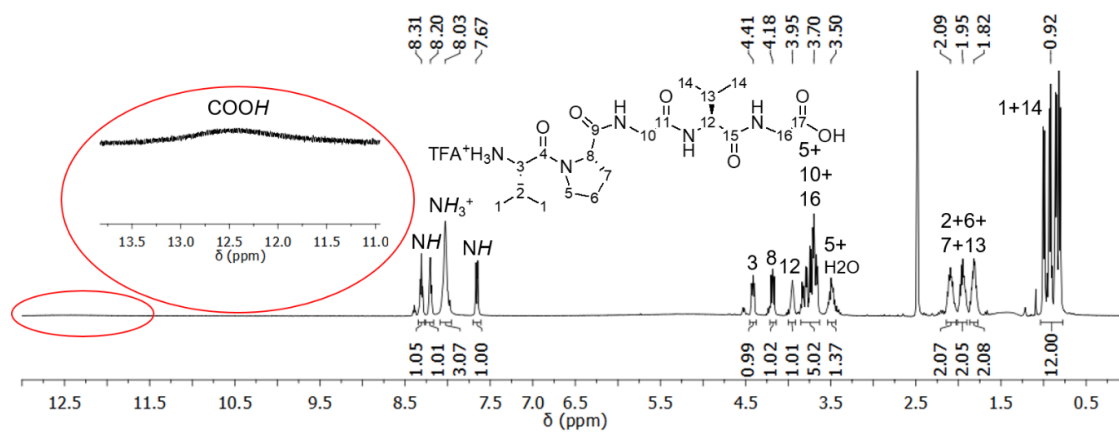


Figure A42. <sup>1</sup>H-NMR spectrum of 19.

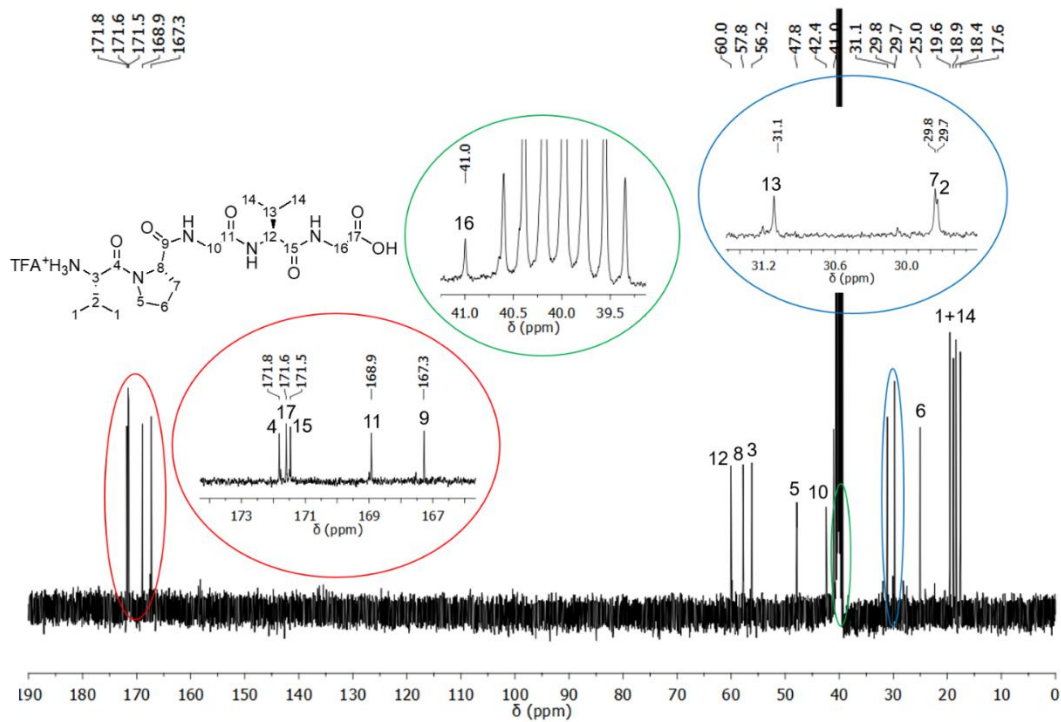


Figure A43.  $^{13}\text{C}$ -NMR spectrum of **19**.

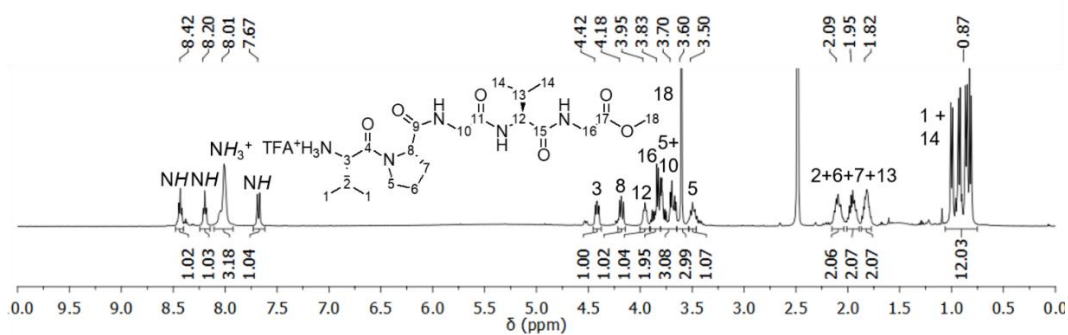


Figure A44.  $^1\text{H}$ -NMR spectrum of **21**.

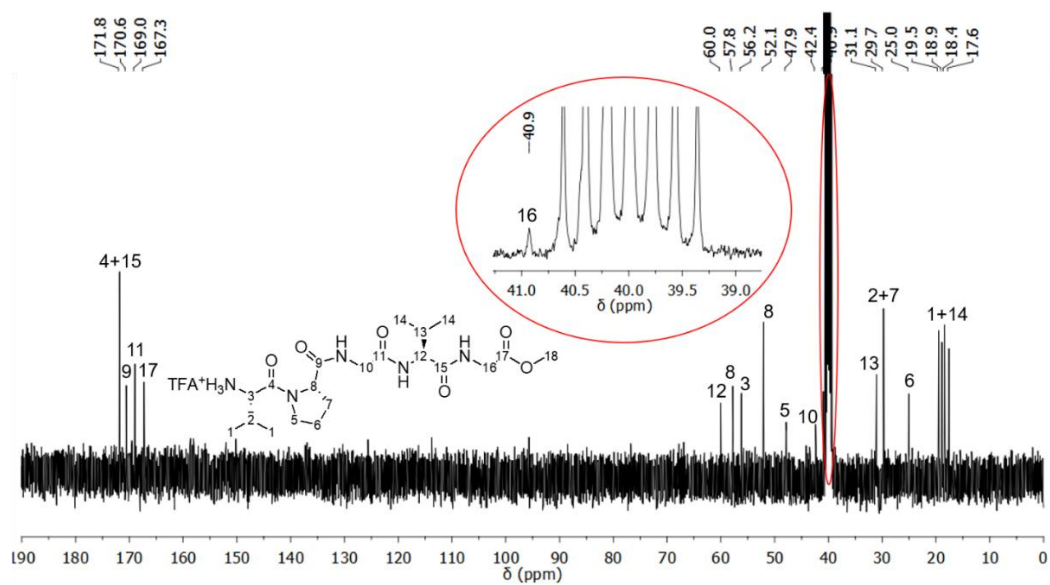


Figure A45.  $^{13}\text{C}$ -NMR spectrum of **21**.

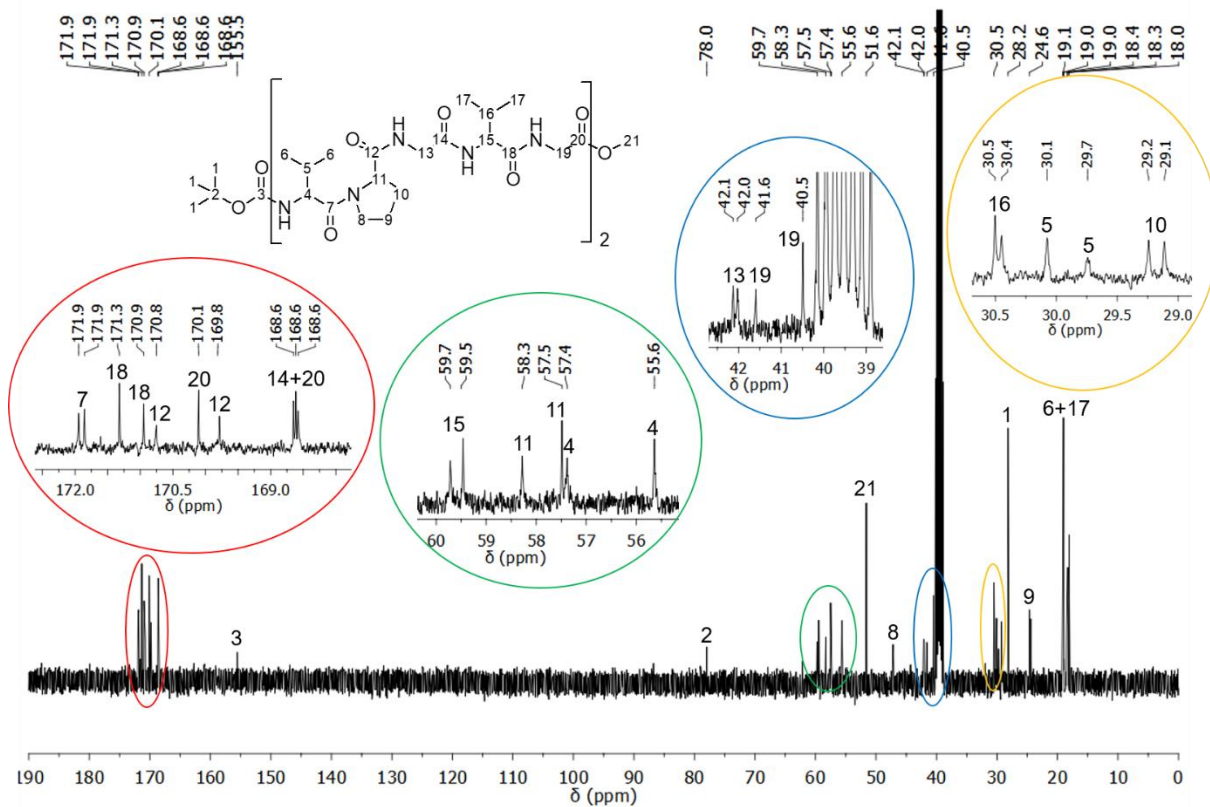


Figure A46.  $^{13}\text{C}$ -NMR spectrum of **22**.



Figure A47. ESI-TOF-MS of **22**.

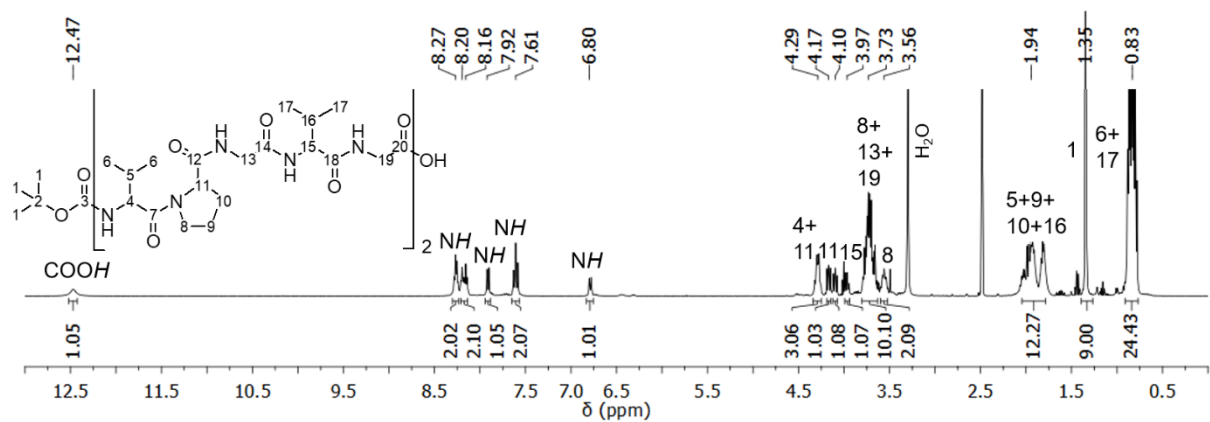


Figure A48.  $^1\text{H}$ -NMR spectrum of **23**.

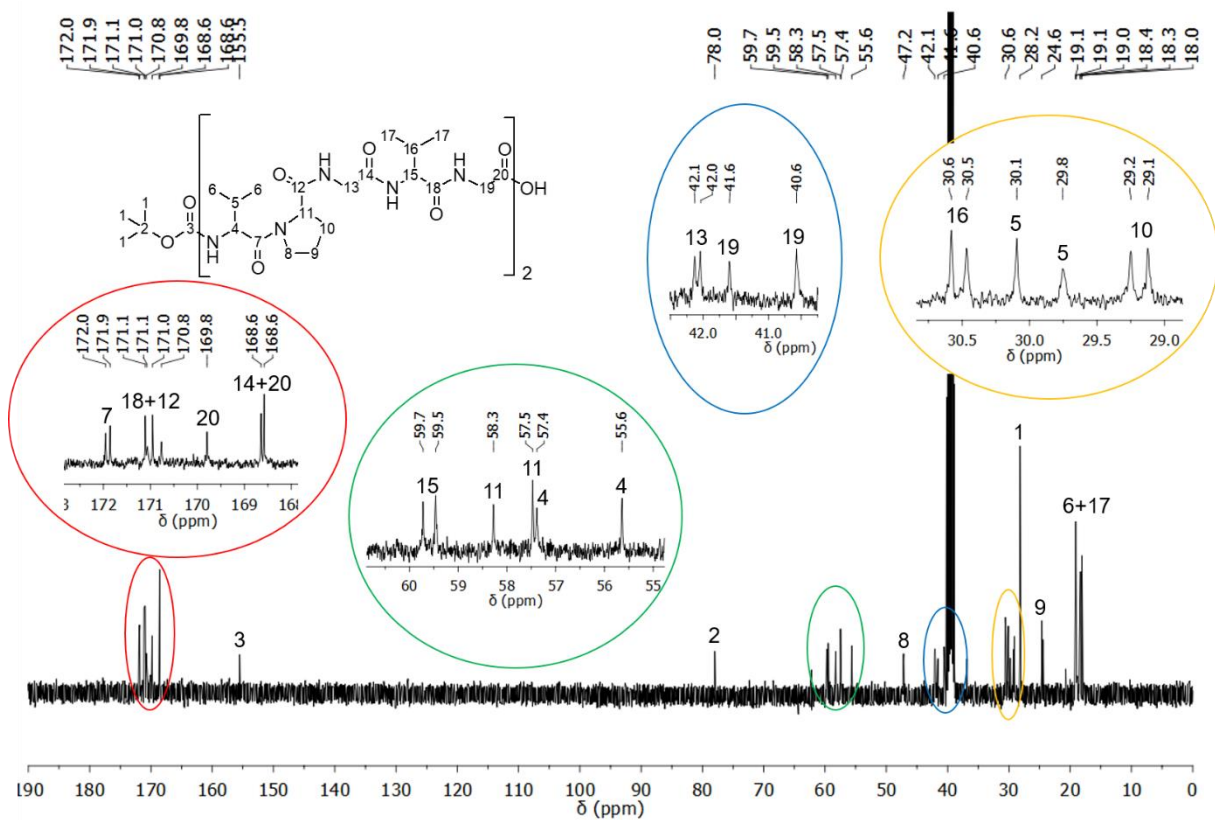


Figure A49.  $^{13}\text{C}$ -NMR spectrum of **23**.

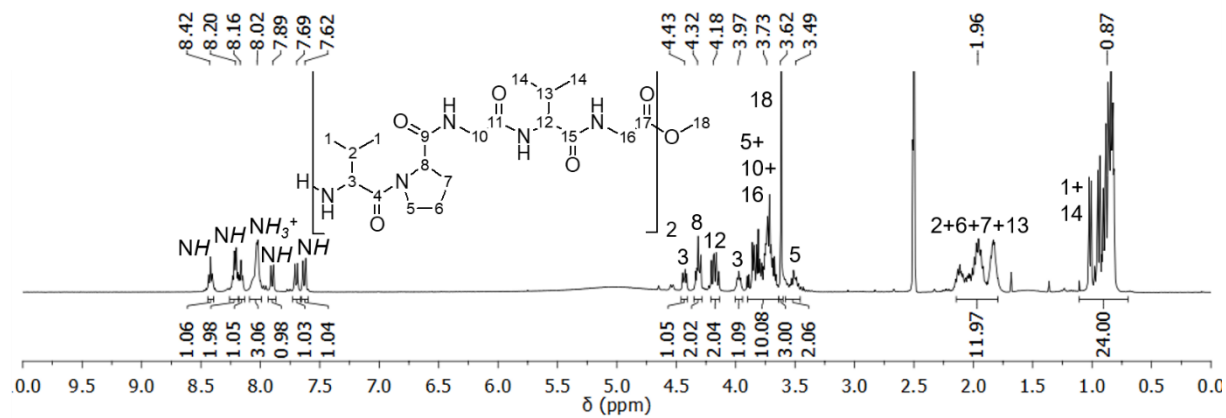


Figure A50.  $^1\text{H}$ -NMR spectrum of **24**.

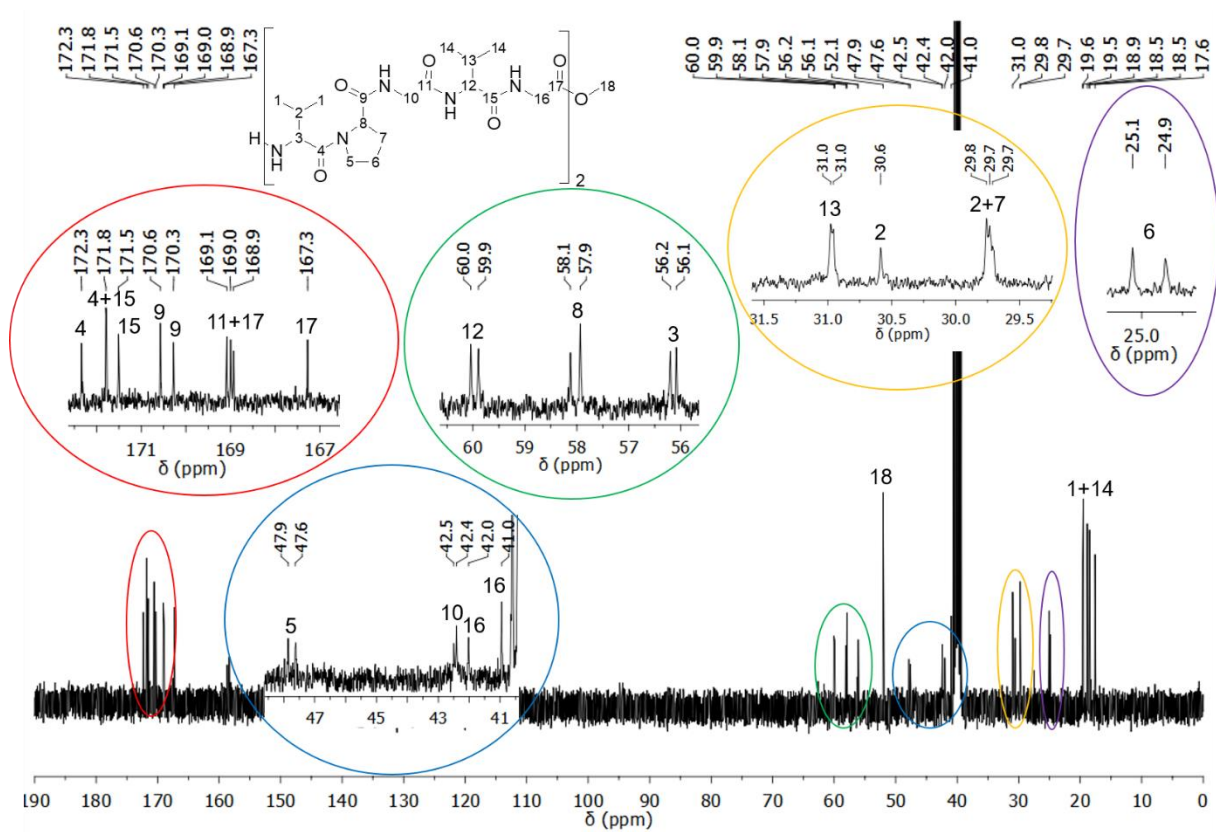


Figure A51.  $^{13}\text{C}$ -NMR spectrum of 24.

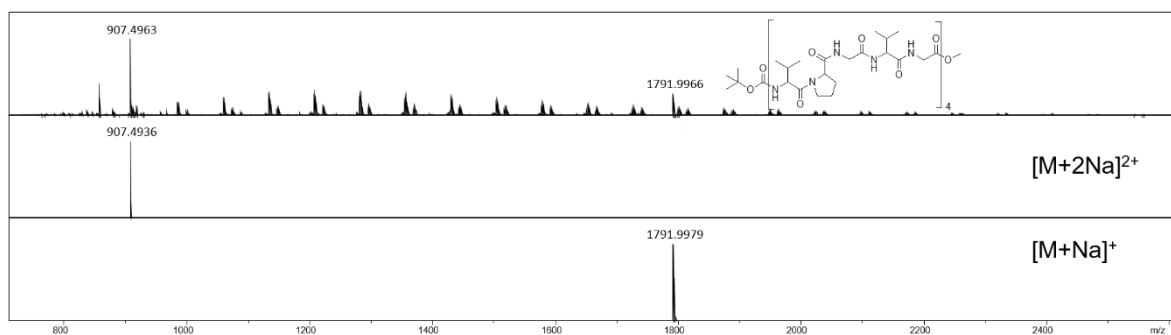


Figure A52. ESI-TOF-MS of 25.

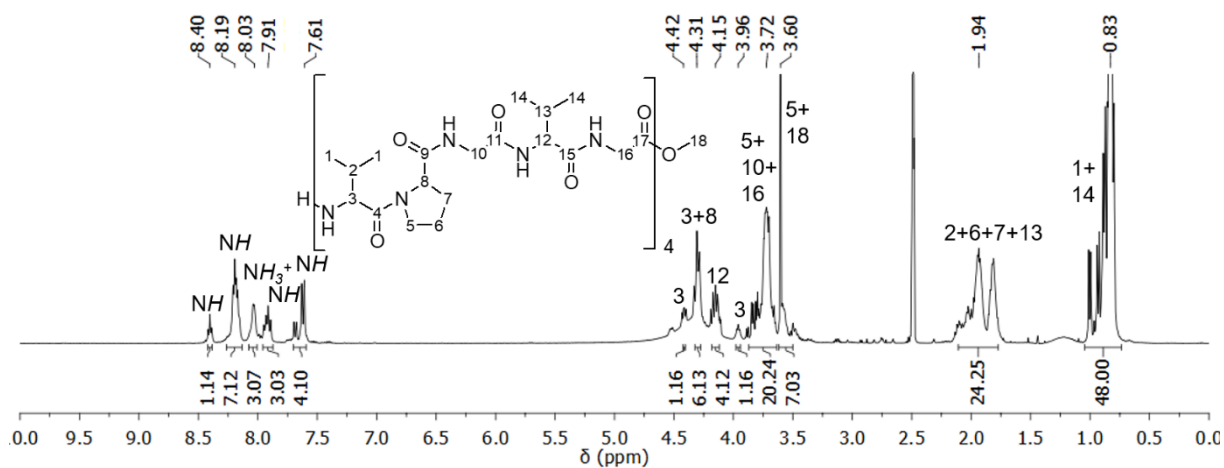


Figure A53.  $^1\text{H}$ -NMR spectrum of 26.

## 7.4 Characterization of the linear mechanocatalysts (27a-g)

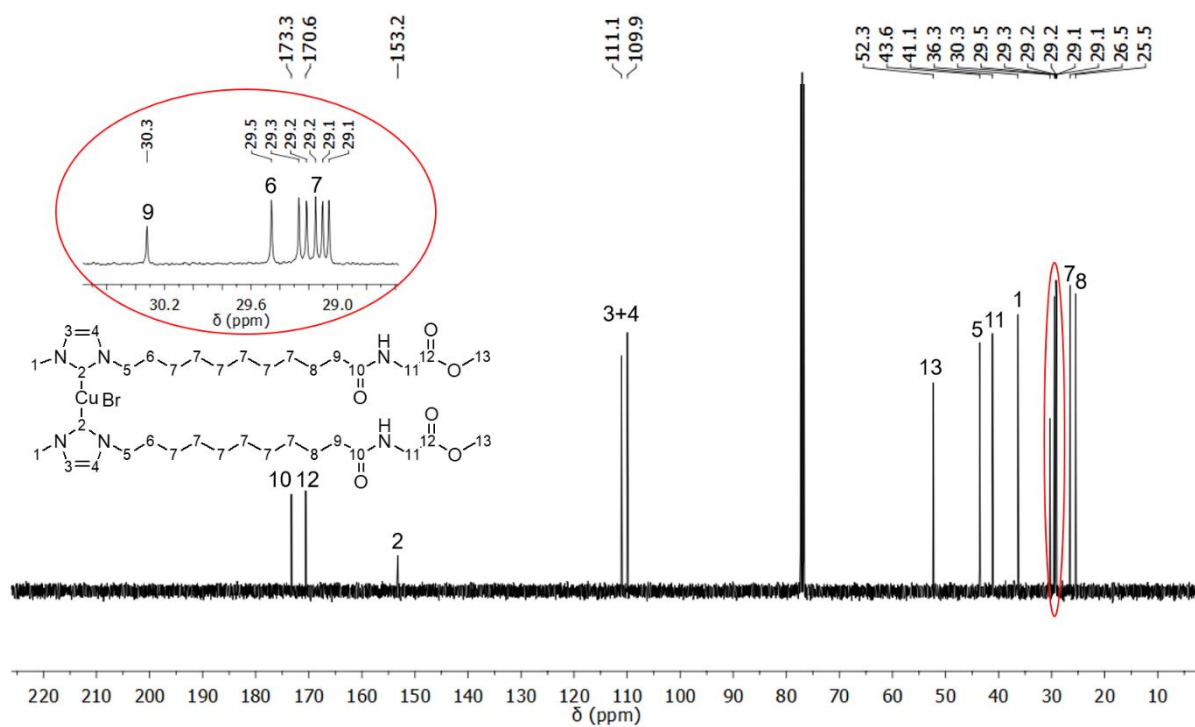


Figure A54.  $^{13}\text{C}$ -NMR spectrum of 27a.

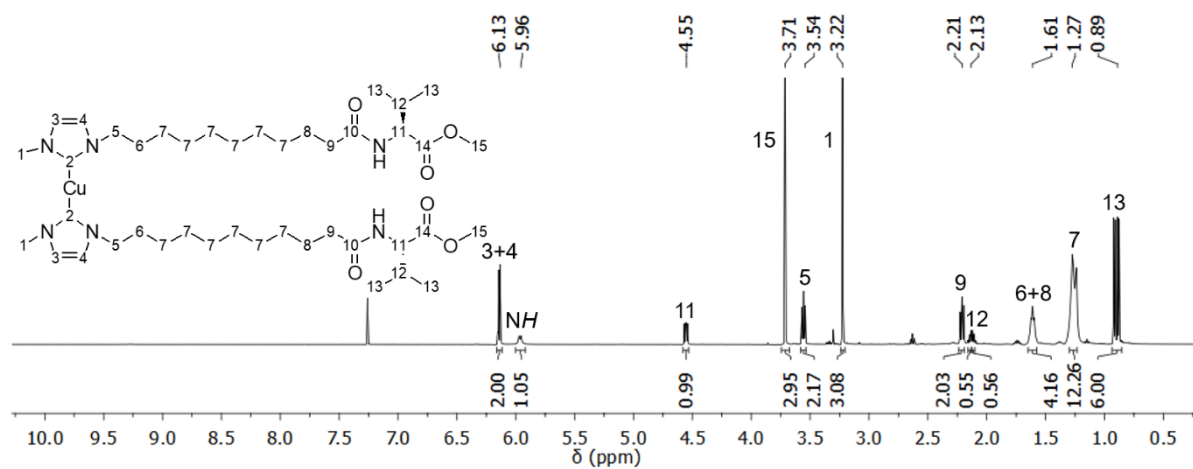


Figure A55.  $^1\text{H}$ -NMR spectrum of 27b.

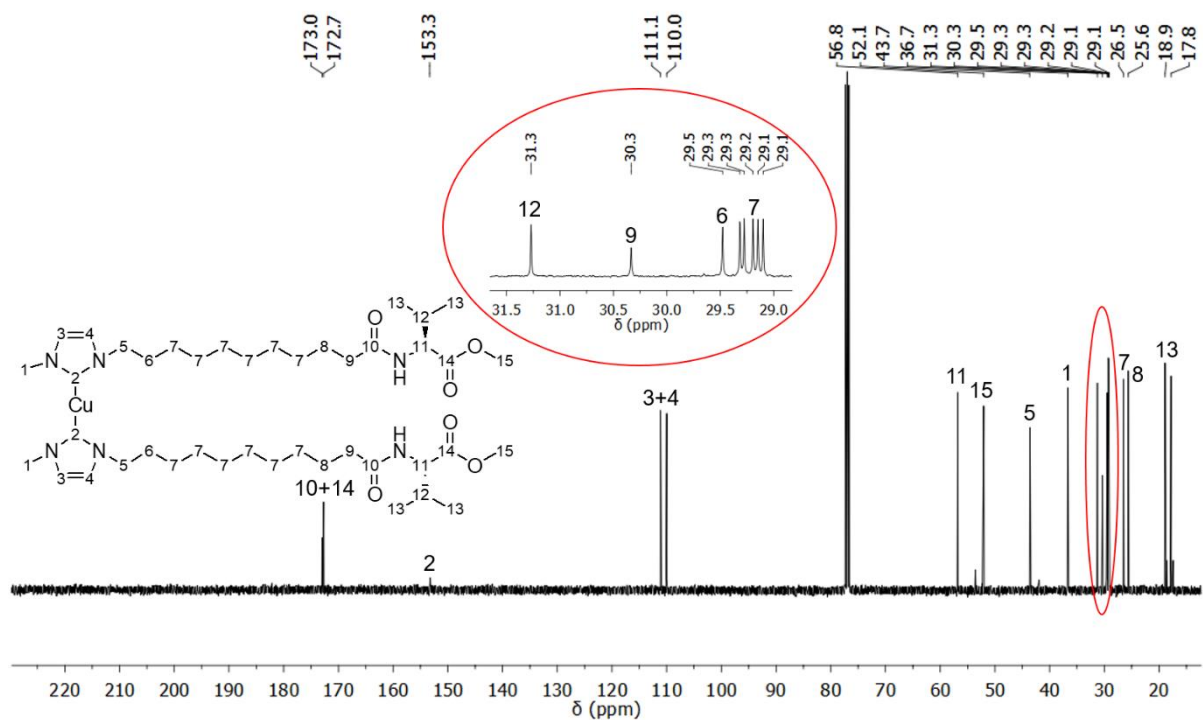


Figure A56.  $^{13}\text{C}$ -NMR spectrum of **27b**.

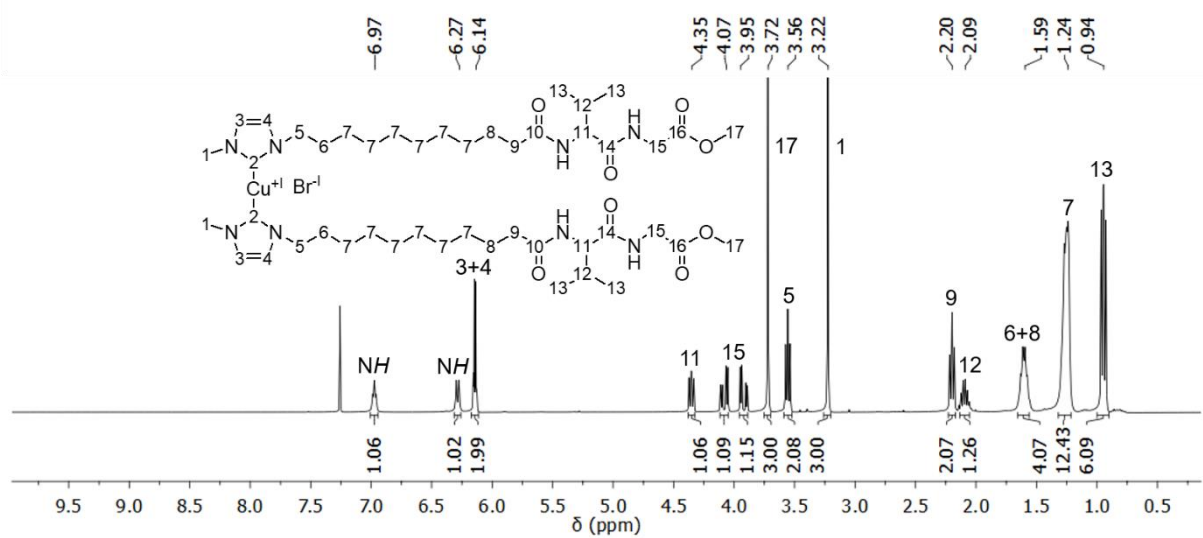
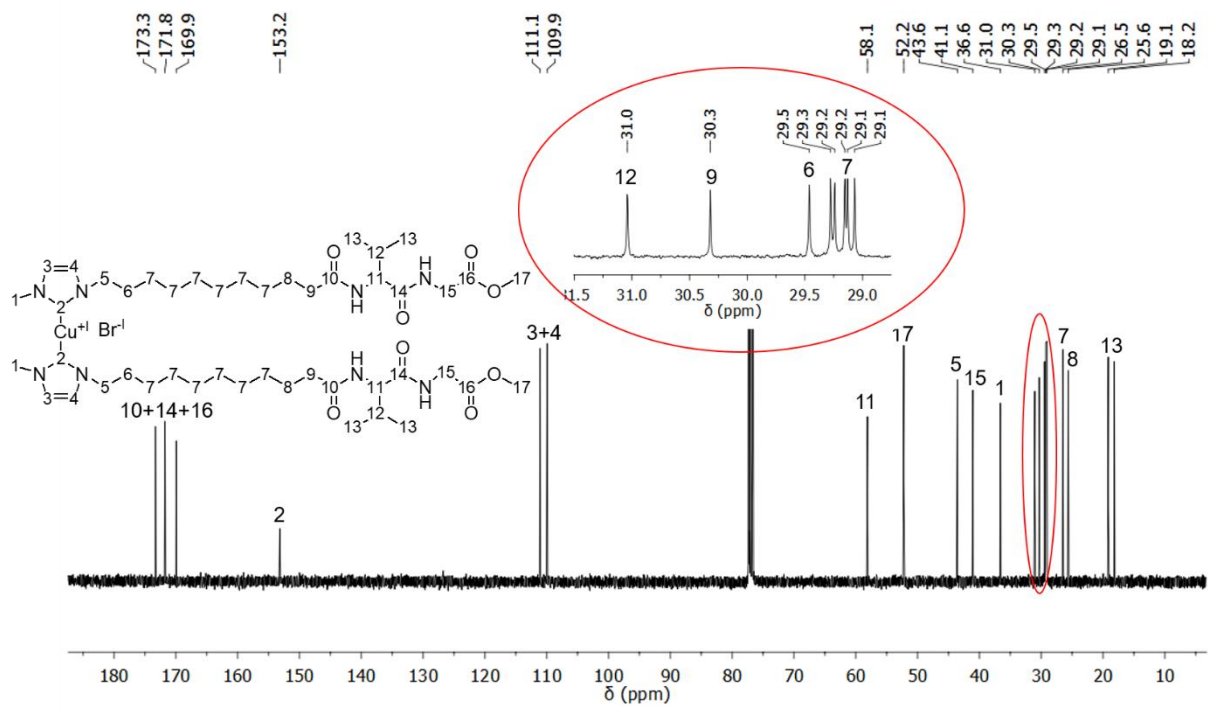
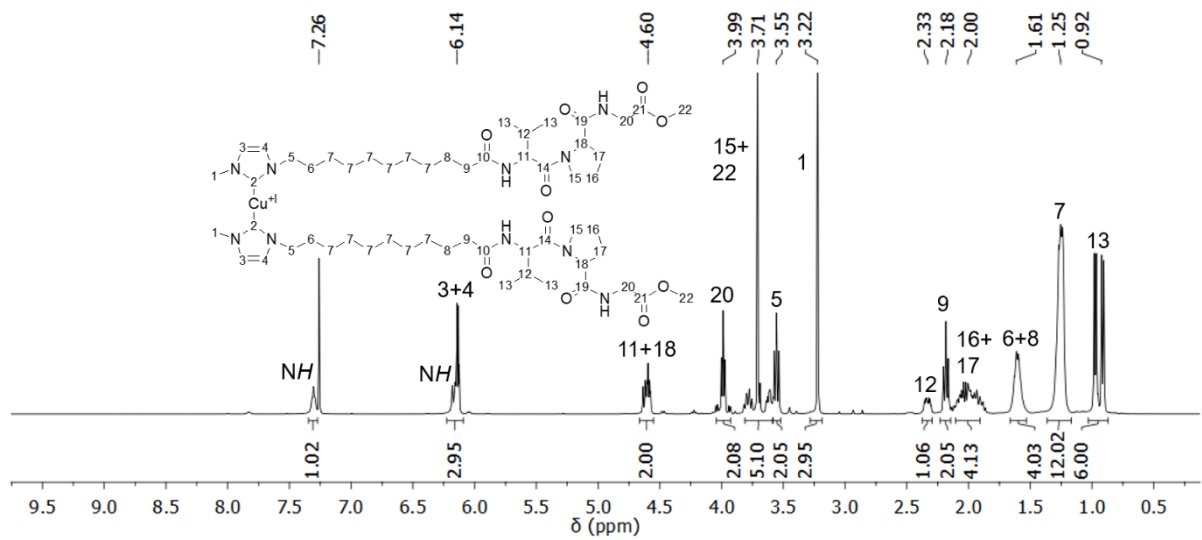


Figure A57.  $^1\text{H}$ -NMR spectrum of **27c**.



**Figure A58.**  $^{13}\text{C}$ -NMR spectrum of **27c**.



**Figure A59.**  $^1\text{H}$ -NMR spectrum of **27d**.

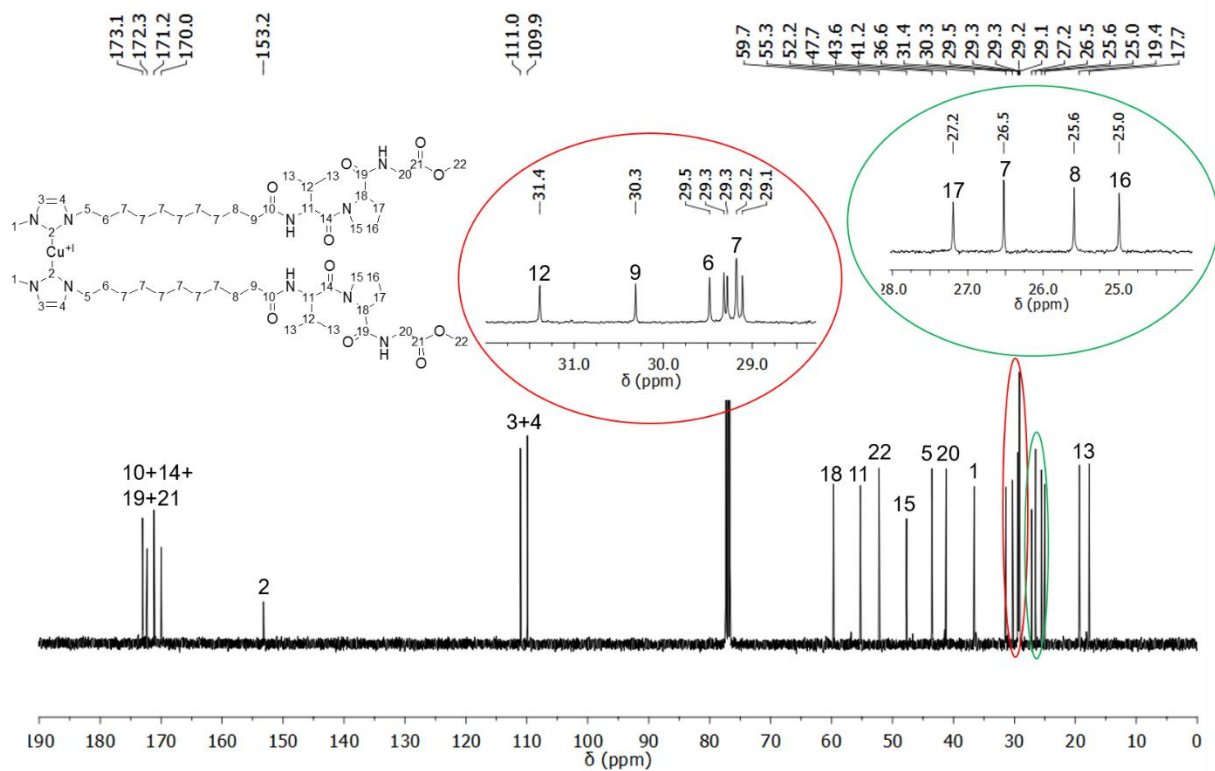


**Figure A60.**  $^{13}\text{C}$ -NMR spectrum of **27d**.

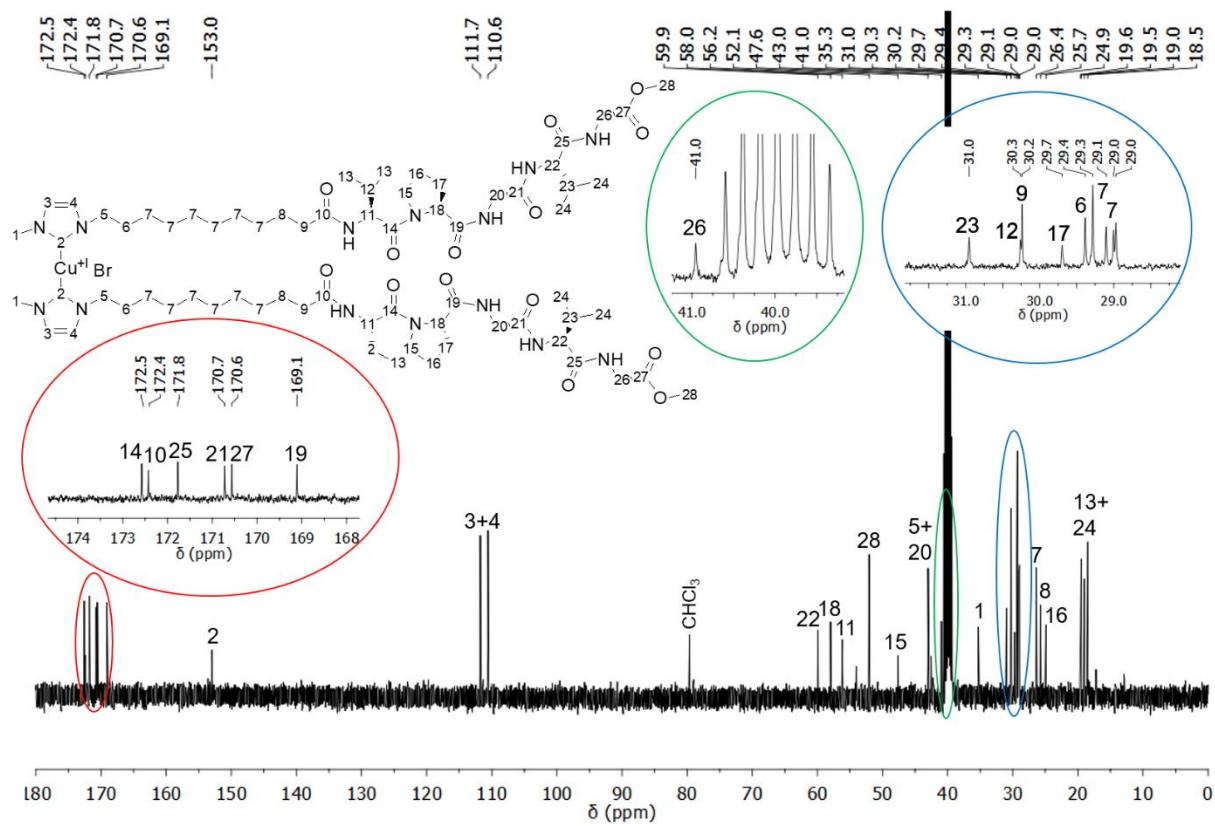


**Figure A61.**  $^{13}\text{C}$ -NMR spectrum of **27e**.

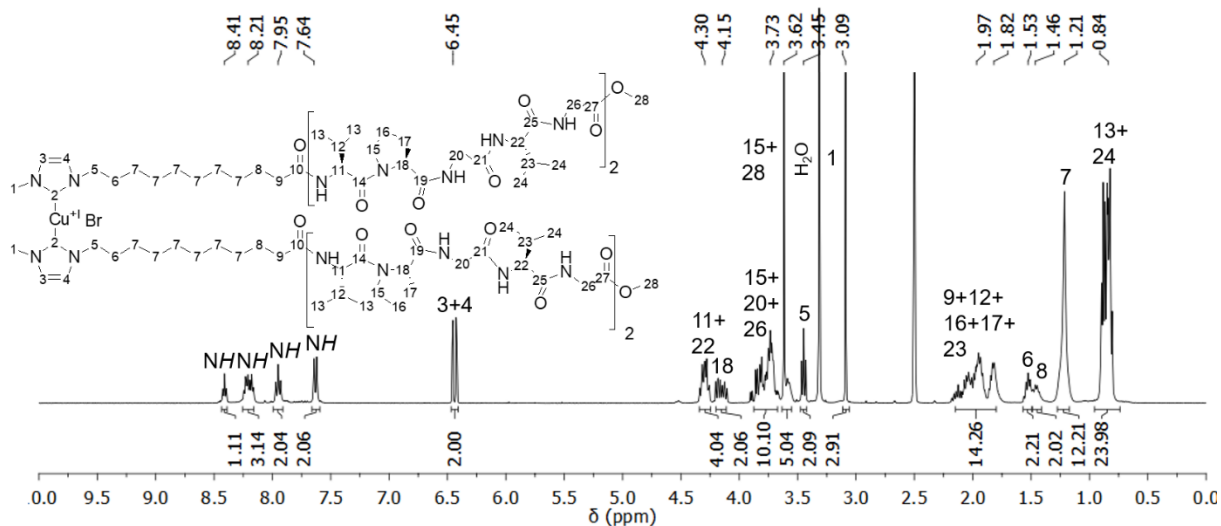


Figure A62.  $^1\text{H-NMR}$  spectrum of 27f.

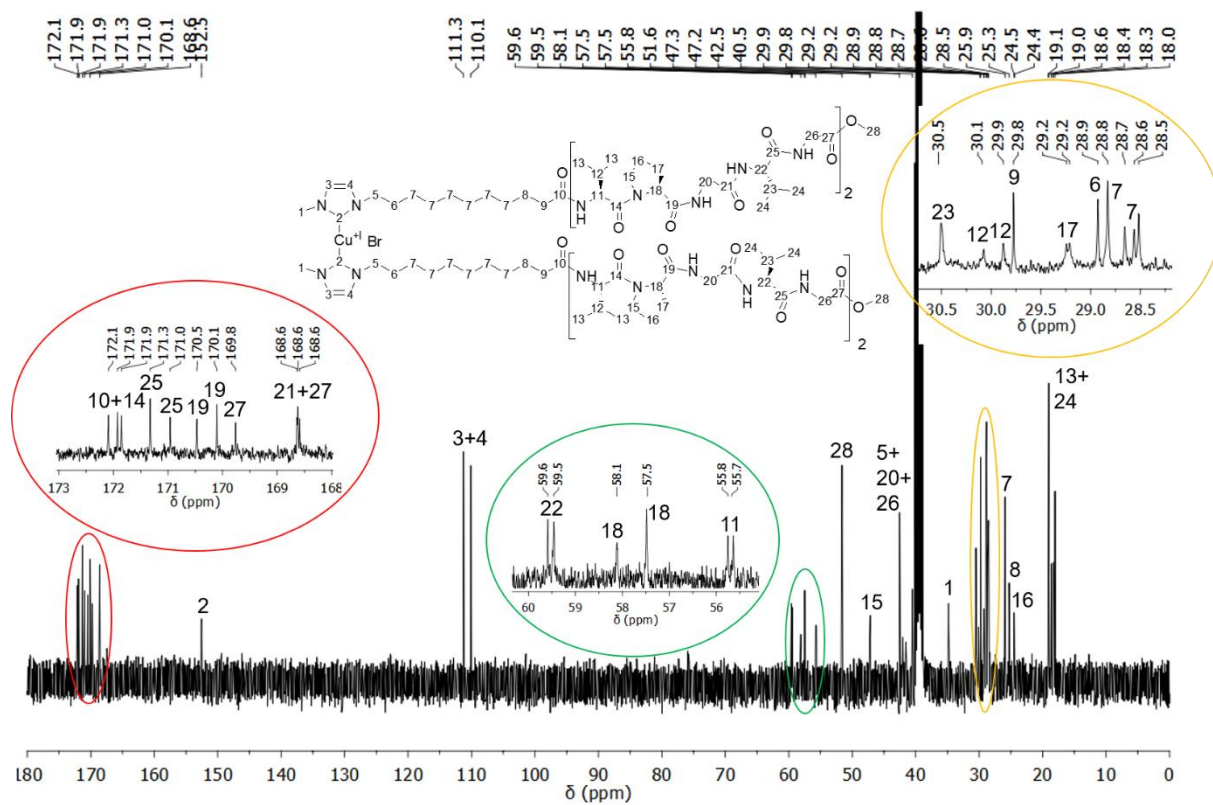


Figure A63.  $^{13}\text{C-NMR}$  spectrum of 27f.

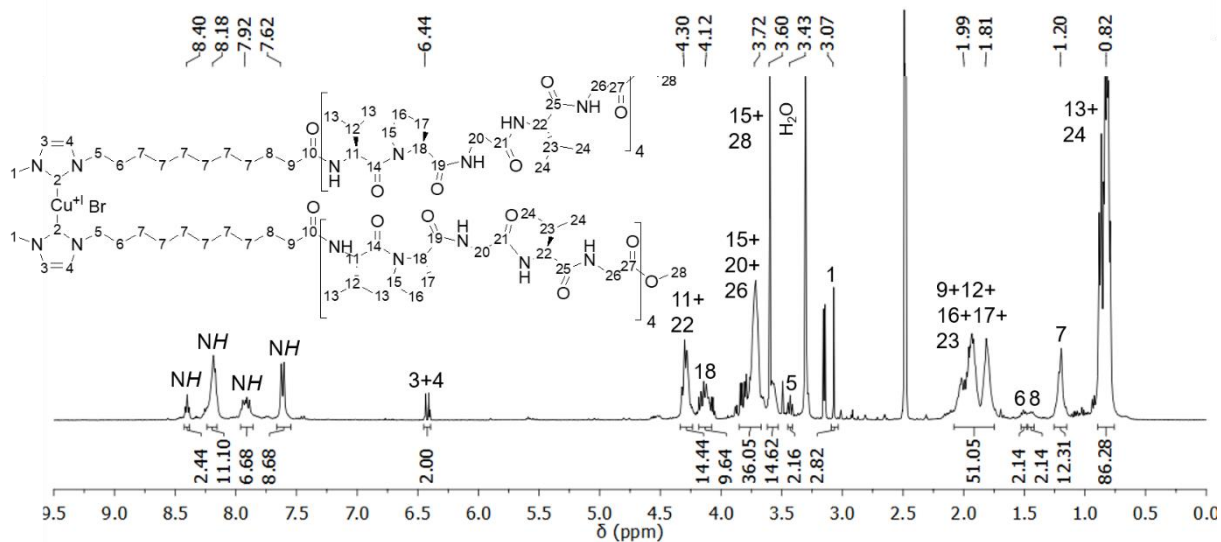


Figure A64.  $^1\text{H-NMR}$  spectrum of **27g**.

### 7.5 Characterization of benzyl azide (**29**)

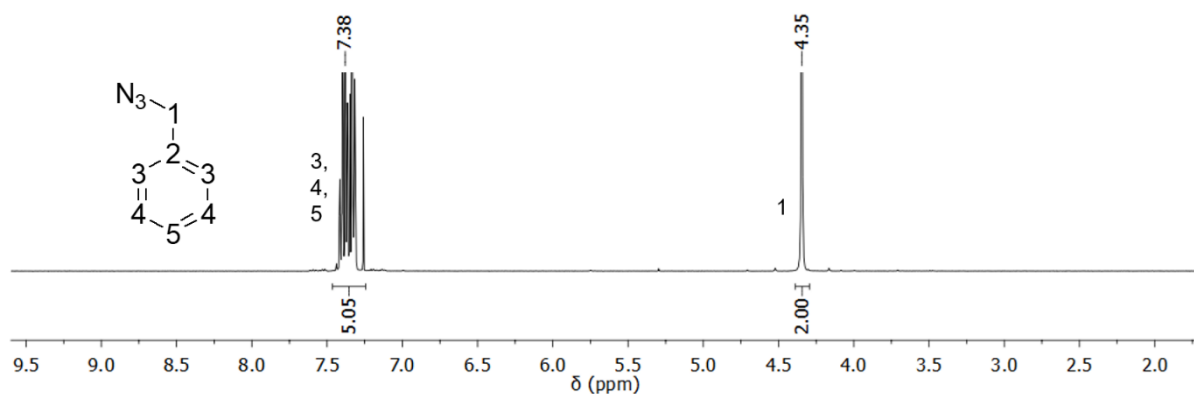


Figure A65.  $^1\text{H-NMR}$  spectrum of **29**.

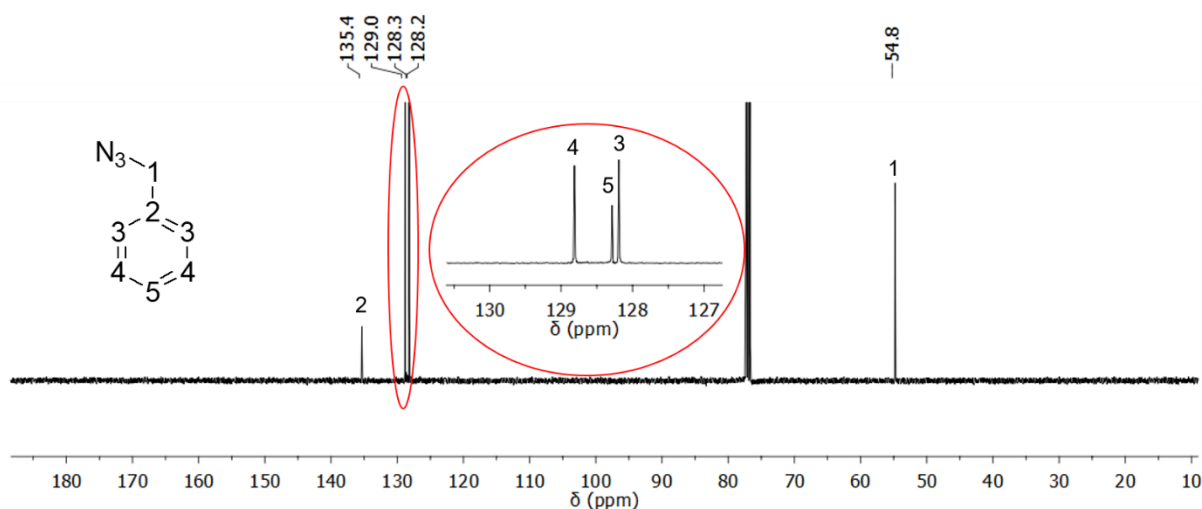
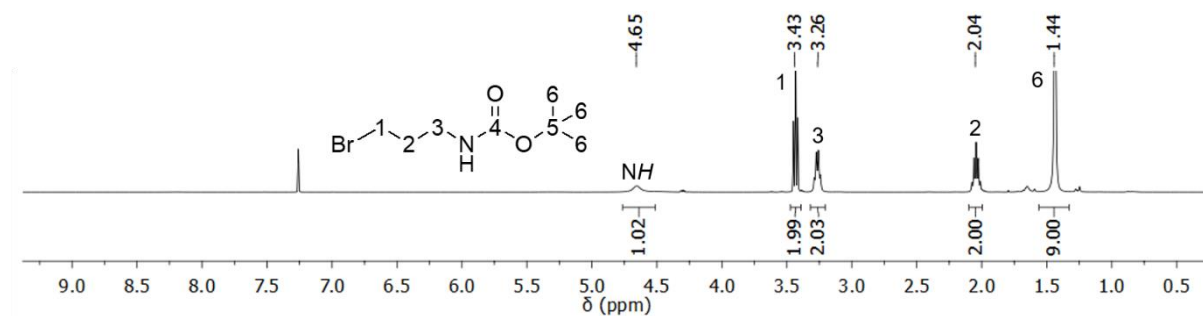
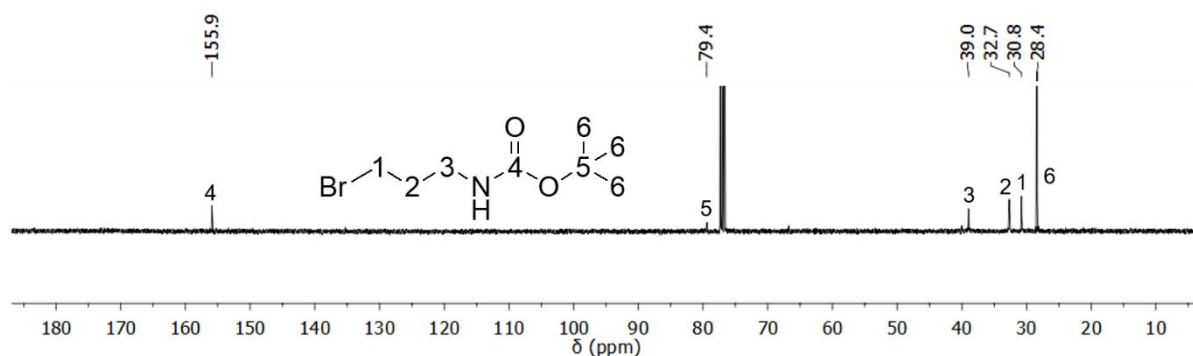


Figure A66.  $^{13}\text{C-NMR}$  spectrum of **29**.

## 7.6 Characterization of the NH<sub>2</sub>-functionalized mechanocatalyst synthesis (31-34)



**Figure A67.** <sup>1</sup>H-NMR spectrum of **31**.



**Figure A68.** <sup>13</sup>C-NMR spectrum of **31**.

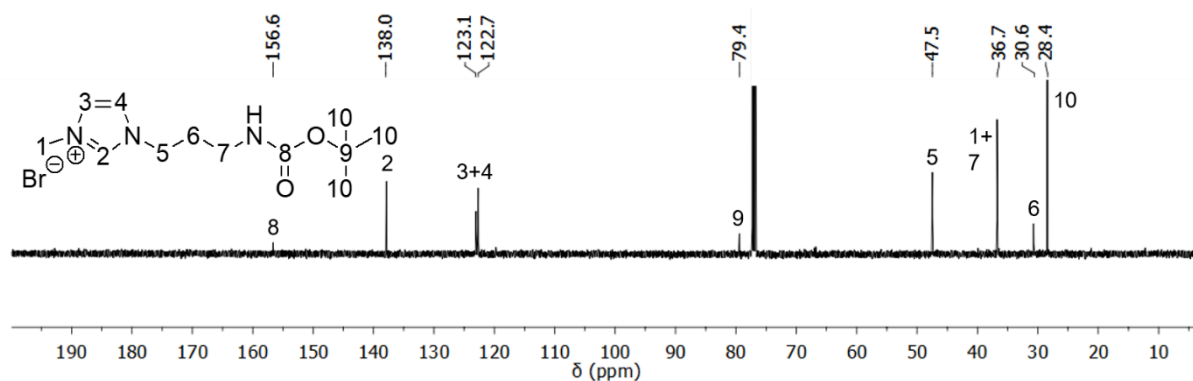


**Figure A69.** <sup>13</sup>C-NMR spectrum of **32**.

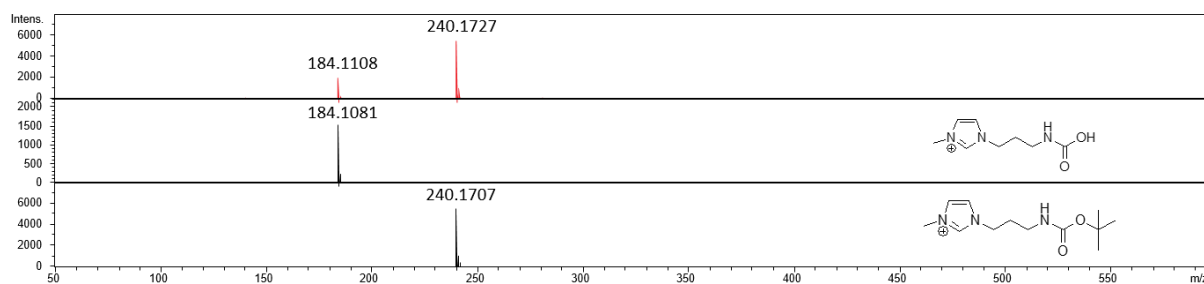


**Figure A70.** ESI-TOF-MS of **32**.

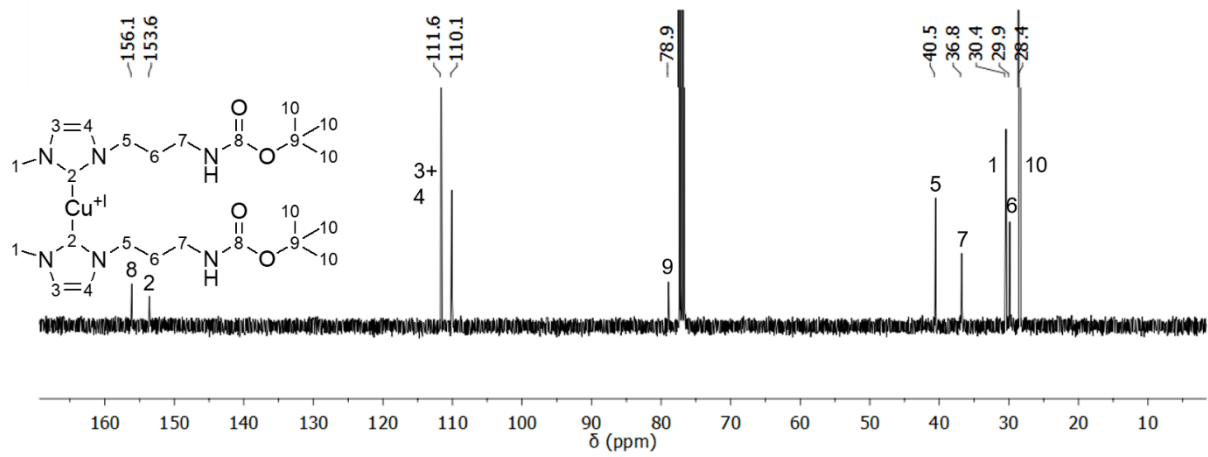


Figure A71.  $^{13}\text{C-NMR}$  spectrum of 33.

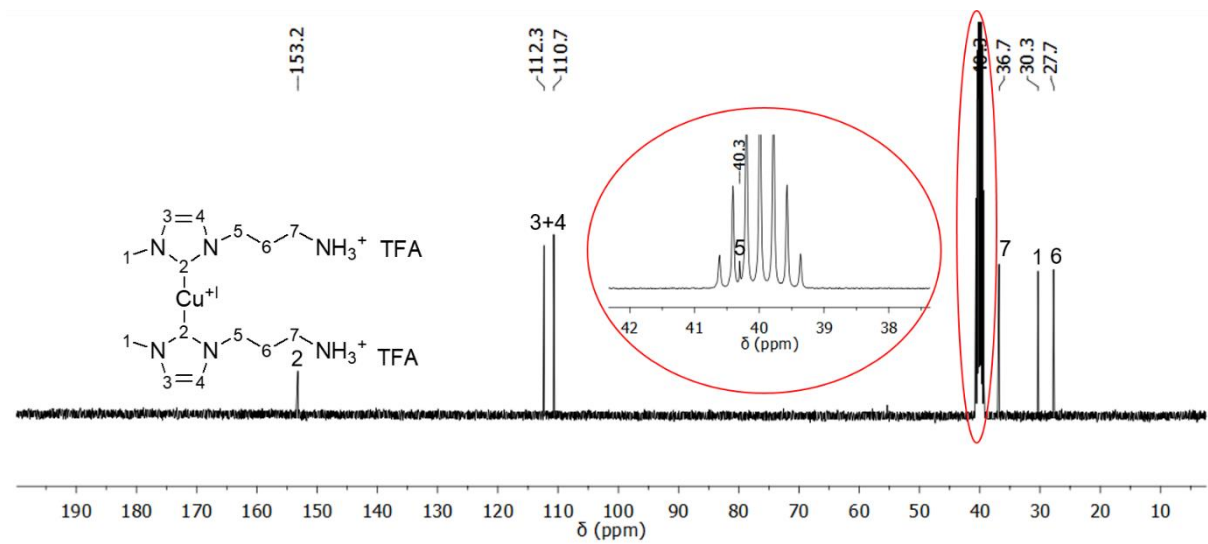


Figure A72.  $^{13}\text{C-NMR}$  spectrum of 34.

## 7.7 Characterization of the chain-extended mechanocatalyst (35a)

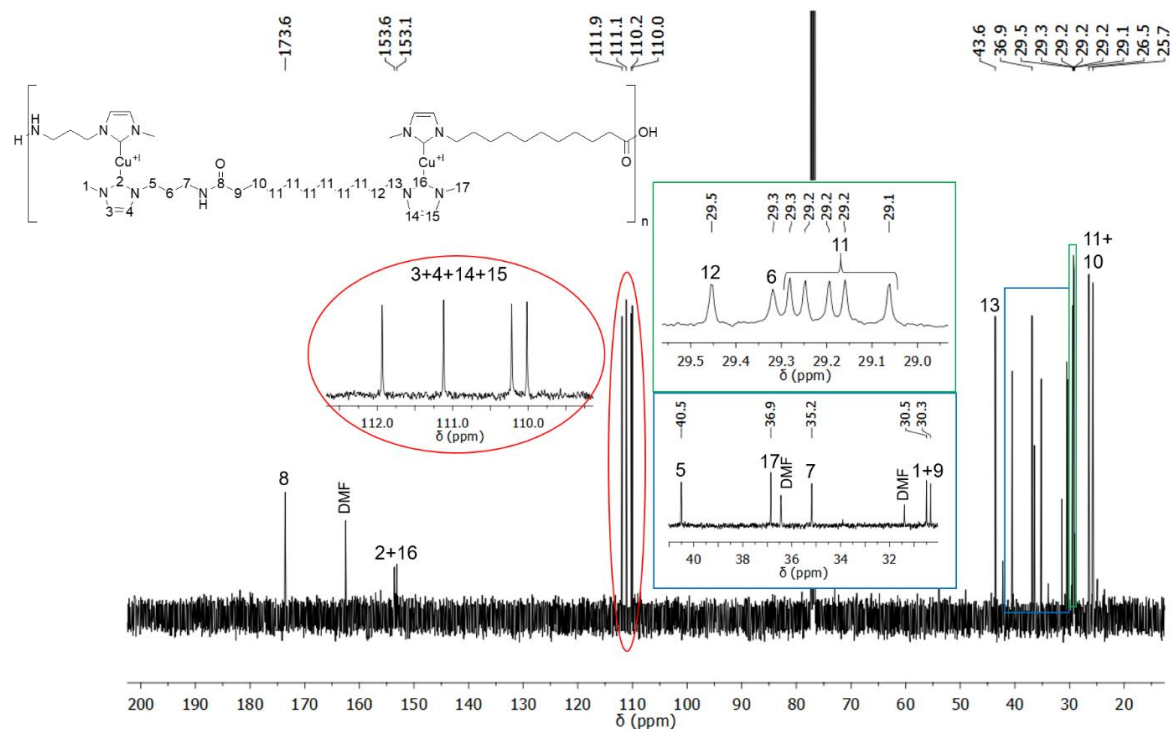


Figure A73.  $^{13}\text{C}$ -NMR spectrum of **35a**.

## 7.8 Characterization of the supramolecular mechanocatalyst synthesis (36-42)

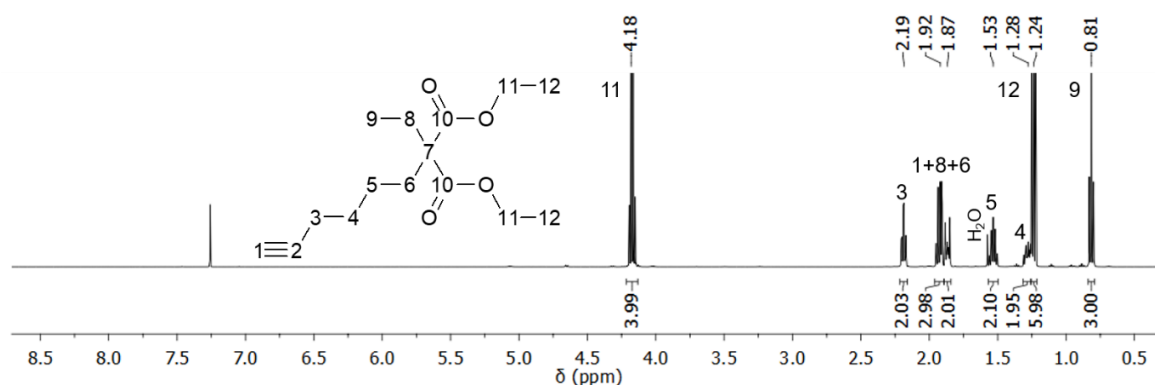


Figure A74.  $^1\text{H}$ -NMR spectrum of **36**.

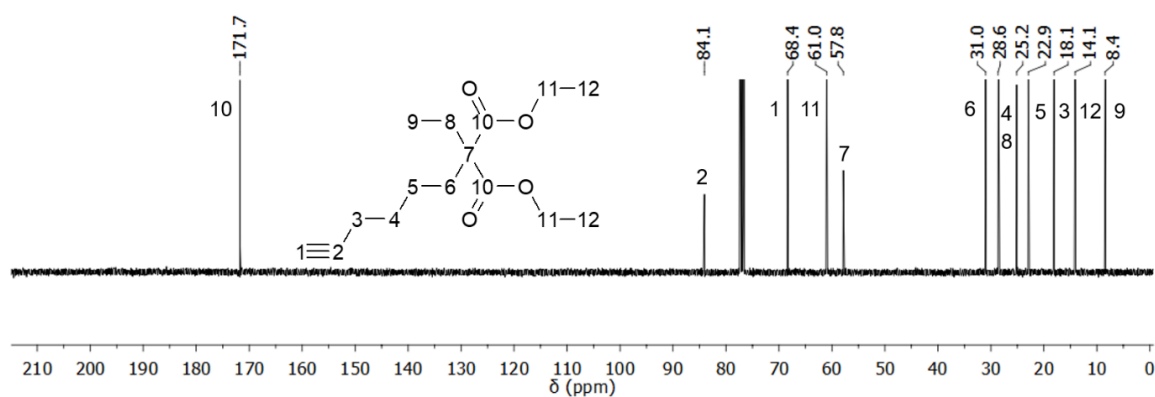
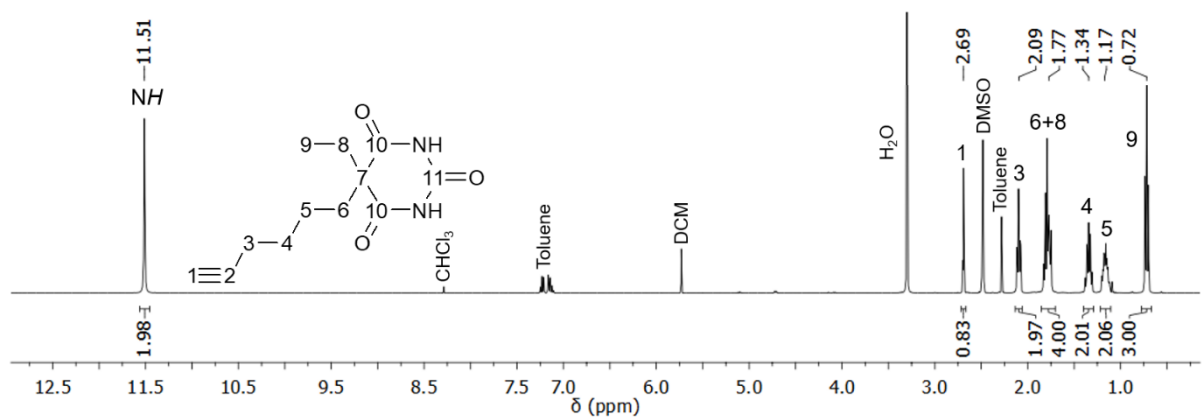
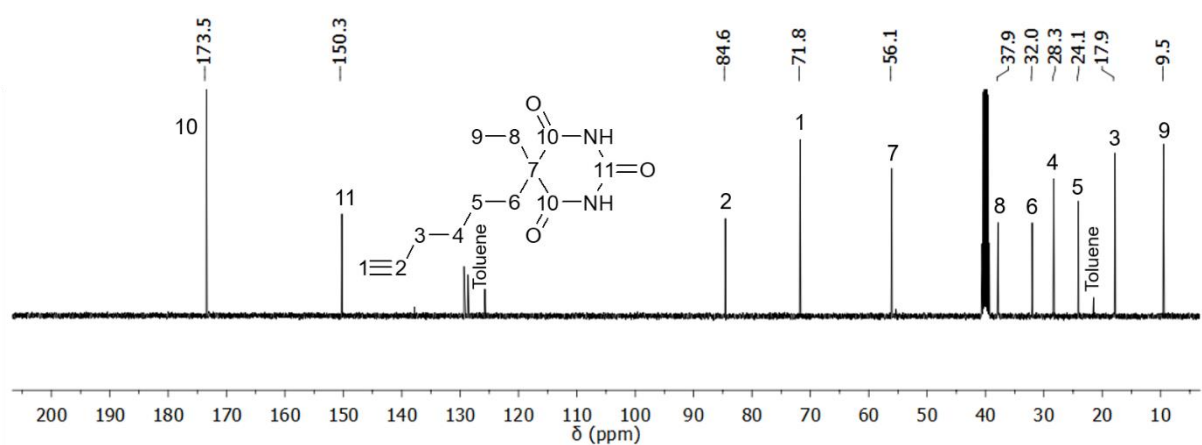


Figure A75.  $^{13}\text{C}$ -NMR spectrum of **36**.



**Figure A76.**  $^1\text{H-NMR}$  spectrum of **37**.



**Figure A77.**  $^{13}\text{C-NMR}$  spectrum of **37**.

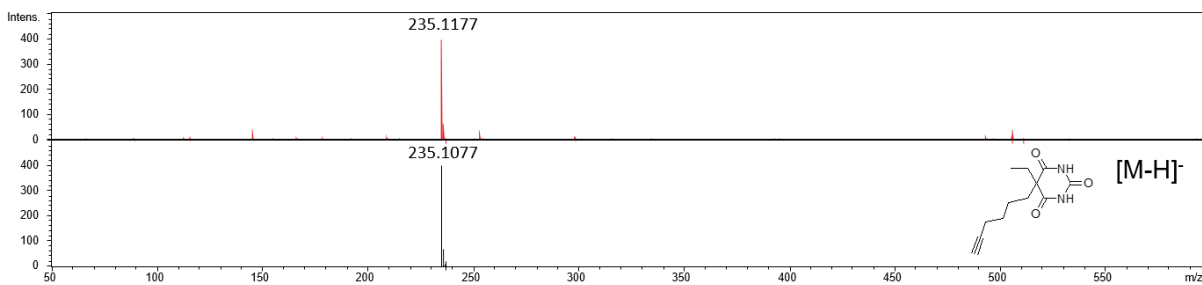


**Figure A78.** ESI-TOF-MS of **37**.

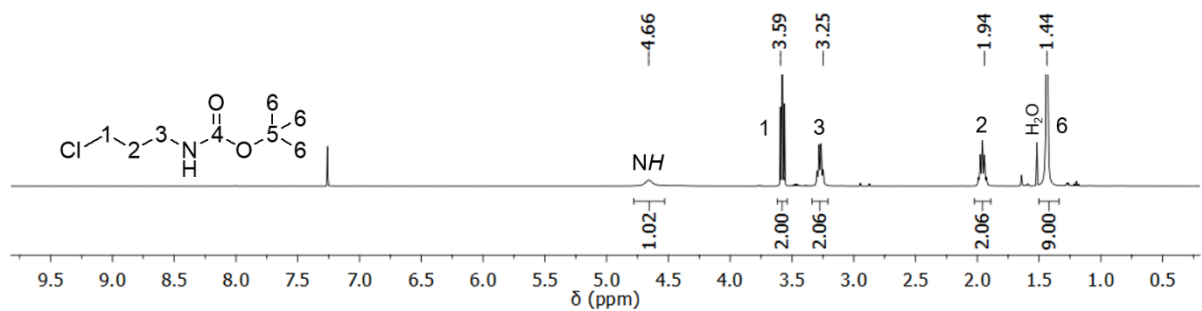


**Figure A79.**  $^1\text{H-NMR}$  spectrum of **38**.

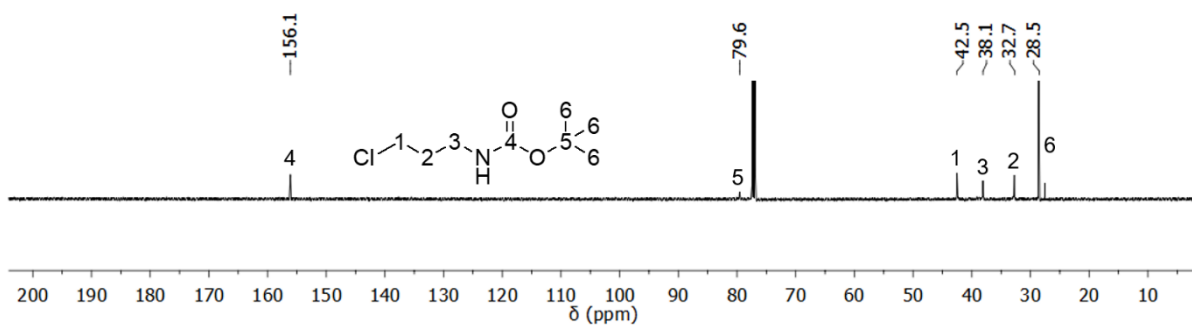


**Figure A80.**  $^{13}\text{C}$ -NMR spectrum of **38**.

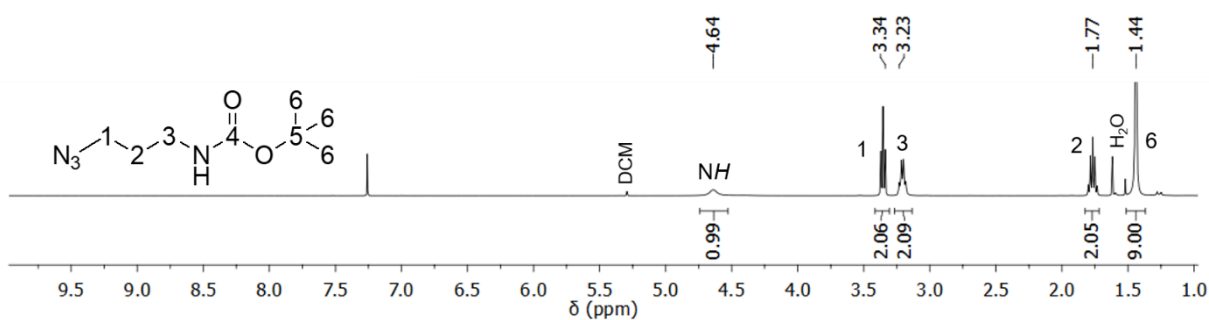


**Figure A81.**  $^1\text{H}$ -NMR spectrum of **39**.

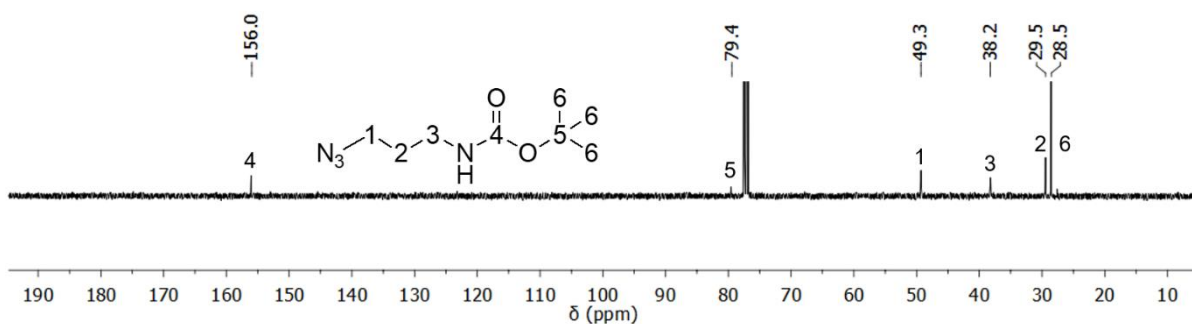


**Figure A82.**  $^{13}\text{C}$ -NMR spectrum of **39**.

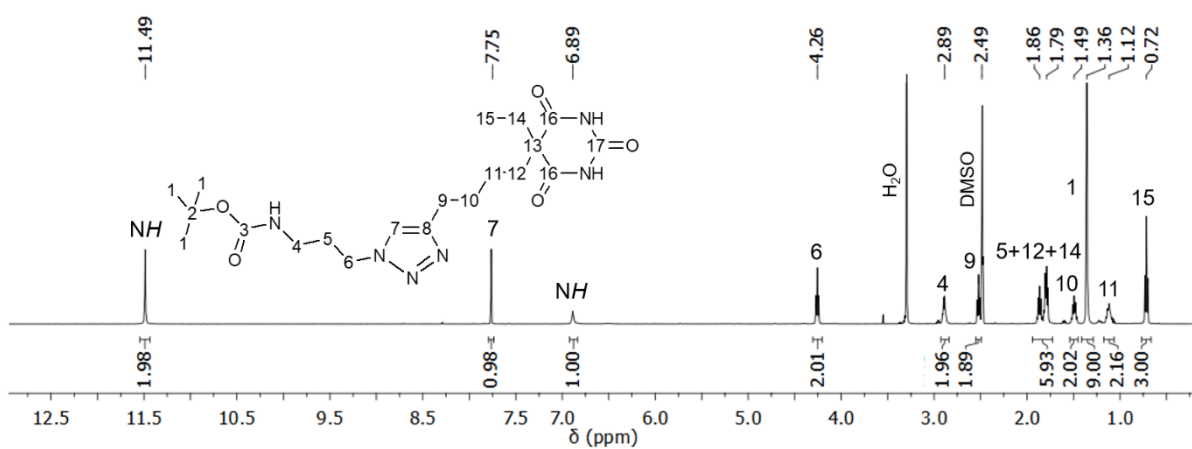


**Figure A83.**  $^1\text{H}$ -NMR spectrum of **40**.

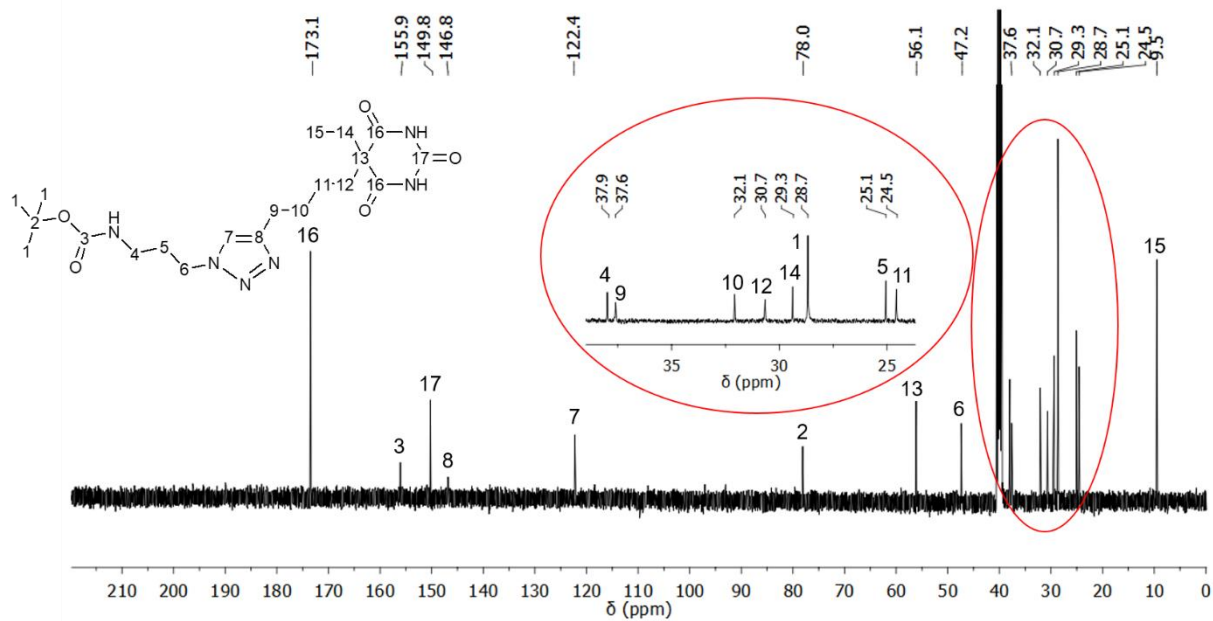


Figure A84. <sup>13</sup>C-NMR spectrum of **40**.

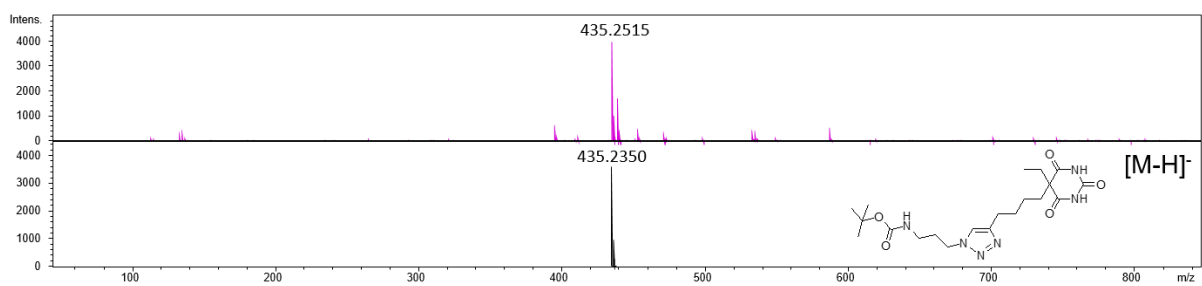


Figure A85. ESI-TOF-MS of **40**.

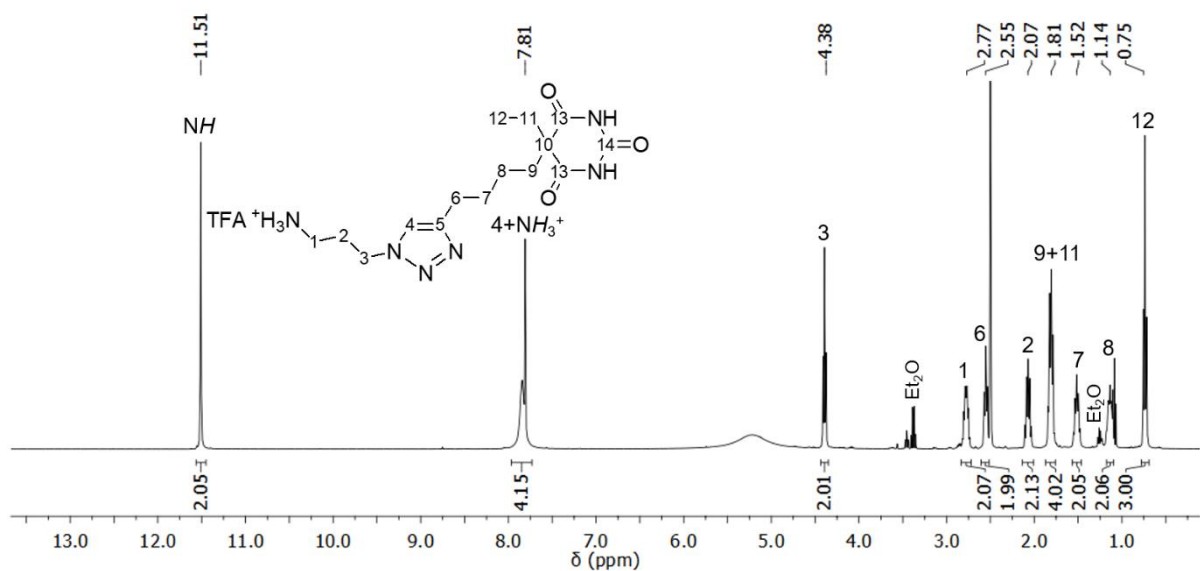
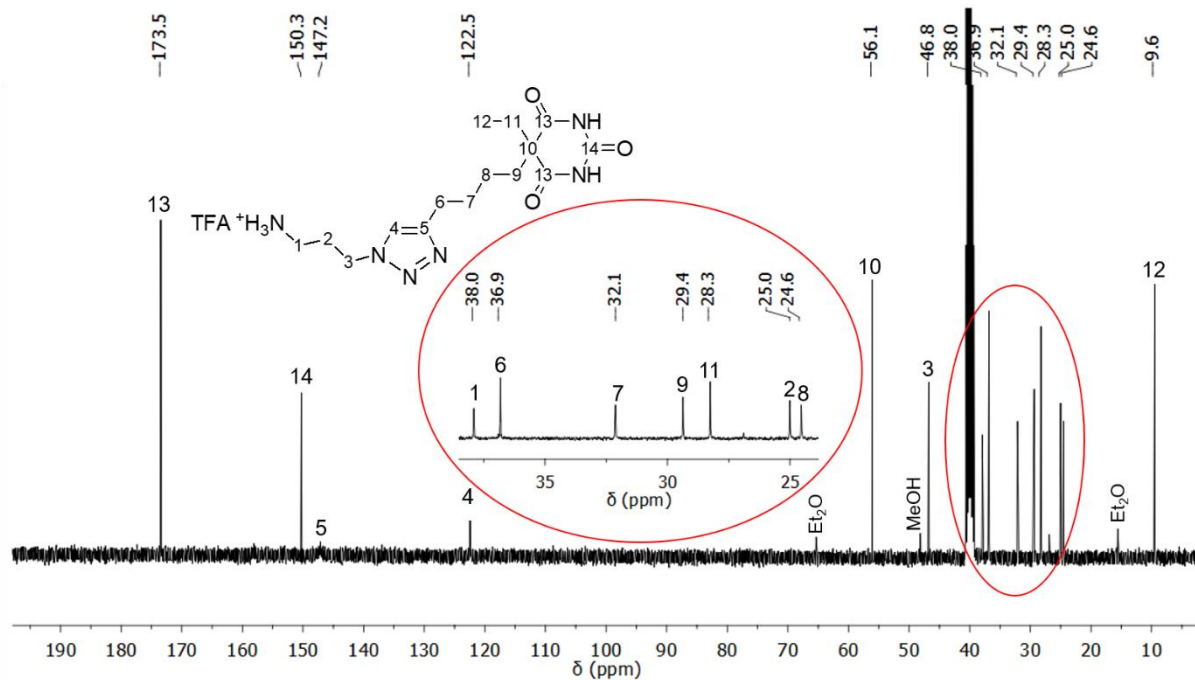
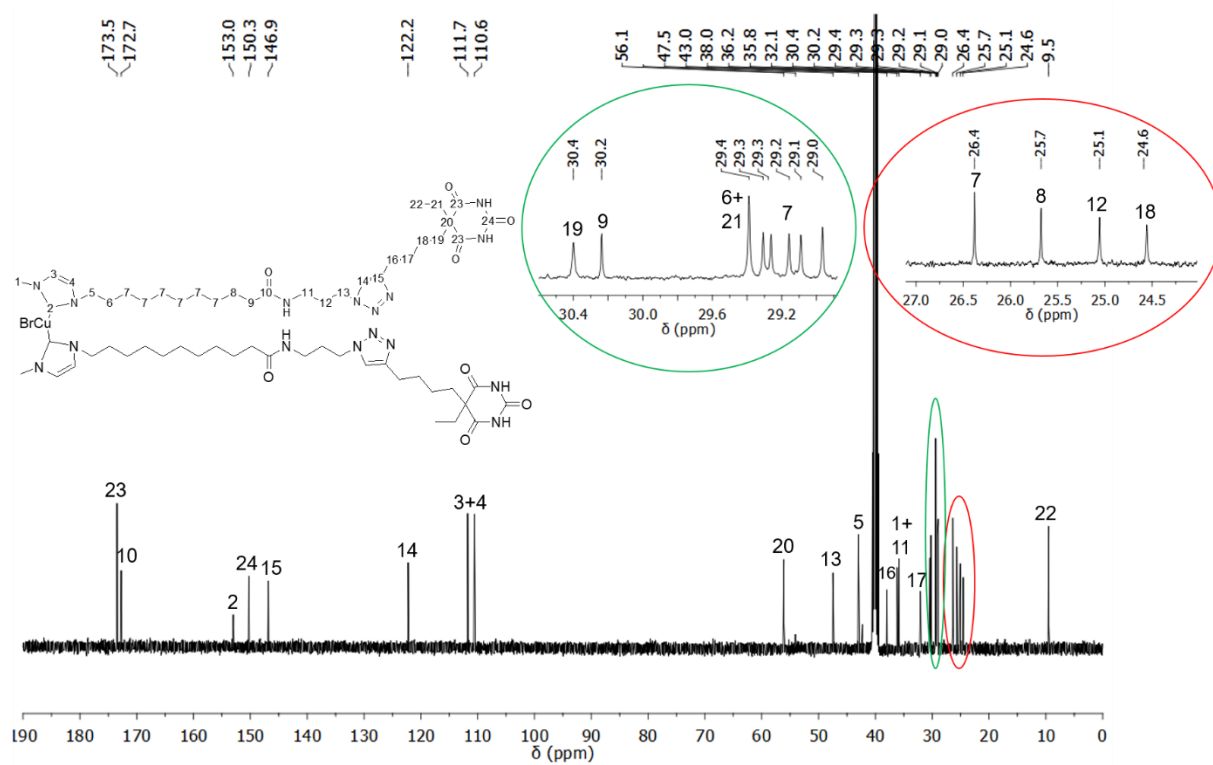


Figure A86. <sup>1</sup>H-NMR spectrum of **41**.



**Figure A87.**  $^{13}\text{C}$ -NMR spectrum of **41**.



**Figure A88.**  $^{13}\text{C}$ -NMR spectrum of **42**.

## 7.9 Characterization of the fluorogenic dye (43-44)

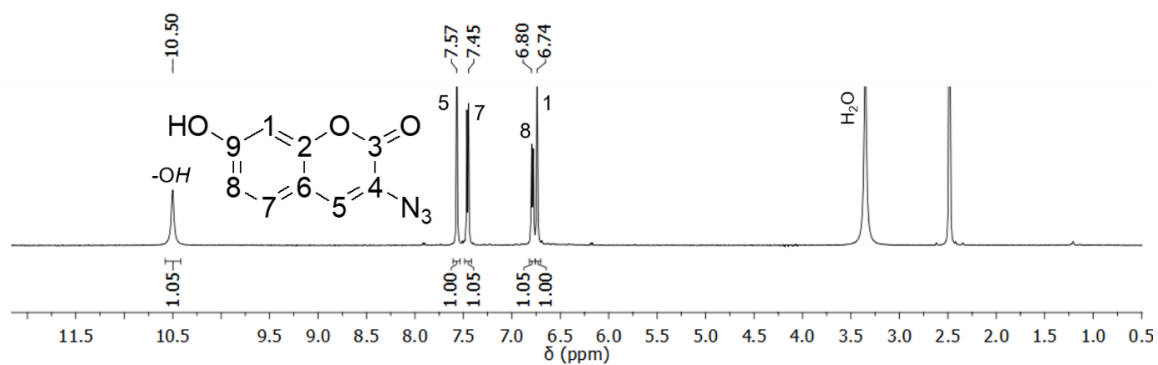


**Figure A89.**  $^1\text{H-NMR}$  spectrum of **43**.

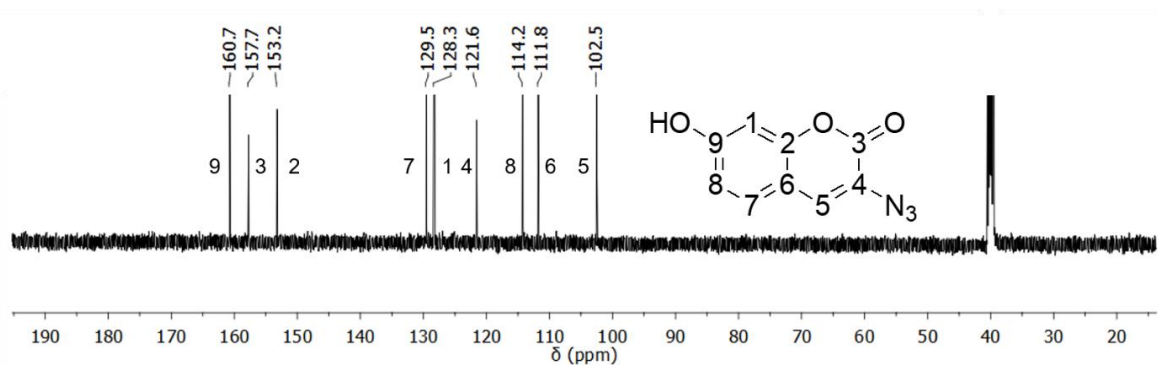


**Figure A90.**  $^{13}\text{C-NMR}$  spectrum of **43**.

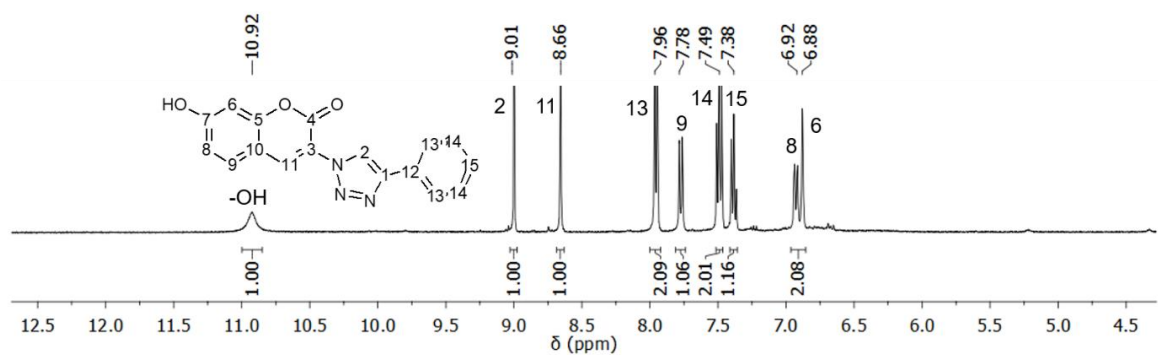


**Figure A91.**  $^1\text{H-NMR}$  spectrum of **44**.

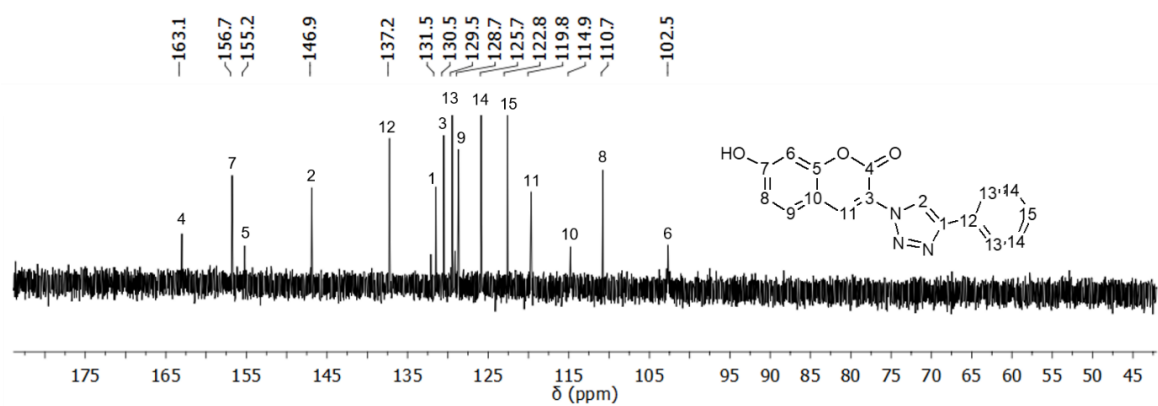


**Figure A92.**  $^{13}\text{C-NMR}$  spectrum of **44**.

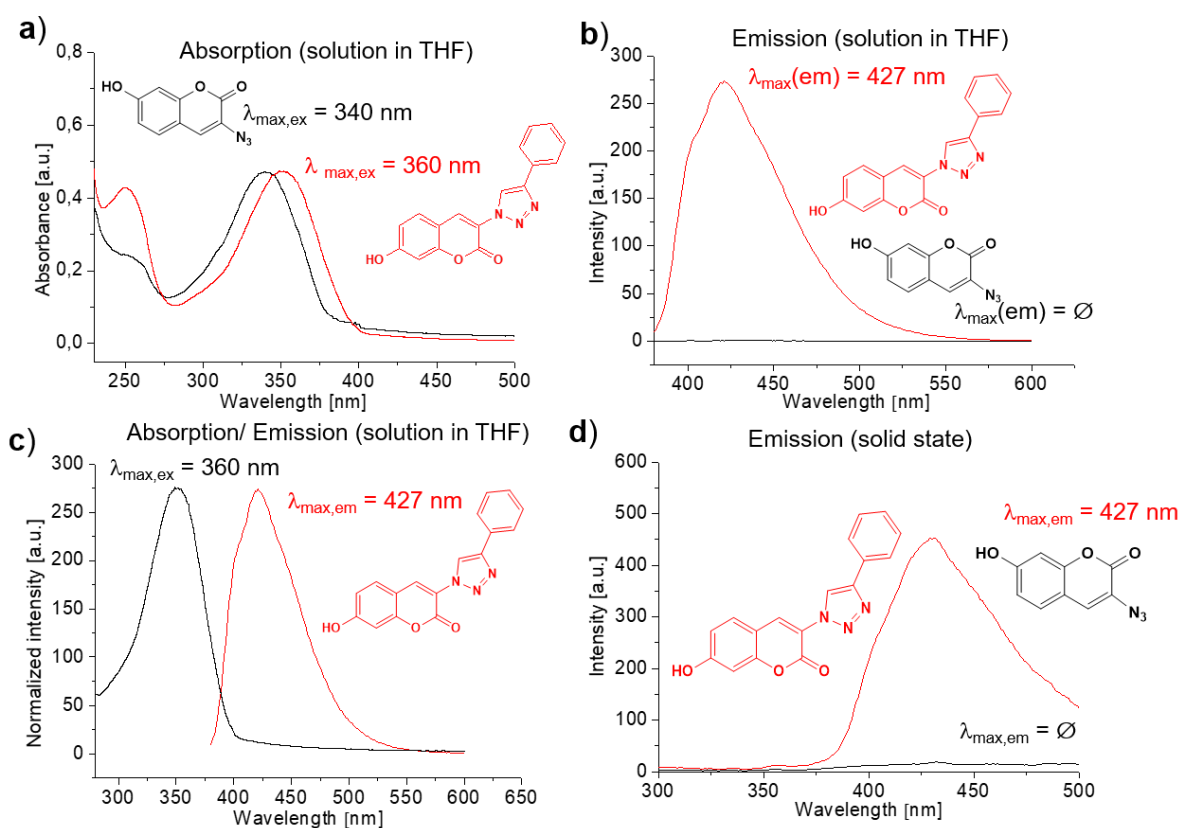


**Figure A93.** a) Measured UV-vis absorption spectra in THF for the non-fluorescent dye **43** (black) and the fluorescent dye **44** (red). b) Measured UV-vis emission spectra in THF for the non-fluorescent dye **43** (black) and the fluorescent dye **44** (red). c) Overlay of the measured UV-vis absorption (black) and emission (red) spectra of the fluorescent dye **44**. d) Measured fluorescence emission spectra for the non-fluorescent dye **43** (black) and the fluorescent dye **44** (red) in the solid state.

### 7.10 Characterization of the PEG modification (46-48)

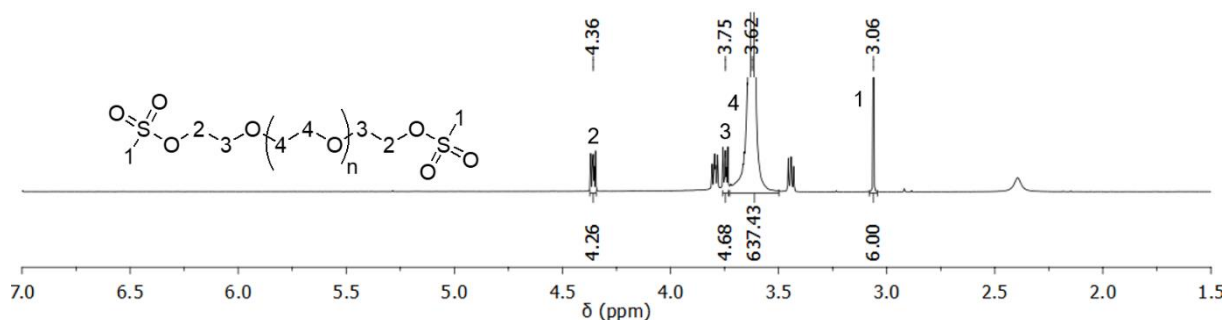


**Figure A94.**  $^1\text{H-NMR}$  spectrum of **46**.





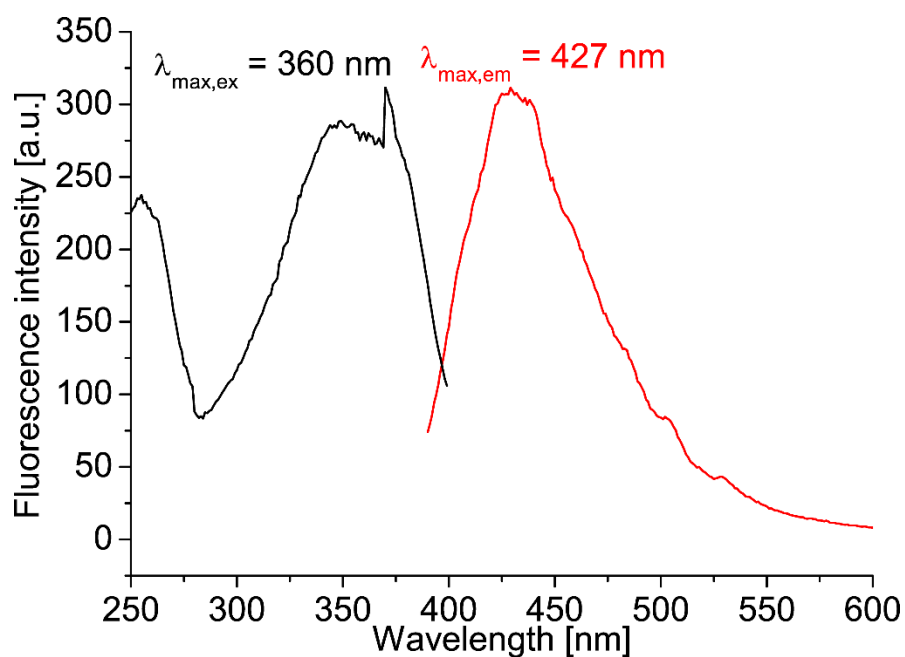


**Figure A100.** Measuring of the excitation and emission wavelength of **44** in the solid state. Incorporation of the fluorescence dye **44** into the barbiturate modified PEG matrix **48** (instead of the PTHF matrix **45**) did not affect the excitation ( $\lambda_{\text{max,ex}} = 360 \text{ nm}$ ) and emission maxima ( $\lambda_{\text{max,em}} = 427 \text{ nm}$ ).

### 7.11 Characterization of crosslinked elastin hydrogels (**49**)

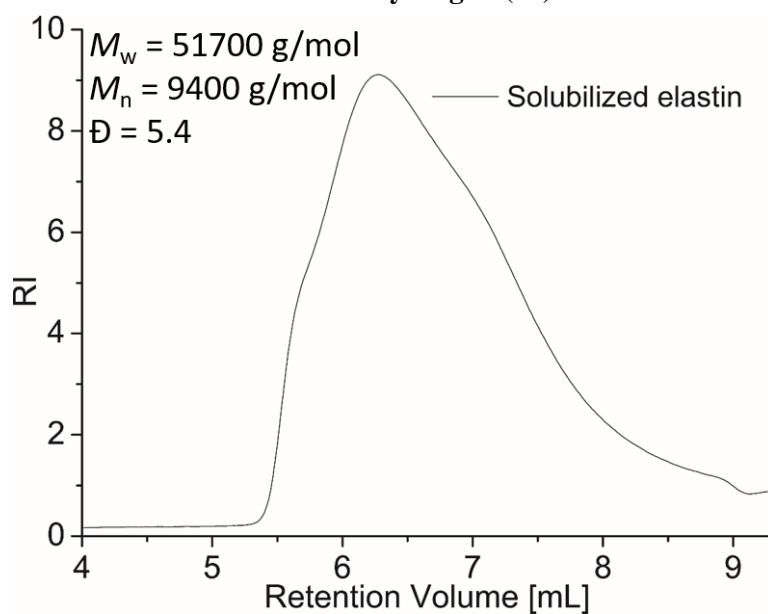


**Figure A101.** GPC traces of commercially obtained solubilized elastin.

**Table A1.** Time dependent mass loss of hydrogel **49h** that was fully swollen in water. Three pieces of the hydrogel (1 x 1 cm) were used for the experiment.

Entry	t = 0 h	t = 1 h	t = 2 h	t = 3 h	t = 4 h	t = 5 h	t = 6 h	t = 7 h	t = 8 h	t = 24 h
1	227 mg (100 %)	163 mg (71.8 %)	109 mg (48 %)	65 mg (28 %)	28 mg (12 %)	7 mg (3.1 %)	3.5 mg (1.5 %)	3.5 mg (1.5 %)	3.5 mg (1.5 %)	3.5 mg (1.5 %)
2	267 mg (100 %)	207 mg (77 %)	154 mg (57 %)	108 mg (40%)	64 mg (24 %)	33 mg (12 %)	12.6 mg (4.7 %)	4.5 mg (1.7 %)	4.2 mg (1.6 %)	4.1 mg (1.5 %)
3	274 mg (100 %)	202 mg (77 %)	140 mg (51 %)	90 mg (33 %)	46 mg (17 %)	15.2 mg (5.5 %)	3.6 mg (1.3 %)	3.5 mg (1.3 %)	3.5 mg (1.3 %)	3.5 mg (1.3 %)
<b>Average</b>										
<b>mass loss</b>	0 %	25.6 %	47.7 %	66.1 %	82.3 %	93.0 %	97.5 %	98.5 %	98.5 %	98.5 %

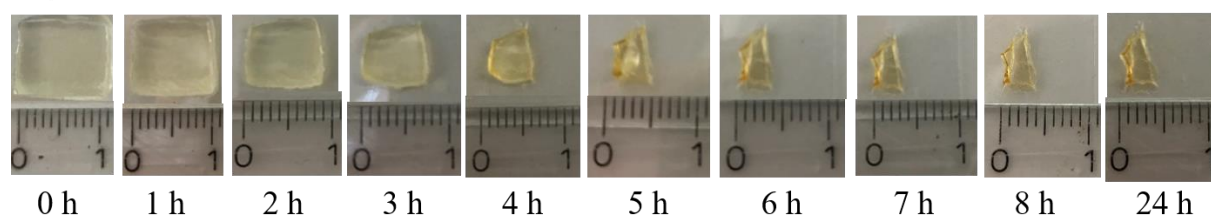
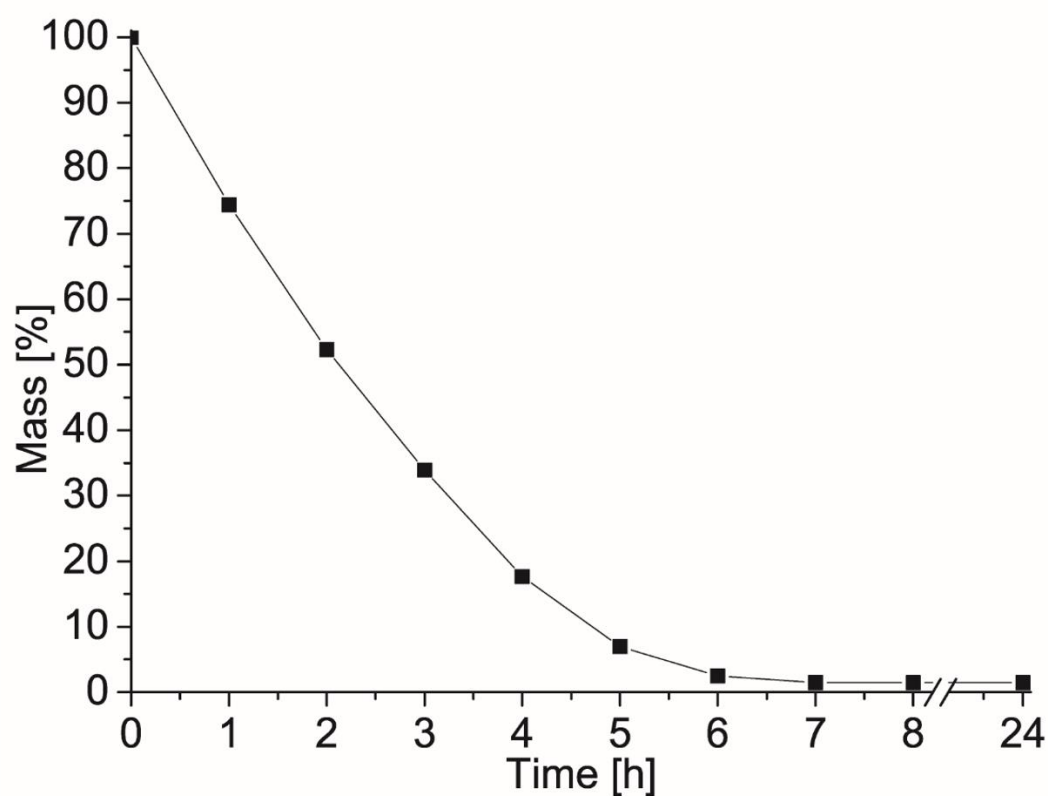
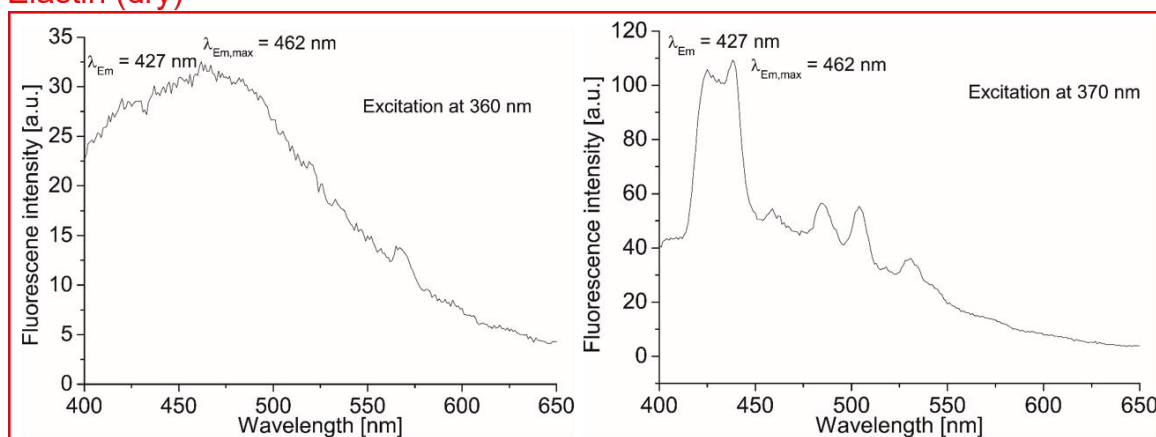
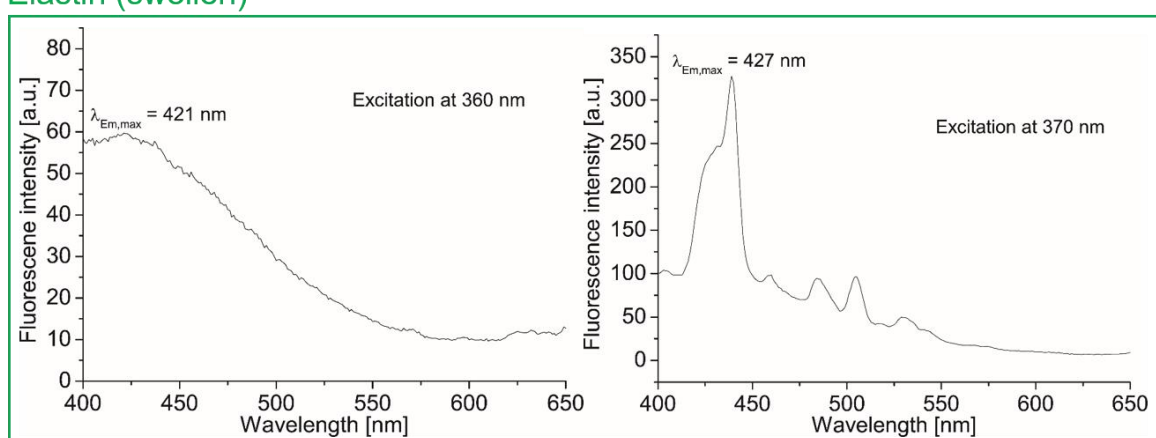


**Figure A102.** Time dependent mass loss of hydrogel **49h** that was fully swollen in water. Three pieces of the hydrogel (1 x 1 cm) were used for the experiment.

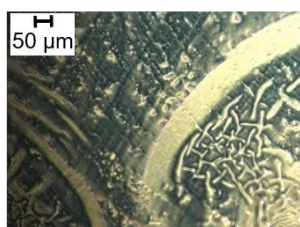
a) Elastin (dry)



b) Elastin (swollen)



c)



d)



**Figure A103.** a) Excitation spectra of dried elastin hydrogels without the precursor dye **43** or the fluorogenic dye **44** at  $\lambda_{Ex} = 360$  nm (left) and  $\lambda_{Ex} = 370$  nm. b) Excitation spectra of swollen elastin hydrogels without the precursor dye **43** or the fluorogenic dye **44** at  $\lambda_{Ex} = 360$  nm (left) and  $\lambda_{Ex} = 370$  nm. c) Optical fluorescence microscopy image of a swollen elastine hydrogel without the precursor dye **43** or the fluorogenic dye **44** under visible light. d) Optical fluorescence microscopy image of a swollen elastine hydrogel without the precursor dye **43** or the fluorogenic dye **44** at an excitation wavelength of  $\lambda_{Ex} = 365$  nm and an emission wavelength of  $\lambda_{Em} = 420$  nm.

## 7.12 Characterization of the histidinium based mechanocatalyst synthesis (51-55)

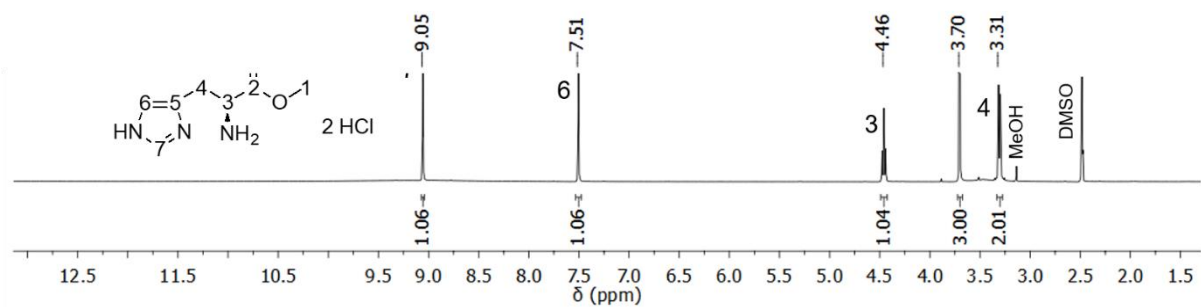


**Figure A104.**  $^1\text{H-NMR}$  spectrum of **51**.

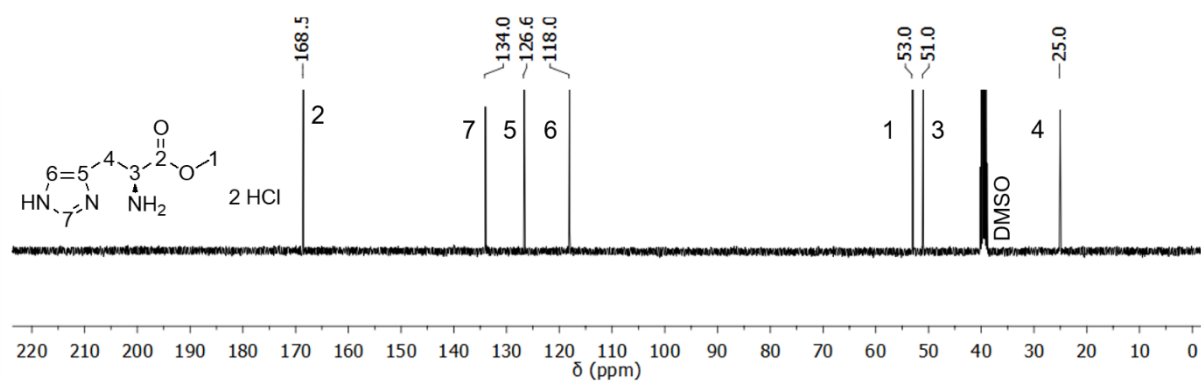


**Figure A105.**  $^{13}\text{C-NMR}$  spectrum of **51**.

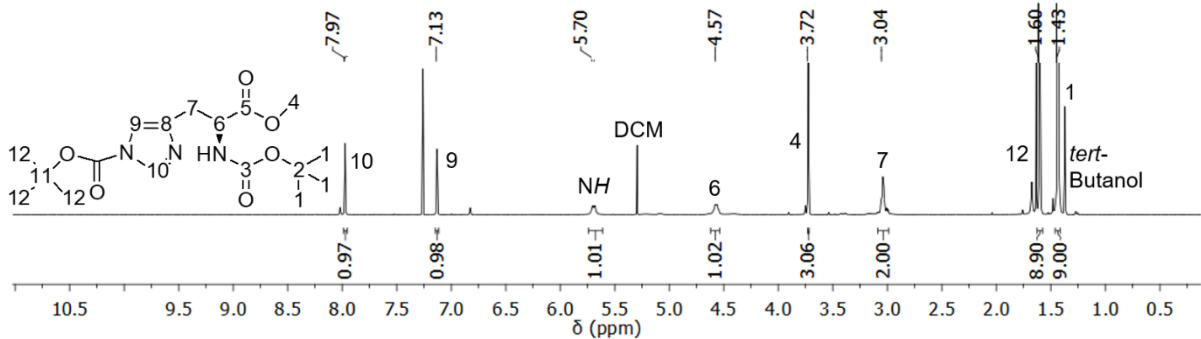


**Figure A106.**  $^1\text{H-NMR}$  spectrum of **52**.

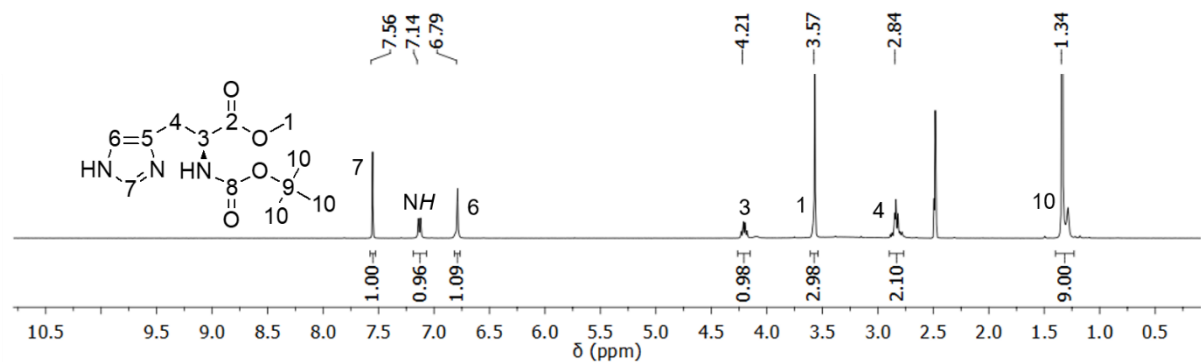


**Figure A107.**  $^1\text{H-NMR}$  spectrum of **53**.

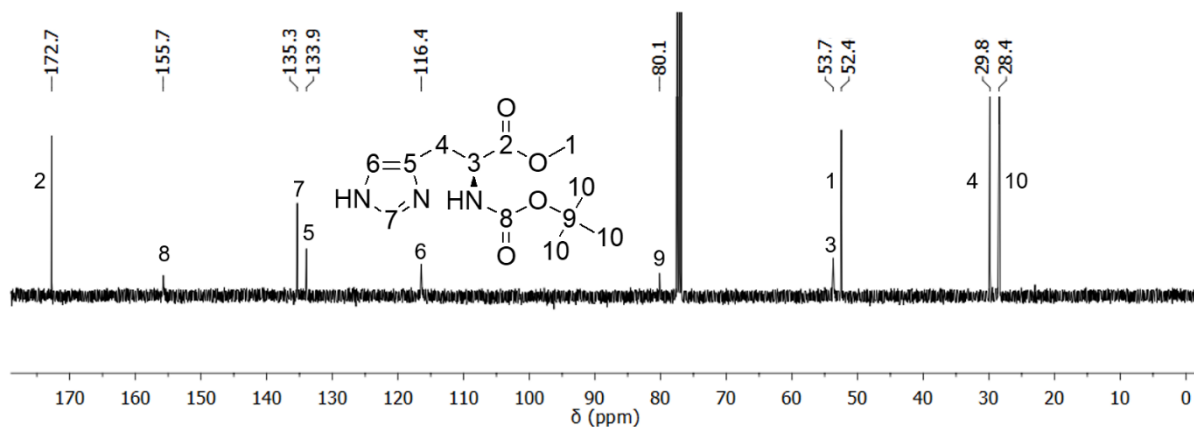


Figure A108.  $^{13}\text{C}$ -NMR spectrum of **53**.

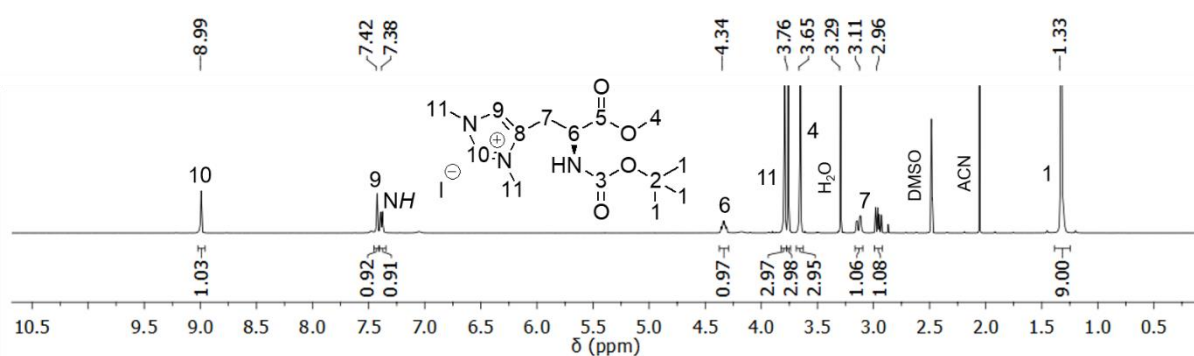


Figure A109.  $^1\text{H}$ -NMR spectrum of **54**.

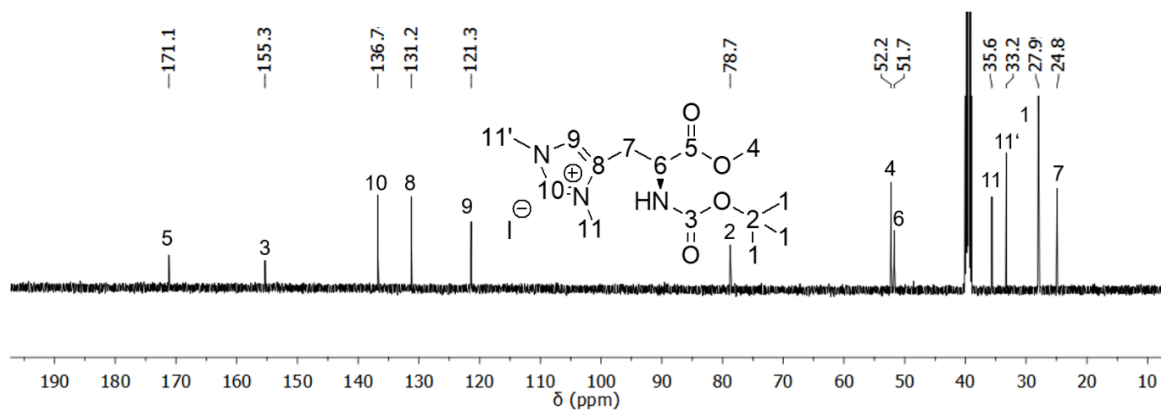


Figure A110.  $^{13}\text{C}$ -NMR spectrum of **54**.

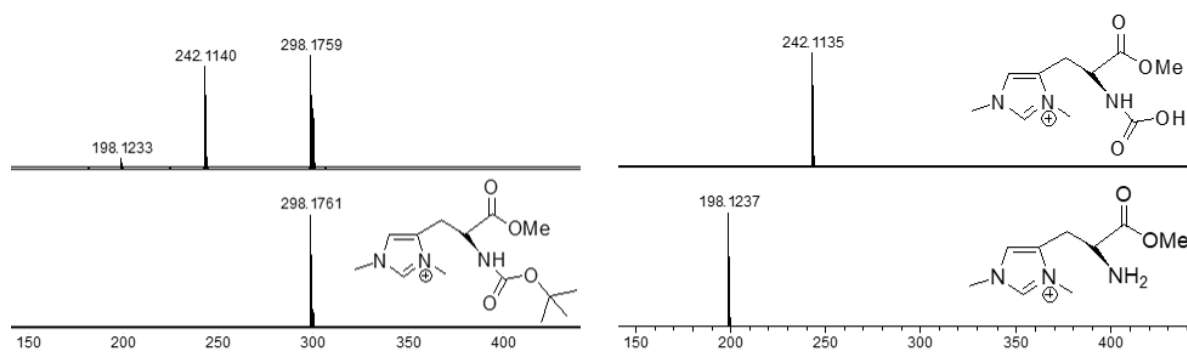
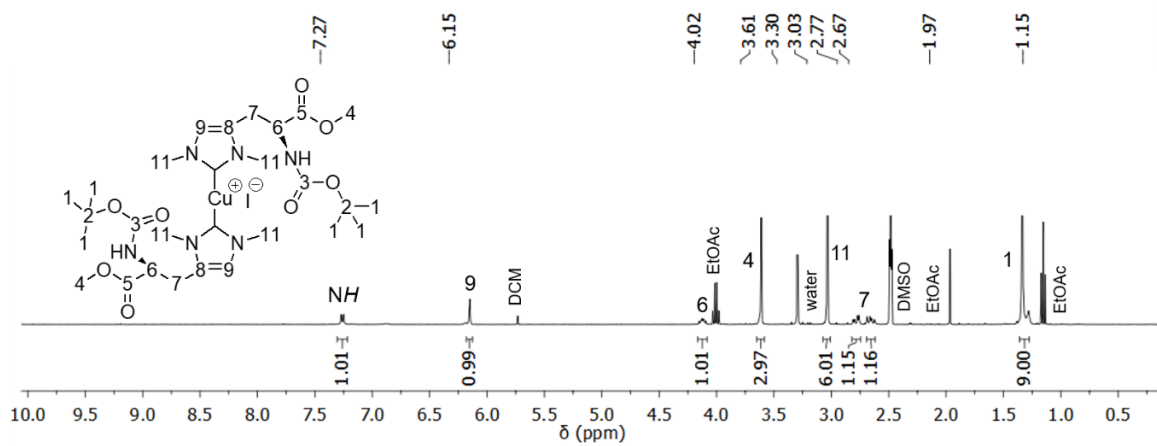
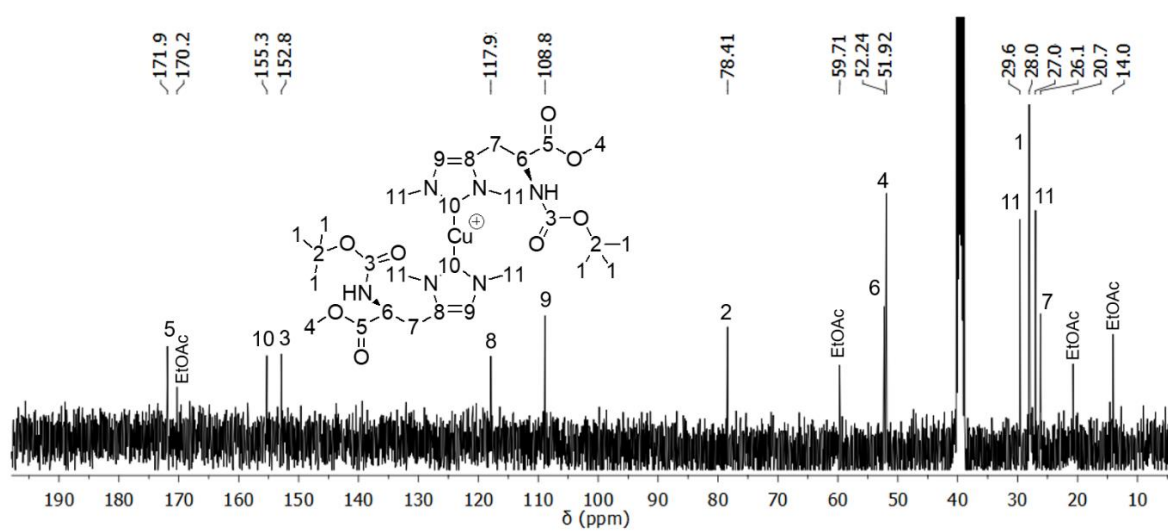


Figure A111. ESI-TOF-MS of **54**.



**Figure A112.** <sup>1</sup>H-NMR spectrum of 55.



**Figure A113.** <sup>13</sup>C-NMR spectrum of 55.

## 8 Curriculum Vitae

### Persönliche Angaben

Sebastian Funtan

Adresse: Osendorfer Straße 6  
06112 Halle (Saale)

Geburtsdatum: 07.08.1989

Geburtsort: Kassel

Familienstand: Verheiratet

### Berufliche Erfahrung

01/2016 – heute      Wissenschaftlicher Mitarbeiter an der Martin-Luther-Universität  
Halle-Wittenberg im Bereich Makromolekulare Chemie  
Promotionsstudium

### Bildungsweg

10/2013 – 11/2015      Masterstudium Chemie an der Martin-Luther-Universität Halle-Wittenberg mit  
Vertiefung im Bereich Makromolekulare Chemie  
10/2009 – 08/2013      Bachelorstudium an der Martin-Luther-Universität Halle-Wittenberg  
08/2006 – 06/2009      Jacob-Grimm-Schule (Oberstufengymnasium), Kassel  
08/2000 – 07/2006      Heinrich-Schütz-Schule (Gesamtschule, Gymnasialzweig), Kassel

### Sprachkenntnisse

Deutsch                      Muttersprache  
Englisch                      fließend in Wort und Schrift  
Spanisch                      Grundkenntnisse

## Publikationsliste

Funtan, S.; Funtan, A.; Paschke, R.; Binder, W. H., Biomimetic Elastin-Like Polypeptides as Materials for the Activation of Mechanophoric Catalysts, *Organic Materials* **2020**, 2 (2), 116.

Funtan, S.; Michael, P.; Binder, W. H., Synthesis and Mechanochemical Activity of Peptide-Based Cu(I) Bis(*N*-Heterocyclic Carbene) Complexes, *Biomimetics* **2019**, 4 (1), 24.

Funtan, S.; Evgrafova, Z.; Adler, J.; Huster, D.; Binder, W. H., Amyloid Beta Aggregation in the Presence of Temperature-Sensitive Polymers, *Polymers* **2016**, 8, 178.

## Konferenzbeiträge

Funtan, S.; Binder, W. H., Mechanocatalytically active polymer networks for force-induced copper(I)-catalyzed azide/alkyne “click” reactions, International Conference on Self-Healing Materials, 25. – 28. Juni 2017, Friedrichshafen, Deutschland, Poster.

Funtan, S.; Binder, W. H., Mechanocatalytically active polymer networks for force-induced copper(I)-catalyzed azide/alkyne “click” reactions, APME (Advanced Polymers *via* Macromolecular Engineering), 21. – 25. Mai 2017, Ghent, Belgien, Poster.

Funtan, S.; Biewend, M.; Kaiser, J.; Binder, W. H., Mechanocatalytically active networks for force-induced copper(I)-catalyzed azide/alkyne “click” reactions, Biennial Meeting of the GDCh-Division Macromolecular Chemistry “Polymers: from Structure to Function”, 11. – 13. September 2016, Halle (Saale), Deutschland, Poster.

Halle (Saale), den

---

Sebastian Funtan

## **9 Eigenständigkeitserklärung**

Ich erkläre hiermit an Eides statt, dass ich die vorliegende Arbeit selbstständig und ohne Benutzung anderer als der in der Arbeit angegebenen Hilfsmittel angefertigt habe. Sämtliche Inhalte, die aus anderen Quellen direkt oder dem Sinn nach entnommen worden sind, wurden als solche kenntlich gemacht.

Außerdem erkläre ich, dass die vorliegende Dissertation an keiner anderen wissenschaftlichen Einrichtung zur Erlangung eines akademischen Grades eingereicht wurde.

Halle (Saale), den

---

Sebastian Funtan